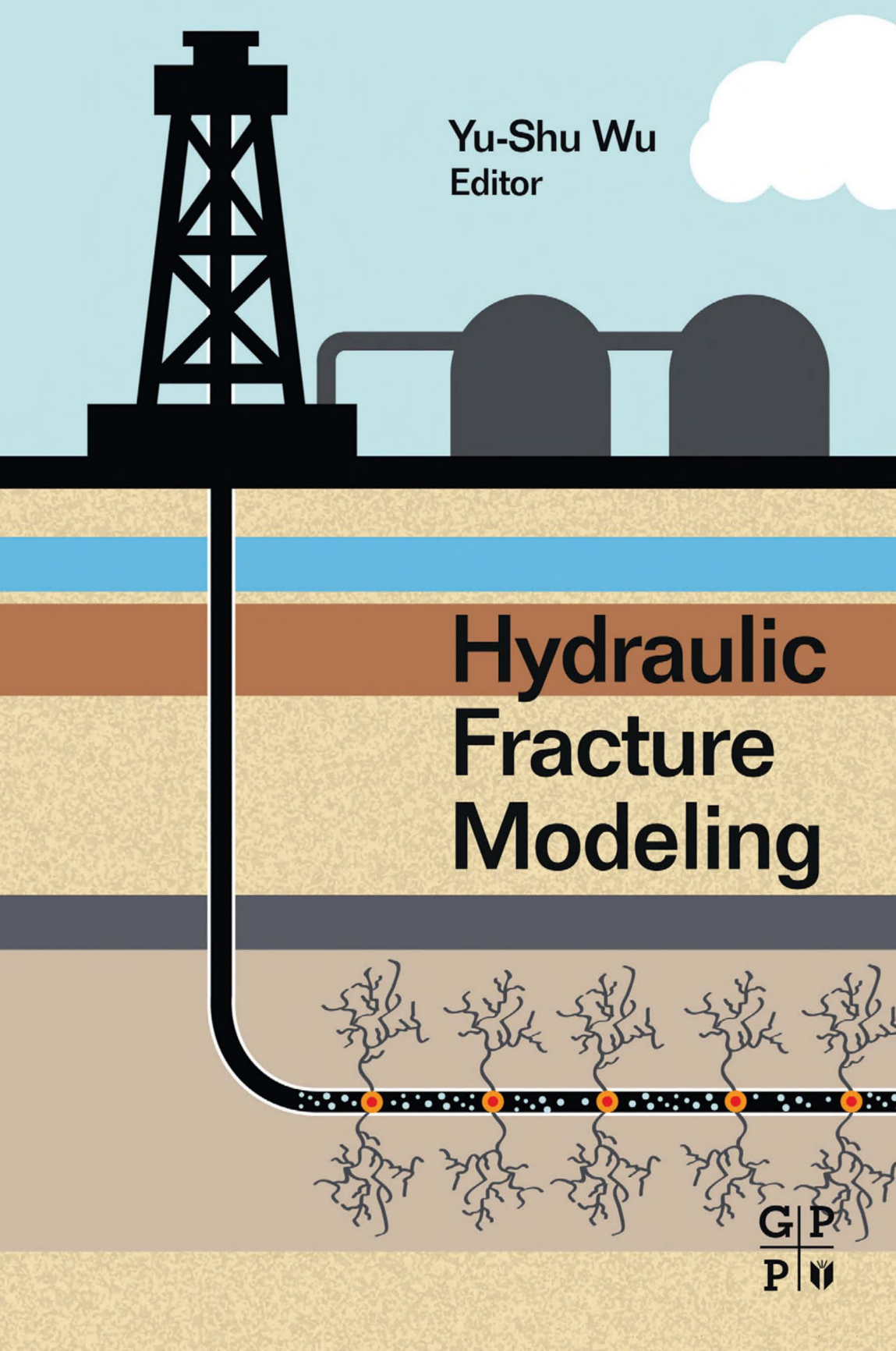
Yu-Shu Wu
Editor
Hydraulic
Fracture
Modeling
G P
P

Hydraulic Fracture Modeling

Editor

Yu-Shu Wu
Colorado School of Mines, Golden, CO, United States

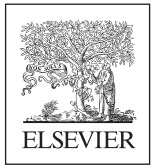

Gulf Professional Publishing
An imprint of Elsevier

Gulf Professional Publishing is an imprint of Elsevier
50 Hampshire Street, 5th Floor, Cambridge, MA 02139, United States
The Boulevard, Langford Lane, Kidlington, Oxford, OX5 1GB, United Kingdom

Notices
Knowledge and best practice in this field are constantly changing. As new research and experience broaden our understanding, changes in research methods, professional practices, or medical treatment may become necessary.

Practitioners and researchers must always rely on their own experience and knowledge in evaluating and using any information, methods, compounds, or experiments described herein. In using such information or methods they should be mindful of their own safety and the safety of others, including parties for whom they have a professional responsibility.

To the fullest extent of the law, neither the Publisher nor the authors, contributors, or editors, assume any liability for any injury and/or damage to persons or property as a matter of products liability, negligence or otherwise, or from any use or operation of any methods, products, instructions, or ideas contained in the material herein.

Library of Congress Cataloging-in-Publication Data
A catalog record for this book is available from the Library of Congress

British Library Cataloguing-in-Publication Data
A catalogue record for this book is available from the British Library

ISBN: 978-0-12-812998-2

Publisher: Joe Hayton
Acquisition Editor: Katie Hammon
Editorial Project Manager: Lindsay Lawrence
Production Project Manager: Anitha Sivaraj
Designer: Greg Harris

Typeset by TNQ Books and Journals

Contents

Contributors

Hazim Abass, Colorado School of Mines, Denver, CO, United States

Binh Bui, Colorado School of Mines, Golden, CO, United States

Yuan Di, Peking University, Beijing, China

Bruno Figueiredo, Uppsala University, Uppsala, Sweden

Jorge L. Garzon, ExxonMobil Upstream Research Company, Spring, TX, United States

Dina Hegazy, Colorado School of Mines, Golden, CO, United States

Mengsu Hu, Lawrence Berkeley National Laboratory, Berkeley, CA, United States

Hai Huang, Idaho National Laboratory, Idaho Falls, ID, United States

Zhao-Qin Huang, China University of Petroleum (East China), Qingdao, China

Jessica Iriarte, Colorado School of Mines, Golden, CO, United States

Daisuke Katsuki, Colorado School of Mines, Golden, CO, United States

Jihoon Kim, Texas A&M University, College Station, TX, United States

Timothy J. Kneafsey, Lawrence Berkeley National Laboratory, Berkeley, CA, United States

Christopher Lamei, Colorado School of Mines, Denver, CO, United States

Paul Meakin, Temple University, Philadelphia, PA, United States

Jennifer L. Miskimins, Colorado School of Mines, Golden, CO, United States

Adriana Paluszny, Imperial College, London, United Kingdom

Jonny Rutqvist, Lawrence Berkeley National Laboratory, Berkeley, CA, United States

Saeed Salimzadeh, Technical University of Denmark, Lyngby, Denmark

Kevin H. Searles, ExxonMobil Upstream Research Company, Spring, TX, United States

Baotang Shen, Shandong University of Science and Technology, Qingdao, China; CSIRO Energy, Queensland Centre for Advanced Technologies, Brisbane, QLD Australia

Theerapat Suppachoknirun, Colorado School of Mines, Golden, CO, United States

Huiying Tang, Southwest Petroleum University, Chengdu, China

Chin-Fu Tsang, Lawrence Berkeley National Laboratory, Berkeley, CA, United States; Uppsala University, Uppsala, Sweden

Azra N. Tutuncu, Colorado School of Mines, Golden, CO, United States

Evan Schankee Um, Lawrence Berkeley National Laboratory, Berkeley, CA, United States

Lei Wang, Colorado School of Mines, Golden, CO, United States

Philip H. Winterfeld, Colorado School of Mines, Golden, CO, United States

Yu-Shu Wu, Colorado School of Mines, Golden, CO, United States

Xia Yan, China University of Petroleum (East China), Qingdao, China

Bowen Yao, Colorado School of Mines, Golden, CO, United States

Jun Yao, China University of Petroleum (East China), Qingdao, China

Qing-Dong Zeng, China University of Petroleum (East China), Qingdao, China

Jing Zhou, Idaho National Laboratory, Idaho Falls, ID, United States

Matias G. Zielonka, ExxonMobil Upstream Research Company, Spring, TX, United States

Robert W. Zimmerman, Imperial College, London, United Kingdom

Preface

This book presents the quantitative approaches developed to model hydraulic fracturing processes and summarizes the fundamentals of rock or hydraulic fracturing technology. Hydraulic fracturing has been the most effective and applied well-stimulation technique, in particular, in development of oil and gas from conventional and unconventional petroleum reservoirs. Even with wide application and decades of success, there is generally a lack of scientific understanding and qualitative investigations into rock hydraulic fracturing processes. As a result, few publications or physics-based knowledge bases exist in the literature regarding such an important topic. Therefore, there is an urgent need for improving and enhancing quantitative approaches to hydraulic fracture modeling for use in several applications, such as petroleum engineering, CO_2 geosequestration, and geothermal energy development.

The book is intended to complement the existing literature on hydraulic fracture modeling by presenting the state-of-the-art and current advances of hydraulic fracturing technology. The chapters of this book are contributed by a team of experts, consisting of professors, researchers, scientists, and engineers working on the forefront of rock and hydraulic fracturing from universities, US national laboratories, and the petroleum industry around the world. The book covers the updated theory and knowledge on rock fracturing modeling, including methods based on rigorous rock mechanics with finite-element and finite difference approaches, as well as traditional techniques using semianalytical solution methods. In addition, we include several recently developed methodologies and new frontiers, such as the extended or discrete finite-element method, displacement discontinuity approach, and thermal and cryogenic fracturing modeling. For highly sophisticated modeling tools, such as hydraulic fracture simulators, model development cannot be considered to be complete until the model is verified and validated for its correctness, accuracy, and applicability. Model verification and validation has been a critical component of model development and application, and we present examples of laboratory and field studies for validation of hydraulic fracture models.

This book focuses on fundamentals, theories, and effective quantitative approaches for rock hydraulic fracturing mechanics, as well as laboratory and field studies of hydraulic fracturing. The book covers various approaches and methodologies of hydraulic fracture modeling from fundamental theories and computational schemes to model validation and application. In addition, several

laboratory and field studies are also presented for model comparison and validation investigations. In an effort to include the new development in several closely related fields, this book also presents numerical modeling approaches for rock fracturing caused by CO_2 injection and thermal and cryogenic fracturing processes.

Because there is a wide range of topics covered in the book, and for the convenience of the readers, the chapters of the book are organized and presented in a stand-alone manner, i.e., chapters could be used or referred to individually. The chapters are structured as follows: Chapter 1 presents a finite-element method for modeling mechanical deformation of porous media rock, accounting for the effects of both poroelasticity and thermoelasticity and coupling with fluid flow in both the pore volume and the fractures. Chapter 2 discusses a framework model for integrated flow−geomechanics−geophysics simulation of planar hydraulic fractures. The model is able to calculate the occurrence time, magnitude, and location of the seismic moment by providing solutions for geomechanics and geological failure. Chapter 3 introduces a displacement discontinuity method into multistage hydraulic fracturing simulation, capable of handling stress interactions or "stress shadow" effects on multistage hydraulic fractures. Chapter 4 shows a quasistatic discrete element method (DEM) for modeling hydraulic and thermal fracturing processes in shale and low permeability crystalline rocks. The DEM model is coupled with models for fluid flow and heat conduction for 2D and 3D simulations of hydraulic fracturing and thermal fracturing in heterogeneous rock formations. Chapter 5 introduces an extended finite-element method (XFEM) for hydraulic fracture modeling, providing the basic mathematical model of hydraulic fracture propagation and numerical methods. In this model, the rock stress field and fluid pressure field are solved by the XFEM method and classical finite-element method, respectively. Chapter 6 discusses the development and validation of a 3D finite-element formulation for modeling fluid-driven hydraulic fracture propagation in a permeable poroelastic medium and presents (1) a model constructed to replicate conditions of a laboratory-scale fluid injection experiment and (2) a model constructed to replicate conditions of a field-scale fluid injection test.

Chapter 7 demonstrates the use of a continuous approach to modeling hydromechanics and hydraulic fracturing in complex fractured rock masses. This fracture continuum modeling approach is developed and applied within the framework of the FLAC3D geomechanical code or the TOUGH-FLAC coupled multiphase flow and geomechanical simulator. Chapter 8 introduces a general 3D hydraulic fracturing model for single-well, multistage fracturing, which accounts for fluid flow and heat transfer in the wellbore. The rock mechanics of fracturing includes fracture initiation, growth, and propagation, as well as fluid flow and heat transfer in the fracture. The model is capable of simulating multiple or multistage fractures that would occur during the fracturing of a horizontal well in an unconventional reservoir, coupled with the stress shadow effect and proppant transport.

Chapter 9 summarizes the fundamentals of the fracture mechanics approach used in FRACOD, a code that predicts the explicit fracturing process in rocks using fracture mechanics principles, and recently related developments. In this chapter, several selected application cases, including hydraulic fracturing and CO_2 geosequestration, are discussed to demonstrate the effectiveness of this approach. Chapter 10 discusses a fully coupled geomechanics and fluid transport model, as well as an integrated workflow in determining the impact of natural and hydraulic fracture interactions and refracturing on production in shale reservoirs. Chapter 11 describes a coupled fluid flow−geomechanical simulation model that can predict caprock failure and fault reactivation. In the model, the geomechanical equations relating stresses and displacements are combined to yield an equation for mean stress, a primary variable, and volumetric strain, a rock property. This formulation is then extended to calculate the stress tensor components and to predict of shear failure, as compared with the experiments of pressure-induced fracturing of a concrete block.

Chapter 12 presents a modeling study of cryogenic fracturing processes under thermal, hydraulic, and mechanical (THM) effects. By coupling all these processes in a THM simulation, this chapter demonstrates a numerical approach suitable for modeling cryogenic fracturing process, which successfully reproduces the experimental results of temperature and pressure profiles, as well as fracture morphology inside the shale samples. Chapter 13 focuses on the use of field-scale data and diagnostics to validate numerical simulations of hydraulic fractures and verify their physical accuracy. This chapter provides the outline or guidance for a hydraulic fracture model validation effort. Chapter 14 presents a systematic modeling study of hydraulic fracture characteristics as observed in experiments, as well as a comprehensive review of rock and hydraulic fracturing experiments in conventional and unconventional rock samples. Chapter 15 presents laboratory studies of subsurface mechanics to support the understanding of fracturing behavior in the field. These laboratory studies focused on various aspects of fracturing, including fracture orientation and borehole orientation with respect to the orientation of principal stresses, rock anisotropy, the effects of various types of discontinuities, leak-off into the formation, and fracturing fluid viscosity. The laboratory-scale studies have advanced in complexity and scale over the previous decades and provided many insights into subsurface fracturing behavior. Finally, Chapter 16 presents an experimental study of hydraulic fracture conductivity under triaxial stress conditions. This study focuses on analyzing the impact, using field core samples, of damage mechanisms on fracture conductivity: proppant embedment and formation spalling.

In summary, this book is intended to bring the latest advances in hydraulic fracture modeling to its readers. Due to the lack of research and development in this area, how to accurately predict hydraulically created fractures, their geometry, and impacts in heterogeneous and complicated formations remains a challenge to engineers, geologists, and scientists working in the field of well-stimulation technology. To achieve the full potential of hydraulic fracture

technology in improving or enhancing petroleum and other natural resource recovery from subsurface reservoirs, minimizing their possible negative impacts on subsurface environments and reducing associated operational costs, more fundamental, multidisciplinary research efforts on fracturing physics and quantitative models/tools are needed. These quantitative methodologies, when developed and validated, will guide better practice and application of hydraulic fracturing from design, operation, and long-term effectiveness in the development of petroleum reservoirs and other resources, as well as subsurface application.

We expect that this book can be used as a supplement to textbooks or as a reference for senior undergraduate and graduate students in petroleum and mining engineering, rock mechanics, soil sciences, geotechnical/foundation, and geoscience. It can also be used as a technical reference for petroleum engineers working on the design and optimization of hydraulic fracturing operations; for geotechnical engineers, soil scientists, and geologists working on building foundation and landslides; and for geothermal engineers, mining engineers, and other scientists and engineers working on subsurface resource recovery and storage.

Yu-Shu Wu
Professor, Department of Petroleum Engineering
Colorado School of Mines
Golden CO 80401, USA
Foundation CMG Chair in Reservoir Simulation

Acknowledgments

The editor would like to express his deep gratitude to Dr. Ramona M. Graves, professor and dean of College of Earth Resource Sciences and Engineering at the Colorado School of Mines, for her support and encouragement for the publication of this book. The editor is very thankful to all the contributors and technical reviewers of the chapters of this book and would also like to thank the editorial and production staff of Elsevier for their work and professionalism. The editor also acknowledges the support from Foundation CMG (Computer Modeling Group).

Chapter 1

Finite-Element Modeling of the Growth and Interaction of Hydraulic Fractures in Poroelastic Rock Formations

Adriana Paluszny[1], Saeed Salimzadeh[2], Robert W. Zimmerman[1]
[1]*Imperial College, London, United Kingdom;* [2]*Technical University of Denmark, Lyngby, Denmark*

1.1 INTRODUCTION

Many analytical models have been developed to investigate different aspects of the hydraulic fracturing process. These models have proved to be very useful in identifying the important factors that influence hydraulic fracture growth and elucidating their effect on the created fracture radius and aperture. However, in general, such models cannot simultaneously account for multiple factors, such as matrix permeability and thermal effects. Furthermore, such models generally take the form of asymptotic solutions, which can be accurate in extreme regions of the parameter space (i.e., viscosity dominated or toughness dominated), but are not accurate in intermediate cases. Finally, analytical solutions are difficult to obtain in situations involving the growth of multiple fractures from a single borehole. Hence, there is a need for a robust numerical approach that can accurately handle all geometries and parameter ranges.

In the broader context of rock fracturing, not necessarily restricted to man-made hydraulic fractures emanating from pressurized boreholes, numerical methods can be extremely useful in understanding the effects of in situ conditions, rock properties, and heterogeneities on the geometric and topological characteristics of fracture networks and their effect on mechanical and flow properties of the rock. Numerical approaches to model fractures within a continuum can be classified into (1) nongeometric methods, in which the fracture is represented as a material property of the mesh, including localized damage and plastic models and (2) geometric methods, in which each fracture is represented explicitly and occupies a volumetric or surface domain that is distinct from the rock matrix. This chapter will focus on geometric methods in

Hydraulic Fracture Modeling. https://doi.org/10.1016/B978-0-12-812998-2.00001-1

which fractures are represented by surfaces and rock property heterogeneities are represented explicitly in the models.

Numerous recent studies have attempted to model fracture propagation in 3D. Nongeometric fracture growth models look at the transition between grain-scale microcracking and cm-scale mesoscale cracking and are generally referred to as "damage" models (Patzák and Jirásek, 2004). These are also known as subgrid or nongeometric models, because they represent multiple "smaller" fractures within a single finite-element triangle or tetrahedron, and therefore do not explicitly represent individual cracks. Phenomenological damage models are material specific, in situ condition specific, and are based on a postulated fracture evolution law. Thus, they have to be fitted to experimental data to be usable. Another type of nongeometric approach is the family of so-called "meshfree" crack methods, including cracking particles, which keep track of fractures implicitly by tagging nodes as being "cracked" during fracture growth (Rabczuk and Belytschko, 2007). These methods also do not explicitly represent individual cracks and rely on secondary reconstruction mechanisms to track fracture surfaces and fronts. Existing multiscale models, such as the "classical" and "cohesive" multiscale models, developed to upscale microfracturing damage models, are based on the existence of a representative elementary volume (REV) (Vernerey and Kabiri, 2014). However, these models break down when applied to quasi-brittle rocks, for which REVs can rarely be identified above the centimeter scale, as fractures tend to exist at all length scales. A multiscale approach must consider both the existence of small scale, microstructure-dependent fractures, as well as the discrete fracture growth of larger fractures.

Discrete fracture growth models are geometric methods that represent fractures "discretely"; they assume that fractures have a body and geometry that change during growth. Such models can make use of a variety of numerical methods, such as the boundary element method (Carter et al., 2000), the finite-element method (Paluszny and Zimmerman, 2011), and the extended finite-element method (Bordas et al., 2008). The finite-element approach defines fracture geometry as part of the mesh, whereas the extended finite element represents fractures as discontinuities that exist within elements of the mesh. The extended finite-element method is constrained in that it allows for only one fracture orientation per element and has a limited "level set" amount of predefined fracture orientations. The finite-element method is, in contrast, more flexible if used as an instrument to inform the growth of a geometric model, as in, for example, the method recently developed by Paluszny and Zimmerman (2011). Models based on stress intensity factors (SIFs) are not generally suited to study smaller scale damage, due to their elevated computational cost and continuity assumptions. However, an innovative method has recently been developed (Paluszny and Zimmerman, 2011) that allows energy-based computations to be carried out on coarse unstructured meshes, without requiring a brick-like mesh, and enables one to model the growth of multiple fractures simultaneously, in three dimensions (Paluszny et al., 2013; Nejati et al., 2015b), at a variety of scales.

1.2 COMPUTATIONAL FRAMEWORK

In this chapter, a numerical framework to model the growth of multiple fractures in three dimensions is described. Fractures are represented discretely, using three-dimensional nonplanar surfaces that are embedded in three-dimensional volumetric domains representing the rock. The framework is suitable for both porous and nonporous rocks. By capturing fracture geometry using surfaces, their high aspect ratio is preserved, and both their geomechanical and flow behavior can be modeled independently in a simultaneous manner. Fractures are represented volumetrically, in the sense that each fracture disk is represented by two superimposed surfaces. Thus, the fracture represents a true discontinuity in the mechanical deformation model. Contact between these surfaces is modeled as part of the simulation, as is the fluid flow through the fracture and the leakoff from the fracture to the matrix. The separation of the fracture walls is tracked during the simulation, yielding a detailed distribution of fracture apertures across the fracture surface. Thus, the aperture distribution on the fracture surface changes as the fluid advances through the fracture and interacts with the in situ stresses. This fracture aperture distribution affects the permeability of the fracture, and in the context of hydraulic fracturing, it also affects the transfer of heat between fracture and matrix, as well as the fluid flow from fracture to matrix. Consequently, it affects the resulting patterns of fractures in a multifracture system.

The rock is assumed to be a linear, elastic, and homogeneous material. In the case of hydraulic fracturing, the main two boundary conditions are the fluid pressure within the fractures and the remote in situ stresses. In addition, a temperature contrast between the fluid and rock can also be accounted for. At each iteration, the thermoporoelastic deformation field is computed. The deformation field depends on the fluid, mechanical, and thermal behavior of both the rock and fluid. A flowchart of the computational procedure is shown in Fig. 1.1.

Energy-based approaches for fracture growth compute SIFs, which can be computed for each fracture modality (I tensile, II and III shear), and can then be directly compared with the toughness of the rock, at different scales. SIFs are measures of the elastic energy change due to fracture growth and are computed at each fracture tip node. By using isoparametric quarter-point elements around the fracture tips (Nejati et al., 2015b), these SIFs can be computed with great accuracy for relatively coarse meshes and result in fracture growth predictions that are independent of both the mesh structure and the mesh refinement. Based on these SIFs, predictions of growth direction and magnitude are made, and the geometric growth of the fracture is computed. At each tip node, a growth vector is computed, resulting in a distributed growth prediction for each fracture. Thus, the numerical framework can capture a scenario in which part of the fracture may be subjected to tension, while another is being subjected to shear, for example. This may result in a variation

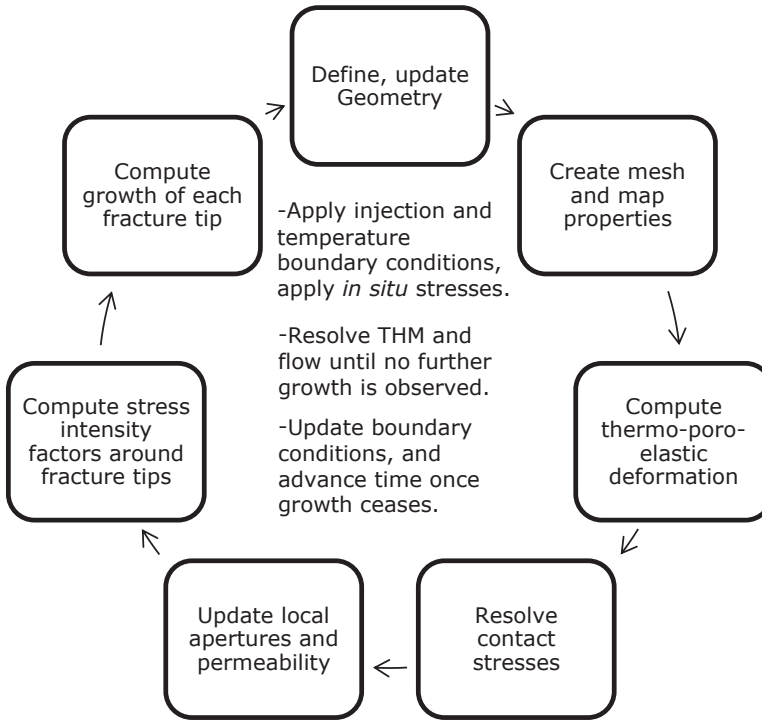

FIGURE 1.1 Schematic representation of the simulation workflow. The numerical framework is based on the finite-element method and assumes that the fractures are represented explicitly by the mesh. Each fracture is composed of two initially overlapping surfaces that may either separate or contact during the deformation. Apertures are computed locally, deformation is poroelastic, and fluid flow is modeled using Darcy's law.

of radii and growth angles across the fracture tip. At each fracture tip node, the direction of fracture propagation is computed from an experimentally validated mixed mode 3D fracture angle criterion that is based on the maximum circumferential stress (Schöllmann et al., 2002). In addition, at each node, the extent of growth is computed independently as a function of the SIFs, relying on semianalytical Paris-type functions that can capture growth modes ranging from brittle to fatigue behavior, by using a material-specific propagation exponent (Lazarus, 2003). This results in fractures that may grow out of their initial plane, if the growth criteria thus specify. This local process is repeated for each fracture, around its tip curve, and for each tip node, in an individual manner. Therefore, multiple fractures can be assessed simultaneously using the same approach, and the interaction between nearby fractures is an emerging behavior of the simulation. Examples of the growth of multiple fractures in 3D are shown in Fig. 1.2.

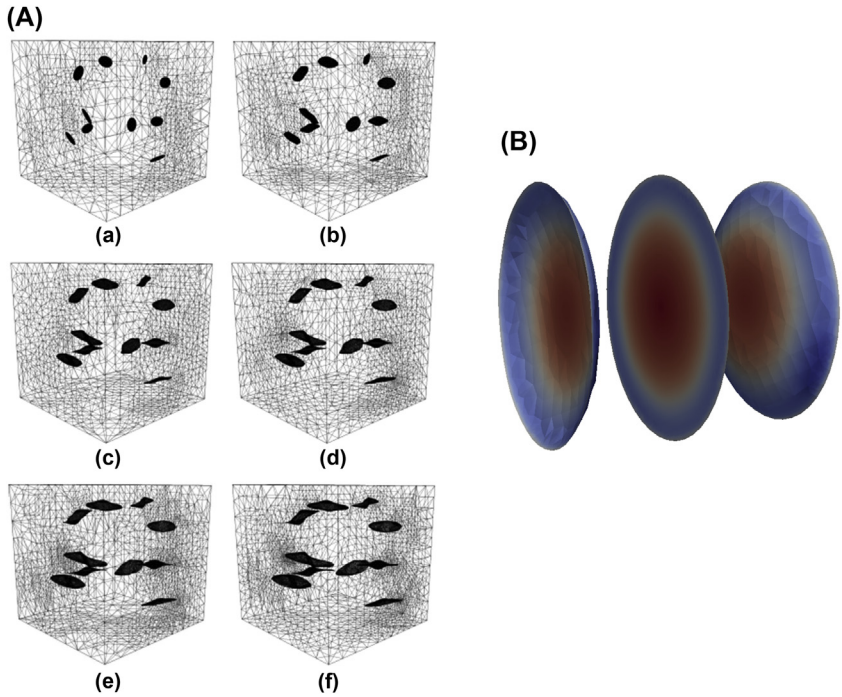

FIGURE 1.2 Example of modeling of the growth fractures using the present numerical framework. (A) Ten fractures grow under tension; (B) three hydraulic fractures grow simultaneously during injection.

1.3 MODELING OF THERMOPOROELASTIC DEFORMATION IN FRACTURED MEDIA

The fully coupled thermohydromechanical (THM) model consists of six interacting submodels and the numerical model for integrated fracture growth prediction. The separate THM submodels are three heat transfer models, two flow models, and the thermomechanical model. Separate flow models are defined for the rock matrix and the fractures, to accurately capture hydraulic loadings on the fracture surfaces, as well as the poroelastic deformation of the deformable rock matrix, and are coupled using fluid leakage terms (Fig. 1.3). The THM scheme to compute temperature, fluid pressure, and displacements at the nodes of the matrix and fractures is a monolithic, fully coupled, three-dimensional finite element–based approach described in detail by Salimzadeh et al. (2017a,b). The presented simulations are for single-phase flow, but the method can be extended to include the effects of multiphase flow within the same framework.

Fluid properties typically vary nonlinearly, and over several orders of magnitude, with changing pressure and temperature. Initially, fluid properties are obtained using lookup tables based on the IAPWS (International

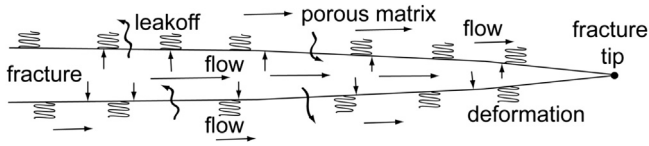

FIGURE 1.3 Schematic representation of the fracture and interaction between the governing equation for (1) mechanical deformation, (2) fluid flow in the fracture, and (3) fluid flow in the matrix.

Association for the Properties of Water and Steam; www.iapws.org) pure water equation of state. For cases where more complex equation of state data are available, these can be incorporated into the simulation. Pressure and temperature equations are solved using a finite-element finite-volume method (FE-FV), in which advective parts of the equations are solved using the finite-volume method and diffusive parts are solved using the finite-element method. Details of this scheme are available in Paluszny et al. (2007). The deformation of the matrix due to stress, temperature, and fluid pressure is governed by the thermomechanical model's governing equation

$$\iiint_{\Omega}\left\{\operatorname{div}\left[\frac{1}{2}\mathbf{D}(\nabla\mathbf{u}+\mathbf{u}\nabla)-\alpha p_m\mathbf{I}-\beta_s K(T_s-T_{s0})\mathbf{I}\right]+\mathbf{F}\right\}dV-\iint_{\Gamma_c}p_f n_c dS=0 \tag{1.1}$$

where $\mathbf{D}$ is the drained stiffness tensor, $\mathbf{u}$ is the displacement vector of the rock solid, α is the Biot coefficient of the matrix, p_m is the matrix fluid pressure, $\mathbf{I}$ is the identity tensor, β_s is the volumetric thermal expansion coefficient of the matrix, K is the bulk modulus of the porous rock, T_s is the current temperature of the solid rock, T_{s0} is the initial temperature of the solid rock, $\mathbf{F}$ is the body force vector per unit volume, p_f is the fluid pressure in the fracture, n_c is the outward unit normal vector to the fracture surface, Ω is the region occupied by the rock mass, and Γ_c is the boundary of the fracture (Zimmerman, 2000).

The first flow model describes flow within the matrix as follows (Salimzadeh and Khalili, 2015):

$$\begin{aligned}&\iiint_{\Omega}\operatorname{div}\left[\frac{\mathbf{k}_m}{\mu_f}(\nabla p_m+\rho_f g)\right]dV\\&=\iiint_{\Omega}\left\{\alpha\frac{\partial(\operatorname{div}\mathbf{u})}{\partial t}+\left[\phi c_f+\frac{(\alpha-\phi)}{K_s}\right]\frac{\partial p_m}{\partial t}-\phi\beta_f\frac{\partial T_m}{\partial t}\right\}dV+\iint_{\Gamma_c}c_L(p_m-p_f)dS\end{aligned} \tag{1.2}$$

where $\mathbf{k}_m$ is the permeability tensor of the matrix, μ_f is the fluid viscosity, ρ_f is the fluid density, $\mathbf{g}$ is the gravitational acceleration vector, ϕ is the matrix porosity, c_f is the fluid compressibility, K_s is the bulk modulus of the solid

grains, β_f is the fluid's volumetric thermal expansion coefficient, T_m is the matrix temperature, and c_L is the fluid leakoff coefficient. The fluid leakoff coefficient couples the two flow models and is defined as $c_L = k_n/\mu_f\delta$ where k_n is the permeability in the direction normal to the fracture and δ is the half-width of the element adjacent to the fracture (Salimzadeh and Khalili, 2015).

Fluid flow through the fracture's walls under nonisothermal conditions is modeled independently by the governing equation of the second flow model as (Zimmerman and Bodvarsson, 1996)

$$\iint_{\Gamma_c} \mathrm{div}\left(\frac{a_f^3}{12\mu_f}\nabla p_f\right) dS = \iint_{\Gamma_c} \left[\frac{\partial \alpha_f}{\partial t} + \alpha_f c_f \frac{\partial p_f}{\partial t} - \alpha_f \beta_f \frac{\partial T_f}{\partial t} - c_L(p_m - p_f)\right] dS \tag{1.3}$$

where α_f is the aperture of the fracture and T_f is the temperature of fluid in the fracture (Salimzadeh et al., 2016a).

There are three heat transfer models: the solid, the fractures, and the rock matrix (Khalili and Selvadurai, 2003). The heat transfer model describing heat transfer through the deformable rock solid is governed by

$$\begin{aligned}&\iiint_{\Omega} \mathrm{div}(\boldsymbol{\lambda}_s \nabla T_s) dV \\ &= \iiint_{\Omega} \left\{\rho_s c_s \frac{\partial T_s}{\partial t} + \beta_s K T_s \frac{\partial(\mathrm{div}\mathbf{u})}{\partial t} + c_{T_m}(T_s - T_m)\right\} dV + \iint_{\Gamma_c} c_{T_f}(T_s - T_f) dS\end{aligned} \tag{1.4}$$

where $\boldsymbol{\lambda}_s$ is the thermal conductivity tensor of the solid, ρ_s is the solid density, c_s is the solid specific heat capacity, c_{T_m} is the solid-matrix heat exchange coefficient, and c_{T_f} is the solid-fracture heat exchange coefficient. Heat exchange between the solid and matrix or fracture is modeled by a thin, thermally resistive layer, such that the heat exchange coefficient is given by $c_{T_f} = \lambda_n/\delta$, where λ_n is the thermal conductivity in the direction normal to the fracture and δ is the half-width of the element adjacent to the fracture.

Similarly, the second heat model for heat transfer through the fracturing fluid is governed by

$$\begin{aligned}&\iiint_{\Gamma} \mathrm{div}(\alpha_f \boldsymbol{\lambda}_f \nabla T_f) dV = \iint_{\Gamma_c} \left[\alpha_f \rho_f C_f \frac{\partial T_f}{\partial t} - \alpha_f \beta_f T_f \frac{\partial p_f}{\partial t}\right] dS \\ &+ \iint_{\Gamma_c} [\alpha_f \rho_f C_f \mathbf{v}_f \cdot \nabla T_f + c_{T_f}(T_f - T_s) + \rho_f C_f c_L(p_m - p_f)(T_f - T_m)] dS\end{aligned} \tag{1.5}$$

where $\boldsymbol{\lambda}_f$ is the isotropic thermal conductivity tensor of the fluid, C_f is the heat capacity of the fluid, and $\mathbf{v}_f$ is the velocity vector of the fluid in the fracture.

Finally, the third heat model, for matrix heat transfer, is governed by the following equation:

$$\iiint_{\Omega} \operatorname{div}(\boldsymbol{\lambda}_f \nabla T_m) dV = \iint_{\Gamma_c} \rho_f c_L C_f (p_m - p_f)(T_m - T_f) dS$$
$$= \iiint_{\Omega} \left\{ \phi \rho_f C_f \frac{\partial T_m}{\partial t} - \phi \beta_f T_m \frac{\partial p_m}{\partial t} + \phi \rho_f C_f \mathbf{v}_m \cdot \nabla T_m + c_{T_m}(T_m - T_s) \right\} dV \tag{1.6}$$

where $\mathbf{v}_f$ is the velocity vector of the fluid in the matrix.

The above equations are solved using the finite-element method for the spatial discretization of the equations and using the finite difference technique for the temporal discretization. To apply these methods, the domain is discretized into a hybrid volumetric-surface mesh that contains both quadratic tetrahedra and triangles.

The procedures and equations described in this work have been implemented into the Geomechanics module (Paluszny and Zimmerman, 2011; Salimzadeh et al., 2017a,b) of the Complex System Modeling Platform (CSMP++), an object-oriented finite element−based API-developed platform for the simulation of complex geological processes (Matthäi et al., 2001). The system of equations resulting from the finite-element method accumulation is solved using the Fraunhofer SAMG Solver library (Stüben, 2001).

Contact between fracture surfaces is modeled using a gap-based augmented Lagrangian approach that resolves the stresses on the fracture surfaces as a function of the local compressive forces, in an iterative manner (Nejati et al., 2016). Thus, under compression the fracture walls are prevented from interpenetration by resolving the frictional forces on fracture walls. Contact resolution is solved iteratively and requires the solution to a nonlinear problem that is solved using the Uzawa algorithm (Nejati et al., 2016). Contact and THM solutions are solved sequentially, thus, for each iteration, one contact and one THM step are solved before the iteration is evaluated.

1.4 MODELING DISCRETE FRACTURE GROWTH

Modal SIFs are computed by evaluating the I-integral over a virtual disk domain (Nejati et al., 2015a). An alternative, displacement correlation technique is also applied side-by-side, for comparison purposes (Nejati et al., 2015b). The mixed-mode three-dimensional Schöllmann method (Schöllmann et al., 2002) is used to compute the growth angle. At each growth iteration, growth vectors are constructed so as to capture changes to the fracture geometry. Growth vectors are translated into the deformation of the fracture surface, or the addition of new fracture surfaces/triangles to the original geometry. As a result, the fracture geometry adapts to the stress state, and the

geometry of the fracture network effectively changes and adapts to the stress state. Thereafter, the mesh is adaptively refined to the new geometry, following the new fracture surface.

Capturing the stress singularity ahead of the fracture tip is the key to accurately estimating the SIFs. Isoparametric quadratic tetrahedra and triangles are defined around the crack tips to capture the $1/\sqrt{r}$ stress and displacement singularities. As the low and displacement equations are solved in a monolithic fully coupled approach, only one type of element is used, and both flow and displacement are computed on isoparametric quadratic elements. Each tip curve is discretized into a set of tip segments. SIFs, for modes I, II, and III, are computed for each segment of the fracture tip.

The SIFs, for modes I, II, and III, can be related to the *J*-integral, which quantifies the amount of energy released to extend the fracture tip for unit length in the direction of the crack plane (Paluszny and Zimmerman, 2011), defined as

$$J = \frac{1}{A_c} \iiint_{V_c} \left(\sigma_{ij} \frac{\partial u_j}{\partial x_k} - W \delta_{ik} \right) \frac{\partial q_k}{\partial x_i} dV, \tag{1.7}$$

where A_c is the amount of fracture surface area created by an extension of the fracture that increases by extension, V_c is the volume of the virtual unit cylinder over which J is computed, W is the strain energy density, δ_{ik} is the Kronecker delta, and q_k is an arbitrary weighting vector that represents the virtual crack extension.

The SIF K is then related to J by

$$J = K^2 / E_{eff}, \tag{1.8}$$

where E_{eff} is computed from the Young's modulus E, Poisson's ratio ν, and the local principal strains $\{\varepsilon_x, \varepsilon_y, \varepsilon_z\}$ as follows:

$$E_{eff} = E \left[\frac{1}{1-\nu^2} + \frac{\nu}{1+\nu} \left(\frac{\varepsilon_z}{\varepsilon_x + \varepsilon_y} \right) \right]. \tag{1.9}$$

There are three different SIFs, which correspond to different deformation modes: K_{I} for the opening mode (mode I), K_{II} for the in-plane shear mode (mode II), and K_{III} for the out-of-plane shear mode (mode III).

Three criteria are needed to model the propagation of the fractures based on the SIFs calculated around the tip: the failure criterion, the propagation magnitude criterion, and the propagation angle criterion. The failure criterion can be expressed as

$$K_v > K_{Ic}, \tag{1.10}$$

where K_{Ic} is the critical SIF, i.e., the rock's "toughness." The term K_v is the component of the SIF in the propagation direction and is given by

$$K_v = \frac{1}{2} \cos(\varphi_0/2) \left[K_{cs} + \sqrt{K_{cs}^2 + 4K_{\mathrm{III}}^2} \right], \tag{1.11}$$

where $K_{cs} = K_{\mathrm{I}} \cos^2(\varphi_0/2) - (3/2)K_{\mathrm{II}} \sin \varphi_0$. The term φ_0 is the deflection angle, which is perpendicular to the crack tip (Schöllmann et al., 2002). At every time step of the simulation, the SIFs $\{K_{\mathrm{I}}, K_{\mathrm{II}}, K_{\mathrm{III}}, K_v\}$ are calculated at each discretized crack tip and then compared against the rock toughness K_{Ic}. Any tips that have K_v values exceeding the rock toughness K_{Ic} are considered to have a failure, after which the fracture tip is extended by a specific extension length that is defined at the beginning of the simulation. To avoid unnecessary growth steps, and considering that the matrix is homogenous, when K_v at one tip reaches K_{Ic} (i.e., growing is triggered), all other tips that have $K_v > 0.3K_{Ic}$ are extended as well. The fracture extension angle is then calculated for these tips based on the propagation angle criterion that allows determining the new ridgeline of fracture tips and updated surface. Once the geometry is updated after each growth step, the model is outsourced to an octree volumetric mesher, and remeshing is done for the entire model.

1.5 EFFECT OF MATRIX POROELASTICITY ON THE GROWTH OF A SINGLE FRACTURE

Analytical methods are able to shed light on specific cases of hydraulic fracture growth, such as the viscosity-dominated, storage-dominated, toughness-dominated, and leakoff-dominated regimes, whereas numerical models are able to handle intermediate regimes (Salimzadeh et al., 2017a,b). The constitutive behavior of the matrix plays an important role in predicting fracture growth in both permeable and impermeable rock formations. In particular, for permeable formations, effects of matrix poroelasticity should not be neglected, as they influence the predicted aperture and lateral extent of the fracture. For toughness-dominated cases, decoupled numerical simulations of hydraulic fracture growth in both permeable and impermeable formations overestimate both fracture apertures and radii during injection. In the case of impermeable formations, the storage-toughness (Savitski and Detournay, 2002) and leakoff-toughness (Bunger et al., 2005) asymptotic solutions provide upper and lower bounds, respectively, to the fracture radii and apertures (Fig. 1.4). In contrast, for permeable formations, the analytical solution for the storage-toughness regime provides an upper bound for both the fracture radii and aperture, but the leakoff-toughness solution fails to provide a lower boundary for the same fracture parameters.

1.6 EFFECT OF INTERACTION ON THE PATHS OF TWO FLUID-DRIVEN PENNY-SHAPED CRACKS

The fluid-driven growth of a single fracture is governed by the interplay between deformation and flow that determines the stress concentrations at the fracture tip. Growth is often examined as a function of in situ or remote stresses, therefore, the far-field stress state is assumed to control the growth of

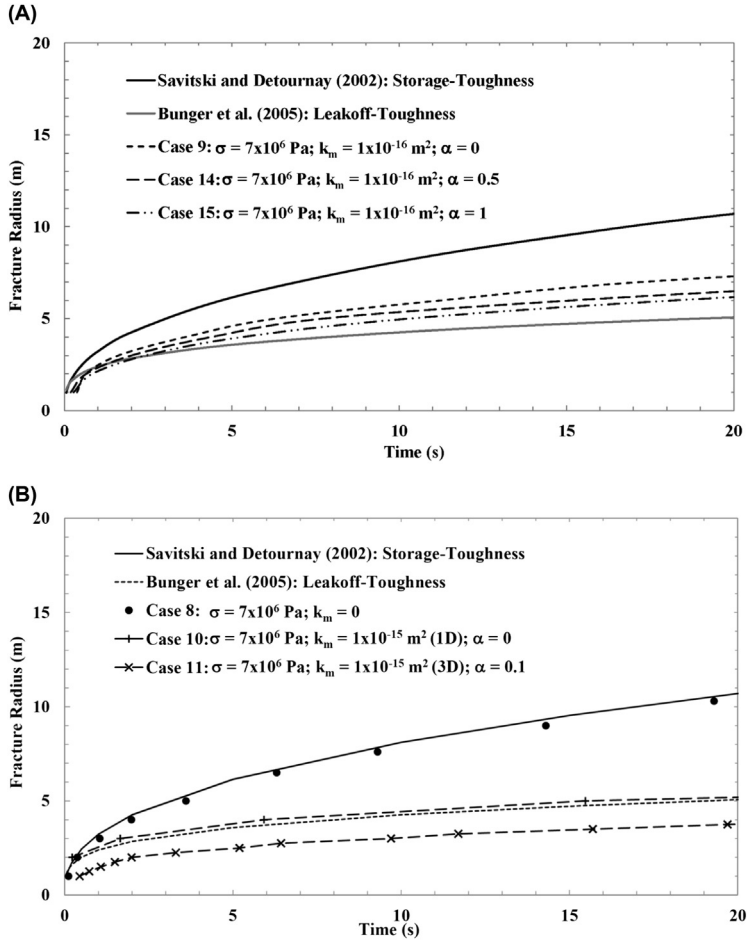

FIGURE 1.4 Fracture radius as a function of time for different regimes, for varying Biot coefficients, for (A) a low permeability matrix and (B) a permeable matrix. Notice how the storage-toughness and leakoff-toughness asymptotic solutions provide bounds for the low permeability matrix case only.

the fractures. However, in cases when more than one fracture grows simultaneously, fractures also interact with each other during growth. Matrix permeability, spacing (Roussel and Sharma, 2011), preexisting fractures (Cruz et al., 2016), geology and matrix heterogeneity (Izadi et al., 2017) are expected to influence the interaction. During simultaneous growth, fractures exert a compressive shadow (Fischer et al., 2004) that influences their curving, and in turn, influence how far they grow into the formation.

First, the case of two penny-shaped cracks is investigated. The cracks are at a fixed spacing and grow simultaneously during fluid injection. The two

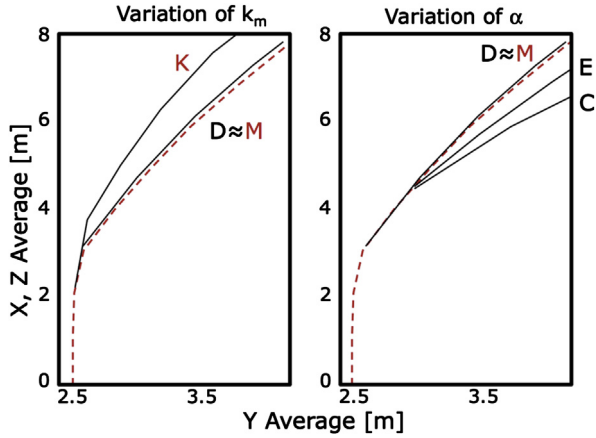

FIGURE 1.5 Fracture paths of an interacting fracture as a function of varying Biot coefficient. As the fracture grows, it deflects from its original plane, in the direction away from the neighboring fracture (see Table 1.1 for properties of cases).

fractures grow along a horizontal well and are under isotropic compressive in situ stresses. Interaction is observed for fractures that grow at a spacing of less than five times their radius, for both permeable and impermeable formations. As fractures interact, they curve away from each other and depart from their original plane of growth (Fig. 1.5). For an impermeable matrix, with $k_m = 0\ \text{m}^2$, and a higher permeability matrix with $k_m = 2 \times 10^{-13}\ \text{m}^2$, the

TABLE 1.1 Biot Coefficient, Permeability, Horizontal and Vertical Stresses, and Spacing Values Assigned for Simulation Runs

ID	Regime	Biot α (-)	k_x, k_y, k_z (m^2)	σ_H, σ_v (MPa)	σ_h (MPa)	Spacing l (m)
M	Viscosity-storage	0	0	20	20	5
K	Toughness-storage	0	0	20	20	5
C	Viscosity-leakoff	1	2×10^{-13}	20	20	5
D	Viscosity-leakoff	0	2×10^{-13}	20	20	5
E	Viscosity-leakoff	0.4	2×10^{-13}	20	20	5

paths are affected by fluid leakoff from the fracture to the matrix. As compared to the impermeable case, fracture interaction in permeable media is more prominent. Thus, fracture interaction is enhanced by the effect of the fluid leaking from the fracture into the adjacent rock formation.

For a higher permeability matrix, 2×10^{-13} m^2, the effect of the rock's poroelastic deformation is investigated. For the hypothetical case in which the Biot coefficient is 0, mechanical and flow simulations are decoupled. This case is unrealistic, as the Biot coefficient would always be higher than the rock porosity (Zimmerman, 2000), but can be investigated to highlight the differences between the permeable and impermeable cases. This case is closest to the impermeable matrix base case, and it represents a scenario under which leakoff does not affect the aperture of the fracture or its growth. For a somewhat higher Biot coefficient of 0.4, the leakoff effect is noticeable, and the interaction effect is increased. For the extreme case of a Biot coefficient of 1, the interaction effect is further increased.

It is worth noting that the differences in fracture paths occur most strongly at the onset of fracture propagation, when the distance between the tips of two adjacent fractures is smallest. For the impermeable cases (M and K), the fracture deviates around 11 degrees from the vertical axis at the onset of growth, whereas for the high and low permeable cases (M and K, respectively; $\alpha = 0$), additional deviations are 19 and 32 degrees, respectively. Once the course of the fracture is set, the path does not undergo significant changes. In contrast, for the poroelastic cases, the difference in angle is much less pronounced (8 and 6 degrees, respectively), as the ensuing paths continue to diverge as the fractures grow. This indicates that permeability and poroelasticity are complementary mechanisms affecting the interaction between fractures, affecting growth at both onset and development of the hydraulic fractures.

In an array of simultaneously stimulated fractures that contains more than two fractures, the interplay of fracture interaction has effects that go beyond the curving of the fracture paths (Fig. 1.6). Five fractures of 1 m radius, initially spaced at 3 m, in a $100 \times 90 \times 90$ m box are stimulated at an injection rate of $Q = 0.005$ m^3/s, for hydrostatic ($\sigma_h = \sigma_H = \sigma_v = 10$ MPa) and nonhydrostatic far-field stress states ($\sigma_h = 10$ MPa, $\sigma_H = 11$ MPa, $\sigma_v = 12$ MPa). For a fixed fracture spacing, fracture interaction depends on the in situ conditions and influences both the fracture paths and the fracture apertures. For isotropic in situ stresses, the boundary fractures exhibit strong deflection from the original path. For the case of the nonisotropic in situ stresses, fractures at the extremes of the array exhibit less curving. For anisotropic stress conditions, the middle fractures are observed to grow further than they would in the isotropic case and sustain larger apertures in the center fracture. For fractures that are stimulated sequentially, curving is also observed to depend on the in situ stresses (Salimzadeh et al., 2017b).

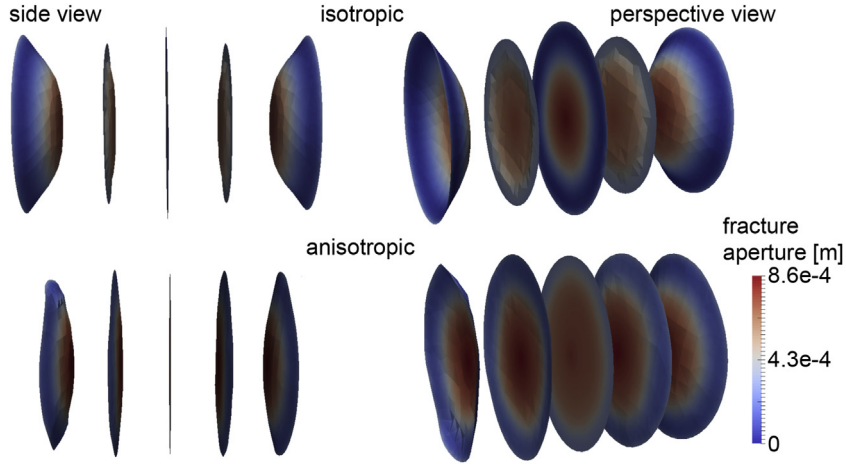

FIGURE 1.6 Five fractures interact during growth for isotropic (top) and anisotropic (bottom) boundary conditions.

1.7 THERMAL EFFECTS ON EARLY STAGES OF HYDRAULIC FRACTURE GROWTH

During hydraulic fracturing, the temperature of the injected fluid is often much lower than that of the matrix rock. Due to thermomechanical coupling in the rock mass, it is expected that this temperature difference may influence stresses at the tip of the fracture and thereby influence the rate of fracture growth. However, the small volume of fluid contained in the fracture quickly enters equilibrium with the rock, and thus, the temperature contrast fails to cause any additional strains in the short term.

Although analytical solutions have been developed for simple scenarios, they do not generally account for processes such as heat transfer between the fracturing fluid and the rock mass or leak-off into a poroelastic rock mass. Thermal effects of the hydraulic fracturing process can be studied numerically, accounting for heat transfer through the solid rock and the fracturing fluid, and for the transfer of thermal energy between the rock and fluid. Fractures provide highly conductive channels, rapidly transferring heat through the formation. In contrast, heat transfer through the solid rock is usually slow and largely independent of the hydraulic properties of the matrix.

Local thermal nonequilibrium between fracture fluid and neighboring rocks leads to heat transfer between them. The rate of heat transfer depends on the temperature differences, as well as the thermal properties of the rock.

Hydraulic fracturing is investigated for local thermal nonequilibrium in an impermeable matrix. Water is injected at a temperature 100°C cooler than the formation, at an injection rate $Q = 0.001$ m^3/s, with a viscosity $/ = 0.1$ Pa s, and a fracture toughness $K_{Ic} = 1$ MPa m$^{0.5}$.

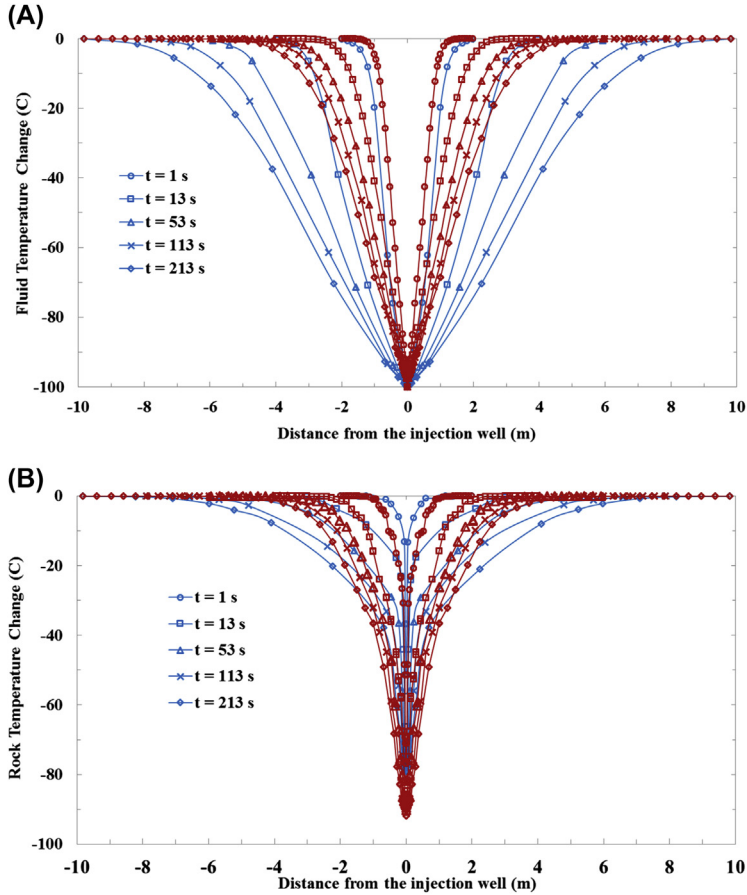

FIGURE 1.7 Temperature change as a function of matrix diffusivity. In blue (light gray in print versions), with a lower value of thermal diffusivity, 1×10^{-6} m^2/s; and in red (dark gray in print versions), with a higher thermal diffusivity, 1×10^{-5} m^2/s. In (A) fluid and (B) rock, temperature change as a function of distance to the injection point, and its progression over injection time (1, 13, 53, 113, and 213 s).

The temperature change along the radial distance along the fracture is plotted as a function of injection time in Fig. 1.7. Two cases are modeled: in blue, with a lower value of thermal diffusivity, 1×10^{-6} m^2/s; and in red, with a higher thermal diffusivity, 1×10^{-5} m^2/s. The initial radius of the fracture is 1 m, and reaches 8 m within the first 150 s of injection. Within this injection window, the large temperature contrast between fluid and rock is rapidly equilibrated as the fluid travels through the fracture. This rapid equilibration is assumed to be primarily due to the small volume of cooler fluid in the fracture. The results show that the thermal diffusivity has a significant effect on the speed at which the fluid temperature reaches equilibrium, with a lower rock

diffusivity causing the fluid to maintain its low temperature for longer. However, in both cases the fluid quickly equilibrates with the rock over the length of the fracture; and in both cases thermal diffusivity does not substantially influence the temperature change of the rock. The temperature contrast between fluid and rock causes local contraction of the rock, occurring most significantly in the vicinity of the well (Salimzadeh et al., 2016).

The effect of the injection rate on the temperature change in the fluid and rock is plotted in Fig. 1.8. In the image, blue represents a lower value of injection rate, $Q = 0.001$ m^3/s, and red depicts a higher injection rate, $Q = 0.01$ m^3/s. Higher

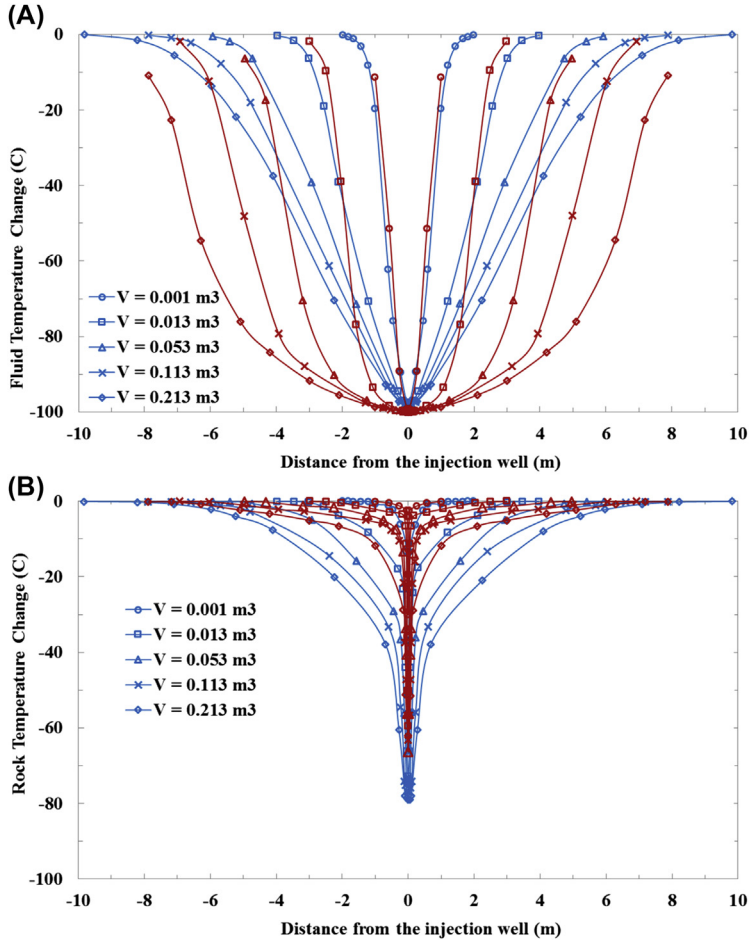

FIGURE 1.8 Temperature change as a function of injection rate. In blue (light gray in print versions), with a lower value of injection rate $Q = 0.001$ m^3/s; and in red (dark gray in print versions), with a higher injection rate, $Q = 0.01$ m^3/s. In (A) fluid and (B) rock, temperature change as a function of distance to the injection point, and its progression over injection volume.

injection rates push the fluids through the system at a higher velocity; therefore, fluids conserve their original temperature during injection and are slower to equilibrate, as compared with the lower injection rate case.

However, for the same amount of injected fluid volume, the rock will undergo much less cooling in the case of the high injection rate, as opposed to the low injection rate case. Thus, larger fracture radii can be achieved with a smaller temperature change.

These results show that temperature contrast does cause a temperature gradient inside the fracture, which is nonlinear, and depends both on the rock diffusivity and the injection rate. An assumption of constant temperature within the fracture may lead to the overestimation of the effect of cold injection on rock contraction and in turn, may overpredict fracture growth enhancement (Usui, 2016).

1.8 CONCLUSIONS

An advanced numerical framework has been presented to model the growth of multiple discrete fractures as a result of the porothermoelastic deformation of a porous matrix. The approach is based on the finite-element method and has been applied to study the effects of matrix permeability, poroelastic behavior of the matrix, and fluid injection temperature, on the overall growth of the fractures. Results highlight the importance of poroelastic and permeability effects, by illustrating the effects of matrix deformation and leakoff on the resultant fracture radii and apertures. For the particular cases investigated herein, we find that matrix cooling during cold injections has a negligible effect on fracture growth at the onset of injection and mainly affects the apertures in the vicinity of the injection well. This analysis is based on very short injection periods and focuses only on the fracturing that takes place at the onset of cold injection. As opposed to asymptotic analytical solutions, the presented simulations can assess a wider variety of geometric settings, and can evaluate complex boundary conditions and reservoir settings that are closer to realistic conditions. The computational framework is flexible and can be adapted to accommodate other constitutive models for the rock and the fluid.

REFERENCES

Bordas, S., Rabczuk, T., Zi, G., 2008. Three-dimensional crack initiation, propagation, branching and junction in non-linear materials by an extended mesh-free method without asymptotic enrichment. Engineering Fracture Mechanics 75 (5), 943–960.

Bunger, A.P., Detournay, E., Garagash, D.I., 2005. Toughness-dominated hydraulic fracture with leak-off. International Journal of Fracture 134, 175–190.

Carter, B.J., Wawrzynek, P.A., Ingraffea, A.R., 2000. Automated 3D crack growth simulation. International Journal of Numerical Methods in Engineering 47, 229–253.

Cruz, L., Izadi, G., Moos, D., Sheridan, J., Fu, P., Settgast, R.R., Ryerson, F.J., 2016. The role of natural fractures (joints) in the Marcellus shale during hydraulic fracture stimulation using full 3D modeling. In: Unconventional Resources Technology Conference, San Antonio, Texas, August 1–3, 2016, pp. 1049–1061.

Fisher, M.K., Heinze, J.R., Harris, C.D., Davidson, B.M., Wright, C.A., Dunn, K.P., 2004. Optimizing horizontal completion techniques in the Barnett shale using microseismic fracture mapping. In: Paper SPE 90051. SPE Annual Technical Conference and Exhibition, Houston, September 26–29, 2004.

Izadi, G., Moos, D., Cruz, L., Gaither, M., Chiaramonte, L., Johnson, S., 2017. Fully coupled 3-D hydraulic fracture growth in the presence of weak horizontal interfaces. In: Society of Petroleum Engineers. SPE Hydraulic Fracturing Technology Conference and Exhibition, January 24–26, 2017, The Woodlands, Texas, USA.

Khalili, N., Selvadurai, A.P.S., 2003. A fully coupled constitutive model for thermo-hydro-mechanical analysis in elastic media with double porosity. Geophysical Research Letters 30 (24), 2268.

Lazarus, V., 2003. Brittle fracture and fatigue propagation paths of 3D plane cracks under uniform remote tensile loading. International Journal of Fracture 122, 23–46.

Matthäi, S.K., Geiger, S., Roberts, S.G., 2001. The Complex Systems Platform csp3.0: Users Guide. Technical report, ETH Zürich Research Reports.

Nejati, M., Paluszny, A., Zimmerman, R.W., 2015a. A disk-shaped domain integral method for the computation of stress intensity factors using tetrahedral meshes,. International Journal of Solids and Structures 69–70, 230–251.

Nejati, M., Paluszny, A., Zimmerman, R.W., 2015b. On the use of quarter-point tetrahedral finite elements in linear elastic fracture mechanics. Engineering Fracture Mechanics 144, 194–221.

Nejati, M., Paluszny, A., Zimmerman, R.W., 2016. A finite element framework for modeling internal frictional contact in three-dimensional fractured media using unstructured tetrahedral meshes. Computer Methods in Applied Mechanics and Engineering 306, 123–150.

Paluszny, A., Matthai, S.K., Hohmeyer, M., 2007. Hybrid finite element-finite volume discretization of complex geologic structures and a new simulation workflow demonstrated on fractured rocks. Geofluids 7 (2), 186–208.

Paluszny, A., Zimmerman, R.W., 2011. Numerical simulation of multiple 3D fracture propagation using arbitrary meshes. Computer Methods in Applied Mechanics and Engineering 200 (9–12), 953–966.

Paluszny, A., Zimmerman, R.W., 2013. Numerical fracture growth modeling using smooth surface geometric deformation. Engineering Fracture Mechanics 108, 19–36.

Patzak, B., Jirasek, M., 2004. Adaptive resolution of localized damage in quasibrittle materials. ASCE Journal of Engineering Mechanics 130, 720–732.

Rabczuk, T., Belytschko, T., 2007. A three-dimensional large deformation meshfree method for arbitrary evolving cracks. Computer Methods in Applied Mechanics and Engineering 196 (29–30), 2777–2799.

Roussel, N.P., Sharma, M.M., 2011. Optimizing Fracture Spacing and Sequencing in Horizontal-well Fracturing. Society of Petroleum Engineers. Paper SPE 127986.

Salimzadeh, S., Paluszny, A., Zimmerman, R.W., 2016. Thermal effects during hydraulic fracturing in low-permeability brittle rocks. In: 50th US Rock Mechanics Symposium, Houston, June 26–29, 2016, Paper ARMA, pp. 16–368.

Salimzadeh, S., Paluszny, A., Zimmerman, R.W., 2017a. Three-dimensional poroelastic effects during hydraulic fracturing in permeable rocks. International Journal of Solids and Structures 108, 153–163.

Salimzadeh, S., Usui, T., Paluszny, A., Zimmerman, R.W., 2017b. Finite element simulations of interactions between multiple hydraulic fractures in a poroelastic rock. International Journal of Rock Mechanics & Mining Sciences 99, 9−20.

Salimzadeh, S., Khalili, N., 2015. A three-phase XFEM model for hydraulic fracturing with cohesive crack propagation,. Computers and Geotechnics 69, 82−92.

Savitski, A.A., Detournay, E., 2002. Propagation of a penny-shaped fluid-driven fracture in an impermeable rock: asymptotic solutions. International Journal of Solids and Structures 39, 6311−6337.

Schöllmann, M., Richard, H.A., Kullmer, G., et al., 2002. A new criterion for the prediction of crack development in multi-axially loaded structures. International Journal of Fracture 117 (2), 129−141.

Stüben, K., 2001. A review of algebraic multi-grid. Journal of Computational and Applied Mathematics 128, 281−309.

Usui, T., 2016. Effects of Poroelasticity on Hydraulic Fracture Interaction (M.Sc. thesis). Imperial College London.

Vernerey, F.J., Kabiri, M., 2014. Adaptive concurrent multiscale model for fracture and crack propagation in heterogeneous media. Computer Methods in Applied Mechanics and Engineering 276, 566−588.

Zimmerman, R.W., 2000. Coupling in poroelasticity and thermoelasticity. International Journal of Rock Mechanics & Mining Sciences 37, 79−87.

Zimmerman, R.W., Bodvarsson, G.S., 1996. Hydraulic conductivity of rock fractures. Transport in Porous Media 23, 1−30.

Chapter 2

A Framework of Integrated Flow–Geomechanics–Geophysics Simulation for Planar Hydraulic Fracture Propagation

Jihoon Kim[1], **Evan Schankee Um**[2]
[1]*Texas A&M University, College Station, TX, United States;* [2]*Lawrence Berkeley National Laboratory, Berkeley, CA, United States*

2.1 INTRODUCTION

There are two approaches for modeling of hydraulic fracturing propagation: analytical and numerical methods. For the analytical approaches, two models are considered: Perkins–Kern–Nordgren (PKN) and Khristianovic–Geertsma–de Klerk (KGD), where different assumptions are applied. For numerical modeling, several methods have been used for the fracturing modeling. For example, the discrete element method considers intact rock and fractures separately and models fracture propagation by splitting nodes (Fu et al., 2012; Ben et al., 2012; Zhang and Wong, 2013). This method is natural because the numerical scheme follows the physical process of fracturing. This discrete element method can be suitable for small-scale problems that can represent intact rock and fractures individually. However, it requires huge computational cost for large-scale problems in a full 3D system. On the other hand, the extended finite element method and the enhanced assumed strain method are based on the continuum approach (Borja, 2008; Moes et al., 1999). These methods use discontinuous interpolation functions for discontinuous displacement to represent fractures and do not require remeshing. However, the applications in the full 3D problems for nonplanar fracture propagation result in considerable complexities and huge coding effort.

Hydraulic Fracture Modeling. https://doi.org/10.1016/B978-0-12-812998-2.00002-3

In reservoir engineering, Ji et al. (2009) proposed a numerical algorithm for hydraulic fracturing, which is based on tensile strength, incorporating poromechanical effects. Dean and Schmidt (2009) essentially used the same fracturing algorithm of Ji et al. (2009), although they used different criteria of the fracture propagation based on rock toughness of fracture mechanics. Kim and Moridis (2013) also used a concept similar to that of Ji et al. (2009). The objective of this chapter is to introduce a coupled modeling approach of fluid flow, geomechanical fracture propagation, and subsequent geoelectrical responses, which can be served as a computational engine for joint interpretation of fracture propagation in a reservoir. In this chapter, we will first overview two analytical models: the PKN and KGD. At the next step, we will deal with full 3D simulation for vertical fracture propagation, followed by its application to geophysical simulation, such as induced seismicity and electromagnetic simulation.

2.2 ANALYTICAL METHODS FOR VERTICAL HYDRAULIC FRACTURES

2.2.1 Two-Dimensional Fracture Models: Perkins–Kern–Nordgren and Khristianovic–Geertsma–de Klerk Fractures

The PKN geometry (Fig. 2.1) involves the following assumptions (Valko and Economides, 1995; Economides and Nolte, 2000; Gidley et al., 1990): (1) the fracture height is considered to be fixed, and it is independent of the total fracture length; (2) the fracturing fluid pressure holds constant in vertical cross sections, perpendicular to the direction of the fracture propagation; (3) the deformation of each vertical section is independent of each other; and (4) the cross section in vertical planes has an elliptical shape.

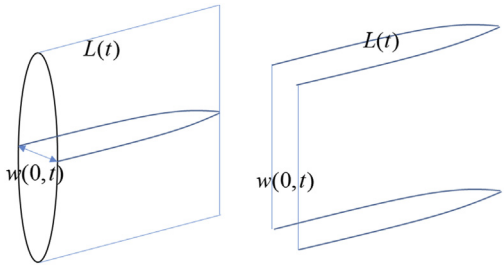

FIGURE 2.1 Schematics of the geometry for Perkins–Kern–Nordgren (left) and Khristianovic–Geertsma–de Klerk (right) hydraulic fractures. $L(t)$ and $w(0,t)$ are the total fracture half-length and the maximum fracture width, respectively.

From the second assumption, the cross sections can have an elliptic shape with the maximum width in the center as

$$w(x,t) = \frac{(1-\nu)Hp_{\text{net}}}{G}, \tag{2.1}$$

where $p_{\text{net}} = (p_f - \sigma_H)$ is the effective stress, ν and G are the Poisson's ratio and the shear modulus of the formation, respectively, H is the height of the fracture, and p_f is the fluid pressure in the fracture.

A PKN hydraulic fracture geometry is determined by the parameters such as the injection rate, the properties of the rock and the fluid, and the leak-off coefficient. The governing equation for the PKN fracture geometry is derived from the conservation of mass (i.e., continuity equation) as follows (Gidley et al., 1990):

$$\frac{\partial q}{\partial x} + \frac{\pi H}{4}\frac{\partial w}{\partial t} = 0, \tag{2.2}$$

where q is the volumetric flow rate per unit height of the fracture, and w is the maximum fracture width at the center. Here, we assume no fluid leak-off and an incompressible fluid. The aperture w is calculated by elastic geomechanics in the state of plane strain.

When the fracturing fluid is assumed to be a Newtonian fluid and laminar flow is supposed, the fluid momentum equation in one dimension is simply written as

$$q = -\frac{w^3 H\pi}{64\mu_f}\frac{\partial p_{\text{net}}}{\partial x}, \tag{2.3}$$

where μ_f is the viscosity of the fracturing fluid. We assume that σ_H is constant. By using Eqs. (2.1) and (2.3), Eq. (2.2) can be written in terms of w as follows:

$$\frac{\partial w}{\partial t} = \frac{G}{64(1-\nu)H\mu_f}\frac{\partial^2 w^2}{\partial x^2}, \tag{2.4}$$

Initial condition: $w(x,0) = 0$,

Boundary condition: $w(x,t) = 0$ for $x > L(t)$ and $q = q_0$ (for one-sided fracture).

On the other hand, the KGD model takes a slightly different assumption, compared with the PKN model: rock stiffness is only considered in the horizontal plane. Thus, the fracture width is independent of the fracture height. Then, the fracture width and flow equations become

$$w(x,t) = \frac{2(1-\nu)Lp_{\text{net}}}{G}\sqrt{1-x^2}, \quad q = -\frac{w^3 H}{12\mu_f}\frac{\partial p_{\text{net}}}{\partial x}, \quad \frac{\partial q}{\partial x} + \frac{\partial w}{\partial t} = 0. \tag{2.5}$$

Then, solving the partial differential equations of the PKN and KGD models with the corresponding fracture widths and flow equations, we obtain (Gidley et al., 1990)

$$L(t) = C_1\left[\frac{Gq_0^3}{(1-\nu)\mu_f H^4}\right]^{0.25} t^{0.8},\quad w(0,t) = C_2\left[\frac{(1-\nu)\mu_f q_0^2}{GH}\right]^{0.25} t^{0.2},$$
$$p(0,t) - \sigma_H = \frac{C_3}{H}\left[\frac{Gq_0^3\mu_f L}{(1-\nu)^3}\right]^{0.25},\quad C_1 = 0.45,\ C_2 = 1.89,\ C_3 = 2.31, \tag{2.6}$$

$$L(t) = C_4\left[\frac{Gq_0^3}{(1-\nu)\mu_f H^3}\right]^{\frac{1}{6}} t^{\frac{2}{3}},\quad w(0,t) = C_5\left[\frac{(1-\nu)\mu_f q_0^3}{GH^3}\right]^{\frac{1}{6}} t^{\frac{1}{3}},$$
$$p(0,t) - \sigma_H = \frac{C_6}{2H}\left[\frac{Gq_0\mu_f H^3}{(1-\nu)^3 L^2}\right]^{0.25},\quad C_4 = 0.48,\ C_5 = 1.32,\ C_6 = 1.19. \tag{2.7}$$

2.2.2 Fracture Propagation and Fracture Widths

From the previous solutions for PKN and KGD fractures, we can easily simulate fracture propagation analytically with different flow and geomechanics parameters as follows, where the input values are $q_0 = 0.0267$ m^3/s, $\nu = 0.2$, $\mu_f = 0.1$ Pa s, $H = 30$ m, and $G = 10$ GPa.

From Fig. 2.2, the hydraulic fracture propagates fast as the shear modulus increases. The PKN fracture propagates faster than the KGD fracture. On the other hand, from Fig. 2.3, the fracture width of the PKN model becomes smaller than that of the KGD model. Also, as the shear modulus increases, the

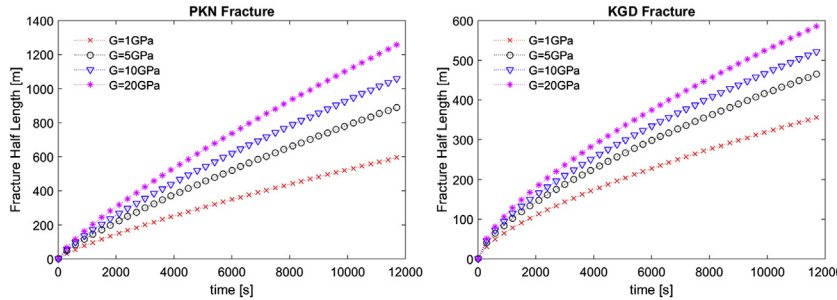

FIGURE 2.2 Fracture propagation of the Perkins–Kern–Nordgren (left) and Khristianovic–Geertsma–de Klerk (right) models.

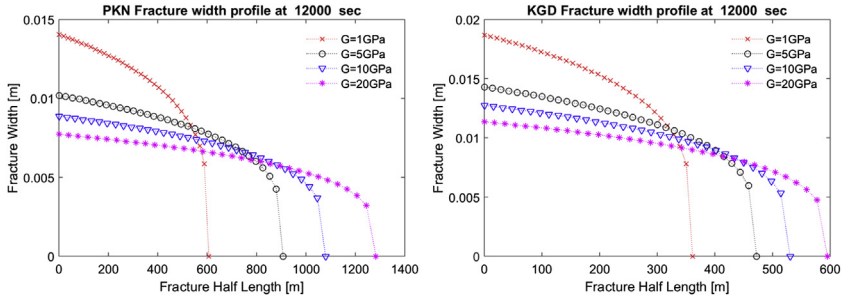

FIGURE 2.3 Fracture width of the Perkins–Kern–Nordgren (left) and Khristianovic–Geertsma–de Klerk (right) models.

fracture width becomes smaller. In other words, more brittle material causes faster fracture propagation with smaller fracture opening.

2.3 NUMERICAL SIMULATION OF VERTICAL HYDRAULIC FRACTURE PROPAGATION IN THREE DIMENSIONS

We first describe the governing equations of flow and geomechanics, followed by constitutive relations, tensile failure, and permeability. In this study, we consider isothermal single-phase flow, assuming the reservoir to be impermeable.

2.3.1 Mathematical Statements and Constitutive Relations

The governing equation of flow comes from mass conservation, written as (Aziz and Settari, 1979)

$$\frac{\partial m_f}{\partial t} + \mathbf{Div}\cdot\mathbf{f} = q_f, \tag{2.8}$$

where m_f, $\mathbf{f}$, and q_f are fluid mass, mass flux, and external source terms, respectively. **Div** is the divergence operator. The subscript f indicates fluid. The mass flux is $\mathbf{f} = \rho_f \mathbf{v}_f$, where ρ_f is fluid density. From the Darcy law, $\mathbf{v}_f$ can be written as

$$\mathbf{v}_f = \frac{k_p}{\mu_f}(\mathbf{Grad}p - \rho_f \mathbf{g}), \tag{2.9}$$

where k_p is the symmetric positive definite rank-2 tensor, and μ_f is fluid viscosity. **Grad** is the gradient operator, and $\mathbf{g}$ is the gravity vector.

The governing equation of geomechanics is derived from linear momentum balance, written as (Coussy, 1995)

$$\mathbf{Div}\cdot\boldsymbol{\sigma} + \rho_b \mathbf{g} = 0, \tag{2.10}$$

where $\boldsymbol{\sigma}$ is total stress and ρ_b is bulk density.

Eq. (2.8) for flow and Eq. (2.10) for geomechanics are coupled by poro-mechanics theory with the following constitutive relations (Coussy, 1995):

$$\delta\sigma = C_{dr}\delta\varepsilon - b\delta p 1, \tag{2.11}$$

$$\frac{\delta m_f}{\rho_f} = b\delta\varepsilon_v + \frac{1}{M}\delta p, \tag{2.12}$$

where ε is the strain, 1 is the rank-2 identity tensor, and b and M are Biot's coefficient and modulus, respectively, written as

$$b = 1 - \frac{K_{dr}}{K_s}, \quad \frac{1}{M} = \phi c_f + \frac{b-\phi}{K_s}, \tag{2.13}$$

where K_{dr} and K_s are the drained bulk modulus and intrinsic solid grain bulk modulus, respectively, c_f is the fluid compressibility, and ϕ is the true porosity, defined as the ratio of the current pore volume to the bulk volume in the deformed configuration. Then, Eq. (2.8) becomes

$$\frac{1}{M}\frac{\partial p_f}{\partial t} + b\frac{\partial \varepsilon_v}{\partial t} + \mathbf{Div}\cdot v_f = \widetilde{q}_f, \tag{2.14}$$

where $q_f = \rho_f \widetilde{q}_f$.

In this chapter, for tensile failure, we use tensile strength−based approach as follows (Ji et al., 2009; Kim and Moridis, 2013):

$$\sigma_c = \sqrt{\beta^{-2}\left(t_t'^2 + t_t'^2\right) + t_n'^2} \le T_c, \tag{2.15}$$

where T_c is tensile strength, and σ_c is the critical stress for tensile failure, which consists of shear $\left(t_t', t_s'\right)$ and normal $\left(t_n'\right)$ effective stresses acting on a planar fracture. In Eq. (2.15), we can account for the contribution of shear effective stress to tensile failure.

Flow capacity within a hydraulic fracture can be modeled by the modified cubic law, written as (Witherspoon et al., 1980)

$$Q_f = a_c \frac{\omega_f^3}{12\mu_f} H(\mathbf{Grad}p_f - \rho_f \mathbf{g}), \tag{2.16}$$

where Q_f is flow rate of water, ω_f is the aperture, fracture opening (width), a_c is a correction factor that reflects the effect of fracture roughness, and H is the fracture plate length.

2.3.2 Numerical Discretization and Examples

We use the finite volume method for flow, in which flow variables take piecewise-constant interpolation (Aziz and Settari, 1979), whereas the finite element method for geomechanics (Hughes, 1987), taking piecewise-linear interpolation of displacement. For time discretization, we use the backward

Euler method. We also use a sequential method to solve the coupled flow and geomechanics problems. Specifically, we use the fixed-stress sequential method in solving two-way coupling in pore volume (Kim et al., 2011). Permeability is calculated based on explicit treatment, depending on failure status and aperture of the fracture as computed at the geomechanics step. Permeability is a strong function of geomechanical failure, and thus, for further accuracy, we take a small time-step size that ensures no fracturing between two fracturing events. At the geomechanics step, pressure within a hydraulic fracture, previously obtained from the flow step, updates the traction boundary, whereas the pressure outside the hydraulic fracture updates the pressure, given in Eq. (2.11). From the given numerical schemes, we can make use of existing flow and geomechanics codes by constructing an interface between them only.

For numerical examples, we discretize the domain for geomechanics with 100, 3, and 22 gridblocks in the x, y, and z directions, respectively. The direction of the minimum compressive principal total stress is normal to the x−z plane. The sizes of the gridblocks in the x, y, and z directions are nonuniform. Specifically, in the x direction, the sizes of the 1st and 2nd gridblocks are 10 m and 2 m; those from the 3rd to the 47th gridblocks are all uniformly 0.5 m; those from the 48th to the 51st gridblocks are 1, 3, 5, 5, 3, 1 m, respectively; those from the 52nd to 98th gridblocks are all uniformly 0.5 m; those of the 99th and 100th gridblocks are 2 m and 10 m. In the y direction, the sizes of the 1st, 2nd, and 3rd gridblocks are 0.01, 2, 40 m, respectively. In the z direction, the sizes of the 1st and 2nd gridblocks are 5 m and 3 m; those from the 3rd to 20th gridblocks are all 1 m; those from the 21st to 22nd gridblocks are 3 m and 5 m.

We take Young's modulus $E = 13.6$ GPa and Poisson's ratio $v = 0.28$. The tensile strength of shale for the reference case is 2 MPa. We assume strong formation on top and bottom layers having tensile strength of 10 MPa. We assume the saline water to be injected at the center ($x = 0$) with total rate of 0.6 kg/s, in the initially fractured areas (Fig. 2.4). Biot's coefficient, b, is taken to be 0.8.

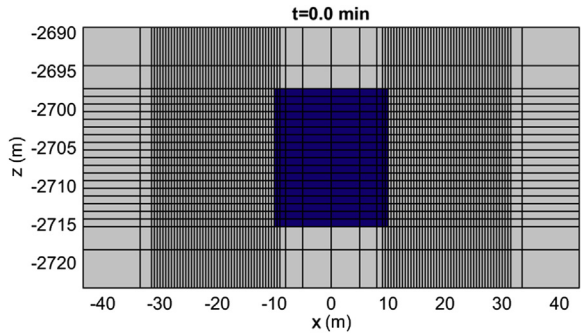

FIGURE 2.4 Initially fractured area for a vertical well.

The initial porosity is 10^{-5}. For the initial conditions, reservoir pressure is initially 32.15 MPa at the top of the domain, with a 12.44 kPa/m gradient. The initial total principal stresses are -46.03 MPa (S_H), -44.67 MPa (S_h), and -67.68 MPa (S_V) at the top of the domain in the x, y, and z directions, respectively, where tensile stress is positive. The corresponding stress gradients are -16.15 kPa/m, -15.68 kPa/m, and -21.57 kPa/m, respectively. Then, for $|S_h|$ of the shale gas reservoir, we assign 5 MPa lower than the aforementioned $|S_h|$. For geomechanics, there are no-horizontal-displacement boundary conditions for the sides, except for the fracture nodes. We have no-vertical-displacement boundary at the bottom. We also consider gravity and bulk of 2560 kg/m^3.

We first simulate propagation of a single fracture with a vertical well. Figs. 2.5 and 2.6 show the fracture propagation and its aperture (fracture width) at different times, respectively. With water injected, the hydraulic fracture propagates further horizontally because the bounding layers have higher tensile strength and higher magnitude of minimum horizontal stress.

From Fig. 2.7, we see that the pressure within the fracture is much higher than that of the reservoir during hydraulic fracturing, causing a significant pressure gradient at the fracture tips. Fig. 2.8 shows evolution of the pressure at the well, which exhibits oscillatory behavior. This oscillation is caused by almost instantaneous opening of the fracture. Although severe oscillation is found at early times due to the small volume of the fracture, the oscillation becomes alleviated as the volume increases.

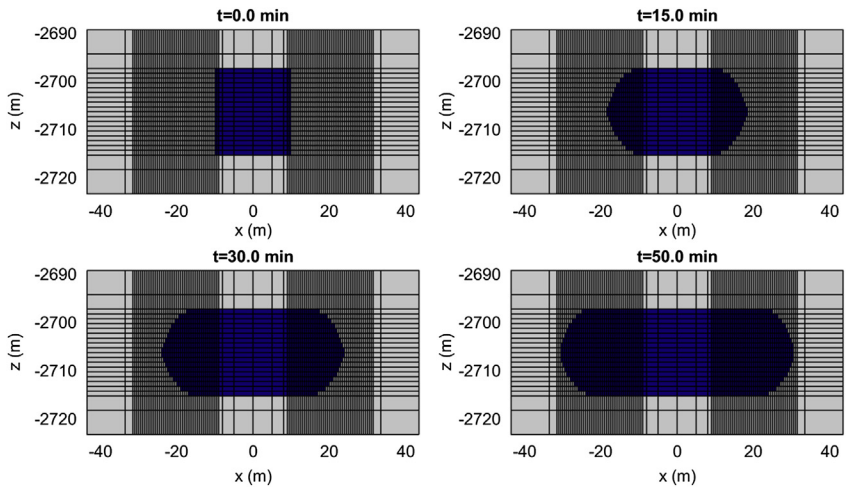

FIGURE 2.5 Fracture propagations at different times.

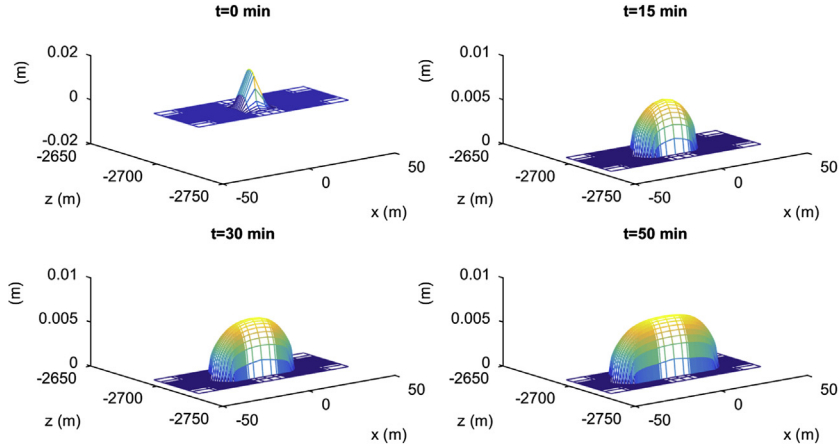

FIGURE 2.6 Half sizes of fracture apertures at different times.

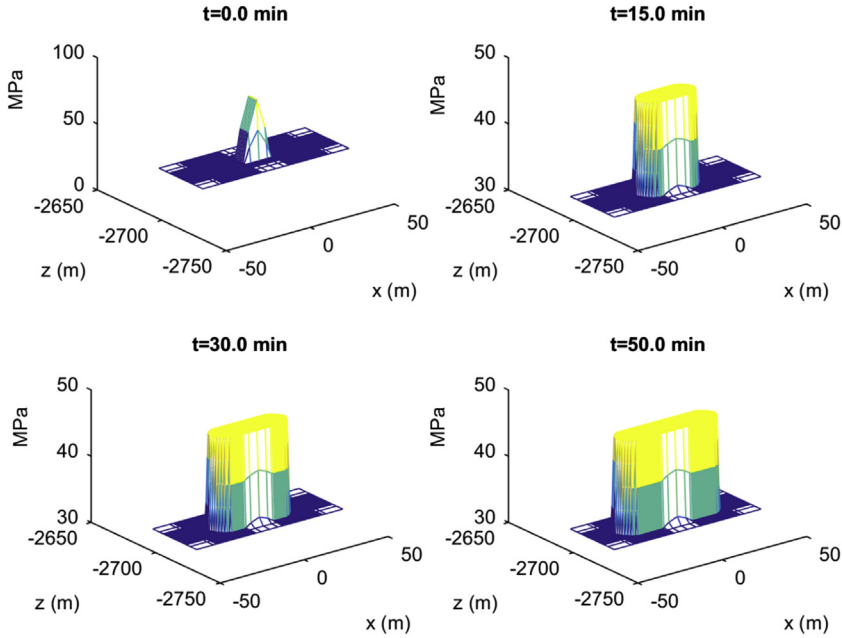

FIGURE 2.7 Pressure distributions at different times.

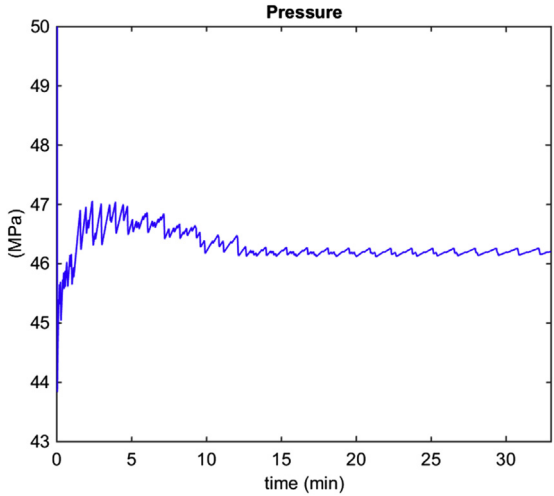

FIGURE 2.8 Evolution of pressure at the injection well.

2.4 JOINT ANALYSIS OF GEOMECHANICS AND GEOPHYSICS

MEQ monitoring has mainly been studied for imaging fractures and fluids (Warpinski et al., 2005; Vermylen and Zoback, 2011). MEQ provides general information about locations of fracturing events. On the other hand, the magnitudes of MEQ are often too small to be reliably recorded in practice. Electrical and electromagnetic (EM) geophysical methods have a potential to complement MEQ because they are sensitive to fluids in pores and fractures and can provide independent information about fluid flow associated with hydraulic fracturing. Thus, in this section, we will perform numerical simulation of induced seismicity (i.e., seismic moment) and the EM survey.

2.4.1 Induced Seismicity

Moment tensors provide a general theoretical framework to describe seismic sources based on generalized force couples, shown in Fig. 2.9.

During the simulation of hydraulic fracturing, we can calculate seismic moment/microearthquake (MEQ) from solution of geomechanics for every event of failure as follows (Aki and Richards, 2002):

$$M_{pq} = \int m_{pq} d\sum, \quad m_{pq} = \lambda v_k u_k \delta_{pq} + \mu(v_p u_q + v_q u_p), \tag{2.17}$$

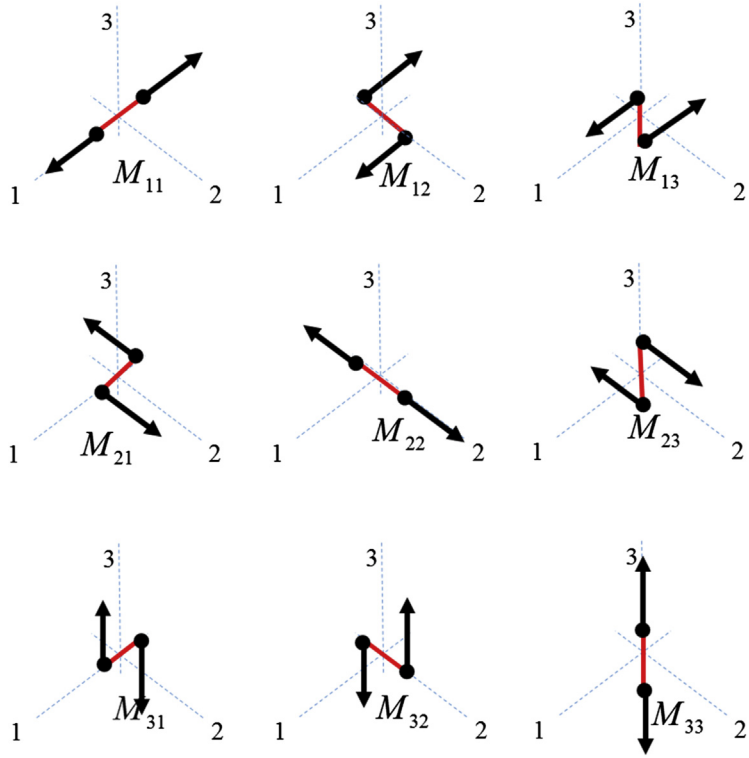

FIGURE 2.9 The system of force couples representing the components of a Cartesian moment tensor. Diagonal elements of the moment tensor represent linear vector dipoles, whereas off-diagonal elements represent force couples with moment (Aki and Richards, 2002).

$$M_w = \frac{\log_{10} M_0 - 16.1}{1.5} + 4.667, \quad M_0 = \|M_{pq}\|_{L2}(N \cdot m), \tag{2.18}$$

where M_{pq} is the seismic moment tensor, λ, μ are Lame's first parameter and shear modulus, respectively, $v_p u_p$ are the vector normal to the fracture plane and the displacement vector, and δ_{pq} is the second-order identity tensor. $\sum$ is the fractured area.

Fig. 2.10 shows distribution of the event locations and the corresponding magnitudes (Mw) that correspond to the previous numerical simulation of hydraulic fracturing. Mw's are between -1 and -3, mostly -2, which are insignificant. This implies that MEQ might not always work well for mapping fractures and flow. Accordingly, the electrical and EM methods can complement MEQ and reduce ambiguity in interpreting fracture and flows as follows.

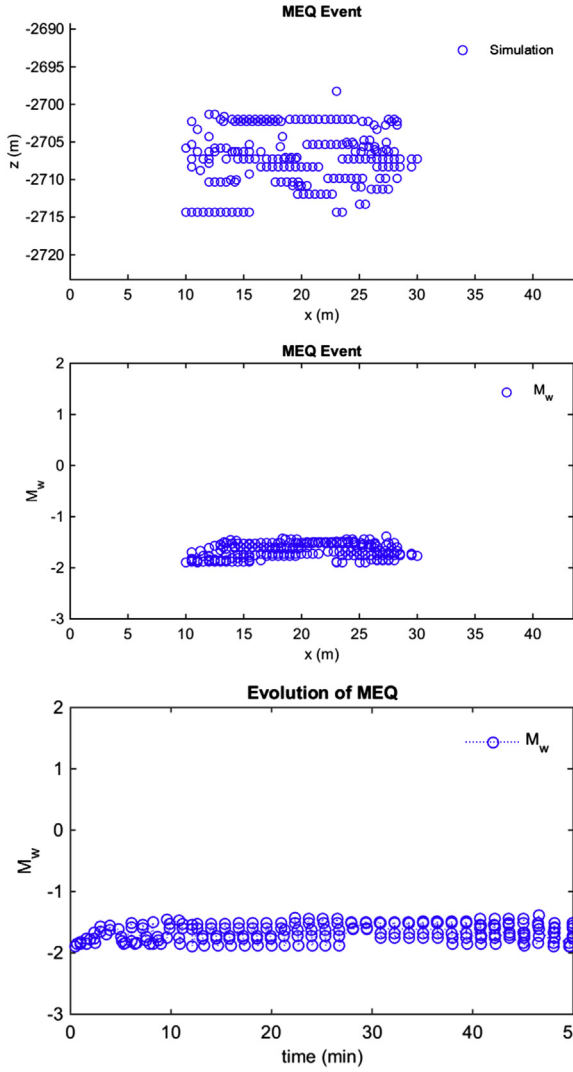

FIGURE 2.10 Distribution of the event locations of the right half domain (top) and the corresponding magnitudes (center and bottom).

2.4.2 Electromagnetic Survey

We investigate detectability of an electrical resistivity method for fracture propagation induced by water-based hydraulic fracturing. The goal of this study is to evaluate the electrical method for detecting hydraulically fractured zones during hydraulic fracturing operations. To achieve this, we use 3D FEM for electrical resistivity modeling (Um et al., 2015), which uses tetrahedral

meshes and accurately and economically discretizes irregular fractured zones not conforming to rectangular Cartesian grids. While fracture propagates, hydrological and petrophysical parameters (e.g., saturations of native and invaded fluids, changes in pore volume and aperture) that are computed by coupled flow−geomechanical simulation are transformed via a rock physics model into electrical conductivity models.

Here, we focus on the surface geophysical configuration because the surface configuration does not require extra observation wells and does not interrupt HF operations. Thus, if successful, the configuration could be widely acceptable, owing to its economic and logistic advantages. Compared with borehole-based methods, however, it is challenging for the surface methods to clearly sense a highly localized fractured zone in depth. To ensure the sufficient sensitivity to a deep hydraulically fractured zone, one can consider injecting highly conductive saline fluid or fluid with electromagnetically anomalous tracers and proppants (e.g., Um et al., 2015; Commer et al., 2015). Such fluid and tracers can raise the magnitude of the weak anomalous signals to a detectable level. It is also proposed to use a steel-cased well as a boosting electric source that directly charges a hydraulic fracture (Schenkel and Morrison, 1994; Commer et al., 2015; Hoversten et al., 2015; Um et al., 2015; Patzer et al., 2017). We apply both approaches to analytical and numerical HF models and demonstrate the sensitivity of the surface electrical method.

Fig. 2.11 shows a surface electric source configuration for imaging a fractured zone in depth. One end point of a 2-km-long *x*-oriented electric source is directly connected to the top of the steel-cased well. In contrast, the other end point is sufficiently distant (i.e., 2 km) from the wellhead such that leak-off of electric currents from the well can be insignificant. The

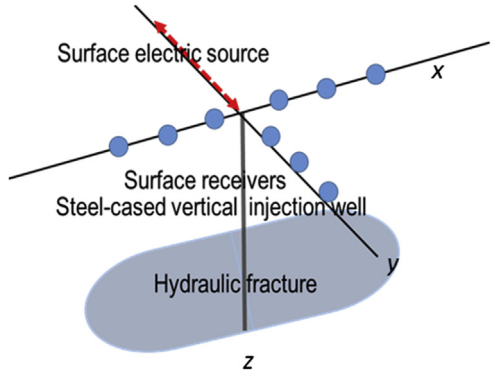

FIGURE 2.11 Schematics of the top-casing electric source method (the $x-z$ plane). The *red line* (dark gray in print version) segment (y-axis) indicates an electric dipole source. The *blue circles* (light gray in print version) are surface electric receivers. The hydraulically fractured zones are mapped into the thin *blue box* (light gray in print version) around the gray steel-cased well.

motivation behind this configuration is that, owing to the high contrast in electrical conductivity between the steel-cased well and its surrounding geology, the high concentration of the electrical current can preferentially flow along the well and directly charge a hydraulic fracture zone. For simplicity, we call this electrical method the top-casing electric source method. Note that our 3D FEM modeling algorithm with unstructured tetrahedral meshes can accurately and efficiently discretize both casing and fracture geometry and generate electric responses to the structures. A reader is referred to Um et al. (2015) for details on tetrahedral mesh generation for 3D multiscale electrical conductivity models that include fine structures such as fractures and a steel-cased injection well.

The resulting coupled flow–geomechanical modeling parameters are converted to an electrical conductivity model (M_e), using a rock physics model. The rock physics model would be available after laboratory tests are performed on cores. One can also consider an electrical conductivity model that is specifically suitable for modeling fluid-filled fractures in rocks. Other petrophysical models to be considered would include Archie's law for clean sand reservoirs or Waxman–Smit's law for shale reservoirs (Waxman and Smits, 1968; Mavko et al., 2009). For simplicity in this study, we use Archie's law written as

$$C_e = \frac{1}{a} C_w \Phi^m S_w^n. \tag{2.19}$$

For numerical study, the rock physics parameters are empirically chosen; both the cementation (m) factor and the saturation (n) factor are set to 2. We consider two conductivity values of injection fluids: seawater and highly conductive saline water (250,000 ppm of NaCl solution). Note that their electrical conductivity is a function of temperature. In this study, we assume that the geothermal gradient is 25°C/km and surface temperature is 25°C. At a given depth, their conductivity can be directly read from the Schlumberger logging chart (Schlumberger, 2009).

Before we apply Archie's law to a set of coupled flow–geomechanics models and perform the geophysical sensitivity study, we first consider electrical responses for the two simple fractured zones, described in Table 2.1. In the table, we take the two different sizes of the hydraulic fractures, after considering the hydraulic fracture propagation by the analytical methods (Figs. 2.2 and 2.3).

The conductivity of the hydraulically active fractured zone is set to 0.5 S/m. Fig. 2.12 shows the detection sensitivity of the top-casing electric source method to the two fracture models. The method clearly distinguishes between the modeling scenarios. The electric field amplitudes along both survey lines are also large enough such that they can be measured in noisy field environments.

TABLE 2.1 Description About the Two Simple Fractured Zone Models

Hydraulically Active Fracture Zone	Length (m)	Height in Depth (m)	Thickness (m)	Conductivity (S/m)
Model 1	$-100 \leq x \leq 100$	$1537.5 \leq z \leq 1662.5$	$-5 \leq y \leq 5$	0.5
Model 2	$-400 \leq x \leq 400$	$1537.5 \leq z \leq 1662.5$	$-5 \leq y \leq 5$	0.5

Next, we consider a more challenging detection scenario where a hydraulically active fractured zone is deep and highly localized around the vertical well. Fig. 2.13 shows distributions of the reservoir porosity of the layer of 2 m thickness that contains the hydraulic fracture, obtained from the previous hydraulic fracturing simulation, assuming that the hydraulic fracture is fully saturated with the invasive fluids.

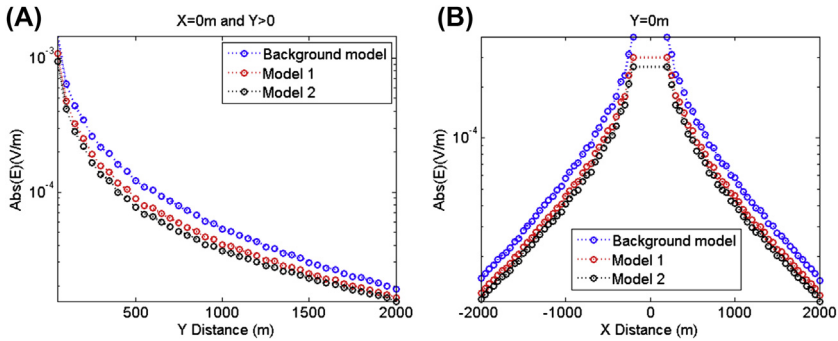

FIGURE 2.12 Survey electric field measurements over the two fracture models and their comparison with the background model (before injection). (A) The electric field measurements along the positive y-axis ($x = 0$). (B) The electric field measurements along the x-axis ($y = 0$).

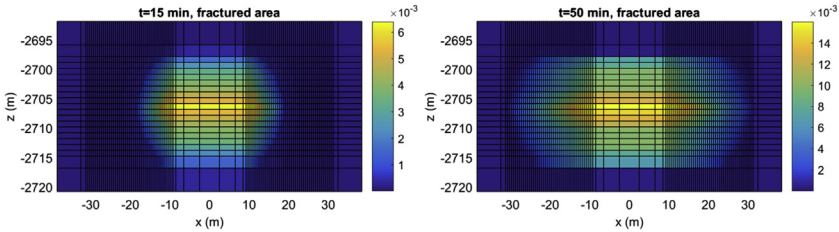

FIGURE 2.13 Porosity values normalized at the 2-m thickness of the hydraulic fracture for different times.

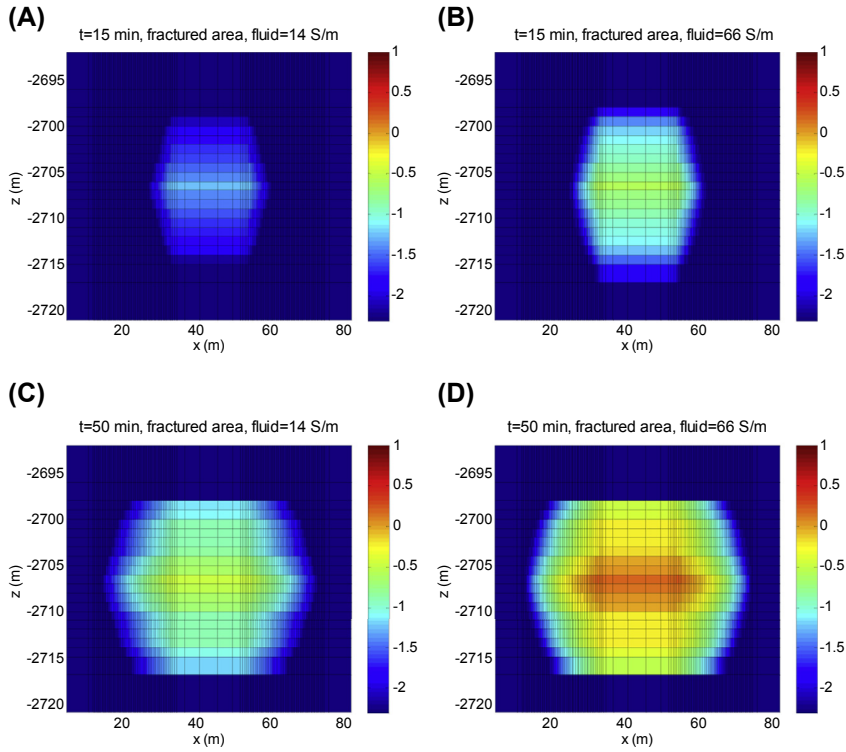

FIGURE 2.14 Spatial distribution of electrical conductivity after the fluid injection. (A) 15 min after seawater injection. (B) 15 min after the highly conductive NaCl solution injection. (C) 50 min after seawater injection. (D) 50 min after the highly conductive NaCl solution injection.

Assuming that the hydraulic fracture is fully saturated with the invasive fluids, we can obtain the electrical conductivity models (Fig. 2.13) by using Eq. (2.19). Fig. 2.14 shows electrical conductivity models at 15 and 50 min after the injection of the two different fluids. To ensure the sensitivity of the top-casing electric source method to such highly localized targets in depth, we consider both seawater and the highly conductive NaCl solution as discussed earlier. At 2.7 km in depth, their conductivity values are about 14 S/m and 66 S/m, respectively. Thus, we examine the role of the fluid conductivity for the sensitivity of the top-casing electric source method.

The electric field measurements over the two fracture models are plotted in Fig. 2.15. Compared with the previous modeling experiments (Fig. 2.12), the overall sensitivity is significantly reduced, due to their small volume and deeper location. First, note that it is quite challenging to detect the highly localized fractured zones in depth when seawater is injected. The relative difference between background and seawater-saturated fracture responses is only 2−3%. Such small perturbations might not always be reliably measured

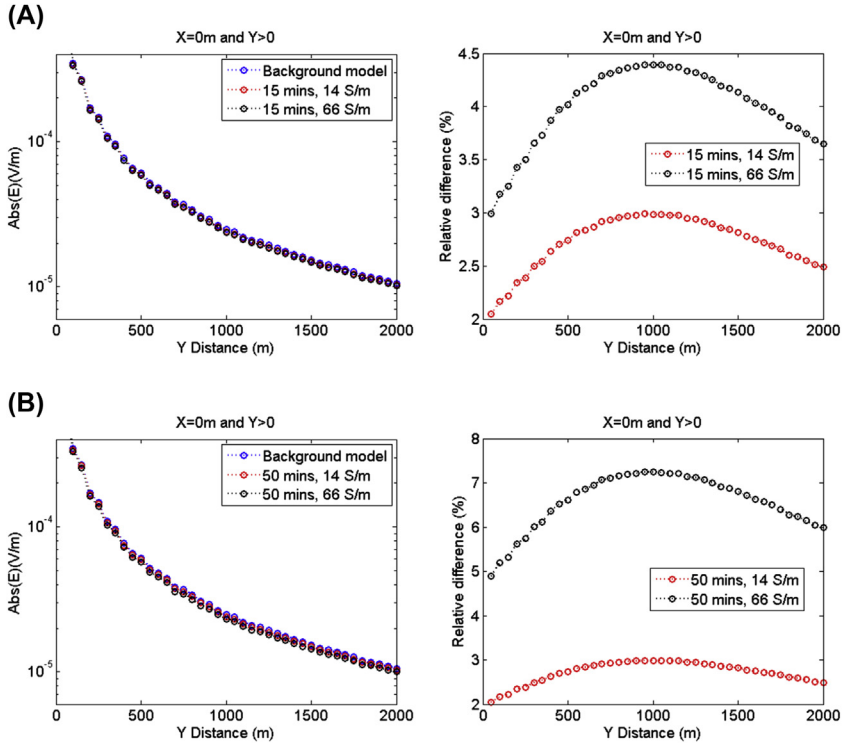

FIGURE 2.15 Electric field measurements along $+y$-axis at $y = 0$ m and relative differences between the background model (before injection) and the fracture models (15 and 50 min after the injection). (A) 15 min after the injection. (B) 50 min after the injection.

in noisy field environments. In contrast, the use of the highly conductive NaCl solution somewhat improves the overall sensitivity, demonstrating that field-specific engineered EM fluids have strong potential for better detection and imaging of deep localized fractured zones.

2.5 SUMMARY

We describe a framework of integrated flow−geomechanics−geophysics simulation, which can be applied to shale gas development with hydraulic fracturing. Specifically, coupled flow and geomechanics enable us to calculate the occurrence time, magnitude, and location of the seismic moment by providing solutions of geomechanics and geological failure. In addition, saturation distribution of the injected water facilitates EM simulation. The integrated simulation can be further used for joint analysis and inversion with various geophysical data combined with well data.

REFERENCES

Aki, K., Richards, P.G., 2002. Quantitative Seismology 1.

Aziz, K., Settari, A., 1979. Petroleum Reservoir Simulation. Elsevier, London.

Ben, Y., Xue, J.Q.M., Wang, Y., Shi, G.-H., 2012. Simulating hydraulic fracturing with discontinuous deformation analysis. In: US Rock Mechanics/Geomechanics Symposium, Chicago, IL, June 24–27, 2012.

Borja, R.I., 2008. Assumed enhanced strain and the extended finite element methods: a unification of concepts. Computer Methods in Applied Mechanics and Engineering 197, 2789–2803.

Commer, M., Hoversten, G.M., Um, E.S., 2015. Transient-electromagnetic finite-difference time-domain earth modeling over steel infrastructure. Geophysics 80, E147–E162.

Coussy, O., 1995. Mechanics of Porous Continua. John Wiley and Sons, Chichester, UK.

Dean, R.H., Schmidt, J.H., 2009. Hydraulic fracture predictions with a fully coupled geomechanical reservoir simulation. SPE Journal 14 (4), 707–714.

Economides, M.J., Nolte, K.G., 2000. Reservoir Stimulation. John Wiley and Sons, Chichester, UK.

Fu, P., Johnson, S.M., Carrigan, C.R., 2012. An explicitly coupled hydro-geomechanical model for simulating hydraulic fracturing in arbitrary discrete fracture networks. International Journal for Numerical and Analytical Methods in Geomechanics 37 (14), 2278–2300.

Gidley, J.L., Holditch, S.A., Nierode, D.E., Ralph, W., Veatch, R.W., 1990. Recent advances in hydraulic fracturing. SPE Monograph Series 12.

Hoversten, G.M., Commer, M., Haber, E., Schwarzbach, C., 2015. Hydro-frac monitoring using ground time-domain electromagnetics. Geophysical Prospecting 63, 1508–1526.

Hughes, T.J.R., 1987. The Finite Element Method: Linear Static and Dynamic Finite Element Analysis. Prentice-Hall, Englewood Cliffs, NJ.

Ji, L., Settari, A., Sullivan, R.B., 2009. A novel hydraulic fracturing model fully coupled with geomechanics and reservoir simulation. SPE Journal 14 (3), 423–430.

Kim, J., Moridis, G.J., 2013. Development of the T+M coupled flow-geomechanical simulator to describe fracture propagation and coupled flow-thermal-geomechanical processes in tight/shale gas systems. Computers & Geosciences 60, 184–198.

Kim, J., Tchelepi, H.A., Juanes, R., 2011. Stability and convergence of sequential methods for coupled flow and geomechanics: fixed-stress and fixed-strain splits. Computer Methods in Applied Mechanics and Engineering 200, 1591–1606.

Mavko, G., Mukerji, T., Dvorkin, J., 2009. The Rock Physics Handbook: Tools for Seismic Analysis of Porous Media. Cambridge University Press, Cambridge.

Moes, N., Dolbow, J., Belytschko, T., 1999. A finite element method for crack growth without remeshing. International Journal for Numerical Methods in Engineering 46, 131–150.

Patzer, C., Tietze, K., Ritter, O., 2017. Steel-cased wells in 3-D controlled source EM modelling. Geophysical Journal International 209, 813–826.

Schenkel, C.J., Morrison, H.F., 1994. Electrical resistivity measurement through metal casing. Geophysics 59, 1072–1082.

Schlumberger, 2009. Log Interpretation Charts.

Um, E.S., Commer, M., Newman, G.A., Hoversten, G.M., 2015. Finite element modelling of transient electromagnetic fields near steel-cased wells. Geophysical Journal International 202, 901–913.

Valko, P., Economides, M.J., 1995. Hydraulic Fracture Mechanics. John Wiley & Sons, New York.

Vermylen, J.P., Zoback, M.D., 2011. Hydraulic fracturing, microseismic magnitudes, and stress evolution in the Barnett Shale, Texas, USA. In: SPE Hydraulic Fracturing Technology Conference, Woodland, Texas, 24–26 January, 2011.

Warpinski, N.R., Kramm, R.C., Heinze, J.R., Waltman, C.K., 2005. Comparison of single- and dual-array microseismic mapping techniques in the Barnett shale. In: SPE ATCE, Dallas, TX, October 9–12, 2005.

Waxman, M.H., Smits, L.J.M., 1968. Electrical conductivities in oil-bearing shaly sands. SPE Journal 8, 107–122.

Witherspoon, P.A., Wang, J.S.Y., Iwai, K., Gale, J.E., 1980. Validity of cubic law for fluid flow in a deformable rock fracture. Water Resources Research 16, 1016–1024.

Zhang, X.P., Wong, L.N.Y., 2013. Loading rate effects on cracking behavior of flaw-contained specimens under uniaxial compression. International Journal of Fracture 180 (1), 93–110.

FURTHER READING

Johnson, R., Shrallow, J., 2011. Ambiguity in Microseismic Monitoring. SEG Annual Meeting Abstract.

Oldenburg, C., Borglin, S.E., Moridis, G.J., 2000. Numerical simulation of ferrofluid flow for subsurface environmental applications. Transport in Porous Media 38, 319–344.

Chapter 3

Simulation of Multistage Hydraulic Fracturing in Unconventional Reservoirs Using Displacement Discontinuity Method (DDM)

Yuan Di[1], **Huiying Tang**[2]
[1]*Peking University, Beijing, China;* [2]*Southwest Petroleum University, Chengdu, China*

Multistage hydraulic fracturing has become a common practice to extract oil and gas from unconventional reservoirs with extremely low permeability. After hydraulic fracturing, an extended fracture network is created to enlarge the contacting area between the wellbore and rock matrix, which could significantly promote the production rate. Placing multiple hydraulic fractures in a horizontal well is a highly effective method to increase per well production. However, multiple, closely spaced fractures could introduce strong interactions among the fractures, often referred to as the "stress shadow" effect. The effect could lead to reduction in fracture width, greater risk of screen-out, and possible change of fracture direction (Yew and Weng, 2014). The model for multistage hydraulic fracturing in unconventional reservoirs should take such stress shadow effect into consideration to properly design the stage length and perforation spacing to achieve optimal performance. In the following sections, a brief explanation of "stress shadow" effect will be given. The current numerical models for multistage hydraulic fracturing are also reviewed. Then, a coupled hydromechanical model based on displacement discontinuity method (DDM), which is capable of considering the stress interactions among hydraulic fractures, is introduced and the applications of this model are followed.

Hydraulic Fracture Modeling. https://doi.org/10.1016/B978-0-12-812998-2.00003-5

3.1 STRESS SHADOW EFFECT

3.1.1 Theoretical Analysis

Sneddon (Sneddon and Elliott, 1946) gave an analytical solution for the stress distribution in the neighborhood of a 2D crack under plane strain assumption in a homogeneous isotropic elastic solid under an internal pressure. This analytical solution laid the foundation of hydraulic fracturing models (Geertsma and De Klerk, 1969; Perkins and Kern, 1961) and can be used to illustrate the stress perturbation caused by an existing hydraulic fracture, which could help explain the effect of stress shadowing on closely spaced hydraulic fractures. The induced stress increments in different directions at $z = 0$ as shown in Fig. 3.1 can be written in the following forms:

$$\begin{aligned}
\Delta\sigma_x &= p_n\left[1 - \frac{x^3}{\left(h_f^2/4 + x^2\right)^{3/2}}\right] \\
\Delta\sigma_z &= p_n\left[1 - \frac{xh_f^2/2 + x^3}{\left(h_f^2/4 + x^2\right)^{3/2}}\right] \\
\Delta\sigma_y &= v(\Delta\sigma_x + \Delta\sigma_z)
\end{aligned} \tag{3.1}$$

where p_n is the internal pressure, h_f is the height of the fracture, and v is the Poisson's ratio.

The change of stress along x direction at $z = 0$ is shown in Fig. 3.2. The compressional stress takes the positive sign in this chapter. From the analytical solution, it is known that the opened fracture will induce extra stresses in the domain; thus, the preexisting or other simultaneously propagating fractures could change the stress state of the current fractures, which results in complex

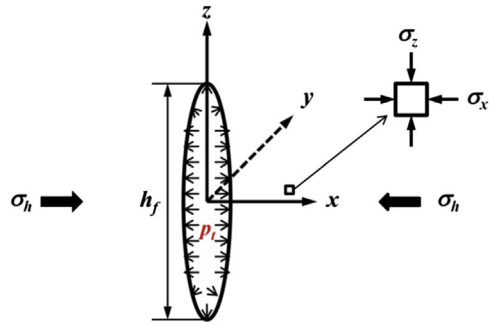

FIGURE 3.1 Schematic of a cross-sectional cut in minimum horizontal stress direction (x direction), which propagates along the maximum horizontal stress direction (y direction) (Dohmen et al., 2014).

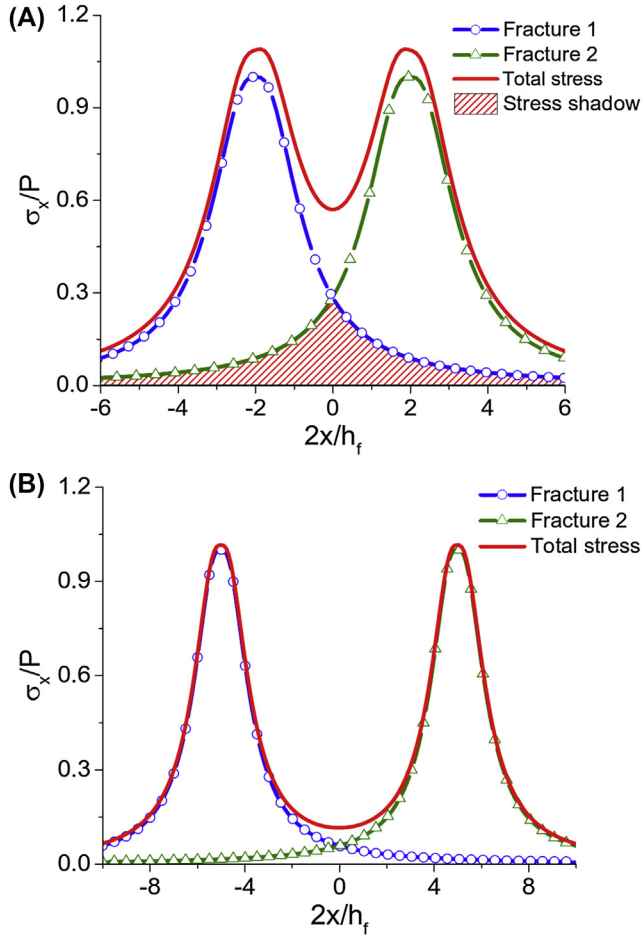

FIGURE 3.2 Distribution of σ_x when two fractures with equal internal pressure exist. The spacings of the fractures are (A) 2 h_f and (B) 5 h_f.

fracture geometries and uneven fracture distributions. Fig. 3.2A and B shows the x stress distribution when two fractures are spaced at 2 h_f and 5 h_f, respectively. The area with red dashed lines, where both fractures induce significant stress perturbations, is the region of stress shadow. When new fractures initiate from the shadowed area, they are under larger compressional stress than the preexisting fractures on the boundaries. The growth of the inner fracture will be retarded or even stopped.

The stress shadow effect not only includes the change of compressional stress applied on fracture surfaces due to the deformations of other fractures, but also the reorientation of stress state, which is an important consequence of the stress interactions among multiple fractures.

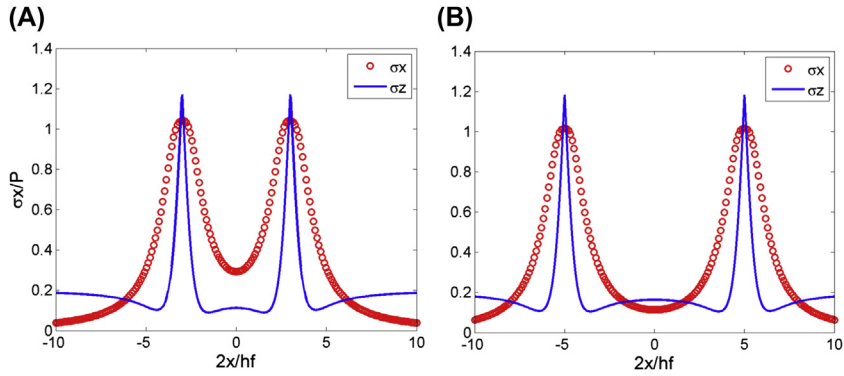

FIGURE 3.3 Distribution of σ_x and σ_z when two fractures with equal internal pressure exist. The spacings between the fractures are (A) 1.5 h_f and (B) 2.5 h_f.

As can be seen from Fig. 3.3, the compression in x direction increases faster than in z direction especially when fractures are placed quite close, which implies the possibility of stress altering the direction of minimum horizontal stress. Because hydraulic fractures are prone to propagate along the direction of least resistance (i.e., the direction perpendicular to minimum horizontal stress), fracture direction could be altered when more than one fracture exists. In multistage hydraulic fracturing, a large number of fractures will be created during the operations. The spacing between perforation clusters could be less than 50 ft (Miller et al., 2011), at which distance the stress shadow effect could be prominent. In the following sections, we will discuss the observations of stress shadowing in experiments and field.

3.1.2 Experimental Observations

The stress shadow effect has also been observed in experiments. Experiments conducted on glass plates with cooling effect showed the stress interactions between simultaneously propagating cracks (Geyer and Nemat-Nasser, 1982). Fig. 3.4 shows the geometries of the cracks after cooling the bottom side. In Fig. 3.4, the glass plate was initially heated to 52°C. When the temperature was homogeneous in the material, evenly distributed cracks were created at the bottom side each with a length of 13 mm and spacing 25 mm. Then, the bottom side was cooled to room temperature. Due to the shrinkage of glass on cooling, tensile stress was generated in the plate, which induced the growth of the initially placed small cracks. As shown in Fig. 3.4, uneven propagation can be observed, and the growth of the cracks between two long cracks was obviously compressed. This experiment illustrated the stress interference between growing fractures, which provided the evidence of the existence of stress shadow effect.

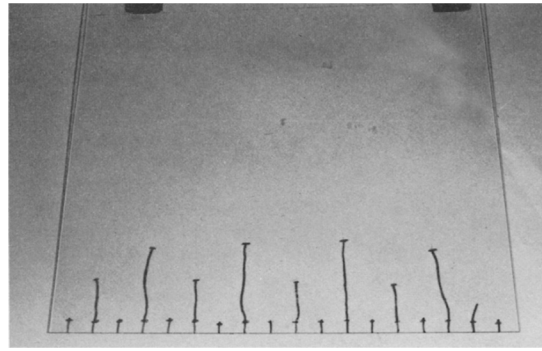

FIGURE 3.4 Geometries of initially equally spaced cracks after cooling the bottom side of the glass plate (Geyer and Nemat-Nasser, 1982).

This experiment was conducted with glass, and the fractures were generated by thermal stress. A hydraulic fracturing experiment was carried out by Abass et al. (1996), which gave better approximations of the field situations. Abass' experiments were aimed to investigate the nonplanar fracture propagation when multiple transverse fractures propagated parallelly or alternatively. Fig. 3.5 is the experimental result when two fractures propagated toward each other with initial offsets. The fracture tips in the middle of perforations propagated slower than the outside wings, which was also the result of stress shadowing between the two fractures. The curving of inner wings was also observed due to the reorientations of stress states.

3.1.3 Field Observations

Stress shadow effect has not only been investigated by theoretical and experimental methods, but also been observed in field measurements. Dohmen et al. (2014) gave an example well in Utica Shale where microseismic events

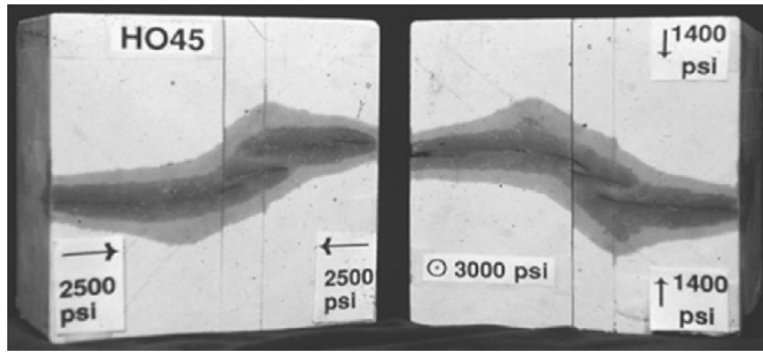

FIGURE 3.5 Fracture geometries after alternative hydraulic fracturing. The stress states were depicted on the rock sample (Abass et al., 1996).

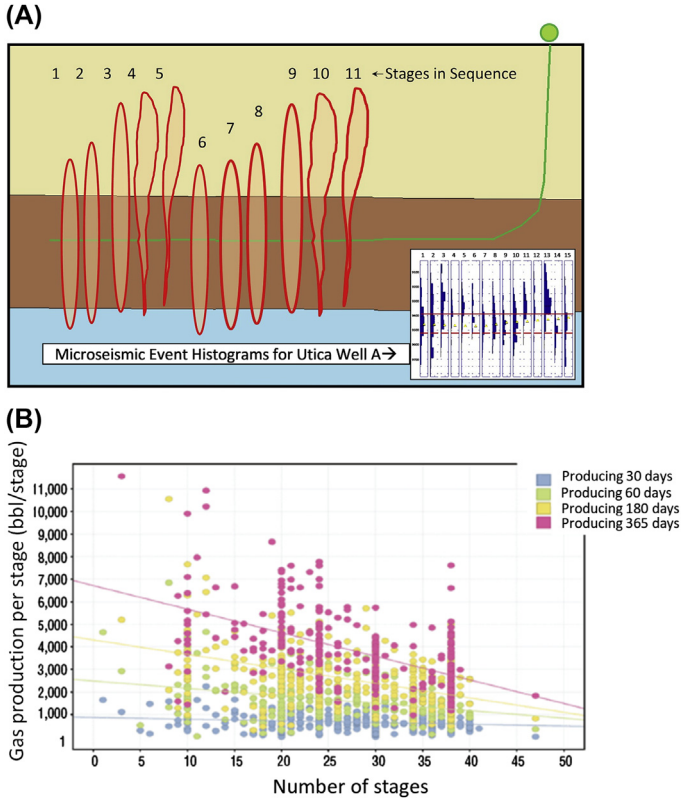

FIGURE 3.6 (A) The microseismic events of a horizontal well in Utica Shale and the schematic of the hydraulic fractures along the wellbore. (B) The relationships between number of stages and production per stage (Dohmen et al., 2014).

showed a clear upward trend along the horizontal borehole as shown in Fig. 3.6A. Dohmen explained the escape of microseismic data from the target zone to upper layers as a result of the extra compression applied on current fractures by previously fractured stages. The compressional stresses in the completion layer were increased by the deformations of hydraulic fractures; thus, the fractures were pushed out and propagated upward because the shadow layers had less in situ stress than deeper layers due to the gravitational effect. In Dohmen's paper, it is also pointed out that the productivity of fractured stages could be influenced by the density of fractures. Fig. 3.6B showed that the more the number of stages along the horizontal well, the less the productivity of each stage, which suggests that very closely spaced fractures may render the final performance, and this phenomenon can be partially explained by the stress shadow effect.

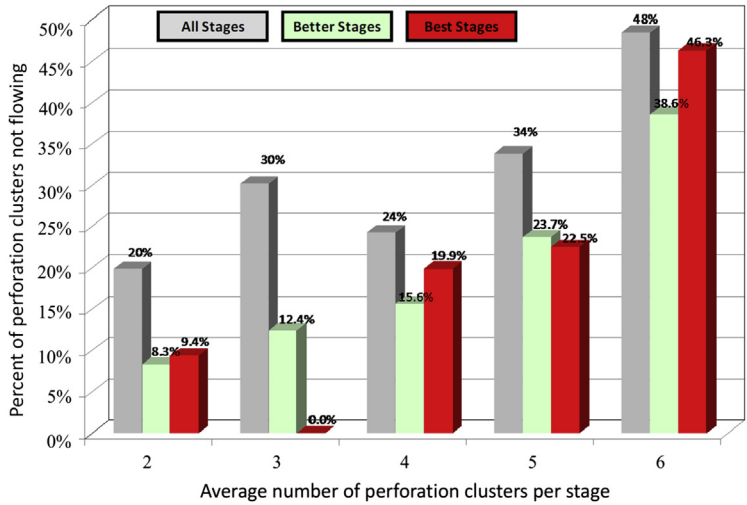

FIGURE 3.7 The relationship between percentage of ineffective perforation clusters and density of clusters per stage (Miller et al., 2011) (better stages represent the stages with production rate 110%−150% higher than the average production rate per stage of all stages; best stages represent the stages with production rate over 150% higher than the average production rate per stage of all stages).

Miller et al. (2011) summarized the treatment operations of more than 100 horizontal wells conducted in main shale gas basins in the United States. The measurement data from FloScan Imager showed that over 30% clusters did not contribute to the production. Meanwhile, the number of ineffective clusters was strongly correlated to the density of clusters in horizontal wells (Fig. 3.7). Similar with the observations in Fig. 3.6B, the production rate was not scalable to the number of perforations. The increase in clusters (i.e., the reduction in fracture spacing) could not bring significant production promotion as expected.

The occurrence of ineffective perforation clusters could also result from the heterogeneity of rock properties or stress distributions. In this chapter, we discuss only the role of the stress interactions among hydraulic fractures in deciding the performance of horizontal wells after stimulations.

3.2 NUMERICAL APPROACHES FOR MULTISTAGE HYDRAULIC FRACTURING IN UNCONVENTIONAL RESERVOIRS

To quantify the stress interactions between hydraulic fractures, numerous models using different numerical methods have been proposed to study the propagation of multiple hydraulic fractures. These models can be divided into three groups: static fracture analysis; fracture propagation modeling; and

coupled wellbore fracture propagation modeling. The static fracture analysis assumed the hydraulic fractures to be of equal length and internal pressure. Astakhov and Germanovich (2000) investigated the width variations when a fluid is passing through a set of parallel joints. Using boundary allocation method, they found the inner joints might be closed by the compression from outer joints, which could not provide highly conductive flow path for hydrocarbons. Rafiee et al. (2012) analyzed the stress difference and orientation changes with different fracture spacing using DDM. Cheng (2012a,b) compared the well performance when changing the distance between hydraulic fractures. It was found that the production enhancement by adding more fractures was not significant when the spacing was already quite small.

The aforementioned work investigated the stress shadowing at the situation when multiple fixed-length fractures exist. However, the propagation of hydraulic fractures is a dynamic process, which is controlled by the reservoir conditions as well as the treatment parameters. Olson (2008) used the 2D DDM to model the elastic deformations of multiple parallel fractures. The internal pressure was assumed to be constant, and fracture propagation velocity is dominated by the stress intensity factor at the fracture tips. Sesetty and Ghassemi (2013) analyzed the influence of fracturing sequence on the effectiveness of fracturing operations. In their paper, the injection rate in each fracture was taken to be the same. In Fig. 3.7, the flow rate in each fracture is not equal. The alternation of stress condition will also change the portion of fluid each perforation cluster could take. A more comprehensive understanding of the multistage hydraulic fracturing requires a model that could consider the fluid flow within wellbore. Lecampion and Desroches (2015) modeled the propagation of multiple radial-shaped fractures with 3D DDM and explicitly simulated the fluid flow in horizontal wells with finite difference method. From Lecampion's simulation results, the inner fractures endured more compression than the outer fracture, which also weakened their ability to take fluid from wells. The propagation of inner fractures was further restricted by the loss of injection fluid. Olson and Wu (2012) used an analytical model for wellbore flow and coupled it with 2D DDM, and conclusions similar with those of Lecampion that the uneven partitioning of fluid among fractures could significantly affect the extent each fracture grew were drawn. Cheng et al. (2016) deducted a semianalytical solution for the propagation of multiple radial fractures with the consideration of wellbore flow and perforation friction. With this semianalytical method, efficient optimization of fracture placement could be achieved. In this chapter, a planar-3D multistage hydraulic fracturing simulation model is proposed based on the DDM, and it is capable of calculating the stress interactions between hydraulic fractures and considers the proppant transport and wellbore fluid flow. A fully hydromechanical coupled numerical program entitled UFrac is also developed. The stress shadow effects in unconventional reservoir stimulation are systematically analyzed.

3.3 SIMULATION OF MULTISTAGE HYDRAULIC FRACTURING IN UNCONVENTIONAL RESERVOIRS USING DISPLACEMENT DISCONTINUITY METHOD

To simulate the simultaneous propagation of multiple fractures and the dynamic partitioning of fluid flow in wellbore, stress interference among fractures should be taken into consideration.

Here, we introduce a planar 3D multiple fracture propagation model using DDM, which fixes the fracture planes to be perpendicular to minimum in situ stress. The assumption of planar 3D geometry can be satisfied when stress difference is strong enough to prevent the fracture curving caused by fracture deformation—induced stresses. Otherwise, nonplanar fracture propagation model should be used (Kumar and Ghassemi, 2016).

Several other important assumptions are made in the model introduced below. We assume the in situ stress state is in a normal faulting regime where the vertical stress is the maximum principal stress. The horizontal wells are assumed to have been drilled along the direction of minimum horizontal stress so that transverse hydraulic fractures will be generated. Hydraulic fractures are assumed to be fully filled with fluid so that no fluid lag exists between fracture front and fluid front. Under the high confining stress in typical shale reservoirs, fluid lag will vanish quickly based on the asymptotic solution analysis (Lecampion and Desroches, 2015).

The model consists of two major parts: the wellbore and the fractures. High-pressure fracturing fluid is pumped into a selected section of the wellbore, and the well pressure increases due to the compression from continuous fluid injection. Hydraulic fractures initiate under this high pressure and extend into the intact reservoir rock. The wellbore and fracture parts are fully coupled to build an integrated numerical frame to simulate the fracturing process (Tang et al., 2016).

Similar with Adachi et al. (2007), hydraulic fracturing fluid, or slurry, is treated as a mixture of interpenetrating fluid and solid components. The fluid components consist mostly of water with some additives, such as gels, surfactants, cross-linkers, friction reducers, and breakers that affect fluid rheology. These fluid additives have a variety of purposes—as inhibitors, acids, biocides, and corrosion inhibitors. The solid components, called proppants, are added to stop the newly formed fractures from closing. Proppant size is assumed to be small enough compared with the fracture width so that proppant distribution can be described by volume fraction. When fracture width approaches proppant size, a block function is used to avoid nonphysical proppant transport.

The model described in this chapter is an extension of the model in Chapter 8, which uses the DDM formulations to calculate the deformation of fractures. The characterization of fluid, calculation of fracturing fluid flow in fractures, modeling of wellbore flow, and temperature redistribution in fractures

and wells are the same with Chapter 8, which will not be described here. In Chapter 8, a principal-stress correction method has been introduced to model the stress shadow effect among multiple propagating fractures. This method helps to make quick estimation of the stress interference based on the superposition of stresses induced by other fractures. However, this method only provides approximation of the fracture-induced stresses by assuming the fractures to be rectangular and is not fully coupled with the flow equations. In this chapter, we will introduce the DDM, which delivers more rigorous calculation of the stress interactions among different fractures. Other modifications of the model in Chapter 8 will also be presented.

3.3.1 Governing Equations for Hydraulic Fracture Growth

The hydraulic fracture is assumed to be planar and perpendicular to the minimum principal stress σ_h. The fracture surface is divided into a series of rectangular grids of size $2a \times 2b$ (a and b are half element lengths in x_1 and x_2 directions as shown in Fig. 3.8). Each element has its local coordinate system with x_3-axis along the normal direction. Before hydraulic fracturing, all fracture grids are defined to be inactive with zero displacements. When the high-velocity fluid is injected, the well pressure, calculated with equations in earlier sections, will build up until fractures start to initiate from the well wall. The fracture grid connecting to the borehole, which is also the first grid being activated, is called the initiation element. As pumping continues, the hydraulically induced fracture will propagate further into the intact reservoir rock to activate more fracture elements.

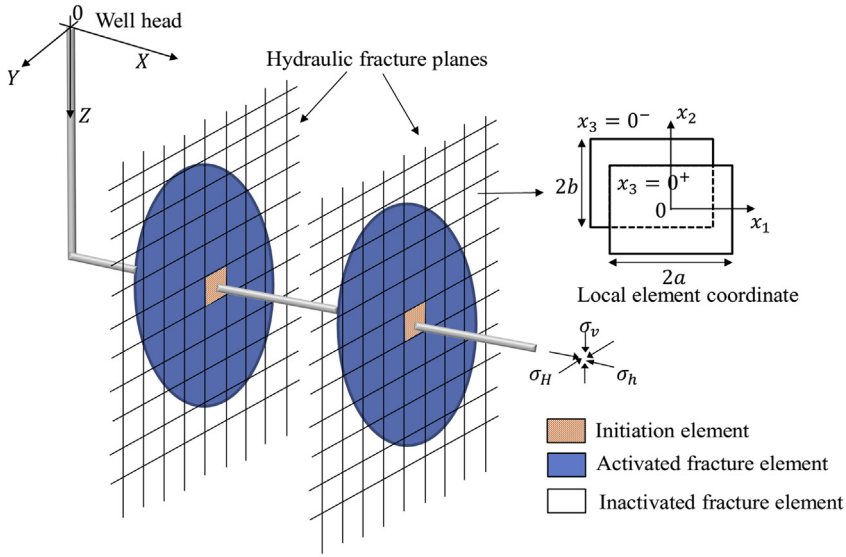

FIGURE 3.8 Schematic of fracture propagation model.

3.3.1.1 Elasticity

Fracture deformations are calculated with the 3D DDM proposed by Okada (1985). It is based on the analytical, elastic solutions of the normal and shear displacements of a finite rectangular discontinuity in half-space. The general idea of DDM is to approximate the distribution of displacement discontinuities of a crack by discretizing it into elements. Knowing the analytical solution of stresses induced by one crack element, the numerical solution of the whole domain can be calculated by superposition. The unknown displacements are obtained by satisfying the boundary conditions on fracture surfaces. DDM is an indirect boundary element method that solves the displacement discontinuities of each fracture element instead of solving the stresses or displacements at the boundaries directly like other boundary element methods. The stress or displacement at any point in the domain is then calculated from the displacement discontinuities. Another indirect boundary element is the fictitious stress method (Crouch et al., 1983), which assumes there is a fictitious stress applied on the boundary element that results in the current stress state. Then these fictitious stresses are solved to get the distribution of other mechanical variables. The poroelastic effect can also be considered with DDM (Tao and Ghassemi, 2010). However, we do not include this mechanism in our model for the reason that the permeability of unconventional reservoir is extremely low, and thus only a small amount of fluid can leak off into the formation, which will not affect stress distribution significantly especially within the short stimulation period.

The displacements of each fracture element are defined in the local coordinate (Fig. 3.9) with z-axis along the normal displacement direction:

$$\begin{aligned} D_x &= u_x(x,y,0^-) - u_x(x,y,0^+) \\ D_y &= u_y(x,y,0^-) - u_y(x,y,0^+) \\ D_z &= u_z(x,y,0^-) - u_z(x,y,0^+) \end{aligned} \tag{3.2}$$

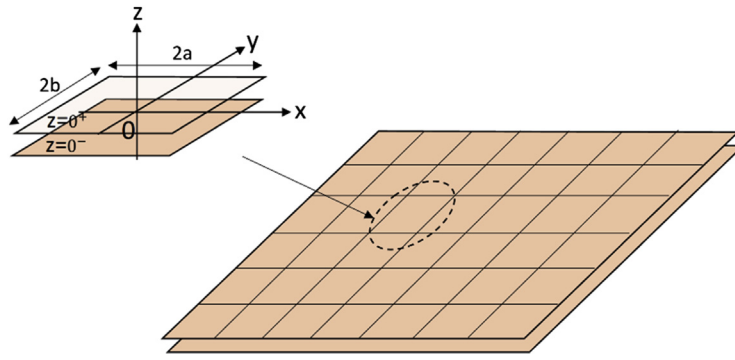

FIGURE 3.9 Schematic of rectangular fracture element.

The displacements and stresses induced by the displacement discontinuities in Eq. (3.2) can be expressed as (Okada, 1985):

$$
\begin{aligned}
u_x &= C\{[2(1-v)I_{,z} - zI_{,xx}]D_x - zI_{,xy}D_y - [(1-2v)I_{,x} + zI_{,xz}]D_z\} \\
u_y &= C\{-zI_{,xy}D_x + [2(1-v)I_{,z} - zI_{,yy}]D_y - [(1-2v)I_{,y} + zI_{,yz}]D_z\} \\
u_x &= C\{[(1-2v)I_{,x} - zI_{,xz}]D_x + [(1-2v)I_{,y} - zI_{,yz}]D_y + [2(1-v)I_{,z} - zI_{,zz}]D_z\} \\
\sigma_{xx} &= 2C\{[2I_{,xz} - zI_{,xxx}]D_x + [2vI_{,yz} - zI_{,xxy}]D_y + [I_{,zz} + (1-2v)I_{,yy} - zI_{,xxz}]D_z\} \\
\sigma_{yy} &= 2C\{[2vI_{,xz} - zI_{,xyy}]D_x + [2I_{,yz} - zI_{,yyy}]D_y + [I_{,zz} + (1-2v)I_{,xx} - zI_{,yyz}]D_z\} \\
\sigma_{zz} &= 2C\{-zI_{,xzz}D_x - zI_{,yzz}D_y + [I_{,zz} - zI_{,zzz}]D_z\} \\
\tau_{xy} &= 2C\{[(1-v)I_{,yz} - zI_{,xxy}]D_x + [(1-v)I_{,xz} - zI_{,xyy}]D_y - [(1-2v)I_{,xy} + zI_{,xyz}]D_z\} \\
\tau_{yz} &= 2C\{-[vI_{,xy} + zI_{,xyz}]D_x + [I_{,zz} + vI_{,xx} - zI_{,yyz}]D_y - zI_{,yzz}D_z\} \\
\tau_{zx} &= 2C\{[I_{,zz} + vI_{,yy} - zI_{,xxz}]D_x - [vI_{,xy} + zI_{,xyz}]D_y - zI_{,xzz}D_z\}
\end{aligned}
\tag{3.3}
$$

where v is the Poisson's ratio; subscripts x, y, and z denote the derivation operations; and C is an elastic constant relating to the rock mass's mechanical properties:

$$
C = \frac{1}{8\pi(1-v)} \tag{3.4}
$$

The function I in Eq. (3.3) is the Green's function of a half infinite space, which can be expressed as:

$$
I(x,y,z) = \iint_S \left[(x-\xi)^2 + (y-\eta)^2 + z^2\right]^{-1/2} d\xi d\eta \tag{3.5}
$$

The expressions of the derivatives of function I in Eq. (3.5) are:

$$
\begin{aligned}
&I_{,x} = \ln(r+\overline{y})||, \quad I_{,y} = \ln(r+\overline{x})||, \quad I_{,z} = -\arctan\left(\frac{\overline{x}\,\overline{y}}{zr}\right)|| \\
&I_{,xx} = \frac{\overline{x}}{r(r+\overline{y})}||, \quad I_{,yy} = \frac{\overline{y}}{r(r+\overline{x})}||, \quad I_{,zz} = \frac{\overline{x}\,\overline{y}(z^2+r^2)}{r\left(z^2+(\overline{y})^2\right)\left(z^2+(\overline{x})^2\right)}|| \\
&I_{,xy} = \frac{1}{r}||, \quad I_{,xz} = \frac{z}{r(r+\overline{y})}||, \quad I_{,yz} = \frac{z}{r(r+\overline{x})}|| \\
&I_{,xxx} = -\frac{(r+\overline{y})(\overline{x}^2 - r^2) + \overline{x}^2 r}{r^3(r+\overline{y})^2}||, \quad I_{,xxy} = -\frac{\overline{x}}{r^3}||, \quad I_{,xxz} = -\frac{\overline{x}z(2r+\overline{y})}{r^3(r+\overline{y})^2}|| \\
&I_{,yyy} = -\frac{(r+\overline{x})(\overline{y}^2 - r^2) + \overline{y}^2 r}{r^3(r+\overline{x})^2}||, \quad I_{,xyy} = -\frac{\overline{y}}{r^3}||, \quad I_{,yyz} = -\frac{\overline{y}z(2r+\overline{x})}{r^3(r+\overline{x})^2}|| \\
&I_{,xzz} = -\frac{(r+\overline{y})(z^2 - r^2) + z^2 r}{r^3(r+\overline{y})^2}||, \quad I_{,xyz} = -\frac{z}{r^3}||, \quad I_{,yzz} = -\frac{(r+\overline{x})(z^2 - r^2) + z^2 r}{r^3(r+\overline{x})^2}|| \\
&I_{,zzz} = -z\overline{x}\,\overline{y}\frac{\left(z^2+\overline{x}^2\right)^2\left(z^2+\overline{y}^2+2r^2\right) + \left(z^2+\overline{y}^2\right)^2\left(z^2+\overline{x}^2+2r^2\right)}{r^3\left(z^2+\overline{x}^2\right)^2\left(z^2+\overline{y}^2\right)^2}||
\end{aligned}
\tag{3.6}
$$

The notation || denotes the operation as below:

$$I(\xi,\eta)|| = I(a,b) - I(a,-b) - I(-a,b) + I(-a,-b) \tag{3.7}$$

Other parameters in Eq. (3.6) have the following expressions:

$$r = \sqrt{(x-\xi)^2 + (y-\eta)^2 + z^2}, \quad \theta = \arctan\left(\frac{(x-\xi)(y-\eta)}{rz}\right)$$
$$\bar{x} = (x-\xi), \qquad \bar{y} = (y-\eta) \tag{3.8}$$

For opened fractures, the total normal stress equals to the fluid pressure, and both strike and dip shear stresses are zero on no-slip fracture surfaces. The stresses applied on the fracture element consist of the in situ stresses and the stresses induced by other elements. The stresses calculated from Eq. (3.3) are defined in the local coordinate of each element. To calculate the induced stresses applying on one element in the normal and shearing directions, the stress tensor should be rotated to the coordinate of the current element to get the following expressions:

$$\begin{aligned}
0 = \tau^i_{xz} &= \sum_j^N A^{ij}_{xx} D^j_x + \sum_j^N A^{ij}_{xy} D^j_y + \sum_j^N A^{ij}_{xz} D^j_z + \tau^i_{xz,0} \\
0 = \tau^i_{yz} &= \sum_j^N A^{ij}_{yx} D^j_x + \sum_j^N A^{ij}_{yy} D^j_y + \sum_j^N A^{ij}_{yz} D^j_z + \tau^i_{yz,0} \\
-p_i = \sigma^i_z &= \sum_j^N A^{ij}_{zx} D^j_x + \sum_j^N A^{ij}_{zy} D^j_y + \sum_j^N A^{ij}_{zz} D^j_z + \sigma^i_{z,0}
\end{aligned} \tag{3.9}$$

where the subscript 0 denotes the in situ stresses. A^{ij} is the influence coefficient, which can be derived from Eq. (3.3) by rotating the stress tensor from element j's local coordinate to element i's coordinate system.

3.3.1.2 Fluid Flow

The openings of fractures are functions of fluid pressure as discussed in the previous section. To obtain the pressure distribution along fractures, a series of fluid flow equations are solved with finite volume method. Slurry equations are first solved to get the mixture velocity. A mass balance equation for each individual component is then solved to update the volume fractions. The general mass conservation equation and momentum equation of the multicomponent slurry are given below:

$$\nabla\cdot\left(\rho_{sl}\vec{v_{sl}}\, w\right) + \frac{\partial}{\partial t}(\rho_{sl} w) + \dot{q}_{sl,wf} - \dot{q}_{\text{leak}}\left(1 - \sum_p c_p\right)\sum_f x_f \rho_f w = 0 \tag{3.10}$$

$$\vec{v_{sl}} = -\frac{k}{\mu_{sl}}\nabla(p + \gamma z) \tag{3.11}$$

where ρ_{sl} is slurry density, $\vec{v_{sl}}$ is overall slurry velocity, w is fracture width, $\dot{q}_{\text{leak}}$ is the leak-off mass flow rate, and $\dot{q}_{sl,wf}$ is the mass exchange between

borehole and fractures. p denotes fluid pressure, μ_{sl} is slurry viscosity, and γ is the hydrostatic gradient. Because matrix permeability in unconventional reservoirs is extremely low, it would be difficult for solid components to flow into the matrix. Thus the leak-off of proppant is neglected. The permeability k can be calculated by assuming that the shape of fracture is a slit:

$$k = \frac{w^2}{12} \tag{3.12}$$

The one-dimensional Carter's leak-off model (Howard and Fast, 1957) is used to model fluid leak-off from fractures into the surrounding matrix:

$$\dot{q}_{\text{leak}} = \frac{C_{\text{leak}}}{\sqrt{t-\tau}} \tag{3.13}$$

where C_{leak} is the leak-off coefficient, τ is the time when fluid first arrives, and t is the current time. Fluid components are assumed to have the same velocity as the slurry, and the slip between proppant and carrying fluid is characterized by gravity-induced settlement:

$$\begin{aligned} v_{fl,x} &= v_{sl,x}; \quad v_{p,x} = \chi v_{sl,x} \\ v_{fl,z} &= v_{sl,z}; \quad v_{p,z} = \chi\left(v_{sl,z} + v_{p,stl}\right) \end{aligned} \tag{3.14}$$

where the subscript x denotes the direction along fracture length, z denotes the direction parallel to the gravity acceleration vector g, fl represents fluid component, p is the proppant component, $v_{p,stl}$ is the settling velocity of proppant relative to slurry, and χ is the block function used to account for proppant bridging, which will be introduced later. Friehauf (2009) presented expressions for proppant velocity in terms of slurry velocity and other variables. Correction factors were introduced that account for inertial effects, the effect of interfering proppant particles, and the effect of the fracture wall. The proppant settling velocity has the form:

$$v_{stl,z} = v_{\text{stokes}} f(N_{re}) g(c_p) h(w) \tag{3.15}$$

where v_{stokes} is the Stoke's settling velocity, $f(N_{re})$ captures inertial effects, $g(c_p)$ models the effect of interfering proppant particles, and $h(w)$ represents the effect of the fracture walls. These expressions are in the forms:

$$\begin{aligned} v_{\text{stokes}} &= \frac{\left(\rho_p - \rho_f\right) g_{\text{frac}} d_p^2}{18\mu_{fl}} \\ f(N_{re}) &= \frac{0.3736\mu_{fl}^{0.57}}{\rho_f^{0.29}\left(\rho_p - \rho_{fl}\right)^{0.29} d_p^{0.86}} \\ g(c_p) &= -5.9\left(\sum_p c_p\right)^3 + 8.8\left(\sum_p c_p\right)^2 - 4.8\left(\sum_p c_p\right) + 1 \end{aligned} \tag{3.16}$$

where d_p is proppant diameter and g_{frac} is the gravity constant projected on the fracture plane. The above expressions for proppant settling velocity are based

on the assumption of spherical particle shape. If irregular or nonspherical proppants are to be considered, the applicability of Friehauf's model should be carefully validated.

Different from Chapter 8, a block function introduced by Shiozawa and McClure (2016) is used to capture proppant bridging when the fracture width is comparable to the proppant diameter.

$$\chi = \begin{cases} 1 & \text{if} \quad w \geq N_{\max} d_p \\ \dfrac{w - N_{\min} d_p}{(N_{\max} - N_{\min}) d_p} & \text{if} \quad N_{\min} d_p \leq w < N_{\max} d_p \\ 0 & \text{if} \quad w < N_{\min} d_p \end{cases} \tag{3.17}$$

Proppants can flow into or out of the fracture element only when fracture aperture is greater than $N_{\min}$ times the proppant diameter. The block function increases linearly from 0 to 1 when the ratio of fracture element width to proppant diameter changes from $N_{\min}$ to $N_{\max}$. Without loss of generality, we choose $N_{\min}$ and $N_{\max}$ to be 2 and 3, respectively.

After calculating the velocities of fluid and solid components, the volume concentration of each component is calculated with mass conservation in the form of advective equations:

$$\begin{aligned} &\nabla \cdot \left[\rho_f \vec{v}_{fl}\, x_f \left(1 - \sum_p c_p \right) w \right] + \frac{\partial}{\partial t} \left[\rho_f x_f \left(1 - \sum_p c_p \right) w \right] - \dot{q}_f = 0 \\ &\nabla \cdot \left[\vec{v}_p\, c_p w \right] + \frac{\partial}{\partial t} [c_p w] - \dot{q}_p = 0 \end{aligned} \tag{3.18}$$

With the above equations, the fluid volume fraction x_f and proppant concentration c_p at the current time step can be solved. Finally, by neglecting pressure loss due to perforation friction, the mass exchange between the wellbore and hydraulic fracture $\dot{q}_{sl,wf}$ is calculated according to Peaceman's (1978) formulation of well index.

$$\dot{q}_{sl,wf} = \frac{T_{wf} \rho_{sl} (P_w - P_f)}{4ab} = \frac{WI \rho_{sl} (P_w - P_f)}{4ab \cdot \mu_{sl}} \tag{3.19}$$

$$WI = -\frac{2\pi k_f w}{\ln(r_w / r_0)}, \quad r_0 = 0.14\sqrt{a^2 + b^2} \tag{3.20}$$

where r_w is the well radius, and a and b are the sizes of initiation fracture element (Fig. 3.8).

3.3.1.3 Fracture Initiation and Propagation

Assuming the formation rock is linear elastic and has a tensile failure strength T_0, the breakdown pressure $P_{b,w}$ for fracturing the surface of the borehole can be calculated with elasticity theory (Timoshenko and Goodier, 1951) to give:

$$P_{b,w} = 3\sigma_h - \sigma_H - P_p + T_0 \tag{3.21}$$

Strictly speaking, the above equation is only applicable to open-hole completion and axial initiation of hydraulic fractures. However, even for horizontal wells where the eventual hydraulic fracture orients transversely to the well and perpendicular to minimum horizontal stress, axial initiation is still favorable (Abbas et al., 2013). Furthermore, this criterion just provides an approximation of the initial pressure in the initiation element (Fig. 3.9), which will not significantly affect the propagation process in later period.

A fixed grid fracture propagation model (Barree, 1983) is used in this paper. Instead of capturing fracture front with implicit level set functions (Peirce and Bunger, 2013), we use a simple correlation to calculate the fracture propagation distance according to the stress intensity factor at the current time step (Mastrojannis et al., 1979; Ribeiro and Sharma, 2013):

$$\Delta d = \max\left\{\Delta d_{\max}\left(\frac{K_{I,d} - K_{IC}}{K_I^{\max} - K_{IC}}\right), 0\right\} \Big| d = a, b \tag{3.22}$$

where $\Delta d_{\max}$ is the maximum propagation length, $K_{I,d}$ is the type I stress intensity factor at the fracture tip along direction of x and y (Fig. 3.9), respectively, $K_I^{\max}$ is the maximum stress intensity factor along the front, and K_{IC} is fracture toughness of reservoir rock. Because the fracture is assumed to be planar, only the type I stress intensity factor is required. Once Δd is larger than the fracture element length, a newly opened element will be added at the front. Note that a large $\Delta d_{\max}$ implies fast propagation velocity. To fill the new element with fluid, however, a longer time is required compared with the situation when a small $\Delta d_{\max}$ is chosen. Thus the overall propagation velocity is similar with different choices of $\Delta d_{\max}$. With DDM, the stress intensity factor K_I can be easily obtained with:

$$K_{I,d} = C\frac{D_n E\sqrt{\pi}}{4(1-\nu^2)\sqrt{d}} \Big| d = a, b \tag{3.23}$$

where E is Young's modulus; ν is Poisson's ratio; d is the half-length of fracture grid, which equals to a or b along different directions; D_n is the normal displacement of tip element; and C is an empirical constant to correct the DDM-based stress intensity factor calculation. The correction factor 0.806 derived by Olson (1991) is used in this paper. Although this value is based on 2D analysis, it also gives good approximation in 3D problems (Sheibani, 2013).

The numerical discretization of this model is similar with that in Chapter 8 except that the mechanical equations are replaced by Eq. (3.9). We also use the same coupling procedure to solve the thermal−hydro−mechanical coupled system.

3.4 MODEL VALIDATION

To validate the model results, comparisons have been made against both existing analytical solutions and with numerical solutions from published works. The fracture deformation and induced stress calculated with DDM and the elastic stress interaction among multiple fractures are validated respectively. Then the radial fracture propagation without fluid leak-off is verified with analytical solutions.

3.4.1 Mechanical Calculation Validation

In this part, the mechanical results based on 3D DDM are validated with analytical solutions and existing numerical results.

For the case of uniformly pressurized radial fractures in a linear elastic material, fracture widths w along radius r and normal stress σ_n in the near tip region follow analytical solutions (Sneddon, 1946):

$$w = \frac{8p_0(1-\nu^2)}{\pi E}\left(c^2 - r^2\right)^{1/2}; \quad \sigma_n = -\frac{2p_0}{\pi}\left(\sin^{-1}\frac{1}{r} - \frac{1}{\sqrt{r^2-1}}\right) \tag{3.24}$$

where p_0 is the fluid pressure, E is the Young's modulus, ν is the Poisson's ratio, and c is the fracture radius. The definition of r is shown in Fig. 3.4 (left). The fracture radius c is chosen to be 1 m, inner pressure equals to 10 Pa, and Poisson's ratio and Young's modulus are 0.1 and 10^5 Pa, respectively.

Three hundred sixteen rectangular elements are used to approximate the radial shape of the fracture in this case. The comparisons between analytical solutions and numerical results calculated with UFrac are given in Fig. 3.10. An excellent match of both fracture deformations and near-tip stresses is observed.

To further verify the stress calculations in a multiple fracture system, a case of three parallel rectangular fractures is tested. The reference results, which are also calculated with DDM, are taken from Wu (2014). Model parameters are listed in Table 3.1. Due to the stress shadow effect, the inner fracture has smaller aperture compared with the outer fractures. The normalized aperture is defined as the ratio of the fracture center aperture to an isolated single fracture aperture. S and H denote the fracture spacing and height, respectively, as depicted in this figure. As fracture spacing increases, the stress interaction between fractures vanishes and each fracture gradually deforms independently when spacing is over roughly 2.5 times longer than fracture height. Again, the results calculated by UFrac match very well with reference solutions (Fig. 3.11).

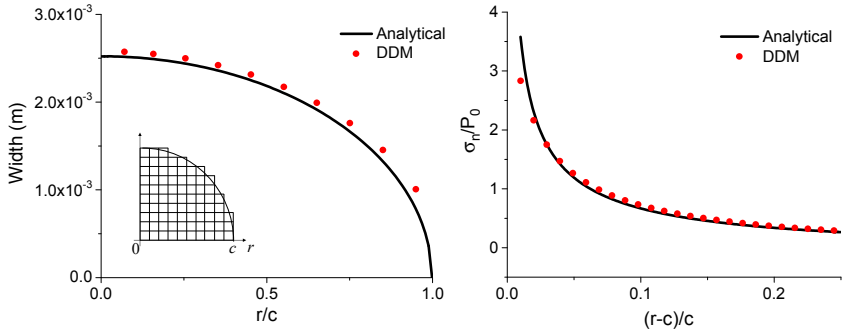

FIGURE 3.10 Radial fracture width (left) and near-tip normal stress (right) comparison between numerical results (UFrac) and analytical solutions.

TABLE 3.1 Input Parameters Used for Three Parallel Fractures

Parameter	Unit	Value
Fracture height	m	30.5
Fracture length	m	121.9
Young's modulus	GPa	6.9
Poisson's ratio	–	0.25
Internal pressure	MPa	40
Minimum horizontal stress	MPa	42
Element number in *x* direction	–	40
Element number in *z* direction	–	10

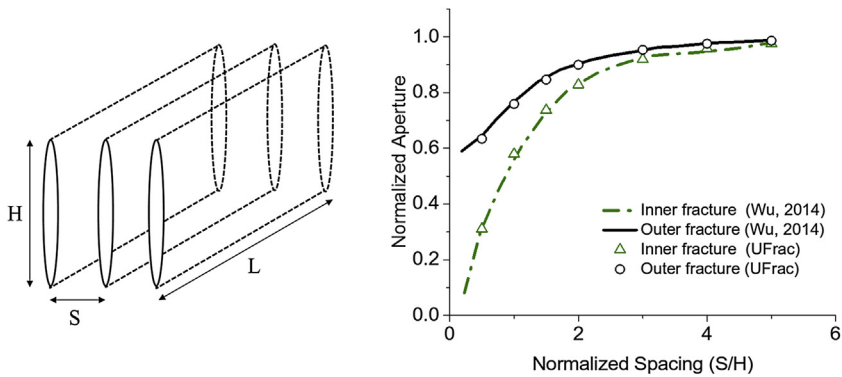

FIGURE 3.11 Illustration of a three-fracture system (left) and the stress shadow effect on the system (right).

3.4.2 Radial Fracture Propagation

For the case when minimum horizontal stress is homogeneous along the vertical direction, radial fractures will be generated. The radius of the radial fractures without leak-off can be calculated as (Geertsma and De Klerk, 1969):

$$R(t) = 0.56\left(\frac{Eq^3}{2\mu(1-\nu^2)}\right)^{1/9} t^{4/9} \tag{3.25}$$

where q is the volumetric injection rate, E is the Young's modulus, ν is the Poisson's ratio, and μ is the fluid viscosity. The values used in the simulation are given in Table 3.1. The maximum propagation distance $\Delta d_{\max}$ is chosen to be 5 m in this case. Different $\Delta d_{\max}$ values have been tested, and the final results are not sensitive to the choice of $\Delta d_{\max}$. Table 3.2 shows the values of the other input parameters used in the simulation.

Fig. 3.12 shows a match of the analytical solution and numerical results. The steplike shape of the numerical solution results from the fact that rectangular grids are used to approximate the fracture radial shape. In early times, the numerical model gives higher propagation velocity because only a few grids are activated in the beginning and such a coarse grid will overestimate the stress intensity factor at the fracture tip. As a result, the model overestimates the velocity as the fracture grows. As fracture propagation continues, more fracture elements are added, and the calculated stress intensity factor starts to stabilize and converge to the actual values. Thus, the numerical solution gradually matches the analytical solution as demonstrated in Fig. 3.12.

TABLE 3.2 Input Parameters for Radial Fracture Propagation Validation

Parameter	Unit	Value
Viscosity	cp	20
Injection rate	bbl/min	20
Young's modulus	GPa	17.24
Poisson's ratio	–	0.25
Minimum horizontal stress	MPa	34.5
Fracture toughness	MPa $\sqrt{m}$	1
Element size in x direction	m	1
Element size in z direction	m	1

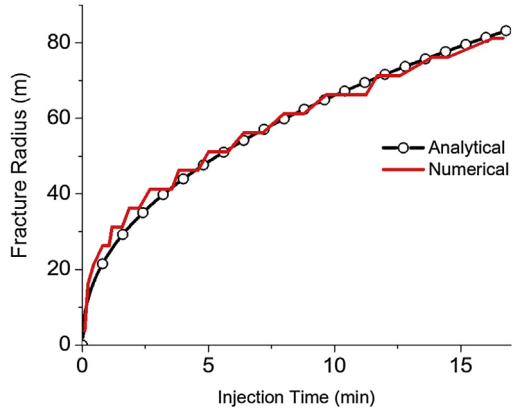

FIGURE 3.12 Fracture radius calculated by numerical and analytical methods.

3.5 APPLICATION

In the previous sections, the details of the integrated hydraulic fracturing simulation model were introduced, and different aspects were verified. In the following section, a set of case studies will be conducted to illustrate the capability of this model to analyze and solve important problems encountered in unconventional reservoir stimulations. The implications and potential use of the simulation results are also discussed.

3.5.1 Fracture Height Growth in Multilayer Formations

Fracture height growth and containment are important not only for operation effectiveness but also for environmental concerns (Fisher and Warpinski, 2012). According to the data provided in Fisher's paper (Fisher and Warpinski, 2012), hydraulic fractures may propagate upward, downward, or be well contained in the target zone depending on stress states, fault distributions, and other reservoir properties.

In this paper, height growth of hydraulic fractures in layered formations is modeled with stress heterogeneity. We assume that the propagating fracture will directly penetrate the layer contacts. For the case where step over or dilation happens, the contacting surfaces should be modeled explicitly with certain constitutive laws (Zhang et al., 2007). In this section, we study two situations: constant in situ stress distribution along the vertical direction and heterogeneous vertical stresses. The parameters used in the simulations are given in Table 3.3. The proppant is injected into the formation with the fracturing fluid since the beginning. The well configuration is shown in Fig. 3.15 with a length of 2500 m in total. Because the wellbore is assumed to

TABLE 3.3 Input Parameters for Case Studies

Parameter	Unit	Value
Viscosity (base fluid)	cp	1
Density (base fluid)	kg/m^3	1020
Injection rate	bbl/min	20
Injection time	min	3
Injected proppant concentration	–	0.2
Proppant diameter	mm	0.45
Proppant density	kg/m^3	2800
Young's modulus	GPa	17.24
Poisson's ratio	–	0.25
Fracture toughness	MPa $\sqrt{m}$	1
Element size in *x* direction	m	3
Element size in *z* direction	m	2

be full of the base fluid before fracturing, the fluid front moves further than the proppant as shown in Fig. 3.13.

With the assumption of homogeneous in situ stress distribution, fracture geometry and proppant transport occurs in a radial pattern (Fig. 3.13A and B). Due to the existence of gravity, the fracture propagates downward further than upward (Fig. 3.14A). For the case of the heterogeneous stress distribution, the minimum horizontal stress at the injection layer is 30 MPa, which is the same with the homogeneous case. The stress distribution along the vertical direction is depicted in Fig. 3.13. The upper layer and lower layer act as stress barriers with stresses 32 and 31.5 MPa, respectively. When layered stress is applied on the fracture surface, the shape of fracture can no longer be described with simple geometry, and the fracture tends to propagate in the layers that have smaller confining stresses (Fig. 3.13C and D). The stress containment in the vertical direction benefits the growth of fracture length in the horizontal direction, and the resulting fracture width is also larger than that in the homogeneous scenario (Fig. 3.14A and C). Because the lower layer has slightly smaller stress, it is easier for fractures to propagate into the lower formation. Meanwhile, after penetrating the upper layer, a less confined layer is encountered, and the fracture width in this layer is recovered (Fig. 3.14C). The stress variation affects not only the shape of the fracture but also the proppant movement within fractures. An approximately homogeneous proppant distribution is observed in the case without stress barriers except for a slight

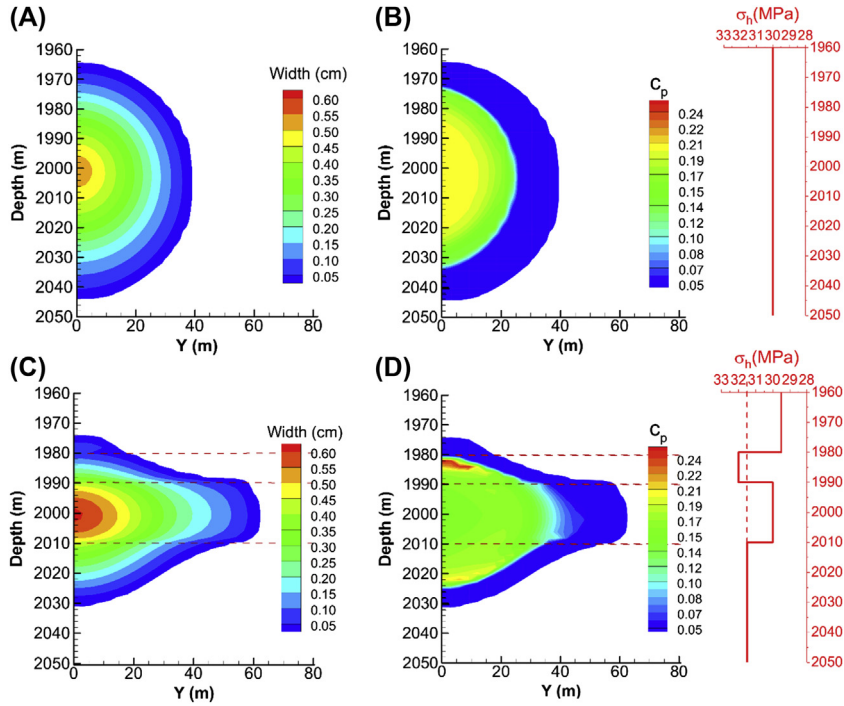

FIGURE 3.13 Fracture width profile (A, C) and proppant volume fraction distribution (B, D) along horizontal direction with different minimum horizontal stress distributions.

proppant bridge built up at the last time step (3 min) (Fig. 3.14B). If the layered stress distribution exists, however, proppants tend to accumulate in high-stress layers. This is because the fracture width at the high-stress layer is significantly smaller than the surrounding layers, which makes it difficult to push the proppant through these narrow parts. At the same time, clear proppant bridges will be formed (Fig. 3.14D). Even though the fracture can cross through the barrier layers, no proppant can reach into these depths, which means these parts of fractures will not contribute to production after fracture shut-ins.

As demonstrated in the aforementioned examples, assumptions such as constant height or circular fracture shape can be easily violated, given practical stress distributions. In situ stress distribution plays a significant role in the determination of the final fracture profile and proppant placement.

3.5.2 Multistage Hydraulic Fracturing

One of the major concerns of hydraulic fracturing is the optimization of fracture spacing. If the fractures are very far away from each other, the total

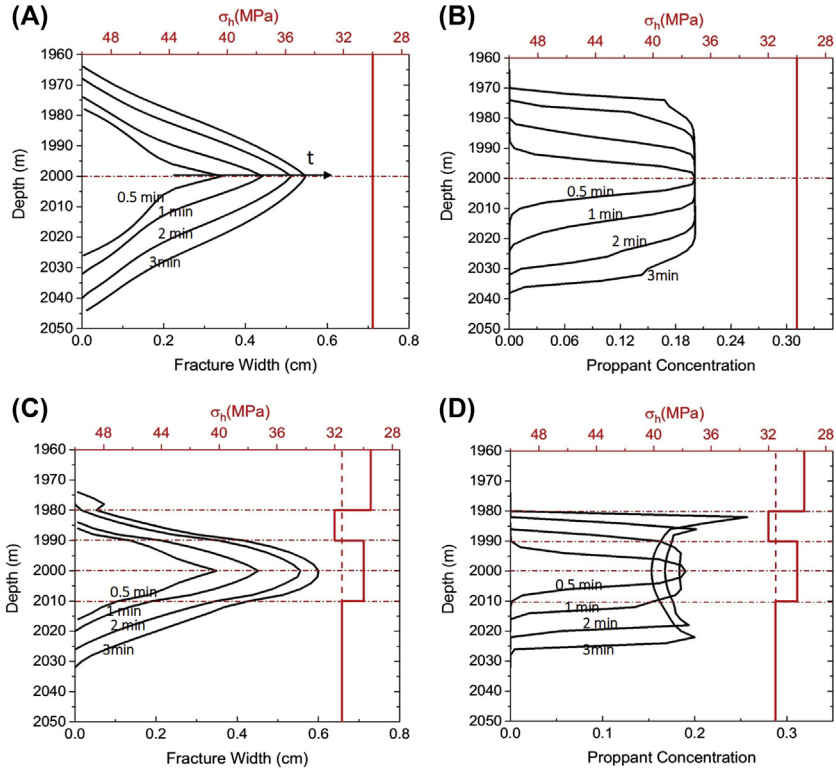

FIGURE 3.14 Fracture width profile (A, C) and proppant volume fracture distribution (B, D) along the vertical direction at the injection point with different minimum horizontal stress distributions. The corresponding times for different profiles are 0.5, 1, 2, and 3 min.

fracture surface area will not be enough to deliver economic production rate. However, if the fractures are very close, the elastic interaction between fractures, also called stress shadow effect, will restrict the fracture size and result in ineffectively stimulated fractures.

First we investigate the effects of perforation spacing on stimulation performance. Four cases, spacing with 20, 40, 60, and 80 m, are modeled with the consideration of gravity. In this case, well friction and fluid leak-off are ignored, and fracture pressure at the injection point is set to be the same as well pressure. Model inputs are listed in Table 3.4. Model configurations, well geometry, parameter definitions, and fracture numbering are illustrated in Fig. 3.15.

Consider simultaneously fracturing of a three-fracture stage in a horizontal well (Fig. 3.15). The vertical part of the well is 2000 m, and the horizontal portion is 500 m. Fractures are equally spaced with distance S. After injecting base fluid for 8 min, the final fracture geometry and width distribution are depicted in Fig. 3.19 with different fracture spacing, varying from 20 to 80 m.

TABLE 3.4 Input Parameters for Case Studies

Parameter	Unit	Value
Horizontal well length	m	500
Well depth	m	2000
Well radius	cm	5
Wellbore roughness	mm	1
Young's modulus	GPa	20
Poisson's ratio	–	0.25
Fracture toughness	MPa	1
Tensile strength	MPa	2
Minimum horizontal stress in target layer $\sigma_{h,0}$ $\sigma_{h,1}$	MPa	30
Minimum horizontal stress in confining layer $\sigma_{h,1}$	MPa	33
Reservoir temperature	°C	80
Injection rate	bbl/min	20
Base fluid density	kg/m^3	1020
Gel density	kg/m^3	1020
Base fluid viscosity	cp	1
Gel viscosity	cp	20
Base fluid specific heat	J/kg	4184
Gel specific heat	J/kg	4184
Fracture-surrounding heat transfer coefficient	J/m^2·s	20
Injected proppant concentration	–	0.2
Proppant diameter	mm	0.45
Proppant density	kg/m^3	2800

Both fracture surface area and width are affected by the distance between fracture perforations (Fig. 3.16). In the early stage, when fractures are relatively small, interference among fractures is not profound. The growth of fractures will increase the deformation-induced stresses, which will enlarge the difference of compression applied on outer and inner fractures. For the case of 20 m spacing, propagation of inner fracture is strongly suppressed by the outer fractures, and almost no fluid can enter the inner fractures, especially at later stage (Fig. 3.17A). With increasing fracture spacing, flow rate is gradually balanced among fractures. In the meantime, the surface area of each

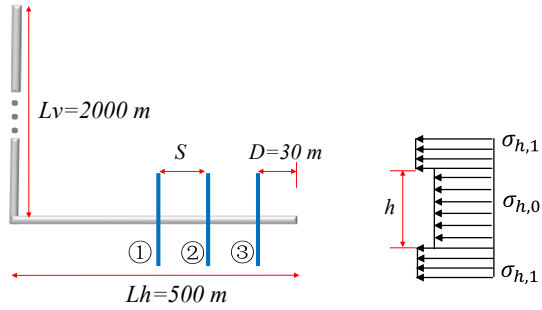

FIGURE 3.15 Schematic of the wellbore and fracture configurations. Three fractures are simultaneously stimulated in the horizontal well segment. The numbering of fractures is 1, 2, and 3 from heel to toe. Different sedimentary layers have different minimum horizontal stresses. Target zone is of height *h*.

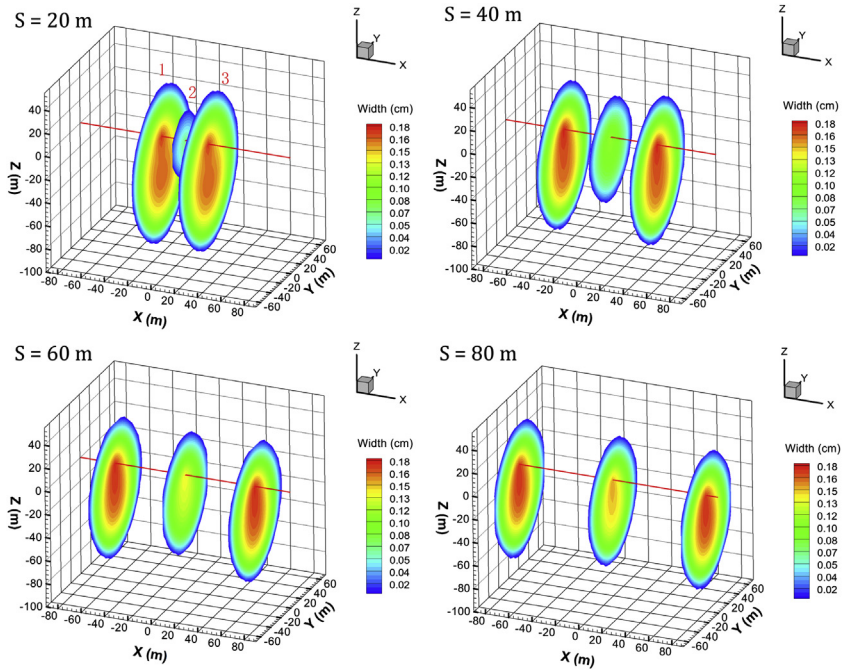

FIGURE 3.16 Fracture geometry and width distribution of a simultaneously stimulated three-fracture stage. Perforation spacing (S) changes from 20 to 80 m.

fracture becomes similar. A monotonic increase in difference among fractures is observed, which implies a time-dependent operation may optimize the stimulation effectiveness. In agreement with the conclusion drawn by previous studies (Cheng, 2012a,b), when fracture spacing is 2.5 times larger than fracture length (in the case 150 m spacing and 60 m fracture radius), the stress

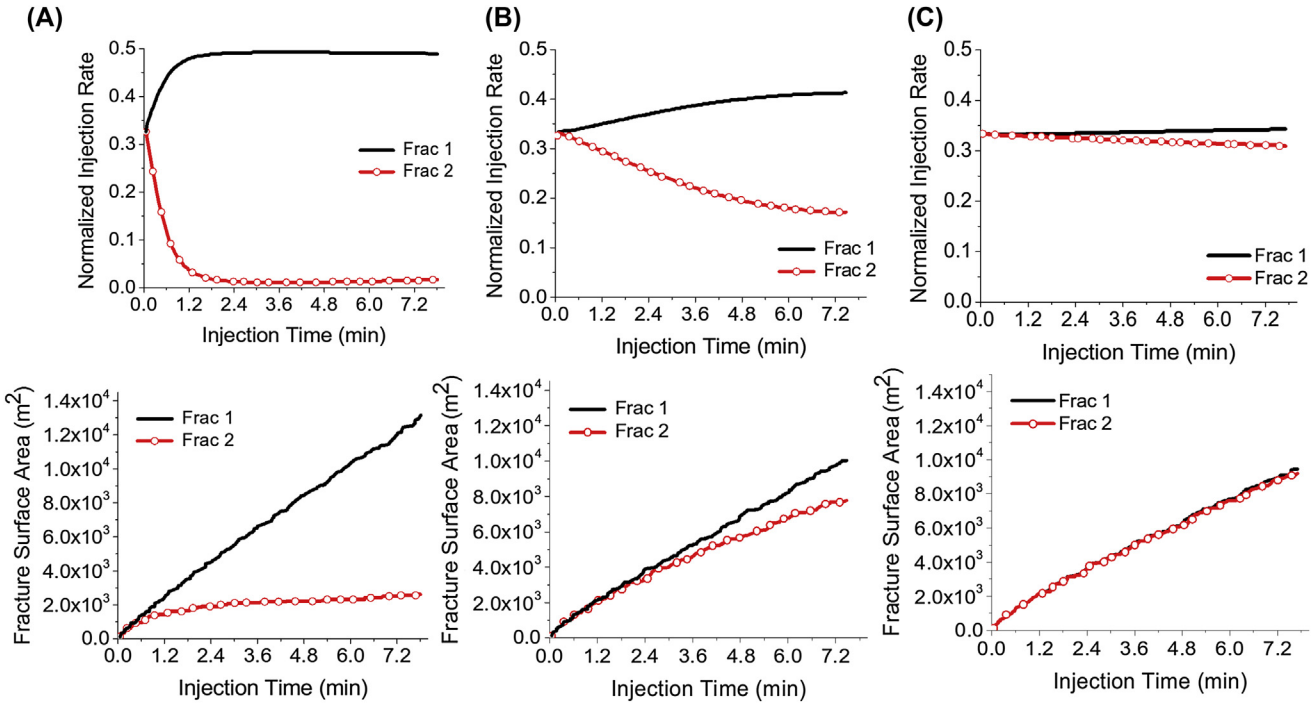

FIGURE 3.17 Flow rate and fracture surface area (defined as the area of one face of fracture) comparison between inner and outer fractures with different fracture spacing: (A) S = 20 m; (B) S = 60 m; (C) S = 150 m.

shadow effect vanishes and each fracture begins to be mechanically independent with few stress interactions (Fig. 3.17C).

Small spacing results in small width of the center fracture, which may also cause problems for proppant transport. Once the fracture width decreases to be comparable with proppant size, the movement of proppant is prohibited and a bridge between proppant-laden fluid and pure fluid will be formed. This phenomenon is called proppant bridging. After injecting pure base fluid for 2 min, proppant with properties listed in Table 3.4 is injected with gel at a constant rate. Well friction is ignored in this case, and the inlet pressure is assumed to be the same among fractures.

When proppant transport is considered, proppant bridging close to the fracture tip is observed (Fig. 3.18B). Due to the compression from outer fractures, the propagation of the inner fracture is prohibited, which results in the accumulation of proppant at the fracture front. Moreover, the middle fracture with smaller aperture forms proppant bridges more easily than other fractures. The combined effect makes proppant movement in inner fractures quite difficult, and only a small portion of the fracture area can be effectively propped. It is clear from Fig. 3.19B that the unevenness of the propped fracture surface area is more severe than the total fracture area. Although the inner fracture keeps growing, the area that is effectively filled with proppant changes little. Because the unpropped part of fractures will be closed when pumping stops, and thus no longer contributes to production, it is important to add the proppant aspect into the model to better evaluate the effective fracture conductivities.

One can also observe from Figs. 3.18 and 3.19 that the symmetry between Frac 1 and Frac 3 (defined in Fig. 3.18A) does not hold when proppant is injected. Before proppant arrives to the current stage, the two outer fractures act the same (Fig. 3.19). When proppant reaches Frac 1, if the injection rate in each fracture is maintained, the resulting pressure buildup in Frac 1 will be

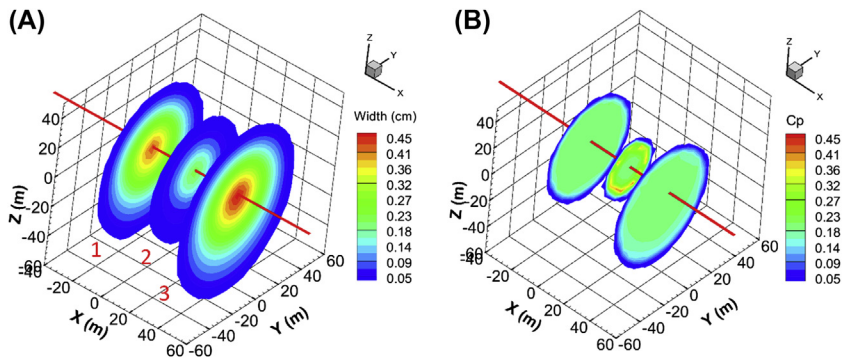

FIGURE 3.18 (A) Fracture width distribution and (B) proppant volume fraction at the end of injection.

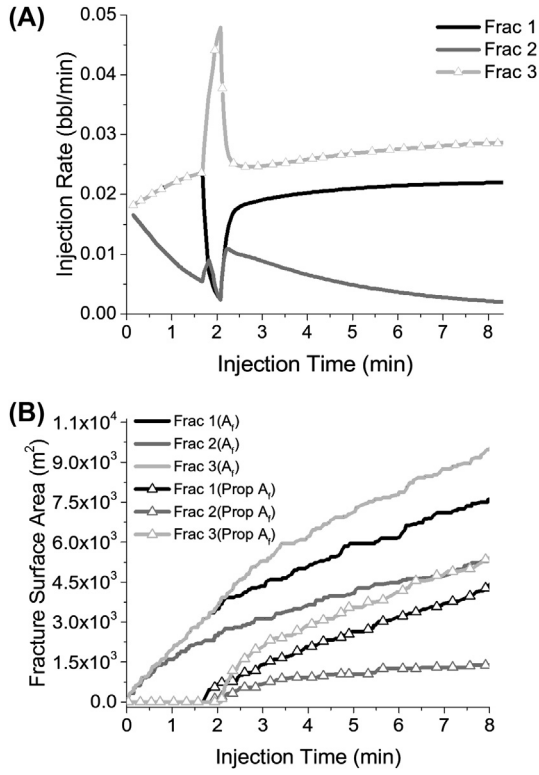

FIGURE 3.19 (A) Injection rate of slurry from wellbore to each fracture. Fracture numbering is the same as in Fig. 3.18. (B) Fracture surface area and propped fracture surface area comparison.

higher than in the fractures that have not received the proppant yet. Because well pressure is assumed to be the same within one stage, the injection rate of the fracture that first accepts proppant (in this case Frac 1) will decrease to maintain pressure equilibrium. As a result, other fractures will receive more fluid and the resulting uneven growth of outer fractures is observed (Fig. 3.18A). After proppant arrives at all fractures, flow partition is stabilized again and a new balance is reached (Fig. 3.19A).

The aforementioned conclusions are based on the assumption of homogeneous in situ stress and only radial-shaped fractures. As illustrated in the previous section, when the fracture is well confined in the target zone with overlying and underlying layers acting as stress containments, Perkins–Kern–Nordgren (PKN)-shaped fractures, which are another typical fracture geometry encountered in hydraulic fracturing, will grow. A case with PKN-shaped fractures is compared with previous radial fracture cases to reveal the role of fracture geometry in simultaneous fracture propagation (Fig. 3.20).

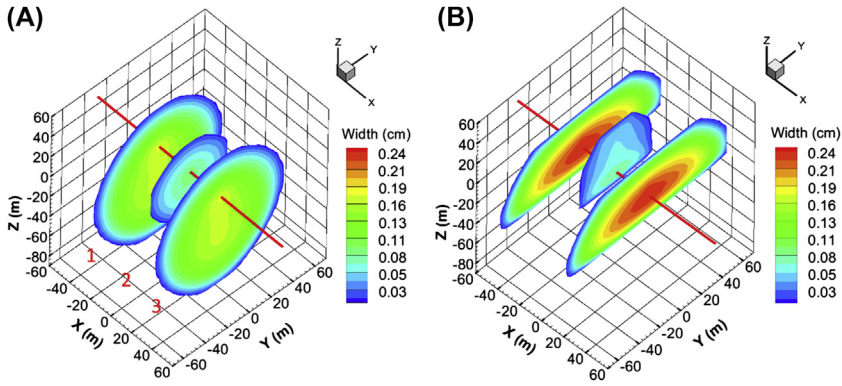

FIGURE 3.20 Impact of fracture geometry on stress interactions. (A) Radial fractures developed in homogeneous in situ stress condition. The *red straight line* represents horizontal well. (B) Perkins–Kern–Nordgren–shaped fractures resulting from stress confinement on adjacent layers. Fracture spacing is 30 m in both cases.

Flow rate partitioning and fracture surface area evolution are compared between these two scenarios (Fig. 3.21). After the end of radial propagation, the middle fracture is under stronger compression in the PKN case. The inner fracture of the PKN shape receives lower flow rate compared with the radial fracture, and finally no fluid can enter it. Meanwhile, the fracture surface area of the PKN outer fracture gradually decreases below the area delivered by radial cases, and the inner fracture area in PKN case is quite similar. These trends can be explained that, at early times, fractures are growing radially in both stress states, and thus similar flow rates and surface areas are observed. Once the stress barrier is reached in the PKN case, the growth ability of the fracture is impaired in the vertical direction and fracture widths start to dilate in the perforation layer. This also explains why outer fracture widths of the PKN fracture are larger as shown in Fig. 3.11. For the same reason, with the same injection volume, the PKN-shaped fractures expand into a smaller area than radial fractures, which have less resistance to propagation (Fig. 3.21A). In addition, because fracture aperture around the injection point of the PKN fracture is larger, the center fracture will endure more compression from outer fractures, which results in more severe unbalanced distribution of flow rate among fractures (Fig. 3.21B). This is clearer when looking at the stress distribution. The normal stress distribution at the depth of the horizontal well is calculated with DDM (Fig. 3.22). The width of each fracture, enlarged with a same constant, is also drawn. In the PKN case, higher compressive stress is observed, which results in a stronger contrast between outer and inner fracture width and length.

When well friction is considered, the larger the distance between the fracture and the heel of the well, the greater the pressure friction loss. As a

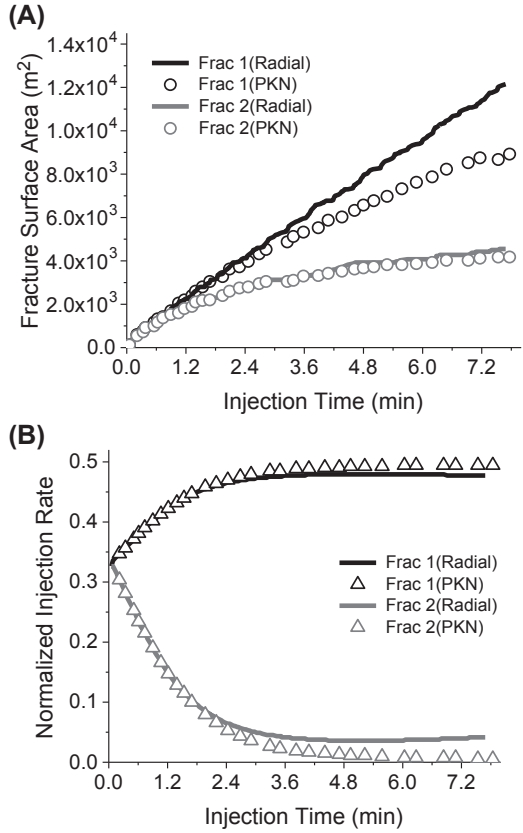

FIGURE 3.21 Comparison of fracture surface area (A) and injection rate (B) in inner (Frac 2) and outer (Frac 1) fractures with different geometries.

result, the fracture close to the injection point will gain most of the pumped fluid. At early stages, when the stress shadowing effect is not significant, the fracture closest to the toe of the well develops slowly due to the friction loss of pressure. As the fracture grows, the compression from outer fractures starts to restrict the propagation of the middle fracture, which gradually becomes the smallest fracture in this stage. If friction exists in the wellbore, the optimized perforation spacing may vary. Based on the aforementioned analysis, suppressing the propagation of fractures close to injection might help other fractures receive more fluid (Fig. 3.23). Consequently, moving the inner fracture closer to the heel of the well could help balance fracture growth within the three-fracture stage (Fig. 3.23A). Moving to the opposite direction (Fig. 3.23C), however, will exaggerate the difference among the fractures.

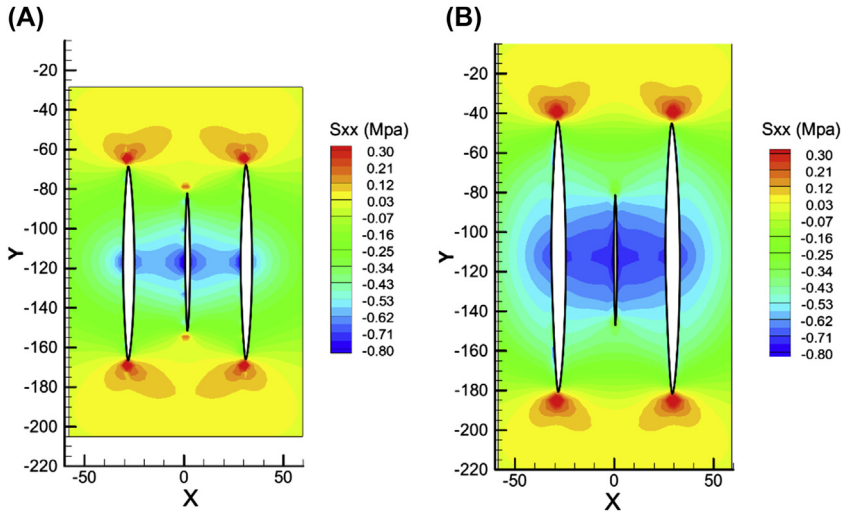

FIGURE 3.22 Fracture deformation−induced normal stress at perforation depth. (A) Radial geometry fractures; (B) Perkins−Kern−Nordgren geometry fractures. Fracture width is enlarged proportionally for display purpose. Compressive stress is taken as negative in this figure.

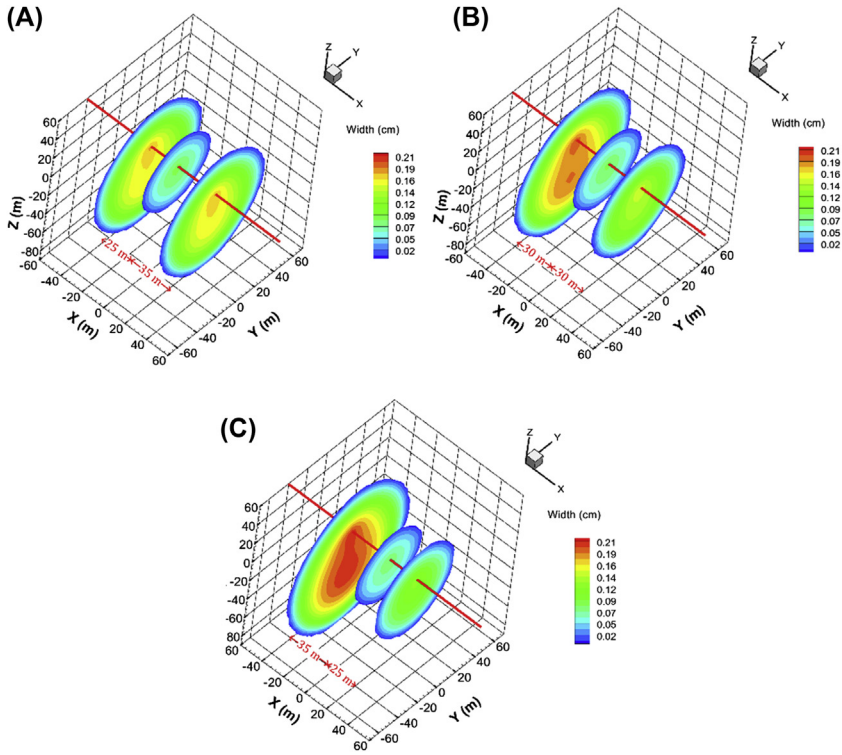

FIGURE 3.23 Fracture geometry with consideration of well friction: (A) uneven spacing with $S = 25$ m between Frac 1 and Frac 2, $S = 35$ m between Frac 2 and Frac 3; (B) equal spacing with $S = 30$ m; (C) uneven spacing with $S = 35$ m between Frac 1 and Frac 2 and $S = 25$ m between Frac 2 and Frac 3.

3.6 CONCLUSIONS

In this chapter, the stress shadow effect in unconventional reservoir stimulation is systematically analyzed. A fully hydromechanical coupled numerical model, which integrates wellbore and fracture parts, is also introduced. The calculation of stress interactions between hydraulic fractures is based on DDM, which is efficient in both storage and time. Several conclusions can be drawn from the simulation results:

- It is necessary to consider the dynamic fluid partitioning among simultaneously propagating fractures. The growth of inner fractures is further restricted due to the lack of injecting fluid.
- The stress shadow effect not only affects the configurations of fractures, but also influences the proppant distribution among fractures. Early proppant bridging may happen in inner fractures, which further prohibits the fracture propagation.
- The strength of the stress shadow effect is related to fracture geometries. With the same spacing, the PKN-shaped outer fracture applies stronger compression on the inner fractures than on radial fractures. Hence, the optimization of fracture spacing should also consider the effect of fracture shapes.
- When well friction exists, the optimal fracture placement will change. More fractures should be placed close to the heel of the well to partially compensate the pressure loss along the wellbore.
- Nonplanar fracture propagation is not considered in this model. For the situation when the in situ stress difference is not obvious, the fracture planes may curve or rotate to form more complex geometries. To get a better estimation of the fracture configurations, a fully 3D fracturing model will be required.

REFERENCES

Abass, H.H., Hedayati, S., Meadows, D.L., 1996. Nonplanar fracture propagation from a horizontal wellbore: experimental study. SPE Production and Facilities 11, 133–137. https://doi.org/10.2118/24823-PA.

Abbas, S., Lecampion, B., Prioul, R., 2013. Competition between transverse and axial hydraulic fractures in horizontal wells. In: SPE Hydraulic Fracturing Technology Conference. Society of Petroleum Engineers.

Adachi, J., Siebrits, E., Peirce, A., Desroches, J., 2007. Computer simulation of hydraulic fractures. International Journal of Rock Mechanics and Mining Sciences 44, 739–757. https://doi.org/10.1016/j.ijrmms.2006.11.006.

Astakhov, D.K., Germanovich, L.N., 2000. Fracture Closure in Extension and Stress Dependent Permeability of Jointed Rock. American Rock Mechanics Association, pp. 841–848.

Barree, R.D., 1983. A practical numerical simulator for three-dimensional fracture propagation in heterogeneous media. In: SPE Reservoir Simulation Symposium. Society of Petroleum Engineers.

Cheng, C., Bunger, A.P., Peirce, A.P., 2016. Optimal Perforation Location and Limited Entry Design for Promoting Simultaneous Growth of Multiple Hydraulic Fractures. Society of Petroleum Engineers.

Cheng, Y., 2012a. Impacts of the number of perforation clusters and cluster spacing on production performance of horizontal shale-gas wells. SPE Reservoir Evaluation and Engineering 15, 31–40. https://doi.org/10.2118/138843-PA.

Cheng, Y., 2012b. Mechanical interaction of multiple fractures-exploring impacts of the selection of the spacing/number of perforation clusters on horizontal shale-gas wells. SPE Journal 17, 992–1001. https://doi.org/10.2118/125769-PA.

Crouch, S.L., Starfield, A.M., Rizzo, F.J., 1983. Boundary element methods in solid mechanics. Journal of Applied Mechanics 50, 704.

Dohmen, T., Zhang, J., Blangy, J.P., 2014. Measurement and Analysis of 3D Stress Shadowing Related to the Spacing of Hydraulic Fracturing in Unconventional Reservoirs. Society of Petroleum Engineers.

Fisher, K.M., Warpinski, N.R., 2012. Hydraulic-fracture-height growth: real data. SPE Production and Operations 27 (1), 8–19.

Friehauf, K.E., 2009. Simulation and Design of Energized Hydraulic Fractures.

Geertsma, J., De Klerk, F., 1969. A rapid method of predicting width and extent of hydraulically induced fractures. Journal of Petroleum Technology 21, 1–571. https://doi.org/10.2118/2458-PA.

Geyer, J.F., Nemat-Nasser, S., 1982. Experimental investigation of thermally induced interacting cracks in brittle solids. International Journal of Solids and Structures 18, 349–356. https://doi.org/10.1016/0020-7683(82)90059-2.

Howard, G.C., Fast, C.R., 1957. Optimum fluid characteristics for fracture extension. In: Drilling and Production Practice. American Petroleum Institute.

Kumar, D., Ghassemi, A., 2016. A three-dimensional analysis of simultaneous and sequential fracturing of horizontal wells. Journal of Petroleum Science and Engineering 146, 1006–1025. https://doi.org/10.1016/j.petrol.2016.07.001.

Lecampion, B., Desroches, J., 2015. Simultaneous initiation and growth of multiple radial hydraulic fractures from a horizontal wellbore. Journal of Mechanics and Physics of Solids 82, 235–258. https://doi.org/10.1016/j.jmps.2015.05.010.

Mastrojannis, E.N., Keer, L.M., Mura, T., 1979. Stress intensity factor for a plane crack under normal pressure. International Journal of Fracture 15, 247–258.

Miller, C., Waters, G., Rylander, E., 2011. Evaluation of production log data from horizontal wells drilled in organic shales. In: North America Unconventional Gas Conference Exhibition SPE 144326. https://doi.org/10.2118/144326-ms.

Okada, Y., 1985. Surface deformation due to shear and tensile faults in a half-space. International Journal of Rock Mechanics and Mining Sciences and Geomechanics Abstracts 75, 1135–1154. https://doi.org/10.1016/0148-9062(86)90674-1.

Olson, J., 2008. Multi-fracture Propagation Modeling: Applications to Hydraulic Fracturing in Shales and Tight Gas Sands. Conf. Paper.

Olson, J., Wu, K., 2012. Sequential vs. simultaneous multizone fracturing in horizontal wells: insights from a non-planar, multifrac numerical model. In: SPE Hydraul. Fracturing Technology Conference. Society of Petroleum Engineers. https://doi.org/10.2118/152602-MS.

Olson, J.E., 1991. Fracture Mechanics Analysis of Joints and Veins (Ph.D. dissertation). Stanford University.

Peaceman, D.W., 1978. Interpretation of well-block pressures in numerical reservoir simulation. Society of Petroleum Engineers Journal 18, 183–194. https://doi.org/10.2118/6893-PA.

Peirce, A., Bunger, A., 2013. Interference fracturing: non-uniform distributions of perforation clusters that promote simultaneous growth of multiple hydraulic fractures. SPE Journal 20, 384–395. https://doi.org/10.2118/172500-PA.

Perkins, T.K., Kern, L.R., 1961. Widths of hydraulic fractures. Journal of Petroleum Technology 13, 937–949. https://doi.org/10.2118/89-PA.

Rafiee, M., Soliman, M., Pirayesh, E., Meybodi, H., 2012. Geomechanical Considerations in Hydraulic Fracturing Designs SPE 162637 13.

Ribeiro, L.H., Sharma, M.M., 2013. A new 3D compositional model for hydraulic fracturing with energized fluids. SPE Production and Operations SPE159812 28, 259–267. https://doi.org/10.2118/115750-PA.

Sesetty, V., Ghassemi, A., 2013. Numerical simulation of sequential and simultaneous hydraulic fracturing. InTech 679–691. https://doi.org/10.5772/56309.

Sheibani, F., 2013. Solving Three Dimensional Problems in Natural and Hydraulic Fracture Development: Insight from Displacement Discontinuity Modeling.

Shiozawa, S., McClure, M., 2016. Simulation of proppant transport with gravitational settling and fracture closure in a three-dimensional hydraulic fracturing simulator. Journal of Petroleum Science and Engineering 138, 298–314. https://doi.org/10.1016/j.petrol.2016.01.002.

Sneddon, I.N., 1946. The distribution of stress in the neighbourhood of a flat elliptical crack in an elastic solid. Proceedings of the Royal Society of London, Series A 187, 229–260. https://doi.org/10.1017/S0305004100025585.

Sneddon, I.N., Elliott, H.A., 1946. The opening of a Griffith crack under internal pressure. Quarterly of Applied Mathematics 4, 262–267.

Tang, H., Winterfeld, P.H., Wu, Y.-S., et al., 2016. Integrated simulation of multi-stage hydraulic fracturing in unconventional reservoirs. Journal of Natural Gas Science and Engineering 36, 875–892.

Tao, Q., Ghassemi, A.A., 2010. Simulation of fluid flow in a naturally fractured poro-thermoelastic reservoir. In: 44th US Rock Mechanics Symposium and 5th US-Canada Rock Mechanics Symposium. American Rock Mechanics Association.

Timoshenko, S., Goodier, J.N., 1951. Theory of elasticity. Journal of Elasticity. https://doi.org/10.1007/BF00046464.

Wu, K., 2014. Numerical Modeling of Complex Hydraulic Fracture Development in Unconventional Reservoirs.

Yew, C.H., Weng, X., 2014. Mechanics of Hydraulic Fracturing. Gulf Professional Publishing.

Zhang, X., Jeffrey, R.G., Thiercelin, M., 2007. Deflection and propagation of fluid-driven fractures at frictional bedding interfaces: a numerical investigation. Journal of Structural Geology 29, 396–410. https://doi.org/10.1016/j.jsg.2006.09.013.

Chapter 4

Quasistatic Discrete Element Modeling of Hydraulic and Thermal Fracturing Processes in Shale and Low-Permeability Crystalline Rocks

Hai Huang[1], **Paul Meakin**[2], **Jing Zhou**[1]
[1]*Idaho National Laboratory, Idaho Falls, ID, United States;* [2]*Temple University, Philadelphia, PA, United States*

4.1 INTRODUCTION

During the last decade, the rates of production of natural gas, natural gas liquids, and oil from low-permeability tight rocks (frequently referred to as "shales") have increased dramatically in the United States because of successful development and deployment of hydraulic fracturing technology (Energy Information Administration, 2015). To understand and optimize the hydraulic fracturing of shales, it is important to better understand and predict the effects of reservoir heterogeneities on fracture propagation. The petroleum industry still routinely applies outdated two-dimensional (2D) (Ouchi et al., 2015; Sesetty and Ghassemi, 2013) or pseudo three-dimensional (pseudo-3D) (Olson, 2004; Wu and Olson, 2015; Rahman and Rahman, 2010) models to design hydraulic fracturing strategies, despite the significant limitations of these models, which are often based on assuming simple fracture geometries and homogeneous rock properties. However, real hydrocarbon-bearing shale formations, and the rocks that surround them, are heterogeneous on all relevant scales, ranging from the characteristic scales of variations of local mineral fabrics, to the scales of fine laminations and natural fractures, and to the scales of larger stratigraphic layers including commercially interesting hydrocarbon bearing formations, the beds and members within them, and the group that they belong to. Because of this complexity, simplified 2D and pseudo-3D models cannot be relied on to fully capture the physics of hydraulic

Hydraulic Fracture Modeling. https://doi.org/10.1016/B978-0-12-812998-2.00004-7

fracturing and produce realistic fracture propagation scenarios and fracture geometries.

Very often the evolving fracture geometry is difficult to monitor and characterize in real time during hydraulic fracturing operations using existing diagnostic methods. Thus physics-based hydraulic fracturing models may not only provide valuable information to guide the design of hydraulic fracturing applications and the planning of monitoring strategies, but they may also improve the interpretation of experimental results and monitoring data. A robust hydraulic fracturing model should at least include the following physics: (1) stress concentration and stress redistribution before, during, and after fracture propagation; (2) fluid pressure transport and dissipations due to viscous flow within hydraulically generated and preexisting fractures, and fluid leak-off from the fractures into the surrounding porous formation; (3) appropriate coupling between fracture opening and fluid flow; and (4) the effects of heterogeneities in rock properties including permeability, tensile strength, and elastic constants.

Thermal and hydraulic fracturing of low-permeability brittle crystalline rocks also plays important roles in engineered geothermal energy systems. The contraction of hot crystalline rocks caused by the injection of cold water into primary fractures increases their apertures and drives the generation of secondary cracks perpendicular to the primary fractures (Shibuya et al., 1985; Nemat-Nasser, 1977; Koh et al., 2011; Kohl et al., 1995; Jing et al., 2000), thus facilitating fluid flow and heat extraction. Experimental investigations (Bahr et al., 1986; Geyer and Nemat-Nasser, 1982) have revealed that during the early stages of cooling, the thermal cracks are densely spaced near the surfaces of the primary fractures, and that they are all of about the same length. As the cooling front propagates into the solid, some of the cracks stop growing because of mutual unloading due to crack−crack interaction mediated by the elastic stress/strain field. In quasi-2D experiments, using materials that are homogeneous on all but very small scales, such as glass, every other crack stops growing at more or less the same time, and a sequence of mutual unloading events progressively reduces the number of propagating cracks, giving rise to a quasihierarchical pattern. In general, thermally induced hierarchical crack growth results from the complex long-range elastic interactions between neighboring cracks, the nonlinear interplay between the growing cracks, and the evolving, stress-generating temperature field. This process has been explained theoretically (Bahr et al., 1986, 1992, 2010; Boeck et al., 1999; Hofmann et al., 2006; Keer et al., 1978; Nemat-Nasser et al., 1980) on the basis of a "bifurcation" stability analysis of the simultaneous growth of an array of equidistant parallel straight cracks in a homogeneous sheet of brittle material cooled along one straight edge. However, most analytical and numerical studies are based on calculation of the transient stress intensity factors (SIFs) K_I or fracture energy release rates for just two parallel straight cracks, both growing perpendicular to the cooled edge of the solid material,

with periodic boundary conditions in the direction parallel to the cooled edge (Bahr and Weiss, 1986). These studies predict only the "bifurcation point" at which one of the two cracks stops growing and the scaling relations between fracture spacing and fracture length. However, they do not predict the emerging crack patterns and the concomitant evolving stress and temperature fields. In practice, thermal cracks are rarely straight and parallel in polycrystalline rocks and other brittle solids.

A variety of rock fracturing models, with different levels of simplifications of the physics associated with fracturing process, has been developed in recent decades. For example, a "wire-mesh" model (Xu et al., 2010), which uses a set of orthogonal and uniformly distributed fractures to approximate the complex fracture network, has been presented. However, this model imposes predetermined fracture spacing and orientation and does not consider the effects of fracture interactions on individual propagation paths. Another widely used method is the displacement discontinuity method (DDM) (Wu and Olson, 2013; Weng, 2015), which is based on the boundary element method (BEM) developed by Crouch (1976). In the DDM model, the fracture propagation length and direction are obtained through calculation of the SIF at the fracture tip in 2D applications or fracture perimeter in 3D applications and an empirical propagation criterion. The DDM reduces the dimensionality of the problem by one through discretizing only the boundaries rather than the whole domain. Therefore, the DDM exhibits much higher computational efficiency, which makes it very suitable for predicting fracture propagation with rapid stress change in large field-scale reservoirs. However, this model is based on the use of *Green's* functions, and, in practice, it is restricted to fracturing of essentially homogeneous linear elastic materials. Dahi-Taleghani and Olson (2011) used a 2D extended finite element method (XFEM) to study fracture propagation in some simple test cases. Although their results seem promising, it is difficult to apply the XFEM method to 3D fracturing, particularly when fractures merge and/or branch. More recently, a commercial XFEM code (Abaqus, 2017) has been used successfully to simulate hydraulic fracturing (Searles et al., 2016, Kumar et al., 2017). At present, no numerical model accurately represents all the coupled processes that may play a significant role in geotechnical hydraulic fracturing. In many scientific and practical applications, both particle-based models such as discrete element model (DEM) and grid-based methods such XFEM are used. They have characteristic strengths and weaknesses and complement each other. XFEM and DEM models are currently the most successful within their respective classes (grid-based and particle-based). However, both require further development and validation, and, in the future, they may be combined in multiscale, multiphysics, multimethod numerical models. The cohesive zone method (CZM) along with the finite element method (FEM) (Huang et al., 2016a; Shin and Sharma, 2014; Haddad and Sepehrnoori, 2014) has also been widely used in hydraulic fracturing simulations. The rock is modeled as a porous elastic medium, and cohesive

elements are inserted to model fracture propagation. An important limitation of this method is that fractures are allowed to propagate only along predefined paths (i.e., along the boundaries of the internal elements of a predefined finite element mesh), and a fine mesh is often required around the fracture perimeter. Lawrence Livermore National Laboratory has developed a fully multiscale, multiphysics, 3D simulator, called GEOS (Settgast et al., 2016; Fu et al., 2013), which is based on coupling a CZM FEM model for geomechanics with a finite volume (FV) approach for fluid flow and has been used to simulate hydraulic fracture propagation in layered, discontinuous, and heterogeneous formations. However, the hydraulic fractures are restricted to propagate along predefined internal element boundaries.

The DEM originally introduced by Cundall and Strack (1979) provides a broadly applicable and versatile approach to model the initiation, coalescence, and propagation of microcracks and macroscopic fracturing processes in heterogeneous rocks. The well-known PFC2D and PFC3D codes developed by ITASCA (Potyondy and Cundall, 2004) have been extensively applied to many rock mechanics phenomena including hydraulic fracturing. Like molecular dynamics and many other particle methods, DEM models simulate the dynamic behavior of materials by integrating the classical equations of motion for a large ensemble of particles. However, unlike molecular dynamics and many other particle methods, DEM models often include the rotational dynamics of the particles, as well as interactions such as friction, and both the properties of the particles and their interactions with other particles may be changed over time to represent chemical transformations, nonlinear elasticity, and other phenomena. Such DEM models are able to capture the propagation of multiple fractures in both homogeneous and heterogeneous rocks, and, in principle, they can also be used to simulate the propagations of elastic waves emitted from fracturing events (Hazzard and Young, 2002; Zhao and Young, 2009). However, dynamic DEM models typically require extremely small time steps to achieve numerical accuracy and stability (substantially less than $\sim r/(E/\rho)^{1/2}$, where r is the radius of the particles used in the DEM model, and E and ρ are the Young's modulus and density of the rock). This means that the time step size of dynamic DEM models is required to be much less than the time required for an elastic wave to travel a distance equal to the particle size. The requirement for such small time steps prohibits the extensive application of fully dynamic DEM models to large-scale hydraulic fracturing problems. To overcome the large computational burden associated with fully dynamic DEM models, Huang and Mattson (2014) developed a quasistatic 2D DEM model coupled with a 2D network flow model for the purpose of modeling hydraulic fracturing processes. This allows much larger time step sizes, determined by the stability criteria for solving the fluid pressure diffusion equation, to be used. In such quasistatic DEM models, instead of solving and integrating the equations of motion for the DEM particles, the DEM network is relaxed into a new mechanical equilibrium under the influence of the applied loads (both pure mechanical loads, which are represented by boundary conditions, and

loads generated by the fluid pressure gradients caused by injection, which are represented by forces acting on the DEM particles) during each time step. Given the fact that the rates of mechanical deformation and relaxation are usually much faster than the rates of fluid pressure diffusion and heat conduction, it is reasonable to expect that such quasistatic models can be used to simulate hydraulic/thermal fracturing processes. To simulate much more rapid geotechnical applications such as the use of explosives or propellants to fracture rocks, a fully dynamic DEM model is then necessary. In general, a fully dynamic model is needed only when inertial effects are important (i.e., when the velocity of fracture propagation is not much smaller than the elastic wave velocity). The average propagation velocity of hydraulic fractures generated by fluid injection to increase hydrocarbon production is 10^4–10^5 times smaller than elastic wave velocities. However, propagation may be intermittent, and slow subcritical critical fracture propagation may be punctuated by periods of fast propagation (bursts) at velocities that approach elastic wave velocities (Baan et al., 2016). Under these conditions, quasistatic DEM models may still be expected to provide realistic results, provided the fracture propagates by only a small fraction of its length during each burst.

In this chapter, we introduce the quasistatic DEM model and how it is coupled with models for fluid flow and heat conduction, and we provide examples of 2D and 3D simulations of hydraulic fracturing and thermal fracturing in heterogeneous rock formations under various conditions.

4.2 QUASISTATIC DISCRETE ELEMENT MODEL

The DEM, originally introduced by Cundall and Strack (1979) over 30 years ago, has been widely used by the geotechnical engineering community to model the mechanical deformation and fracturing of polycrystalline rocks at various scales, ranging from grain-scale microcracks to large-scale faults associated with earthquakes (Cundall, 2001; Herrmann et al., 1989; Potyondy and Cundall, 2004; Dalguer et al., 2003). In DEM models, as illustrated by Fig. 4.1, a volume of rock is represented by a network of nodes (also referred to as particles) of variable sizes connected by mechanical elements that can be endowed with a variety of rheomechanical properties, depending on the application. In the works discussed in this chapter, the nodes were connected by elastic beams. The force and moment exerting on a node i by a neighboring node j are given by

$$\overrightarrow{F}_{i,j} = k_n\left(d_{i,j} - d_{i,j}^0\right)\overrightarrow{n}_{i,j} + k_s\frac{1}{2}\left(\phi_{i,j} + \phi_{j,i}\right)\overrightarrow{s}_{i,j}, \tag{4.1}$$

$$M_{i,j} = k_s d_{i,j}\left[\frac{\Phi}{12}\left(\phi_{i,j} - \phi_{j,i}\right) + \frac{1}{2}\left(\frac{2}{3}\phi_{i,j} + \frac{1}{3}\phi_{j,i}\right)\right]. \tag{4.2}$$

Here k_n and k_s are the normal and shear force constants; $d_{i,j} = |\overrightarrow{\mathrm{x}}_i - \overrightarrow{\mathrm{x}}_j|$ is the distance between the centers of two DEM nodes (the centers of the

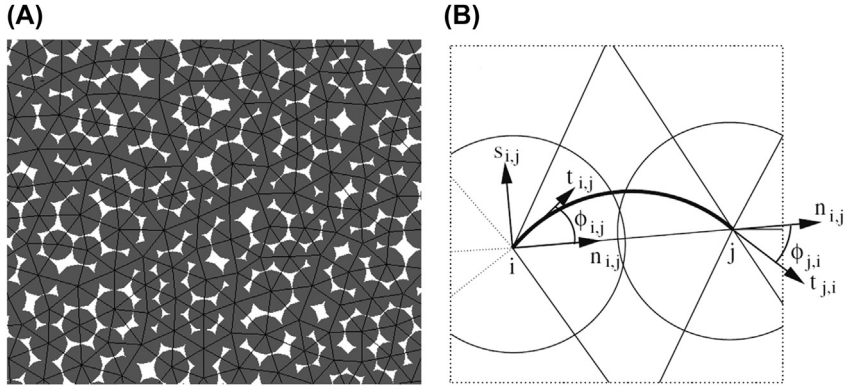

FIGURE 4.1 Illustration of a two-dimensional discrete element model (DEM): (A) A discrete element network generated by randomly packing disks of variable sizes with a uniform size distribution (between a minimum and maximum size) and (B) a bent elastic beam connecting nodes *i* and *j* used in the DEM. *From Huang, H., Meakin, P., Malthe-Sorenssen, A., 2016b. Physics-based simulation of multiple interacting crack growth in brittle rocks driven by thermal cooling. International Journal for Numerical and Analytical Methods in Geomechanics 40 (16), 2163–2177, with permission from John Wiley and Sons.*

corresponding particles), i and j; and $d_{i,j}^0 = r_i + r_j$ is the initial equilibrium (stress free) distance, where r_i is the radius of the ith particle. $\overrightarrow{n}_{i,j}$ and $\overrightarrow{s}_{i,j}$ are the unit vectors parallel and perpendicular to the center line connecting nodes i and j; $\phi_{i,j}$ is the rotation angle in the local frame of the beam; $\overrightarrow{t}_{i,j}$ is the unit vector parallel to the tangent of the bent beam at node i. For an isotropic elastic medium, there are two independent elastic constants—the two Lame coefficients (usually represented by λ and μ) or the Young's modulus E_0 and shear modulus G_0 are commonly used. If a regular square (Herrmann et al., 1989) or triangular (Malthe-Sørenssen et al., 2006) lattice is used in the simulation, an isotropic 2D elastic medium with known Young's modulus and shear modulus can be simulated by using model parameters k_n, k_s, and Φ given by

$$k_n = E_0 A/d \tag{4.3}$$

$$k_s = 12E_0 I\left[d^2(1+\Phi)\right] \tag{4.4}$$

$$\Phi = 12E_0 I/G_0 A d^2, \tag{4.5}$$

where A is the cross-sectional area of the elastic beam and I is the geometric part of its moment of inertia. The Young's modulus E_0 and Poisson's ratio ν can also be used as the independent elastic constants, and G_0, E_0, and ν are related by $G_0 = E_0/[2(1+\nu)]$. Because a random DEM network was used in our simulations (to avoid the effects of the lattice symmetry on the fracturing pattern and represent the small-scale heterogeneities that are present in all

materials), k_n and k_s must be calibrated against the desired values of E_0 and ν. At mechanical equilibrium, the total force and moment acting on every DEM node must vanish, giving rise to elasticity equations in the continuum limit.

Once a mechanical load is applied, an overrelaxation algorithm is used to relax the DEM network to a new state of mechanical equilibrium in which the net forces and moments are zero for all the DEM particles. After the mechanical relaxation, all of the beams that satisfy the failure criterion (Salencon, 1983),

$$\tau = \left(F_{i,j}/F_c\right)^2 + \max\left(\left|M_{i,j}/M_c\right|, \left|M_{j,i}/M_c\right|\right) > 1, \tag{4.6}$$

are identified and, if one or more beam satisfies the failure criterion, the beam that most exceeds the failure criterion is then irreversibly removed from the DEM network, giving rise to crack initiation; the DEM network is then relaxed to a new equilibrium. This network relaxation and beam removal process continues a number of times until there is no beam that meets the failure criteria under the current mechanical load, mimicking crack growth. F_c and M_c are the critical beam force and moment. The beam rupture criterion of Eq. (4.6) is derived from Tresca's and von Mises's general yielding criteria for the material that the beam is composed of (Herrmann et al., 1989; Tzschichholz and Herrmann, 1995; Tzschichholz et al., 1994). F_c and M_c are closely related to the beam length and jointly determined by the critical longitudinal tensile strain of the beam ε_c and the critical beam rotational angle ϕ_c above which the beam will break, even in the absence of tensile strain (representing shear failure under compression). Typical values for ε_c and ϕ_c range from $\sim 10^{-3}$ to $\sim 10^{-2}$ for rocks and many other polycrystalline brittle solids. After a beam has broken, stress is transferred throughout the system by the long-range elastic interactions, but mainly to neighboring beams, and they are likely to break immediately or after a short lapse in time. A sequence of "coupled" beam-breaking events mimics the fracture propagation process, and this makes DEM models a powerful method for studying the random initiation and propagation of hydraulic and/or thermally driven cracks.

The DEM model parameters k_n, k_s, ε_c, and ϕ_c must be calibrated to accurately represent the macroscopic mechanical properties of brittle rocks such as the Young's modulus E_0, Poisson's ratio ν, tensile strength σ_t, and compressive strength σ_c. The calibration of DEM model parameters was performed by simulating uniaxial tensile/compression tests (see details in Huang et al., 2016b).

4.3 FRACTURING OF BRITTLE CRYSTALLINE ROCK BY THERMAL COOLING

In this section, we illustrate the methodology of coupling a quasistatic DEM model with heat conduction and its applications to modeling fracturing of

brittle crystalline rocks induced by thermal cooling. Heat conduction through the rock matrix is described by the classical heat conduction equation:

$$\rho c_v \frac{\partial T}{\partial t} = \nabla \cdot K \nabla T, \tag{4.7}$$

where ρ is the rock density (kg/m^3), c_v is the heat capacity (J/kg°K), K is the thermal conductivity (W/m°K), and T is the temperature (in Kelvin). The volume reduction of rock (area reduction in 2D model) due to cooling is modeled by reducing the radii r_i of the DEM nodes according to

$$r_i(t) = r_i(0)[1 + \alpha \Delta T_i]^{1/d}, \tag{4.8}$$

where $r_i(0)$ is the radius under ambient conditions (the initial temperature T_0 of the rock), α is the volumetric thermal expansion coefficient, d is the dimensionality of the problem (2 and 3 for 2D and 3D problems, respectively), and ΔT_i is the temperature change for the ith DEM node. By choosing a characteristic length L^* and a characteristic time t^*, and defining the dimensionless length, time, and gradient as $L' = L/L^*$, $t' = t/t^*$, and $\nabla' = L^*\nabla$, respectively, Eq. (4.7) can be rewritten in the form:

$$\rho c_v \frac{\partial T}{\partial t^* t'} = \frac{1}{L^*} \nabla' \cdot K \left(\frac{1}{L^*} \nabla' T \right). \tag{4.9}$$

By normalizing the temperature T in Eq. (4.9) by the initial temperature of the hot rock T_0 and the temperature of cold water T_{water} via $T' = (T - T_{\text{water}})/(T_0 - T_{\text{water}})$, and then rearranging coefficients on both sides of Eq. (4.9), and dropping the prime superscript, Eq. (4.9) becomes a dimensionless heat diffusion equation

$$\frac{\partial T}{\partial t} = \nabla \cdot \frac{K}{\rho c_v} \frac{t^*}{L^{*2}} \nabla T = \nabla \cdot D \nabla T, \tag{4.10}$$

where $D = Kt^*/\rho c_v (L^*)^2$ is the dimensionless thermal diffusivity, and T is the dimensionless temperature, with a maximum of $T = 1$, corresponding to the initial temperature of the hot rock, and minimum of $T = 0$, the temperature of the cold water in contact with the hot rock. This dimensionless temperature diffusion equation can be solved numerically using the conventional implicit FV discretization

$$\Delta V_i \frac{T_i^{t+\Delta t} - T_i^t}{\Delta t} = \sum_{j=1}^{n} D A_{i,j} \frac{T_j^{t+\Delta t} - T_i^{t+\Delta t}}{d_{i,j}}, \tag{4.11}$$

on the DEM network, where D is the thermal diffusivity, where T_i and ΔV_i are the temperature and control volume of the ith DEM node, respectively. $A_{i,j}$ is the cross-sectional area between DEM nodes i and j, n is the number of neighbor nodes in contact with the ith DEM node, and $d_{i,j}$ is the distance between the centroids of the ith and jth DEM particles.

The simulation of a coupled heat conduction–fracturing processes consists of interleaved temperature diffusion, mechanical relaxation of the DEM network, and beam-breaking steps. During each time step, the new temperature field is obtained first by using Eq. (4.11). The radii of all the DEM nodes are then adjusted according to Eq. (4.8) to account for thermal contraction. The reduction in the sizes of the DEM particles generates a tensile load within the rock, and the DEM network is relaxed to mechanical equilibrium. The beam that mostly exceeds the failure criteria, which is usually near a crack tip, is then removed from the DEM network and the network is again relaxed into a new state of mechanical equilibrium. The mechanical relaxation and beam-breaking operations are repeated during each time step, mimicking crack initiation and propagation, until no additional beam-breaking occurs, and the simulation then proceeds to a new time step. This quasistatic approach to modeling thermal cracking is reasonable, because the rate of heat conduction is typically much slower than the rate of mechanical relaxation.

Many previous theoretical and numerical investigations of thermal fracture propagation were based on the assumption that the fracturing material is homogeneous and the cracks are linear, parallel to each other and parallel to the temperature gradient. However, because of the local, short-length-scale disorder, including variations in mineral grain and grain boundary materials and geometries, and the presence of pores and microfractures, the mechanical properties are inhomogeneous, and this results in random fracture initiation, which plays an important role in crack growth. In our simulations, the local inhomogeneity is represented by (1) a random distribution of particle sizes in the DEM network and (2) random distributions of the force constants k_n, critical tensile strains ε_c, and critical rotation angles ϕ_c of each beam. The resulting small-scale heterogeneity has a profound impact, and it must be included to generate realistic fracture patterns.

The coupled DEM–heat conduction model was used to simulate the initiation and growth of thermal cracks using a total volumetric thermal strain $\alpha\Delta T$ of 0.4%—a moderate thermal stress load (the macroscopic critical tensile strain of the simulated rock sample is $\sim$0.175%). The simulations were carried out on a 400×200 domain with an initial dimensionless temperature of $T = 1$ everywhere, as shown in Fig. 4.2. The top boundary was assumed to be mechanically free to mimic a cooled primary fracture (open and unstressed) surface, and it was held at a prescribed temperature of $T = 0$ to represent contact with a cold, rapidly flowing fluid. The left and right boundaries were periodic for both displacements and temperature to mimic a long, primary fracture (the model domain captures only a small portion of the primary fracture). The bottom boundary was treated as a no heat flux boundary with zero vertical displacement.

Fig. 4.2 shows the simulated fracture patterns at three stages after the hot brittle rock was cooled along one surface. In this case, all of the thermal cracks are more or less parallel to the average temperature gradient. During the early

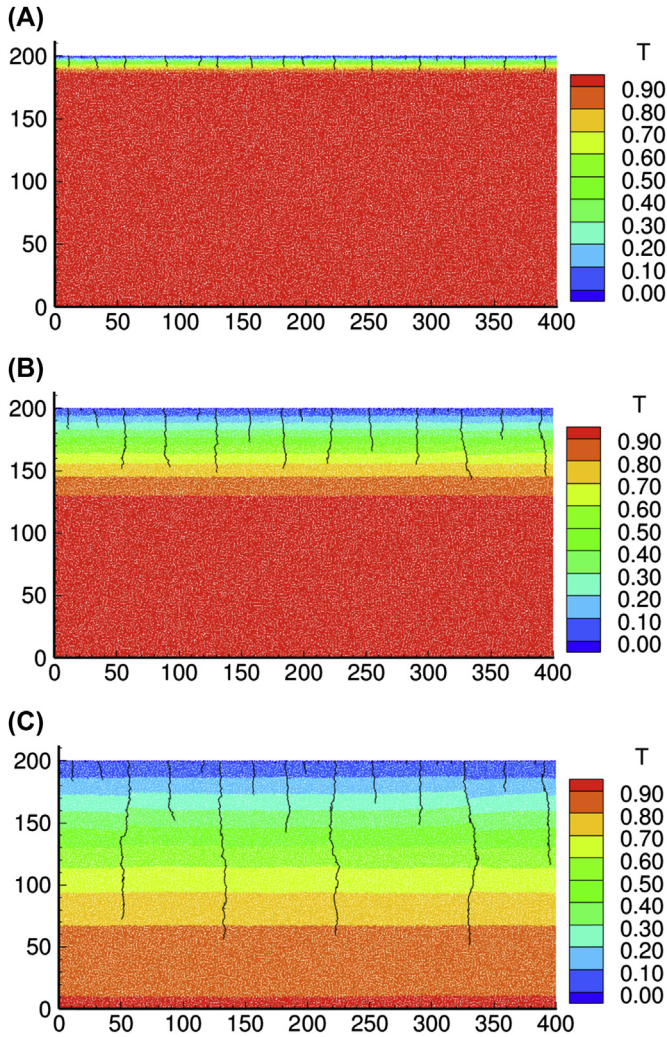

FIGURE 4.2 Simulated initiation and growth patterns of thermal cracks and associated temperature field at different times for a moderate thermal strain load: (A) $t = 150$; (B) $t = 300$; and (C) $t = 17{,}000$. Colors are used to indicate the dimensionless temperature field and the color scale is shown at the right-hand side of each part of the figure. *From Huang, H., Meakin, P., Malthe-Sorenssen, A., 2016b. Physics-based simulation of multiple interacting crack growth in brittle rocks driven by thermal cooling. International Journal for Numerical and Analytical Methods in Geomechanics 40 (16), 2163–2177, with permission from John Wiley and Sons.*

stage of cooling (Fig. 4.2A), a strong thermal gradient was established near the top (cooled) surface, and an array of many small, more or less parallel, and equally spaced cracks of about the same length was formed due to thermal contraction. In thermal fracturing processes, the average spacing between

(or equivalently the number of) macroscopic cracks is determined by the principle of minimum total potential energy (elastic strain energy + fracture surface energy) at a given thermal strain load. Crack initiation and propagation are also strongly influenced by the short-length-scale heterogeneity. These two important features are well captured by the coupled DEM−heat conduction model. As the cooling front penetrated further (Fig. 4.2B and C), some cracks (more or less every other one) stopped growing while the others continued to grow, and the number of growing cracks decreased monotonically and almost stepwise, with increasing time, forming an approximately hierarchical cracking pattern. The simulated hierarchical cracking pattern shown in Fig. 4.2 is very similar to patternsobserved in experimental studies (Bahr et al., 1986; Geyer and Nemat-Nasser, 1982).

The approximately hierarchical cracking pattern can be explained by crack−crack mechanical interactions via the stress−strain fields. Fig. 4.3 shows the stress fields (the horizontal component of the stress tensor) at various times corresponding to those shown in Fig. 4.2. During the early stage of cooling (Fig. 4.3A), an array of more or less equally spaced thermal cracks grew in the direction perpendicular to the cooled surface. Stress is concentrated at the tips of all of the cracks, but crack−crack interaction, mediated by the long-range elastic Green's function, screens the stress/strain fields near the tips of the shorter cracks, and the stress is high enough to drive crack propagation only at the tips of the longer cracks. As the cooling front penetrates deeper into the rock (Fig. 4.3B and C), some cracks propagate further than others, and the stress decreases at the tips of the fractures that fall behind, and eventually some of the shorter cracks stop growing. As shown in the insert in Fig. 4.3B, when cracks propagate, the rock on opposite sides of the cracks moves apart, and the cracks open. This reduces the stress near the tips of neighboring fractures—a phenomenon referred to as stress shadowing. As a consequence, when an array of parallel cracks propagates simultaneously at a given load, they "compete" with each other, and there are "winners" that continue to grow and "losers" that do not. As shown in Fig. 4.3, cracks experiencing stress reduction around their tips stopped propagating, while those that maintain a high stress around their tips continue to propagate. The reduction in stress at the tip of a crack due to the presence of a neighboring crack increases as the relative length of the neighboring crack increases (the influence of a crack on the stress/strain field extends over a range on the order of the crack length). Growth of a long crack (or failure to grow) has the strongest influence on the nearest cracks of comparable length, which also have lengths that are on the order of the distance between them or greater. Consequently, an array of parallel, initially dense cracks, such as that shown in Fig. 4.3A, undergo multiple stages of "space-coarsening," forming a distinct quasihierarchical crack pattern as shown in Figs. 4.2 and 4.3. The local, short-length-scale heterogeneity has large effects on the locations of individual cracks and the local crack propagation pathways, but the formation of a

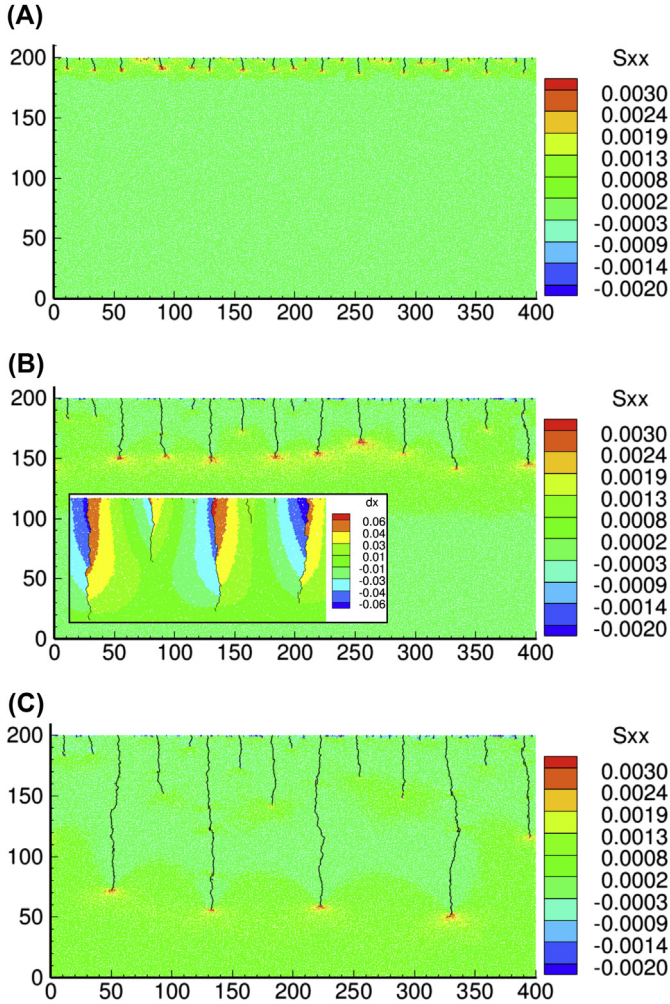

FIGURE 4.3 Simulated initiation and growth patterns of thermal cracks and associated horizontal stress component S_{xx} field at different times for a moderate thermal strain load: (A) $t = 150$; (B) $t = 300$; and (C) $t = 17{,}000$. The insert in part (B) shows the detailed displacement field near a few of the cracks. Colors are used to indicate the dimensionless S_{xx} element of the stress tensor, and the color scale is shown at the right-hand side of each part of the figure. The insert in the middle part ($t = 300$) of the figure shows the dimensionless displacement, dx, in the direction parallel to the cooled surface, and the corresponding color scale is shown in right-hand side of the insert. *From Huang, H., Meakin, P., Malthe-Sorenssen, A., 2016b. Physics-based simulation of multiple interacting crack growth in brittle rocks driven by thermal cooling. International Journal for Numerical and Analytical Methods in Geomechanics 40 (16), 2163–2177, with permission from John Wiley and Sons.*

quasihierarchical cracking pattern and its statistical properties do not depend on the local heterogeneity. Of course, crack propagation is regulated by the temperature field, which determines the average crack spacing on larger scales via the principle of minimum total potential energy, a principle often used in linear elastic fracturing mechanics (Griffith, 1921; Irwin, 1957).

Fig. 4.4 shows the simulated fracturing process under a larger thermal strain load, $\alpha\Delta T$, of 1.0%. This simulation was carried out using the extreme assumption that there is no heat conduction across the cracks. At the beginning of the cooling (Fig. 4.4A), a densely spaced array of small cracks that are more or less parallel to each other was formed, similar to the cracking patterns formed at small-to-moderate thermal strain loads, but with many more cracks initiated due to the larger initial thermal strain load. Thus the crack−crack competition for growth started earlier because of the smaller spacing between adjacent cracks. As shown in Fig. 4.4A, these parallel thermal cracks started to form hierarchical fracturing pattern shortly after the cooling started. As the cooling front penetrated deeper into the rock, as shown in Fig. 4.4B, this hierarchical fracturing pattern became more obvious. However, at this stage, while the longer cracks continued to propagate more or less vertically, some of the shorter cracks started to bend away from the vertical direction instead of simply ceasing to grow, as they did in the smaller thermal strain load simulations. The crack bending become more obvious as the cooling front continued to propagate deeper into the rock, as shown in Fig. 4.4C. Some cracks continued to propagate more or less vertically, whereas others curved strongly and approached or joined long "vertically" propagating cracks in an approximately horizontal direction. Similar behavior has been observed in experiments (Geyer and Nemat-Nasser, 1982). The curved cracks significantly altered the temperature field, because heat transport across the cracks was turned off in these simulations.

The simulation results strongly indicate that the coupled heat conduction−DEM model is a valuable tool for studying the complex nonlinear interplay between crack propagation and the evolving temperature fields in brittle rocks. The key physical processes involved in thermally driven cracking process, such as random initiation of cracks (largely influenced by local heterogeneity), subsequent crack propagation and crack "space-coarsening" based on the principle of minimum total potential energy under evolving, stress-generating temperature field, are well captured by the model and become "emergent" behavior of the model itself. We did not consider the effect of initial in situ stress because we were more interested in the changes of stress due to thermal contraction/diffusion and fracturing. As illustrated in the later sections of this chapter, it is straightforward and convenient to impose various in situ confining stress states into the DEM model by simply shrinking or expanding the DEM network accordingly.

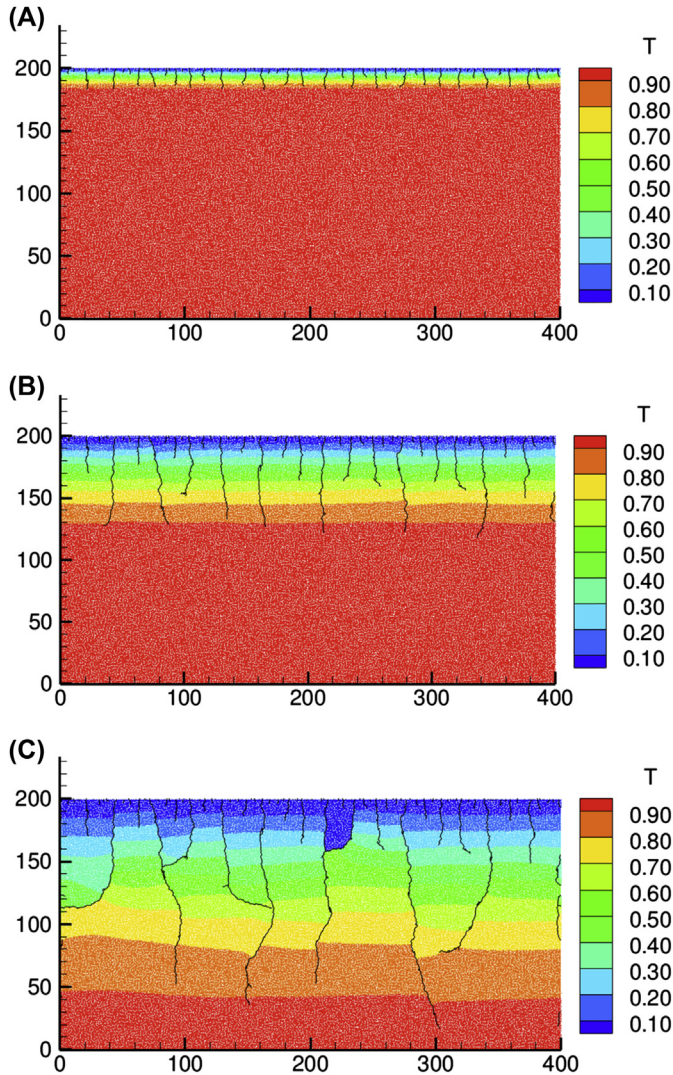

FIGURE 4.4 Simulated initiation and growth patterns of thermal cracks and associated temperature field under large thermal strain load condition at different times with no heat transport across crack apertures: (A) $t = 150$; (B) $t = 300$; and (C) $t = 15{,}000$. Colors are used to indicate the dimensionless temperature field and the color scale is shown at the right-hand side of each part of the figure. *From Huang, H., Meakin, P., Malthe-Sorenssen, A., 2016b. Physics-based simulation of multiple interacting crack growth in brittle rocks driven by thermal cooling. International Journal for Numerical and Analytical Methods in Geomechanics 40 (16), 2163–2177, with permission from John Wiley and Sons.*

4.4 HYDRAULIC FRACTURING MODELING BY COUPLED QUASISTATIC DISCRETE ELEMENT MODEL AND CONJUGATE NETWORK FLOW MODEL

4.4.1 Methodology of Coupled Discrete Element Model and Dual Network Flow Model

In this subsection, we illustrate how the quasistatic DEM model can be coupled with a dual network fluid flow model to simulate hydraulic fracturing. The coupled quasistatic DEM−network flow model enables the physics-based modeling of hydraulic fracturing model with high computational efficiency. Fig. 4.5 illustrates how the coupling method between the two models is implemented. Rock is represented by an assembly of randomly generated, nonuniformly sized circular rigid particles that may be connected by elastic beams. The elastic beams form the first type of lattice—a disordered geomechanical network. The enclosed beams form a set of control volumes for network flow simulations. One single dual flow node is assigned to each enclosed beam loop. The dual flow lattice is generated by connecting all of the dual nodes to provide possible channels for fluid flow.

The governing equation for fluid flow is assumed to take the form:

$$\frac{\partial(n\rho_f)}{\partial t} = \nabla\left(\frac{\rho_f k_0}{\mu}\nabla P\right) + \rho_f Q, \tag{4.12}$$

where n is the porosity of the rock, ρ_f is the fluid density, k_0 is the formation permeability, μ is the fluid viscosity, P is fluid pressure, and Q is the volu-

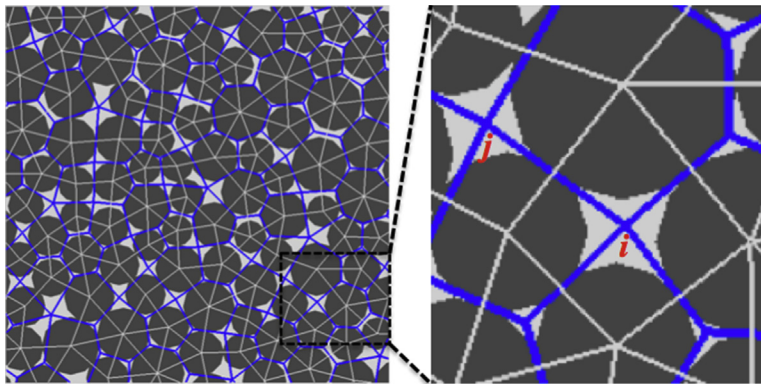

FIGURE 4.5 Illustration of the coupled discrete element model (DEM)−network flow model: circular discrete elements connected by elastic beam lattice (in white) and a network flow lattice (in blue [light gray in print version]) dual to the DEM lattice. The graph on the right shows the control volume of a flow node in more detail.

metric injection rate. Using the definitions for fluid compressibility $c_f = \frac{1}{\rho_f}\frac{\partial \rho_f}{\partial P}$ and rock matrix bulk compressibility (inverse of the bulk modulus) $c_n = \frac{1}{n}\frac{\partial n}{\partial P}$, the term on the left-hand side of Eq. (4.12) can be rewritten as

$$\frac{\partial(n\rho_f)}{\partial t} = (\rho_f n c_f + \rho_f n c_n)\frac{\partial P}{\partial t}. \tag{4.13}$$

Substituting Eq. (4.13) into Eq. (4.12), defining total compressibility as $c_T = c_f + c_n$, and rearranging terms, we obtain

$$\frac{\partial(nP)}{\partial t} = \nabla\left(\frac{k_0}{c_T\mu}\nabla P\right) + \frac{Q}{c_T}. \tag{4.14}$$

By choosing a characteristic length L^* and a characteristic time t^*, Eq. (4.14) can be rewritten in a dimensionless form:

$$\frac{\partial(nP)}{\partial t'} = \nabla'\left(\frac{k_0}{c_T\mu}\frac{t^*}{L^{*2}}\nabla' P\right) + \frac{Qt'}{c_T} = \nabla'(\lambda\nabla' P) + \frac{Qt^*}{c_T}. \tag{4.15}$$

By further normalizing the fluid pressure P by the Young's modulus E and dropping the prime sign in Eq. (4.15), we finally obtain the dimensionless fluid pressure diffusion equation

$$\frac{\partial(np)}{\partial t} = \nabla(\lambda\nabla p) + Q^*, \tag{4.16}$$

with dimensionless pressure $p = P/E$, dimensionless injection rate $Q^* = Qt^*/(c_T E)$, and dimensionless pressure diffusivity $\lambda = k_0 t^*/c_T\mu L^{*2}$.

As illustrated in Fig. 4.5, a network flow model using a lattice dual to the DEM lattice is used to discretize Eq. (4.16) by a conventional FV scheme:

$$\Delta V_i n_n \frac{p_i^{t+\Delta t} - p_i^t}{\Delta t} = \sum_{j=1}^{\text{neighbor}} \lambda_{ij} A_{ij} \frac{p_j^{t+\Delta t} - p_i^{t+\Delta t}}{d_{ij}} + Q^* \Delta V_i, \tag{4.17}$$

where ΔV_i is the control volume associated with flow node i, d_{ij} is the distance between nodes i and j, A_{ij} is the cross-sectional area between flow nodes i and j. It is worth noting that, unlike the thermal conduction equation that is solved on the DEM lattice as illustrated in the previous section, the flow equation is solved on a flow network dual to the DEM lattice. In the coupled DEM–network flow model, fractures are represented by a connected set of segments that coincide with the faces of the lattice that is dual to the beam lattice used in the DEM model. Consequently, it is more realistic to calculate fluid flow along the fracture(s) from the permeabilities of the segments that lie on faces of the dual lattice, treated as slits with parallel faces, than to calculate the fluid flow along the fractures using a connected set of channels along the edges (beams) of the DEM lattice. An advantage of this approach is that the aperture widths

can be calculated directly from the distances between the DEM model particles on either side of each slit-shaped segment and their diameters.

The forces and moments acting on individual elements of the discrete element network including the contribution of the fluid pressure gradient are given by

$$\vec{F}_{i,j} = k_n\left(d_{i,j} - d_{i,j}^0\right)\vec{n}_{i,j} + k_s\frac{1}{2}\left(\phi_{i,j} + \phi_{j,i}\right)\vec{s}_{i,j} - \nabla P\cdot\pi r_i^2, \tag{4.18}$$

$$\vec{M}_{i,j} = k_s d_{i,j}\left[\frac{\Phi}{12}\left(\phi_{i,j} - \phi_{j,i}\right) + \frac{1}{2}\left(\frac{2}{3}\phi_{i,j} + \frac{1}{3}\phi_{j,i}\right)\right], \tag{4.19}$$

where ∇P is the fluid pressure gradient acting on individual DEM particle, which can be obtained from the nodal pressures on the dual flow lattice. As fluid pressure (and pressure gradient) increases due to fluid injection during hydraulic stimulation, the force exerting on the DEM particles increases and deforms the mechanical bonds and breaks them if the deformation reaches a prescribed threshold value, thereby initiating fracturing or propagating a preexisting fracture. As shown in Fig. 4.5, each mechanical bond intersects the flow network, and when a mechanical bond is broken, a microfracture connects the two associated fluid nodes of the flow network with a new permeability given by

$$k = b^2/12 \tag{4.20}$$

Here b is the aperture of the microfracture (the separation distance between the two neighbor DEM particles subject to fracturing). The new permeability is then used to calculate the hydraulic diffusivity λ_{ij} in Eq. (4.17). In addition, when a beam is broken or the pressure field changes the positions of all of the nodes in the DEM change, and the permeabilities between all of the fluid nodes connected by fractures or fracture segments are recalculated from Eq. (4.20) each time that the DEM network is relaxed to a new mechanical equilibrium.

The simulation of coupled DEM−network flow model consists of interleaved fluid flow, mechanical relaxation of the DEM network, recalculation of fracture permeability, and beam-breaking steps. During each time step, the new fluid pressure field (in both fractures and matrix) is obtained by using Eq. (4.17). Then the new fluid pressure field is applied to DEM network according to Eqs. (4.18) and (4.19); the DEM network is then relaxed to a new mechanical equilibrium and the fracture permeability is recalculated. The beam that most exceeds the failure criteria, which is usually near a crack tip, is then removed from the DEM network, and the network is again relaxed into a new state of mechanical equilibrium. The mechanical relaxation and beam-breaking are repeated a number of times during each time step, mimicking crack initiation and propagation, until no additional beam-breaking occurs, and the simulation then proceeds to a new time step.

Our coupled DEM—network flow model accounts for both flow in fractures and flow into the rock matrix, unlike most other network flow models that typically only account for fluid flow in fractures, or use some ad hoc leak-off factor. One distinct advantage of the model is that fracturing is naturally described by the breakage of elastic beams between DEM elements without complex and empirical ad hoc assumptions about the fracture initiation and propagation direction. The crack path and the lengths of individual propagation events are natural outcomes of the quasistatic DEM model itself, based on minimum total potential energy principal (i.e., relaxation into a new mechanical equilibrium that minimizes the elastic potential energy under a given load).

4.4.2 Simultaneous Propagation of Interacting Fractures

The first example of simulations conducted with the coupled DEM and network flow model is a 2D simulation of the propagation and interaction between two fractures that grow simultaneously from a single horizontal wellbore. The rock formation is assumed to be homogeneous and isotropic on large length scales, but small-scale heterogeneity is represented in the model by the random packing procedure used to generate the geometry of the DEM model and perturbations added to the force constants and failure thresholds of individual beams. As shown in Fig. 4.6, a cased horizontal wellbore is located

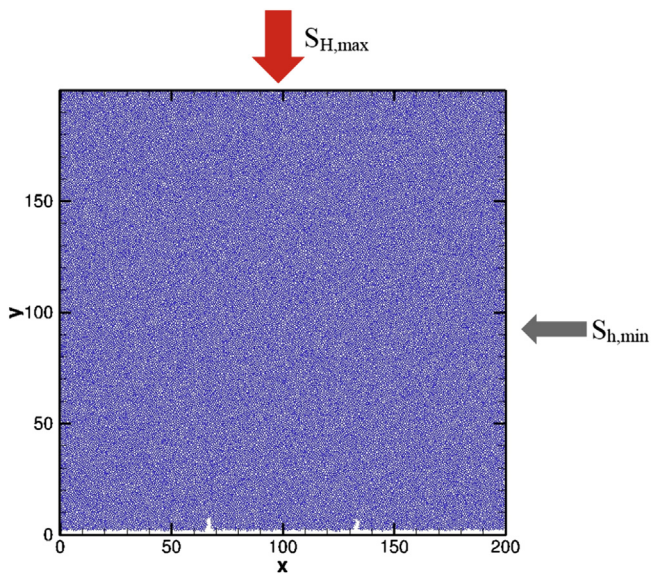

FIGURE 4.6 Model setup with a horizontal wellbore at the bottom and two perforations. The unit of length is feet.

TABLE 4.1 Input Parameters for Simultaneous Hydraulic Fracture Propagations

Input Parameters	
Young's modulus (GPa)	40
Poisson's ratio	0.269
Maximum horizontal stress (MPa)	48
Stress anisotropy ratio	$S_{h,\min}/S_{H,\max} = 0.9$ ($S_{H,\max} - S_{h,\min} = 4.8$ MPa)
Injection rate (bbl/min)	50
Injection viscosity (cP)	200
Formation permeability (nD)	100
Formation porosity	0.1
Fracture height (ft)	100
Perforation spacing (ft)	40

at the bottom of the domain and aligned with the minimum horizontal compressive stress direction. The domain size is 200×200 ft filled with 51,000 DEM particles, and the overall porosity of the domain is 10%. Two perforations were initiated from the wellbore simply by removing a few DEM particles adjacent to the wellbore out from the model domain. The input rock properties and stress conditions are summarized in Table 4.1. The maximum horizontal compressive stress is orientated in the y-direction. The simulated result of induced fracture geometry is shown in Fig. 4.7.

As shown in Fig. 4.7, the two hydraulic fractures repel each other as they propagate. The opening of one hydraulic fracture will exert additional closing forces on neighboring cracks via the long-range elastic interaction, a well-known "stress shadowing" effect, leading to a "repelling-growth" pattern of two interacting fractures. The simulated "repelling-growth" pattern is consistent with predictions from other multiple nonplanar hydraulic fracture simulators based on the BEM (Weng et al., 2011; Wu, 2014).

4.4.3 Interaction Between Propagating Hydraulic Fracture and Natural Fracture

In this example, the interaction of a single propagating hydraulic fracture with a natural fracture at various orientations will be examined. Preexisting natural fractures are introduced by prebreaking or weakening the elastic bonds that intersect the natural fractures. In essence, the beams represent the cohesive and frictional strength of the undamaged rock and the natural fractures. Friction

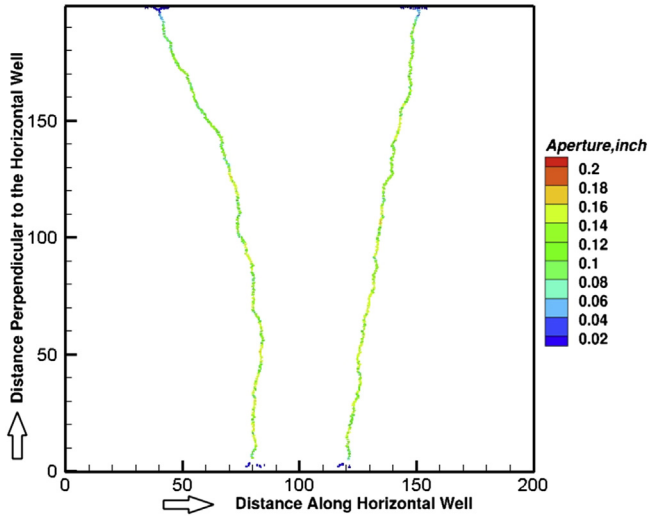

FIGURE 4.7 Induced hydraulic fracture geometry with stress ratio $S_{h,\min}/S_{H,\max} = 0.9$.

and repulsive forces between particles that are not connected by unbroken beams were not included because the DEM model was used to simulate hydraulic fracturing for conditions under which mode I (opening mode hydraulic fracturing) is dominant. These forces play an essential role in DEM modeling of granular dynamics (Cundall and Strack, 1979), and they can easily be added when required. The natural fractures can be fully open or cemented, depending on the type and extent of mineralization. Fig. 4.8 shows the schematic model setup that is considered in this example simulation. The reservoir is homogeneous on long length scales (much larger than the scale of the DEM particles) and isotropic with dimensions of 200 × 200 ft. The radii of the circular DEM particles vary between 0.4 and 0.6 ft, and nearly 51,000 particles were used for this simulation. A horizontal well with single perforation is located at the bottom of the model domain and aligned along the minimum compressive principal stress direction. Only one primary hydraulic fracture is expected to initiate and propagate along the maximum compressive stress direction. In this 2D model, it is assumed that the induced fracture has a constant height in the z-direction (pseudo-3D), i.e., both the hydraulic fracture and natural fracture are confined vertically within a thin stratum. The maximum horizontal compressive stress is oriented in the y-direction. The relevant rock properties and injection parameters are provided in Table 4.2.

Four different intersection angles α (the angle between natural fracture and maximum horizontal compressive stress, or equivalently the average propagation direction of hydraulic fracture), 90, 75, 45, and 30 degrees, were used in simulations. A relatively large in situ stress ratio of 0.7 ($S_{h,\min}/S_{H,\max} = 0.7$) is

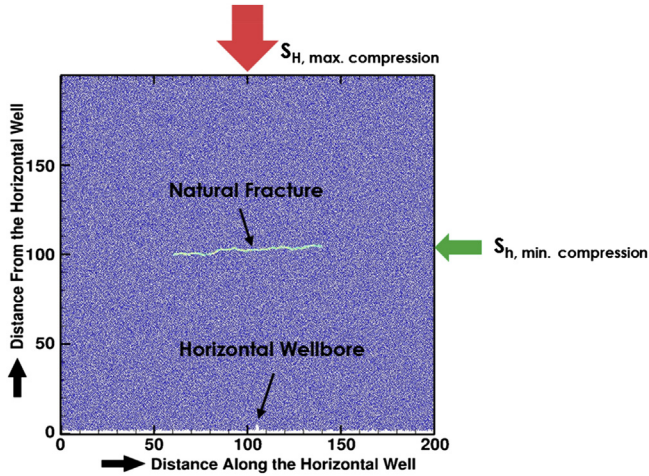

FIGURE 4.8 Top view of a reservoir with one natural fracture located at the center of the domain is shown. Hydraulic fracture is induced through a single perforation in a horizontal well. The maximum horizontal stress is in a direction perpendicular to the horizontal well and is shown by the *red arrow* (gray in print version). *From Zhou, J., et al., 2017. A dual lattice discrete element model to understand hydraulic fracturing in a naturally fractured system. Hydraulic Fracturing Journal 4 (2).*

TABLE 4.2 Input Parameters for Simulating Interactions Between Hydraulic Fracture and Natural Fracture

Parameters	Value
Young's modulus (GPa)	40
Poisson's ratio	0.27
Maximum horizontal compressive stress, $S_{H,max}$ (MPa)	48
Stress ratio (minimum/maximum)	0.7
Formation permeability (nano-Darcy)	100
Formation porosity	0.1
Formation tensile strength (MPa)	27
Natural fracture length (ft)	80
Natural fracture cohesion	0
Hydraulic fracture height (constant) (ft)	100

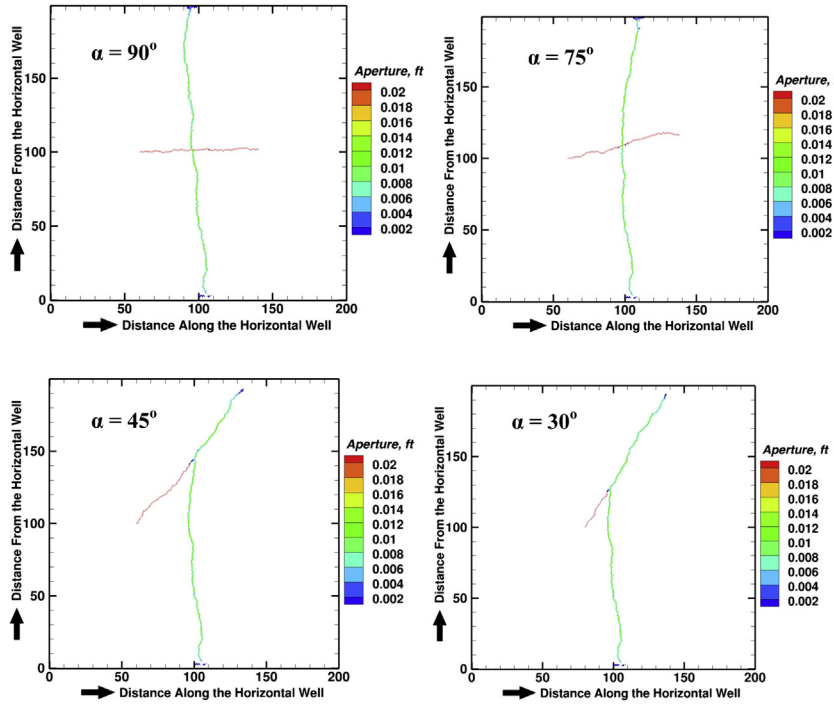

FIGURE 4.9 Induced fracture geometry with different intercepting angles. *From Zhou, J., et al., 2017. A dual lattice discrete element model to understand hydraulic fracturing in a naturally fractured system. Hydraulic Fracturing Journal 4 (2).*

used for all cases. The permeability and cohesive (or tensile) strength of the natural fracture are 1 md and 0 psi, respectively, representing a more permeable flow pathway with no fracture healing—an extreme condition in favor the diversion of hydraulic fractures. The injected fluid viscosity is 10 *cP*. The final fracturing patterns are shown in Fig. 4.9.

At large intersection angles (90 and 75 degrees), the simulated hydraulic fracture cuts through the natural fracture, even though the natural fracture is much more permeable than the undamaged rock (so fracturing fluid can easily leak into it) and it has no tensile strength. This behavior may be due to the relatively large in situ stress ratio of 0.7 between the minimum and maximum horizontal compressive stresses applied to the model. In contrast, at smaller intersection angles (45 and 30 degrees), when the hydraulic fracture approached the natural fracture, it was "arrested" by the highly permeable natural fracture. The natural fracture was opened due to pressurization of the fluid within it, and the hydraulic fracture continued to propagate from the far-end tip of the natural fracture. The key observations in the bottom two panels are that with closer collinearity between the hydraulic and the natural fracture,

there was a greater potential for the hydraulic fracture to be captured by the natural fracture, if the natural fractures are more permeable than the rock matrix, and can be considered to be "weak" planar defects (a tensile strength of zero was used in this extreme case). Warpinski and Teufel (1987) experimentally observed that decreasing the intersection angle is more favorable for impeding the direct crossing and propagation of the hydraulic fracture, and the subsequent reactivation the natural fracture. Although not shown here, similar behavior can be observed using different random realizations with the same set of mechanical/flow parameters, and the macroscale results do not change much from realization to realization.

In addition to orientations of natural fractures, a large number of other factors, including the in situ stress differential ratio, permeability and tensile/shear strengths of natural fractures, injection rate, and viscosity of the fracturing fluid, would collectively have profound effects on the interaction between propagating hydraulic fracture and natural fractures. It is not the objective of this chapter to present a full spectrum of sensitivity studies on these parameters; however, the coupled DEM−network flow model provides a valuable tool to account for these parameters in a single model.

4.4.4 Three-Dimensional Simulations of Hydraulic Fracturing

Although the 2D coupled quasistatic DEM model as illustrated previously has been successfully applied to generate "realistic" crack morphologies for thermally driven and hydraulic fracturing processes, it provides interesting insights into the physics behind fracturing process (Zhou et al., 2015a,b, 2016), and it has limited applicability to the hydraulic fracturing of real shale formations. In this subsection, we extend the 2D coupled quasistatic DEM and network flow model into 3D and present several 3D simulation results.

In the 3D model, the rock volume is represented by an assembly of spherical DEM elements of variable sizes (instead of the circular disks as used in the 2D model) that are usually selected randomly from a prescribed size distribution. A random packing procedure is then used to generate a closely packed ensemble that represents the rock volume. The DEM lattice used in the 3D model is then formed by the Delaunay tessellation of the DEM particles. The Delaunay tessellation decomposes the domain into nonoverlapping tetrahedra with each vertex representing a DEM particle and each edge representing an elastic beam connecting two adjacent DEM particles. A dual flow node is then assigned to the center of each tetrahedron and it is connected to the adjacent flow nodes. Fig. 4.10 illustrates the dual-lattice construction of the coupled DEM−network flow model in 3D. In Fig. 4.10, points A, B, C,…, G represent the DEM particles. Via Delaunay tessellation, four DEM tetrahedra are formed according to their locations (<ABCD>, <ABCE>, <ABDF>, and <ACDG>) with each edge representing an elastic beam connecting two

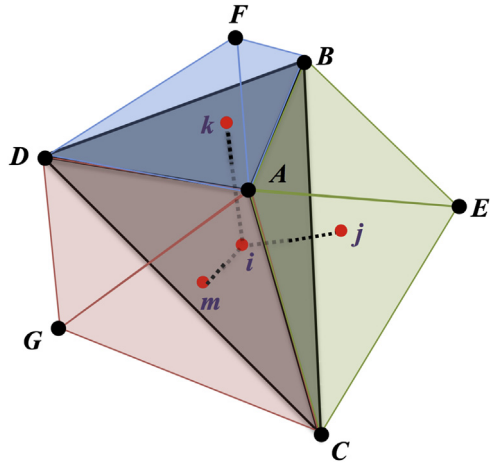

FIGURE 4.10 A three-dimensional discrete element model lattice (*solid lines*) and dual flow network lattice (*dotted lines*).

adjacent DEM particles. Each tetrahedron has four neighboring tetrahedra with shared facets. Each tetrahedron contains a flow node (i, j, k, m in Fig. 4.10). By connecting these flow nodes, a dual flow network is then constructed. For example, three possible flow paths for flow node i ($i \Leftrightarrow j$, $i \Leftrightarrow k$, $i \Leftrightarrow m$) are shown in Fig. 4.10 (there is also a fourth flow path, $i \Leftrightarrow n$, between node i and node n, which lies in front of tetrahedron <ABCD> and is not shown in the figure).

Similar to the 2D DEM model, the force and moment exerted on DEM particle A by a neighboring DEM particle B via the elastic beam $A-B$ that connects them (e.g., $A-B$ beam in Fig. 4.10) has the following form:

$$\vec{F}_{A,B} = F^n_{A,B}\vec{n}_{A,B} + F^s_{A,B}\vec{s}_{A,B} \tag{4.21}$$

and

$$\vec{M}_{A,B} = M^n_{A,B}\vec{n}_{A,B} + M^s_{A,B}\vec{\zeta}_{A,B}, \tag{4.22}$$

where $F^n_{A,B}$ and $F^s_{A,B}$ are the normal (along the beam) and perpendicular force components. Here $\vec{n}_{A,B}$ is the unit vectors parallel to the center line connecting DEM nodes A and B (current locations) and $\vec{s}_{A,B}$ is the unit vector perpendicular to $\vec{n}_{A,B}$, in the plane that contains both the current beam unit vector $\vec{n}_{A,B}$ and the initial beam unit vector $\vec{n}^0_{A,B}$. Therefore $\vec{n}_{A,B} \cdot \vec{s}_{A,B} = 0$. $\vec{\zeta}_{A,B}$ *is the unit vector pointing in the direction of the out-of-the-plane beam bending moment and it is equal to the cross product between* $\vec{n}_{A,B}$ and $\vec{s}_{A,B}$. $F^n_{A,B}$ and $F^s_{A,B}$ can be calculated as

$$F_{A,B}^{n} = \overline{k}_{n}^{A,B} S \Delta d_{A,B}^{n} \tag{4.23}$$

and

$$F_{A,B}^{s} = \overline{k}_{s}^{A,B} S \Delta d_{A,B}^{s}, \tag{4.24}$$

where $\overline{k}_{n}^{A,B}$ and $\overline{k}_{s}^{A,B}$ are the beam ($A-B$) normal and shear (bending) stiffness constants per unit cross-sectional area of the beam. Each beam has a circular cross section with an area of $S = \pi \overline{R}^2$, where $\overline{R}$ is the average of the radii or the two DEM particles that it connects, and $\Delta d_{A,B}^{n}$ and $\Delta d_{A,B}^{s}$ are the normal $\left(\overrightarrow{n}_{A,B}\right)$ and perpendicular $\left(\overrightarrow{s}_{A,B}\right)$ components of the relative displacement vector of the two DEM nodes connected by beam ($A-B$).

The torsional and bending moments of the beam can be obtained from

$$M_{A,B}^{n} = -\overline{k}_{s}^{A,B} J \Delta \theta^{n} \tag{4.25}$$

and

$$M_{A,B}^{s} = -\overline{k}_{n}^{A,B} I \Delta \theta^{s}, \tag{4.26}$$

where $\Delta\theta^{n}$ and $\Delta\theta^{s}$ are the twisting and bending angles of the beam between DEM particles A and B. I is the moment of inertia (corresponding to bending of the beam) and J is the polar moment of inertia of the beam (corresponding to beam twisting) (see Potyondy (Potyondy and Cundall, 2004) for details), calculated by

$$I = \frac{1}{4} \pi \overline{R}^4 \tag{4.27}$$

and

$$J = \frac{1}{2} \pi \overline{R}^4. \tag{4.28}$$

Once a mechanical load is applied (the load is imposed by fluid injection in this case), a successive overrelaxation algorithm is used to relax the 3D DEM network into a new state of mechanical equilibrium in which the net force and moment are zero for all individual DEM particles. The effective tensile and shear strains of a beam are calculated as

$$\varepsilon = \left(\frac{F^{n}}{\overline{k}_{n} A} + \frac{|M^{s}| \overline{R}}{\overline{k}_{n} I} \right) \Big/ L_0, \tag{4.29}$$

and

$$\varphi = \left(\frac{|F^{s}|}{\overline{k}_{s} A} + \frac{|M^{n}| \overline{R}}{\overline{k}_{s} A} \right) \Big/ L_0, \tag{4.30}$$

where L_0 is the initial beam length. Similar to the 2D model, if the tensile strain of a beam exceeds its prescribed critical tensile strain ($\varepsilon \geq \varepsilon_c$) or its

shear strain exceeds its prescribed critical shear strain ($\varphi \geq \varphi_c$), it is irreversibly removed from the DEM network, giving rise to fracture initiation and growth. Here ε_c is the critical longitudinal tensile strain (the maximum tensile strain that the bond can sustain) and φ_c is the critical relative shear strain above which the beam will break, even in the absence of tensile strain. This criterion can simulate both tensile-induced and shear-induced rock failure. Typical values for ε_c and φ_c range from $\sim 10^{-4}$ to $\sim 10^{-2}$ for rocks and many other polycrystalline brittle solids.

The coupling between the 3D quasistatic DEM model and the 3D flow model is implemented using essentially the same method that is used in the 2D model described in Section 4.1. The 3D network flow model accounts for flow within both the fractures and Darcy flow within the porous matrix with continuity of both the fluid pressure and flux across the fracture surfaces. Although we considered only laminar flow of Newtonian fluids in this work, the flow model could be extended to include the effects of turbulent flow and more complex rheologies by using semiempirical relationships between the pressure gradient and flow velocity in both the fractures and surrounding permeable rock.

The 3D model was used to simulate hydraulic fracture propagation from a vertical wellbore, as shown in Fig. 4.11. In this example, we assumed that the rock is homogeneous and isotropic on large length scales but heterogeneous on

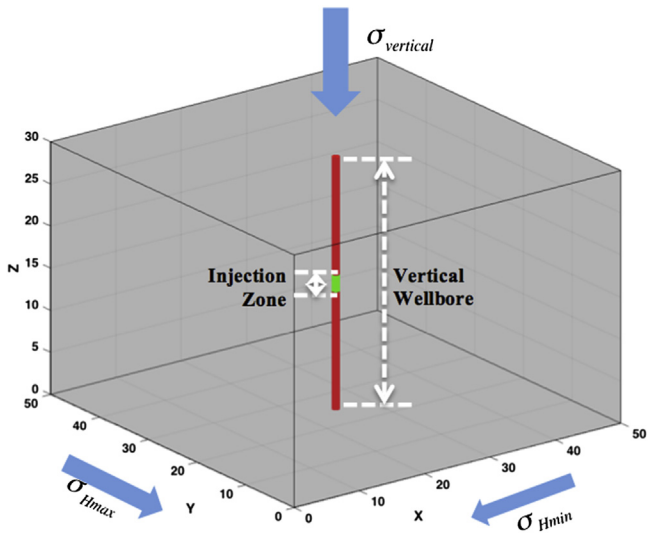

FIGURE 4.11 Model setup used in the three-dimensional discrete element model simulations with a vertical wellbore. The well is "cased and cemented" except for an interval of 3 ft, indicated in green (light gray in print version), through which the fluid is injected into the formation. The properties of the injected fluid are very similar to those of water at room temperature (Table 4.3).

small length scales (the individual beam stiffnesses, tensile strengths, and shear strengths were still selected randomly from the corresponding distribution functions). The model domain size was chosen to be $50 \times 50 \times 30$ ft (15.24 m on a side). An open vertical cylindrical wellbore was inserted at the center of the model domain, and it penetrated the whole depth (red cylinder) with a diameter of 1 ft (0.3048 m). Fluid was injected into the formation only through the middle part of the vertical well (the green segment in Fig. 4.11) with a height of 3 ft (0.91 m) at a rate of 2 L/min. The overburden stress (S_{vertical}) was oriented in the *Z*-direction, the maximum compressive horizontal stress ($S_{H,\max}$) was oriented in the *Y*-direction, and the minimum compressive horizontal stress ($S_{H,\min}$) was oriented along the *X*-direction. The geological and operation parameters are summarized in Table 4.3. A total of 118,634 DEM particles of variable sizes, ranging from 0.4 to 0.6 ft (0.12–0.18 m) were randomly generated and packed into the model domain to form the DEM lattice and associated dual flow network. The permeability of the rock matrix was 100 nano-Darcy (1.0×10^{-19} m^2), representing an ultralow-permeability formation.

TABLE 4.3 Input Parameters and Rock Properties Used in 3D Simulations

Parameters	Value
Young's modulus (GPa)	40
Poisson's ratio	0.23
Shear modulus (GPa)	17.9
Density (g/cm^3)	2.95
Uniaxial compressive strength (MPa)	105
Uniaxial tensile strength (MPa)	14
Formation permeability (nano-Darcy)	100
Formation porosity	0.06
Injection rate (L/min)	2.0
Injection fluid viscosity (Pa·s)	1.0×10^{-3} (viscosity of water is 0.89×10^{-3} Pa s at 25°C)
Injection fluid density (g/cm^3)	1.0
Injection fluid compressibility (Pa^{-1})	4.58×10^{-10}
Overburden stress (MPa)	44
Maximum horizontal stress (MPa)	30.35
Minimum horizontal stress (MPa)	25.07

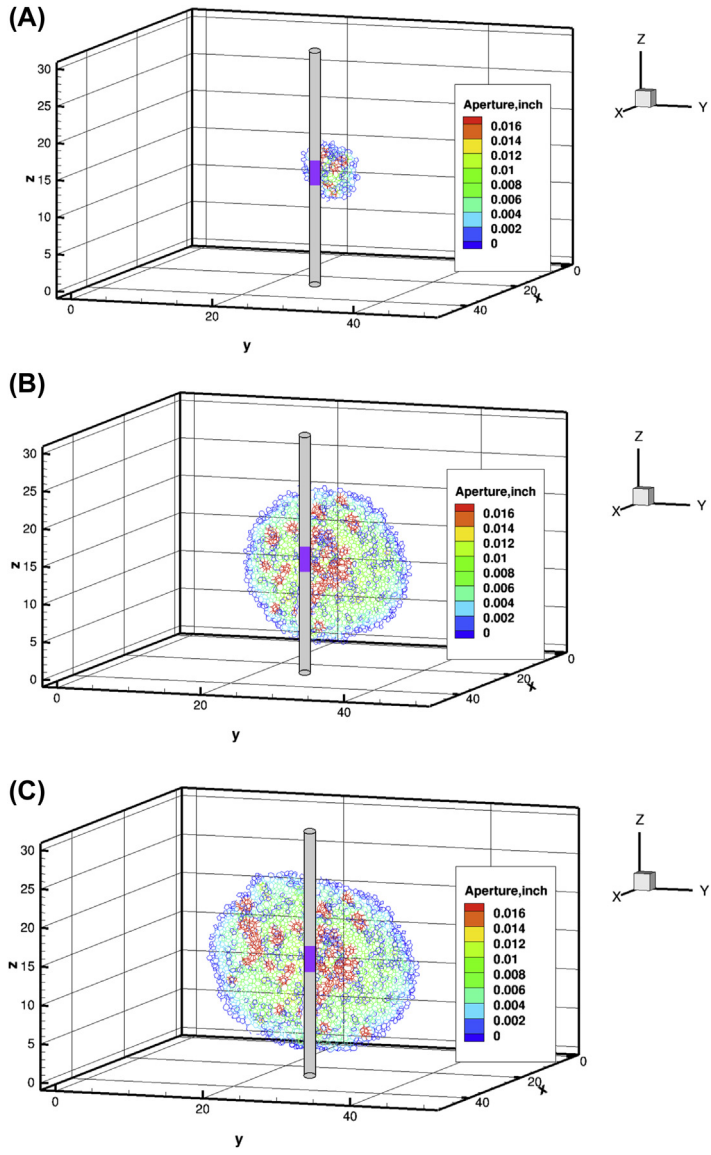

FIGURE 4.12 Simulated three-dimensional hydraulic fracture morphologies at different times: (A) $t = 35$ s; (B) $t = 145$ s; and (C) $t = 345$ s. The color scale indicates the width of the hydraulic fracture aperture.

Fig. 4.12 shows how the simulated hydraulic fracture propagated over time. As the fluid was injected at a constant rate, the pressure in the wellbore rapidly increased due to the low compressibility of the injected fluid and the rigidity of the formation. Once the wellbore pressure was large enough (~35 s after

injection starts) to break the beams between DEM particles adjacent to the wellbore, a nearly vertical fracture was initiated and started to propagate (Fig. 4.12A). Once the fracture was initiated, it "popped open," and a crack with a relatively large radius of ~ 1.2 m, and an average aperture of $\sim 2.0 \times 10^{-4}$ m, was formed. Due to the local mechanical heterogeneity incorporated into the model, the initial crack did not assume an ideal biwing penny shape, but instead it was quite asymmetric. As more fluid was injected, the fracture continued to propagate more or less along the plane perpendicular to the direction of the minimum horizontal principal compressive stress (the *X*-axis in this simulation) and eventually grew into a more or less a penny-shaped fracture (Fig. 4.12B and C). Unlike the uniform fracture front growth expected in a homogeneous material (unless unstable critical fracture propagation occurs), the simulated growth of the fracture front at any given moment is nonuniform, with some parts of the crack front advancing while others remain stationary. The uniform growth concept is valid only in a statistical sense during the late stages of fracture propagation. In addition, because randomness was introduced into the mechanical properties of beams, the fracture propagation was not perfectly symmetric. Another general trend observed in all of the hydraulic fracturing simulations is that the fracture aperture closer to the wellbore is the largest and its size decreases with the increasing distance from the wellbore, as expected. Some local fluctuations of the fracture apertures, due to the local mechanical heterogeneity included in the model, are also observed in the simulations, indicating a rough walled hydraulic fracture that fluctuates about the average plane of the fracture. We believe that these deviations from the behavior expected for hydraulic fracturing of a homogeneous formation are realistic for natural rocks, which are never truly homogeneous.

Fig. 4.13 shows how the wellbore pressure evolved during the simulated hydraulic fracturing process. After fluid injection began, the pressure increased

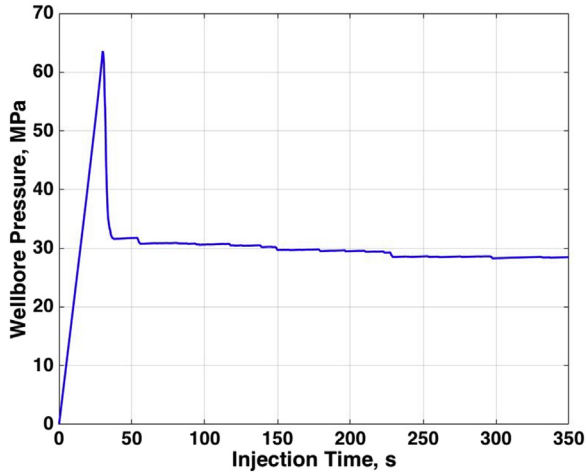

FIGURE 4.13 Wellbore pressure versus injection time.

rapidly until a peak pressure (the breakdown pressure) was reached. At this point in time, fracture propagation began, and the pressure decreased rapidly until the fracture began to propagate with a stable, reduced pressure called the propagation pressure, which decreased slowly with increasing time. The estimated breakdown pressure, which was reached about 35 s after injection began, was 64 MPa, and the estimated propagation pressure was 28 MPa as the quasiasymptotic steady state in which the fluid injection rate and leak-off rate are balanced. The rapid decrease in pressure after the breakdown pressure was reached is attributed to fast fracture propagation, which rapidly increases the fluid volume. As the crack propagates further, the fluid pressure needed to maintain crack growth, at a slower velocity, decreases.

One of the dominant features of shale and other sedimentary rock formations is their layered structure, with variations in mineral compositions, rock mechanical properties such as the Young's modulus and critical tensile strength, and permeability from one layer to another, all of which may affect the hydraulic fracture process. Fig. 4.14 shows two scenarios with stratigraphic

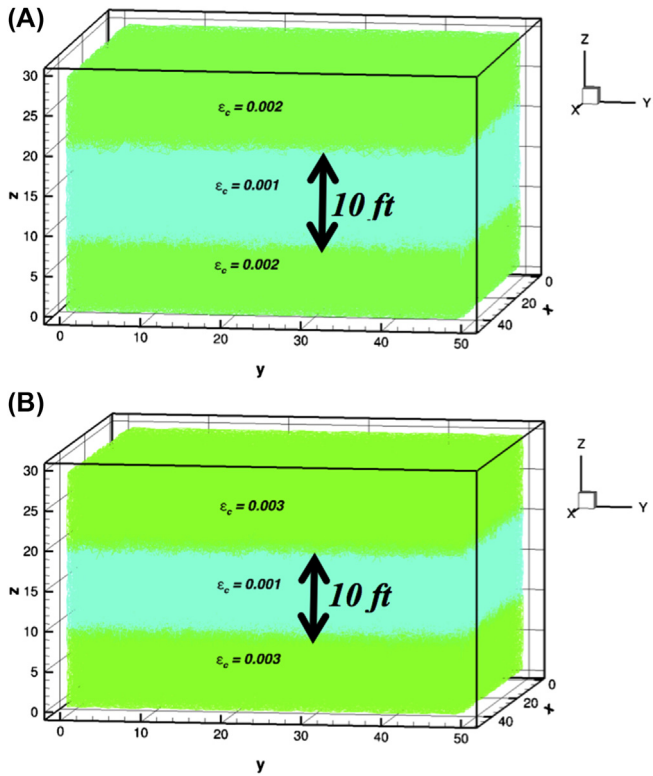

FIGURE 4.14 Formation consisting of a weak middle layer and strong adjacent layers: (A) tensile strength ratio of $\varepsilon_c^{\text{top/bot}} \Big/ \varepsilon_c^{\text{mid}} = 2$ and (B) tensile strength ratio of $\varepsilon_c^{\text{top/bot}} \Big/ \varepsilon_c^{\text{mid}} = 3$.

variations of rock tensile strengths. The model domain was separated into three horizontal layers: the top and bottom layers had the same mechanical properties, whereas the middle layer had different ones. Because fracture height containment plays an important role in selecting the perforation intervals or landing depth, two different cases were investigated to illustrate the effect of layered mechanical heterogeneity on fracture morphology. In case A (Fig. 4.14A), the critical tensile strength ratio between the top and bottom layers and middle layer was 2 $\left(\varepsilon_c^{\text{top/bot}} \Big/ \varepsilon_c^{\text{mid}} = 2\right)$, and the critical tensile strength ratio of case B was 3 (Fig. 4.14B, $\varepsilon_c^{\text{top/bot}} \Big/ \varepsilon_c^{\text{mid}} = 3$). All other model parameters were identical to those used in the previous example.

The simulated final fracture growth patterns for the two cases are shown in Fig. 4.15. Instead of growing into a penny-shaped crack in a statistically

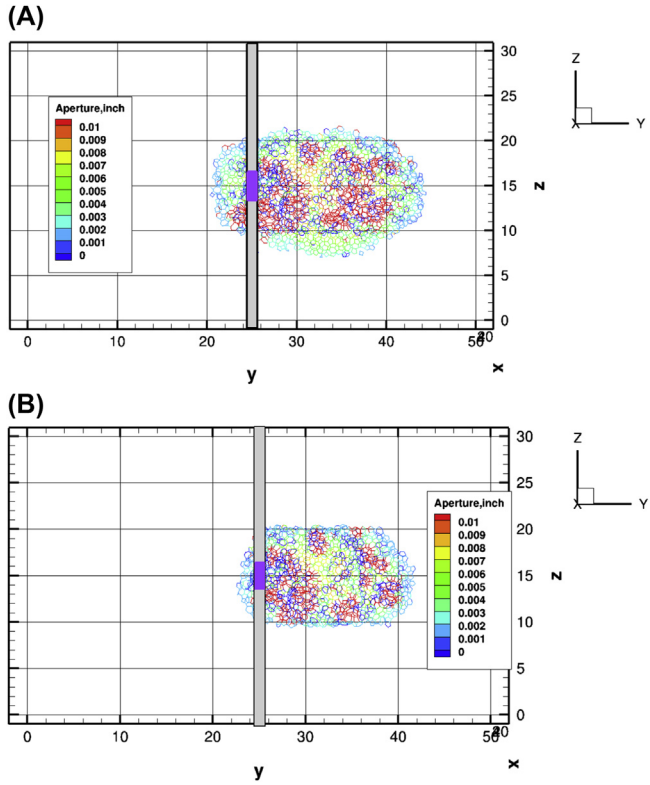

FIGURE 4.15 Hydraulic fracture in a formation consisting of a weak middle layer and strong lower and upper layers with a tensile strength ratio of (A) 2 $\left(\varepsilon_c^{\text{top/bot}} \Big/ \varepsilon_c^{\text{mid}} = 2\right)$ and (B) 3 $\left(\varepsilon_c^{\text{top/bot}} \Big/ \varepsilon_c^{\text{mid}} = 3\right)$. The color scale indicates the width of the hydraulic fracture aperture.

homogeneous formation as shown in the previous example, the induced fracture geometry turned from a penny shape into a more or less rectangular fracture as the hydraulic fractures reached the stronger confining layers. In both cases the hydraulic fractures still propagated along the plane perpendicular to the direction of the least horizontal principal compressive stress, as expected. Once the induced fracture reached the stronger upper and lower layers, vertical growth of the hydraulic fractures was suppressed. In addition, by comparing the fracture geometries shown in Fig. 4.15, it can be seen that when the tensile strength ratio between the layers was moderately small (≤ 2), some vertical propagation of the fracture into the stronger layers did occur. However, when this ratio was sufficiently large ($\rightarrow \geq 3$), the hydraulic fracture was entirely "contained" within the weaker layer. Under these circumstances, a 2D model, such as those presented in Sections 4.2 and 4.3, might provide results that are realistic enough to provide useful insights, but only when the fracture lengths are much greater than the thickness of the weak layer and if mechanical coupling and flow coupling with the overlying and underlying stronger layers are taken into account. One important implication of these results is that because stratigraphic mechanical heterogeneities are ubiquitous in sedimentary basins, hydraulic fracture may propagate over a greater distance horizontally than would be expected if there was no stratigraphic mechanical strength heterogeneity. Similarly, strong stratigraphic mechanical heterogeneity may inhibit vertical fracture propagation and make it less likely for hydraulic fractures to propagate through large distances vertically—into overlying freshwater aquifers, for example. Of course, other heterogeneities such as heterogeneous permeability, porosity, modulus, vertical stress gradient, and toughness would have to be taken into account at specific hydraulic fracturing sites.

REFERENCES

Abaqus, 2017. Abaqus Analysis Guide, SIMULIA User Assistance. Dassault Systémes Simulia Corp., Johnston, RI.

van der Baan, M., Eaton, D.W., Preisig, G., 2016. Stick-split mechanism for anthropogenic fluid-induced tensile rock failure. Geology 44 (7), 503−506.

Bahr, H.-A., Bahr, U., Petzold, A., 1992. 1-D deterministic crack pattern formation as a growth process with restrictions. EPL (Europhysics Letters) 19 (6), 485−490.

Bahr, H.-A., Weiss, H.-J., 1986. Heuristic approach to thermal shock damage due to single and multiple crack growth. Theoretical and Applied Fracture Mechanics 6 (1), 57−62.

Bahr, H.A., et al., 2010. Scaling behavior of thermal shock crack patterns and tunneling cracks driven by cooling or drying. Journal of the Mechanics and Physics of Solids 58 (9), 1411−1421.

Bahr, H.A., Fischer, G., Weiss, H.J., 1986. Thermal-shock crack patterns explained by single and multiple crack propagation. Journal of Materials Science 21 (8), 2716−2720.

Boeck, T., et al., 1999. Self-driven propagation of crack arrays: a stationary two-dimensional model. Physical Review E: Statistical, Nonlinear, and Soft Matter Physics 59 (2), 1408−1416.

Crouch, S.L., 1976. Solution of plane elasticity problems by the displacement discontinuity method. International Journal for Numerical Methods in Engineering 10 (2).

Cundall, P.A., 2001. A discontinuous future for numerical modelling in geomechanics? Proceedings of the Institution of Civil Engineers – Geotechnical Engineering 149 (1), 41–47.

Cundall, P.A., Strack, O.D., 1979. A discrete numerical model for granular assemblies. Géotechnique 29 (1), 47–65.

Dahi-Taleghani, A., Olson, J., September 2011. Numerical modeling of multistranded-hydraulic-fracture propagation: accounting for the interaction between induced and natural fractures. SPE Journal 16, 575–581.

Dalguer, L.A., Irikura, K., Riera, J.D., 2003. Simulation of tensile crack generation by three-dimensional dynamic shear rupture propagation during an earthquake. Journal of Geophysical Research Solid Earth 108 (B3). Available from: https://doi.org/10.1029/2001JB001738.

Energy Information Administration, U.S., 2015. Annual Energy Outlook 2015.

Fu, P., Johnson, S.M., Carrigan, C.R., 2013. An explicitly coupled hydro-geomechanical model for simulating hydraulic fracturing in arbitrary discrete fracture networks. International Journal for Numerical and Analytical Methods in Geomechanics 37 (14), 2278–2300.

Geyer, J.F., Nemat-Nasser, S., 1982. Experimental investigation of thermally induced interacting cracks in brittle solids. International Journal of Solids and Structures 18 (4), 349–356.

Griffith, A.A., 1921. The phenomena of rupture and flow in solids. Philosophical Transactions of the Royal Society of London 221 (582–593), 163–198.

Haddad, M., Sepehrnoori, K., 2014. Simulation of multiple-stage fracturing in quasibrittle shale formations using pore pressure cohesive zone model. In: Unconventional Resources Technology Conference, Denver, Colorado, USA, 25–27 August, Tulsa, OK, USA. American Association of Petroleum Geologists. Available from: http://search.datapages.com/data/doi/10.15530/urtec-2014-1922219.

Hazzard, J.F., Young, R.P., 2002. Moment tensors and micromechanical models. Tectonophysics 356 (1–3), 181–197.

Herrmann, J., Hansen, A., Roux, S., 1989. Fracture of disordered, elastic lattices in 2 dimensions. Physical Review B 39 (1), 637–648.

Hofmann, M., et al., 2006. Self-driven tunneling crack arrays – a 3D-fracture mechanics bifurcation analysis. International Journal of Fracture 141 (3–4), 345–356.

Huang, H., Mattson, E., 2014. Physics-based modeling of hydraulic fracture propagation and permeability evolution of fracture network in shale gas formation. In: 2014 ARMA 48th US Rock Mechanics/Geomechanics Symposium, Minneapolis, MN, 1–4 June 2014.

Huang, J., et al., 2016a. Simulation of coupled fracture propagation and well performance under different refracturing designs in shale reservoirs. In: SPE Low Permeability Symposium, Denver, Colorado, USA, 5–6 May.

Huang, H., Meakin, P., Malthe-Sorenssen, A., 2016b. Physics-based simulation of multiple interacting crack growth in brittle rocks driven by thermal cooling. International Journal for Numerical and Analytical Methods in Geomechanics 40 (16), 2163–2177.

Irwin, G.R., 1957. Analysis of stresses and strains near the end of a crack traversing a plate. Journal of Applied Mechanics E24, 351–369.

Jing, Z., et al., 2000. A three-dimensional stochastic rock mechanics model of engineered geothermal systems in fractured crystalline rock. Journal of Geophysical Research Solid Earth 105 (B10), 23663–23679.

Keer, L.M., Nemat-Nasser, S., Oranratnachai, A., 1978. Unstable growth of thermally induced interacting cracks in brittle solids: further results. International Journal of Solids and Structures 14 (6), 409–430.

Koh, J., Roshan, H., Rahman, S.S., 2011. A numerical study on the long term thermo-poroelastic effects of cold water injection into naturally fractured geothermal reservoirs. Computers and Geotechnics 38 (5), 669–682. Available from: https://doi.org/10.1016/j.compgeo.2011.03.007.

Kohl, T., et al., 1995. Coupled hydraulic, thermal and mechanical considerations for the simulation of hot dry rock reservoirs. Geothermics 24 (3), 345–359.

Kumar, S., Searles, K.H., Gosavi, S.V., 2017. Modeling of fluid-driven fractures using XFEM. In: 51th U.S. Rock Mechanics/Geomechanics Symposium. San Francisco, California, pp. 25–28. June.

Malthe-Sørenssen, A., Jamtveit, B., Meakin, P., 2006. Fracture patterns generated by diffusion controlled volume changing reactions. Physical Review Letters 96 (24), 1–4.

Nemat-Nasser, S., 1977. Geothermal energy: heat extraction from hot dry rook masses. Journal of Pressure Vessel Technology 99 (4), 612–613.

Nemat-Nasser, S., Sumi, Y., Keer, L.M., 1980. Unstable growth of tension cracks in brittle solids: stable and unstable bifurcations, snap-through, and imperfection sensitivity. International Journal of Solids and Structures 16 (11), 1017–1035.

Olson, J.E., 2004. Predicting Fracture Swarms—the Influence of Subcritical Crack Growth and the Crack-tip Process Zone on Joint Spacing in Rock, vol. 231. Geological Society, London, Special Publications, pp. 73–88. https://doi.org/10.1144/GSL.SP.2004.231.01.05.

Ouchi, H., et al., 2015. A peridynamics model for the propagation of hydraulic fractures in heterogeneous, naturally fractured reservoirs. In: SPE Hydraulic Fracturing Technology Conference Held in the Woodlands, Texas, USA, 3–5 February.

Potyondy, D.O., Cundall, P.A., 2004. A bonded-particle model for rock. International Journal of Rock Mechanics and Mining Sciences 41 (8), 1329–1364. Available from: http://linkinghub.elsevier.com/retrieve/pii/S1365160904002874.

Rahman, M.M., Rahman, M.K., 2010. A review of hydraulic fracture models and development of an improved pseudo-3D model for stimulating tight oil/gas sand. Energy Sources, Part A: Recovery, Utilization, and Environmental Effects 32 (15), 1416–1436.

Salencon, J., 1983. Calcul à la rupture et analyse limite. Presses de l'ecole nationale des ponts et chaussee, Paris.

Searles, K.H., et al., 2016. Fully-coupled 3D hydraulic fracture models: development, validation, and application to O&G problems. In: SPE Hydraulic Fracturing Technology Conference held in The Woodlands. Texas, USA, pp. 9–11. February.

Sesetty, V., Ghassemi, A., 2013. Numerical simulation of sequential and simultaneous hydraulic fracturing. In: Effective and Sustainable Hydraulic Fracturing. https://doi.org/10.5772/56309.

Settgast, R.R., et al., 2016. A fully coupled method for massively parallel simulation of hydraulically driven fractures in 3-dimensions. International Journal for Numerical and Analytical Methods in Geomechanics. https://doi.org/10.1002/nag.2557.

Shibuya, Y., et al., 1985. Multiple artificial geothermal cracks in a hot dry rock mass for extraction of heat. Journal of Energy Resources Technology 107 (2), 274–279. Available from: http://link.aip.org/link/JERTD2/v107/i2/p274/s1&Agg=doi%5Cn http://energyresources.asmedigitalcollection.asme.org/article.aspx?articleid=1412522.

Shin, D.H., Sharma, M.M., 2014. Factors controlling the simultaneous propagation of multiple competing fractures in a horizontal well. In: SPE 168599 Hydraulic Fracturing Technology Conference, Woodlands, Texas, USA, 4–6 February.

Tzschichholz, F., et al., 1994. Beam model for hydraulic fracturing. Physical Review B 49 (10), 7056–7059. Available from: http://journals.aps.org/prb/abstract/10.1103/PhysRevB.49.7056.

Tzschichholz, F., Herrmann, H.J., 1995. Simulations of pressure fluctuations and acoustic emission in hydraulic fracturing. Physical Review E 51 (3), 1961−1970.

Warpinski, N.R., Teufel, L.W., 1987. Influence of geologic discontinuities on hydraulic fracture propagation. Journal of Petroleum Technology 39 (02).

Weng, X., 2015. Modeling of complex hydraulic fractures in naturally fractured formation. Journal of Unconventional Oil and Gas Resources 9, 114−135. Available from: http://linkinghub.elsevier.com/retrieve/pii/S2213397614000354.

Weng, X., et al., 2011. Modeling of hydraulic fracture network propagation in a naturally fractured formation. In: SPE 140253 Hydraulic Fracturing Technology Conference, Woodlands, Texas, USA, 24−26 January. Society of Petroleum Engineers. Available from: http://www.onepetro.org/doi/10.2118/140253-MS.

Wu, K., 2014. Numerical Modeling of Complex Hydraulic Fracture Development in Unconventional Reservoirs. The University of Texas at Austin.

Wu, K., Olson, J.E., 2013. Simultaneous multi-frac treatments: fully coupled fluid flow and fracture mechanics for horizontal wells. In: SPE 167626 Annual Technical Conference and Exhibition, New Orleans, USA, 30 September−2 October.

Wu, K., Olson, J.E., 2015. A simplified three-dimensional displacement discontinuity method for multiple fracture simulations. International Journal of Fracture 193 (2), 191−204. Available from: https://doi.org/10.1007/s10704-015-0023-4.

Xu, W., et al., 2010. Wiremesh: a novel shale fracturing simulator models. In: International Oil and Gas Conference and Exhibition in China, 8−10 June. Society of Petroleum Engineers, Beijing.

Zhao, X.P., Young, R.P., 2009. Numerical simulation of seismicity induced by hydraulic fracturing in naturally fractured reservoirs. In: SPE 124690 Annual Technical Conference and Exhibition Held in New Orleans, Louisiana, USA, 4−7 October.

Zhou, J., et al., 2017. A dual lattice discrete element model to understand hydraulic fracturing in a naturally fractured system. Hydraulic Fracturing Journal 4 (2).

Zhou, J., Huang, H., Deo, M., 2015a. A new physics-based modeling of multiple non-planar hydraulic fractures propagation. In: URTeC 2170875. Unconventional Resources Technology Conference Held in San Antonio, Texas, USA, 20−22 July.

Zhou, J., Huang, H., Deo, M., 2015b. Modeling the interaction between hydraulic and natural fractures using dual-lattice discrete element method. In: 49th US Rock Mechanics/Geomechanics Symposium Held in San Francisco, CA, USA, 28 June−1 July.

Zhou, J., Huang, H., Deo, M., 2016. Simulation of hydraulic and natural fracture interaction using a coupled DFN-DEM model. In: 50th US Rock Mechanics/Geomechanics Symposium, 26−29 June, Houston, Texas.

Chapter 5

Hydraulic Fracturing Modeling and Its Extension to Reservoir Simulation Based on Extended Finite-Element Method (XFEM)

Zhao-Qin Huang, Qing-Dong Zeng, Xia Yan, Jun Yao
China University of Petroleum (East China), Qingdao, China

5.1 INTRODUCTION

Horizontal well drilling and hydraulic fracturing have become key technologies in the development of shale gas reservoirs (George, 2010). The application of hydraulic fracturing is also essential for other tight sand reservoirs and hot dry rock geothermal systems (Bruel, 1995). The complexity of fracture geometrical configuration is closely related to the geological complexity of formation, including the existence of natural fractures, rock anisotropy, and heterogeneity. To design and optimize the treatment of hydraulic fracturing, it is important to understand how hydraulic fracture propagates in the formation and the effects of reservoir heterogeneities on fracture propagation.

For shale and tight reservoirs, simulation of hydraulic fracturing is a complicated process, as it involves coupling of the following physical elements: (1) the mechanical deformation induced by the fluid pressure on the fracture surfaces; (2) the flow of fluid within the fracture; (3) the fracture propagation; (4) fracture height growth; (5) interaction between hydraulic and natural fractures; (6) interaction among adjacent hydraulic fractures; and (7) proppant transport in the fracture networks. In recent years, a great number of numerical models have been developed to simulate hydraulic fracture propagation in shale and tight reservoirs. The solving methods can be divided into the following kinds: finite-element method (FEM) (Chen, 2012; Fu et al., 2013), extended finite-element method (XFEM) (Lecampion, 2009; Taleghani, 2009), displacement discontinuity method (Weng et al., 2011; Wu and Olson, 2015), discrete element method (De Pater and Beugelsdijk, 2005; Morgan and Aral, 2014), and discrete fracture network method (Meyer and Bazan, 2011; Wengyue et al., 2010). Each method

Hydraulic Fracture Modeling. https://doi.org/10.1016/B978-0-12-812998-2.00005-9

has advantages and disadvantages. For continuum methods, it is possible to compute the stress field precisely, whereas for noncontinuum methods, it is convenient to simulate arbitrary fracture propagation. The hydraulic fracture models have been reviewed in Adachi et al. (2007) and Weng (2015). However, it is mainly focused on the application of XFEM in fracturing simulation in this chapter.

In the frame of classical FEM, the fracture is restricted to the interelement boundaries, which leads to the problem of mesh dependency. However, the XFEM has many advantages over the classical FEM, especially for problems with discontinuities and moving boundaries. The XFEM is originally proposed (Belytschko and Black, 1999; Moes et al., 1999) for discontinuous problems, which has been widely used in many fields due to flexibility in meshing. This method allows fracture propagates along an arbitrary path without remeshing by locally enriching the finite-element model in the vicinity of the fracture. The level set method is proposed to represent the fracture location, including the location of fracture tips, and fracture propagation is modeled by updating the level set functions (Stolarska et al., 2001). This method has also been extended to three dimensional crack modeling (Gravouil et al., 2002; Moes et al., 2002; Sukumar et al., 2000). The problem of crack growth with frictional contact is resolved by adapting the iterative scheme used by the LATIN method in the frame of XFEM (Dolbow et al., 2001). Other investigations include modeling cohesive cracks (Mergheim et al., 2005; Zi and Belytschko, 2003) and dynamic crack propagation (Belytschko et al., 2003). The XFEM has been well reviewed in Belytschko et al. (2009) and Fries and Belytschko (2010).

As for the application of the extended finite element to hydraulic fracturing simulation, the fracture surface is not stress free, and the fracture propagation is caused by the injection of fracturing fluid, which is a kind of fluid−solid coupled process. Lecampion used the XFEM to solve hydraulic fracturing problems by accounting for two different propagation regimes including the toughness-dominated regime and viscosity-dominated regime (Lecampion, 2009). Ren explored numerical modeling for concrete hydraulic fracturing with the XFEM by assuming that water pressure is constant and imposed on the fracture surfaces (Ren et al., 2009). Taleghani solved hydraulic fracture propagation by coupling fluid flow in the fracture with rock mass deformation (Taleghani, 2009). Gordeliy and Peirce described coupled algorithms that use the XFEM to solve the propagation of hydraulic fractures in an elastic medium and proposed implicit level set schemes for modeling hydraulic fractures (Gordeliy and Peirce, 2013a,b). Mohammadnejad and Khoei proposed a fully coupled numerical model for modeling the hydraulic fracture propagation in porous media using the XFEM in conjunction with the cohesive crack model, and the governing equations are derived within the framework of the generalized Biot theory (Mohammadnejad and Khoei, 2013a). Besides, they extended the model to simulate cohesive crack propagation in multiphase

porous media (Mohammadnejad and Khoei, 2013b). Gupta and Duarte extended the method to the simulation of nonplanar three dimensional hydraulic fractures (Gupta and Duarte, 2016). Liu extended the method to an elastoplastic medium, in which the fracture propagation process is governed by a cohesive fracture model (Liu et al., 2016). Many evidences indicate that natural fracture is abundant in shale rocks, and the effect of natural fracture on the hydraulic fracture is very important to understand how the fracture network is formed. Taleghani used the XFEM to model hydraulic fracture approach of natural fracture by using the energy release rate criterion (Taleghani, 2011). Khoei also presented an extended finite-element model to simulate the mechanism of interaction between hydraulic fracturing and frictional natural fault in impermeable media (Khoei et al., 2015). These applications of XFEM described previously in modeling hydraulic fracture propagation are just in the start-up stage, but they have shown great promise, especially for coupled geomechanics and reservoir models.

In this chapter, the basic mathematical model of hydraulic fracture propagation and numerical methods will be described in detail. The rock stress field and fluid pressure field are solved by XFEM and classical FEM, respectively. Then, the numerical model is validated and the effects of rock properties, fluid properties, and natural fracture on fracture propagation are analyzed. Moreover, modeling of simultaneous propagation of multicluster fractures is performed, in which fracture tips are located by using an implicit level set method.

5.2 MATHEMATICAL MODEL OF HYDRAULIC FRACTURE PROPAGATION

5.2.1 Underlying Assumptions

The hydraulic fracture propagation model is illustrated in Fig. 5.1. The fracturing fluid is injected to initiate and extend fractures in reservoir rock. For simplicity, the fluid is assumed incompressible, and its leak-off into the formation satisfies the Carter model. Rock deformation obeys linear elasticity theory. Moreover, the propagation of fractures is assumed in the quasi-static state.

5.2.2 Governing Equations

The mathematical model of hydraulic fracture propagation can be divided into two parts: rock deformation and fluid flow.

Rock deformation is caused by combined effects of remote in situ stresses and fluid pressure in the fracture. The governing equations can be given by the linear elasticity theory.

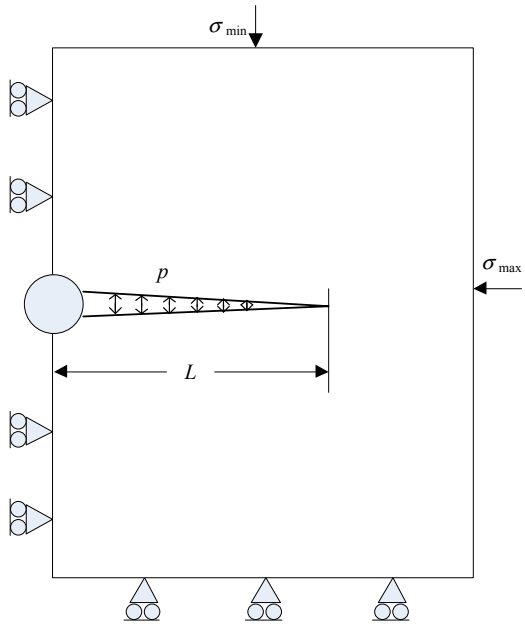

FIGURE 5.1 Schematic diagram of hydraulic fracture propagation.

The equation of equilibrium gives

$$\nabla \cdot \boldsymbol{\sigma} + \boldsymbol{f} = 0 \tag{5.1}$$

where $\boldsymbol{\sigma}$ is stress tensor and $\boldsymbol{f}$ is the body force.

The constitutive equation gives

$$\boldsymbol{\sigma} = \boldsymbol{C} : \boldsymbol{\varepsilon}(\boldsymbol{u}) \tag{5.2}$$

where $\boldsymbol{\varepsilon}$ is strain tensor, which is related to displacement tensor $\boldsymbol{u}$ by the geometric equation. $\boldsymbol{C}$ is the elasticity tensor, which can be calculated by rock mechanical parameters, including elastic modulus and Poisson's ratio.

Under the assumption of small strain and displacement, the geometric equation gives

$$\boldsymbol{\varepsilon}(\boldsymbol{u}) = \frac{1}{2}\left(\nabla \boldsymbol{u} + (\nabla \boldsymbol{u})^T\right) \tag{5.3}$$

Fluid flow along fracture width direction is neglected because the fracture width is much smaller than the fracture length, so fluid flow in the fracture can be simplified to 1D flow along fracture length direction.

According to Poiseuille's law, the equation of motion can be given as

$$\frac{\partial p(s,t)}{\partial s} = -\frac{12\mu q(s,t)}{w^3(s,t)} \tag{5.4}$$

where s is distance along the fracture; t is time; $p(s, t)$ denotes fluid pressure at point s and time t; q is the flux; μ is the fluid viscosity; and w is the fracture width.

Neglecting compressibility of fluid, the equation of conservation can be written as

$$\frac{\partial q(s,t)}{\partial s}+\frac{\partial w(s,t)}{\partial t}+q_L=0 \tag{5.5}$$

where q_L is the fluid leak-off velocity from fracture surface into formation, which can be expressed by the Carter leak-off model as follows:

$$q_L=\frac{2C_L}{\sqrt{t-\tau_0(s)}},\ \ t>\tau_0(s) \tag{5.6}$$

where C_L is the total leak-off coefficient and $\tau_0(s)$ is the time when point s is first exposed to fracturing fluid.

Besides the local conservation equation, the global conservation equation is needed for the computation of time increment.

$$\int_0^t Q_0\mathrm{d}t=\int_0^L \Delta w\mathrm{d}s+\int_0^L 2C_L\left[\sqrt{t-\tau(s)}-\sqrt{t-\Delta t-\tau(s)}\right]\mathrm{d}s \tag{5.7}$$

where Q_0 is the given injection rate and L is the length of fracture.

The boundaries for rock deformation include outer boundary and fracture boundary. Imposed displacement and stresses are defined at the outer boundary, and fluid pressure is acting on the fracture surface. The boundary conditions can be given by

$$\boldsymbol{u}|_{\Gamma_\mathrm{g}}=\boldsymbol{g} \tag{5.8}$$

$$\boldsymbol{\sigma}\cdot\boldsymbol{n}|_{\Gamma_\mathrm{h}}=\boldsymbol{h} \tag{5.9}$$

$$\sigma_\mathrm{n}|_{\Gamma_\mathrm{f}^+}=\sigma_\mathrm{n}|_{\Gamma_\mathrm{f}^-}=-p(s,t) \tag{5.10}$$

where Γ_g is the imposed displacement boundary and $\boldsymbol{g}$ is the imposed displacement. Γ_h is the imposed stress boundary, and $\boldsymbol{h}$ is the imposed stress. Γ_f is the fracture surface boundary, and p is the fluid pressure.

For fluid flow in the fracture, the injection rate is given at the inlet of fracture and fracture width equals to zero at the tip, which can be written as

$$q(0,t)=Q_0 \tag{5.11}$$

$$w(L,t)=0 \tag{5.12}$$

5.2.3 Fracture Propagation Criteria

The well-known criteria for fracture propagation consist of maximum circumferential stress criterion, maximum energy release rate criterion, and maximum strain energy density criterion. Here the maximum circumferential

stress criterion is selected to determine fracture growth, which states that when the stress intensity factor at the crack tip exceeds the rock toughness, the fracture will expand and propagate along the direction of the maximum circumferential stress. Thus, it must satisfy the following condition for fracture propagation:

$$\cos\left(\frac{\theta_M}{2}\right)\left(K_I\cos^2\left(\frac{\theta_M}{2}\right)-\frac{3}{2}K_{II}\sin\theta_M\right)\geq K_{IC} \tag{5.13}$$

where θ_M is the angle of maximum circumferential stress direction. K_I and K_{II} are stress intensity factors of mode I and mode II.

The deflection angle can be given as

$$\theta_M = 2\arctan\left(\frac{K_I \pm \sqrt{K_I^2+8K_{II}^2}}{4K_{II}}\right) \tag{5.14}$$

To estimate Eqs. (5.13) and (5.14), the stress intensity factors at the fracture tip should be computed. Several techniques have been proposed in the literature to extract stress intensity factors using numerical results. Many of these methods are based on the *J*-integral (Rice, 1967) or one of its variations such as the M-integral or the domain equivalent integral (Li et al., 1985; Moran and Shih, 1987). The interaction integral method is a popular approach for the extraction of stress intensity factors. This method is derived from *J*-integral by considering auxiliary fields. Here the interaction integral method is selected to calculate stress intensity factors, which will be described briefly.

According to the definition of *J*-integral, *J*-integral around fracture tip can be given by

$$J=\int_{\Gamma\cup\Gamma_c^+\cup\Gamma_c^-}\left(\frac{1}{2}\sigma_{ik}\varepsilon_{ik}\delta_{1j}-\sigma_{ij}u_{i,1}\right)n_j\mathrm{d}s \tag{5.15}$$

where Γ is the boundary of integration domain, and Γ_c^+ and Γ_c^- are crack surface boundaries. n_j is the jth component of outward normal vector to the boundary. δ is the Kronecker delta function.

Using the divergence theorem, Eq. (5.15) can be deduced to a domain integral as

$$J=\int_A\left(\sigma_{ij}u_{i,1}-\frac{1}{2}\sigma_{ik}\varepsilon_{ik}\delta_{1j}\right)\omega_j\mathrm{d}A+\int_{\Gamma_c^+\cup\Gamma_c^-}\left(\frac{1}{2}\sigma_{ik}\varepsilon_{ik}\delta_{1j}-\sigma_{ij}u_{i,1}\right)\omega n_j\mathrm{d}s \tag{5.16}$$

where ω is the weight function defined on integration domain.

For a linear elastic material, the *J*-integral is equal to strain energy release rate

$$J=\frac{K_I^2+K_{II}^2}{E^*} \tag{5.17}$$

where $E^* = E$ for plane stress and $E^* = E/(1-\nu^2)$ for plane strain.

To extract stress intensity factors, the auxiliary state is superposed to the given state of stress. The J-integral of two states can be given as

$$J^{(1,2)} = \frac{\left(K_{\mathrm{I}}^{(1)} + K_{\mathrm{I}}^{(2)}\right)^2}{E^*} + \frac{\left(K_{\mathrm{II}}^{(1)} + K_{\mathrm{II}}^{(2)}\right)^2}{E^*} \tag{5.18}$$

where superscripts (1) and (2) correspond to two states of stress.

Eq. (5.18) can be decomposed as

$$J^{(1,2)} = J^1 + J^2 + I^{1,2}$$

$$= \left(\frac{\left(K_{\mathrm{I}}^{(1)}\right)^2 + \left(K_{\mathrm{II}}^{(1)}\right)^2}{E^*}\right) + \left(\frac{\left(K_{\mathrm{I}}^{(2)}\right)^2 + \left(K_{\mathrm{II}}^{(2)}\right)^2}{E^*}\right) + \frac{2\left(K_{\mathrm{I}}^{(1)}K_{\mathrm{I}}^{(2)} + K_{\mathrm{II}}^{(1)}K_{\mathrm{II}}^{(2)}\right)}{E^*} \tag{5.19}$$

Therefore, the interaction integral is expressed by

$$I^{1,2} = \frac{2\left(K_{\mathrm{I}}^{(1)}K_{\mathrm{I}}^{(2)} + K_{\mathrm{II}}^{(1)}K_{\mathrm{II}}^{(2)}\right)}{E^*} \tag{5.20}$$

According to the definition of J-integral, the interaction integral can be deduced as

$$I^{1,2} = \int_A \left(\sigma_{ij}^{(1)}u_{i,1}^{(2)} + \sigma_{ij}^{(2)}u_{i,1}^{(1)} - \sigma_{ik}^{(1)}\varepsilon_{ik}^{(2)}\delta_{1j}\right)\omega_j \mathrm{d}A$$

$$+ \int_{\Gamma_{c^+}\cup\Gamma_{c^-}} \left(\sigma_{ik}^{(1)}\varepsilon_{ik}^{(2)}\delta_{1j} - \sigma_{ij}^{(1)}u_{i,1}^{(2)} - \sigma_{ij}^{(2)}u_{i,1}^{(1)}\right)\omega n_j \mathrm{d}s \tag{5.21}$$

Choosing the auxiliary state as the pure mode I asymptotic field $\left(K_{\mathrm{I}}^{(2)} = 1,\ K_{\mathrm{II}}^{(2)} = 0\right)$, K_{I} for the given state can be calculated as

$$K_{\mathrm{I}}^{(1)} = \frac{E^*}{2} I^{1,\text{Mode I}} \tag{5.22}$$

In a similar way, K_{II} for the given state can be calculated as

$$K_{\mathrm{II}}^{(1)} = \frac{E^*}{2} I^{1,\text{Mode II}} \tag{5.23}$$

5.3 NUMERICAL SCHEME FOR HYDRAULIC FRACTURING

5.3.1 Stress Field With Extended Finite-Element Method

In the framework of FEM, modeling of crack propagation needs applying various remeshing strategies. However, the transfer of data between meshes

requires great computational efforts. The XFEM has been widely used for discontinuous problems. It allows fracture propagates across the grid element by using the level set method without remeshing. Therefore, the XFEM is used to solve rock displacements in the hydraulic fracturing problem.

The XFEM is realized by the partition of unity concept (Melenk and Babuska, 1996). A partition of unity in a domain Ω is a set of functions Φ_I such that

$$\sum \Phi_I(\boldsymbol{x}) = 1, \quad \forall \boldsymbol{x} \in \Omega \tag{5.24}$$

The displacement field can be decomposed into two parts: the continuous displacement field and the discontinuous part, and the approximation expression can be written as follows:

$$u^{\mathrm{h}}(\boldsymbol{x}) = \sum_{I \in N} N_I(\boldsymbol{x}) u_I + \sum_{I \in N^{\mathrm{cr}}} N_I(\boldsymbol{x})(H(\varphi(\boldsymbol{x})) - H(\varphi(\boldsymbol{x}_I)))a_I$$

$$+ \sum_{I \in N^{\mathrm{tip}}} N_I(\boldsymbol{x}) \sum_{k=1}^{4} \left(F^k(\boldsymbol{x}) - F^k(\boldsymbol{x}_I)\right) b_I^k \tag{5.25}$$

where $\boldsymbol{x}$ is the position vector. N is the set of all nodes in the discretized model. N^{cr} is the set of nodes of all elements containing cracks but not crack tips. N^{tip} is the set of nodes of all elements containing the crack tip. N_I is the finite-element shape function. $H(\varphi(\boldsymbol{x}))$ is the Heaviside step function, and $\varphi(\boldsymbol{x})$ is the signed distance function. $F(\boldsymbol{x})$ is the enriched functions for tip elements. u_I is the nodal displacements. a_I and b_I are degrees for enriched nodes.

The virtual work principle of stress field can be written as follows:

$$\int_{\Omega} \boldsymbol{\varepsilon}(\boldsymbol{u}) : \boldsymbol{C} : \boldsymbol{\varepsilon}(\boldsymbol{v}) \mathrm{d}\Omega = \int_{\Omega} \boldsymbol{f} \cdot \boldsymbol{v} \mathrm{d}\Omega + \int_{\Gamma_{\mathrm{h}}} \boldsymbol{h} \cdot \boldsymbol{v} \mathrm{d}\Gamma + \int_{\Gamma_{\mathrm{f}}} p \cdot ||\boldsymbol{v}|| \mathrm{d}\Gamma, \quad \forall \boldsymbol{v} \in \boldsymbol{U}_0 \tag{5.26}$$

where $\boldsymbol{v}$ is the virtual displacement and $||v||$ is the opening between the two surfaces of fracture, which can be given by

$$||v|| = \boldsymbol{n} \cdot (\boldsymbol{v}^+ - \boldsymbol{v}^-) = 2\boldsymbol{n} \cdot \sum_{I \in N_{\mathrm{cr}}} N_I a_I + 2\boldsymbol{n} \cdot \sqrt{r} \sum_{I \in N_{\mathrm{tip}}} N_I b_I^1 \tag{5.27}$$

By substituting the defined displacement approximation Eq. (5.25) into the weak form, the discrete equations can be written as

$$\boldsymbol{K}\boldsymbol{u}^{\mathrm{h}} = \boldsymbol{f} \tag{5.28}$$

The stiffness matrix $\boldsymbol{K}$ can be formulated as follows:

$$K_{ij}^{e} = \begin{bmatrix} k_{ij}^{uu} & k_{ij}^{ua} & k_{ij}^{ub} \\ k_{ij}^{au} & k_{ij}^{aa} & k_{ij}^{ab} \\ k_{ij}^{bu} & k_{ij}^{ba} & k_{ij}^{bb} \end{bmatrix} \tag{5.29}$$

$$k_{ij}^{rs} = \int_{\Omega^e} \left(B_i^r\right)^T D B_j^s \mathrm{d}\Omega, \quad (r,s = u,a,b) \tag{5.30}$$

$$B_i^u = \begin{bmatrix} N_{i,x} & 0 \\ 0 & N_{i,y} \\ N_{i,y} & N_{i,x} \end{bmatrix} \tag{5.31}$$

$$B_i^a = \begin{bmatrix} (N_i[H(\varphi(x)) - H(\varphi(x_i))])_{,x} & 0 \\ 0 & (N_i[H(\varphi(x)) - H(\varphi(x_i))])_{,y} \\ (N_i[H(\varphi(x)) - H(\varphi(x_i))])_{,y} & (N_i[H(\varphi(x)) - H(\varphi(x_i))])_{,x} \end{bmatrix} \tag{5.32}$$

$$B_i^b = \begin{bmatrix} \left(N_i\left[F_i^k(x) - F_i^k(x_i)\right]\right)_{,x} & 0 \\ 0 & \left(N_i\left[F_i^k(x) - F_i^k(x_i)\right]\right)_{,y} \\ \left(N_i\left[F_i^k(x) - F_i^k(x_i)\right]\right)_{,y} & \left(N_i\left[F_i^k(x) - F_i^k(x_i)\right]\right)_{,x} \end{bmatrix} \tag{5.33}$$

5.3.2 Pressure Field With Finite-Element Method

Substituting Eqs. (5.4) and (5.6) into Eq. (5.5) gives the fluid flow equation in the fracture as

$$\frac{\partial w}{\partial t} + \frac{2C_L}{\sqrt{t - \tau_0(s)}} = \frac{1}{12\mu} \frac{\partial}{\partial s}\left(w^3 \frac{\partial p}{\partial s}\right) \tag{5.34}$$

The fluid pressure inside the fracture is approximated by

$$p(s) = \sum_{i=1}^{n_f} N_i(s) p_i \tag{5.35}$$

where N_i is the shape function for node i, p_i is the corresponding nodal value for fluid pressure, and n_f is the number of total nodes.

The weak form of Eq. (5.35) can be written as

$$\int_0^L \frac{\Delta w}{\Delta t} N_i(s)\mathrm{d}s + \int_0^L \frac{2C_L N_i(s)}{\sqrt{t-\tau(s)}}\,\mathrm{d}s = \frac{1}{12\mu}\int_0^L \frac{\partial}{\partial s}\left(w^3\frac{\partial p}{\partial s}\right)N_i(s)\mathrm{d}s \tag{5.36}$$

Integrating the right-hand side of Eq. (5.36) by parts results in

$$\frac{1}{12\mu}\int_0^L \frac{\partial}{\partial s}\left(w^3\frac{\partial p}{\partial s}\right)N_i(s)\mathrm{d}s = \frac{1}{12\mu}w^3\frac{\partial p}{\partial s}N_i(s)\Big|_0^L - \sum_{j=1}^{n_f}\frac{p_j}{12\mu}\int_0^L w^3\frac{\partial N_i}{\partial s}\frac{\partial N_j}{\partial s}\,\mathrm{d}s \tag{5.37}$$

Therefore, according to the fluid-flux boundary condition, the derived weak form can be rewritten as

$$\sum_{j=1}^{n_f}\frac{p_j}{12\mu}\int_0^L w^3\frac{\partial N_i}{\partial s}\frac{\partial N_j}{\partial s}\mathrm{d}s = Q_0 N_i(0) - \int_0^L \frac{\Delta w}{\Delta t}N_i(s)\mathrm{d}s - \int_0^L \frac{2C_L N_i(s)}{\sqrt{t-\tau(s)}}\,\mathrm{d}s \tag{5.38}$$

5.3.3 Coupling Schemes

To solve the hydraulic fracture propagation model, the coupled equations of rock stress field and fluid pressure field are solved by Picard iteration method. First, fluid pressure is given a guess, and then the fracture width can be obtained by solving rock stress field. Second, the global conservation equation is solved using the bisection method to get time increment Δt, and after that the fluid pressure is obtained by solving the pressure field equation. Convergence is checked by comparing the relative error between consecutive values of pressure. If convergence is not reached, fracture width is updated to continue the iteration. Otherwise, if convergence is reached, stress intensity factors are calculated to check whether fracture tips satisfy the fracture propagation criterion. The block diagram of iteration process is shown in Fig. 5.2.

5.4 NUMERICAL CASES AND RESULTS ANALYSIS

In this part, first the validation of established model is carried out. Then, the effects of rock properties, fluid properties, and natural fracture on hydraulic fracture propagation will be analyzed in detail.

5.4.1 Validation of Numerical Model

To validate the correctness of established models, 2D plane strain hydraulic fracture propagation is simulated and its result is compared with an analytical solution of Khristianovic–Geertsma–de Klerk (KGD) model. The model

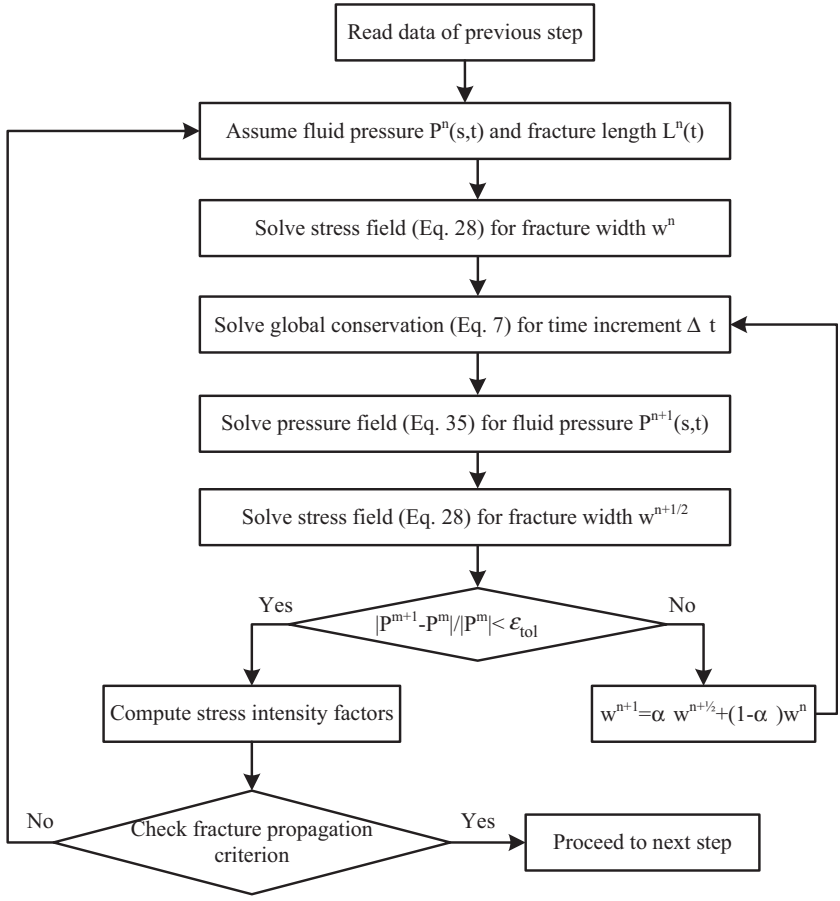

FIGURE 5.2 Block diagram of iteration process.

parameters are set as follows: elastic modulus $E = 25$ GPa, Poisson's ratio $\nu = 0.25$, half injection rate $Q_0 = 0.443 \times 10^{-3}$ m^3/s, fluid viscosity $\mu = 0.1$ Pa·s, and leak-off coefficient $C_L = 0$ m/s$^{0.5}$.

The solutions of fracture half-length and maximum fracture width versus injection time are given as follows (Spence and Sharp, 1985):

$$L(t) = 0.68\left[\frac{GQ_0^3}{(1-\nu)\mu}\right]^{\frac{1}{6}} t^{\frac{2}{3}} \tag{5.39}$$

$$w_{\max}(t) = 1.87\left[\frac{(1-\nu)\mu Q_0^3}{G}\right]^{\frac{1}{6}} t^{\frac{1}{3}} \tag{5.40}$$

where G is the shear modulus.

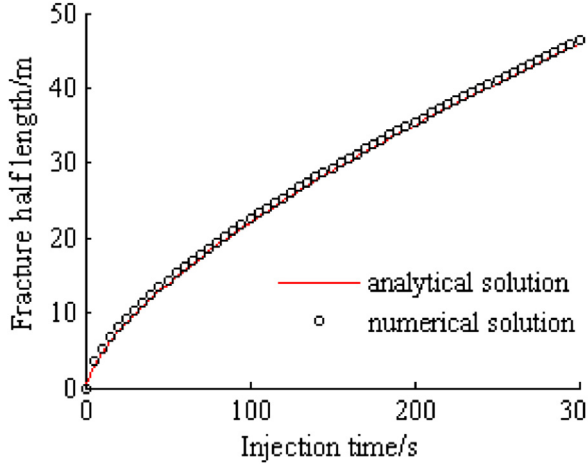

FIGURE 5.3 Comparison of fracture half-length between analytical and numerical solution.

The comparisons between the numerical solution and analytical solution are shown in Figs. 5.3 and 5.4. It can be shown that the predicted fracture half-length and fracture maximum width from this model are well consistent with results from KGD model.

5.4.2 The Effect of Rock Properties

Fracture geometrical configuration is essential to fracturing design, and rock properties have a great impact on the final fracture geometry. Therefore, the

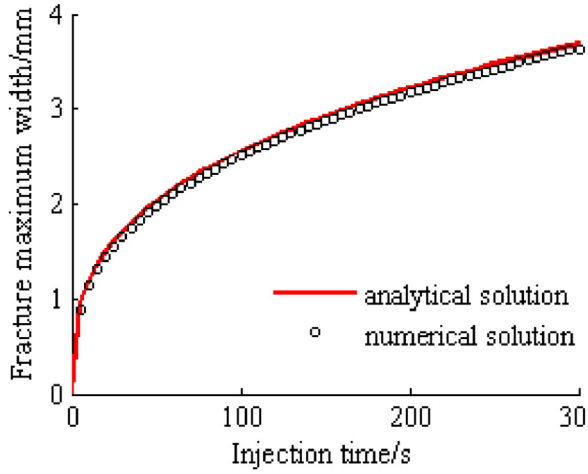

FIGURE 5.4 Comparison of fracture maximum width between analytical and numerical solution.

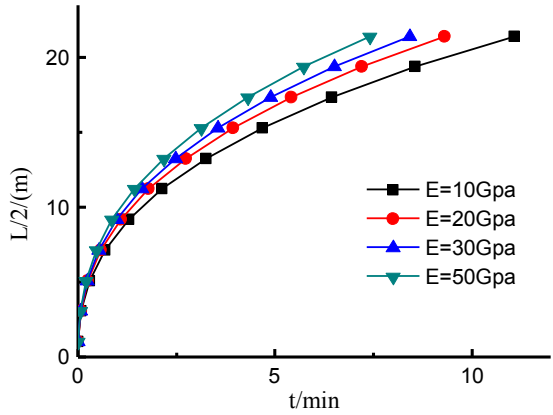

FIGURE 5.5 Fracture half-length versus time for different elastic modulus.

effects of elastic modulus and Poisson's ratio on fracture geometrical parameters are analyzed first, and then the effect of rock anisotropy and heterogeneity is analyzed.

The effects of elastic modulus and Poisson's ratio on fracture half-length and width are shown in Figs. 5.5–5.8. The results show that as elastic modulus increases, fracture half-length increases, whereas fracture width decreases when other model parameters are fixed. This means that as elastic modulus increases, the final geometry of fracture tends to have longer length but narrower width. It can also be shown that Poisson's ratio has an opposite impact on fracture geometrical parameters, but the impact is trivial.

Consider hydraulic fracture propagating in anisotropic formation as shown in Fig. 5.9. Horizontal bedding planes are abundant in oil and gas reservoirs;

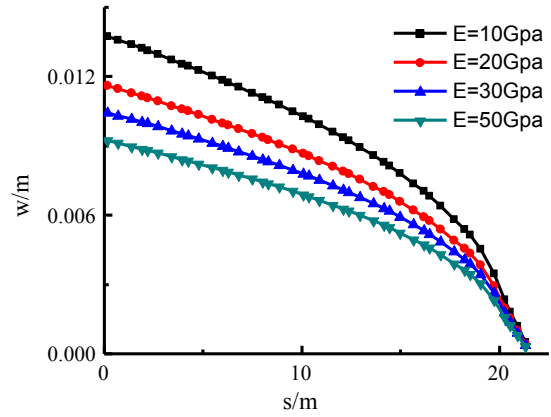

FIGURE 5.6 Fracture width distribution for different elastic modulus.

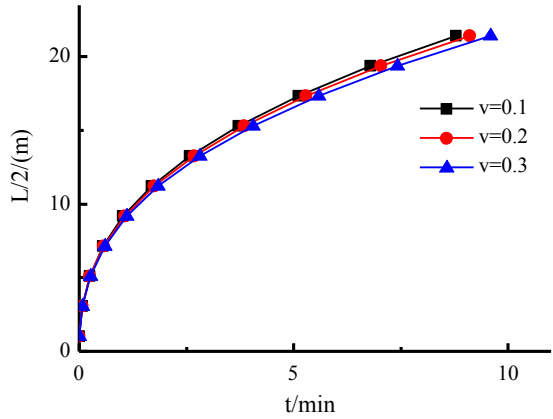

FIGURE 5.7 Fracture half-length versus time for different Poisson's ratios.

however, many natural fractures lay vertically in the rocks, which leads to the layer being seen as orthotropic material.

When three dimension is reduced to two dimension, there are two scenarios including plane stress and plane strain. For plane stress, the constitutive equation in the local coordinate system of material principal direction can be reduced to

$$\begin{bmatrix} \varepsilon_{x'} \\ \varepsilon_{y'} \\ \tau_{x'y'} \end{bmatrix} = \begin{bmatrix} 1/E_1 & -\nu_{12}/E_2 & 0 \\ & 1/E_2 & 0 \\ & & 1/G_{12} \end{bmatrix} \begin{bmatrix} \sigma_{x'} \\ \sigma_{y'} \\ \gamma_{x'y'} \end{bmatrix} \tag{5.41}$$

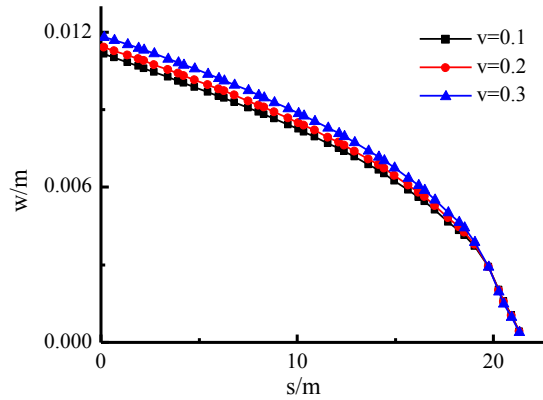

FIGURE 5.8 Fracture width distribution for different Poisson's ratios.

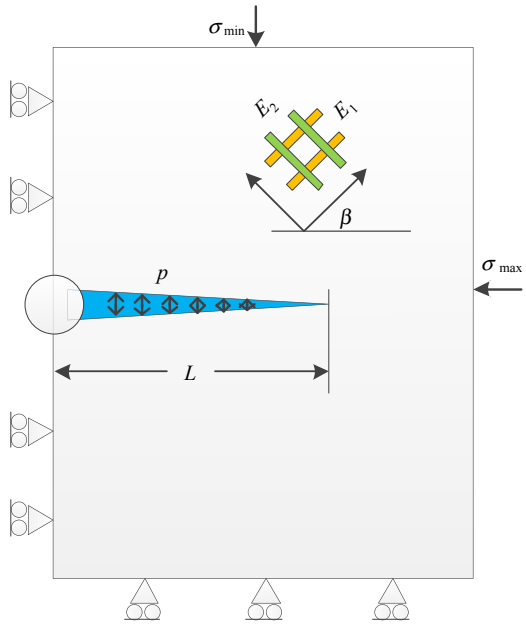

FIGURE 5.9 Physical model of hydraulic fracture propagating in anisotropic formation with material angle β.

In addition, for plane strain the constitutive equation can be deduced as

$$\begin{bmatrix} \varepsilon_{x'} \\ \varepsilon_{y'} \\ \tau_{x'y'} \end{bmatrix} = \begin{bmatrix} 1/E_1 - \nu_{13}^2/E_3 & -\nu_{12}/E_2 - \nu_{13}\nu_{23}/E_3 & 0 \\ & 1/E_2 - \nu_{23}^2/E_3 & 0 \\ & & 1/G_{12} \end{bmatrix} \begin{bmatrix} \sigma_{x'} \\ \sigma_{y'} \\ \gamma_{x'y'} \end{bmatrix} \tag{5.42}$$

For isotropic material, the maximum circumferential tensile stress criterion is commonly used to determine fracture propagation, whereas for anisotropic material, the criterion is transformed to the maximization of the ratio of the maximum circumferential tensile stress over the material critical tensile strength, which can be presented as

$$\max \frac{K_\theta}{K_{\mathrm{IC}}} \tag{5.43}$$

where K_θ is related to the circumferential stress σ_θ and can be expressed as follows:

$$K_\theta = \frac{\sigma_\theta}{\sqrt{2\pi r}} = K_{\mathrm{I}}\mathrm{Re}[A(s_1 B - s_2 C)] + K_{\mathrm{II}}\mathrm{Re}[A(B - C)] \tag{5.44}$$

where r and θ are polar coordinates with the origin at the crack tip. K_{I} and K_{II} are stress intensity factors of mode I and mode II, respectively. s_1 and s_2 are

roots of the material characteristic equation, which can be obtained using equilibrium and compatibility conditions (Lekhnitskii, 1963):

$$S_{11}s^4 - 2S_{16}s^3 + (2S_{12} + S_{66})s^2 - 2S_{26}s + S_{22} = 0 \tag{5.45}$$

where S_{11}, S_{12}, S_{16}, S_{22}, S_{26}, and S_{66} are elements of rock compliance matrix.

In Eq. (5.44), the coefficients A, B, and C are related to s_1 and s_2, which can be expressed as

$$A = \frac{1}{s_1 - s_2} \tag{5.46}$$

$$B = (s_2 \sin\theta + \cos\theta)^{3/2} \tag{5.47}$$

$$C = (s_1 \sin\theta + \cos\theta)^{3/2} \tag{5.48}$$

According to Saouma, the critical stress intensity factors are assumed to be inversely proportional to elastic modulus (Saouma et al., 1987), which can be given as

$$\frac{K_{IC}^1}{K_{IC}^2} = \frac{E_2}{E_1} \tag{5.49}$$

In Eq. (5.25), the enriched functions for tip elements are extracted from the analytical tip solution for orthotropic materials, which can be expressed as

$$\{F_l\} = \left[\sqrt{r}\cos\frac{\theta_1}{2}\sqrt{g_1(\theta)},\ \sqrt{r}\cos\frac{\theta_2}{2}\sqrt{g_2(\theta)},\ \sqrt{r}\sin\frac{\theta_1}{2}\sqrt{g_1(\theta)},\ \sqrt{r}\sin\frac{\theta_2}{2}\sqrt{g_2(\theta)}\right] \tag{5.50}$$

where θ_k and g_k are related to the roots s_1 and s_2 of the material characteristic Eq. (5.45), which can be written as

$$\theta_k = \arctan\left(\frac{s_{ky}\sin\theta}{\cos\theta + s_{kx}\sin\theta}\right) \tag{5.51}$$

$$g_k(\theta) = \sqrt{(cos\ \theta + s_{kx}\ sin\ \theta)^2 + (s_{ky}\ sin\ \theta)^2} \tag{5.52}$$

where s_{kx} and s_{ky} are the real and imaginary parts of root s_k.

When the material principal axes are not aligned with the principal stress directions, the propagation direction may divert from the initial direction of maximum principal stress. The hydraulic fracture propagation paths are quite different when material angles are set as different values, which are shown in Fig. 5.10. When the material angle β is 0, the propagation path of hydraulic fracture remains a straight line. However, when the material angle is larger than 0, the propagation path changes to a curved line. If the material angle satisfies $0° < \beta < 90°$, the hydraulic fracture will divert toward the positive

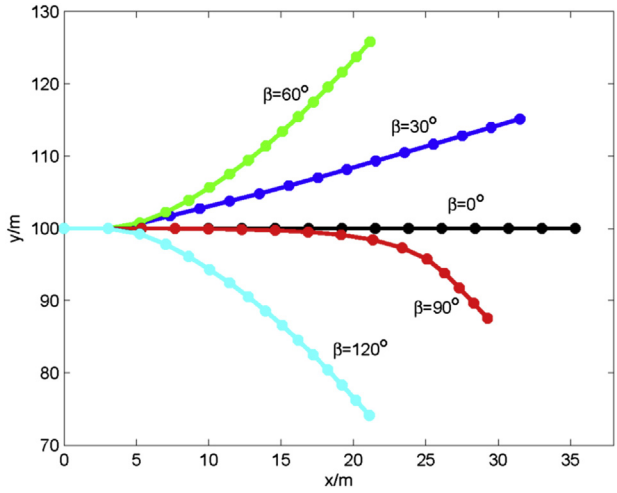

FIGURE 5.10 Fracture propagation paths for different material angles.

direction of y axis. If the material angle satisfies $90^\circ < \beta < 180^\circ$, the hydraulic fracture will divert toward the negative direction of y axis. Moreover, the propagation path of material angle $\beta = 60^\circ$ is symmetric to that of material angle $\beta = 120^\circ$ with respect to the propagation path of $\beta = 0^\circ$. It can be seen that when the material angle β is not equal to 0, the propagation direction of fracture has a tendency to be aligned with the direction of material main axis. When the material angle $\beta = 90^\circ$, the fracture may divert toward the positive or negative direction of y axis. However, because of the boundary condition, it only diverts to the negative direction, as shown in Fig. 5.10.

The normal stress contour of y direction is also plotted in Fig. 5.11. From the figure we can see that the normal stress is significantly influenced by fracture trajectory, namely that the material angle has important influence on the redistribution of stress in the formation.

As for rock inhomogeneity, the elastic modulus is assumed to obey the Weibull distribution. The density function of the Weibull distribution is expressed as

$$f(x) = \alpha\gamma^{-\alpha} \exp\left[-\left(\frac{x}{\gamma}\right)^{\alpha}\right], \; x \geq 0 \tag{5.53}$$

where f is probability density, x is random variable, α is shape factor, and γ is mean value of variable.

The cumulative distribution function can be given as

$$F(x) = 1 - exp\left(-\left(\frac{x}{\gamma}\right)^{\alpha}\right) \tag{5.54}$$

where F is cumulative probability density.

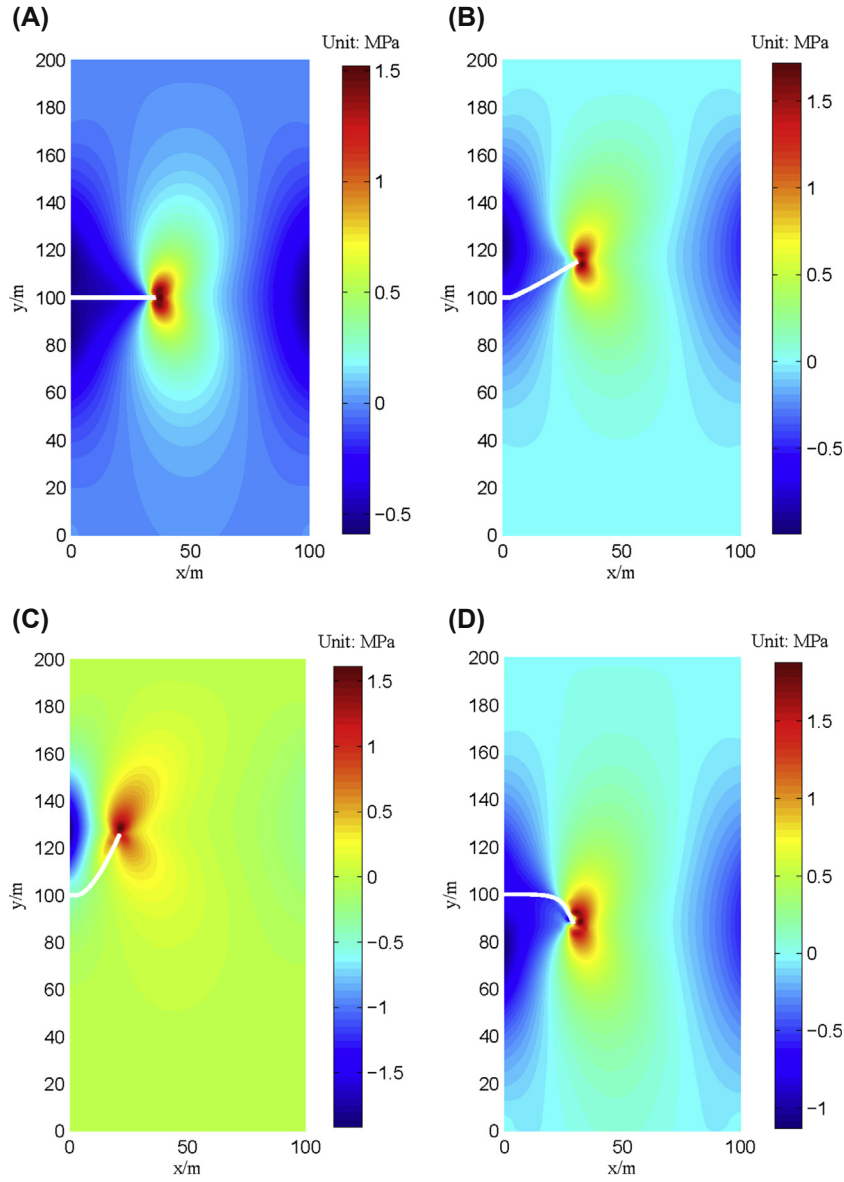

FIGURE 5.11 Fracture trajectories and normal stress contour of y direction for different material angles: the white line represents fracture. (A) $\beta = 0°$; (B) $\beta = 30°$; (C) $\beta = 60°$; (D) $\beta = 90°$.

According to transformation of inverse function, a random variable obeying the Weibull distribution can be calculated with the following equation.

$$x = \gamma[-ln(1 - r_x)]^{1/\alpha} \tag{5.55}$$

where r_x is a random number between 0 and 1.

The mean value of elastic modulus is 27 GPa, and shape factors are set for 1.5, 2.5, and 5. Hence the elastic modulus for each grid can be calculated as Eq. (5.55), and then the elasticity tensor matrix is constructed for each grid. The fracture half-length versus injection time is plotted in Fig. 5.12 for different shape factors. It can be seen that as shape factor decreases, fracture half-length decreases correspondingly. This means that as rock inhomogeneity increases, the final geometry of fracture tends to have shorter length and wider width.

5.4.3 The Effect of Fluid Properties

In this part, the effect of rheological properties of fracturing fluid on fracture geometrical parameters is analyzed. When fracturing fluid is a power-law fluid, the flow equation is changed to

$$\frac{\partial p}{\partial s} = -\frac{2K_c q^n}{w^{2n+1}}\left(\frac{4n+2}{n}\right)^n \tag{5.56}$$

where n is the rheological index and K_c is the consistency index.

Therefore, the weak form of fluid flow equation can be expressed with the standard finite-element shape function

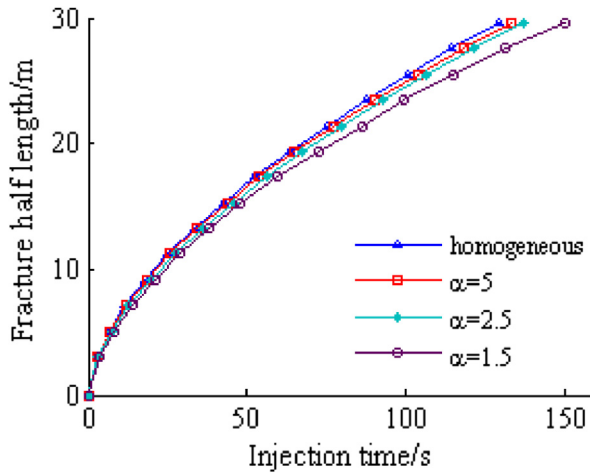

FIGURE 5.12 Fracture half-length versus injection time for different shape factors.

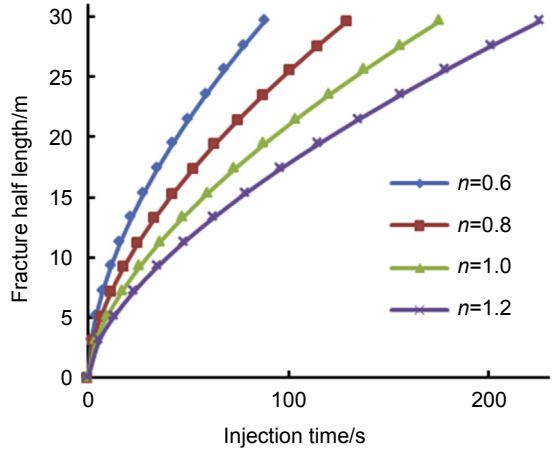

FIGURE 5.13 Fracture half-length distribution when different rheological indices are set.

$$\sum_{j=1}^{N}\frac{p_j}{12\mu}\int_0^L\frac{n}{4n+2}\left(\frac{1}{2K_c}\right)^{\frac{1}{n}}w^{\frac{2n+1}{n}}\left(-\frac{\partial p}{\partial s}\right)^{\frac{1}{n}-1}\frac{\partial N_i}{\partial s}\frac{\partial N_j}{\partial s}\mathrm{d}s$$
$$=Q_0N_i(0)-\int_0^L\frac{\Delta w}{\Delta t}N_i(x)\mathrm{d}s-\int_0^L\frac{2C_LN_i(s)}{\sqrt{t-\tau(s)}}\mathrm{d}s \tag{5.57}$$

The results of fracture half-length with different rheological and consistency indices are shown in Figs. 5.13 and 5.14. It can be shown that as rheological index increases, fracture half-length decreases. Moreover, as consistency index increases, fracture half-length decreases. It can be concluded that the rheological parameters of fracturing fluid have great impact on fracture geometrical parameters.

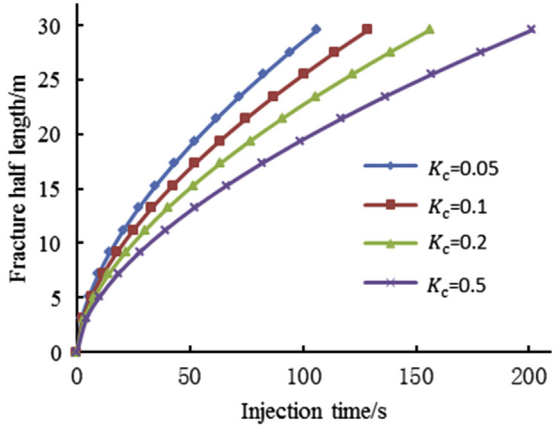

FIGURE 5.14 Fracture half-length distribution when different consistency indices are set.

5.4.4 The Effect of Natural Fracture

Renshaw and Pollard (1995) developed a simple criterion for predicting whether a fracture will propagate across a frictional interface orthogonal to the approaching fracture (Renshaw and Pollard, 1995). The criterion was extended to a fracture crossing frictional interfaces at nonorthogonal angles by Gu and Weng (2010). However, these criterions do not account for the effect of fluid pressure. When the length of natural fracture is large and its permeability is much larger than that of the surrounding matrix rock, and the propagation rate of hydraulic fracture is relatively low so that the fracturing fluid flows first into natural fracture quickly, then the fluid pressure effect should be taken into account (Zeng and Yao, 2016). Otherwise, the criterion of Gu and Weng should be adopted.

Consider the model of a hydraulic fracture intersecting a natural fracture as shown in Fig. 5.15. The intersection angle between hydraulic fracture and natural fracture is β. Assuming compression is positive, the combined stress near the hydraulic fracture tip can be approximately calculated by

$$\sigma_{xx} = \sigma_{\mathrm{H}} - \frac{K_I}{\sqrt{2\pi r}}\cos\frac{\theta}{2}\left(1 - \sin\frac{\theta}{2}\sin\frac{3\theta}{2}\right) \tag{5.58}$$

$$\sigma_{yy} = \sigma_{\mathrm{h}} - \frac{K_I}{\sqrt{2\pi r}}\cos\frac{\theta}{2}\left(1 + \sin\frac{\theta}{2}\sin\frac{3\theta}{2}\right) \tag{5.59}$$

$$\tau_{xy} = -\frac{K_I}{\sqrt{2\pi r}}\sin\frac{\theta}{2}\cos\frac{\theta}{2}\cos\frac{3\theta}{2} \tag{5.60}$$

where σ_{xx} and σ_{yy} are normal stresses in the x-direction and y-direction, respectively, Pa; τ_{xy} is the shear stress, Pa; σ_{H} and σ_{h} are maximum principal stress and minimum principal stress, respectively, Pa; r, and θ are polar coordinates of the fracture tip.

To reinitiate the fracture on the opposite side of the natural fracture, the maximum principal stress must reach the rock tensile strength, then the critical

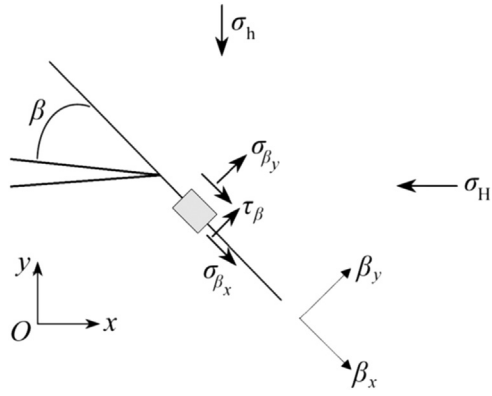

FIGURE 5.15 Schematic of hydraulic fracture approaching natural fracture.

radius r_c can be solved. As the hydraulic facture propagates across the natural fracture, it requires another condition. The stresses acting on the natural fracture must not cause slip of the interface. For a frictional surface, the condition that slip along the interface does not occur must satisfy

$$\left|\tau_\beta\right| < S_0 + c_f \sigma_{\beta_y} \tag{5.61}$$

where τ_β is shear stress along the interface, Pa; σ_{β_y} is normal stress on the interface, Pa; c_f is the coefficient of friction; and S_0 is the cohesion of the interface, Pa.

Because the permeability of natural fracture is larger than that of the matrix, when the hydraulic fracture intersects the natural fracture, the fluid flows into the natural fracture first. Furthermore, the natural fracture may as well be filled by fluid before the intersection. So accounting for the fluid pressure, the combined normal stress on the natural fracture is

$$\sigma_{\beta_y} = \sigma_{\text{tip},\beta_y} - p_f \tag{5.62}$$

where p_f is the fluid pressure, Pa, and this pressure is assumed to be equal to the pressure of fluid in the tip element; $\sigma_{\text{tip},\beta_y}$ is the normal stress acting on the natural fracture by projecting the near-tip stresses, Pa, which can be calculated by

$$\sigma_{\text{tip},\beta_y} = \sigma_{xx} \sin^2 \beta + \sigma_{yy} \cos^2 \beta + 2\tau_{xy} \sin \beta \cos \beta \tag{5.63}$$

The above equations can be solved numerically for the crossing criterion. When neglecting the effect of sliding stress and fluid pressure, the criterion reduced to the extended criterion developed by Gu and Weng, as shown in the semilog plot (Fig. 5.16). The minimum principal stress is fixed at 50 MPa, and

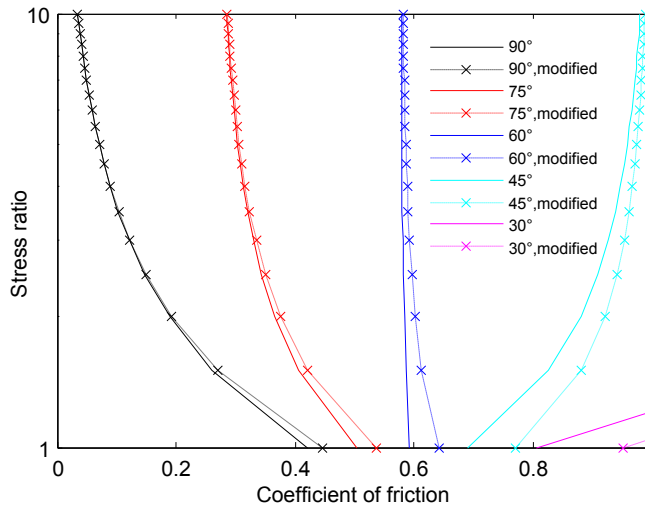

FIGURE 5.16 The results of crossing curve for Gu's criterion and modified criterion.

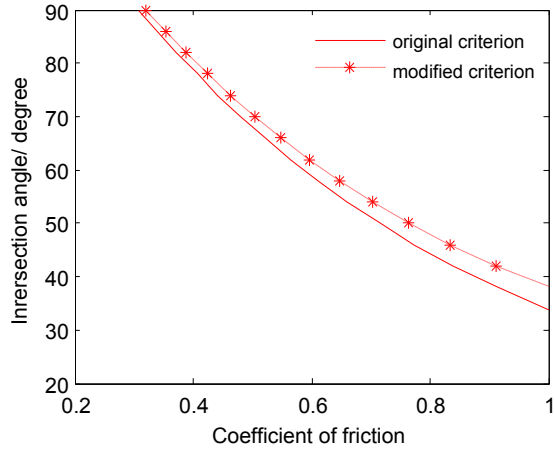

FIGURE 5.17 The crossing curves solved by Gu's criterion and modified criterion.

stress ratio is the ratio of maximum principal stress to minimum principal stress. The right to crossing curves means the hydraulic fracture propagates across the natural fracture. When the fluid pressure in the natural fracture is given as 5 MPa, the modified criterion moves to the right of crossing curves, which makes the arrest of hydraulic fracture by natural fracture easier.

In some block of Longmaxi Group shale, the maximum principal stress is 67 MPa and minimum principal stress is 50 MPa. According to these field data, stress ratio can be calculated as 1.34; thus the crossing curve can be plotted as shown in Fig. 5.17. In the figure, the modified criterion is above the crossing curve of Gu and Weng criterion.

Based on the modified criterion, hydraulic fracture approaching a natural fracture at an angle of 30° is simulated, and the results are shown in Fig. 5.18. As shown in the figure, the hydraulic fracture diverts into the natural fracture and reopens the natural fracture.

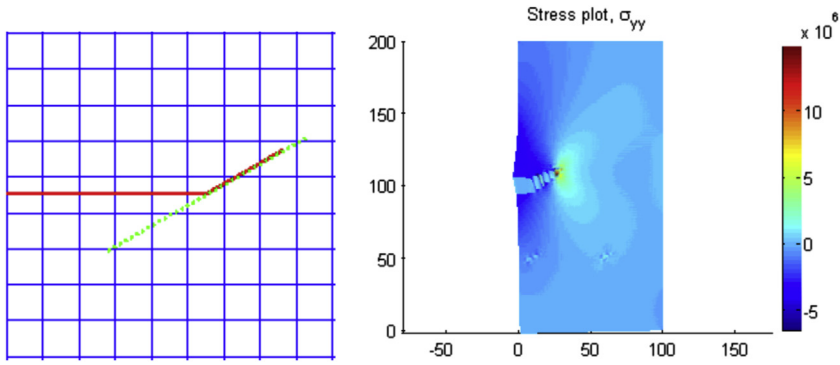

FIGURE 5.18 Propagation path of hydraulic fracture.

5.5 MODELING OF SIMULTANEOUS PROPAGATION OF MULTIPLE CLUSTER FRACTURES

5.5.1 Problem Formulations

Multiple fractures propagate simultaneously in multistage hydraulic fracturing process. There exists stress shadowing between these fractures, which influences fracture propagation and fracture geometry. Fractures do not propagate parallel and are of different lengths and widths. The central fracture always experiences elevated stress concentration, resulting in much smaller fracture width compared with the edge fractures. To understand the interaction between fractures, simultaneous propagation of multiple fractures is modeled in this part with an implicit level set method based on tip asymptotic solutions.

Due to the effect of stress shadowing, each fracture has different propagating rate and direction, and the injection rate into each fracture is a dynamic distribution process. The schematic of simultaneous propagation of multiple fractures is shown in Fig. 5.19.

Modeling fluid flow in the wellbore is needed to capture the distribution of injection rate into each fracture. According to Kirchoff's first law, the injection rate of all fractures sums up to the total injection rate.

$$Q_{\mathrm{T}} = \sum_{i=1}^{N} Q_i \tag{5.64}$$

where Q_{T} is the total injection rate, Q_i is injection rate of fracture i, and N is fracture number.

According to Kirchoff's second law, fluid pressure must satisfy

$$p_0 = p_{\mathrm{w},i} + \Delta p_{\mathrm{pf},i} + \Delta p_{\mathrm{cf},i} \tag{5.65}$$

where p_0 is fluid pressure at the heel of the wellbore, $p_{\mathrm{w},i}$ is the fluid pressure at the inlet of fracture i, $\Delta p_{\mathrm{pf},i}$ is the pressure drop through the perforation to

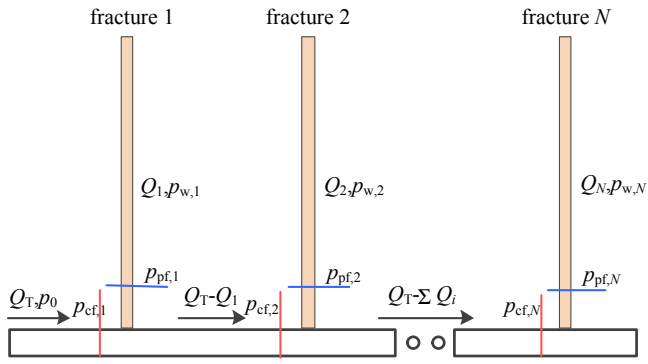

FIGURE 5.19 Schematic of simultaneous propagation of multiple fractures.

fracture i, and $\Delta p_{\mathrm{cf},i}$ is the pressure drop due to the friction along the wellbore to fracture i.

The pressure drop due to perforation can be calculated as

$$\Delta p_{\mathrm{pf}} = \frac{\rho_{\mathrm{s}}}{0.323\rho_{\mathrm{w}} n_{\mathrm{p}}^2 d_{\mathrm{p}}^4} Q^2 \tag{5.66}$$

where ρ_{s} is the density of slurry; ρ_{w} is the density of water; n_{p} is the number of perforations; d_{p} is the diameter of the perforation; and Q is the fluid rate.

The pressure drop due to friction along the wellbore can be calculated by laminar flow equation.

$$p_{\mathrm{cf},i} = C_{\mathrm{cf}} \sum_{j=1}^{i} (x_j - x_{j-1}) Q_{\mathrm{w},j} \tag{5.67}$$

$$Q_{\mathrm{w},j} = Q_{\mathrm{T}} - \sum_{k=1}^{j-1} Q_k \tag{5.68}$$

$$C_{\mathrm{cf}} = \frac{128\mu}{\pi D^4} \tag{5.69}$$

where C_{cf} is friction coefficient; x_j is the distance between fracture j and wellbore heel; and D is the wellbore diameter.

5.5.2 Tip Asymptotic Solution

When multiple fractures propagate simultaneously, the propagation rate of fracture tip is different from each other due to stress shadowing. Here an implicit level set scheme based on tip asymptotic solution is adopted to determine fracture growth length (Gordeliy and Peirce, 2013b).

First, the tip asymptotic solution is described. Research results show that besides rock and fluid parameters, fracture width near the tip only depends on the local propagating rate of the fracture tip. It means that there is a tip asymptotic solution, and many studies have been devoted to find the solution. It is found that the tip asymptotic solution is determined by two competing processes, including the energy required to break rocks and energy dissipated in the fluid flow. When the former energy is much greater than the latter, it is called toughness-dominated regime. Otherwise, when the latter energy is much greater than the former, it is called viscosity-dominated regime. However, in the field-fracturing process the tip asymptotic solution is often in the intermediate regime between toughness dominated and viscosity dominated. Linkov (2014) derived the universal solution for these three regimes.

$$\Omega_{k\mu}\left(\xi_{k\mu}\right) = A_{k\mu}\xi_{k\mu}^{\alpha} \tag{5.70}$$

$$\alpha = \begin{cases} 1/2, & \xi_{k\mu} \le 10^{-5} \\ 0.599, & 10^{-5} \le \xi_{k\mu} \le 1 \\ 2/3, & \xi_{k\mu} \ge 1 \end{cases}, \quad A_{k\mu} = \begin{cases} 1, & \xi_{k\mu} \le 10^{-5} \\ 2^{1/3}3^{5/6}, & 10^{-5} \le \xi_{k\mu} \le 1 \\ 2^{1/3}3^{5/6}, & \xi_{k\mu} \ge 1 \end{cases} \tag{5.71}$$

In Eq. (5.70), $\Omega_{k\mu}$ is the scaled fracture width and $\xi_{k\mu}$ is the scaled distance to fracture tip. The scaling can be given as

$$\Omega_{k\mu} = \frac{3\pi^2 E' \mu v_* w}{256 K_{IC}^4} \tag{5.72}$$

$$\xi_{k\mu} = \frac{9\pi^3 E' \mu^2 v_*^2 r}{2048 K_{IC}^6} \tag{5.73}$$

where E' is the elastic modulus for plane strain state, Pa; r is the distance to fracture tip, m; v_* is the propagating rate of fracture tip, m/s; and K_{IC} is rock toughness, $Pa \cdot m^{1/2}$.

The log−log plot of tip asymptotic solution is shown in Fig. 5.20. The slope of the toughness asymptote and viscosity asymptote is 1/2 and 2/3, respectively. The universal asymptotic solution coincides with the toughness asymptote in the toughness-dominated regime and the viscosity asymptote in the viscosity-dominated regime.

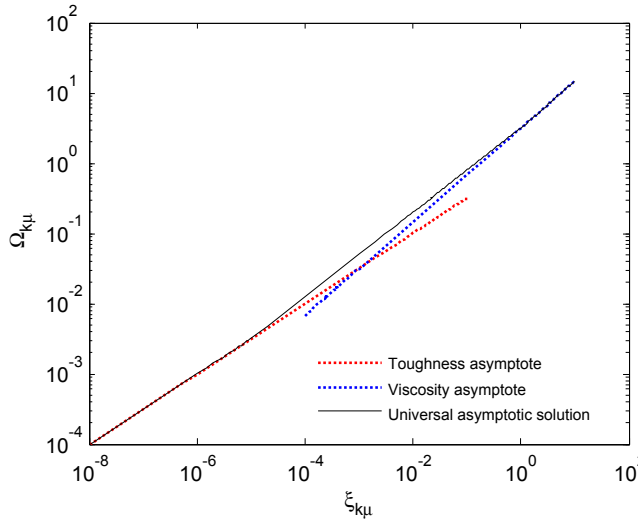

FIGURE 5.20 Log−log plot of tip asymptotic solution.

5.5.3 Numerical Algorithm

The numerical solution for multiple fractures is different from that of single fractures and will be described in detail as follows. The numerical solution includes four parts: stress field, pressure field, iteration process, and inversion of fracture growth length.

First, the stress field is solved with localized mixed-hybrid method in which the fracture opening displacement in a neighborhood Σ_t of the fracture tip is prescribed, whereas the pressure is prescribed in the interior of the fracture $\Sigma_c = \Sigma - \Sigma_t$:

$$w^i(r) = w^i_{\text{tip}}(L-s), \quad s \in \Sigma^i_t \tag{5.74}$$

$$p^i(s) = p^i_c(s), \quad s \in \Sigma^i_c \tag{5.75}$$

where i denotes fracture i and w_{tip} represents fracture tip asymptotic solution.

The weak form of rock deformation can be written as

$$\begin{aligned} 0 = &\int_{V_0 \setminus \Sigma} \boldsymbol{\varepsilon}(\boldsymbol{v}^h) : \boldsymbol{\sigma}(\boldsymbol{u}^h) dV + \sum_{i=1}^{N} \int_{B_i \setminus \Sigma^i_t} \boldsymbol{\varepsilon}(\boldsymbol{v}^h) : \boldsymbol{\sigma}^h dV + \sum_{i=1}^{N} \int_{B_i \setminus \Sigma^i_t} \boldsymbol{\tau}^h(\boldsymbol{\varepsilon}(\boldsymbol{u}^h) \\ &- \boldsymbol{C}^{-1} : \boldsymbol{\sigma}^h) dV + \sum_{i=1}^{N} \int_{\Sigma^i_c} [\![\boldsymbol{v}^h]\!] \cdot (-p^i_c(s)\boldsymbol{n}) ds + \sum_{i=1}^{N} \int_{B_i \setminus \Sigma^i_t} ([\![\boldsymbol{v}^h]\!] \cdot \boldsymbol{n}) \\ &(\boldsymbol{n} \cdot \{\boldsymbol{\sigma}^h\} \cdot \boldsymbol{n}) + (\boldsymbol{n} \cdot \{\boldsymbol{\tau}^h\} \cdot \boldsymbol{n}) \left([\![\boldsymbol{u}^h]\!] - w^i_{\text{tip}}(r) \right) ds \end{aligned} \tag{5.76}$$

where V is discretized into a mesh of nonoverlapping elements e: $V = \bigcup_{e \in F} V^h_e$. The subset of elements that overlaps with the fracture tip region Σ^i_t is denoted as $\mathcal{B}_i : \mathcal{B}_i = \left\{ e \in \mathcal{F} \middle| V^h_e \cap \Sigma^i_t \neq \varnothing \right\}$; The rest element that does not overlap with any fracture tip region is denoted as V_0: $V_0 = V \setminus \bigcup_{i \in \{1,2,\ldots N\}} \mathcal{B}_i$.

In the equation, $[\![\cdot]\!]$ and $\{ \cdot \}$ are operators, which can be defined as

$$[\![\boldsymbol{v}]\!] = \boldsymbol{v}^+ - \boldsymbol{v}^- \tag{5.77}$$

$$\{\boldsymbol{\sigma}\} = \frac{1}{2}(\boldsymbol{\sigma}^+ + \boldsymbol{\sigma}^-) \tag{5.78}$$

The approximate formulation of displacement for multiple fractures in the frame of XFEM can be given as

$$\begin{aligned} u^h(\boldsymbol{x}) = &\sum_{I \in N_e} N_I(\boldsymbol{x}) u_I + \sum_{i=1}^{N} \sum_{I \in N^i_c} N_I(\boldsymbol{x}) (H_i(\varphi(\boldsymbol{x})) - H_i(\varphi(\boldsymbol{x}_I)) a^i_I \\ &+ \sum_{i=1}^{N} \sum_{I \in N^i_t} \sum_{\alpha=1}^{4} N_I(\boldsymbol{x}) \left(\psi^u_\alpha(\boldsymbol{x}) - \psi^u_\alpha(\boldsymbol{x}_I) \right) b^i_{I\alpha} + \sum_{j=1}^{n_J} \sum_{I \in N_J} N_I(\boldsymbol{x}) (J(\boldsymbol{x}) - J(\boldsymbol{x}_I)) d_{Ij} \end{aligned} \tag{5.79}$$

where N_e is the set of all nodes in the discretized model, N_c is the set of nodes of all elements containing cracks but not crack tips, N_t is the set of nodes of all elements containing the crack tip, and N_J is the set of nodes that are enriched for the junction; N_I are the finite-element shape functions, $H(\xi)$ is the Heaviside step function, $\varphi(\boldsymbol{x})$ is the signed distance function, ψ^{μ} is the enriched functions for tip elements, and $J(\boldsymbol{x})$ is the junction function; u_I is the nodal degree, a_I is the enriched degree for Heaviside function, b_I is the enriched degree for tip function, and d_I is the enriched degree for junction function.

The intersection element is enriched with the junction function, which is similar to the Heaviside function. Consider the intersection consisting of two cracks denoted by cracks I and II, then the junction function $J(\boldsymbol{x})$ can be expressed in terms of the Heaviside function as

$$J(\boldsymbol{x}) = \begin{cases} H(\varphi_I(\boldsymbol{x})) - H(\varphi_I(\boldsymbol{x}_i)), \varphi_I(\boldsymbol{x})\varphi_I(\boldsymbol{x}_i) > 0 \\ H(\varphi_{II}(\boldsymbol{x})) - H(\varphi_{II}(\boldsymbol{x}_i)), \varphi_I(\boldsymbol{x})\varphi_I(\boldsymbol{x}_i) < 0 \end{cases} \tag{5.80}$$

The approximate formulation of stress in the frame of XFEM can be written as

$$\sigma^h(\boldsymbol{x}) = \sum_{I \in N_B} N_I(\boldsymbol{x}) a_I + \sum_{I \in N_B} N_I(\boldsymbol{x}) \sum_{j=1}^{4} \left(\psi_j^{\sigma}(\boldsymbol{x}) - \psi_j^{\sigma}(\boldsymbol{x}_I) \right) c_I^j \tag{5.82}$$

where ψ^{μ} is the enriched functions of stress for tip elements.

The appropriate enriched function for displacement and corresponding stress fields are in the following form:

$$\psi^{\mu,\lambda} = r\{sin(\lambda\theta),\ cos(\lambda\theta),\ sin(\lambda - 2)\theta,\ cos(\lambda - 2)\theta\} \tag{5.83}$$

$$\psi^{\sigma,\lambda} = r^{\lambda-1}\{sin(\lambda - 1)\theta,\ cos(\lambda - 1)\theta,\ sin(\lambda - 3)\theta,\ cos(\lambda - 3)\theta\} \tag{5.84}$$

where λ is the asymptotic index in the tip asymptotic solution.

Second, the fluid pressure field is solved simultaneously for multiple fractures. The weak form is similar to that of single fracture propagation.

$$\frac{p_i^j}{12\mu} \int_0^{L_i} w_i^3 \frac{\partial N_k}{\partial s} \frac{\partial N_j}{\partial s} \mathrm{d}s = Q_i N_k(0) - \int_0^{L_i} \frac{\Delta w_i}{\Delta t} N_k(s) \mathrm{d}s - \int_0^{L_i} \frac{2C_l N_k(s)}{\sqrt{t - \tau_0(s)}} \mathrm{d}s \tag{5.85}$$

Due to the linearity of elasticity problem, the problem can be divided into two elastic boundary value problems as follows.

The problem solution is denoted as $w_i^{j+1/2}$ with the following boundary condition:

$$\sigma_n^+ = \sigma_n^- = -p_i^{j+1/2},\ s \in \Sigma_c^i,\ j = 1, 2, \ldots n_i,\ i = 1, 2, \ldots N \tag{5.86}$$

$$[\![\boldsymbol{w}]\!] \cdot \boldsymbol{n} = 0,\ s \in \Sigma_t^i,\ i = 1, 2, \ldots N \tag{5.87}$$

The problem solution is denoted $w_{t,i}$ with the following boundary condition:

$$\sigma_n^+ = \sigma_n^- = 0,\ s \in \Sigma_c^i,\ i = 1, 2, \ldots N \tag{5.88}$$

$$[\![\boldsymbol{w}]\!] \cdot \boldsymbol{n} = w_t^i (L_i - x),\ x \in \Sigma_t^i,\ i = 1, 2, \ldots N \tag{5.89}$$

Both aforementioned boundary value problems can be solved by using the method described for stress field. Therefore, the whole solution for problem can be superposed as

$$w(x) = \sum_{i=1}^{N} w_{t,i}(x) + \sum_{i=1}^{N} \sum_{j=1}^{n_i} w_i^{j+1/2}(x) \tag{5.90}$$

Then, the stress field and pressure field need to be solved by an iterative process. The time step is fixed, and growth length for each fracture tip is inverted by tip asymptotic solution, which will be described briefly in the following part. The unknown variables include fracture width $w_i = \left(w_i^1, w_i^2, \ldots w_i^{n_i}\right)$, fluid pressure $p_i = \left(p_i^{1/2}, p_i^{3/2}, \ldots p_i^{n_i+1/2}\right)$, injection rate into each fracture Q_i, and fluid pressure at the wellbore heel. The total number of unknowns is $N + 1 + 2\Sigma n_i$. According to the iterative method, the equal number equations are needed to solve the problem. The discretization of Eq. (5.90) has Σn_i equations, and discretization of Eq. (5.85) has Σn_i equations. Eqs. (5.64) and (5.65) describing fluid flow in the wellbore has $N + 1$ equations. So the total number of equations is the same as that of unknowns. The Newton–Raphson method is used to solve the whole equation set.

Finally, the inversion method of fracture growth length is presented. When fracture width of each element is given, the element next to tip element is selected to retrieve the fracture length for current time step. The distance between the center of the element next to tip element and injection point can be obtained and is denoted by s. Its fracture width is also known, denoted by w.

The fracture half-length is assumed to be equal to L for current time step, and then the propagation rate of fracture tip can be given as

$$v_* = \frac{L - L^0}{\Delta t} \tag{5.91}$$

where L^0 is fracture half-length for previous time step, m.

According to tip asymptotic solution w_t, it can be deduced as

$$w - w_t(L - s, v_*) = 0 \tag{5.92}$$

The tip asymptotic solution is a function of tip propagation rate and distance to tip. The tip asymptotic solution is expressed in explicit equations as Eqs. (5.70) and (5.71). To obtain fracture half-length, it needs to solve Eq. (5.92) by iterative method because of the nonlinearity.

5.5.4 Numerical Results

To analyze the effect of fracture spacing on fracture propagation, simultaneous propagation of three fractures is modeled with a fracture spacing of 10 and 15 m. The cloud diagram of stress change along the minimum principal stress direction is shown in Fig. 5.21, and fracture width distribution is shown in Fig. 5.22. It can be seen that as fracture spacing decreases, the fracture widths of upper and middle fractures decrease. The reason for this is that as fracture

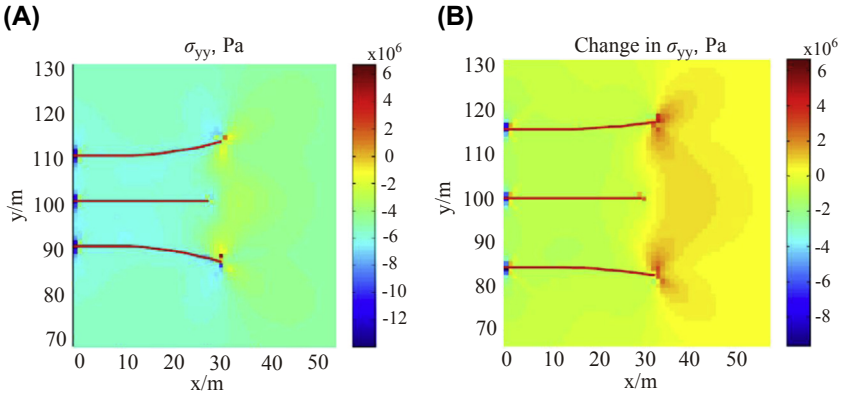

FIGURE 5.21 Cloud diagram of stress change along minimum principal stress direction. (A) $D = 10$ m and (B) $D = 15$ m.

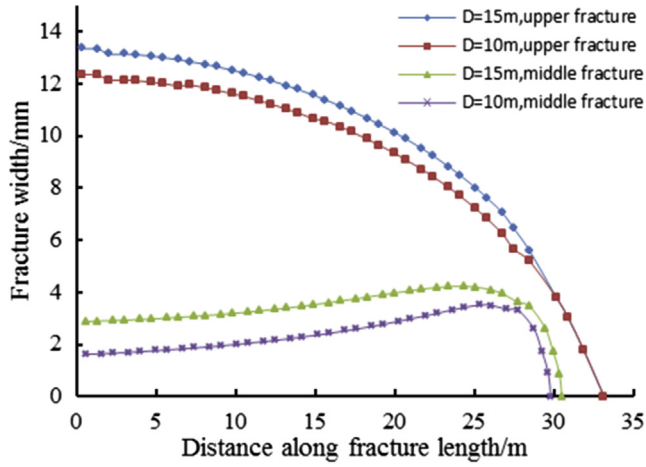

FIGURE 5.22 Fracture width distribution along fracture propagation direction.

spacing decreases, the stress interference between fractures becomes severe, and then fractures experience larger compressive stress, which can also be seen from Fig. 5.21. It can also be shown in Fig. 5.21 that the propagation paths of fractures develop into curved lines, especially two-side fractures. Moreover, as fracture spacing decreases, the curvature of propagation path increases.

To investigate the effect of stress anisotropy on fracture propagation, the minimum principal stress is fixed at 5 MPa, whereas the maximum principal stress is set as 10 and 20 MPa. The cloud diagram of stress change along the minimum principal stress direction is shown in Fig. 5.23. It can be shown that the curvature of the propagation path of two-edge fractures when stress difference is 15 MPa is smaller than that when stress difference is 5 MPa. It means that stronger stress anisotropy leads to smaller curvature of propagation path.

5.6 EXTENSIONS TO RESERVOIR HYDROMECHANICAL SIMULATION

After hydraulic fracturing, a reservoir usually possesses multiscale fractures (e.g., hydraulic fractures and natural/induced fractures) and becomes more stress sensitive. In this section, an adaptive hybrid model (HM) is proposed to model the coupled flow and mechanical processes in these reservoirs. In our HM, the single porosity model is applied in the region outside the stimulated reservoir volume (SRV). The matrix and natural/induced fractures in the SRV region are modeled by a double porosity model which can accurately simulate the matrix fracture fluid exchange for the entire transient period. The hydraulic fractures filled with proppants are modeled explicitly by nonmatching grids

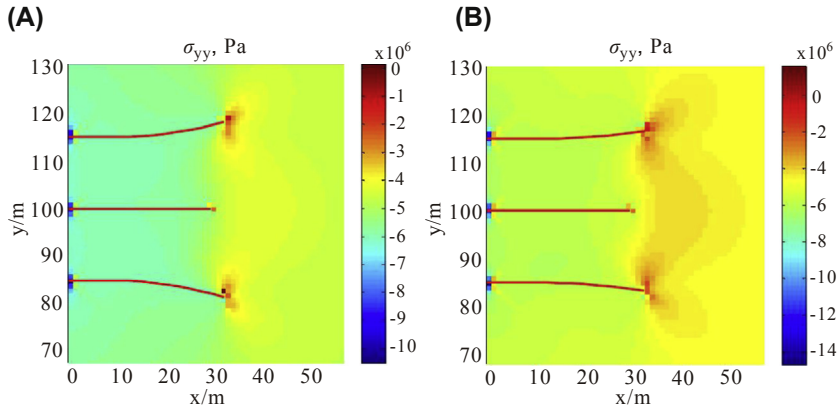

FIGURE 5.23 Cloud diagram of stress change along the minimum principal stress direction. (A) $\Delta\sigma = 5$ MPa and (B) $\Delta\sigma = 15$ MPa.

model: the embedded discrete fracture model (EDFM) (Yan et al., 2016). Furthermore, a mixed space discretization, i.e., finite volume method (FVM) for porous flow and stabilized XFEM for geomechanics, and modified fixed stress sequential implicit methods are applied to solve the HM. The accuracy and robustness of the proposed method are demonstrated through several numerical examples.

5.6.1 Coupling Scheme for Extended Finite-Element Method and Embedded Discrete Fracture Model

The EDFM and XFEM do not need the grids to be matching with the hydraulic fractures and can achieve high accuracy without requiring highly refined grids; thus, the orthogonal grids are used for the geometry discretization, and hydraulic fractures are discretized according to the intersections of hydraulic fractures and orthogonal grids, as illustrated in Fig. 5.24. Therefore, the challenges associated with matching refined grids are bypassed entirely. In addition, an improved Multiple INteracting Continua (MINC) method is used to generate the nested grid by combining the MINC and multiple subregion (MSR) method (Gong et al., 2008) inside the matrix block. The matrix block is discretized by the MINC nested elements from the exterior (natural/induced fractures) to a transition location ($D_p = 0.04\,L$, this is an optimal value for the square and cube); then the MSR nested elements based on pressure contours are applied in the remaining region.

The governing equation for fluid flow is obtained from the general mass balance (Wu, 2015), and its integral form can be written as

$$\frac{\partial}{\partial t}\int_{\Omega} A_\beta \mathrm{d}\Omega + \int_{\Gamma} \boldsymbol{F}_\beta \cdot \boldsymbol{n}\mathrm{d}\Gamma = \int_{\Omega} q_\beta \mathrm{d}\Omega \tag{5.93}$$

where the subscript β indicates fluid phases; $\boldsymbol{n}$ is the normal vector of the boundary Γ; A, $\boldsymbol{F}$, and q are the mass accumulation, mass flux, and source

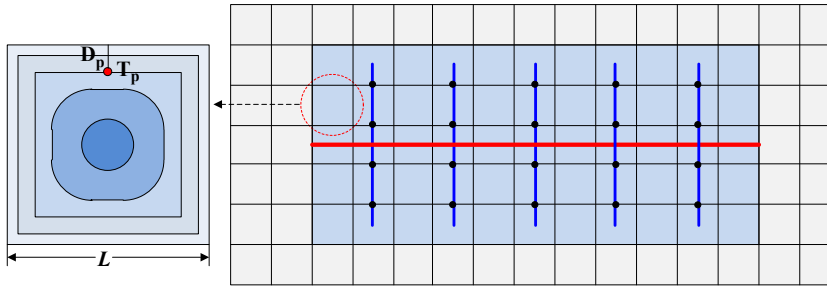

FIGURE 5.24 Schematic of the gridding (the *blue* [light gray in print version] *and red* [dark gray in print version] *lines* are hydraulic fractures and horizontal well, respectively).

terms on the domain Ω, respectively. The mass accumulation of phase β is expressed as

$$A_\beta = \phi S_\beta \rho_\beta \tag{5.94}$$

where ϕ is the Lagrange porosity, and its formulas are given in Eqs. (5.97) and (5.99); S_β and ρ_β are saturation and density of phase β, respectively.

The mass flux term in Eq. (5.93) is given by

$$\boldsymbol{F}_\beta = -\rho_\beta \frac{k_{r\beta}}{\mu_\beta} k\left(\nabla p_\beta - \rho_\beta g \nabla D\right) \tag{5.95}$$

where k is absolute permeability; $k_{r\beta}$ and μ_β are relative permeability and viscosity of phase β, respectively; g is the gravity acceleration; and D is depth.

The governing equations for geomechanics are based on quasi-static and linear elasticity assumption (the sign convention is adopted positive for tension and negative for compression), and it can be found in Ren et al. (2016). The effective stress (Biot, 1941) and Lagrange porosity equations of the single porosity model applied in the region out of SRV are written as

$$\boldsymbol{\sigma} = \boldsymbol{C}\boldsymbol{\varepsilon} - \alpha p_t \mathbf{I} \tag{5.96}$$

$$\Delta\phi = \frac{(1-\alpha)(\alpha-\phi)}{K}\Delta p_t + \alpha \Delta\varepsilon_v \tag{5.97}$$

where $\boldsymbol{C}$ and α are the elasticity tensor and Biot coefficient of matrix; $p_t = p_w S_w + p_g S_g$ is the total pressure; $\mathbf{I}$ is a unit tensor; and K is the drained bulk modulus of matrix.

The effective stress (Kim et al., 2012) and Lagrange porosity equations for the multiple porosity model applied in the SRV region are written as

$$\boldsymbol{\sigma} = \boldsymbol{C}_{up}\boldsymbol{\varepsilon} + \sum\nolimits_l K_{dr} b_l p_{tl} \mathbf{I} \tag{5.98}$$

$$\Delta\phi_l = \left(\frac{\alpha_l^2}{K_l} + \frac{\alpha_l - \phi_l}{K_s}\right)\Delta p_{tl} - \frac{b_l}{\eta_l} K_{dr}\left(\Delta\varepsilon_v + \sum\nolimits_i^{n_m} b_i \Delta p_{ti}\right) \tag{5.99}$$

where subscript l indicates the lth subelement within a gridblock; K_{dr} and $\boldsymbol{C}_{up}$ are the upscaled drained bulk modulus and elasticity tensor at the level of gridbolcks, respectively; $\alpha_l = 1 - K_l/K_s$, K_l, and η_l are the Biot coefficient, drained bulk modulus, and volume fraction for lth subelement, respectively; K_s is the intrinsic solid grain bulk modulus; ε_v is the total volumetric strain of a gridblock; and n_m is the number of subelements in each gridblock. $b_l = -\alpha_l \eta_l / K_l$ is a coupling coefficient, and K_{dr} and $\boldsymbol{C}_{up}$ are described as

$$\frac{1}{K_{dr}} = \sum_{l=1}^{n_m} \frac{\eta_l}{K_l}, \quad \boldsymbol{C}_{up} = K_{dr} \sum_{l=1}^{n_m} \frac{\eta_l}{K_l} \boldsymbol{C}_l \tag{5.100}$$

The permeabilities of matrix, natural/induced fractures, and hydraulic fractures are all affected by the deformation of reservoirs. Based on the Kozeny−Carman model (Liu et al., 2011), the dynamic matrix permeability k_m can be written as

$$k_m = k_{m0}\left(\frac{\phi_m}{\phi_{m0}}\right)^3\left(\frac{1-\phi_{m0}}{1-\phi_m}\right)^2 \tag{5.101}$$

where k_m and ϕ_m are matrix permeability and porosity, and 0 represents the initial state.

In a multiple porosity model based on the MINC method (Pruess, 1985), the permeability of natural/induced fractures k_f (i.e., the first subelement) is defined as

$$k_f = d_f^3 \Big/ (6L) \tag{5.102}$$

where d_f is the fracture aperture and L is the fracture spacing. The isotropic deformation of gridblocks is assumed in this study, and the following equations can be obtained:

$$1+\varepsilon_f = \frac{V_f}{V_{f0}} = \frac{L^2-(L-d_f)^2}{L_0^2-(L_0-d_{f0})^2} = \frac{d_f(2L-d_f)}{d_{f0}(2L_0-d_{f0})} \approx \frac{d_f L}{d_{f0}L_0} = \frac{d_f}{d_{f0}}(1+\varepsilon_v)^{\frac{1}{2}} \tag{5.103}$$

where $\varepsilon_f = \varepsilon_v K_{dr}/K_f$ and V_f are the volumetric strain and volume of fractures, respectively; K_f is the drained bulk modulus of fractures. Then the dynamic permeability of natural/induced fractures can be inferred by combining Eqs. (5.102) and (5.103).

$$k_f = k_{f0}\left(\frac{d_f}{d_{f0}}\right)^3\frac{L_0}{L} = k_{f0}\left(1+\frac{K_{dr}}{K_f}\varepsilon_v\right)^3(1+\varepsilon_v)^{-2} \tag{5.104}$$

Experimental and theoretical works have established that flow in hydraulic fractures is very closely governed by the Darcy's law (Witherspoon et al., 1980), with permeability k_F proportional to the square of fracture aperture d_F; therefore the dynamic permeability of hydraulic fractures can be written as

$$k_F = k_{F0}\left(\frac{d_F}{d_{F0}}\right)^2 \tag{5.105}$$

The displacement difference between hydraulic fracture interfaces can be calculated by the stabilized XFEM in this study; therefore the fracture aperture d_F can be obtained as follows.

$$d_F = d_{F0} + [\![\boldsymbol{u}]\!]\cdot\boldsymbol{n}_F \tag{5.106}$$

For capillary pressure functions, the impact of rock deformation (i.e., pore change) is accounted by using the Leverett function (Leverett, 1941)

$$p_c = C_p p_{c0} \sqrt{\frac{\phi}{k} \frac{k_0}{\phi_0}} \tag{5.107}$$

where p_c is the capillary pressure and C_p is a constant.

It is noted that only normal deformation of hydraulic fractures is assumed in this section, while the shear slip and related dilation will be included in future study for specific cases. In addition, one can use an alternative, table lookup approach for the correlation of reservoir parameters as a function of effective stress, from laboratory studies, for a given shale reservoir.

A mixed space discretization is used in this study: the FVM is used for fluid flow, where pressure and saturation are located at element centers. On the other hand, space discretization for geomechanics is by using the XFEM, in which the displacement vector is located at grid vertices. The mixed space discretization can yield the benefits such as local mass conservation and excellent numerical stability in space. Note that in multiple porosity model, the flow model is solved at subelement level, whereas the geomechanics model is solved at gridblock level.

A key point of the HM for fluid flow is the calculation of transmissibility T_{ij} between connecting elements in different domains. In the region out of SRV, there are two types of transmissivity (global flow): T_{mm} (matrix to matrix) and T_{mf} (matrix to natural/induced fractures). In the SRV region, it is assumed that matrix and natural/induced fractures exchange fluid locally within each gridblock, while global flow occurs through natural/induced and hydraulic fractures. This means there are five types of transmissivity: T_{mm} (matrix to matrix), T_{mf} (matrix to natural/induced fractures), T_{ff} (natural/induced fractures to natural/induced fractures), T_{fF} (natural/induced fractures to hydraulic fractures), and T_{FF} (hydraulic fractures to hydraulic fractures). In this study, the improved MINC method (Fig. 5.24) is applied to calculate the T_{mm} and T_{mf}, and the EDFM method (Moinfar et al., 2012; Yan et al., 2016) is used to calculate the T_{fF} and T_{FF}. In addition, the star−delta transmissivity (Karimi-Fard et al., 2004) is used to handle intersecting hydraulic fractures.

To solve the hydromechanical process accurately, there are two strategies: fully coupled (Hu et al., 2013; Huang et al., 2015; Winterfeld and Wu, 2016) and sequential implicit methods (Kim et al., 2011, 2012). The fully coupled method provides unconditional stability and high accuracy. However, this method requires a unified hydromechanical simulator, huge computational cost, and complicated code management. To avoid these disadvantages, sequential methods are typically used, providing sufficient precision and flexible code management.

In this section, a modified fixed stress sequential implicit method is applied to solve the HM. Specifically, the flow problem is first solved (fixing the total

stress field), and then the geomechanics problem is solved based on the fluid pressures and saturations obtained from flow problem. This sequential implicit method can provide unconditional numerical stability and high accuracy (Kim et al., 2011, 2012), and it can easily be implemented by using the Lagrange porosity, as follows

$$\phi^{n+1}-\phi^{n}=\frac{(1-\alpha)(\alpha-\phi^{n})}{K}\left(p_{\mathrm{t}}^{n+1}-p_{\mathrm{t}}^{n}\right)+\overbrace{\alpha\left(\varepsilon_{\mathrm{v}}^{n+1}-\varepsilon_{\mathrm{v}}^{n}\right)}^{\text{correction term}},\quad \text{out of SRV} \tag{5.108}$$

$$\phi_{l}^{n+1}-\phi_{l}^{n}=\left(\frac{\alpha_{l}^{2}}{K_{l}}+\frac{\alpha_{l}-\phi_{l}^{n}}{K_{\mathrm{s}}}\right)\left(p_{tl}^{n+1}-p_{tl}^{n}\right)$$
$$-\overbrace{\frac{b_{l}}{\eta_{l}}K_{\mathrm{dr}}\left(\left(\varepsilon_{\mathrm{v}}^{n+1}-\varepsilon_{\mathrm{v}}^{n}\right)+\sum_{i}^{n_{\mathrm{m}}}b_{i}\left(p_{ti}^{n}-p_{ti}^{n-1}\right)\right)}^{\text{correction term}},\quad \text{in SRV} \tag{5.109}$$

where the superscript n indicates time level. The correction term can correct the inconsistency between the porosity estimated from the pore compressibility in the flow problem and the strain from geomechanics.

5.6.2 Numerical Examples

Fig. 5.25A shows a 2D shale reservoir (700 m × 340 m) with five hydraulic fractures. The SRV region in this reservoir is 540 m × 220 m. This reservoir is initially saturated with gas, and the initial pressure is 25 MPa. For flow, we have no flow at boundaries, and a constant pressure (10 MPa) is applied at the production well. For geomechanics, constant forces are applied on the top and right boundaries, and the left and bottom boundaries are fixed in x-direction and y-direction, respectively. Some parameters are provided in Table 5.1. The parameters of the matrix in the region out of SRV are the same as the parameters of the fourth matrix subelement in the SRV region. The absolute permeability of natural/induced fractures is calculated by Eq. (5.102). In this example, the proppants in hydraulic fractures are ignored, and the absolute permeability of hydraulic fractures is assumed to be a constant. The computational grids of the standard finite-element model (SFEM) (grid number: 49,396) and the proposed method (35 × 17) are shown in Fig. 5.25. The refined grids and the fully coupled and fully implicit scheme are used in the SFEM, which is implemented by the COMSOL Multiphysics software (COMSOL, 2015).

Two cases are presented to verify the proposed method. In Case 1, the absolute permeabilities of matrix and natural/induced fractures are assumed to be constant. In Case 2, the dynamic absolute permeabilities of matrix and natural/induced fractures are adopted. The pressure and x-displacement fields

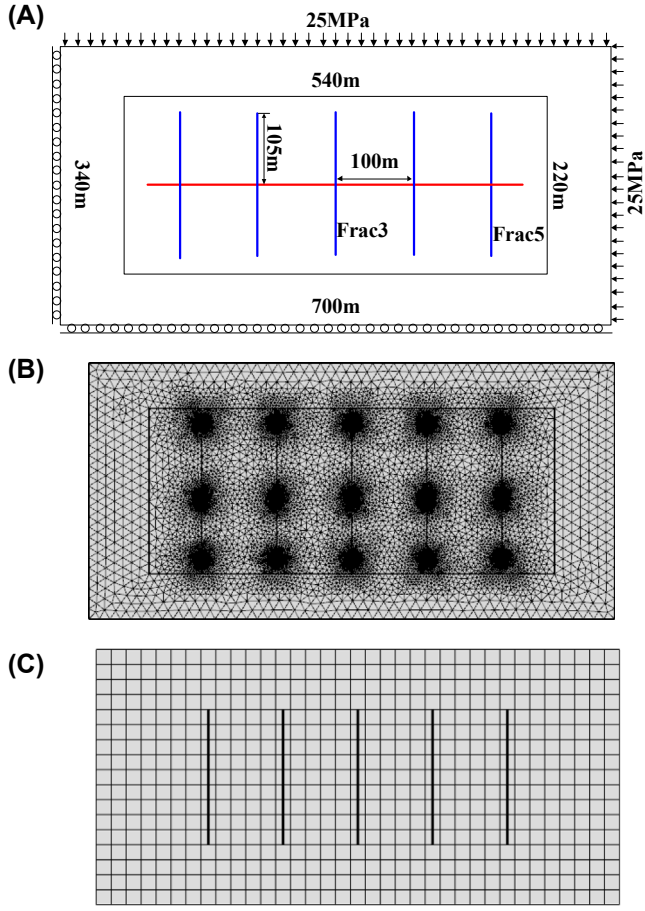

FIGURE 5.25 Schematic of the shale reservoir and computational grids. (A) Schematic of the shale reservoir. (B) Computational grids for the standard finite-element model. (C) Computational grids for the proposed method.

of Case 2 after 20 years are shown in Fig. 5.26, and the results of the SFEM and proposed method are qualitatively close.

The comparisons of cumulative gas for two cases and the relative displacements between fracture interfaces (Frac3 and Frac5 as shown in Fig. 5.27) for Case 2, which are calculated by the SFEM (reference) and proposed method (HM), are plotted in Fig. 5.27, and excellent agreements between results of the proposed method and the references can be seen. In addition, it also shows that the stress sensitivity (permeability variation) of the

TABLE 5.1 Parameters of Shale Reservoir

Name	Value
Initial absolute permeabilities of matrix and hydraulic fractures, m^2	5.0E-20, 8.33E-12
Natural fracture spacing, initial natural, and hydraulic fracture apertures, m	10, 5.0E-6, 0.001
Initial porosities of matrix, natural fractures, and hydraulic fractures	0.08, 1.0, 0.75
Volume fraction of matrices 1, 2, 3, 4	0.154, 0.213, 0.379, 0.254
Drained bulk modulus of natural fractures and matrices, GPa	0.05, 5, 40, 40, 40
Intrinsic solid grain bulk modulus (K_s), GPa	400
Poisson's ratios of natural fracture and matrices	0.1, 0.2, 0.25, 0.25, 0.25
Irreducible saturations of water and gas	0, 0
Formation thickness, m	10.0

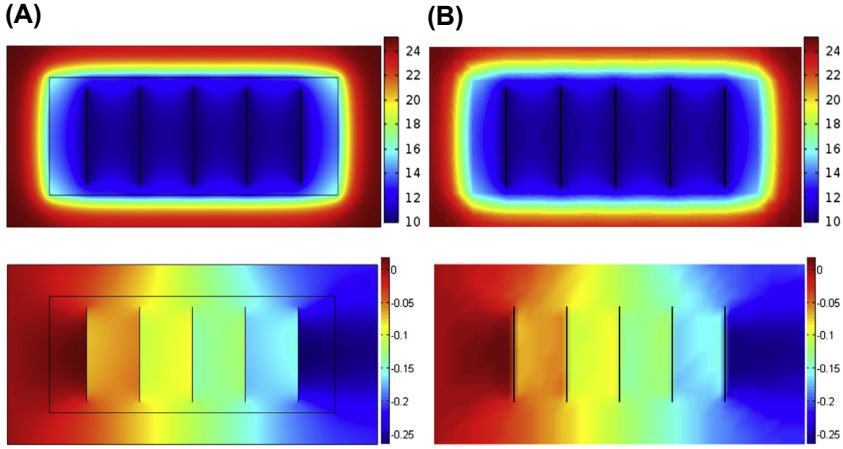

FIGURE 5.26 Pressure and displacement comparisons of the standard finite-element model (SFEM) and the proposed method after 20 years. (A) Pressure field of the SFEM, MPa. (B) Pressure field of the proposed method, MPa. (C) *x*-displacement field of the SFEM, m. (D) *x*-displacement field of the proposed method, m.

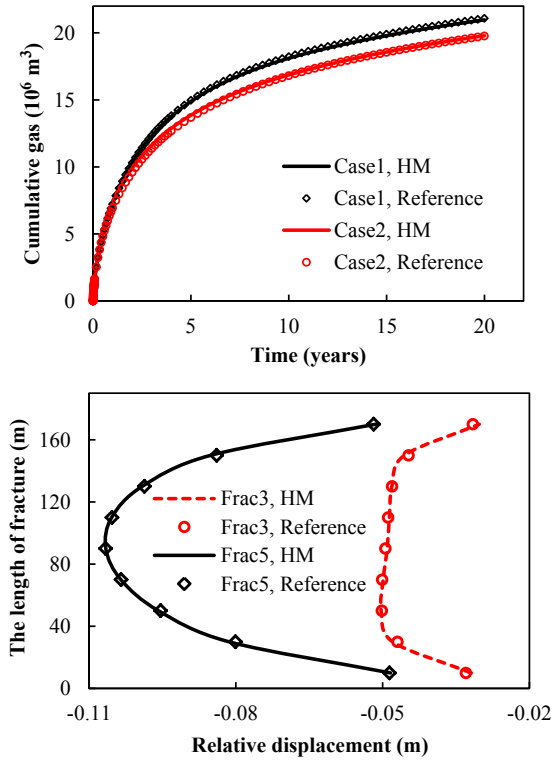

FIGURE 5.27 Comparisons of cumulative gas (top) and relative displacements (bottom) calculated by different methods.

natural/induced fractures and matrix has a significant impact on the gas production in the shale reservoirs.

5.7 CONCLUSIONS

In this chapter, based on the XFEM, fully hydromechanical-coupled model of hydraulic fracture propagation is presented. Its extension to reservoir simulation coupling with EDFM also has been developed. Due to the discontinuity caused by fractures, the XFEM is adopted to capture stress variation. Several conclusions can be drawn from the simulation results:

- When hydraulic fracture propagates in anisotropic formation, the propagation behavior is influenced by comprehensive factors including material angle, elastic modulus ratio, shear modulus, and initial principal stress difference. When material angle is larger than 0, the fracture will change its propagation direction and might divert to the material principal direction. As for rock heterogeneity, when elastic modulus obeys the Weibull

distribution, the strong heterogeneity of it could induce short and wide fracture.

- When non-Newton fluid is used as fracturing fluid, the larger the rheological index and consistency index, the shorter and wider the fracture. The rheological parameters of fracturing fluid not only have great impact on fracture geometrical parameters, but also could affect the settlement of proppant.
- Accounting for fluid pressure in the interaction between hydraulic fracture and natural fracture will make the crossing criterion curve move to the right side and make the arrest of hydraulic fracture by natural fracture easier. The greater the principal stress difference and approaching angle, the easier the hydraulic fracture propagates cross natural fracture.
- When multicluster fractures propagate simultaneously, fracture spacing has significant influence on their propagation path and geometry. Decreasing the fracture spacing will enhance the effect of stress shadowing and result in large differences between fractures. Strong stress anisotropy could lead to a small curvature of the propagation path and a large difference of fluid flow distribution between fractures.
- The EDFM and XFEM do not need the grids to be matching with the hydraulic fractures and can achieve high accuracy without requiring highly refined grids; thus the simple orthogonal grids can be directly used for the geometry discretization, and hydraulic fractures are discretized according to the geometry intersections of hydraulic fractures and orthogonal grids.

ACKNOWLEDGMENTS

The authors gratefully acknowledge support from the National Nature Science Foundation of China (Grant No. 51404292), the Fundamental Research Funds for the Central Universities (17CX06007), and the National Science and Technology Major Project (2016ZX05060-010).

REFERENCES

Adachi, J., Siebrits, E., Peirce, A., 2007. Computer simulation of hydraulic fractures. International Journal of Rock Mechanics & Mining Sciences 44 (5), 739−757.

Belytschko, T., Black, T., 1999. Elastic crack growth in finite elements with minimal remeshing. International Journal for Numerical Methods in Engineering 45 (5), 601−620.

Belytschko, T., Chen, H., Xu, J., Zi, G., 2003. Dynamic crack propagation based on loss of hyperbolicity and a new discontinuous enrichment. International Journal for Numerical Methods in Engineering 58 (12), 1873−1905.

Belytschko, T., Gracie, R., Ventura, G., 2009. A review of extended/generalized finite element methods for material modeling. Modelling and Simulation in Materials Science and Engineering 17 (4), 043001.

Biot, M.A., 1941. General theory of three-dimensional consolidation. Journal of Applied Physics 12 (2), 155−164.

Bruel, D., 1995. Heat extraction modelling from forced fluid flow through stimulated fractured rock masses: application to the Rosemanowes hot dry rock reservoir. Geothermics 24 (3), 361–374.

Chen, Z., 2012. Finite element modelling of viscosity-dominated hydraulic fractures. Journal of Petroleum Science and Engineering 88–89 (2), 136–144.

De Pater, C., Beugelsdijk, L., 2005. Experiments and numerical simulation of hydraulic fracturing in naturally fractured rock. In: Paper Presented at the Alaska Rocks 2005, the 40th US Symposium on Rock Mechanics (USRMS).

Dolbow, J., Moës, N., Belytschko, T., 2001. An extended finite element method for modeling crack growth with frictional contact. Computer Methods in Applied Mechanics and Engineering 190 (51), 6825–6846.

Fries, T.P., Belytschko, T., 2010. The extended/generalized finite element method: an overview of the method and its applications. International Journal for Numerical Methods in Engineering 84 (3), 253–304.

Fu, P., Johnson, S.M., Carrigan, C.R., 2013. An explicitly coupled hydro-geomechanical model for simulating hydraulic fracturing in arbitrary discrete fracture networks. International Journal for Numerical and Analytical Methods in Geomechanics 37 (14), 2278–2300.

George, E.K., 2010. Thirty years of gas shale fracturing: what have we learned?. In: Paper Presented at the SPE Annual Technical Conference and Exhibition. Italy, Florence.

Gong, B., Karimi-Fard, M., Durlofsky, L.J., 2008. Upscaling discrete fracture characterizations to dual-porosity, dual-permeability models for efficient simulation of flow with strong gravitational effects. SPE Journal 13 (1), 58.

Gordeliy, E., Peirce, A., 2013a. Coupling schemes for modeling hydraulic fracture propagation using the XFEM. Computer Methods in Applied Mechanics and Engineering 253, 305–322.

Gordeliy, E., Peirce, A., 2013b. Implicit level set schemes for modeling hydraulic fractures using the XFEM. Computer Methods in Applied Mechanics and Engineering 266, 125–143.

Gravouil, A., Moës, N., Belytschko, T., 2002. Non-planar 3D crack growth by the extended finite element and level sets—part II: level set update. International Journal for Numerical Methods in Engineering 53 (11), 2569–2586.

Gu, H., Weng, X., 2010. Criterion for fractures crossing frictional interfaces at non-orthogonal angles. In: Paper Presented at the 44th US Rock Mechanics Symposium and 5th US-Canada Rock Mechanics Symposium, Salt Lake City, UT.

Gupta, P., Duarte, C., 2016. Coupled formulation and algorithms for the simulation of non-planar three-dimensional hydraulic fractures using the generalized finite element method. International Journal for Numerical and Analytical Methods in Geomechanics 40 (10), 1402–1437.

Hu, L., Winterfeld, P.H., Fakcharoenphol, P., Wu, Y.S., 2013. A novel fully-coupled flow and geomechanics model in enhanced geothermal reservoirs. Journal of Petroleum Science and Engineering 107, 1–11.

Huang, Z.Q., Winterfeld, P.H., Xiong, Y., Wu, Y.S., Yao, J., 2015. Parallel simulation of fully-coupled thermal-hydro-mechanical processes in CO_2 leakage through fluid-driven fracture zones. International Journal of Greenhouse Gas Control 34, 39–51.

Karimi-Fard, M., Durlofsky, L., Aziz, K., 2004. An efficient discrete-fracture model applicable for general-purpose reservoir simulators. SPE Journal 9 (02), 227–236.

Khoei, A., Hirmand, M., Vahab, M., Bazargan, M., 2015. An enriched FEM technique for modeling hydraulically driven cohesive fracture propagation in impermeable media with frictional natural faults: numerical and experimental investigations. International Journal for Numerical Methods in Engineering 104 (6), 439–468.

Kim, J., Tchelepi, H.A., Juanes, R., 2011. Stability and convergence of sequential methods for coupled flow and geomechanics: fixed-stress and fixed-strain splits. Computer Methods in Applied Mechanics and Engineering 200 (13), 1591–1606.

Kim, J., Sonnenthal, E.L., Rutqvist, J., 2012. Formulation and sequential numerical algorithms of coupled fluid/heat flow and geomechanics for multiple porosity materials. International Journal for Numerical Methods in Engineering 92 (5), 425–456.

Lecampion, B., 2009. An extended finite element method for hydraulic fracture problems. Communications in Numerical Methods in Engineering 25 (2), 121–133.

Lekhnitskii, S., 1963. Of an Anisotropic Elastic Body, vol. 525. Holden-Day, San Francisco.

Leverett, M., 1941. Capillary behavior in porous solids. Transactions of the AIME 142 (01), 152–169.

Li, F.Z., Shih, C.F., Needleman, A., 1985. A comparison of methods for calculating energy release rates. Engineering Fracture Mechanics 21 (2), 405–421.

Linkov, A.M., 2014. Universal asymptotic umbrella for hydraulic fracture modeling. arXiv:1404.4165.

Liu, J., Chen, Z., Elsworth, D., Qu, H., Chen, D., 2011. Interactions of multiple processes during CBM extraction: a critical review. International Journal of Coal Geology 87 (3–4), 175–189.

Liu, F., Gordon, P., Meier, H., Valiveti, D., 2016. A stabilized extended finite element framework for hydraulic fracturing simulations. International Journal for Numerical and Analytical Methods in Geomechanics. https://doi.org/10.1002/nag.2565.

Melenk, J.M., Babuska, I., 1996. The partition of unity finite element method: basic theory and applications. Computer Methods in Applied Mechanics and Engineering 139 (1), 289–314.

Mergheim, J., Kuhl, E., Steinmann, P., 2005. A finite element method for the computational modelling of cohesive cracks. International Journal for Numerical Methods in Engineering 63 (2), 276–289.

Meyer, B., Bazan, L., 2011. A discrete fracture network model for hydraulically induced fractures-theory, parametric and case studies. In: Paper Presented at the SPE Hydraulic Fracturing Technology Conference.

Moes, N., Dolbow, J., Belytschko, T., 1999. A finite element method for crack growth without remeshing. International Journal for Numerical Methods in Engineering 46 (4), 131–150.

Moes, N., Gravouil, A., Belytschko, T., 2002. Non-planar 3D crack growth by the extended finite element and level sets – Part I: mechanical model. International Journal for Numerical Methods in Engineering 53 (11), 2549–2568. https://doi.org/10.1002/nme.429.

Mohammadnejad, T., Khoei, A., 2013a. An extended finite element method for hydraulic fracture propagation in deformable porous media with the cohesive crack model. Finite Elements in Analysis and Design 73, 77–95.

Mohammadnejad, T., Khoei, A., 2013b. Hydro-mechanical modeling of cohesive crack propagation in multiphase porous media using the extended finite element method. International Journal for Numerical and Analytical Methods in Geomechanics 37 (10), 1247–1279.

Moinfar, A., Varavei, A., Sepehrnoori, K., Johns Russell, T., 2012. Development of a Novel and Computationally-Efficient Discrete-Fracture Model to Study IOR Processes in Naturally Fractured Reservoirs. Society of Petroleum Engineers.

Moran, B., Shih, C., 1987. Crack tip and associated domain integrals from momentum and energy balance. Engineering Fracture Mechanics 27 (6), 615–642.

Morgan, W.E., Aral, M.M., 2014. An implicitly coupled hydro-geomechanical model for hydraulic fracture simulation with the discontinuous deformation analysis. International Journal of Rock Mechanics & Mining Sciences 73, 82–94.

Multiphysics, COMSOL, 2015. v. 5.2. COMSOL AB, Stockholm, Sweden.

Pruess, K., 1985. A practical method for modeling fluid and heat flow in fractured porous media. Society of Petroleum Engineers Journal 25 (01), 14–26.

Ren, Q., Dong, Y., Yu, T., 2009. Numerical modeling of concrete hydraulic fracturing with extended finite element method. Science in China Series E: Technological Sciences 52 (3), 559–565.

Ren, G., Jiang, J., Younis, R.M., 2016. Fully Coupled Geomechanics and Reservoir Simulation for Naturally and Hydraulically Fractured Reservoirs. American Rock Mechanics Association.

Renshaw, C.E., Pollard, D.D., 1995. An experimentally verified criterion for propagation across unbounded frictional interfaces in brittle, linear elastic materials. International Journal of Rock Mechanics Mining Sciences & Geomechanics 32 (3), 237–249.

Rice, J.R., 1967. A path independent integral and the approximate analysis of strain concentration by notches and cracks. Journal of Applied Mechanics 35 (2), 379–386.

Saouma, V.E., Ayari, M.L., Leavell, D.A., 1987. Mixed mode crack propagation in homogeneous anisotropic solids. Engineering Fracture Mechanics 27 (2), 171–184.

Spence, D., Sharp, P., 1985. Self-similar solutions for elastohydrodynamic cavity flow. Proceedings of the Royal Society of London A: Mathematical, Physical and Engineering Sciences 400 (1819), 289–313.

Stolarska, M., Chopp, D., Moës, N., Belytschko, T., 2001. Modelling crack growth by level sets in the extended finite element method. International Journal for Numerical Methods in Engineering 51 (8), 943–960.

Sukumar, N., Moës, N., Moran, B., Belytschko, T., 2000. Extended finite element method for three-dimensional crack modelling. International Journal for Numerical Methods in Engineering 48 (11), 1549–1570.

Taleghani, A.D., 2009. Analysis of Hydraulic Fracture Propagation in Fractured Reservoirs: An Improved Model for the Interaction Between Induced and Natural Fractures (Ph.D.). The University of Texas, Austin.

Taleghani, A.D., 2011. Modeling simultaneous growth of multi-branch hydraulic fractures: accounting for the interaction between induced and natural fractures. In: Paper Presented at the 45th US Rock Mechanics/Geomechanics Symposium.

Weng, X., 2015. Modeling of complex hydraulic fractures in naturally fractured formation. Journal of Unconventional Oil & Gas Resources 9, 114–135.

Weng, X., Kresse, O., Cohen, C., 2011. Modeling of hydraulic-fracture-network propagation in a naturally fractured formation. SPE Production & Operations 26 (4), 368–380.

Wengyue, X., Ganguly, U., Xiaowei, W., June 8–10, 2010. Wiremesh: a novel shale fracturing simulator. In: Paper Presented at the CPS/SPE International Oil & Gas Conference and Exhibition, Beijing, China.

Winterfeld, P.H., Wu, Y.-S., 2016. Simulation of coupled thermal/hydrological/mechanical phenomena in porous media. SPE Journal 21 (03), 1041–1049.

Witherspoon, P.A., Wang, J.S.Y., Iwai, K., Gale, J.E., 1980. Validity of Cubic Law for fluid flow in a deformable rock fracture. Water Resources Research 16 (6), 1016–1024.

Wu, Y.S., 2015. Multiphase Fluid Flow in Porous and Fractured Reservoirs. Gulf Professional Publishing.

Wu, K., Olson, J.E., 2015. Simultaneous multifracture treatments: fully coupled fluid flow and fracture mechanics for horizontal wells. SPE Journal 20 (2), 337–346.

Yan, X., Huang, Z., Yao, J., Li, Y., Fan, D., 2016. An efficient embedded discrete fracture model based on mimetic finite difference method. Journal of Petroleum Science and Engineering 145, 11–21.

Zeng, Q., Yao, J., 2016. Numerical simulation of fracture network generation in naturally fractured reservoirs. Journal of Natural Gas Science and Engineering 30, 430−443.

Zi, G., Belytschko, T., 2003. New crack-tip elements for XFEM and applications to cohesive cracks. International Journal for Numerical Methods in Engineering 57 (15), 2221−2240.

Chapter 6

Fully Coupled 3-D Hydraulic Fracture Models—Development and Validation

Kevin H. Searles, Matias G. Zielonka, Jorge L. Garzon
ExxonMobil Upstream Research Company, Spring, TX, United States

6.1 INTRODUCTION

The problem of fluid-driven (hydraulic) fractures propagating in a permeable poroelastic medium has widespread application within the oil and gas industry. For example, the intended nucleation and propagation of hydraulic fractures may be desired to enhance rock formation permeability and productivity of wells producing from unconventional reservoirs (e.g., shale gas, tight oil). Similarly, the intended growth of hydraulic fractures may serve to improve the injectivity of water disposal wells or wells used for storage and containment of rock cuttings while drilling. The nucleation and propagation of hydraulic fractures may also be unintended, as in the case of drilling fluids lost to the formation while circulating returns. Whether the growth of hydraulic fractures is intentional or not, it is often desired (and perhaps required) to know the extent of fracture growth. In the case of enhancing well productivity from unconventional reservoirs, knowledge of fracture geometry is required to accurately predict inflow performance. For the case of disposal of rock cuttings while drilling, knowledge of fracture geometry is an important requirement for seeking permit approvals. To maintain a stable borehole and avoid collapse while drilling, it is required to understand the margin between the in situ gradients of pore fluid pressure and fracture nucleation.

Measurement of the actual hydraulic fracture geometry associated with any of the aforementioned processes is neither practical nor possible in most cases. Resorting to an analytical approach for a direct solution to fracture geometry presents its own set of challenges as a boundary value problem. Even though the physics governing fracture growth is coupled and described by a set of

Hydraulic Fracture Modeling. https://doi.org/10.1016/B978-0-12-812998-2.00006-0

differential equations, constructing and solving them is unwieldy without making some simplifying assumptions. If too many assumptions are made to render a solution more tractable, it may no longer represent the underlying physical processes. By considering an alternative treatment such as the finite element method, we can better approximate the real problem.

In the first part of this chapter, we discuss the physical processes associated with hydraulic fracturing that are highly coupled in nature. We then go into detail and review the system of unknowns, governing equations, and constitutive relation that describe the coupled interactions. The governing equations and constitutive relation are underpinned by the theory of linear poroelasticity and include continuity and momentum for fluid in the fracture and fluid in the permeable porous medium comprising the fracture.

Next, the methodology for modeling the coupled mechanical and flow behaviors through pores and fractures is described at length. After describing the mechanical and flow behavior modeling, we introduce the framework for implementation based on the use of cohesive elements and the extended finite element method (XFEM). This is followed by verification of certain limiting cases of the numerical results against referenced analytical benchmarks. The analytical benchmarks are asymptotic expansions to limiting propagation regimes for semiinfinite cracks propagating in elastic media (Bunger et al., 2005; Detournay et al., 2006; Garagash, 2006; Garagash et al., 2011; Hu and Garagash, 2010; Peirce and Detournay, 2008; Savitski and Detournay, 2002). The expansions are considered on a basis of the competing dissipative processes, viz., solid toughness, fracture fluid viscosity, and the competing fluid balance components, viz., fracture fluid storage, leak-off.

Finally, it is demonstrated that the numerical treatment has been made tractable for solving example problems having greater time and length scales, e.g., laboratory and field scales. The problems presented in support of this include (1) a model constructed to replicate conditions of a laboratory-scale fluid injection experiment and (2) a model constructed to replicate conditions of a field-scale fluid injection test considering a representative geologic scenario.

6.2 NUMERICAL FORMULATION

Development of modeling capabilities in 3-D to simulate the nucleation and propagation of hydraulic fractures is an arduous task. The difficulty arises primarily from the strongly nonlinear coupling between multiple physical processes that govern fracture growth. These processes include nucleation and propagation, the flow of fluid in the fracture, the exchange of fluid between the fracture and adjoining porous medium, and mechanical deformation of the porous medium. The task of simulating the nucleation and propagation of hydraulic fractures is further complicated by considering the porous medium as a layered, heterogeneous geologic system of varying properties that is

subjected to oriented in situ confining stresses of nonuniform magnitudes. Moreover, the flow of fluid in the fracture may often exhibit nonlinear rheological behavior with history-dependent fluid exchange between the fracture and adjoining porous medium.

Numerous approaches have been followed to develop numerical modeling capabilities for simulating the nucleation and propagation of hydraulic fractures (Carrier and Granet, 2012; Detournay et al., 2006; Garagash, 2006; Ortiz and Pandolfi, 1999; Peirce and Detournay, 2008). Many of these approaches are rooted in academic research codes that are not practical for representing actual subsurface conditions and often lack the computational capabilities (e.g., massively parallel) required for solving large 3-D domains representing realistic field-scale problems (Abbas et al., 2014; Dahi-Taleghani and Olson, 2011).

There are also a number of computationally inexpensive hydraulic fracturing simulators that are commercially available and are designed to provide fast-running solutions to fracture geometry, fluid flow, and net treating pressure (Cleary, 1980; Meyer, 1989; Warpinski et al., 1994). These commercially available hydraulic fracturing simulators are based on certain simplifying assumptions: (1) fracture geometry can be described with few geometric parameters; (2) fracture geometry is planar and symmetric with respect to the borehole; (3) fracture propagation is in accordance with linear elastic fracture mechanics without consideration of poroelastic effects; (4) loss of fluid from the fracture to the adjacent porous medium is one-dimensional and decoupled from deformation of the porous medium; and (5) the porous medium is unbounded and linear elastic resulting in an integral equation for fracture opening and pressure. The utility of these simulators lies in their ability to rapidly predict broad trends in fracture geometry with varying input parameters and in predicting upper and lower bounds of operating parameters. The accuracy of the predictions is restricted to situations in which the nonlinear coupling between multiple physical processes can be neglected.

Accurate 3-D modeling capabilities to simulate the nucleation and propagation of hydraulic fractures while considering realistic representations of geology, stress state, well configuration, and surface operating conditions demand a more advanced multiphysics numerical simulator. Toward this end, we consider the development of such capabilities based on the general-purpose, nonlinear finite element software application Abaqus/Standard (Abaqus® 2017). These newly developed capabilities build on the existing implicit solution procedure in Abaqus/Standard for nonlinear soils consolidation while leveraging cohesive elements and XFEM to model propagating discontinuities.

In this work, two new element classes have been introduced into the soils consolidation procedure for solving the diffusion of fluid in porous media coupled with deformation of the porous matrix. First, pressure-deformation cohesive elements are introduced for modeling the loss of normal

mechanical strength (fracture opening) due to damage coupled with increasing flow of fluid through the fracture and fluid leak-off. Second, enriched versions of the pressure-deformation continuum elements are introduced for activating arbitrarily oriented discontinuities in both displacements and pore fluid pressure while simultaneously modeling the flow of fluid through the fracture and fluid leak-off.

As previously stated, the coupled physical processes governing the growth of a hydraulic fracture include nucleation and propagation, fluid flow in the fracture, the exchange of fluid between the fracture and adjoining porous medium, and mechanical deformation of the porous medium. The governing equations for each of the coupled processes, as well as the kinetic and constitutive relations adopted for the fracture fluid, pore fluid, and porous medium, include the following (Zielonka et al., 2014a):

- Equilibrium equation for the porous medium
- Constitutive equation for the porous medium (Biot's theory of poroelasticity)
- Continuity equation for the pore fluid
- Momentum equation for the pore fluid (Darcy's law)
- Continuity equation for the fracture fluid
- Momentum equation for the fracture fluid (Reynold's lubrication equation)

The governing equations and constitutive relations, i.e., Biot's theory of poroelasticity for porous media, Darcy's law for pore fluid flow, Reynold's lubrication theory for fracture fluid flow, and cohesive zone concepts to describe fracture nucleation and propagation (Abaqus®, 2017; Charlez, 1997), are summarized in what follows.

6.2.1 Fluid Flow in the Porous Medium

The mechanical behavior of the porous medium can be represented on the basis of an isotropic, poroelastic material undergoing quasi-static deformation. The equilibrium equation that is enforced in the absence of body forces is stated as

$$\sigma_{ij,j} = 0 \tag{6.1}$$

while the poroelastic constitutive relation for small strains is given by

$$\sigma_{ij} - \sigma_{ij}^{0} = 2G\varepsilon_{ij} + \left(K - \frac{2}{3}G\right)\varepsilon_{kk}\delta_{ij} - \alpha(p - p_0)\delta_{ij} \tag{6.2}$$

where the relationships for the dry elastic shear and bulk moduli are

$$2G = \frac{E}{1+\nu}, \quad 3K = \frac{E}{1-2\nu} \tag{6.3}$$

and in which α is the Biot's coefficient; E is the dry Young's modulus; and ν is the dry Poisson's ratio. By defining the Terzaghi effective stresses σ' for fully saturated porous media as (Abaqus®, 2017; Charlez, 1997)

$$\sigma'_{ij} = \sigma_{ij} + p\delta_{ij} \tag{6.4}$$

the constitutive relation then takes the following form:

$$\sigma'_{ij} - \sigma'^{0}_{ij} = 2G\varepsilon_{ij} + \left(K - \frac{2}{3}G\right)\varepsilon_{kk}\delta_{ij} - (\alpha - 1)(p - p_0)\delta_{ij} \tag{6.5}$$

Furthermore, when the effective strains ε'_{ij} are written as

$$\varepsilon'_{ij} = \varepsilon_{ij} - \frac{\alpha - 1}{3K}(p - p_0)\delta_{ij} \tag{6.6}$$

then the constitutive relation becomes

$$\sigma'_{ij} - \sigma'^{0}_{ij} = 2G\varepsilon'_{ij} + \left(K - \frac{2}{3}G\right)\varepsilon'_{kk}\delta_{ij} \tag{6.7}$$

We notice that the above identity Eq. (6.7) is the same constitutive relation as that for linear elastic materials with elastic stresses and strains expressed in terms of Terzaghi effective stresses $\sigma\prime$ and effective strains $\varepsilon\prime$. In Abaqus/Standard, the above equivalence is adopted for translating total stresses and strains into Terzaghi effective stresses and effective strains.

If it is assumed that the volumetric strains are sufficiently small, i.e., infinitesimal, the continuity equation for the pore fluid can be stated as

$$\frac{1}{M}\dot{p} + \alpha\dot{\varepsilon}_{kk} + v_{k,k} = 0 \tag{6.8}$$

where the seepage velocity of the pore fluid is $v_{k,k}$, and the Biot modulus is M. The relationships between the Biot modulus M and Biot coefficient α, and the dry elastic bulk modulus K are

$$\frac{1}{M} = \frac{\phi_0}{K_f} + \frac{\alpha - \phi_0}{K_s}, \quad \frac{1}{K_s} = \frac{1 - \alpha}{K} \tag{6.9}$$

In Eq. (6.9), the quantities K_s and K_f are the bulk moduli for the solid grains and fluid, and ϕ_0 is the initial porosity of the porous medium. The flow of pore fluid through the interconnected network of pores is assumed to be governed by Darcy's law and is expressed by the relationship:

$$v_i = -\frac{k}{\mu}p_{,i} = -\frac{\overline{k}}{\gamma}p_{,i} \tag{6.10}$$

in which the permeability is k; the hydraulic conductivity is $\overline{k}$; the viscosity of the pore fluid is μ, and the specific weight of the pore fluid is γ. On combining Eq. (6.10) with the continuity equation Eq. (6.8), the diffusion equation for the pore fluid becomes

$$\frac{1}{M}\dot{p} + \alpha\dot{\varepsilon}_{kk} = \frac{\overline{k}}{\gamma}p_{kk} \tag{6.11}$$

6.2.2 Fracture Nucleation and Propagation

The process of fracture nucleation and propagation can be abstracted as a progressive transition between the fully intact state and the fully damaged state of a material. The intact state is characterized by continuity of displacements and nonzero tractions in all material directions. The fully damaged state is characterized by a displacement discontinuity along a material interface with no tractions normal to the interface. In this work, the transition is modeled by a cohesive material law as a loss of material strength due to progressive damage along a zero- or finite-thickness interface. The orientation of this interface for cohesive elements is defined a priori while it is solution-dependent for the XFEM implementation. The cohesive material law representing the gradual loss of material strength due to increasing separation is described by a traction–separation relation (Abaqus®, 2017; Ortiz and Pandolfi, 1999).

The traction–separation cohesive law employed in the XFEM implementation assumes a linear softening relationship, which is defined by the cohesive energy G_c (area under the softening portion of the traction–separation curve) and cohesive strength T_0 of the material. For the implementation based on cohesive elements, it is further assumed that the traction–separation behavior before crack nucleation and the onset of damage is linear with an initial stiffness of K_0. As illustrated by Fig. 6.1, the cohesive traction T evolves linearly during softening from the intact strength T_0 at nucleation to zero (fully damaged) at a total separation of g_1.

If unloading occurs along the cohesive interface before separation, the traction T_p is assumed to linearly ramp down according to K_p (damaged stiffness):

$$T = K_p g, \quad 0 \leq g \leq g_p \tag{6.12}$$

Before the onset of interface damage and crack nucleation, fluid is permitted to flow through the interface according to Darcy's law. At the onset of crack nucleation ($T = T_0$), the flow through the damaged interface (fracture) begins to transition from Darcy flow to flow through a crack (Poiseuille flow) at a fluid pressure p_f. Therefore, for the fluid pressure p_f, the total tractions acting on (and resisted by) the interface are

$$T = K_p g - (1 - D)\alpha_0 p_f - D p_f, \quad g_0 \leq g \leq g_1 \tag{6.13}$$

where α_0 is the Biot coefficient of the undamaged material, and the variable D is a scalar measure of damage. More details on the aforementioned flow transitioning are recounted in the next section.

6.2.3 Fluid Flow in the Fracture

Realistic simulation of the fluid-driven fracturing process requires modeling the flow of multiple fluid behaviors including Newtonian and complex non-Newtonian fluids. For fluids that are temperature-sensitive, the modeling of heat transfer is also required. The basis for modeling the flow of fluids in

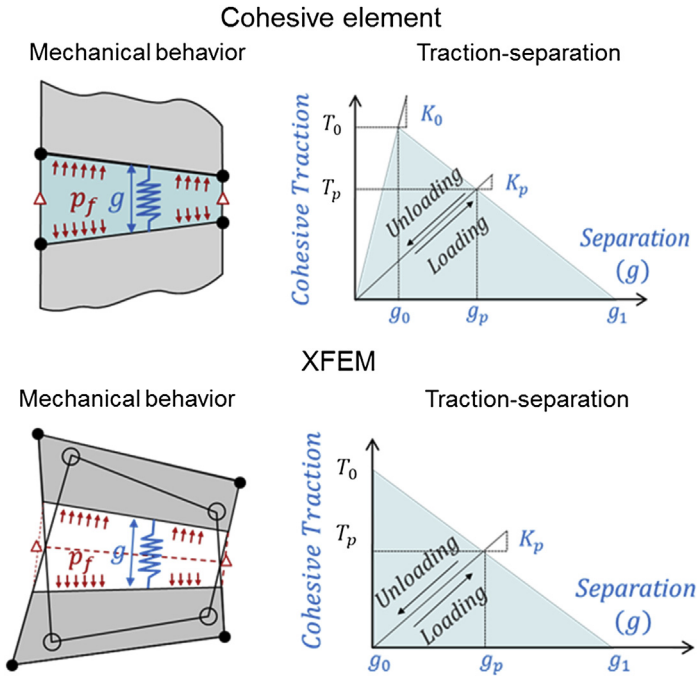

FIGURE 6.1 Linear cohesive traction−separation law for cohesive element and extended finite element method implementations. *Modified from Zielonka, M.G., Searles, K.H., Ning, J., Buechler, S.R., 2014a. Development and validation of fully coupled hydraulic fracturing simulation capabilities. In: 2014 SIMULIA Community Conference, 19−22 May, Providence, Rhode Island, USA, pp. 1−31.*

fully damaged cohesive elements or XFEM-enriched continuum elements is that of plane Poiseuille flow. Referring to Fig. 6.2, the solution method is centered on the application of tangential flow continuity for an incompressible fluid, including fluid infiltration through the top and bottom fracture faces.

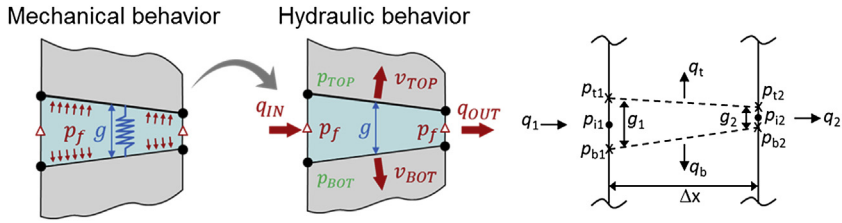

FIGURE 6.2 Configuration for modeling the Poiseuille flow of viscous fluids in damaged cohesive or extended finite element method−enriched continuum elements.

Based on analysis of a control volume, the incremental form of the continuity equation for tangential flow can be defined as (Boone and Ingraffea, 1990)

$$-q_1 g_1 + q_2 g_2 + \left(\frac{g^{t+1} - g^t}{\Delta t}\right)\Delta x + (q_t + q_b)\Delta x = 0 \tag{6.14}$$

where q_1, q_2 are the tangential flows entering and exiting the crack inlet and outlet, respectively, over some distance Δx; g_1, g_2 are the incremental relative crack openings; and q_t, q_b are the fluid losses exiting normal to the top and bottom fracture surfaces (accounting for filter cake resistance). The equivalent weak form of the previous Eq. (6.14) becomes

$$\int_L \left[\frac{\partial(qg)}{\partial x} + \left(\frac{g^{t+1} - g^t}{\Delta t}\right) + q_t + q_b\right]\delta p_i w dx = 0 \tag{6.15}$$

In Eq. (6.15), w is the element thickness; the product $q \cdot g$ represents the flow of incompressible fluid (per unit width) between parallel plates, i.e., plane Poiseuille flow; δp_i is the fluid pressure at the fracture midplane; g is the fracture opening; dx is an infinitesimal length along the fracture, and L is the fracture length. The fluid loss normal to the top (q_t) and bottom (q_b) fracture surfaces can be expressed as

$$\begin{cases} q_t = C_t(p_i - p_t) \\ q_b = C_b(p_i - p_b) \end{cases} \tag{6.16}$$

where $p_{t/b}$ are the pore pressures at the top and bottom fracture surfaces in the adjacent host formation, and $C_{t/b}$ are the coefficients of filter cake resistance (fouling) for the top and bottom fracture surfaces, respectively. On rewriting Eq. (6.15) and applying the divergence theorem to the first term:

$$(Q\delta p^*)|_{x=0}^{x=L} - \int_L Q\frac{d\delta p^*}{dx}dx + \int_L \frac{dg}{dx}\delta p^* dx + \int_L (q_t + q_b)\delta p^* dx = 0 \tag{6.17}$$

where Q is the tangential flow rate and δp^* is the virtual fluid pressure inside the fracture.

In fully developed, laminar flow of non-Newtonian fluids having a yield stress dependence (e.g., Herschel−Bulkley), the momentum equation relating tangential flow rate and pressure drop for Poiseuille flow can be given as (Cherny and Lapin, 2016)

$$Q = \left(\frac{g^2}{2\left(\frac{1}{\alpha}+2\right)\left(\frac{1}{\alpha}+1\right)}\right)\left(\frac{(g)(-\partial P/\partial x)}{2K}\right)^{\frac{1}{\alpha}}\left(1 - \frac{2\tau_0}{(g)(-\partial P/\partial x)}\right)^{\frac{1}{\alpha}+1}$$
$$\left(\frac{1}{\alpha} + 1 + \frac{2\tau_0}{(g)(-\partial P/\partial x)}\right) \tag{6.18}$$

For Eq. (6.18), K is the flow consistency index; α is the flow behavior index, and τ_0 is the yield stress for generalized non-Newtonian fluids. In deriving this equation, the limits of integration are taken from $-g/2$ to $g/2$ assuming that $g = 0$ is the midplane. By recognizing that the momentum equation for fluids having other non-Newtonian viscosity characteristics is a special case of the Herschel–Bulkley type, it follows

$$\mathrm{Q} = \left(\frac{g^2}{12}\right)\left(\frac{(g)(-\partial \mathrm{P}/\partial \mathrm{x})}{2\mu_0}\right)\left(1 - \frac{2\tau_0}{(g)(-\partial \mathrm{P}/\partial \mathrm{x})}\right)^2\left(2 + \frac{2\tau_0}{(g)(-\partial \mathrm{P}/\partial \mathrm{x})}\right) \tag{6.19}$$

for a Bingham plastic fluid in which $\alpha = 1$ and $\mathrm{K} = \mu_0$ the Bingham viscosity;

$$\mathrm{Q} = \left(\frac{g^2}{2\left(\frac{1}{\alpha} + 2\right)}\right)\left(\frac{(g)(-\partial \mathrm{P}/\partial \mathrm{x})}{2\mathrm{K}}\right)^{\frac{1}{\alpha}} \tag{6.20}$$

for an Ostwald–de Waele (power-law) fluid in which $\tau_0 = 0$ and;

$$\mathrm{Q} = \left(\frac{g^2}{6}\right)\left(\frac{(g)(-\partial \mathrm{P}/\partial \mathrm{x})}{2\mu}\right) \tag{6.21}$$

for a Newtonian fluid in which $\alpha = 1$ and $\mathrm{K} = \mu$ the Newtonian viscosity.

As mentioned previously, the fracture fluid flow is based on Poiseuille flow, i.e., steady, incompressible laminar flow between parallel plates. Fluid loss normal to the fracture surfaces (leak-off) reflects resistance due to the deposition of filter cake and associated fouling effects. For undamaged cohesive or enriched continuum elements, the fluid is permitted to flow according to Darcy's law. In this work, a flow transition scheme is adopted whereby the changing nature of flow through an initially undamaged porous medium (Darcy flow) to flow in a fracture (Poiseuille) is approximated, as the medium is progressively damaged.

The general specification for transitioning from Darcy to Poiseuille flow can be expressed in the following manner, using a Newtonian fluid to illustrate the method:

$$\mathrm{Q} = -w\left[\left(1 - \mathrm{D}\widehat{\mathrm{F}}\left(\widehat{g}\right)\right)\frac{\mathrm{k}}{\mu_\mathrm{f}}g_{\mathrm{init}} + \mathrm{D}\widehat{\mathrm{F}}\left(\widehat{g}\right)\frac{\widehat{g}^3}{12\mu_\mathrm{f}}\right](\nabla \mathrm{P} - \rho_\mathrm{f} g) \tag{6.22}$$

In Eq. (6.22), w is the element thickness; the variable D is the scalar measure of damage; μ_f is the Newtonian viscosity of the fracture fluid; ρ_f is the density of the fracture fluid; k is the intrinsic Darcy permeability of the porous medium; $\nabla \mathrm{P}$ is the pressure gradient; g is the acceleration due to gravity; g_{init} is an initial gap to prevent numerical issues associated with a "no flow"

condition; $\widehat{g}$ is the difference between current and initial element geometric thickness; and $\widehat{\mathrm{F}}\left(\widehat{g}\right)$ is a conditional state function given as

$$\widehat{\mathrm{F}}\left(\widehat{g}\right) = \begin{cases} 0 & \widehat{g} < 0 \\ \dfrac{\widehat{g}}{g_{\mathrm{init}}} & 0 < \widehat{g} < g_{\mathrm{init}} \\ 1 & g_{\mathrm{init}} < \widehat{g} \end{cases} \tag{6.23}$$

As specified by the conditions for the $\widehat{\mathrm{F}}\left(\widehat{g}\right)$ function, the transition method is reversible and supports transitioning from Poiseuille flow back to Darcy flow if a damaged element closes.

For the foregoing transition method, the expressions given by Eqs. (6.22) and (6.23) are based on the flow of a Newtonian fluid. When considering a non-Newtonian fluid, the same expressions can be adopted, provided the correct permeability and fluid viscosity are used. For example, if we consider a non-Newtonian fluid having viscosity characteristics of the Herschel−Bulkley type, then the viscosity μ_{f} should be replaced by the appropriate apparent viscosity μ_{app}:

$$\frac{\tau}{\dot{\gamma}} = \mu_{\mathrm{app}} = \frac{\tau_0}{\dot{\gamma}} + \mathrm{K}\dot{\gamma}^{\alpha-1} \tag{6.24}$$

where the magnitude of shear rate $\dot{\gamma} = \sqrt{2tr\mathrm{D}^2}$ is defined with respect to the rate of deformation matrix $[\mathrm{D_{ik}}] = {}^1\!/_2\ (\mathrm{V_{i,k}} + \mathrm{V_{k,i}})$ and given in the form

$$\dot{\gamma} = \sqrt{2\mathrm{D_{ik}}\mathrm{D_{ik}}} = \sqrt{\left(\frac{\partial \mathrm{V_x}}{\partial \mathrm{z}}\right)^2 + \left(\frac{\partial \mathrm{V_y}}{\partial \mathrm{z}}\right)^2} \tag{6.25}$$

In Eq. (6.25), the fluid velocities $\mathrm{V_x}$ and $\mathrm{V_y}$ are in reference to the x-y plane of the fracture (refer to Fig. 6.3). It is assumed that flow is symmetric about the z-axis with no slippage at $\mathrm{z} = -g/2$ and $\mathrm{z} = +g/2$.

The permeability found in Eq. (6.22) should also be the appropriate measure for the flow of a non-Newtonian fluid in a porous medium. One of the more suitable methods for defining this measure is to assume that the porous medium is an assembly of flow channels or bundle of capillary tubes. The details of such a method are not elaborated here; we instead refer the interested reader to the works of others such as Al-Fariss and Pinder (1987).

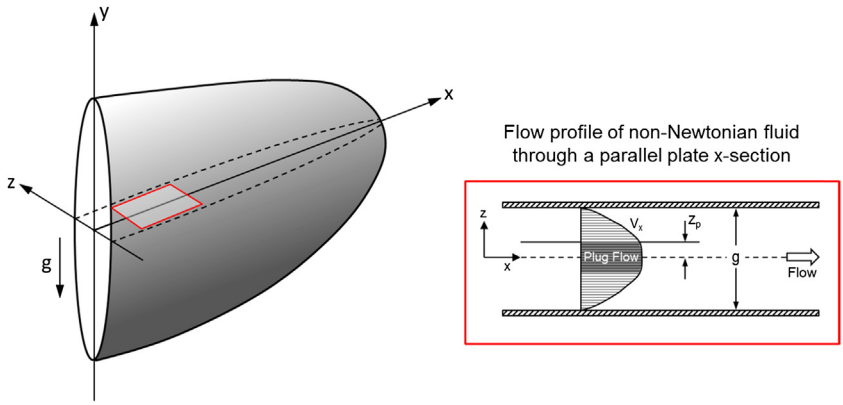

FIGURE 6.3 Illustration of the 2-D flow domain for viscous fluids in a vertically oriented hydraulic fracture.

6.3 IMPLEMENTATION SCHEME

The basis for modeling fluid-driven, hydraulic fractures propagating in a permeable poroelastic medium is a 3-D finite element formulation. The fully coupled formulation for hydraulic fracture growth is implemented in a finite element solver (Abaqus®, 2017) using both cohesive elements and the XFEM.

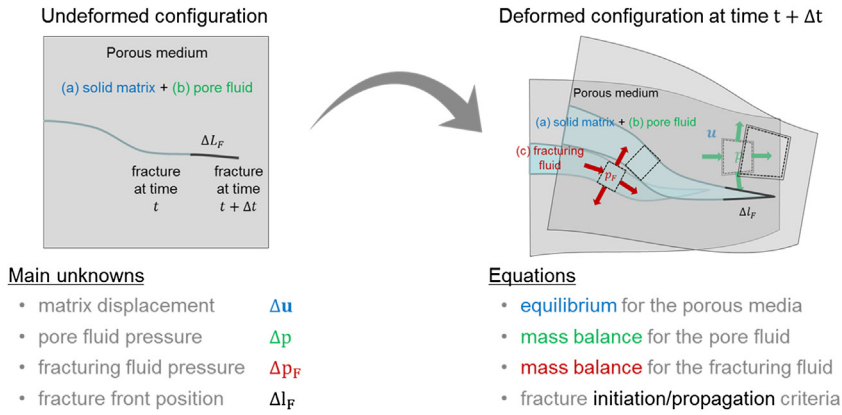

FIGURE 6.4 Graphical illustration of the main unknowns and system of equations for solving the hydraulic fracture problem. *Modified from Zielonka, M.G., Searles, K.H., Ning, J., Buechler, S.R., Du, Z., Xia, L., Wohlever, C., 2014b. An extended finite element method for hydraulic fracturing of fully saturated porous media. In: Eleventh World Congress on Computational Mechanics (WCCM XI), 20–25 July, Barcelona, Spain, pp. 1–32.*

The solution to the problem is fully implicit where the system of equations for equilibrium, pore fluid mass balance, and fracture fluid mass balance are solved in a simultaneous fashion. The main unknowns are the deformation of the porous medium (matrix), the pore fluid pressure, the fracture fluid pressure, and the position of the fracture front. The unknowns and system of equations are further illustrated graphically in Fig. 6.4.

For a representative vertical hydraulic fracture as illustrated in Fig. 6.3, the dimensions in the x-y plane are orders of magnitude greater compared with the fracture opening (z direction). Owing to a much smaller opening (width) dimension, pressure variations across the fracture width are assumed to be negligible. The derivatives of the flow velocities in the x-y plane are also assumed to be larger in comparison with the other derivatives. Therefore, according to Clifton and Wang (1988), Clifton (1989), Ouyang (1994), and Yew (1997), the fracture fluid continuity equation can be expressed by

$$\frac{\partial}{\partial t}(\rho_f g) + \frac{\partial(\rho_f V_x g)}{\partial x} + \frac{\partial(\rho_f V_y g)}{\partial y} = -(q_t + q_b)\rho_f \tag{6.26}$$

or alternatively, in a slightly more compact notation:

$$\frac{\partial}{\partial t}(\rho_f g) + \nabla\cdot(\mathbf{V} g \rho_f) = -q_l \rho_f \tag{6.27}$$

where ρ_f is the mean density of the fracture fluid and q_l is the combined fluid loss from the top and bottom fracture surfaces.

By way of the aforementioned considerations, and ignoring inertia and accelerations, it can be shown that the momentum balance governing fluid motion in the fracture is written as

$$-\frac{\partial P}{\partial x} = \frac{\partial}{\partial z}\left(\mu_{app}\frac{\partial V_x}{\partial z}\right) = \frac{\partial}{\partial z}\left(\frac{\partial \tau_{zx}}{\partial z}\right), \quad -\frac{\partial P}{\partial y} - \rho_f g = \frac{\partial}{\partial z}\left(\mu_{app}\frac{\partial V_y}{\partial z}\right) = \frac{\partial}{\partial z}\left(\frac{\partial \tau_{zy}}{\partial z}\right) \tag{6.28}$$

The momentum balance can be further generalized by equating the L.H.S. of the above equations to an external force vector or modified pressure gradient. Adopting the notation of Lakhtychkin et al. (2012), the applied external force vector or modified pressure gradient $\mathscr{G}$ is written as

$$\mathscr{G} = \overrightarrow{\left(-\frac{\partial P}{\partial x}, -\frac{\partial P}{\partial y} - \rho_f g\right)} \tag{6.29}$$

where the term $\mathscr{G} = \partial\tau_{z\xi}/\partial z$ is a component of $\mathscr{G}$ oriented collinearly to the local normal of the fracture front. This leads to the following definitions for the fluid velocity $V_\xi(z)$:

$$V_\xi = \left(\frac{\mathscr{G}}{K}\right)^{\frac{1}{\alpha}}\left(\frac{1}{\frac{1}{\alpha}+1}\right)\left(\frac{g}{2}\right)^{\frac{1}{\alpha}+1}\left[\left(1-\frac{2\tau_0}{(g)(\mathscr{G})}\right)^{\frac{1}{\alpha}+1}-\left(2\left(\frac{z}{g}\right)-1-\frac{2\tau_0}{(g)(\mathscr{G})}\right)^{\frac{1}{\alpha}+1}\right],$$

$$\left(\frac{g}{2}\right)\left(1+\frac{2\tau_0}{(g)(\mathscr{G})}\right) \le z \le g$$

$$V_\xi = \left(\frac{\mathscr{G}}{K}\right)^{\frac{1}{\alpha}}\left(\frac{1}{\frac{1}{\alpha}+1}\right)\left(\frac{g}{2}\right)^{\frac{1}{\alpha}+1}\left[\left(1-\frac{2\tau_0}{(g)(\mathscr{G})}\right)^{\frac{1}{\alpha}+1}-\left(1-\frac{2\tau_0}{(g)(\mathscr{G})}-2\left(\frac{z}{g}\right)\right)^{\frac{1}{\alpha}+1}\right],$$

$$0 \le z \le \left(\frac{g}{2}\right)\left(1-\frac{2\tau_0}{(g)(\mathscr{G})}\right) \tag{6.30}$$

for a Herschel–Bulkley fluid;

$$V_\xi = \left(\frac{\mathscr{G}(g)^2}{2\mu_0}\right)\left[\left(\frac{z}{g}\right)-\left(\frac{z}{g}\right)^2\right]-\left(\frac{\tau_0(g)}{\mu_0}\right)\left(1-\frac{z}{g}\right), \quad \left(\frac{g}{2}\right)\left(1+\frac{2\tau_0}{(g)(\mathscr{G})}\right) \le z \le g$$

$$V_\xi = \left(\frac{\mathscr{G}(g)^2}{2\mu_0}\right)\left[\left(\frac{z}{g}\right)-\left(\frac{z}{g}\right)^2\right]-\left(\frac{\tau_0(g)}{\mu_0}\right)\left(\frac{z}{g}\right), \quad 0 \le z \le \left(\frac{g}{2}\right)\left(1-\frac{2\tau_0}{(g)(\mathscr{G})}\right) \tag{6.31}$$

for a Bingham plastic fluid in which $\alpha = 1$ and $K = \mu_0$ the Bingham viscosity;

$$V_\xi = \left(\frac{\mathscr{G}}{K}\right)^{\frac{1}{\alpha}}\left(\frac{1}{\frac{1}{\alpha}+1}\right)\left(\frac{g}{2}\right)^{\frac{1}{\alpha}+1}\left[1-\left(2\left(\frac{z}{g}\right)-1\right)^{\frac{1}{\alpha}+1}\right] \tag{6.32}$$

for an Ostwald–de Waele (power-law) fluid in which $\tau_0 = 0$ and;

$$V_\xi = \left(\frac{\mathscr{G}}{\mu}\right)\left(\frac{g}{2}\right)^2\left[\frac{z}{g}-\left(\frac{z}{g}\right)^2\right] \tag{6.33}$$

for a Newtonian fluid in which $\alpha = 1$ and $K = \mu$ the Newtonian viscosity.

Recall that the fluid loss term q_l given by the R.H.S. of Eq. (6.27) acts as a source term, i.e., the more the fluid infiltrates through the fracture surfaces at ($z = \pm g/2$), the higher the filter cake resistance due to deposition and wall-building effects. The basic leak-off theory for a filter cake defines the fluid leak-off term with the following equation:

$$q_l(x,y,t) = \frac{2C_w}{\sqrt{t-\psi(x,y)}} + 2S_p\dot{\delta}(t-\psi(x,y)) \tag{6.34}$$

where $C_w = C_{t/b}$ is the usual coefficient of filter cake resistance; $\psi(x,y)$ is the time at which the fracture surface location at (x,y) was first exposed to fluid; S_p is the spurt loss, which represents a rapid loss of filtrate at an early time before the filter cake begins to deposit; and $\dot{\delta}$ is the Dirac delta function. The

coefficient of filter cake resistance can be derived as (Mayerhofer et al., 1991; Mayerhofer and Economides, 1994)

$$C_w = \sqrt{\frac{\mathscr{K}_c b_c \Delta P_c}{2\mu_{app}}}, \quad b_c = \frac{\mathscr{V}_w}{\mathscr{V}_s} \tag{6.35}$$

in which $\mathscr{K}_c$ is the filter cake permeability; b_c is the constant of deposition; $\Delta P_c = p_i - p_{t/b}$ is the pressure differential across the filter cake; μ_{app} is the apparent viscosity of the fracture fluid; and $\mathscr{V}_w$ and $\mathscr{V}_s$ are the volumes of the filtrate and filter cake, respectively. The relation between filter cake permeability $\mathscr{K}_c$ and filter cake thickness z_c can be established by introducing the hydraulic filter cake resistance as $R_c = z_c/K_c$.

6.3.1 Cohesive Elements

As described previously, the evolution of a hydraulic fracture is modeled by way of introducing zero- or finite-thickness interface elements with separation resisted by gradually decreasing tensile tractions. For the cohesive element implementation, these interface elements are defined a priori and placed between continuum element faces. For the enriched XFEM implementation, they are inserted within the existing continuum elements and oriented automatically during the course of the simulation.

The coupled pressure-deformation cohesive elements are implemented as standard linear isoparametric elements with displacement and pore fluid pressure degrees of freedom (DOFs). The DOFs are associated with the element corner nodes as depicted in Fig. 6.5 (nodes 1, 2, 3, 4). The elements must be inserted a priori and placed between the faces of the adjacent pressure diffusion-stress continuum elements to model progressive damage and fracture nucleation. Referring to Fig. 6.5, the elements also have additional pressure DOFs to accommodate coupling of the fluid flow equations as described in the preceding sections. These DOFs are located at the center of the element edges (midplane) perpendicular to the plane of the fracture and are utilized for interpolating the fluid pressure (p_f, p_i) at nodes 5 and 6.

The cohesive elements can have an arbitrary undeformed geometric thickness t_{init} because the instantaneous gap g in the fracture fluid flow equation is defined as the difference between the deformed and undeformed thickness, i.e., $g = t_{curr} - t_{init}$. Before the onset of damage, the top and bottom faces of the unopened fracture are subjected to the pore fluid pressure p acting to increase separation, which is resisted by effective tractions:

$$T = K_0 g - p \tag{6.36}$$

where K_0 is the initial stiffness of the cohesive element before failure. After damage initiation, the pore fluid is displaced by the fracture fluid pressurizing

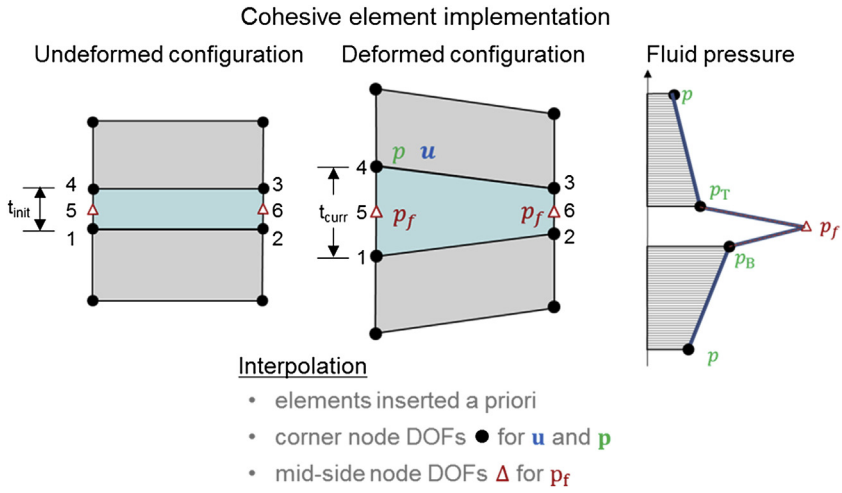

FIGURE 6.5 Coupled pressure-deformation cohesive elements with displacement and pore fluid pressure degrees of freedom (DOFs). *Modified from Searles, K.H., Zielonka, M.G., Ning, J., Garzon, J.L., Kostov, N.M., Sanz, P.F., Biediger, E.A.O., 2016. Fully coupled 3D hydraulic fracture models: development, validation and application to O&G problems. Society of Petroleum Engineers SPE 179121-MS. In: SPE Hydraulic Fracturing Technology Conference, 9–11 February, The Woodlands, Texas, USA, pp. 1–21.*

the interface. The total tractions acting on the top and bottom surfaces of the opening fracture are then

$$\mathrm{T} = \mathrm{K_p} g - (1 - \mathrm{D})\alpha_0 \mathrm{p_f} - \mathrm{D}\mathrm{p_f} \tag{6.37}$$

where $\mathrm{K_p}$ is the damaged stiffness; D is the scalar damage; α_0 is the undamaged Biot coefficient; and $\mathrm{p_f}$ is the fracture fluid pressure (cf. Fig. 6.1).

6.3.2 Extended Finite Elements

The XFEM implementation is based on the so-called phantom node approach (Abaqus®, 2017; Remmers et al., 2008; Song et al., 2006; Sukumar and Prevost, 2003; Van der Meer and Sluys, 2009). Each enriched pressure diffusion-stress continuum element is internally duplicated with the addition of corner phantom nodes depicted in Fig. 6.6. The original nodes are represented with full circles and the corner phantom nodes are represented with hollow circles. Prior to the onset of damage, a single copy of the element is active. On damage initiation, displacement and pore fluid pressure DOFs associated with the phantom nodes are activated. Both copies of the element are then allowed to deform independently with pore fluid pressure diffusion while behavior of the created interface is enforced by a traction–separation law.

The solution to the fracture fluid flow equations is initiated on the basis of the midplane pressure ($\mathrm{p_f}$, $\mathrm{p_i}$) that is interpolated from edge phantom nodes

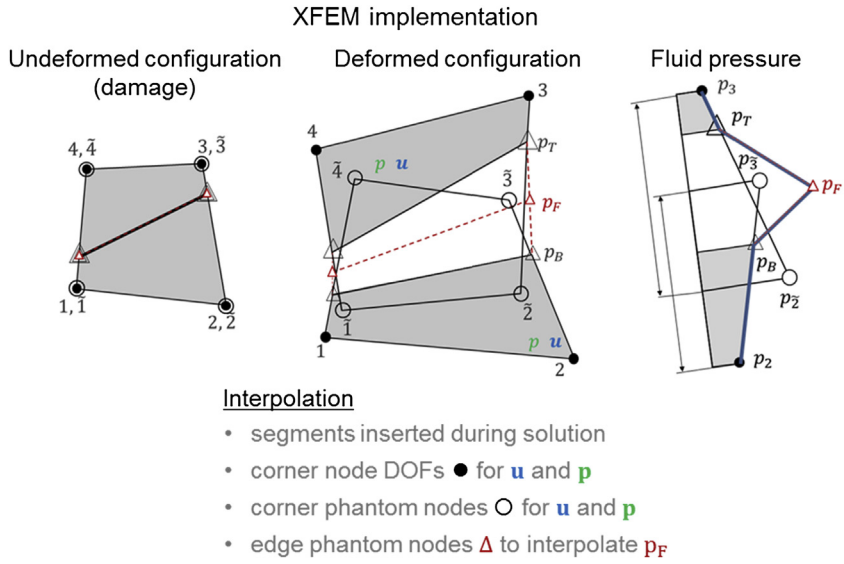

FIGURE 6.6 Enriched pressure diffusion-stress continuum elements having phantom nodes with displacement and pore fluid pressure degrees of freedom (DOFs). *Modified from Searles, K.H., Zielonka, M.G., Ning, J., Garzon, J.L., Kostov, N.M., Sanz, P.F., Biediger, E.A.O., 2016. Fully-coupled 3D hydraulic fracture models: development, validation and application to O&G problems. Society of Petroleum Engineers SPE 179121-MS. In: SPE Hydraulic Fracturing Technology Conference, 9–11 February, The Woodlands, Texas, USA, pp. 1–21; Zielonka, M.G., Searles, K.H., Ning, J., Buechler, S.R., Du, Z., Xia, L., Wohlever, C., 2014b. An extended finite element method for hydraulic fracturing of fully saturated porous media. In: Eleventh World Congress on Computational Mechanics (WCCM XI), 20–25 July, Barcelona, Spain, pp. 1–32.*

(shown as red triangles in Fig. 6.6). The pore fluid pressures p_T and p_B (equivalent to p_{t1} and p_{b1} in Fig. 6.2) acting on the top and bottom fracture surfaces, respectively, are interpolated from pore fluid pressure DOFs at the corner nodes (real and phantom). The difference in pressures between p_f and $p_{T/B}$ determines the amount of fluid which infiltrates through the fracture surfaces at ($z = \pm g/2$). When p_f increases enough to overcome the effective intact strength of the porous medium, the fracture will begin to propagate through one or more enriched elements ahead of the fracture tip.

In the context of this work, the fracture is extended through one or more enriched continuum elements ahead of the fracture tip according to a local or nonlocal stress measure. The local stress measure governing fracture evolution is implemented based on a scheme that is most representative of the tip condition required for fracture propagation. For the purpose of illustration, let us assume that two quadrilateral elements, Elements 1 and 2, are joined at a common edge and share nodes (cf. Fig. 6.7). The elements are 2-D plane strain, bilinear displacement elements with additional pore fluid pressure DOFs. Element 1 is defined by four nodes (n_1, n_2, n_3, n_4) and four internal

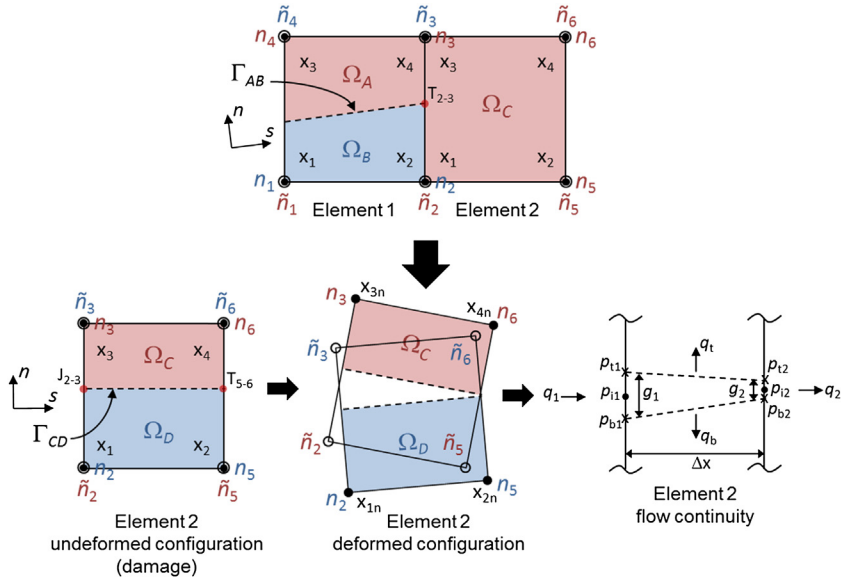

FIGURE 6.7 Construction of a discontinuity (fracture) using the phantom node method.

Gauss quadrature points (x_1, x_2, x_3, x_4). Element 2 is similarly defined by four nodes (n_2, n_5, n_6, n_3) and four internal Gauss quadrature points (x_1, x_2, x_3, x_4).

When Element 1 is cut by fracture segment Γ_{AB}, it is divided into two subdomains Ω_A and Ω_B. The discontinuity is constructed by activating phantom nodes ($\tilde{n}_1$, $\tilde{n}_2$, $\tilde{n}_3$, $\tilde{n}_4$) on top of the existing nodes (n_1, n_2, n_3, n_4). The jump in the displacement field over the fracture segment is such that closure is enforced where the discontinuity bisects the common edge of both Elements 1 and 2, i.e., crack tip ($T_{2\text{-}3}$).

To more accurately evaluate when Element 2 fractures and the tip $T_{2\text{-}3}$ propagates through the entire element, a representative state of principal stress at the tip is sought. For one possible scheme, the state of Element 2 is defined by taking a centroid average of the quadrature point (x_1, x_2, x_3, x_4) principal stress values. When the centroid average of these values exceeds a critical value, a new fracture segment Γ_{CD} is inserted in Element 2. The new fracture segment in Element 2 joins $J_{2\text{-}3}$ to the existing fracture tip and is oriented in the orthogonal direction (or element local 1, 2) relative to the orientation of the centroid average principal stress.

In another possible scheme, the state for Element 2 is defined by extrapolating from the quadrature point (x_1, x_2, x_3, x_4) principal stress values back to the tip location, i.e., where the discontinuity bisects the common edge of Elements 1 and 2. When the principal stress value at the tip derived from extrapolation exceeds a critical value, a new fracture segment Γ_{CD} *is* inserted in Element 2. The new segment within Element 2 joins $J_{2\text{-}3}$ to the existing tip

and is oriented in a local direction relative to the orientation of extrapolated principal stress. A variation on this scheme involves inserting the new fracture segment Γ_{CD} in Element 2 based on the tip extrapolated principal value and orienting it in a local direction relative to the orientation of the centroid average principal stress.

The subregion connectivity for the newly split Element 2 is C ($\tilde{n}_2$, $\tilde{n}_5$, n_6, n_3) and D (n_2, n_5, $\tilde{n}_6$, $\tilde{n}_3$) as shown in the deformed configuration (Fig. 6.7), and the resulting two new subregions can move apart. Contribution to the jump in the displacement field is realized for subregion C by integration over the active subdomain Ω_C and for subregion D by integration over the active subdomain Ω_D. For the subdomain integration, the quadrature points (x_1, x_2, x_3, x_4) are reevaluated (B-matrices) at the nodal locations (x_{1n}, x_{2n}, x_{3n}, x_{4n}). The jump in displacement (in global coordinates) over the fracture segment within Element 2 is the difference in displacement fields ($\mathbf{u}$) between C and D (Song et al., 2006; Van der Meer and Sluys, 2009):

$$[\![\mathbf{u}]\!](\mathbf{x}) = \mathbf{N}(\mathbf{x})(\mathbf{u}_C - \mathbf{u}_D), \quad \mathbf{x} \in \Gamma_{CD} \tag{6.38}$$

where $\mathbf{N}(\mathbf{x})$ are the usual finite element shape functions. The jump in displacement can be recast in a local (s-n) coordinate system with normal and shear components as

$$[\![\bar{\mathbf{u}}]\!] = \left\{[\![u]\!]_n; [\![u]\!]_s\right\}^T = \mathbf{Q}[\![\mathbf{u}]\!] \tag{6.39}$$

where

$$\mathbf{Q} = \begin{bmatrix} -\sin\theta & \cos\theta \\ \cos\theta & \sin\theta \end{bmatrix} \tag{6.40}$$

Closure is enforced when phantom nodes have not been activated (or added) at the element boundary containing the fracture tip. Activation (or addition) of phantom nodes occurs when the fracture segment propagates entirely through to the next adjacent element.

The aforementioned schemes for a local measure are convenient to apply but may be error prone without sufficient mesh refinement where there is a large variation in stress ahead of the fracture tip. One way to lessen the error is to introduce a *nonlocal* scheme for averaging the principal stress field over some domain surrounding the tip. Referring to Fig. 6.8, the orientation of the fracture segment within Element 2 may be based on Gaussian weighting of the maximum principal stress over some characteristic domain ahead of the fracture tip. Fracture nucleation at $T_{2\text{-}3}$ is defined by extrapolating from the quadrature point (x_1, x_2, x_3, x_4) principal stress values back to the location of tip, i.e., where the discontinuity bisects the common edge of Element 1 and Element 2.

When the principal stress at the tip exceeds a critical value, a new fracture segment Γ_{CD} is inserted in Element 2. The new fracture segment in Element 2

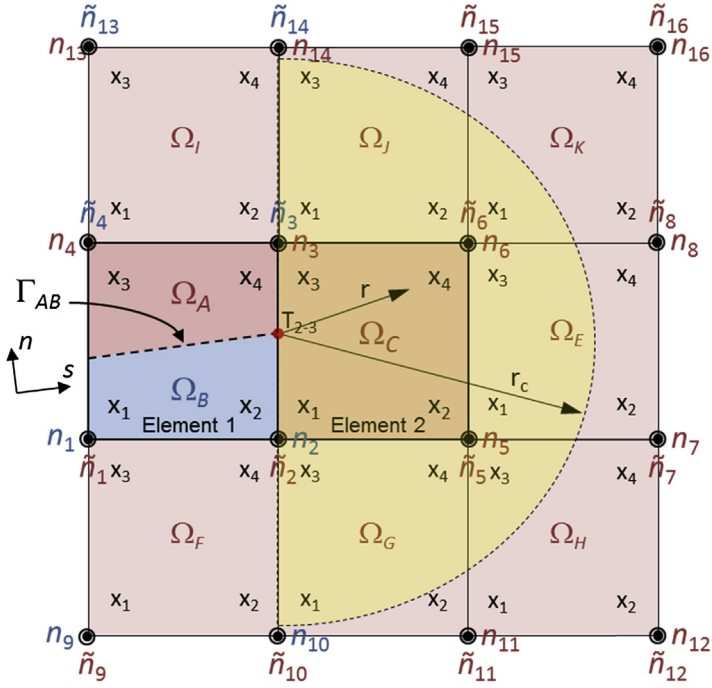

FIGURE 6.8 Discontinuity (fracture) constructed using the phantom node method with a nonlocal averaging domain (defined by r_c) to evaluate crack evolution.

joins the existing fracture segment at $J_{2\text{-}3}$ and is oriented in the direction determined by a weighted average over the characteristic 2-D (semicircular) or 3-D (semispherical) domain defined by area A or volume V and radius r_c:

$$\begin{aligned}\boldsymbol{\sigma}_{\text{ave}}^{\text{tip}} &= \int_{\text{A}} \boldsymbol{\sigma}\omega \text{dA} \Big/ \int_{\text{A}} \omega \text{dA} \\ \boldsymbol{\sigma}_{\text{ave}}^{\text{tip}} &= \int_{\text{V}} \boldsymbol{\sigma}\omega \text{dV} \Big/ \int_{\text{V}} \omega \text{dV}\end{aligned} \tag{6.41}$$

The radius r_c of the characteristic 2-D or 3-D domain (measured from the tip) is taken as a default value of $2l$, where l is a characteristic length of an element near the fracture tip. The weight function ω is a Gaussian function given by (Wells and Sluys, 2001)

$$\omega(\text{r}) = \frac{1}{(2\pi)^{3/2}\text{r}_\text{c}^3} \exp\left(-\frac{\text{r}^2}{2\text{r}_\text{c}^2}\right) \tag{6.42}$$

where r_c is the interaction radius and r is the distance of a point away from the tip of the fracture segment.

The orientation of the fracture segment within Element 2 may also be based on cubic spline weighting of the maximum principal stress over some characteristic domain ahead of the fracture tip. The weight function ω is a cubic spline function given by (Song, 2008)

$$\omega(r) = \begin{cases} 4\left(\frac{r}{r_c} - 1\right)\left(\frac{r}{r_c}\right)^2 + \frac{2}{3} & 0 < r < \frac{r_c}{2} \\ \frac{4}{3}\left(1 - \frac{r}{r_c}\right)^3 & \frac{r_c}{2} \le r \le r_c \\ 0 & \text{otherwise} \end{cases} \tag{6.43}$$

where again, r_c is the interaction radius and r is the distance of a point away from the tip of the fracture.

6.4 SOLUTION VERIFICATION

In this section, the cohesive element and XFEM implementations previously discussed are applied to simplified model configurations for a propagating hydraulic fracture:

- Vertical planar KGD (Khristianovich-Geertsma-de Klerk) fracture propagating within a prismatic-shaped domain (Charlez, 1997; Geertsma and De Klerk, 1969; Yew, 1997)
- Horizontal radial ("penny-shaped") fracture propagating within a cylindrical domain (Cleary, 1980; Charlez, 1997; Yew, 1997)

The purpose of such model configurations is to function as verification examples for assessing the accuracy of the numerical solution. Because these configurations are based on simplified fracture geometries that are symmetric, they lend themselves to comparisons with known solutions for a certain set of assumptions.

There are no readily available closed-form solutions to the KGD or radial fracture propagation problem when the coupled processes are fully considered in the analysis. However, by way of a more restrictive theoretical framework, analytical solutions are available in the form of regular asymptotic expansions to limiting propagation regimes (Bunger et al., 2005; Detournay et al., 2006; Garagash, 2006; Garagash et al., 2011; Hu and Garagash, 2010; Peirce and Detournay, 2008; Savitski and Detournay, 2002). The analytical solutions result from considering (1) an infinite linear elastic domain, (2) an impervious medium, (3) linear elastic fracture mechanics, and (4) fluid loss modeled according to Carter's leak-off model (Howard and Fast, 1957; Charlez, 1997).

According to the more restrictive theoretical framework, the equations governing the problem simplify to (1) the equilibrium equation for an infinite linear elastic domain represented as a singular integral equation relating

fracture opening and fluid pressure, (2) the local and global mass balance equations for the fracture fluid, and (3) a fracture propagation criterion also expressed as a singular integral equation relating fracture pressure and fracture toughness. Nondimensional analysis of this reduced system of equations reveals two sets of competing physical processes. The first set of physical processes consists of competing dissipative mechanisms, i.e., energy dissipated due to fluid viscosity and energy dissipated due to fracture propagation. The second set of physical processes consists of the competing components of fluid balance, i.e., storage within the fracture and loss from the fracture into the surrounding medium. From the sets of competing processes (dissipative, fluid balance), four principal limiting regimes of propagation emerge depending on which of the processes dominates:

- Toughness- and storage-dominated propagation regime (K)
- Viscosity- and storage-dominated propagation regime (M)
- Toughness- and leak-off-dominated propagation regime $(\widetilde{\mathrm{K}})$
- Viscosity- and leak-off-dominated propagation regime $(\widetilde{\mathrm{M}})$

These four principal limiting regimes of propagation can be conceptualized as a rectangular parametric space (cf. Fig. 6.9) where each of the limiting regimes corresponds to one of the vertices (K, M, $\widetilde{\mathrm{K}}$, $\widetilde{\mathrm{M}}$) of the rectangle.

Verification of the numerical solutions for the vertical KGD and horizontal radial model configurations are made in the next section considering both the

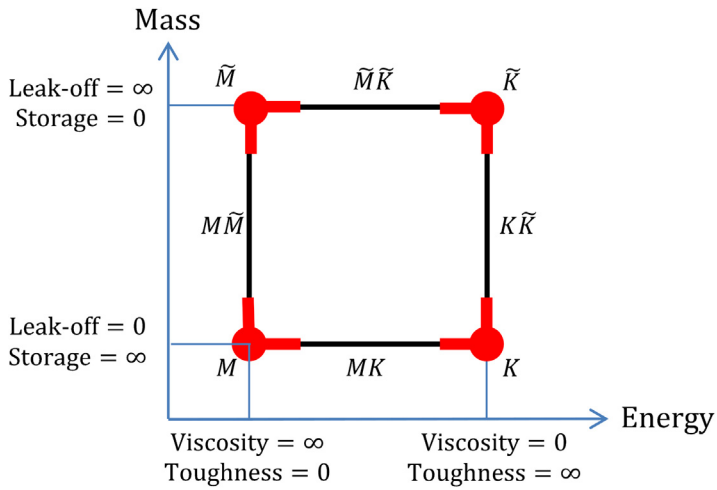

FIGURE 6.9 Diagram of the parametric space representing the four limiting regimes of fracture propagation. *Adapted from Searles, K.H., Zielonka, M.G., Ning, J., Garzon, J.L., Kostov, N.M., Sanz, P.F., Biediger, E.A.O., 2016. Fully-coupled 3D hydraulic fracture models: development, validation and application to O&G problems. Society of Petroleum Engineers SPE 179121-MS, p. 14. Copyright 2016, SPE. Reproduced with permission of SPE. Further reproduction prohibited without permission.*

toughness-storage-dominated (*near*-K) and viscosity-storage-dominated (*near*-M) regimes. The *near*-K and *near*-M asymptotic expansions (small-time solution) are used to verify the numerical solution for each implementation (cohesive elements and XFEM), with judiciously chosen material parameters, loads, and boundary conditions that reproduce each of these propagation regimes. Dimensions of the model domains are chosen to be much larger than fracture width and length; the permeability is defined to minimize poroelastic effects, and mechanical properties are selected to minimize the size of the cohesive zone relative to the fracture size.

6.4.1 Vertical Planar Khristianovich-Geertsma-de Klerk Fracture

The first model problem consists of a vertical planar KGD fracture propagating within a prismatic-shaped domain as shown in Fig. 6.10.

The domain is modeled as a porous medium with the following properties: Young's modulus E; Poisson's ratio ν; fracture toughness K_{IC}; porosity ϕ; Biot's coefficient α; Biot's modulus M; and hydraulic conductivity $\bar{k}$. The fracture fluid is an incompressible Newtonian fluid of viscosity μ_f, which is injected along a vertical wellbore at a constant rate per unit of vertical length Q. The problem unknowns are the fracture width $g(r, t)$, the net fluid pressure $p(r, t) = p_f(r, t) - \sigma_0$, and the fracture length R(t).

The porous medium is discretized with linear coupled pressure diffusion-stress continuum elements. The medium is assumed to be fully saturated with no confining stresses. For the cohesive element implementation, coupled pressure-deformation cohesive elements are inserted a priori along the midplane of the model domain. The nodes connecting the continuum elements to the cohesive elements are shared nodes. For the XFEM implementation, an equivalent mesh is used whereby the midplane discretized with cohesive elements is replaced by a set of enriched coupled pore fluid diffusion-stress elements.

The normal displacements at boundary surfaces and symmetry planes are constrained, and pore fluid pressure is set to a uniform value of $p = 0$ on all model boundaries. The corner phantom nodes on symmetry and boundary surfaces are constrained to move within these surfaces. The fracture fluid pressure DOFs are associated with the fracture midplane nodes of the cohesive elements and the edge phantom nodes of the enriched elements. Concentrated fluid flow is applied directly to these midplane and phantom edge nodes.

The results for the vertical planar KGD fracture problem are shown in Figs. 6.11 and 6.12. The results presented in Fig. 6.11A–D display the time variation of net fluid pressure $p(r_{0.1}, t) = p_f(r_{0.1}, t) - \sigma_0$ and fracture width $g(r_{0.1}, t)$ (evaluated at the injection node $r = 0.01$) for both implementations. The results presented in Fig. 6.12A–D display the maximum variation of the net fluid pressure and fracture width as a function of length R along the midplane of

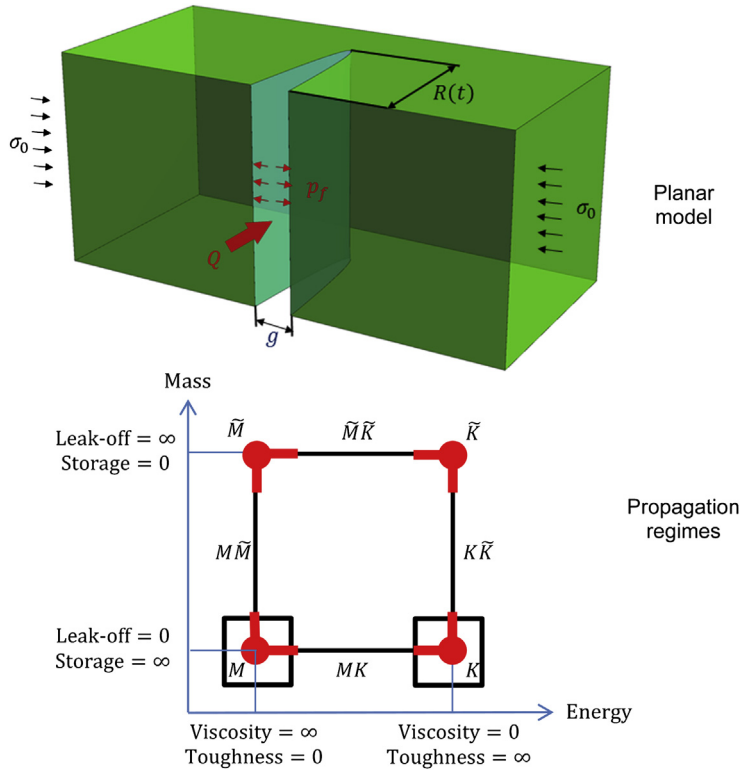

FIGURE 6.10 Illustration of the model configuration for the vertical planar Khristianovich-Geertsma-de Klerk fracture problem. *Modified from Searles, K.H., Zielonka, M.G., Ning, J., Garzon, J.L., Kostov, N.M., Sanz, P.F., Biediger, E.A.O., 2016. Fully-coupled 3D hydraulic fracture models: development, validation and application to O&G problems. Society of Petroleum Engineers SPE 179121-MS. In: SPE Hydraulic Fracturing Technology Conference, 9–11 February, The Woodlands, Texas, USA, pp. 1–21; Zielonka, M.G., Searles, K.H., Ning, J., Buechler, S.R., 2014a. Development and validation of fully-coupled hydraulic fracturing simulation capabilities. 2014 SIMULIA Community Conference, 19–22 May 2016, Providence, Rhode Island, USA, pp. 1–31.*

the fracture. Reasonably good agreement is found between the numerical and analytical solutions for both implementations. For the sake of brevity, only results for the toughness-storage (K-*vertex)*-dominated and viscosity-storage (M-*vertex)*-dominated propagation regimes are presented. More detail regarding model setup and analysis for the KGD problem can be found elsewhere (Zielonka et al., 2014a,b).

6.4.2 Radial (Penny-Shaped) Fracture

The second model problem consists of a horizontal, radial (penny-shaped) fracture propagating within a cylindrical domain as shown in Fig. 6.13.

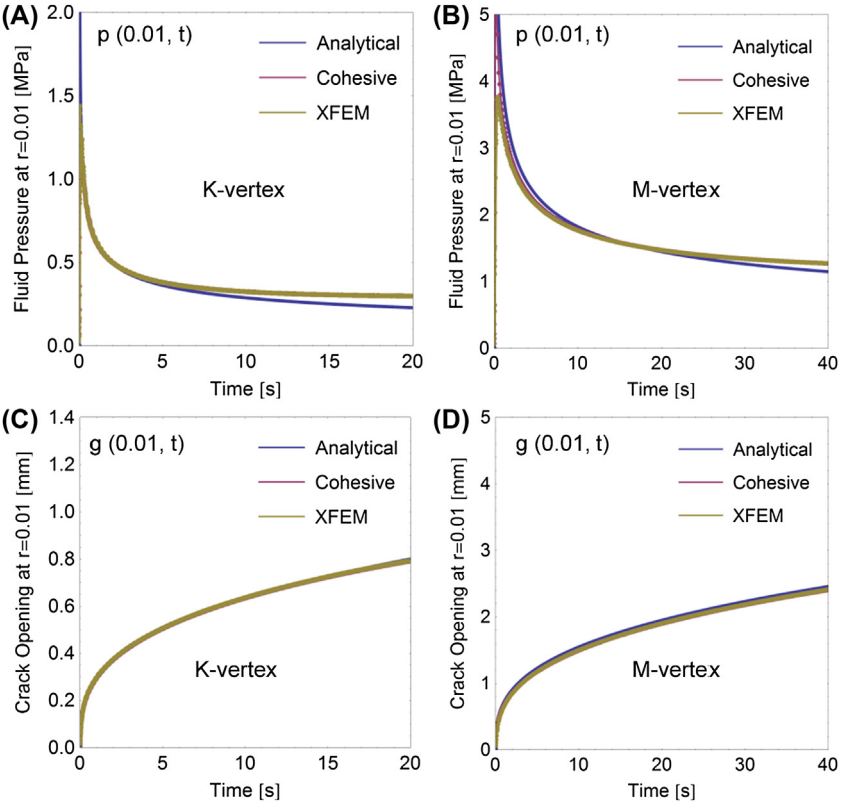

FIGURE 6.11 Time variation of net fluid pressure (A, B) and fracture width (C, D) for the vertical planar Khristianovich-Geertsma-de Klerk fracture problem.

Like the previous KGD problem, the domain for this problem is modeled as a porous medium having the same properties: Young's modulus E; Poisson's ratio ν; fracture toughness K_{IC}; porosity ϕ; Biot's coefficient α; Biot's modulus M; and hydraulic conductivity $\bar{k}$. The fracture fluid is also the same, i.e., an incompressible Newtonian fluid of viscosity μ_f, which is injected along a vertical wellbore at a constant rate per unit of vertical length Q. The problem unknowns are the fracture width $g(r, t)$, the net fluid pressure $p(r, t) = p_f(r, t) - \sigma_0$, and the fracture radius R(t).

The porous medium is also discretized with coupled pressure diffusion-stress continuum elements, and the medium is assumed to be fully saturated with no confining stresses. Coupled pressure-deformation cohesive elements are inserted a priori along the midplane of the model domain. The nodes connecting the continuum elements to the cohesive elements are shared nodes. An equivalent mesh is also used for the XFEM implementation whereby the midplane discretized with cohesive elements is replaced by a set of enriched coupled pore fluid diffusion-stress elements.

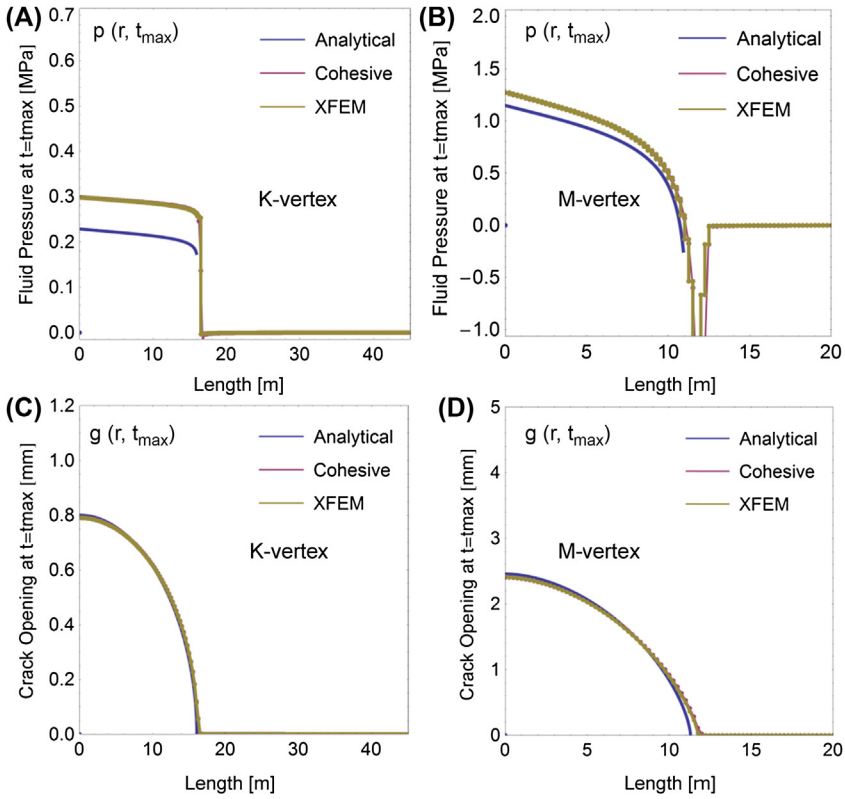

FIGURE 6.12 Maximum variation of the net fluid pressure (A, B) and fracture width (C, D) as a function of length R along the midplane for the vertical planar KGD fracture problem.

The normal displacements at boundary surfaces and symmetry planes are constrained, and pore fluid pressure is set to a uniform value on all model boundaries. The fracture fluid pressure DOFs are associated with the fracture midplane nodes of the cohesive elements and the edge phantom nodes of the enriched elements. Fluid flow is applied directly to these midplane and phantom edge nodes.

The results for the radial penny-shaped fracture problem are shown in Figs. 6.14 and 6.15. The results presented in Fig. 6.14A–D display the time variation of net fluid pressure $p(r_{0.1}, t) = p_f(r_{0.1}, t) - \sigma_0$ and fracture width $g(r_{0.1}, t)$ (evaluated at the injection node $r = 0.01$) for both implementations. The results presented in Fig. 6.15A–D display the maximum variation of the net fluid pressure and fracture width as a function of radius R along the midplane of the fracture. Reasonably good agreement is found between the numerical and analytical solutions for both implementations. Again, for the sake of brevity, only results for the toughness-storage (K-*vertex*)-dominated and

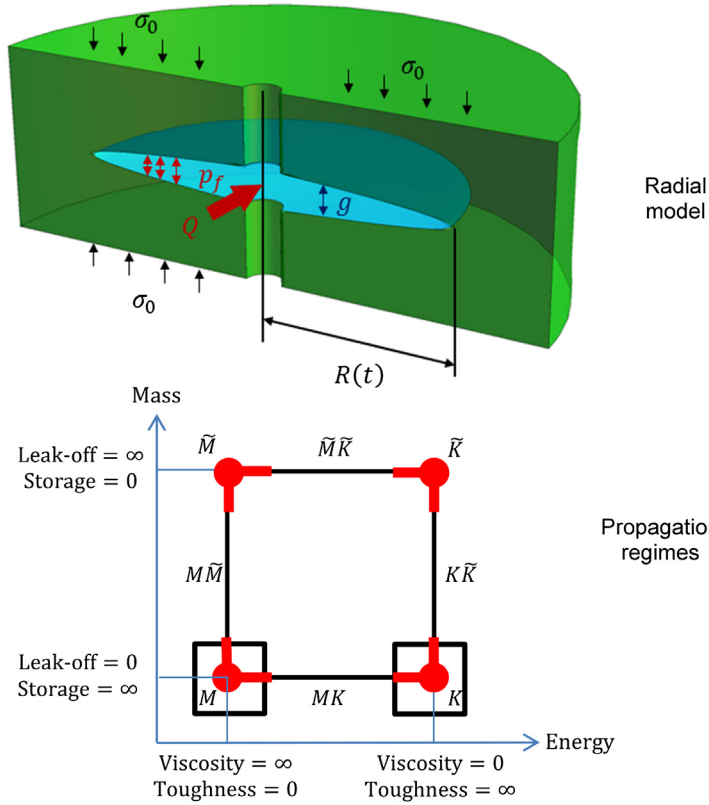

FIGURE 6.13 Illustration of the model configuration for the radial penny-shaped fracture problem. *Modified from Searles, K.H., Zielonka, M.G., Ning, J., Garzon, J.L., Kostov, N.M., Sanz, P.F., Biediger, E.A.O., 2016. Fully-coupled 3D hydraulic fracture models: development, validation and application to O&G problems. Society of Petroleum Engineers SPE 179121-MS. In: SPE Hydraulic Fracturing Technology Conference, 9–11 February, The Woodlands, Texas, USA, pp. 1–21; Zielonka, M.G., Searles, K.H., Ning, J., Buechler, S.R., 2014a. Development and validation of fully coupled hydraulic fracturing simulation capabilities. In: 2014 SIMULIA Community Conference, 19–22 May, Providence, Rhode Island, USA, pp. 1–31.*

viscosity-storage (M-*vertex*)-dominated propagation regimes are presented. More detail regarding model setup and analysis for the penny-shaped problem can also be found in Zielonka et al., 2014a,b for the interested reader.

6.5 MODEL VALIDATION

In this section, we demonstrate that the numerical treatment has been made tractable for solving example problems having greater time and length scales, e.g., laboratory and field scales. The problems presented in support of this include (1) a model constructed to replicate conditions of a laboratory-scale

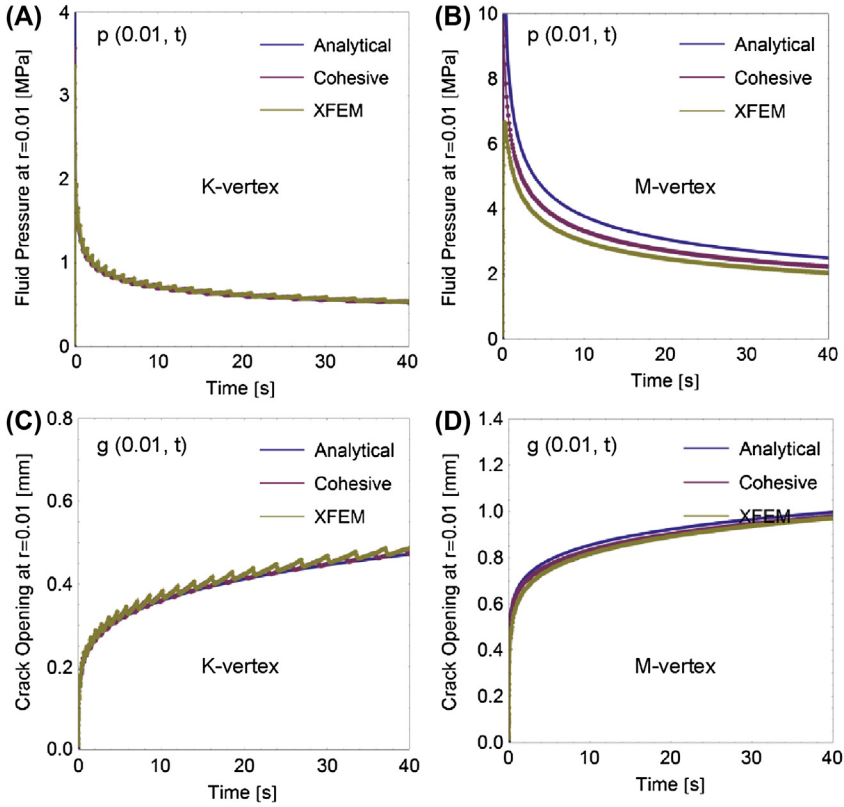

FIGURE 6.14 Time variation of net fluid pressure (A, B) and fracture width (C, D) for the radial penny-shaped fracture problem.

fluid injection experiment and (2) a model constructed to replicate conditions of a field-scale fluid injection test considering a representative geologic scenario.

For the laboratory-scale problem, unique experimental facilities have been developed based on a polyaxial test cell apparatus for conducting fluid injection tests in hydrostone and natural rock samples. The utility of the polyaxial test cell apparatus is to characterize first-order physical processes governing the nucleation and propagation of hydraulic fractures. The testable physical processes include the fracture fluid behavior, fracture fluid infiltration (leak-off), fracture mechanics, and poroelastic and capillary effects. The dependence of the processes on test conditions and properties can also be studied using the apparatus. The test conditions that can be varied during a test to study their impact include the injection rate, test duration, and applied confining stresses. The properties that can be varied with each test sample include elastic constants, fracture toughness, porosity, permeability, and initial saturation.

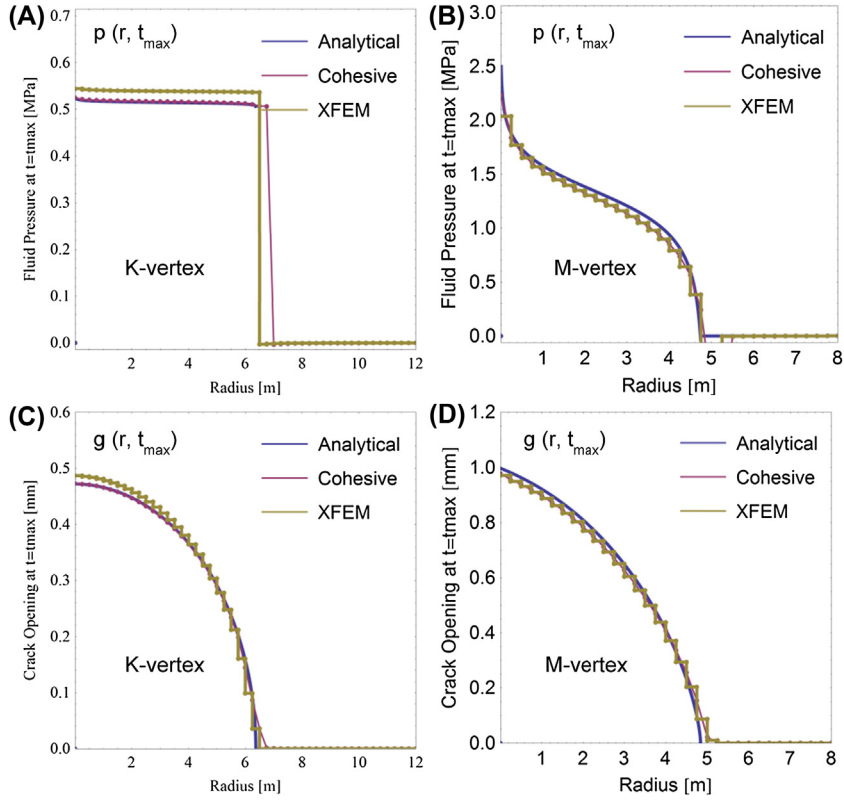

FIGURE 6.15 Maximum variation of the net fluid pressure (A, B) and fracture width (C, D) as a function of radius R along the midplane for the radial penny-shaped fracture problem.

The polyaxial test cell apparatus shown in Fig. 6.16A can apply loads to surfaces of the hydrostone or natural rock sample in Fig. 6.16B along three orthogonal, mutually independent axes. The computer-controlled hydraulic system is capable of applying up to 10^6 lbs of force and 20×10^3 psi of fluid pressure to represent most subsurface in situ conditions. Rock samples are prepared from quarried outcrop sections, whereas reconstituted hydrostone samples are prepared using an internally standardized sample preparation process. For fabricating the hydrostone samples, a 12 in. $\times$ 12 in. $\times$ 18 in. casting is created with a metal wellbore and a 2 in. open-hole section located at the center of the sample. As presented in Fig. 6.16C, plug samples are also created from the same batch to measure the mechanical and flow properties.

A suite of parametric experimental studies has been previously conducted to cover a range of test conditions and mechanical and flow properties. Test results from the studies suggest good test repeatability and provide some basis for interpreting surface pressure response from field-scale injection tests. From

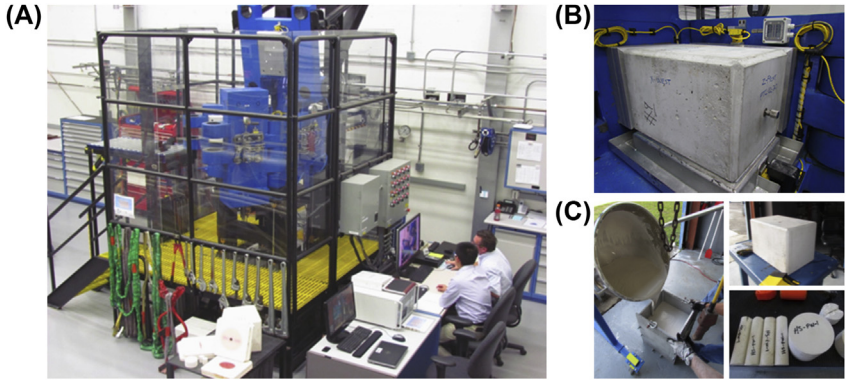

FIGURE 6.16 (A) Polyaxial test cell apparatus for conducting fluid injection tests; (B) as-cast sample for injection test; and (C) as-cast plugs for measurement of properties.

the suite of parametric studies, a case in point is presented below to demonstrate model validation for the viscosity-storage (*near*-M)-dominated propagation regime.

6.5.1 Laboratory-Scale Model

The representative laboratory-scale finite element model employed for simulating the polyaxial test cell experiment is depicted in Fig. 6.17. For simplicity, the 3-D model is assumed to be symmetric with respect to the y-z plane, and only one half of the domain is considered in the analysis. Compressive stresses of $S_x = 1000$ psi, $S_y = 500$ psi, and $S_z = 1500$ psi are applied to the sample

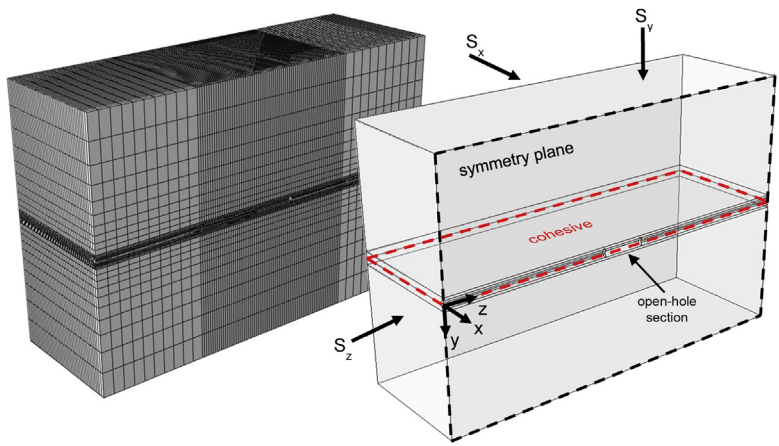

FIGURE 6.17 The 3-D finite element model employed for replicating the polyaxial test cell experiment.

surfaces oriented in the x, y, and z directions, respectively. The hydraulic fracture is discretized using coupled pressure-deformation cohesive elements, and the surrounding hydrostone is discretized with linear coupled pressure diffusion-stress continuum elements. The characteristic element length (l_e) of the cohesive elements is 0.057 and 0.075 in. for the adjacent continuum elements. The fracture is expected to nucleate in the open-hole section and propagate within the x-z plane, i.e., normal to the minimum stress (S_y).

The model input parameters to characterize the hydrostone (cf. Table 6.1) and fracture fluid are derived from measurements taken on fluid samples and hydrostone core plugs cast during the fabrication process. For this particular validation case, the Darcy permeability of the hydrostone sample is 0.28 millidarcy (mD), and a highly viscous fluid (45870 cSt, 0.876 sg) is pumped at a flow rate Q_0 of 2.5 mL/min into the initially unsaturated sample. As already stated, fracture propagation is anticipated to be in the *near*-M viscosity-storage regime with negligible fluid infiltration.

The experimental and finite element model results for this case are presented in Figs. 6.18 and 6.19. In Fig. 6.18A, the injection pressure versus time response is shown for both the polyaxial test cell (dashed black line) and 3-D

TABLE 6.1 Finite Element Model Input Parameters to Characterize the Hydrostone

Young's Modulus, E (Mpsi)	Poisson's Ratio, ν	Cohesive Strength, T_0 (ksi)	Fracture Toughness, K_{IC} (psi$\sqrt{in}$)	Porosity, ϕ (%)	Permeability, k (mD)
3.5	0.22	1.1	432	14	0.28

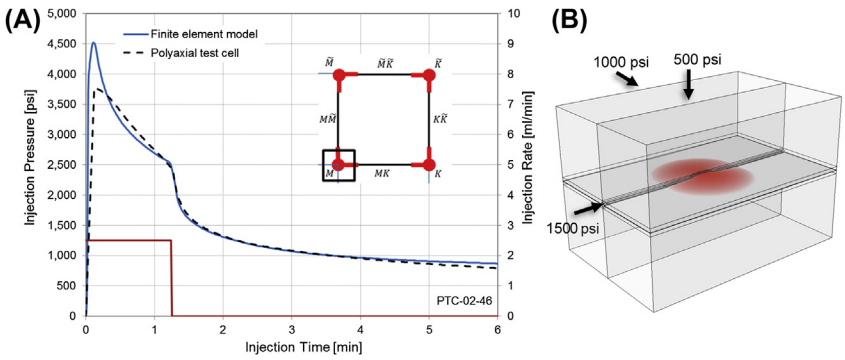

FIGURE 6.18 Comparison of pressure versus time response from the test and model (A); and predicted fracture extent from the model (B).

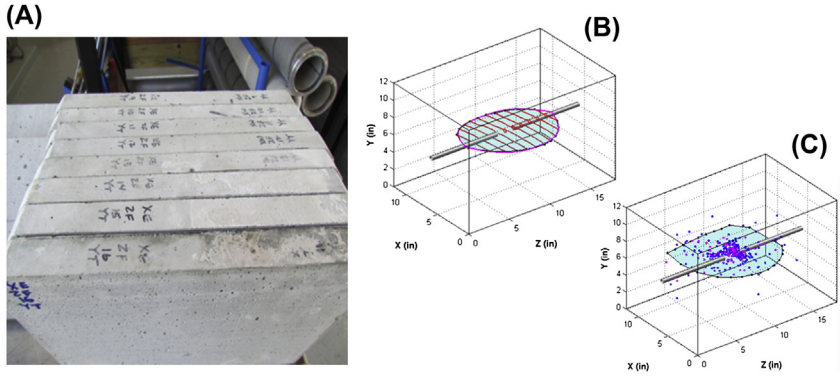

FIGURE 6.19 Posttest hydrostone sample divided into sections of equal thickness along the z-axis (A); fracture reconstruction from the serial sections (B); and interpretation of fracture extent from measured acoustic emission activity (C).

finite element model (blue line). For the modeled pressure versus time response, the corresponding fracture extent is shown in Fig. 6.18B. To make a comparison between the modeled and actual fracture extents, the actual fracture is reconstructed from serial sections of the test sample shown in Fig. 6.19A. Following the reconstruction process, the extent of the actual fracture can be estimated by fitting a surface through the assembled images of each cross section as depicted in Fig. 6.19B.

In addition to the serial reconstruction, the fracture extent is also interpreted from acoustic emission activity recorded by 24 piezoelectric transducers. The result of the interpretation, as presented in Fig. 6.19C, is compared with the reconstructed fracture extent, and both are then used as the basis for validating the model result.

It appears from Fig. 6.18A that there is reasonable agreement between the test and the model through most of the test duration, including matching the post shut-in (falloff) behavior. The measured injection pressure at shut-in is 2704 psi versus a predicted shut-in pressure of 2663 psi. The most notable discrepancy is the difference between the measured and modeled fracture nucleation (breakdown) pressures. The measured breakdown pressure is 3766 psi while the predicted breakdown pressure is 4503 psi.

There are many factors that might contribute to the noted differences in breakdown pressure. The most likely of these include one or more of the following: test cell system compliance (not modeled); lack of resolved cohesive-diffusive lengths near the fracture tip; incorrect fluid lag region; and partial saturation. The influence of each of these contributing factors on breakdown pressure is not discussed in this section. For an in-depth discussion on the sensitivity of breakdown pressure to these factors, the reader is encouraged to review the works of Chen et al. (2009), Cleary, (1979), De Pater et al. (1994), and Detournay et al. (1989), to name a few.

6.5.2 Field-Scale Model

A finite element model has also been constructed to replicate conditions of a field-scale fluid injection test considering a typical geologic setting. For this case, a fluid injection test has been conducted for an offshore operation in which seawater is injected into the subsurface at a low flow rate for a specified duration. Over the duration, the flow rate is held constant, and flowing bottomhole pressure (FBHP) is measured. Once the FBHP has stabilized, the flow rate is ramped up by a predetermined amount and held constant until the FBHP again stabilizes. This "step-rate" process is continued until the FBHP indicates that fracture nucleation and propagation have occurred.

With the fracture propagation pressure held more or less constant, injection is stopped (shut-in), and falloff behavior is observed. For this particular test, the injection process is started a second time to reopen the existing fracture created during the first pumping sequence. The reason for reopening the fracture and continuing to propagate it further is to quantify the reopening pressure and verify falloff characteristics.

The representative field-scale finite element model employed for simulating the abovementioned injection test is depicted in Fig. 6.20. The dimensions of the half-symmetry (x-y plane) model are 800 m in x, 800 m in y, and 900 m in the z direction. To reduce the total number of elements and computations, the 3-D model is further assumed to be symmetric with respect to the z-y plane, i.e., only a quarter of the whole domain is considered.

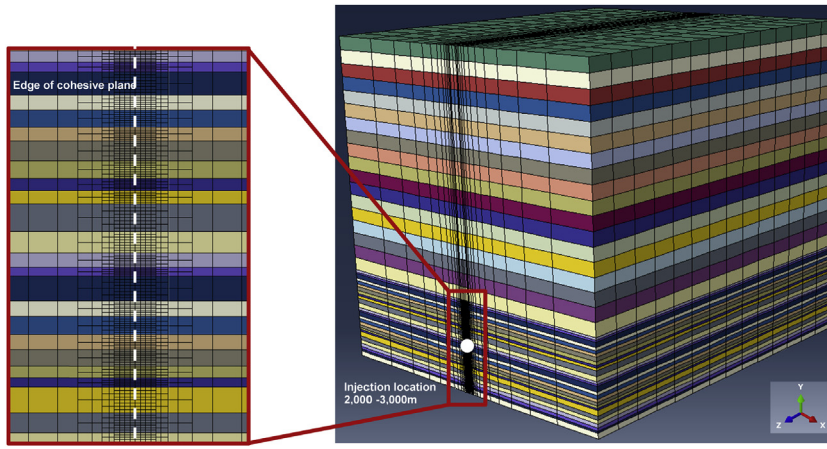

FIGURE 6.20 The 3-D finite element model used for simulating the case of a field-scale, step-rate injection test. *Adapted from Searles, K.H., Zielonka, M.G., Ning, J., Garzon, J.L., Kostov, N.M., Sanz, P.F., Biediger, E.A.O., 2016. Fully-coupled 3D hydraulic fracture models: development, validation and application to O&G problems. Society of Petroleum Engineers SPE 179121-MS. In: SPE Hydraulic Fracturing Technology Conference, 9–11 February, The Woodlands, Texas, USA, p. 15. Copyright 2016, SPE. Reproduced with permission of SPE. Further reproduction prohibited without permission.*

The plane of the fracture is discretized with coupled pressure-deformation cohesive elements while the surrounding rock is partitioned and discretized with linear coupled pressure diffusion-stress continuum elements. The characteristic element length (l_e) of the cohesive elements is on the order of 1−2 m. The use of multipoint constraints enables the transition from a very fine mesh within the plane of the fracture to a much coarser mesh away from the fracture. The fracture is anticipated to nucleate and propagate within the z-y plane, i.e., normal to the direction of the minimum in situ stress (S_x).

The surrounding rock for this case is partitioned into 46 distinct material section definitions. The model parameters to characterize the initial conditions and material properties for each of the partitions are derived from an internally developed, integrated workflow. The basis for the integrated workflow is the application of a theoretical rock physics model derived from differential effective medium theory (Keys and Xu, 2002; Xu and White, 1995). The inputs to the integrated workflow are taken from measurements made by well logging tools including gamma ray; density; porosity; permeability; and compressional and shear wave slowness.

The outputs resulting from the application of the rock physics model include synthetic compressional and shear velocities; Young's modulus; Poisson's ratio; void ratio (porosity); permeability; cohesive strength; fracture toughness; and initial stress and pore fluid pressure gradients. Where possible, the outputs are further calibrated to any available laboratory measurements on core plugs and measurements on in situ stresses. When assigning these outputs to representative material definitions for each of the model partitions, suitable zoning and upscaling techniques must also be used. Such techniques are often required because the vertical resolution of data from well logging tools is usually greater than the partitioned model domain. Some examples of outputs where zoning and upscaling have been applied are shown in Fig. 6.21.

The key results for the case of the field-scale, step-rate injection test and finite element model are depicted in Fig. 6.22. The duration of the test and simulation is 210 min, and the actual injection schedule is prescribed as a boundary condition for the model. The corrected bottom-hole injection pressure versus time response is denoted by the dashed black line while the modeled response is denoted by the blue line. The red line indicates the prescribed injection rate with multiple, stepped rates occurring within the first 30−60 min of the test. The stepped rates range from 1 to 6 bbl/min and are followed by shut-in and subsequent repressurization periods. During the first step-rate portion of the test, it is observed that the corrected pressure response shows characteristics of a fracture that has nucleated and propagated.

The finite element model results show reasonably good agreement with the field-scale injection test results. The most notable discrepancy between the test and the model appears to be over the time interval between 30 and 35 min. This difference is due to the actual time required to completely fill the

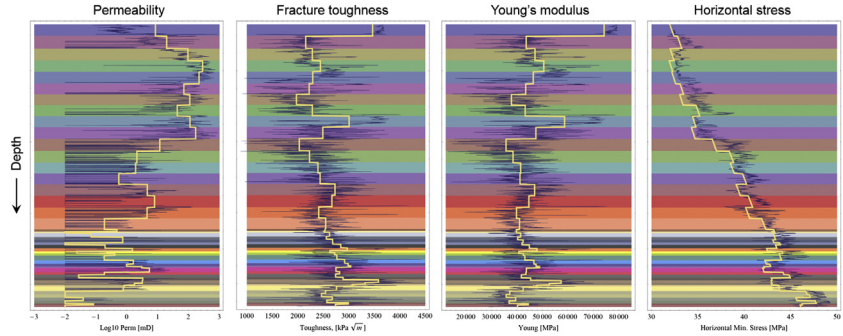

FIGURE 6.21 Examples of zoning and upscaling (46 partitions) applied to outputs derived from the rock physics model. *Adapted from Searles, K.H., Zielonka, M.G., Ning, J., Garzon, J.L., Kostov, N.M., Sanz, P.F., Biediger, E.A.O., 2016. Fully-coupled 3D hydraulic fracture models: development, validation and application to O&G problems. Society of Petroleum Engineers SPE 179121-MS, p. 15. Copyright 2016, SPE. Reproduced with permission of SPE. Further reproduction prohibited without permission.*

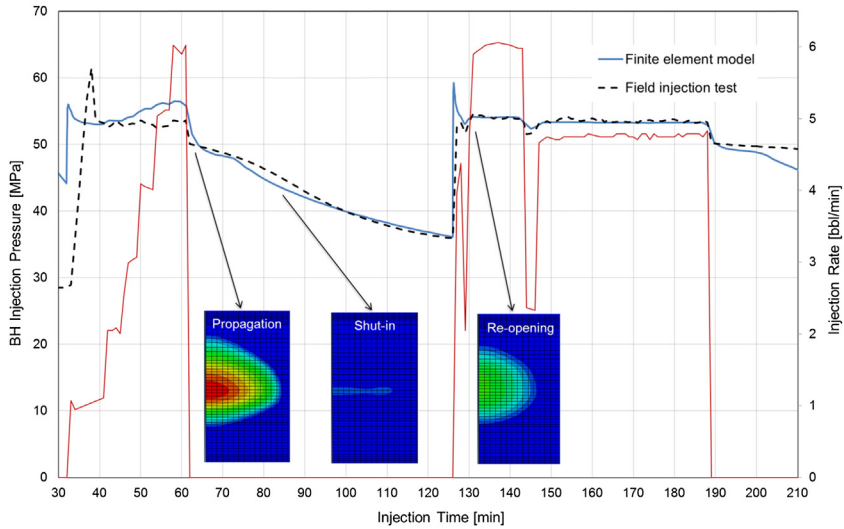

FIGURE 6.22 Comparison of bottom-hole (BH) injection pressure versus time response between the field-scale step-rate test and the 3D finite element model. *Adapted from Searles, K.H., Zielonka, M.G., Ning, J., Garzon, J.L., Kostov, N.M., Sanz, P.F., Biediger, E.A.O., 2016. Fully-coupled 3D hydraulic fracture models: development, validation and application to O&G problems. Society of Petroleum Engineers SPE 179121-MS, p. 16. Copyright 2016, SPE. Reproduced with permission of SPE. Further reproduction prohibited without permission.*

wellbore with injection fluid. In contrast, the modeled wellbore is assumed to be completely filled from the start of the simulation. Because of this difference, the predicted breakdown pressure (cf. Fig. 6.22) is observed to occur earlier in comparison with the actual breakdown pressure.

After approximately 75 min, there appears to be a transition from bilinear flow (fracture) to radial flow (porous medium) where the rate of pressure decay is mostly dependent on the intrinsic permeability of the surrounding rock. The reasonably good agreement between the actual and modeled pressure response during this time tends to suggest that the permeability profile derived from the rock physics–based workflow is representative of the in situ permeability variation.

It is worth mentioning that the similarity between the actual injection test and finite element model results has been obtained based on the first-pass estimates of the material definitions and initial conditions from the previously stated workflow. We do anticipate that a much better match of the measured pressure versus time response can be achieved through minor adjustments to the model parameters.

6.6 CONCLUSION

In this chapter, we discussed the coupled physical processes associated with hydraulic fracturing. We reviewed the system of unknowns, governing equations, and constitutive relation that describe the coupled interactions. The governing equations and constitutive relation included continuity and momentum for fluid in the fracture, and the fluid in the permeable porous medium comprising the fracture.

The methodology for modeling the coupled mechanical and flow behaviors was described at length. The framework was also presented for implementation based on the use of cohesive elements and the XFEM. This was followed by verification of certain limiting cases of the numerical results against analytical benchmarks. The benchmarks were the asymptotic expansions to limiting propagation regimes for semiinfinite cracks propagating in impervious elastic media. Such expansions were considered on a basis of the competing dissipative processes and fluid balance components.

Finally, it was demonstrated that the numerical treatment can be made tractable for solving example problems having greater time and length scales e.g., laboratory and field scales. The problems presented in support of this include (1) a model constructed to replicate conditions of a laboratory-scale fluid injection experiment and (2) a model constructed to replicate conditions of a field-scale fluid injection test considering a representative geologic scenario.

NOMENCLATURE

$\sigma_{ij}, \sigma'_{ij}$ Total and effective stress components (psi)
$\varepsilon_{ij}, \varepsilon'_{ij}$ Total and effective strain components
p Pore fluid pressure (psi)
$\mathbf{p_f}$ Fracture fluid pressure (psi)
q Fracture fluid flux (in.^{2}/s)
α Biot's coefficient
$\mathbf{K_s}$, $\mathbf{K_f}$ Bulk moduli for the solid grains and fluid (psi)
E Young's modulus (psi)
G Shear modulus (psi)
M Biot's modulus (psi)
ν Poisson's ratio
$\mathbf{v_{k,k}}$ Pore fluid seepage velocity components (in./s)
ϕ Porosity of the porous medium
k Intrinsic permeability of the porous medium (in.^{2})
$\overline{\mathbf{k}}$ Hydraulic conductivity of the porous medium (in./s)
μ Viscosity of the pore fluid (cP)
$\mathbf{T_0}$ Cohesive strength of the porous medium (psi)
$\mathbf{G_c}$ Cohesive energy of the porous medium (psi-in.)
$\mathbf{K_{IC}}$ Mode I fracture toughness of the medium (psi$\sqrt{}$in.)
g Width of the hydraulic fracture (in.)
g_0 Separation at the onset of damage
g_1 Separation at full damage
w Cohesive element thickness (in.)
D Scalar measure of material damage
K Flow consistency index, non-Newtonian fluid (psi-s^n)
n Flow behavior index, non-Newtonian fluid
τ_0 Yield stress, non-Newtonian fluid (psi)
τ_{ij} Shear stress incurred by the fracture fluid (psi)
$\dot{\gamma}$ Shear rate applied to the fracture fluid (1/s)
$\mathbf{V_x}$, $\mathbf{V_y}$ Fracture fluid velocity components (in./s)
$\mathbf{V_\xi}$ Local fracture fluid velocity (in./s)
ρ_f Mean density of the fracture fluid (lbs/in.^{3})
g Acceleration due to gravity (in./s^2)
$\mathbf{C_w}$ Coefficient of filter cake resistance
$\mathbf{S_p}$ Instantaneous loss of filtrate, spurt loss (in.^{3})
$\mathscr{V}_w$ Volumes of filtrate and filter cake (in.^{3})
$\mathbf{R_c}$ Hydraulic resistance of filter cake (1/in.)
$\mathbf{r_c}$ Interaction radius of 2-D or 3-D domain (in.)
$\mathbf{S_x}$, $\mathbf{S_y}$, $\mathbf{S_z}$ Compressive normal stresses (psi)

ACKNOWLEDGMENTS

The authors wish to thank ExxonMobil Upstream Research Company (EMURC) for permission to publish this manuscript. The authors also wish to thank our colleague Gilbert Kao (EMURC) and the entire staff at the Friendswood laboratory facility for commissioning the polyaxial test cell apparatus and conducting the many intricate experiments to support model validation.

REFERENCES

Abaqus® Analysis Guide, 2017. SIMULIA User Assistance 2017. Dassault Systémes Simulia Corp., Johnston, RI. "Abaqus" is a registered trademark of Dassault Systemes Simulia Corporation.

Abbas, S., Gordeliy, E., Peirce, A., Lecampion, B., Chuprakov, D., Prioul, R., 2014. Limited height growth and reduced opening of hydraulic fractures due to fracture offsets: an XFEM application. Society of Petroleum Engineers SPE-168622-MS. In: SPE Hydraulic Fracturing Technology Conference, 4–6 February, The Woodlands, Texas, USA, pp. 1–13.

Al-Fariss, T., Pinder, K.L., 1987. Flow through porous media of a shear-thinning liquid with yield stress. The Canadian Journal of Chemical Engineering 65 (3), 391–405.

Boone, T.J., Ingraffea, A.R., 1990. A numerical procedure for simulation of hydraulically-driven fracture propagation in poroelastic media. International Journal for Numerical and Analytical Methods in Geomechanics 14, 27–47.

Bunger, A.P., Detournay, E., Garagash, D.I., 2005. Toughness-dominated hydraulic fracture with leak-off. International Journal of Fracture 134, 175–190.

Carrier, B., Granet, S., 2012. Numerical modeling of hydraulic fracture problem in permeable medium using cohesive zone model. Engineering Fracture Mechanics 79, 312–328.

Charlez, P.A., 1997. Rock Mechanics: Petroleum Applications, vol. 2. Editions Technip, Paris.

Chen, Z., Bunger, A.P., Zhang, X., Jeffrey, R.G., 2009. Cohesive zone finite element- based modeling of hydraulic fractures. Acta Mechanica Solida Sinica 22 (5), 443–452.

Cherny, S.G., Lapin, V.N., 2016. 3D model of hydraulic fracture with Herschel-Bulkley compressible fluid pumping. Procedia Structural Integrity 2, 2479–2486.

Cleary, M.P., June 4–6, 1979. Rate and structure sensitivity in hydraulic fracturing of fluid-saturated porous formations. American Rock Mechanics Association ARMA-79-0127. In: Twentieth U.S. Symposium on Rock Mechanics (USRMS), Austin, Texas, USA, pp. 127–142.

Cleary, M.P., 1980. Comprehensive design formulae for hydraulic fracturing. Society of Petroleum Engineers SPE-9259-MS. In: SPE Annual Technical Conference and Exhibition, 21–24 September, Dallas, Texas, USA, pp. 1–20.

Clifton, R.J., 1989. Three-dimensional fracture propagation models. In: Gidley, J.L., Holditch, S.A., Nierode, D.E., Veatch Jr., R.W. (Eds.), Recent Advances in Hydraulic Fracturing, SPE Monograph Series, vol. 12. Society of Petroleum Engineers, Texas, USA, pp. 95–108.

Clifton, R.J., Wang, J.-J., 1988. Multiple fluids, proppant transport, and thermal effects in three-dimensional simulation of hydraulic fracturing. Society of Petroleum Engineers SPE 18198. In: SPE Annual Technical Conference and Exhibition, 2–5 October, Houston, Texas, USA, pp. 1–14.

Dahi-Taleghani, A., Olson, J.E., 2011. Numerical modeling of multistranded-hydraulic- fracture propagation: accounting for the interaction between induced and natural fractures. Society of Petroleum Engineers Journal 16 (3), 575–581. SPE-124884-PA.

De Pater, C.J., Weijers, L., Savic, M., Wolf, K.H.A.A., Van den Hoek, P.J., Barr, D.T., 1994. Experimental study of nonlinear effects in hydraulic fracture propagation. Society of Petroleum Engineers SPE 25893-PA SPE Production and Facilities 9 (4), 239–246.

Detournay, E., Cheng, A.H.D., Rogiers, J.C., McLennan, J.D., 1989. Poroelasticity considerations in in situ stress determination by hydraulic fracturing. International Journal of Rock Mechanics and Mining Sciences & Geomechanics Abstracts 26 (6), 507–513.

Detournay, E., Adachi, J.I., Garagash, D.I., Savitski, A.A., 2006. Interpretation and Design of Hydraulic Fracturing Treatments. US Patent 7111681B2.

Garagash, D.I., 2006. Plane-strain propagation of a fluid-driven fracture during injection and shut-in: asymptotics of large toughness. Engineering Fracture Mechanics 73, 456–481.

Garagash, D.I., Detournay, E., Adachi, J.I., 2011. Multiscale tip asymptotics in hydraulic fracture with leak-off. Journal of Fluid Mechanics 669, 260–297.

Geertsma, J., De Klerk, F., 1969. A rapid method of predicting width and extent of hydraulically induced fractures. Society of Petroleum Engineers SPE 2458-PA Journal of Petroleum Technology 21 (12), 1571–1581.

Howard, G.C., Fast, C.R., 1957. Optimum fluid characteristics for fracture extension. In: Drilling and Production Practices, vol. 24. API, pp. 261–270.

Hu, J., Garagash, D.I., 2010. Plane-strain propagation of a fluid-driven crack in a permeable rock with fracture toughness. Journal of Engineering Mechanics 136 (9), 1152–1166.

Keys, R.G., Xu, S., 2002. An approximation for the Xu-White velocity model. Geophysics 67 (5), 1406–1414.

Lakhtychkin, A., Eskin, D., Vinogradov, O., 2012. Modelling of transport of two proppant-laden immiscible power-law fluids through an expanding fracture. The Canadian Journal of Chemical Engineering 90, 528–543.

Mayerhofer, M.J., Economides, M.J., 1994. Experimental study of fracturing fluid loss. Journal of Canadian Petroleum Technology 33 (8), 49–56.

Mayerhofer, M.J., Economides, M.J., Leoben, M.U., Nolte, K.G., 1991. An experimental and fundamental interpretation of fracturing filter-cake fluid loss. Society of Petroleum Engineers SPE 22873–MS. In: SPE Annual Technical Conference and Exhibition, 6–9 October, Dallas, Texas, USA, pp. 557–567.

Meyer, B.R., 1989. Three-dimensional hydraulic fracturing simulation on personal computers: theory and comparison studies. Society of Petroleum Engineers SPE 19329–MS. In: SPE Eastern Regional Meeting, 24–27 October, Morgantown, West Virginia, USA, pp. 1–18.

Ortiz, M., Pandolfi, A., 1999. Finite-deformation irreversible cohesive elements for three-dimensional crack-propagation analysis. International Journal for Numerical Methods in Engineering 44 (9), 1267–1282.

Ouyang, S., 1994. Propagation of Hydraulically Induced Fractures with Proppant Transport (Ph.D. dissertation). The University of Texas at Austin, Austin, TX.

Peirce, A., Detournay, E., 2008. An implicit level set method for modeling hydraulically driven fractures. Computer Methods in Applied Mechanics and Engineering 197, 2858–2885.

Remmers, J.J.C., de Borst, R., Needleman, A., 2008. The simulation of dynamic crack propagation using the cohesive segments method. Journal of the Mechanics and Physics of Solids 56, 70–92.

Savitski, A.A., Detournay, E., 2002. Propagation of a penny-shaped fluid-driven fracture in an impermeable rock: asymptotic solutions. International Journal of Solids and Structures 39, 6311–6337.

Searles, K.H., Zielonka, M.G., Ning, J., Garzon, J.L., Kostov, N.M., Sanz, P.F., Biediger, E.A.O., 2016. Fully-coupled 3D hydraulic fracture models: development, validation and application to O&G problems. Society of Petroleum Engineers SPE 179121-MS. In: SPE Hydraulic Fracturing Technology Conference, 9–11 February, 2016, The Woodlands, Texas, USA, pp. 1–21.

Song, J.-H., 2008. Computations of the Dynamic Fracture of Quasi-Brittle Plane and Shell Structures by the Extended Finite Element Method (Ph.D. dissertation). Northwestern University, Evanston, Illinois.

Song, J.-H., Areias, P.M.A., Belytschko, T., 2006. A method for dynamic crack and shear band propagation with phantom nodes. International Journal for Numerical Methods in Engineering 67, 868–893.

Sukumar, N., Prevost, J.H., 2003. Modeling quasi-static crack growth with the extended finite element method part I: computer implementation. International Journal for Solids and Structures 40, 7513–7537.

Van der Meer, F.P., Sluys, L.J., 2009. A phantom node formulation with mixed mode cohesive law for splitting laminates. International Journal of Fracture 158, 107–124.

Warpinski, N.R., Moschovidis, Z.A., Parker, C.D., Abou-Sayed, I.S., 1994. Comparison study of hydraulic fracturing models-test case: GRI staged field experiment no. 3. Society of Petroleum Engineers SPE 25890-PA SPE Production and Facilities 9 (1), 7–16.

Wells, G.N., Sluys, L.J., 2001. A new method for modeling cohesive cracks using finite elements. International Journal for Numerical Methods in Engineering 50, 2667–2682.

Xu, S., White, R.E., 1995. A new velocity model for clay-sand mixtures. Geophysical Prospecting 43, 91–118.

Yew, C.H., 1997. Mechanics of Hydraulic Fracturing, first ed. Gulf Professional Publishing Company, Texas, USA.

Zielonka, M.G., Searles, K.H., Ning, J., Buechler, S.R., 2014a. Development and validation of fully-coupled hydraulic fracturing simulation capabilities. In: 2014 SIMULIA Community Conference, 19–22 May, Providence, Rhode Island, USA, pp. 1–31.

Zielonka, M.G., Searles, K.H., Ning, J., Buechler, S.R., Du, Z., Xia, L., Wohlever, C., 2014b. An extended finite element method for hydraulic fracturing of fully saturated porous media. In: Eleventh World Congress on Computational Mechanics (WCCM XI), 20–25 July, Barcelona, Spain, pp. 1–32.

FURTHER READING

Garzon, J., Zielonka, M., Searles, K.H., Sanz, P., 2015. Advanced fracture modeling capabilities for cuttings re-injection. In: 2015 SIMULIA Community Conference, 19–21 May, Berlin, Germany, pp. 1–15.

Chapter 7

Continuum Modeling of Hydraulic Fracturing in Complex Fractured Rock Masses

Jonny Rutqvist[1], Bruno Figueiredo[2], Mengsu Hu[1], Chin-Fu Tsang[1,2]
[1]*Lawrence Berkeley National Laboratory, Berkeley, CA, United States;* [2]*Uppsala University, Uppsala, Sweden*

7.1 INTRODUCTION

To date, a number of approaches have been developed to simulate the hydromechanics of fractured rocks and hydraulic fracturing. Depending on how to deal with the fractures, these approaches are categorized into continuous, discontinuous, and hybrid approaches. In continuous approaches, the fractures are usually modeled as heterogeneity by using the same dimension for fractures as for the rock matrix (such as approaches by Rutqvist et al., 2009, 2013a; Li et al., 2012; Wangen, 2013; Chau et al., 2016; Pogacnik et al., 2016; Gan and Elsworth, 2016). In discontinuous approaches, the fractures are commonly regarded as discontinuities mechanically with a reduced dimensional model for fluid flow in the fractures, such as the approach developed by Fu et al. (2013). A detailed review on discontinuous approaches for hydraulic fracturing modeling was done by Lisjak and Grasselli (2014). The hybrid approaches include the coupling of conventional continuous and discontinuous methods, such as finite-discrete element method (FDEM, including ELFEN by Rockfield Software Ltd., 2004; Y-Geo by Munjiza, 2004; Latham et al., 2013) and more recently developed methods such as extended finite element method (XFEM, Salimzadeha and Khalilib, 2015), which allow fractures across solid elements. Among these approaches, continuous approaches remain to be a practical approach for modeling hydraulic fracturing involving a complex fracture network. The following advantages can be highlighted: (1) compared with discontinuous approaches, continuous approaches have the capability and high accuracy to represent the constitutive behavior for both the rock matrix

Hydraulic Fracture Modeling. https://doi.org/10.1016/B978-0-12-812998-2.00007-2

and the fractures and (2) compared with hybrid approaches, continuous approaches are more convenient and practical to deal with complex fracture networks because there is no need to update the topology for initiated fractures.

In this chapter we present and demonstrate the use of a continuous approach to model hydromechanics and hydraulic fracturing of complex fractured rock masses. This fracture continuum modeling approach is developed and applied within the framework of the FLAC3D geomechanical code (Itasca, 2012), or the TOUGH-FLAC coupled multiphase flow and geomechanical simulator (Rutqvist et al., 2002; Rutqvist, 2011). The basic idea of the fracture continuum approach is to map discrete fractures onto a fine numerical grid of continuum elements and modify the properties of those continuum elements adequately and as accurately as possible to represent the hydraulic and mechanical behavior of the fractures. In the next section, we will describe how this is done using FLAC3D and TOUGH-FLAC. Then we will demonstrate the use of the fracture continuum method for modeling hydromechanical behavior complex fractured rock, for modeling fracture propagation across geological features, and for modeling of a classical hydraulic fracturing stress measurement operation from a vertical well.

7.2 TOUGH-FLAC SIMULATOR AND FRACTURE CONTINUUM APPROACH

In this section we first introduce the TOUGH-FLAC simulator and thereafter the fracture continuum approach that is developed and applied within the framework of the FLAC3D and TOUGH-FLAC simulators.

7.2.1 TOUGH-FLAC Simulator

Hydraulic fracturing is a coupled hydromechanical process where the interaction of fluid flow and deformation is significant. The initiation of new fractures or opening/shearing of existing fractures dramatically changes the stress and pressure distribution and also the mechanical and hydraulic properties. This process involves direct and indirect couplings, as summarized and defined by Rutqvist and Stephansson (2003). To model coupled multiphase flow, heat transport, and geomechanics, the TOUGH-FLAC simulator was developed by Rutqvist et al. (2002) and later applied for the analysis of various geological activities, such as CO_2 geological storage, geothermal exploration, and nuclear waste disposal (Rutqvist, 2011, 2017). In this simulator, TOUGH2 (Pruess et al., 2012) is used for solving multiphase flow and heat transport equations, whereas FLAC3D (Itasca, 2012) is used for solving geomechanical stress−strain equations. The two codes are sequentially coupled and TOUGH-FLAC simulation runs seamlessly. A schematic of couplings between TOUGH2 and FLAC3D in TOUGH-FLAC is shown in Fig. 7.1.

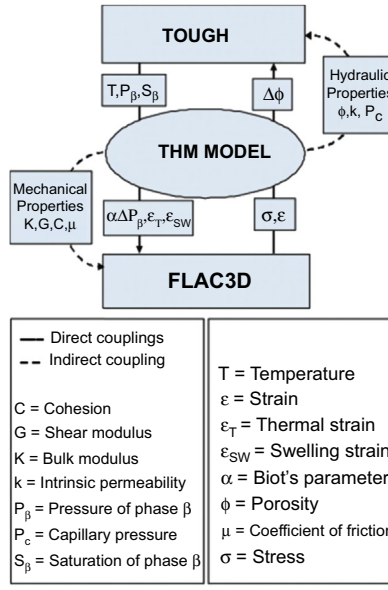

FIGURE 7.1 Schematic of linking TOUGH family code with FLAC3D for a coupled thermo–hydro–mechanical simulation (Rutqvist, 2011).

For fractured media, an empirical model has been applied to update permeability for changes in the three-dimensional stress field (e.g., Rutqvist et al., 2002). The arrow on the left side of Fig. 7.1 depicts the flow of data obtained from TOUGH (namely pressure P, temperature T, and phase saturations S_β) to FLAC3D for estimating their impact on the effective stress $\alpha\Delta P_\beta$ (α being Biot's effective stress parameter), as well as on thermal and swelling strains (ε_T and ε_{sw}, respectively). In addition, changes in P, T, and S_β may also result in changes in other mechanical properties, as listed in Fig. 7.1. These include bulk modulus K, shear modulus G, cohesion C, and coefficient of internal friction μ.

7.2.2 Fracture Continuum Approach

Natural fractures usually have complex and heterogeneous structures, with branching, damaged fracture surfaces, partially fracture filling, and maybe curved. A natural fracture across a rock mass is rarely a perfect plane or single-trace fracture. To represent such features of fractures, a fracture continuum model was developed. The initial development and application of such a fracture continuum model within the framework of TOUGH-FLAC was conducted for modeling coupled hydromechanical behavior of fractured rocks associated with nuclear waste disposal research (Rutqvist et al., 2009, 2013a).

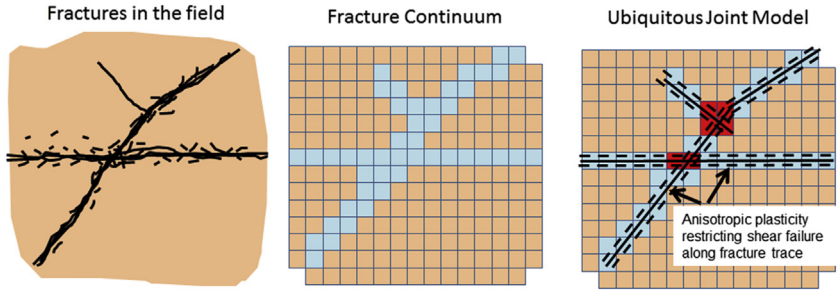

FIGURE 7.2 Concept of fracture continuum model of natural fractures and their intersections, and application of the ubiquitous joint model available in FLAC3D for fracture mechanical behavior.

As shown in Fig. 7.2, in this approach, the traces of fractures are mapped across continuum elements. From a hydraulic perspective, the fracture continuum model is able to capture the permeability along and across the fractures. Along a fracture, fluid flow might approximately obey the cubic relation between fracture aperture and flow transmissivity. Fluid storage within the fracture is associated with an equivalent void aperture that may be significantly impacted by damage and secondary microfractures of the fracture surfaces. In addition, fluid storage is impacted by the change in porosity due to mechanical deformation.

The fracture continuum model for hydraulic simulations has been incorporated in TOUGH2 previously using different techniques (e.g., Doughty et al., 2002). A simple approach in the case of a permeable fracture is to assign enhanced (isotropic) permeability to the continuum element according to

$$k_{FC} = k_{\text{matrix}} + k_{\text{fracture}} = k_{\text{matrix}} + \frac{b_h^3}{12d} \tag{7.1}$$

where b_h is the hydraulic conducting aperture of a fracture intersecting the continuum element and d represents the size (or width) of the continuum element. This is a simplification based on the cubic relation between the aperture of a single fracture and its flow transmissivity. Despite the simplifications in this formulation, it provides a reasonable conceptual model to link fracture stress and strain changes to permeability.

Related to mechanics of fractures, a simple approach is to consider the softening and weakening of elements that are intersected by a fracture. For example, the equivalent modulus, E_{FC}, of continuum fracture elements could be calculated as (Rutqvist et a., 2013a; Figueiredo et al., 2015)

$$\frac{1}{E_{FC}} = \frac{1}{E_R} + \frac{1}{k_n d} \tag{7.2}$$

where again d is the width of the continuum element, k_n is the fracture normal stiffness, and E_R is the Young's modulus of the intact rock matrix. Weakening

of the shear and tensile strength can be accommodated by reducing the shear strength (cohesion and coefficient of friction) and tensile (cutoff) strength based on the Mohr–Coulomb criterion. In a first-order approximation, an isotropic elastoplastic model with isotropic elastic tensor and isotropic Mohr-Coulomb criterion can be applied. Even in the case of isotropic elastoplasticity, large shear strain can only be accommodated within the weak elements lining up along the trace of a fracture. Similarly, substantial tensile strain after tensile failure can only be accommodated in the direction normal to the fracture trace. The capability of such a model to capture the shear offset displacement along a fracture was verified for modeling of shear reactivation of a larger-scale fault in Cappa and Rutqvist (2011). Another option is to utilize the transversely orthotropic elastoplastic constitutive model available in FLAC3D (Itasca, 2012). The FLAC3D ubiquitous joint model considers the isotropic strength of the matrix rock as well as shear and tensile strength of weak planes with given orientation. In this case, we can orient the weak planes in the ubiquitous joint model along the local fracture trace so that shear failure and tensile failure would only be initialized for the local fracture orientation (Fig. 7.2).

For hydromechanical coupling, various options may be considered for permeability changes, including relations between stress, strain, and permeability. For hydraulic fracturing applications, an approach developed by Rutqvist et at. (2012) can be used. Here the initiation and propagation of a fracture along a row of fracture continuum elements should be simulated. In Rutqvist et al. (2012), based on laboratory experiments with concrete, the concept of crack-opening displacement (COD) was employed (Fig. 7.3). In the application of the COD concept, a strain threshold for permeability, i.e., a threshold around which flow can permeate the fracture was considered. The fracture permeability is expressed as

$$k = k_0 + k_f = k_0 + A\left(\varepsilon_n - \varepsilon_n^t\right)^3 \tag{7.3}$$

where k_0 is the initial fracture permeability, A is a constant, and ε_n^t is a threshold strain related to the required COD for onset of permeability changes.

For proper modeling of intact rock undergoing tension or shear failure, Figueiredo et al. (2015) implemented and applied an elastic–brittle stress–strain relation, with the degradation of the mechanical properties of continuum elements undergoing failure by tension or shear. Such an elastic–brittle model captures localized failure in certain elements and disturbance of the local stress field, which may lead to progressive failure of surrounding elements (Fang and Harrison, 2002; Li et al., 2015). For the elements that undergo tensile or shear yielding, stiffness and strength properties are degraded according to a damage variable (Fig. 7.4). As an alternative to this approach, the strain-softening ubiquitous joint model in FLAC3D can be used

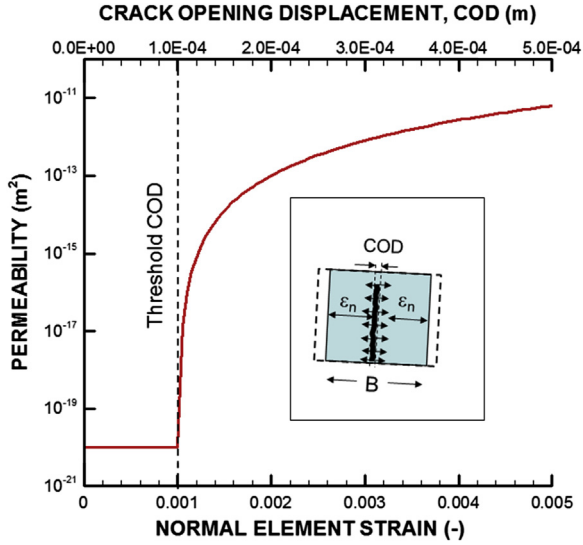

FIGURE 7.3 Relationship between crack-opening displacement and permeability during fracturing initiation. *Modified from Rutqvist, J., Kim, H.-M., Ryu, D.-W., Synn, J.-H., Song, W.-K., 2012. Modeling of coupled thermodynamic and geomechanical performance of underground compressed air energy storage in lined rock caverns. International Journal of Rock Mechanics & Mining Sciences 52, 71–81.*

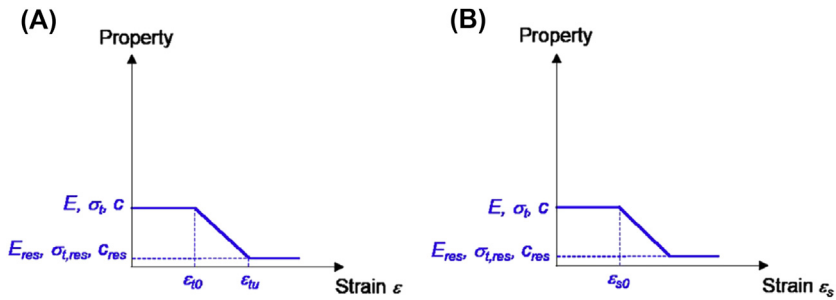

FIGURE 7.4 Degradation of the stiffness and strength properties for the failure elements of the intact rock by (A) tension and (B) shear: E, σ_t, and c are the initial values for elastic modulus, tensile strength, and cohesion, respectively; E_{res}, $\sigma_{t,res}$, and c_{res} are their residual values, respectively, ε_{t0} is the strain threshold of tension damage, ε_{tu} is the limit strain of tensile strength, and ε_{s0} is the strain threshold of shear damage (Figueiredo et al., 2015).

for modeling fluid-driven fracture propagation, by reducing the tensile strength as a function of plastic tensile strain (Rutqvist et al., 2015). With such an approach, the brittle to ductile or cohesive fracture behavior can be modeled simply by changing the plastic strain increment required for complete loss of tensile strength.

7.3 VERIFICATION AND DEMONSTRATION

In this section, we demonstrate the use of the fracture continuum method for modeling of (1) hydromechanical behavior complex fractured rocks, (2) fracture propagation across geological features, and (3) a classical hydraulic fracturing stress measurement operation, using either FLAC3D or the TOUGH-FLAC simulator.

7.3.1 Hydromechanics in Complex Fractured Rock

The continuum fracture model for modeling a complex rock mass was demonstrated in a number of theoretical studies in the international DECOVALEX (DEvelopment of COupled models and their VALidation against EXperiments) project (Rutqvist et al., 2009, 2013a). This project also involved code intercomparison, including comparison of simulation results for discontinuous and continuous methods of representing complex discrete fracture networks. The discontinuous methods were typically represented by distinct element method models, or by hydrological discrete fracture network models, with ad hoc geomechanics in the form of simplified stress analysis (Rutqvist et al., 2009, 2013a). Typically, for the models applied in those cases, the discontinuous models could represent discontinuous fracture behavior, but only for a subset of idealized straight fractures, and did not include damage to the intact rock between fractures. The continuum fracture models, on the other hand, could represent damage occurring in both fractures and intermediate intact rock bridges between fractures. Another advantage with continuum representation was its ability to easily represent curved fractures and detailed geometry of both large and small fractures.

In a DECOVALEX task related to the evolution of the excavation-disturbed zone (EDZ) around nuclear waste emplacement tunnels, TOUGH-FLAC with continuum fracture approach was applied (Rutqvist et al., 2009). The geometry of the fracture pattern was obtained from detailed fracture mappings near a drift at the Äspö Hard Rock Laboratory (HRL), Sweden. Fig. 7.5 shows the fracture pattern from field mapping and the representation in the TOUGH-FLAC continuum model. In the TOUGH-FLAC model, squares with 5 cm side length were used to form the mesh. Stress boundary conditions on the near-field model shown in Fig. 7.5(right) were derived from separate repository-scale thermo–hydro–mechanical simulation. A pragmatic approach to calculate damage-induced permeability changes in both the rock matrix and fractures was based on a strain-versus-permeability relation calibrated against field studies of EDZ at Äspö HRL. Fig. 7.5 shows the calculated permeability after excavation and 100 years of heating from heat-releasing nuclear waste package emplaced within the tunnel. After 100 years, strong thermal stress produced high deviatoric stress around the tunnel, leading to shear failure in both the fractures and matrix rock. As shown in Fig. 7.5, the permeability of

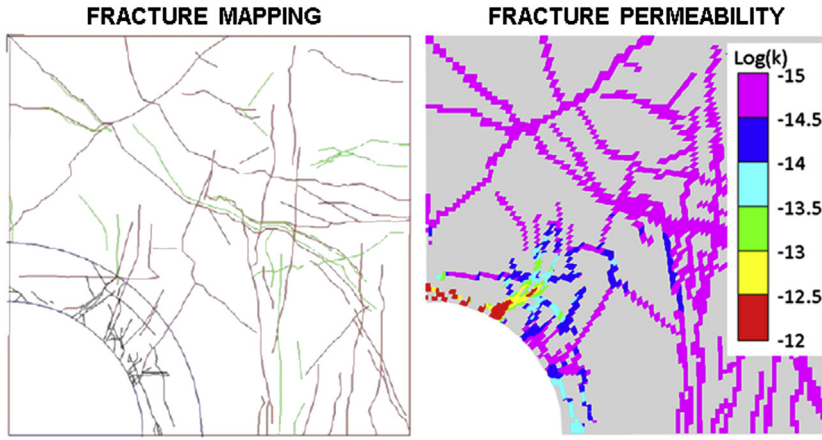

FIGURE 7.5 Modeling of fracture hydromechanics in a fracture rock mass surrounding a simulated nuclear waste emplacement tunnel. Fracture pattern developed based on fracture mapping at the Äspö Hard Rock Laboratory (left) and fracture continuum model with calculated fracture permeability after excavation and 100-years heating from the heat-releasing waste canister emplaced within the tunnel (right). *Modified from Rutqvist, J., Bäckström, A., Chijimatsu, M., Feng, X.-T., Pan, P.-Z., Hudson, J., Jing, L., Kobayashi, A., Koyama, T., Lee, H.-S., Huang, X.-H., Rinne, M., Shen, B., 2009. Multiple-code simulation study of the long-term EDZ evolution of geological nuclear waste repositories. Environmental Geology 57, 1313–1324.*

fractures was increased several orders of magnitude within the EDZ, especially on top of the tunnel.

In another DECOVALEX task, a 20×20 m model domain containing more than 7000 fractures was simulated. The task was to evaluate coupled thermo–hydro–mechanical–chemical processes, i.e., coupled hydromechanical changes in the fracture network during external loading and their effect on solute transport through the fractured media (Rutqvist et al., 2013a). By increasing the horizontal-to-vertical stress ratio from 1 to 5, the shear stress was increased across the model domain.

Here we will focus on some key aspects of this simulation to demonstrate some advantages of the fracture continuum approach. Using the fracture continuum modeling approach, it is straightforward to include an arbitrary number of fractures into the model as an element intersecting a fracture trace is simply flagged as a fracture element with different mechanical and hydraulic properties. Fig. 7.6 shows a model with a fracture network of 7767 fractures (Fig. 7.6, left) and another model in which fractures with length smaller than 2 m were neglected (Fig. 7.6, right). The model has 160,000 elements, and each element has a side length of 0.05 m. Fig. 7.7 shows shear strain and volumetric strain when the model is loaded at a horizontal-to-vertical stress ratio of 5, i.e., at high shear stress across the sample. The figure shows that if fractures less than 2 m long are neglected, very limited shearing occurs in a

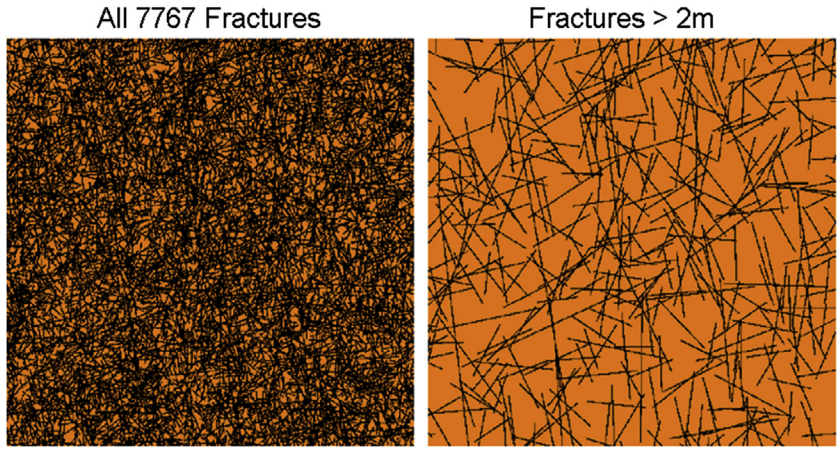

FIGURE 7.6 Fracture continuum model including all 7767 fractures (left) and a fracture continuum model in which fractures with trace length less than 2 m have been neglected (right).

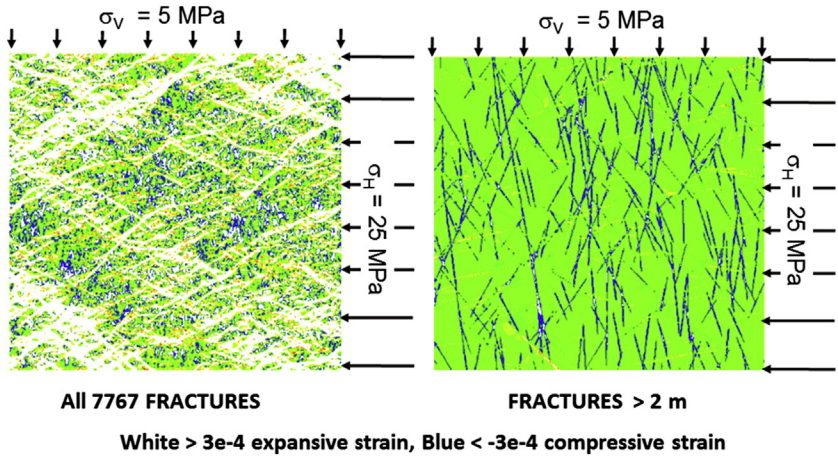

FIGURE 7.7 Simulation results of volumetric strain at a horizontal-to-vertical stress ratio of 5 when including all 7767 fractures (left) and when neglecting fractures of trace length less than 2 m (right). The left figure shows significant shear dilation (white areas) from shear failure and coalescence of sheared fractures, whereas the right figure with smaller fractures neglected shows mainly compression (blue [gray in print version]) of subvertical fractures and only limited shear dilation on some inclined fractures (yellow (white in print version)).

few optimally oriented fractures, whereas the dominant mode of fracture deformation is the closure of subvertical fractures. On the other hand, if all the fractures are included, distinct shear bands are formed with coalescence of shear failure along both large-scale and small-scale fractures. Within those shear bands, the volumetric strain shows expansion as a result of shear dilation. Thus, neglecting the small-scale fractures produces a completely different

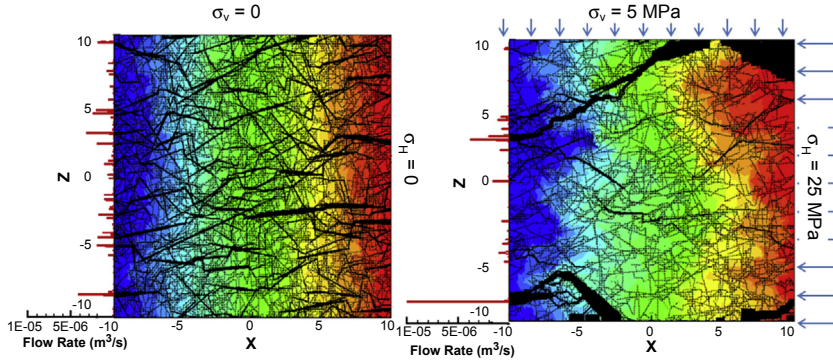

FIGURE 7.8 Simulation results of flow through fractured rock mass (7767 fractures) exposed to a hydraulic gradient under increased shear stress. The fluid pressure goes from 0.3 MPa (red [light gray in print version]) on the right boundary to 0.1 MPa (blue [dark gray in print version]) on the left boundary resulting in a pressure gradient of 10 kPa/m. The thickness of the black lines along each fracture is proportional to the mass flow rate to show channeling along large aperture fractures. Outflow distribution through the left boundary is plotted in a histogram for each numerical grid element along the boundary.

mechanical response that would lead to a fundamentally different response in permeability. When including all the fractures, the shearing causes distinct flow channeling as shown in Fig. 7.8. This behavior could not be captured if small-scale and dead-end fractures are neglected from the model.

This case of 7767 fractures within a 20 × 20 m model domain is a case of very densely fractured rock that, in practice, could be represented by an equivalent continuum model approach, or a combination where the larger throughgoing fractures are explicitly represented and fractured rock domains between those main fractures are represented by an equivalent continuum model. In Rutqvist et al. (2013a), this model domain was also represented by a dual-continuum approach using different element sizes in which the stress-dependent permeability was calculated using a crack-tensor model and a simplified approach for considering shear slip along fractures. The results were in reasonable good agreement with a discrete fracture model in terms of stress-dependent flow through the model domain. Thus, in this particular case either an equivalent continuum model or a discrete fracture model considering all fractures would be adequate, whereas a discrete fracture model simplified to only include fractures larger than 2 m would not be sufficient.

7.3.2 Fracture Propagation Across Discontinuities and Geological Layers

In this section, we use the fracture continuum model for modeling fracture propagation to study the effects of preexisting fractures, faults, and geological layers. The simulations are conducted using FLAC3D (Itasca, 2012), with an

elastic–brittle stress relation based on degradation of material properties (Fang and Harrison, 2002; Li et al., 2015) (Fig. 7.4).

7.3.2.1 Verification of the Model for Fracture Propagation

This section aims to verify the use of a continuum mechanics–based model to simulate the fracture propagation in intact rock with a single fracture. Here we test the continuum approach for modeling of the formation and propagation of wing cracks from a preexisting fracture and compare the numerical results with an analytical approximation in an infinite elastic medium and another numerical solution using displacement discontinuity method (DDM) by Mutlu and Pollard (2008). To study this case of fracture propagation, a rock domain with one fracture inclined at 45 degrees with the horizontal direction is considered, and differential boundary stresses S_H and S_h are applied (Fig. 7.9). The length f of the preexisting fracture is 2 m. The model is a square region with sides measuring 50 m. The mesh consists of 56,000 elements and is more refined in a square region around the fracture, where the elements are squares with sides of 0.05 m (Fig. 7.9). The Young's modulus and Poisson's ratio are 20 GPa and 0.2, respectively. The compressive maximum boundary stress S_H is

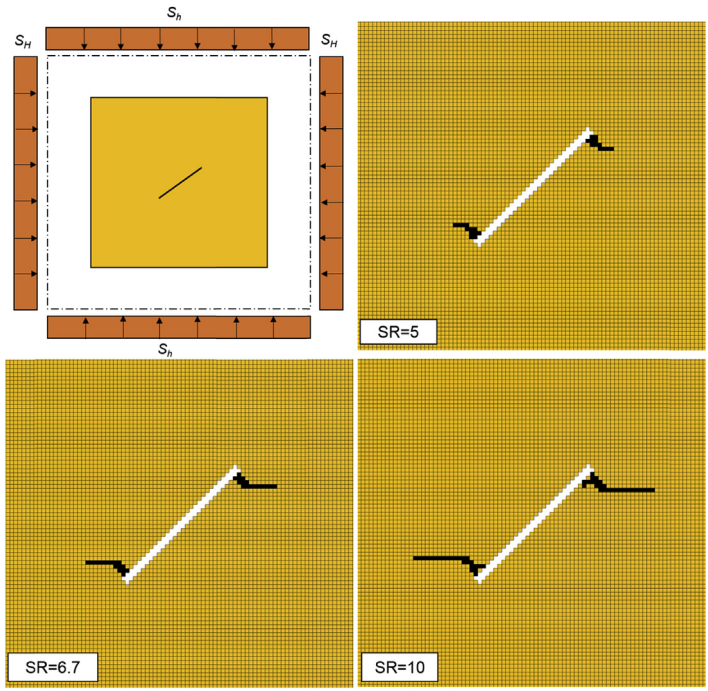

FIGURE 7.9 Results for a single fracture propagation with different stress regimes simulated by the continuum-based model.

40 MPa, and the stress ratios (*SRs*) between the maximum horizontal S_H and minimum horizontal S_h boundary stress are considered to be 4, 5, 6.7, and 10, respectively (Fig. 7.9).

Results for fracture propagation obtained with the continuum-based model for a stress ratio of 5, 6.7 and 10, are presented in Fig. 7.9. The figure shows that as expected the extent of fracture propagation increases with the ratio between the maximum and minimum boundary stresses. The figure shows that at the initiation of the wing cracks from the two ends of the preexisting fracture, the fracture propagation is not confined to a single row of elements because the wing cracks are curved. When the wing cracks have propagated a certain distance away from the preexisting fracture, the fracture propagation turns into a straight fracture in the direction perpendicular to the minimum principal stress. Fig. 7.10 shows a comparison of the length w of the fracture extension (wing cracks by tension), normalized by the half-length f of the fracture with that obtained by the analytical approximation and the DDM. The analytical results are obtained by assuming that the propagating fracture follows a straight path. They show that the ratio w/f given by the analytical approximation is less than that estimated from our model by about 0.08 for $SR = 4$, 0.07 for $SR = 5$, 0.02 for $SR = 6.7$, and 0.15 for $SR = 10$. These differences are not surprising because the analytical approximation is valid for a simplified case of straight wing cracks, whereas the numerical model simulates fracture propagation along a curved path. These differences are of the same order of magnitude as those observed between the analytical approximation for simplified straight wing cracks and the results of a 2D

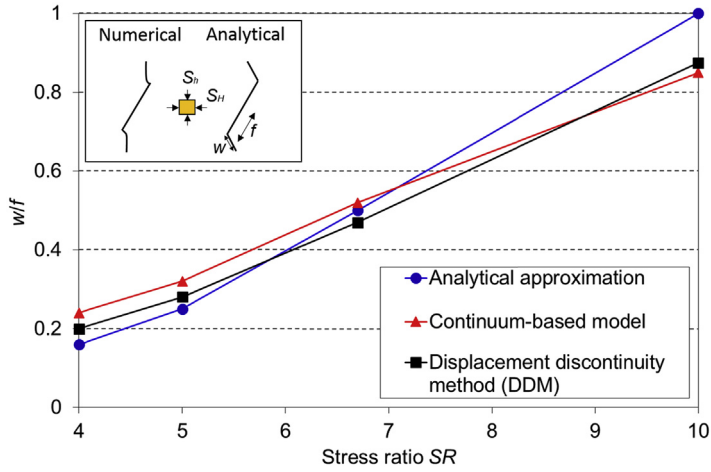

FIGURE 7.10 Variation of the dimensionless length w/f of the wing cracks as a function of the stress ratio (SR) between the maximum horizontal S_H and minimum horizontal S_h boundary stresses (below) (w/f is measured along the curved fracture propagation from the continuum mechanics–based model and the displacement discontinuity method, whereas it is measured along a straight path in the analytical approximation).

DDM, as illustrated in Fig. 7.10. The differences are acceptable because of the assumptions inherent to each numerical method. In the DDM method, the preexisting fracture, with zero thickness, is approximated with very short displacement discontinuity elements, and the intact rock is assumed to be elastic. In our continuum-based model with an elastic−brittle stress relation based on degradation of material properties, the mesh is orthogonal, the preexisting fracture is approximated by elements with a finite thickness, and initial and residual values for the tensile strength need to be assigned into the intact rock. These assumptions cause slight differences in the curvature of the wing crack, which in turn leads to slight differences in the wing crack length.

7.3.2.2 *The Effects of Nearby Fractures on Hydraulically Induced Fracture Propagation*

In this example, we study the effect of nearby fractures on hydraulic fracture propagation. For this example, two rock domains, FD1 and FD2, each with dimensions 50 × 50 m, were considered (Fig. 7.11). The rock domains FD1

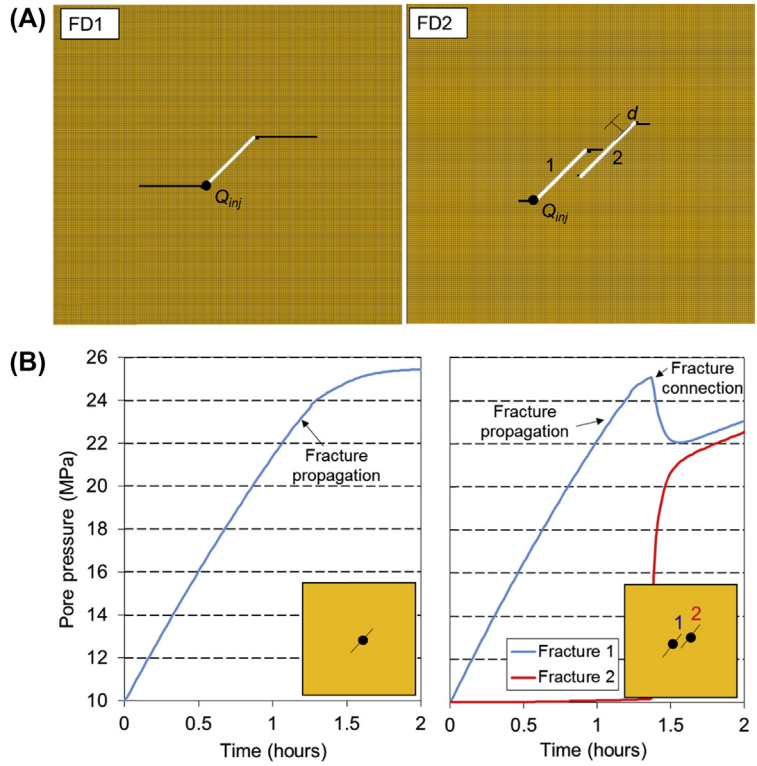

FIGURE 7.11 (A) Tension failure regions and (B) variation with time (hours) of the fluid pore pressure (MPa) in the center of fractures (results obtained for the rock domains FD1 [left] and FD2 [right]).

and FD2 are horizontal and include a single fracture and two fractures, respectively. The length of the fractures is 2 m. In FD2, the left-hand and right-hand side fractures are named 1 and 2, respectively, and the closest distance between them is 0.25 m. The fractures were assumed to be parallel with an angle of 45 degrees from the maximum principal stress direction, which is horizontal. The mesh and elastic parameters referred in Section 7.3.2.1 are used. The initial permeabilities of the fractures and intact rock are 4.5×10^{-14} m^2 and 10^{-18} m^2, respectively.

The rock domains FD1 and FD2 are assumed to be located at a depth of 1000 m. At this depth, the vertical stress is assumed to be 27 MPa and perpendicular to the rock domains. The minimum horizontal boundary stress S_h is equal to the vertical stress. The ratio between the maximum horizontal S_H and minimum horizontal S_h boundary stresses is 2. The initial fluid pore pressure is 10 MPa. Water is injected at a constant rate of $Q_{inj} = 4.0 \times 10^{-4}$ m^3/s in one borehole for 2 h. After 2 h, water injection is stopped, but simulation continues for another hour. The borehole is vertical (perpendicular to FD1 and FD2) and intersects the only fracture in FD1 and only fracture 1 on the left-hand side in FD2 (Fig. 7.11A). A 2D model with a 0.0025 m^3 grid block is considered. This pressurization rate enables reaching a maximum injection pressure of about 2.5 times the initial pore pressure. Fig. 7.11B shows the failure regions by tension in the intact rock for FD1 and FD2 rock domains after 2 h of injection and the variation of the fluid pore pressure with time in the center of the fractures.

In both rock domains, the fracture starts to propagate at a fluid pressure of approximately 23 MPa. This is when the tensile stress caused by fluid pressure increase exceeds the tensile strength of the intact rock around the fracture tip. As the fracture propagates, the permeability and porosity of the elements failed by tension increases. This leads to fluid penetration and pore pressure increase in adjacent elements, which, in turn, leads to tension failure in those elements. As observed in Fig. 7.11B, the evolution of fluid pressure in rock domains FD1 and FD2 is different because the FD2 involves connection of fracture 1 with fracture 2, which does not exist in FD1. There is also a significant difference in the propagation length. In FD2, fractures propagate much shorter because fracture 2 is inclined to the principal stress directions and has softer properties than those of the surrounding intact rock. In such a scenario, when the two fractures connect, the pore pressure decreases and becomes smaller than the minimum pressure necessary to continue propagating the fracture.

7.3.2.3 The Influence of Complex Geological Settings on Hydraulically Induced Fracture Propagation

In a second example, the influence of confining formations and preexisting geological settings (bedding plane, fault) on the hydraulically induced fracture propagation is studied. Fluid is injected in a 2-m-long vertical fracture in a

shale-gas reservoir. Initially, the injection fracture has similar permeability and stiffness as the surrounding shale formation but with no cohesion and tensile strength. The fracture is aligned with the maximum principal stress direction, which is vertical.

Three scenarios are considered. In scenario 1, a shale-gas reservoir with a thickness of 20 m located between two 15-m-thick confining formations is considered. In scenario 2, in addition to the previous scenario, one preexisting horizontal bedding plane located 1 m above the injection fracture upper tip is considered. In scenario 3, in addition to scenario 1, a preexisting fault with a dip angle of 60 degrees located near the injection fracture is considered. In scenario 3, the center of the preexisting fault is 1.0 m horizontally and 0.8 m vertically from the tip of the injection fracture (Fig. 7.12).

The rock domain is a 50 m × 50 m square region, with a thickness of 1 m. The shale-gas reservoir is located 2000 m deep. At this depth, the vertical stress is around 54 MPa. The ratio between the minimum horizontal boundary stress (in the plane of the rock domain) and the vertical stress is equal to 0.7. The initial pore pressure is 20 MPa. The elastic modulus is 30 GPa for the shale, confining formations, and bedding plane, and 5 GPa for the preexisting fault. With exception of the confining formations where the initial permeability is 10^{-16} m^2, the initial permeability is 10^{-19} m^2. Hydraulic fracturing stimulation is conducted by injecting water at a constant rate for 2 h. It is assumed that the borehole is horizontal, locates in the plane of the analyzed rock domain, and intersects the injection fracture in the shale-gas reservoir (Rutqvist et al., 2013b). Water is injected at a rate of 2×10^{-6} kg/s into each 0.04 m^3 grid block of the 2-m-long injection fracture. After 30-min injection,

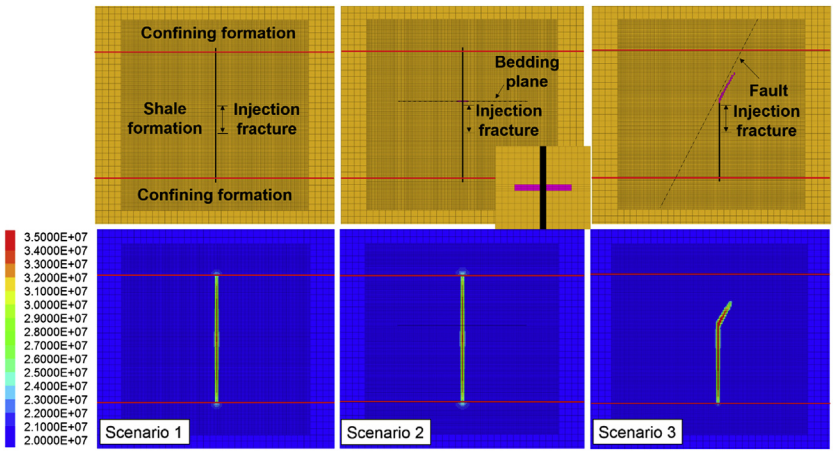

FIGURE 7.12 Failure regions (above) and pore pressure field (Pa) (below) at the end of the 2-h water injection (tension and shear failure regions are represented by the black and pink [gray in print version] colors, respectively).

the fluid pressure in the center of the injection fracture reaches as high as approximately 2.5 times the initial fluid pressure. After 2 h, water injection is stopped, but simulation of hydromechanical behavior continues for another hour.

The developed 2D FLAC3D (Itasca, 2012) model is used to study the coupled hydromechanical effects in scenarios 1, 2, and 3 as results of hydraulic fracturing stimulation (Figueiredo et al., 2017). The mesh consists of 24,100 elements and is more refined in a square region with 30 m side length around the injection fracture where the elements are squares with 0.20 m side length. A plane strain analysis was carried out. Fig. 7.12 shows the failure regions and fluid pressure field after 2 h of injection for scenarios 1, 2, and 3. The upper and lower limits of the shale reservoir are represented by two red lines. In all these scenarios, before the end of the injection period, the fracture reaches the confining formations. As those confining formations have an initial permeability three orders of magnitude larger than that of the shale formation, the pore pressure at the fracture tip decreases, and the fracture propagation is limited. After shutting in, the pore pressure decreases even more and the fracture practically does not propagate any longer.

Fig. 7.13 shows the evolution of the pore pressure at the center of the injection fracture (point 1) and at the intersection of the fault with the fracture (point 2). In Fig. 7.13, the dashed lines indicate the time at which the propagating fracture intersects with the preexisting bedding plane or the fault. The

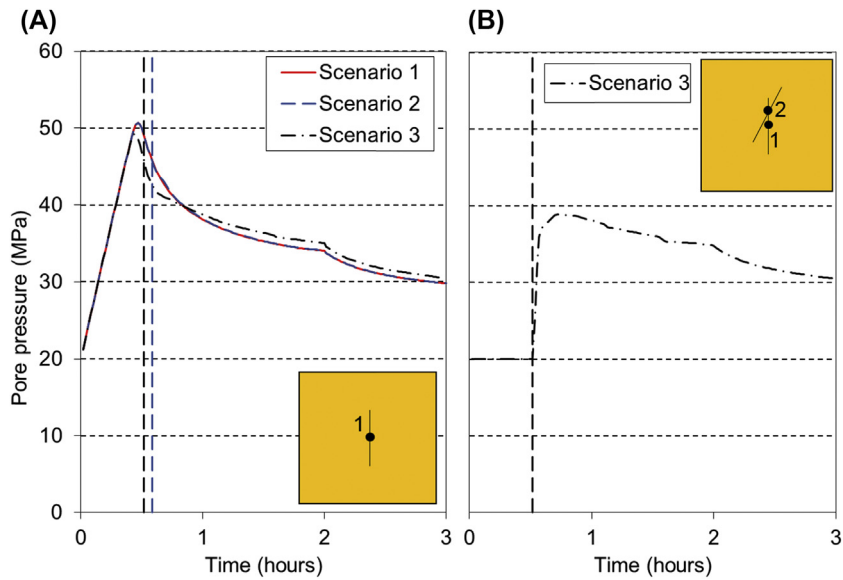

FIGURE 7.13 Evolution of pore pressure (MPa) in the (A) center of the injection fracture (point 1) and (B) the fault (point 2) in scenario 3.

simulation shows that the fracture propagation and pressure evolution are practically the same in scenarios 1 and 2, whereas some significant difference can be observed for scenario 3 due to the activation of the inclined fault. In scenario 2, the bedding plane does not significantly affect the results because the bedding plane is oriented perpendicular to the main propagating fracture and the shear displacement is not enough to cause a significant pore pressure decrease and arrest the propagating fracture. In scenario 3, when fracture propagation reaches the fault, shear failure occurs in the fault element at the intersection with the propagating fracture, and the fracture does not propagate beyond it. At this point, the pore pressure in the fault (point 2) increases abruptly from 20 MPa to approximately 37 MPa (Fig. 7.13). Because of changes in the fault permeability, the fluid flows more along the fault, leading to shear failure and dilation in the adjacent elements. After 2 h of injection, the length of the shear rupture zone in the fault is 5.1 m along the fault.

7.3.3 Classical Hydraulic Fracturing Stress Measurement Operation

Hydraulic fracturing is a classic method for in situ stress measurement (Rutqvist et al., 2000; Haimson and Cornet, 2003). Normally, several stages are involved, including fracture initiation from a well, fracture propagation driven by fluid pressure, fracture closure during shut-in, and fluid venting of the borehole. By using the continuum fracture modeling approach, it is possible to model all these stages. Starting from an intact borehole, tensile failure forms a hydraulic fracture, which subsequently propagates with continuous fluid injection. Here we demonstrate the approach of using the FLAC3D ubiquitous joint model for the fracture continuum with a strain-softening tensile strength. The aperture changes during the fracture propagating through the continuum mesh is based on the concept of COD, and it is related to the tensile strain normal to the fracture plane and the size of the element in a direction normal to the fracture plane (Fig. 7.3 and Eq. 7.3). The permeability is governed by a cubic relation between fracture aperture and fracture transmissivity. The variation of fracture aperture along with fracture propagation results in a change in fracture porosity that plays a critical role in determining the fluid storage within the fracture elements during fracture propagation. Such a problem involves strong pore−volume coupling between flow and mechanics. On the other hand, TOUGH-FLAC is based on sequential coupling between flow and mechanics. Therefore, it is critical to verify the model against analytical solutions of fluid-driven fracture growth.

To verify the model for fluid-driven fracture growth we conducted a simulation test against solutions based on the KGD model (Fig. 7.14). A rather coarse mesh was used with elements dedicated as fracture element with a size of 2×4 m. Despite the coarse model discretization with 4-m-long elements along the fracture, a good agreement was achieved with the KGD model

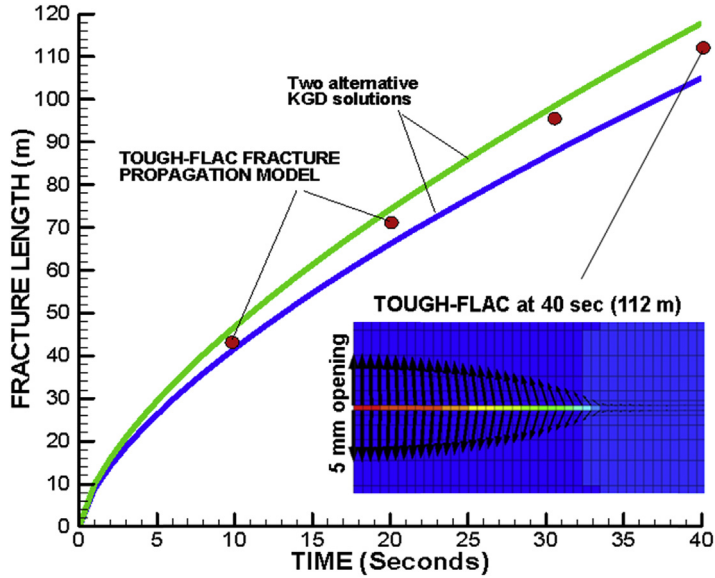

FIGURE 7.14 Verification of the fracture continuum model implemented in TOUGH-FLAC for modeling fluid-driven fracture propagation. Two alternative KGD solutions are plotted based on Fu et al. (2013). The insert of the model shows displacement vectors (black arrows) of grid nodes located above and below the fracture continuum elements after 40 s when the fracture is 112 m long.

solution. Two alternative KGD solutions are shown (Fu et al., 2013) and the TOUGH-FLAC numerical results fall between the two KGD solutions.

The fracture continuum model approach with TOUGH-FLAC is further demonstrated for 3D modeling of the breakdown cycle related to classical hydraulic fracturing stress measurement from a vertical borehole. The model is based on field hydraulic fracturing experiments that were conducted at the Kismet site in the Sanford Underground Research Laboratory, South Dakota (Oldenburg et al., 2017). The model is shown in Fig. 7.15, which is a 1/8 symmetric model of the full 3D experimental condition. Fig. 7.16 shows the borehole pressure evolution for simulation of a typical breakdown cycle of the hydraulic fracturing operation. A constant injection rate of 1.2 L/min is simulated (with 1/8 of this number in the 1/8th symmetric model). The permeability of the rock matrix is 1×10^{-21} m^2 and the Young's modulus is 77 MPa. The horizontal stress normal to the fracture was set to 20 MPa, and the stress parallel to the fracture was set to 40 MPa, based on the best estimation at the field site (Oldenburg et al., 2017). In the strain-softening model, the tensile strength is set to 1 MPa with a drop to zero tensile strength after a plastic tensile strain of 1×10^{-5}, which represents a brittle failure. It takes about 20 s to reach breakdown, which is signified by the onset of unstable fracture propagation. The injection then continues at a constant rate until 50 s, when the well is shut in. The simulated shut-in pressure is close to the

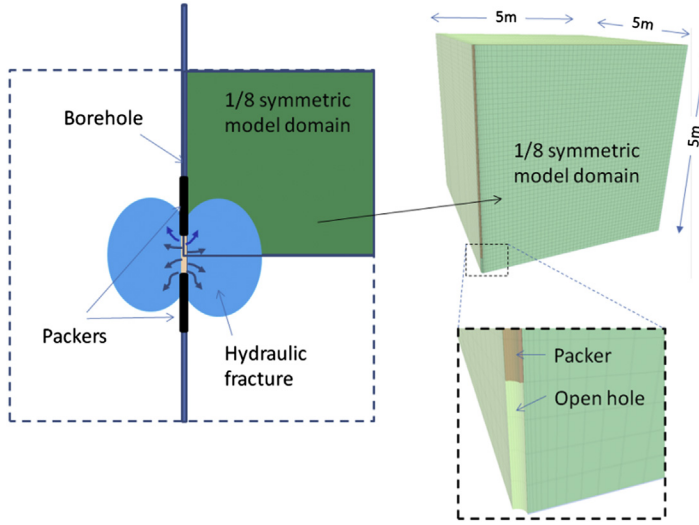

FIGURE 7.15 3D TOUGH-FLAC model grid for modeling classical hydraulic fracturing stress measurement from a vertical borehole. A 1/8th symmetric model is used in the actual simulations.

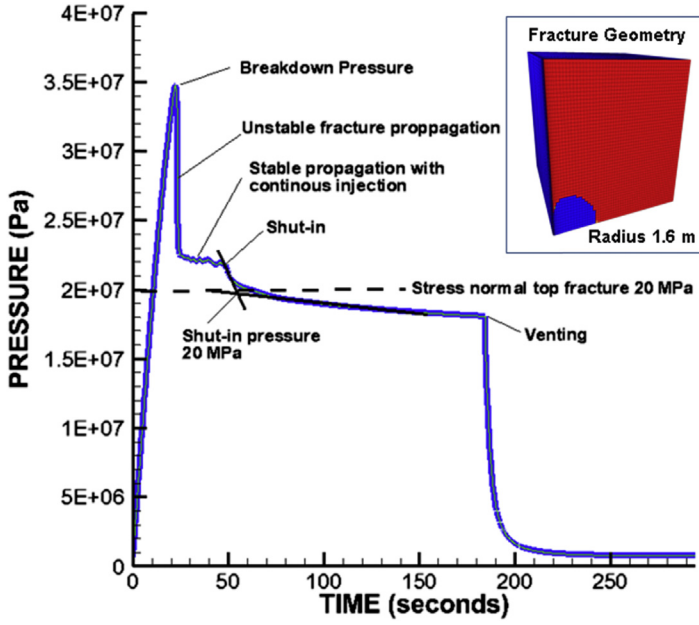

FIGURE 7.16 Results of TOUGH-FLAC modeling of the breakdown cycle related to a classical hydraulic fracturing stress measurement from the vertical borehole. The fracture continuum elements are 5 mm thick in this case. The model insert shows the fracture geometry at the end of the simulation.

theoretical value of 20 MPa as this value should be close to the stress normal to the fracture. After 190 s, the pressure in the well is released and the fracture is vented for reopening cycle. Fig. 7.16 also shows the extent of the fracture at the end of the simulation. The fracture has propagated to a radius of about 1.6 m. The fracture could be propagated longer in a subsequent fracture reopening sequence of a hydraulic fracturing stress measurement operation. However, if much longer than 1.6 m radius, the fracture would become relatively large compared with the domain size, and the numerical results could be affected by outer boundaries.

7.4 CONCLUDING REMARKS

Continuous approaches are practical for modeling fractures and hydraulic fracturing because of their capability to represent complex fracture geometry and constitutive behavior and their convenience to represent complex fracture networks without the need to update the topology. In this chapter, we presented and demonstrated a continuous approach, i.e., a fracture continuum approach, to model hydraulic fracturing of complex fractured rock masses with coupled hydromechanical effects. The fracture continuum approach was here developed and applied within the framework of the FLAC3D geomechanical code (Itasca, 2012) and the coupled multiphase flow and geomechanical simulator TOUGH-FLAC (Rutqvist et al., 2002; Rutqvist, 2011). This approach is relatively simple to implement and it is practical for discretization of complex fractured rock masses, including curvature of fractures, dense intersections of fractures, and dead-end fractures. The creation of new fractures and their propagation is accommodated through the existing mesh. Based on this continuum fracture approach, we presented examples involving coupled hydromechanical analysis for complex fractured rock masses and fracture propagation in 2D and 3D, respectively. From our simulations, we showed that neglecting the small-scale or dead-end fractures (such as frequently employed in discontinuous modeling) may produce a completely different mechanical response that would lead to a fundamentally different response in fluid flow. Our simulations of fracture propagation show the great impact of rock mass heterogeneities, far from the ideal case of homogeneous rock. Finally, the applicability of the present fracture continuum approach for realistic 3D fracture propagation at the meter-scale was demonstrated.

For modeling larger-scale fractured rock masses, e.g., kilometer-scale, it will not be possible to discretize all small-scale fractures. Therefore, an equivalent continuum approach may be more practical, although dominant discrete flow features could still be accommodated in the continuum approach, for example, major faults (e.g., Rutqvist et al., 2016; Jeanne et al., 2014). Still, the fracture continuum approach is an approximation of the real discontinuous behavior of fractures. Like any other numerical methods, the fracture continuum approach requires fine discretization to capture details of the complex

fracture network and stresses around the propagating fractures. An alternative promising approach for unified discontinuous and continuous modeling of hydromechanical behavior in fractured rock has recently been suggested by Hu et al. (2017), based on the numerical manifold method.

ACKNOWLEDGMENTS

The authors gratefully acknowledge financial support from the U.S. Department of Energy to the Lawrence Berkeley National Laboratory under contract No. DE-AC02-05CH11231 and from the Swedish Geological Survey (SGU), grant number 1724, and the EU project, grant number 640979, to the Uppsala University.

REFERENCES

Cappa, F., Rutqvist, J., 2011. Modeling of coupled deformation and permeability evolution during fault reactivation induced by deep underground injection of CO_2. International Journal of Greenhouse Gas Control 5, 336–346.

Chau, V.T., Bažant, Z.P., Su, Y., 2016. Growth model for large branched three-dimensional hydraulic crack system in gas or oil shale. Philosophical Transactions of the Royal Society A 374, 20150418.

Doughty, C., Salve, R., Wang, J.S.Y., 2002. Liquid-release tests in unsaturated fractured welded tuffs: II. Numerical modeling. Journal of Hydrology 256, 80–105.

Fang, Z., Harrison, J.P., 2002. Development of a local degradation approach to the modeling of brittle fracture in heterogeneous rocks. International Journal of Rock Mechanics and Mining Sciences 39, 443–457.

Figueiredo, B., Tsang, C.F., Rutqvist, J., Niemj, A., 2017. Study of hydraulic fracturing processes in shale formations with complex geological settings. Journal of Petroleum Science and Engineering 152, 361–374.

Figueiredo, B., Tsang, C.F., Rutqvist, J., Niemi, A., 2015. A Numerical study of changes in deep fractured rock permeability due to coupled hydro-mechanical effects. International Journal of Rock Mechanics & Mining Sciences 79, 70–85.

Fu, P., Johnson, S.M., Carrigan, C.R., 2013. An explicitly coupled hydro-geomechanical model for simulating hydraulic fracturing in arbitrary discrete fracture networks. International Journal for Numerical and Analytical Methods in Geomechanics 37, 2278–2300.

Gan, Q., Elsworth, D., 2016. A continuum model for coupled stress and fluid flow in discrete fracture networks. Geomechanics and Geophysics for Geo-Energy and Geo-Resources 2, 43–61.

Haimson, B.C., Cornet, F.H., 2003. ISRM Suggested methods for rock stress estimation—Part 3: hydraulic fracturing (HF) and/or hydraulic testing of pre-existing fractures (HTPF). International Journal of Rock Mechanics & Mining Sciences 40, 1011–1020.

Hu, M., Rutqvist, J., Wang, Y., 2017. A numerical manifold method model for analyzing fully coupled hydro-mechanical processes in porous rock masses with discrete fractures. Advances in Water Resources 102, 111–126.

Itasca, 2012. FLAC3D, Version 5.0. User's Manual. Itasca Consulting Group, Minneapolis.

Jeanne, P., Rutqvist, J., Hartline, C., Garcia, J., Dobson, P.F., Walters, M., 2014. Reservoir structure and properties from geomechanical modeling and microseismicity analyses associated with an enhanced geothermal system at the Geysers, California. Geothermics 51, 460–469.

Latham, J.-P., Xiang, J., Belayneh, M., Nick, H.M., Tsang, C.F., Blunt, M.J., 2013. Modelling stress-dependent permeability in fractured rock including effects of propagating and bending fractures. International Journal of Rock Mechanics and Mining Sciences 57, 100−112.

Li, L., Tang, C., Li, G., Wang, S., Liang, Z., Zhang, Y., 2012. Numerical simulation of 3D hydraulic fracturing based on an improved flow-stress-damage model and a parallel FEM technique. Rock Mechanics and Rock Engineering 45 (5), 801−818.

Li, Y., Zhou, H., Zhu, W., Li, S., Liu, J., 2015. Numerical study of crack propagation in brittle joined rock mass influenced by fracture water pressure. Nature Materials 8, 3364−3376.

Lisjak, A., Grasselli, G., 2014. A review of discrete modeling techniques for fracturing processes in discontinuous rock masses. Journal of Rock Mechanics and Geotechnical Engineering 6 (4), 301−314.

Munjiza, A., 2004. The Combined Finite-discrete Element Method. John Wiley & Sons Ltd., Chichester, UK.

Mutlu, O., Pollard, D., 2008. On the patterns of wing crack along an outcrop scale flaw: a numerical modeling approach using complementarity. Journal of Geophysical Research 113, B06403. https://doi.org/10.1029/2007JB005284.

Oldenburg, et al., 2017. Hydraulic fracturing experiments at 1500 m Depthin a deep mine: highlights from the kISMET project. In: Proceedings, 42nd Workshop on Geothermal Reservoir Engineering, Stanford University, Stanford, California, February 13-15, 2017. SGP-TR-212.

Pogacnik, J., Elsworth, D., O'Sullivan, M., O'Sullivan, J., 2016. A damage mechanics approach to the simulation of hydraulic fracturing/shearing around a geothermal injection well. Computers & Geotechnics 71, 338−351.

Pruess, K., Oldenburg, C., Moridis, G., 2012. TOUGH2 User's Guide, Version 2.1, LBNL-43134 (Revised). Lawrence Berkeley National Laboratory, Berkeley, California.

Rockfield Software Ltd., 2004. ELFEN 2D/3D Numerical Modelling Package. Rockfield Software Ltd., Swansea, UK.

Rutqvist, J., 2011. Status of the TOUGH-FLAC simulator and recent applications related to coupled fluid flow and crustal deformations. Computers and Geosciences 37 (6), 739−750.

Rutqvist, J., 2017. An overview of TOUGH-based geomechanics models. Computers & Geosciences 108, 56−63.

Rutqvist, J., Stephansson, O., 2003. The role of hydromechanical coupling in fractured rock engineering. Hydrogeology Journal 11 (1), 7−40.

Rutqvist, J., Stephansson, O., Tsang, C.-F., 2000. Uncertainty in estimate of maximum principal stress from hydraulic fracturing due to the presence of the induced fracture. International Journal of Rock Mechanics and Mining Sciences 37, 107−120.

Rutqvist, J., Wu, Y.-S., Tsang, C.-F., Bodvarsson, G., 2002. A modeling approach for analysis of coupled multiphase fluid flow, heat transfer, and deformation in fractured porous rock. International Journal of Rock Mechanics and Mining Sciences 39 (4), 429−442.

Rutqvist, J., Bäckström, A., Chijimatsu, M., Feng, X.-T., Pan, P.-Z., Hudson, J., Jing, L., Kobayashi, A., Koyama, T., Lee, H.-S., Huang, X.-H., Rinne, M., Shen, B., 2009. Multiple-code simulation study of the long-term EDZ evolution of geological nuclear waste repositories. Environmental Geology 57, 1313−1324.

Rutqvist, J., Kim, H.-M., Ryu, D.-W., Synn, J.-H., Song, W.-K., 2012. Modeling of coupled thermodynamic and geomechanical performance of underground compressed air energy storage in lined rock caverns. International Journal of Rock Mechanics & Mining Sciences 52, 71−81.

Rutqvist, J., Leung, C., Hoch, A., Wang, Y., Wang, Z., 2013a. Linked multicontinuum and crack tensor approach for modeling of coupled geomechanics, fluid flow and transport in fractured rock. International Journal of Rock Mechanics and Geotechnical Engineering 5, 18–31.

Rutqvist, J., Rinaldi, A.P., Cappa, F., Moridis, G.J., 2013b. Modeling of fault reactivation and induced seismicity during hydraulic fracturing of shale-gas reservoirs. Journal of Petroleum Science and Engineering 107, 31–44.

Rutqvist, J., Rinaldi, A.P., Cappa, F., Moridis, G.J., 2015. Modeling of fault activation and seismicity by injection directly into a fault zone associated with hydraulic fracturing of shale-gas reservoirs. Journal of Petroleum Science and Engineering 127, 377–386.

Rutqvist, J., Rinaldi, A.P., Cappa, F., Jeanne, P., Mazzoldi, A., Urpi, L., Guglielmi, Y., Vilarrasa, V., 2016. Fault activation and induced seismicity in geologic carbon storage—Lessons learned from recent modeling studies. Journal of Rock Mechanics and Geotechnical Engineering 8, 775–966.

Salimzadeha, S., Khalilib, N., 2015. A three-phase XFEM model for hydraulic fracturing with cohesive crack propagation. Computers and Geotechnics 69, 82–92.

Wangen, M., 2013. Finite element modeling of hydraulic fracturing in 3D. Computers & Geosciences 17, 647–659.

Chapter 8

Development of a Hydraulic Fracturing Simulator for Single-Well Fracturing Design in Unconventional Reservoirs

Philip H. Winterfeld, Yu-Shu Wu
Colorado School of Mines, Golden, CO, United States

8.1 INTRODUCTION

One of the earliest hydraulic fracturing simulators was formulated by Perkins and Kern (1961), who applied the plane strain crack solution by Sneddon (1946) to obtain the PK (Perkins−Kern) model. This model was later extended by Nordgren (1972) and was called the PKN (Perkins−Kern−Nordgren) model. Khristianovic and Zheltov (1955) and Geertsma and de Klerk (1969) both developed the KGD (Khristianovic−Geertsma−de Klerk) model. The PKN model is applicable to long fractures with constant height and elliptical cross section; the KGD model is applicable to short fractures under plane strain. These simple models were subsequently modified, for example, their extension to power law fluids (Daneshy, 1973). Later models (Mack and Warpinski, 2000) include pseudo three-dimensional models, an extension of the work of Simonson et al. (1978) to multiple layers. These models consist of cell-based and lumped ones. In the lumped models, the fracture vertical cross section consists of two half-ellipses whose dimensions change according to the amount of fluid in the fracture. In the cell-based models, the fracture is represented as a series of series of PKN-like cells that have varying height. Planar three-dimensional models represent the fracture as a two-dimensional grid that may be fixed or moving. The fracture is planar and perpendicular to the minimum stress direction. In general,A three-dimensional models, the planar fracture requirement is relaxed and the fracture may be truly three-dimensional.

Hydraulic Fracture Modeling. https://doi.org/10.1016/B978-0-12-812998-2.00008-4

We present here a general three-dimensional hydraulic fracturing model that accounts for fluid flow and heat transfer in the wellbore and the rock mechanics of fracturing including fracture initiation, growth, and propagation, as well as fluid flow and heat transfer in the fracture. The model is capable of simulating multiple fractures that would occur during fracturing of a horizontal well in an unconventional reservoir and includes geomechanical effects such as the stress shadow effect, the effect on fracture growth from superposition of induced stresses by near-by fractures. In future work, we will couple this model to a reservoir model to optimize fracturing as well as production after fracturing has occurred.

8.2 FRACTURE FLUID CHARACTERIZATION

The slurry used in hydraulic fracturing contains a mixture of fluid and solid species. The fluid species consist mostly of water with some additives, such as gels, surfactants, cross-linkers, friction reducers, and breakers that effect fluid rheology, and others with a variety of purposes such as inhibitors, acids, biocides, and corrosion inhibitors. The solid species, called proppants, are added to stop the newly formed fractures from closing completely by forming a rigid, porous medium at a sufficiently large volume fraction. The permeability of this porous proppant medium depends on factors such as proppant roundness and grain size. Because produced fluid will be flowing through this medium, its permeability should be maximized.

In the analysis that follows, we consider the slurry to be composed of conserved proppant and fluid components. A proppant component would generally correspond to single proppant species; a fluid component could be any mixture of the above fluid species, namely water plus a number of additives. Two important physical properties of slurry are density and viscosity. The slurry density, ρ_{sl}, is a weighted sum of the solid and fluid component densities:

$$\rho_{sl} = \sum_p c_p \rho_p + \left(1 - \sum_p c_p\right) \sum_f x_f \rho_f \tag{8.1}$$

where subscripts p and f refer to proppant and fluid components, respectively, c is proppant component volume fraction, ρ is density, and x is fluid component volume fraction in the fluid portion of slurry. The proppant component density is constant and the fluid component is slightly compressible:

$$\rho_f = \rho_{f,0}(1 + C_f(P - P_{\text{ref}})) \tag{8.2}$$

where ρ_{f0} is fluid component density at reference pressure, P_{ref}, and C_f is fluid component compressibility.

Slurry viscosity, μ_{sl}, has contributions from fluid and proppant components. This dependence is often expressed as the fluid viscosity, μ_{fl},

multiplied by a correction factor, $f(c_p)$, which is a function of proppant volume fraction:

$$\mu_{sl} = \mu_{fl} f(c_p) \tag{8.3}$$

A number of expressions have appeared in the literature for these corrections; one example, from Nicodemo et al. (1974), is an exponential relation:

$$\mu_{sl} = \mu_{fl} \left(1 - \frac{\sum_p c_p}{c_{\max}} \right)^{-n} \tag{8.4}$$

where $c_{\max}$ is the proppant volume fraction at which slurry is a rigid porous medium and n is an exponent typically between 1.0 and 2.5. The viscosity of the fluid portion of slurry depends on fluid component volume fraction and fluid component viscosity, μ_f:

$$\mu_{fl} = \mu_{fl}(\mu_f, x_f) \tag{8.5}$$

One common fluid viscosity expression is the exponentially weighted product shown below:

$$\mu_{fl} = \prod_f \mu_f^{x_f} \tag{8.6}$$

Fracture fluid component viscosity may be Newtonian, power law, or others. The effective viscosity of a power law fluid depends on shear rate and increases without bound for decreasing shear rate. Actual fluids exhibit power law behavior only for a range of shear rates and transition to Newtonian behavior at sufficiently low shear rates. When a fracture fluid component is specified as power law, this maximum Newtonian viscosity parameter is input in addition to the usual parameters that describe a power-law fluid, the flow consistency index, and flow behavior index.

8.3 FRACTURE MASS CONSERVATION EQUATIONS

The general mass balance for a conserved, flowing species is:

$$\nabla \cdot (\rho \vec{v}) + \frac{\partial \rho}{\partial t} + q = 0 \tag{8.7}$$

where $\mathrm{v}\rightarrow$ is velocity and q is the source/sink term. We consider a fracture to be a thin slit in the Cartesian y-direction and integrate Eq. (8.7) over that width to yield:

$$\frac{\partial}{\partial x}(\rho \vec{v} w) + \frac{\partial}{\partial z}(\rho \vec{v} w) + \frac{\partial (\rho w)}{\partial t} + q = 0 \tag{8.8}$$

where w is the fracture width and other terms, such as density and velocity, are understood to be averages over the fracture width.

Slurry fluid and proppant components are conserved. A version of Eq. (8.8) for a fluid component is obtained by defining the fluid mass per unit volume as the product of fluid density and fluid component volume fraction in the overall fluid volume, and defining the fluid velocity as the fluid superficial velocity averaged over the fracture width. The source/sink terms consist of fluid leak-off, the flow of fluid through the porous fracture wall, and flow of fluid between the completed zones along the wellbore (the surroundings) and the fracture. Then:

$$\frac{\partial}{\partial x}\left[\rho_f x_f\left(1-\sum_p c_p\right)\overrightarrow{v_{fl}}w\right]+\frac{\partial}{\partial z}\left[\rho_f x_f\left(1-\sum_p c_p\right)\overrightarrow{v_{fl}}w\right] +\frac{\partial}{\partial t}\left[\rho_f x_f\left(1-\sum_p c_p\right)w\right]+\rho_f x_f q_{\text{leak}}+\rho_f x_f\left(1-\sum_p c_p\right)q_{\text{surr}}=0 \tag{8.9}$$

where subscript leak refers to fluid leak-off and subscript surr refers to the surroundings.

A version of Eq. (8.8) for a proppant component is obtained by defining the proppant mass per unit volume as the product of proppant grain density and proppant volume fraction, and defining the proppant velocity as the proppant superficial velocity averaged over the fracture width. Unlike fluid, proppant velocity does vary for each proppant component. In addition, proppant does not leak off through the fracture face, so the term leak in Eq. (8.9) is absent. Then:

$$\frac{\partial}{\partial x}\left(\rho_p c_p\overrightarrow{v_p}w\right)+\frac{\partial}{\partial z}\left(\rho_p c_p\overrightarrow{v_p}w\right)+\frac{\partial}{\partial t}\left(\rho_p c_p w\right)+\rho_p c_p q_{\text{surr}}=0 \tag{8.10}$$

Proppant is assumed to be incompressible. Because a fracture occupies a relatively small depth range, we consider fluid component density in Eq. (8.10) as constant. Then, Eqs. (8.9) and (8.10) become:

$$\frac{\partial}{\partial x}\left[x_f\left(1-\sum_p c_p\right)\overrightarrow{v_{fl}}w\right]+\frac{\partial}{\partial z}\left[x_f\left(1-\sum_p c_p\right)\overrightarrow{v_{fl}}w\right] +\frac{\partial}{\partial t}\left[x_f\left(1-\sum_p c_p\right)w\right]+x_f q_{\text{leak}}+x_f\left(1-\sum_p c_p\right)q_{\text{surr}}=0 \tag{8.11}$$

and

$$\frac{\partial}{\partial x}\left(c_p\overrightarrow{v_p}w\right)+\frac{\partial}{\partial y}\left(c_p\overrightarrow{v_p}w\right)+\frac{\partial}{\partial t}\left(c_p w\right)+c_p q_{\text{surr}}=0 \tag{8.12}$$

If we sum Eq. (8.11) over fluid components, Eq. (8.12) over proppant components, and add the results together, we obtain an overall slurry conservation equation:

$$\frac{\partial}{\partial x}\left[\left(1-\sum_p c_p\right)\overrightarrow{v_f}+\sum_p c_p\overrightarrow{v_p}\right]w+\frac{\partial}{\partial z}\left[\left(1-\sum_p c_p\right)\overrightarrow{v_f}+\sum_p c_p\overrightarrow{v_p}\right]w + \frac{\partial w}{\partial t}+q_{\text{leak}}+q_{\text{surr}}=0 \tag{8.13}$$

We equate the coefficient of w in the length derivatives to the slurry velocity, a weighted sum of fluid and proppant velocities:

$$\overrightarrow{v_{sl}}=\left(1-\sum_p c_p\right)\overrightarrow{v_{fl}}+\sum_p c_p\overrightarrow{v_p} \tag{8.14}$$

Eq. (8.13) then becomes:

$$\frac{\partial}{\partial x}(\overrightarrow{v_{sl}}w)+\frac{\partial}{\partial z}(\overrightarrow{v_{sl}}w)+\frac{\partial w}{\partial t}+q_{\text{leak}}+q_{\text{surr}}=0 \tag{8.15}$$

Slurry velocity is assumed to be that for laminar flow of a fluid through a slit of width w:

$$\overrightarrow{v_{sl}}=-\frac{w^2}{12\mu_{sl}}\nabla(P+\gamma_{sl}z) \tag{8.16}$$

where P is the fracture pressure and γ_{sl} is the slurry gradient. For fluid rheology other than Newtonian, the slurry viscosity in Eq. (8.16) is considered to be an effective one.

Proppant component and fluid velocities generally differ because proppant is denser than fluid and consists of discrete granules that can interact with each other and with the fracture wall. Proppant z-direction velocity is the sum of the slurry velocity plus a proppant settling velocity that accounts for the difference in fluid and proppant component densities:

$$v_{p,z}=v_{sl}+v_{p,\text{stl}} \tag{8.17}$$

where $v_{p,z}$ is proppant component velocity and $v_{p,\text{stl}}$ is proppant component settling velocity. Proppant settling velocity is based on Stoke's law, which gives the terminal velocity of a sphere in an infinite fluid, and correction factors that account for other effects. Stoke's law is:

$$v_{p,\text{stokes}}=\frac{(\rho_p-\rho_{fl})gd_p^2}{18\mu_{fl}} \tag{8.18}$$

where $v_{p,\text{stokes}}$ is the Stoke's velocity and d_p is the proppant grain diameter. One example of corrections for other effects is from the work of Friehauf (2009), who presents modifications to Stoke's law that account for inertial effects, the effect of interfering proppant particles, and the effect of the fracture wall. These modifications to Stoke's law result in a proppant settling velocity that has the following form:

$$v_{p,\text{stl}} = v_{p,\text{stokes}} f_1(N_{\text{Re}}) f_2(c_p) f_3(w) \tag{8.19}$$

where N_{Re} is Reynold's Number, $f_1(N_{\text{Re}})$ captures inertial effects, $f_2(c_p)$ captures the effect of interfering proppant particles, and $f_3(w)$ captures the effect of the fracture wall. These expressions, modified for the presence of multiple proppant components, are:

$$f_1(N_{\text{Re}}) = \frac{0.3736\mu_{fl}^{0.57}}{\rho_{fl}^{0.29}\left(\rho_p - \rho_{fl}\right)^{0.29} d_p^{0.86}} \tag{8.20}$$

$$f_2(c_p) = -5.9\left(\sum_p c_p\right)^3 + 8.8\left(\sum_p c_p\right)^2 - 4.8\left(\sum_p c_p\right) + 1 \tag{8.21}$$

$$f_3(w) = 0.563\left(\frac{d_p}{w}\right)^2 - 1.563\left(\frac{d_p}{w}\right) + 1 \tag{8.22}$$

For the direction perpendicular to the gravity vector, the proppant velocity is effected by the fracture wall and other proppant particles. Friehauf (2009) modified this velocity by introducing a multiplicative retardation factor for the slurry velocity that accounts for both of these:

$$v_{p,x} = f_{\text{ret}}(c_p, w) v_{sl,x} \tag{8.23}$$

This multiplicative factor is given by:

$$f_{\text{ret}}(c_p, w) = 1 + \left(\frac{d_p}{w_c}\right) - 2.02\left(\frac{d_p}{w_c}\right)^2 \tag{8.24}$$

and

$$\frac{1}{w_c^2} = 1.411\left(\frac{1}{d_p^2} - \frac{1}{w^2}\right)\left(\sum_p c_p\right)^{0.8} \tag{8.25}$$

Fluid velocity is then obtained from slurry velocity and proppant velocity by rearranging Eq. (8.14):

$$\vec{v}_{fl} = \frac{\vec{v}_{sl} - \sum_p c_p \vec{v}_p}{\left(1 - \sum_p c_p\right)} \tag{8.26}$$

8.4 FRACTURE ENERGY EQUATION

The general energy balance for a conserved, flowing species that takes into account advection and conduction is:

$$\nabla \cdot \left(\rho \overline{h} \overrightarrow{v}\right) + K\nabla^2 T + \frac{\partial \rho \overline{u}}{\partial t} + q_e = 0 \tag{8.27}$$

where K is thermal conductivity, $\overline{h}$ is specific enthalpy, $\overline{u}$ is specific internal energy, and q_e is the energy source/sink term. As we did for fracture flow, we consider the fracture to be a thin slit in the Cartesian y-direction and integrate Eq. (8.27) over that width to yield:

$$\frac{\partial}{\partial x}\left(\rho \overline{h} \overrightarrow{v}\right)_{sl} w + \frac{\partial}{\partial z}\left(\rho \overline{h} \overrightarrow{v}\right)_{sl} w + \frac{\partial (\rho \overline{u})_{sl} w}{\partial t} + q_{\text{cond}} + q_{\text{leak}} \sum_f x_f \rho_f \overline{h}_f + q_{e,\text{surr}} = 0 \tag{8.28}$$

We neglect conduction except for heat loss per unit area through the fracture faces, denoted by q_{cond}. The surroundings (surr) term accounts for energy transport resulting from flow of slurry between the fracture and the surroundings.

Specific enthalpy and internal energy are dependent on slurry composition:

$$\overline{h}_{sl} = \sum_p c_p \overline{h}_p + \left(1 - \sum_p c_p\right) \sum_f x_f \overline{h}_f \tag{8.29}$$

and

$$\overline{u}_{sl} = \sum_p c_p \overline{u}_p + \left(1 - \sum_p c_p\right) \sum_f x_f \overline{u}_f \tag{8.30}$$

where $\overline{h}_i$ and $\overline{u}_i$ are proppant or fluid component specific enthalpy and internal energy, respectively. Specific enthalpy and internal energy are assumed to be equal and given by:

$$\overline{h}_x = \overline{u}_x = C_x(T - T_{\text{ref}}), \quad x = p,f \tag{8.31}$$

where C is the conserved species heat capacity. The heat loss per unit area through the fracture faces is formulated as being heat loss through a semi-infinite medium. This heat loss is given by:

$$q_{\text{cond}} = 2\sqrt{\frac{K_{\text{res}} \rho_{\text{res}} C_{\text{res}}}{\pi(t - \tau)}}(T - T_{\text{res}}) \tag{8.32}$$

where K_{res} is reservoir thermal conductivity, ρ_{res} is reservoir density, C_{res} is reservoir heat capacity, and τ is the time that heat loss commences from that area of the fracture face.

8.5 FRACTURE MECHANICS EQUATIONS

In this section, we consider fracture mechanics, the determination of fracture width and the fracture extension criterion. The slurry in a fracture exerts a force on the fracture wall (the fracture pressure) that is opposed by the stress exerted by the reservoir (the minimum principal stress). The fracture width is dependent on the difference between those two forces, the net pressure. Our fracture width equation is based on the solution for the deflection caused by a load distributed over the boundary of a semiinfinite elastic medium, presented by Timoshenko and Goodier (1951):

$$u(\overrightarrow{r}) = \int_A \frac{(1-\upsilon^2)}{\pi E r} P_{\text{net}} dA \tag{8.33}$$

where u is the deflection, E is Young's modulus, ν is Poisson's ratio, P_{net} is the applied load, and A is the area the load acts on.

We insert a factor of 2 into Eq. (8.33) because the fracture consists of two identical faces, each of which is a deflection that is described by Eq. (8.33). The fracture is finite in area with the width vanishing at the fracture boundary. Because Eq. (8.33) yields a width profile over an infinite plane, we assume the fracture width is zero everywhere outside the fracture face. This zero-width condition is imposed by a hypothetical net pressure acting on the area outside the fracture. Then:

$$w(\overrightarrow{r} \in F) = \int_{\overrightarrow{r} \in F} \frac{2(1-\upsilon^2)}{\pi E r} (P_f - \sigma_{\min}) dA + \int_{\overrightarrow{r} \notin F} \frac{2(1-\upsilon^2)}{\pi E r} P_{\text{net}} dA \tag{8.34}$$

and

$$w(\overrightarrow{r} \notin F) = \int_{\overrightarrow{r} \in F} \frac{2(1-\upsilon^2)}{\pi E r} (P_f - \sigma_{\min}) dA + \int_{\overrightarrow{r} \notin F} \frac{2(1-\upsilon^2)}{\pi E r} P_{\text{net}} dA = 0 \tag{8.35}$$

where F is the fracture face area, P_f is the fracture pressure, $\sigma_{\min}$ is the minimum principal stress, and P_{net} is the net pressure acting outside of the fracture area.

Continued injection of fluid into a fracture causes the fracture width to increase and the fracture to extend. The criterion for fracture extension is obtained from the stress intensity factor at the fracture tip, given by Yew (1997) as:

$$K_I = \frac{E}{8(1-\upsilon^2)} \left(\frac{2\pi}{r}\right)^{\frac{1}{2}} w_{fr}(r) \tag{8.36}$$

where K_I is the stress intensity factor at the fracture tip and r is the inward normal distance from the fracture front. The movement of the fracture front is given as a front velocity that has the form (Mastrojannis et al., 1980):

$$v = C_{\text{ext}}\left(\frac{K_I - K_{IC}}{K_{IC}}\right)^n \tag{8.37}$$

where C_{ext} and n are parameters that depend on the medium and K_{IC} is rock toughness, a rock property.

8.6 FLUID LEAK-OFF FORMULATION

The higher fracture pressure relative to the permeable reservoir pressure causes fluid to leak off from the fracture into the reservoir. A fluid leak-off formulation that is widely used in hydraulic fracturing simulation has been outlined by Schechter (1992). Fluid leak-off occurs through a composite of three regions: a growing filter cake region at the fracture wall, a growing invaded zone starting at the fracture wall, and an infinite region of compressible fluid in the reservoir or formation, as illustrated in Fig. 8.1.

A fluid flow formulation is developed for each of these regions, and the results are combined to yield an overall fluid loss coefficient. For the Compressed Formation Fluids Zone, there is single-phase flow of a slightly compressible fluid in a semiinfinite medium, and the fluid velocity, v_N, at the surface of the medium is given by:

$$v_N = \sqrt{\frac{\phi_{\text{res}} k_{\text{res}} \beta_{\text{res}}}{\pi \mu_{\text{res}}}}\,\frac{P_I - P_R}{\sqrt{t-\tau}} = \alpha_c \frac{P_I - P_R}{\sqrt{t-\tau}} \tag{8.38}$$

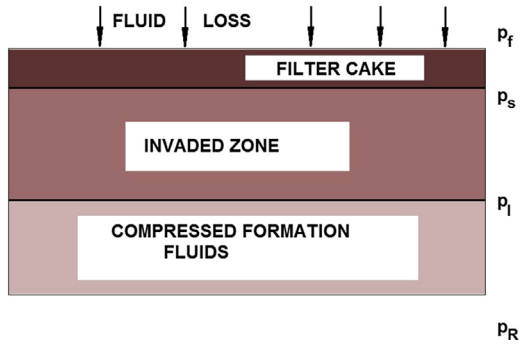

FIGURE 8.1 Illustration of zones for leak-off model. *From Schechter, R.S., 1992. Oil Well Stimulation. Prentice Hall, Englewood Cliffs, NJ.*

where the subscript res refers to the reservoir, β is compressibility, τ is the time leak-off commences, and the pressures are defined in Fig. 8.1. For the Invaded Zone, the fluid velocity obeys Darcy's law and the zone grows as fluid enters it. The fluid velocity in the Invaded Zone is given by:

$$v_N = \sqrt{\frac{\phi_{\text{res}} k_{\text{res}} (P_S - P_I + P_{\text{cap}})}{2\mu_{\text{res}}(t-\tau)}} = \alpha_v \sqrt{\frac{(P_S - P_I + P_{\text{cap}})}{t-\tau}} \tag{8.39}$$

where P_{cap} is the capillary pressure between the invading fluid and the reservoir fluid. For the filter cake zone, the fluid velocity is given by:

$$v_N = \alpha_w \sqrt{\frac{P_f - P_S}{t-\tau}} \tag{8.40}$$

where α_w is related to the slope, m_w, of a plot of filtrate volume versus the square root of time, which is usually obtained in the laboratory:

$$m_w = 2\alpha_w \sqrt{P_f - P_s} \tag{8.41}$$

The velocities in Eqs. (8.38)–(8.40) are all equal, and these equations are combined by summing their respective pressure drops. Then, fluid leak-off velocity is related to time and an overall leak-off coefficient:

$$v_N = \frac{C_{\text{leak}}}{\sqrt{t-\tau}} \tag{8.42}$$

where

$$C_{\text{leak}} = \frac{-\frac{1}{\alpha_c \Delta P} + \sqrt{\left(\frac{1}{\alpha_c \Delta P}\right)^2 + 4\left(\frac{1}{\alpha_v^2 \Delta P} + \frac{1}{\alpha_w^2 \Delta P}\right)}}{2\left(\frac{1}{\alpha_v^2 \Delta P} + \frac{1}{\alpha_w^2 \Delta P}\right)} \tag{8.43}$$

and

$$\Delta P = P_f - P_R + P_{\text{cap}} \tag{8.44}$$

8.7 WELLBORE MASS, FLOW, AND ENERGY EQUATIONS

Slurry, injected at the surface, traverses the wellbore before entering the fractures (or before fracture initiation, leaking off into the porous formation). In this section, we formulate the mass and energy conservation equations that govern fluid and heat flow in the wellbore.

We represent the wellbore as a series of connected well segments that follow the well trajectory. We define a global three-dimensional Cartesian coordinate system where the x-direction points east and the y-direction points

north. Each well segment has a starting and ending measured depth and true vertical depth, and an azimuth angle that is measured clockwise from the y-axis. Given a well segment starting at point i and ending at point $i+1$, the relationships between Cartesian coordinates and well trajectory measurements are:

$$x_{i+1} = x_i + \sqrt{(MD_{i+1} - MD_i)^2 - (TVD_{i+1} - TVD_i)^2}\sin(\theta_i) \tag{8.45}$$

and

$$y_{i+1} = y_i + \sqrt{(MD_{i+1} - MD_i)^2 - (TVD_{i+1} - TVD_i)^2}\cos(\theta_i) \tag{8.46}$$

and

$$z_{i+1} = z_i + (TVD_{i+1} - TVD_i) \tag{8.47}$$

where θ_i is the well segment azimuth angle, TVD refers to true vertical depth, and MD refers to measured depth.

Each well segment has constant outer and inner radii that define an annulus through which slurry flows. We represent slurry flow as flow of a series of slurry segments that travel through the wellbore in a pistonlike manner. Each slurry segment is composed of a single fluid and proppant component. The proppant component is incompressible and the fluid component is slightly compressible with density given by Eq. (8.2). Fig. 8.2 shows a schematic of a wellbore. There are two well segments, one originating at the wellhead, point 3, and extending to point 2, and the other originating at point 2 and extending to the wellbore bottom, point 1. There are three slurry segments in the wellbore whose boundaries are denoted by S_i. The numbering of these slurry segment boundaries starts at one, the wellbore bottom, and increases as the wellbore is traversed toward the wellhead, with the last segment boundary being S_{N+1},

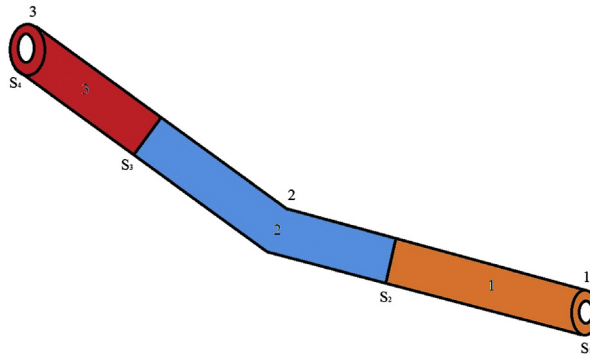

FIGURE 8.2 Schematic of a wellbore with two wellbore segments and three slurry segments.

located at the wellhead, where N is the number of slurry segments. Slurry is injected into the wellbore at the wellhead and leaves the wellbore through completed intervals along it. This slurry either flows into the fractures or is lost to the formation. As slurry is injected into the wellbore, the locations of the slurry segment boundaries change with time with the exception of the wellbore bottom and the wellhead, which are fixed.

A mass balance for the fluid or proppant component in slurry segment i is:

$$\frac{\partial}{\partial t}\left(\int_{S_{i+1}}^{S_i} A\rho_j x_j dS\right) + \int_{S_{i+1}}^{S_i} T_{ws}\rho_j x_j (P_w - P_{\text{surr}}) dS - \delta_{iN} q_{\text{inj}} \rho_j x_j = 0, \;\; j = f, p \tag{8.48}$$

where A is the annular area for slurry flow, x denotes component volume fraction, T_{ws} is transmissibility per unit length for slurry loss to the surroundings, P_w is wellbore pressure, P_{surr} is surroundings pressure, and q_{inj} is slurry injection rate, which applies only to slurry segment N via the Kronecker delta. The subscripts f and p refer to the well segment fluid and proppant components, respectively. The transmissibility per unit length for slurry loss to the surroundings is only nonzero along completed intervals.

The pressure along the wellbore has frictional and gravitational components and is obtained from:

$$\frac{\partial P_w}{\partial S} = \left(\rho_f x_f + \rho_p x_p\right)\overline{g}\cdot\widehat{S} + \frac{\partial P_{w,\text{fric}}}{\partial S} \tag{8.49}$$

where $\overline{g}$ is the gravitational vector and $\widehat{S}$ is the unit vector along the wellbore trajectory. The frictional portion of the pressure gradient, $P_{w,\text{fric}}$, is obtained from a correlation that is a function of slurry composition and wellbore geometry. One example is the well-known friction factor:

$$\frac{\partial P_{w,\text{fric}}}{\partial S} = \frac{4f}{D_h}\left(\rho_f x_f + \rho_p x_p\right) v_{sl}^2 \tag{8.50}$$

where f is friction factor and D_h is hydraulic diameter. Friction factor is correlated with Reynold's number. For laminar flow, friction factor is $16/N_{\text{Re}}$ and correlations for turbulent flow include the Colebrook equation:

$$\frac{1}{\sqrt{f}} = -2\log_{10}\left(\frac{\varepsilon}{3.7D_h} + \frac{2.51}{N_{\text{Re}}\sqrt{f}}\right) \tag{8.51}$$

where ε is pipe roughness, and a relation given by Valko and Economides (1995):

$$\begin{aligned}\ln(f) = {} & 28.135 + (-29.379 \\ & + (8.2405 - 0.86227\ln(\ln(N_{\text{Re}})))\ln(\ln(N_{\text{Re}})))\ln(\ln(N_{\text{Re}}))\end{aligned} \tag{8.52}$$

In addition, an equation given by Lord and McGowan (1986) relates friction pressure to pipe diameter and volumetric flow rate and gives results similar to the Colebrook equation for smooth pipe:

$$\frac{\partial P_{w,\text{fric}}}{\partial S} = -8.7623 \cdot D^{-4.8} q^{1.8} \tag{8.53}$$

where D is pipe diameter and quantities are in SI units.

An energy balance for a slurry segment is:

$$\begin{gathered}\frac{\partial}{\partial t}\left(\int_{S_{i+1}}^{S_i} A\left(\rho_f x_f \overline{u}_f + \rho_p x_p \overline{u}_p\right) dS\right) + \int_{S_{i+1}}^{S_i} T_{ws}\left(\rho_f x_f \overline{h}_p + \rho_p x_p \overline{h}_p\right) \\ (P_w - P_s) dS - \delta_{iN} q_{\text{inj}}\left(\rho_f x_f \overline{h}_f + \rho_p x_p \overline{h}_p\right) + \int_{S_{i+1}}^{S_i} \pi D_o q_{\text{loss}} dS = 0\end{gathered} \tag{8.54}$$

where q_{loss} is the rate of heat loss per unit area from the slurry to the surroundings and D_o is the outer wellbore diameter for fluid flow. Heat loss from the slurry to the surroundings is conceptualized as heat flow through a series of uniform concentric media. For example, heat can flow first through the outer wellbore casing, then through the cement, and finally into the formation, which is considered to extend to infinity. We derive an expression for this heat loss through concentric media. The temperature profile for transient heat flow through a uniform infinite medium with a point heat source at the origin is:

$$T(r,t) - T_\infty = \frac{Q_0}{4\pi k_{th}} E_1\left(\frac{\alpha_{th} r^2}{4(t-\tau)}\right) \tag{8.55}$$

and the heat flow, Q, at any radius and time is:

$$Q = Q_0 e^{-\left(\frac{\alpha_{th} r^2}{4(t-\tau)}\right)} \tag{8.56}$$

where k_{th} is thermal conductivity, α_{th} is thermal diffusivity, Q_0 is heat source magnitude (per unit length), τ is the time at which the heat source is activated, and E_1 is the exponential integral function. For steady-state heat flow through a uniform annulus, the temperature difference is given by:

$$T_i - T_{i+1} = \frac{Q_{ss}}{2\pi k_{th,i}} \ln\left(\frac{r_{i+1}}{r_i}\right) \tag{8.57}$$

where Q_{ss} is the steady-state heat flow (per unit length). We consider N uniform annular composite media with the last extending to infinity, as shown in Fig. 8.3. Initially, all composites are at the ambient reservoir temperature, T_∞. The innermost composite (numbered as 1 in Fig. 8.3) is initially heated. At first, this heat flow is approximated as that through an infinite medium and there is no heat flow through the other composites; at a sufficiently later time, heat flow

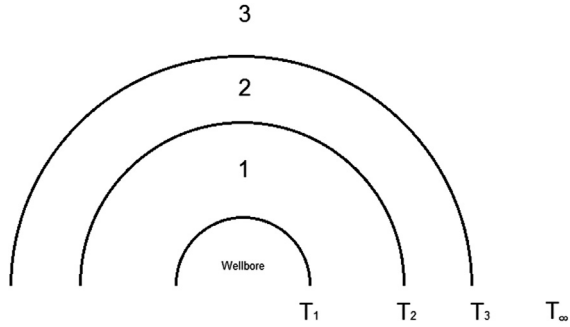

FIGURE 8.3 Schematic of a wellbore surrounded by two finite composite media and a third infinite-extending one.

through this composite transitions to the steady-state approximation and transient heat flow starts to occur through the next composite (numbered as 2 in Fig. 8.3). This process continues until all inner composites are at steady state; the outer infinite-extending composite, of course, never reaches steady state.

We derive an overall heat transfer coefficient for this composite medium. Heat flow through composites numbered 1 through j is assumed to be steady state and heat flow through composite $j+1$ is assumed to be transient. Eq. (8.57) gives the temperature difference for each of the j steady state composites. Eq. (8.55) gives the temperature difference for the transient composite, $j+1$. The temperature at the inner boundary of composite $j+1$ equals that of the outer boundary of composite j; we set the heat source magnitude of infinitely acting composite $j+1$ to the value that would equal the steady-state heat flow at the composite j outer boundary. Then, the temperature difference across composite $j+1$ becomes:

$$T_{j+1} - T_\infty = \frac{Q_{ss} e^{\left(\frac{\alpha_{th,j+1} r_{j+1}^2}{4(t-\tau_{j+1})}\right)}}{4\pi k_{th,j+1}} E_1\left(\frac{\alpha_{th,j+1} r_{j+1}^2}{4(t-\tau_{j+1})}\right) \tag{8.58}$$

Summing Eq. (8.57) from 1 to j and adding Eq. (8.58) yields a relationship between the wellbore heat loss, Q (with the *ss* subscript dropped), and the temperature difference between the wellbore slurry (inner boundary of composite 1) and the ambient reservoir:

$$T_1 - T_\infty = Q\left\{\sum_{i=1}^{j} \frac{1}{2\pi k_{th,i}} \ln\left(\frac{r_{i+1}}{r_i}\right) + \frac{e^{\left(\frac{\alpha_{th,j+1} r_{j+1}^2}{4(t-\tau_{j+1})}\right)}}{4\pi k_{th,j+1}} E_1\left(\frac{\alpha_{th,j+1} r_{j+1}^2}{4(t-\tau_{j+1})}\right)\right\} \tag{8.59}$$

The transition of a composite from transient to steady-state heat flow occurs when the ratio of the transient temperature difference to the steady state one equals a characteristic temperature ratio that is smaller than 1 (chosen to be 0.8 in practice):

$$\frac{T_j - T_{j+1}|_{\text{trans}}}{T_j - T_{j+1}|_{ss}} = \frac{e^{z_j^2} E_1\left(\frac{\alpha_j r_j^2}{4(t-\tau_j)}\right) - e^{z_{j+1}^2} E_1\left(\frac{\alpha_j r_{j+1}^2}{4(t-\tau_j)}\right)}{2\ln\left(\frac{r_{j+1}}{r_j}\right)} = \varepsilon_{\text{rat}} \qquad (8.60)$$

where ε_{rat} is the characteristic temperature ratio.

8.8 STRESS SHADOW EFFECT

The fracture width depends on the net pressure, the difference between the fracture pressure and the minimum principal stress. The presence of a fracture induces a stress in the nearby formation that is proportional to the net pressure. This induced stress can affect the opening of nearby fractures because it is superposed on the ambient stress field and changes the minimum stress magnitude and direction nearby. This induced stress phenomenon is referred to as the stress shadow effect.

An estimation of the stress shadow effect was done by Warpinski and Branagan (1989) using the solution, derived by Sneddon (1946), for the stress field around an infinitely long, two-dimensional crack in a homogeneous, isotropic elastic material. To apply this solution to our simulator, we first define a local coordinate system (l,m,n) where the crack is oriented along the m-direction, the direction normal to the crack plane is the n-direction, and the direction along the infinite crack length is the l-direction, as shown in Fig. 8.4. In addition, the n-direction axis intersects the midpoint of the m-direction

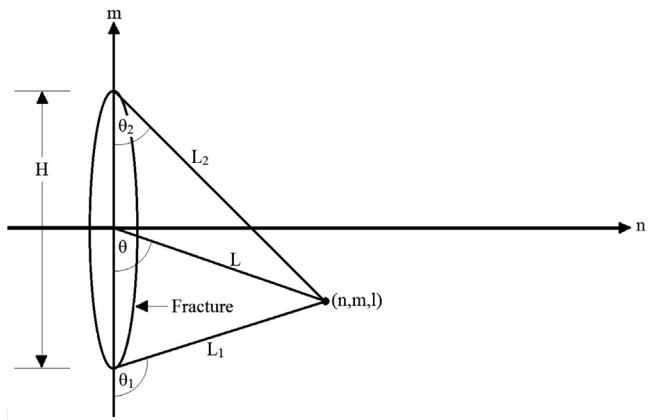

FIGURE 8.4 Schematic of two-dimensional fracture with parameter definitions for stress shadow calculation. The l-coordinate is perpendicular to the figure plane.

crack height. The transformation of this coordinate system to our global coordinate system is obtained from the n-direction unit vector, given by:

$$\widehat{n} = n_x\widehat{i} + n_y\widehat{j} + n_z\widehat{k} \tag{8.61}$$

The l-direction is defined as having no gravity, so the unit vector in the l-direction is obtained from:

$$\widehat{l} = \widehat{n} \times \widehat{k} = \det\begin{vmatrix} \widehat{i} & \widehat{j} & \widehat{k} \\ n_x & n_y & n_z \\ 0 & 0 & 1 \end{vmatrix} = \frac{n_y\widehat{i} - n_x\widehat{j}}{\sqrt{n_x^2 + n_y^2}} \tag{8.62}$$

Finally, the m-direction is orthogonal to the l-direction and the n-direction:

$$\begin{aligned} \widehat{m} = \widehat{l} \times \widehat{n} &= \det\begin{vmatrix} \widehat{i} & \widehat{j} & \widehat{k} \\ \dfrac{-n_y}{\sqrt{n_x^2 + n_y^2}} & \dfrac{n_x}{\sqrt{n_x^2 + n_y^2}} & 0 \\ n_x & n_y & n_z \end{vmatrix} \\ &= \frac{\dfrac{n_x n_z\widehat{i}}{\sqrt{n_x^2 + n_y^2}} + \dfrac{n_y n_z\widehat{j}}{\sqrt{n_x^2 + n_y^2}} - \dfrac{\left(n_x^2 + n_y^2\right)\widehat{k}}{\sqrt{n_x^2 + n_y^2}}}{\sqrt{n_x^2 + n_y^2 + n_z^2}} \end{aligned} \tag{8.63}$$

The transformation from global to local coordinates is then:

$$\begin{bmatrix} \dfrac{n_x n_z}{\sqrt{n_x^2 + n_y^2}\sqrt{n_x^2 + n_y^2 + n_z^2}} & \dfrac{n_y n_z}{\sqrt{n_x^2 + n_y^2}\sqrt{n_x^2 + n_y^2 + n_z^2}} & -\dfrac{\left(n_x^2 + n_y^2\right)}{\sqrt{n_x^2 + n_y^2}\sqrt{n_x^2 + n_y^2 + n_z^2}} \\ \dfrac{n_y}{\sqrt{n_x^2 + n_y^2}} & -\dfrac{n_x}{\sqrt{n_x^2 + n_y^2}} & 0 \\ n_x & n_y & n_z \end{bmatrix} \begin{bmatrix} \widehat{i} \\ \widehat{j} \\ \widehat{k} \end{bmatrix} = \begin{bmatrix} \widehat{l} \\ \widehat{m} \\ n \end{bmatrix} \tag{8.64}$$

The expressions for induced stresses (Warpinski and Branagan, 1989) in terms of our local coordinate system are:

$$\begin{aligned} \tau_{nn} = -(P_f - \sigma_{\min})\Bigg\{ &\frac{L}{\sqrt{L_1 L_2}}\cos\left[\theta - \frac{1}{2}(\theta_1 + \theta_2)\right] \\ &+ \frac{2L\sin(\theta)}{h}\left(\frac{H^2}{4L_1 L_2}\right)^{\frac{3}{2}}\sin\left[\frac{3}{2}(\theta_1 + \theta_2)\right] - 1\Bigg\} \end{aligned} \tag{8.65}$$

$$\tau_{mm} = -(P_f - \sigma_{\min})\left\{\frac{L}{\sqrt{L_1 L_2}}\cos\left[\theta - \frac{1}{2}(\theta_1 + \theta_2)\right] - \frac{2L\sin(\theta)}{h}\left(\frac{H^2}{4L_1 L_2}\right)^{\frac{3}{2}}\sin\left[\frac{3}{2}(\theta_1 + \theta_2)\right] - 1\right\} \tag{8.66}$$

$$\tau_{nm} = -(P_f - \sigma_{\min})\left\{\frac{2L\sin(\theta)}{h}\left(\frac{H^2}{4L_1 L_2}\right)^{\frac{3}{2}}\cos\left[\frac{3}{2}(\theta_1 + \theta_2)\right]\right\} \tag{8.67}$$

$$\tau_{ll} = \mu(\tau_{nn} + \tau_{mm}) \tag{8.68}$$

The fracture height is H, and the lengths and angles in Fig. 8.4 are the following:

$$L = \sqrt{n^2 + m^2} \tag{8.69}$$

$$L_1 = \sqrt{n^2 + \left(m + \frac{H}{2}\right)^2} \tag{8.70}$$

$$L_2 = \sqrt{n^2 + \left(m - \frac{H}{2}\right)^2} \tag{8.71}$$

$$\theta = \tan^{-1}\left(\frac{n}{-m}\right) \tag{8.72}$$

$$\theta_1 = \tan^{-1}\left(\frac{n}{-m - \frac{H}{2}}\right) \tag{8.73}$$

$$\theta_2 = \tan^{-1}\left(\frac{n}{\frac{H}{2} - m}\right) \tag{8.74}$$

If any of the angles in Eqs. (8.72)–(8.74) are negative, then π would be added to them.

An actual fracture would have a finite length in the l-direction, so we modify the above formulation to account for that. We can write Eqs. (8.65)–(8.67) as:

$$\tau_{nn} = -(P_f - \sigma_{\min}) f_1(H, n, m) \tag{8.75}$$

$$\tau_{mm} = -(P_f - \sigma_{\min}) f_2(H, n, m) \tag{8.76}$$

$$\tau_{nm} = -(P_f - \sigma_{\min}) f_3(H, n, m) \tag{8.77}$$

If we consider the fracture to be rectangular, we can apply the Warpinski and Branagan (1989) approach along the finite fracture length, W, as well as along the fracture height, H, as we have done above. These induced stresses would then be:

$$\tau_{nn} = -(P_f - \sigma_{\min}) f_1(W, n, l) \tag{8.78}$$

$$\tau_{ll} = -(P_f - \sigma_{\min}) f_2(W, n, l) \tag{8.79}$$

$$\tau_{nl} = -(P_f - \sigma_{\min}) f_3(W, n, l) \tag{8.80}$$

The terms multiplying the net pressure in Eqs. (8.78)–(8.80) are the variation of induced stresses along the finite fracture length (for an infinite fracture height), and those multiplying net pressure in Eqs. (8.75)–(8.77) are the variation of induced stresses along the finite fracture height (for an infinite fracture length). In Eqs. (8.75)–(8.77), we account for the variation of induced stress along the fracture length by attaching a multiplicative factor obtained by normalizing the fracture length variation of the *nn*-component in Eq. (8.78). In Eqs. (8.78)–(8.80), we account for the variation of induced stress along the fracture height by attaching a multiplicative factor obtained by normalizing the fracture height variation of the *nn*-component in Eq. (8.75). The induced stress components from the stress shadow effect then become:

$$\tau_{nn} = -\frac{(P_f - \sigma_{\min})}{2}\left(f_1(H, n, m)\frac{f_1(W, n, l)}{f_1(W, n, 0)} + f_1(W, n, l)\frac{f_1(H, n, m)}{f_1(H, n, 0)}\right) \tag{8.81}$$

$$\tau_{mm} = -(P_f - \sigma_{\min}) f_2(H, n, m)\frac{f_1(W, n, l)}{f_1(W, n, 0)} \tag{8.82}$$

$$\tau_{nm} = -(P_f - \sigma_{\min}) f_3(H, n, m)\frac{f_1(W, n, l)}{f_1(W, n, 0)} \tag{8.83}$$

$$\tau_{ll} = -(P_f - \sigma_{\min}) f_2(W, n, l)\frac{f_1(H, n, m)}{f_1(H, n, 0)} \tag{8.84}$$

$$\tau_{nl} = -(P_f - \sigma_{\min}) f_3(W, n, l)\frac{f_1(H, n, m)}{f_1(H, n, 0)} \tag{8.85}$$

Because the above process yields two versions for the *nn* stress tensor component, we include both as an average in Eq. (8.81).

We input the stress field as principal stresses, which are either a function of true vertical depth or calculated from reference quantities. In the latter, the z-direction principal stress (σ_3) is normal to the earth's surface, and the other two principal stresses (σ_1,σ_2) act in the horizontal plane. The equilibrium equation for the z-direction principal stress, with no shear stresses, is:

$$\frac{d\sigma_3}{dz} + F_{b,z} = 0 \tag{8.86}$$

The body force term is the weight of the overburden, which consists of rock (r) and fluid (f):

$$F_{b,z} = (\rho_f \phi + \rho_r (1 - \phi))g \tag{8.87}$$

Integrating Eq. (8.86) from reference depth z_0 to z gives the zz-principal stress component:

$$\sigma_3 = \sigma_{3,0} - \int_{z_0}^{z} F_{b,z} dz \tag{8.88}$$

Winterfeld and Wu (2015) present equations for principal horizontal stress components. Assuming no shear stresses and no horizontal variation, these equations become:

$$\frac{d^2}{dz^2}\left(\sigma_1 - h(P,T) - \frac{3\upsilon}{1+\upsilon}(\sigma_m - h(P,T))\right) = 0 \tag{8.89}$$

$$\frac{d^2}{dz^2}\left(\sigma_2 - h(P,T) - \frac{3\upsilon}{1+\upsilon}(\sigma_m - h(P,T))\right) = 0 \tag{8.90}$$

where $\sigma_m$is the mean stress and υ is Poisson's ratio. We integrate these equations twice to yield:

$$\sigma_1 - h(P,T) - \frac{3\upsilon}{1+\upsilon}(\sigma_m - h(P,T)) = D_{11}(z - z_0) + D_{12} \tag{8.91}$$

$$\sigma_2 - h(P,T) - \frac{3\upsilon}{1+\upsilon}(\sigma_m - h(P,T)) = D_{21}(z - z_0) + D_{22} \tag{8.92}$$

The integration constants D_{12} and D_{22} are evaluated at reference depth, z_0. The integration constants D_{11} and D_{21} are chosen to reflect the lithostatic environment. We express this as the following horizontal to vertical stress ratios:

$$\lim_{z \to z_r} \frac{\sigma_1 - \sigma_{1,r}}{\sigma_3 - \sigma_{3,r}} = R_{13} \tag{8.93}$$

and

$$\lim_{z \to z_r} \frac{\sigma_2 - \sigma_{2,r}}{\sigma_3 - \sigma_{3,r}} = R_{23} \tag{8.94}$$

where the subscript r refers to the reference depth. Eqs. (8.91) and (8.92) are solved simultaneously for the horizontal plane principal stresses. The orientation of the principal stresses in the horizontal plane with respect to the global coordinate system is also specified.

The total stress tensor is the sum of the input stress field and the induced one from the stress shadow effect:

$$\boldsymbol{\tau}_{\text{total}} = \boldsymbol{\tau}_{\text{input}} + \boldsymbol{\tau}_{\text{induced}} \tag{8.95}$$

where the components of the induced stress tensor are given by Eqs. (8.81)–(8.85). The eigenvalues of the total stress tensor give the principal stresses and the corresponding eigenvectors are the principal stress directions. The fracture width is calculated using the minimum of these principal stresses and the fracture orientation is perpendicular to the direction of this minimum principal stress.

8.9 GOVERNING EQUATION SOLUTION

The equations governing our hydraulic fracturing simulator are solved using the integral finite difference method (Narashimhan and Witherspoon, 1976). In this method, the simulation domain is subdivided into subdomains and the governing equations are integrated over a subdomain with flux terms expressed as an integral over the subdomain boundary using the divergence theorem. The definitions of the geometric parameters used in the following derivation of this method are illustrated in Fig. 8.5. We consider a generalized conservation equation of the form:

$$\frac{\partial M^k}{\partial t} = \nabla \cdot \overline{F}^k + q^k \tag{8.96}$$

where k refers to conserved quantity, M is quantity per unit volume, F is flux, and q is source/sink term. Integrating Eq. (8.96) over a subdomain V_n yields:

$$\frac{\partial}{\partial t}\int_{V_n} M^k \, dV = \int_{\Gamma_n} \overline{F}^k \cdot \hat{n} d\Gamma + \int_{V_n} q^k dV \tag{8.97}$$

Integrals over V_n are replaced with averages:

$$\int_{V_n} M^k dV = M_n^k V_n \tag{8.98}$$

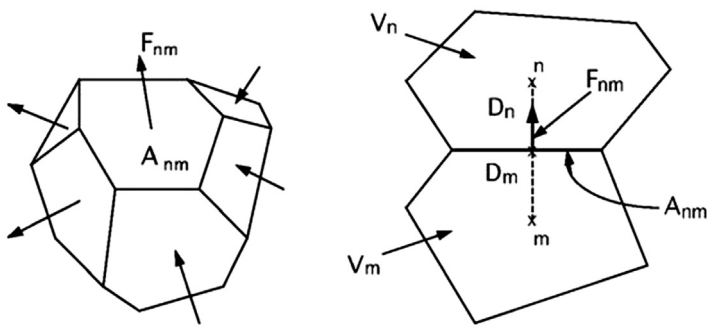

FIGURE 8.5 Parameter definitions for the integral finite difference method. *Adapted from Pruess K., TOUGH2—A General Purpose Numerical Simulator for Multiphase Fluid and Heat Flow, Report LBL-29400. 1991, Lawrence Berkeley National Laboratory, Berkeley, CA.*

Integrals over the subdomain boundary are replaced with discrete sums over boundary-averaged segments:

$$\int_{\Gamma_n} \overline{F}^k \cdot \hat{n} d\Gamma = \sum_m A_{nm} F_{nm}^k \tag{8.99}$$

where the subscript n denotes an averaged quantity over V_n, A_{nm} is the boundary segment common to V_n and V_m, and the double subscript nm denotes an averaged quantity over boundary segment A_{nm}. The time derivative is approximated by the standard first-order finite difference approximation. Applying these approximations to Eq. (8.96) yields:

$$\left[M_n^k\right]^{l+1} - \left[M_n^k\right]^l - \frac{\Delta t}{V_n}\left[\sum_m A_{nm} F_{nm}^k + V_n q_n^k\right] = 0 \tag{8.100}$$

where l is time level.

These governing equations (Eq. 8.100) expressed in residual vector form are:

$$\overline{R}\left(\overline{x}^{l+1}\right) = 0 \tag{8.101}$$

where $\overline{x}^{l+1}$ is the primary variable vector at time level $l+1$. This vector of equations is solved by the Newton–Raphson method. The Newton–Raphson method is an iterative procedure used to solve systems of nonlinear equations. Denoting iteration number by subscript p, the following system of equations result from applying the Newton–Raphson method to Eq. (8.101):

$$\overline{\overline{J}}\left(\overline{x}_p^{l+1}\right)\left(\overline{x}_p^{l+1} - \overline{x}_p^l\right) = -\overline{R}\left(\overline{x}_p^{l+1}\right) \tag{8.102}$$

where the Jacobian matrix, $\overline{\overline{J}}\left(\overline{x}_p^{l+1}\right)$, is defined as:

$$\left[\overline{\overline{J}}\left(\overline{x}_p^{l+1}\right)\right]_{ij} = \frac{\partial R_i(\overline{x})}{\partial x_j} \tag{8.103}$$

The Jacobian matrix is evaluated by numerical differentiation:

$$\frac{\partial R_i(\overline{x})}{\partial x_j} \approx \frac{R_i\left(\overline{x}(\forall i \neq j,\ \ x_j + \varepsilon_j)\right) - R_i(\overline{x})}{\varepsilon_j} \tag{8.104}$$

where ε_j is the increment for primary variable x_j. Eq. (8.102) is a set of algebraic equations of the form $Ax = b$, which we solve using an iterative matrix solution technique. The iteration is converged when all residuals R_i are less than a prescribed tolerance, ε_{tol}:

$$\left|\frac{R_i\left(\overline{x}_p^{l+1}\right)}{M_i\left(\overline{x}_p^{l+1}\right)}\right| \leq \varepsilon_{\text{tol}} \tag{8.105}$$

8.10 FRACTURE DISCRETIZATION

The governing equations for the fractures depend on two spatial dimensions because they are derived from an average over the fracture width. Consequently, we discretize the fractures into a two-dimensional grid that is uniform and Cartesian. Because multiple completed zones may produce multiple fractures that are approximately parallel, this grid has an additional dimension equal to the number of these parallel fractures. Each gridblock has a position expressed in global coordinates and various properties including a normal vector that defines its orientation. A local coordinate system (l,m,n), described earlier, is determined by that normal vector. Fig. 8.6 shows the fracture grid that would arise if there were two completed intervals along the wellbore and the two associated fractures were approximately parallel.

These fracture gridblocks are either active or inactive. Before fracture initiation, all fracture gridblocks are inactive. At fracture initiation, fracture gridblocks containing completions become active, meaning they contain fluid and proppant and have a nonzero fracture width. As the fracture extends, inactive gridblocks that neighbor active ones become active. The fracture boundary consists of active fracture gridblocks that border inactive ones. The number of rows and columns of the fracture grid are chosen large enough such that the fracture will never reach the grid outer boundary.

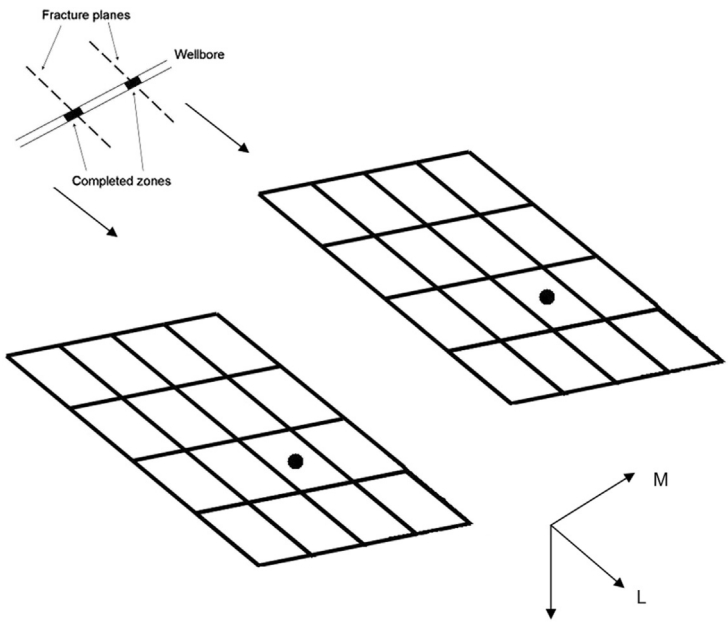

FIGURE 8.6 Fracture grid for two completed zones and approximately parallel fractures. Large dots indicate gridblocks containing the completions.

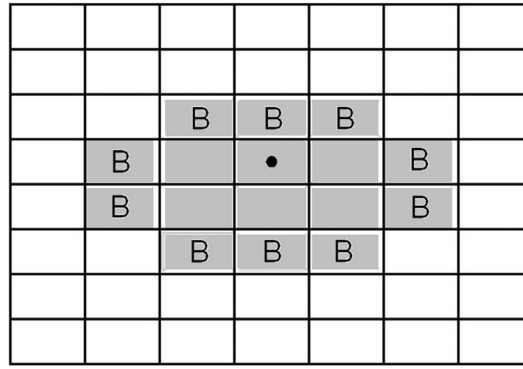

FIGURE 8.7 Fracture grid showing active gridblocks (shaded) and inactive (unshaded) ones. Gridblocks on the fracture boundary contain a "B." The gridblock with the large dot contains completions.

Fig. 8.7 shows an example of a fracture grid with active, inactive, and boundary gridblocks.

Each gridblock's normal vector is orthogonal to the minimum principal stress direction, and this vector is calculated when the gridblock becomes active. The stress tensor components for a gridblock are obtained by the superposition of the input stresses and those induced by the stress shadow effect. The principal stresses and directions are obtained by determining the eigenvalues and eigenvectors of the stress tensor. The minimum principal stress eigenvector is the gridblock normal vector and this vector does not change after the gridblock becomes active. Varying gridblock normal vectors result in fractures that are nonplanar.

A fracture gridblock occupies a depth range given by its local m-direction range projected along the global z-direction. Some parameters associated with fracture gridblocks, such as rock properties, are input as a function of depth. The value of these properties associated with a fracture gridblock is their average over the fracture gridblock depth range.

8.11 DISCRETIZED FRACTURE MASS AND ENERGY CONSERVATION EQUATIONS

The integral finite difference method is applied to the fracture conservation equations by integration over a two-dimensional fracture gridblock, replacing the integrals by averages, and evaluating the time derivative using the standard difference approximation. A fracture gridblock, located in row and column (i,j) in the grid, has four neighbors that are located in the following rows and columns: $(i+1,j)$, $(i-1,j)$, $(i,j+1)$, and $(i,j-1)$. Application of the integral

finite difference method to the overall slurry balance (Eq. 8.15) results in the following:

$$\left[(P+\gamma z)_{i,j}-(P+\gamma z)_{i+1,j}\right]^m\left[\frac{w^3}{12\mu_{sl}}\right]^m_{i+\frac{1}{2}j}$$

$$\frac{\Delta x}{\Delta z}+\left[(P+\gamma z)_{i,j}-(P+\gamma z)_{i-1,j}\right]^m\left[\frac{w^3}{12\mu_{sl}}\right]^m_{i-\frac{1}{2},j}$$

$$\frac{\Delta x}{\Delta z}+\left[(P+\gamma z)_{i,j}-(P+\gamma z)_{i,j+1}\right]^m\left[\frac{w^3}{12\mu_{sl}}\right]^m_{i,j+\frac{1}{2}}$$

$$\frac{\Delta z}{\Delta x}+\left[(P+\gamma z)_{i,j}-(P+\gamma z)_{i,j-1}\right]^m\left[\frac{w^3}{12\mu_{sl}}\right]^m_{i,j-\frac{1}{2}}$$

$$\frac{\Delta z}{\Delta x}+\frac{\Delta x\Delta z}{\Delta t}\left(w_i^{l+1}-w_i^{l}\right)-T^m_{wf,i}\left(P^{l+1}_{w,i}-P^{l+1}_{f,i}\right)+2\Delta x\Delta z\frac{C^m_{\text{leak}}}{\sqrt{t-\tau_i}}=0 \tag{8.106}$$

where Δt is the time step size, Δx is the gridblock length along the local l-direction, Δz is the gridblock length along the local m-direction, l is previous time step, $l+1$ is current time step, and m signifies that some terms in the brackets are evaluated at time step l and others at time step $l+1$. Application of the integral finite difference method to the proppant balance (Eq. 8.10) yields the following:

$$\left[c_p f_{\text{ret}}\left(c_{p,w}\right)\right]^m_{i,j+\frac{1}{2}}\left[(P+\gamma z)_{i,j}-(P+\gamma z)_{i,j+1}\right]^m\left[\frac{w^3}{12\mu_{sl}}\right]^m_{i,j+\frac{1}{2}}$$

$$\frac{\Delta z}{\Delta x}+\left[c_p f_{\text{ret}}\left(c_{p,w}\right)\right]^m_{i,j-\frac{1}{2}}\left[(P+\gamma z)_{i,j}-(P+\gamma z)_{i,j-1}\right]^m\left[\frac{w^3}{12\mu_{sl}}\right]^m_{i,j-\frac{1}{2}}$$

$$\frac{\Delta z}{\Delta x}+\left[c_p\right]^m_{i+\frac{1}{2},j}\left[(P+\gamma z)_{i,j}-(P+\gamma z)_{i+1,j}\right]^m\left[\frac{w^3}{12\mu_{sl}}\right]^m_{i+\frac{1}{2},j}\frac{\Delta x}{\Delta z}+\left[c_p w v_{p,\text{stl}}\right]^m_{i+\frac{1}{2},j}$$

$$\Delta x+\left[c_p\right]^m_{i-\frac{1}{2},j}\left[(P+\gamma z)_{i,j}-(P+\gamma z)_{i-1,j}\right]^m\left[\frac{w^3}{12\mu_{sl}}\right]^m_{i-\frac{1}{2},j}\frac{\Delta x}{\Delta z}-\left[c_p w v_{p,\text{stl}}\right]^m_{i-\frac{1}{2},j}$$

$$\Delta x+\frac{\Delta x\Delta z}{\Delta t}\left[\left(c_p w_i\right)^{l+1}-\left(c_p w_i\right)^{l}\right]-c_p^{l+1}T^m_{wf,i}\left(P^{l+1}_{w,i}-P^{l+1}_{f,i}\right)=0 \tag{8.107}$$

Application of the integral finite difference method to the fluid balance (Eq. 8.9) yields the following:

$$
\begin{aligned}
&[x_f]^{l+1}_{i,j+\frac{1}{2}}\left\{\begin{array}{l}\left[(P+\gamma z)_{i,j}-(P+\gamma z)_{i,j+1}\right]^m\left[\dfrac{w^3}{12\mu_{sl}}\right]^m_{i,j+\frac{1}{2}}-\\ \\ \displaystyle\sum_p\left[c_p f_{\mathrm{ret}}\left(c_{p,w}\right)\right]^m_{i,j+\frac{1}{2}}\left[(P+\gamma z)_{i,j}-(P+\gamma z)_{i,j+1}\right]^m\left[\dfrac{w^3}{12\mu_{sl}}\right]^m_{i,j+\frac{1}{2}}\end{array}\right\}\frac{\Delta z}{\Delta x}+\\
&[x_f]^{l+1}_{i,j-\frac{1}{2}}\left\{\begin{array}{l}\left[(P+\gamma z)_{i,j}-(P+\gamma z)_{i,j-1}\right]^m\left[\dfrac{w^3}{12\mu_{sl}}\right]^m_{i,j-\frac{1}{2}}-\\ \\ \displaystyle\sum_p\left[c_p f_{\mathrm{ret}}\left(c_{p,w}\right)\right]^m_{i,j-\frac{1}{2}}\left[(P+\gamma z)_{i,j}-(P+\gamma z)_{i,j-1}\right]^m\left[\dfrac{w^3}{12\mu_{sl}}\right]^m_{i,j-\frac{1}{2}}\end{array}\right\}\frac{\Delta z}{\Delta x}+\\
&[x_f]^{l+1}_{i+\frac{1}{2}j}\left\{\begin{array}{l}\left[(P+\gamma z)_{i,j}-(P+\gamma z)_{i+1,j}\right]^m\left[\dfrac{w^3}{12\mu_{sl}}\right]^m_{i+\frac{1}{2}j}-\\ \\ \displaystyle\sum_p\left[c_p\right]^m_{i+\frac{1}{2}j}\left[(P+\gamma z)_{i,j}-(P+\gamma z)_{i+1,j}\right]^m\left[\dfrac{w^3}{12\mu_{sl}}\right]^m_{i+\frac{1}{2}j}\dfrac{\Delta x}{\Delta z}-\displaystyle\sum_p\left[c_p w v_{p,\mathrm{stl}}\right]^m_{i+\frac{1}{2}j}\Delta x\end{array}\right\}\frac{\Delta x}{\Delta z}+\\
&[x_f]^{l+1}_{i-\frac{1}{2}j}\left\{\begin{array}{l}\left[(P+\gamma z)_{i,j}-(P+\gamma z)_{i-1,j}\right]^m\left[\dfrac{w^3}{12\mu_{sl}}\right]^m_{i-\frac{1}{2}j}-\\ \\ \displaystyle\sum_p\left[c_p\right]^m_{i-\frac{1}{2}j}\left[(P+\gamma z)_{i,j}-(P+\gamma z)_{i-1,j}\right]^m\left[\dfrac{w^3}{12\mu_{sl}}\right]^m_{i-\frac{1}{2}j}\dfrac{\Delta x}{\Delta z}+\displaystyle\sum_p\left[c_p w v_{p,stl}\right]^m_{i-\frac{1}{2}j}\Delta x\end{array}\right\}\frac{\Delta x}{\Delta z}+\\
&\frac{\Delta x\Delta z}{\Delta t}\left\{\left[wx_f\left(1-\sum_p c_p\right)\right]^{l+1}_i-\left[wx_f\left(1-\sum_p c_p\right)\right]^l_i\right\}-\\
&\left[x_f\left(1-\sum_p c_p\right)\right]^{l+1}_{wf}T^m_{wf,i}\left(P^{l+1}_{w,i}-P^{l+1}_{f,i}\right)+2\Delta x\Delta z x_f^{l+1}\frac{C^m_{\mathrm{leak}}}{\sqrt{t-\tau_i}}=0
\end{aligned}
\tag{8.108}
$$

Application of the integral finite difference method to the energy balance (Eq. 8.28) yields the following:

$$\left[\overline{h}_{sl}\right]_{i+\frac{1}{2},j}^{l+1}\left[(P+\gamma z)_{i,j}-(P+\gamma z)_{i+1,j}\right]^{m}\left[\frac{w^3}{12\mu_{sl}}\right]_{i+\frac{1}{2},j}^{m}$$

$$\frac{\Delta x}{\Delta z}+\left[\overline{h}_{sl}\right]_{i-\frac{1}{2},j}^{l+1}\left[(P+\gamma z)_{i,j}-(P+\gamma z)_{i-1,j}\right]^{m}\left[\frac{w^3}{12\mu_{sl}}\right]_{i-\frac{1}{2},j}^{m}$$

$$\frac{\Delta x}{\Delta z}+\left[\overline{h}_{sl}\right]_{i,j+\frac{1}{2}}^{l+1}\left[(P+\gamma z)_{i,j}-(P+\gamma z)_{i,j+1}\right]^{m}\left[\frac{w^3}{12\mu_{sl}}\right]_{i,j+\frac{1}{2}}^{m}$$

$$\frac{\Delta z}{\Delta x}+\left[\overline{h}_{sl}\right]_{i,j-\frac{1}{2}}^{l+1}\left[(P+\gamma z)_{i,j}-(P+\gamma z)_{i,j-1}\right]^{m}\left[\frac{w^3}{12\mu_{sl}}\right]_{i,j-\frac{1}{2}}^{m}$$

$$\frac{\Delta z}{\Delta x}+\frac{\Delta x\Delta z}{\Delta t}\left([\overline{u}w]_i^{l+1}-[\overline{u}w]_i^{l}\right)-\left[\overline{h}_{sl}\right]_{wf}^{l+1}T_{wf,i}^{m}\left(P_{w,i}^{l+1}-P_{f,i}^{l+1}\right)+$$

$$2\Delta x\Delta z\sum_f\left[x_f\rho_f\overline{h}_f\right]_i^{l+1}\frac{C_{\text{leak}}^{m}}{\sqrt{t-\tau_i}}+2\Delta x\Delta z\sqrt{\frac{K_{\text{res}}\rho_{\text{res}}C_{\text{res}}}{\pi(t-\tau)}}\left(T_i^{l+1}-T_{\text{res},i}\right)=0 \tag{8.109}$$

8.12 DISCRETIZED FRACTURE MECHANICS EQUATIONS

In the finite difference approximation to Eqs. (8.34) and (8.35), we replace the integrals with sums over discrete gridblocks:

$$w(\overrightarrow{r}\in F)=\sum_{j\in F}\left[\frac{2(1-\upsilon^2)}{\pi E}(P_f-\sigma_{\min})\right]_j\frac{A_j}{r_{ij}}+\sum_{j\notin F}\left[\frac{2(1-\upsilon^2)}{\pi E}P_{\text{net}}\right]_j\frac{A_j}{r_{ij}} \tag{8.110}$$

and

$$w(\overrightarrow{r}\notin F)=\sum_{j\in F}\left[\frac{2(1-\upsilon^2)}{\pi E}(P_f-\sigma_{\min})\right]_j\frac{A_j}{r_{ij}}+\sum_{j\notin F}\left[\frac{2(1-\upsilon^2)}{\pi E}P_{\text{net}}\right]_j\frac{A_j}{r_{ij}}=0 \tag{8.111}$$

To increase computational speed, we make the following modifications to Eqs. (8.110) and (8.111). The fracture area F consists of active gridblocks, and the rest of the gridblocks are inactive. We approximate the sum over inactive gridblocks in Eqs. (8.110) and (8.111) as only over inactive gridblocks connected to at least one boundary gridblock, and assume the net pressures

associated with those inactive gridblocks are equal. We approximate the fracture pressure for active gridblocks by that in gridblock i plus a constant gradient factor. Eqs. (8.110) and (8.111) then become:

$$w(\overrightarrow{r} \in F) = \sum_{j \in F} \left[\frac{2\left(1-\upsilon_j^2\right)}{\pi E_j} \left(P_i^{l+1} + \rho_{\text{avg}} g(z_j - z_i) - \sigma_{\text{min},j}^m \right) \right] \frac{A_j}{r_{ij}} + P_{\text{net,avg}}^{l+1} \sum_{j \in I} \left[\frac{2(1-\upsilon^2)}{\pi E} \right]_j \frac{A_j}{r_{ij}} \tag{8.112}$$

and

$$\sum_{i \in B} w(\overrightarrow{r} \in B) = \sum_{i \in I} \left\{ \sum_{j \in F} \left[\frac{2(1-\upsilon^2)}{\pi E} \left(P_f^{l+1} - \sigma_{\text{min},j}^m \right) \right]_j \frac{A_j}{r_{ij}} + P_{\text{net,avg}}^{l+1} \sum_{j \in I} \left[\frac{2(1-\upsilon^2)}{\pi E} \right]_j \frac{A_j}{r_{ij}} \right\} = 0 \tag{8.113}$$

where I is the set of inactive gridblocks connected to at least one boundary gridblock. The minimum principal stress is written with the superscript m because it can vary over time due to the stress shadow effect.

Fracture extension occurs when inactive gridblocks adjacent to active ones become activated. For each boundary gridblock, l-direction and m-direction fracture front distances are tracked; when these distances exceed half the gridblock dimension in that direction, the adjacent gridblock in that direction is activated. These front distances are a function of stress intensity factor (Eq. 8.36), which is approximated as:

$$K_{I,i} = \left(\frac{E}{8(1-\upsilon)} \sqrt{\frac{4\pi}{\sqrt{\Delta s_l \Delta s_m}}} w \right)\Bigg|_i \tag{8.114}$$

When an inactive gridblock becomes activated, the stress tensor associated with that gridblock is assembled from the superposition of the input stress field and the induced one from the stress shadow effect (Eq. 8.95). The eigenvector of the minimum principal stress is the normal vector of the gridblock, and this vector does not change with time. The minimum principal stress is updated every time step for each active gridblock by assembling the stress tensor and obtaining the minimum eigenvalue.

8.13 DISCRETIZED WELLBORE MASS AND ENERGY CONSERVATION EQUATIONS

The wellbore mass and energy conservation equations, Eqs. (8.48) and (8.54), are integrated over an injected slurry segment volume that is located along the

measured depth interval S_{i+1} to S_i. We replace these integrals by averages, evaluate the time derivative using the standard difference approximation, and obtain the following. For fluid and proppant:

$$\begin{aligned}&\left[\rho_{y,i}x_{y,i}(S_i - S_{i+1})\right]^{l+1} - \left[\rho_{y,i}x_{y,i}(S_i - S_{i+1})\right]^{l} + \frac{\Delta t}{A_i}\\&\left(T_{ws}\rho_{y,ws}x_{y,ws}\left(P_{w,i} - P_{\text{surr}}\right)(S_i - S_{i+1}) - q_{\text{inj}}\rho_{y,\text{inj}}x_{y,\text{inj}}\right) = 0;\ y = f, p\end{aligned} \tag{8.115}$$

and for energy:

$$\begin{aligned}&\left[\rho_{sl,i}\overline{u}_{sl,i}(S_i - S_{i+1})\right]^{l+1} - \left[\rho_{sl,i}\overline{u}_{sl,i}(S_i - S_{i+1})\right]^{l}\\&+\frac{\Delta t}{A_i}\left(T_{ws}\rho_{sl,ws}\overline{h}_{sl,ws}\left(P_{w,i} - P_s\right)(S_i - S_{i+1}) - q_{\text{inj}}\rho_{sl,\text{inj}}\overline{h}_{sl,\text{inj}}\right)\\&+2\pi R_i H_i\left[\left(T_{w,i} - T_{\text{surr},i}\right)(S_i - S_{i+1})\right]^{l+1} = 0\end{aligned} \tag{8.116}$$

where the subscript surr refers to the surroundings, which can be either the fracture or the formation.

The wellbore pressure equation, Eq. (8.49), is integrated from the wellhead ($S = 0$ at pressure $P_{w,0}$) to an arbitrary measured depth, S, yielding:

$$\left[\begin{array}{l}P_{w,j} - P_{w,0} - \displaystyle\sum_{j=1}^{i-1}\overline{g}\cdot\widehat{S}_{j,j+1}\left(\rho_f x_f + \rho_p x_p\right)\big|_j(S_j - S_{j+1}) - \overline{g}\bullet\widehat{S}_{i,i+1}\\\qquad\qquad\left(\rho_f x_f + \rho_p x_p\right)\big|_j(S - S_{i+1}) -\\\displaystyle\sum_{j=1}^{i-1}\Delta P_{\text{fric},j} - \frac{\Delta P_{\text{fric},i}}{S_i - S_{i+1}}(S - S_{i+1})\end{array}\right]^{l+1} = 0 \tag{8.117}$$

where the subscript j, $j+1$ refers to the wellbore segment bounded by measured depths S_j and S_{j+1} and the friction pressure difference is that for a wellbore segment.

8.14 WELLBORE–SURROUNDINGS TRANSFER

In the fracture and wellbore mass and energy conservation equations, there are expressions for exchange of conserved species and energy between the wellbore and the surroundings, namely, the fracture or the formation. The volumetric flow rate for this exchange is:

$$q_{wf} = T_{wf}\left(P_{w,i} - P_{\text{sur}}\right) \tag{8.118}$$

In this section, we derive expressions for T_{wf}. For flow into the fractures, which are represented as slits of width w, the transmissibility is:

$$T_f = \frac{w^3}{12\mu_{sl}} \tag{8.119}$$

If fluid would flow through the perforations before entering the fractures, there is an additional pressure drop across the perforations, given by (McClain, 1963) as:

$$\Delta P_{\text{prf}} = 0.8074 \frac{\rho_{sl} q_{wf}^2}{n_{\text{prf}}^2 d_{\text{prf}}^2 C_{\text{prf}}^2} \tag{8.120}$$

where n_{prf} is the number of perforations per unit length, d_{prf} is perforation diameter, and C_{prf} is the perforation discharge coefficient. Eq. (8.120) can be rearranged to yield a perforation transmissibility:

$$q_{wf} = \frac{n_{\text{prf}}^2 d_{\text{prf}}^2 C_{\text{prf}}^2}{0.8074 \rho_{sl} q_{wf}} \Delta P_{\text{prf}} = T_{\text{prf}} \Delta P_{\text{prf}} \tag{8.121}$$

The overall transmissibility for flow from the wellbore into the fractures is the harmonic average of those for flow into the fractures and through the perforations:

$$\frac{1}{T_{wf}} = \frac{1}{T_f} + \frac{1}{T_{\text{prf}}} \tag{8.122}$$

Before fracture initiation, fluid flows from the wellbore into the formation. We model this flow as steady-state flow of injected fluid through a growing invaded zone that is surrounded by an infinitely extending, transient, slightly compressible reservoir zone. The pressure drop for the invaded zone is:

$$\Delta P_{wI} = \frac{\ln\left(\frac{r_I}{r_w}\right) \mu_{sl} q_{wf}}{2\pi k_{\text{res}}} \tag{8.123}$$

where r_w is the radius of the wellbore and r_I is the radius of the invaded zone. The invaded zone radius is determined by the cumulative volume of fluid that has flowed into the formation (V_{loss}):

$$r_I = \sqrt{r_w^2 + \frac{V_{\text{loss}}}{\pi \phi}} \tag{8.124}$$

The pressure drop for the compressible zone is estimated from the pressure drop associated with a point injector in an infinite, radial porous medium (Horner, 1951):

$$\Delta P_{If} = \frac{\mu_{\text{res}} q_{wf}}{4\pi k_{\text{res}}} (\ln(\eta) + 0.57772) \tag{8.125}$$

and

$$\eta = \frac{r^2 \phi \mu_{\text{res}} C_{t,\text{res}}}{4 k_{\text{res}} t} \tag{8.126}$$

where $C_{t,\text{res}}$ is the reservoir fluid compressibility.

For pistonlike displacement, the relation between radius, time, and injection rate per unit length for a point injector in an infinite, radial porous medium is:

$$q_{wf} t = \pi r^2 \phi \tag{8.127}$$

We substitute Eq. (8.127) into Eq. (8.126) to yield:

$$\eta = \frac{q_{wf} \mu_{\text{res}} C_{t,\text{res}}}{4 k_{\text{res}}} \tag{8.128}$$

The transmissibility for flow in the invaded zone is:

$$T_{wI} = \frac{2\pi k_{\text{res}}}{\ln\left(\frac{r_I}{r_w}\right)\mu_{sl}} \tag{8.129}$$

and that for the compressible zone is:

$$T_{If} = \frac{4\pi k_{\text{res}}}{\mu_{\text{res}}(\ln(\eta) + 0.57772)} \tag{8.130}$$

The overall transmissibility is the harmonic sum of Eqs. (8.129) and (8.130):

$$\frac{1}{T_{wf}} = \frac{1}{T_{wI}} + \frac{1}{T_{If}} \tag{8.131}$$

8.15 SOLUTION OF FINITE DIFFERENCE FLOW, ENERGY, AND FRACTURE MECHANICS EQUATIONS

The set of discretized of flow and energy equations for the wellbore and fracture, and the fracture mechanics equations, are solved using Newton's method, outlined previously. These equations are expressed as a residual vector that is a function of the primary variable vector. The primary variable vector consists of wellbore primary variables: the slurry segment boundaries (S_i), fluid volume fractions (x_i), temperature ($T_{w,i}$), and the wellhead pressure, (P_{w0}):

$$\mathbf{x}_{wb} = \left[x_1, x_2, x_3, \ldots x_{N_s}, S_2, S_3, \ldots S_{N_s}, T_1, T_2, T_3, \ldots T_{N_s}, P_{w,0}\right] \tag{8.132}$$

where N_s is the number of wellbore slurry segments. These primary variables correspond to the following governing equations:

1. Fluid component conservation in each slurry segment (N_s equations)
2. Proppant component conservation in each slurry segment (N_s equations)
3. Energy conservation in each slurry segment (N_s equations)

The number of wellbore primary variables and equations are both $3N_s$. There are two additional slurry segment boundaries, numbered 1 and $N_s + 1$ that are fixed (wellhead and wellbore bottom locations) and not included in the primary variable vector.

The fracture primary variables for each active gridblock are pressure, width, proppant component volume fractions, and fluid component volume fractions. The fracture primary variable vector is thus:

$$\mathbf{x}_{\text{frac}} = \begin{bmatrix} \left(P, w, T, c_1, c_2, c_3, \ldots c_{N_p}, x_1, x_2, x_3, \ldots x_{N_f-1}\right)_1, \\ \left(P, w, T, c_1, c_2, c_3, \ldots c_{N_p}, x_1, x_2, x_3, \ldots x_{N_f-1}\right)_2, \\ \left(P, w, T, c_1, c_2, c_3, \ldots c_{N_p}, x_1, x_2, x_3, \ldots x_{N_f-1}\right)_3, \ldots \\ \left(P, w, T, c_1, c_2, c_3, \ldots c_{N_p}, x_1, x_2, x_3, \ldots x_{N_f-1}\right)_{N_{\text{act}}}, \; P_{\text{net}} \end{bmatrix} \tag{8.133}$$

where N_p is the number of proppant components, N_f is the number of fluid components, and N_{act} is the number of active fracture gridblocks. These primary variables correspond to the following governing equations:

1. Fracture mechanics equation for nonzero fracture width (N_{act} equations)
2. Fracture mechanics equation for zero fracture width (one equation)
3. Slurry conservation (N_{act} equations)
4. Proppant component conservation (N_p N_{act} equations)
5. Fluid component conservation (($N_f - 1$) N_{act} equations)
6. Energy conservation (N_{act} equations)

The number of fracture primary variables and equations are both $(N_f + N_p + 2)N_{act} + 1$. Fluid component volume fraction numbered N_f is not included in the primary variable vector because, for each gridblock, fluid component volume fractions sum to 1.

The governing equations for the wellbore and fracture are solved in a sequential manner. First, fracture pressure, width, and all wellbore primary variables except temperature are solved. Second, fracture fluid and proppant volume fractions are solved. Finally, fracture and wellbore temperatures are solved.

In general, the Jacobian matrix consists of submatrices associated with the fracture (F) and the wellbore (W), with the set of algebraic equations represented as:

$$\begin{bmatrix} F & FW \\ WF & W \end{bmatrix} \begin{bmatrix} X_F \\ X_W \end{bmatrix} = \begin{bmatrix} R_F \\ R_W \end{bmatrix} \tag{8.134}$$

where X refers to state variables and R refers to residuals. This system of equations is solved by first factoring the Jacobian matrix as:

$$\begin{bmatrix} F & FW \\ WF & W \end{bmatrix} = \begin{bmatrix} F & 0 \\ WF & (W - WF \cdot F^{-1} \cdot FW) \end{bmatrix} \begin{bmatrix} I & (F^{-1} \cdot FW) \\ 0 & I \end{bmatrix} \tag{8.135}$$

Then, the system of equations are solved by the following steps:

1. $F \cdot Y_F = R_F$
2. $F \cdot D = FW$
3. $(W - WF \cdot D) \cdot X_W = R_W - WF \cdot Y_F$
4. $X_F = Y_F - D \cdot X_W$

In steps 1 and 2, the fracture matrix F is solved iteratively using the stabilized biconjugate gradient. In step 3, the wellbore matrix W is solved directly.

8.16 TIME STEP SIZE SELECTION

There are two options for time step size, Δt, selection: constant throughout the simulation or variable. In the latter, the time step size is calculated based on the condition of stability for flow in a single gridblock, as shown in Fig. 8.8. In that system, a conserved species is transported into a volume V at a rate qx_i where q is the flow rate and x_i is the species concentration, a constant, and also transported out of the volume at a rate qx where x is the species concentration in the volume. A mass balance around the volume yields the following, in dimensionless form:

$$1 - \Psi(\tau) = \frac{d\Psi(\tau)}{d\tau} \tag{8.136}$$

$$\tau(0) = 0 \tag{8.137}$$

where

$$\Psi = \frac{x - x_0}{x_i - x_0} \tag{8.138}$$

$$\tau = \frac{qt}{V} \tag{8.139}$$

The explicit finite difference version of Eq. (8.136) is:

$$1 - \Psi^n = \frac{\Psi^{n+1} - \Psi^n}{\Delta\tau} \tag{8.140}$$

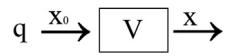

FIGURE 8.8 Single gridblock system.

Eq. (8.140) has the following analytical solution:

$$\Psi^n = 1 - (1 - \Delta\tau)^n \tag{8.141}$$

For this solution to be stable, the dimensionless time step size, called the Courant number, N_c, must be less than 1:

$$N_c = \frac{q\Delta t}{V} < 1 \tag{8.142}$$

We calculate the Courant number of each active fracture gridblock by using the net inflow as q and the gridblock volume as V. Time step size adjustment is based on the maximum of these Courant numbers, $N_{c,\max}$, over the fracture grid, the target Courant number, $N_{c,\text{targ}}$, and the time step multiple parameter, $F_{\Delta t}$:

$$\Delta t^{l+1} = \max\left(\frac{1}{F_{\Delta t}}, \min\left(F_{\Delta t}, \frac{N_{c,\text{targ}}}{N_c}\right)\right)\Delta t^l \tag{8.143}$$

Eq. (8.142) applies to an explicit finite difference approximation; however, our finite difference contains a great deal of implicit terms, although it is not fully implicit and unconditionally stable. Consequently, target Courant numbers greater than one can give stable results.

8.17 EXAMPLE PROBLEMS

We describe three simulations to provide model verification and application examples. The first two, radial fracture propagation and PKN-like fracture propagation, are presented for model validation and are compared with analytical solutions as well as to another hydraulic fracturing simulator. The last one is a simulation of field data that illustrates some of the simulators capabilities, including the stress shadow effect.

8.17.1 Radial Fracture Propagation

The radial fracture propagation problem is a simulation of fracture propagation in the horizontal plane with no leak-off, gravity, or temperature effects (Ribeiro and Sharma, 2012). Slurry consists of one incompressible Newtonian fluid component with 40 cp (0.04 Pa s) viscosity and no proppant. Young's modulus is 2.5×10^6 psi (17.24 GPa), Poisson's ratio is 0.25, the minimum stress is 5000 psi (34.47 MPa), and slurry is injected at 20 bbl/min (0.053 m^3/s) for 30 min (1800 s) via a point source. Gridblocks are square with length of 32.81 ft (10 m). Fig. 8.9 shows simulated fracture width after 30 min of injection, and Fig. 8.10 shows the results from Ribeiro and Sharma (2012), who ran the same problem on another fracturing simulator. The fracture width profiles from both simulators are very similar. Ribeiro and Sharma (2012) also compared fracture radius versus time with an analytical solution for radial

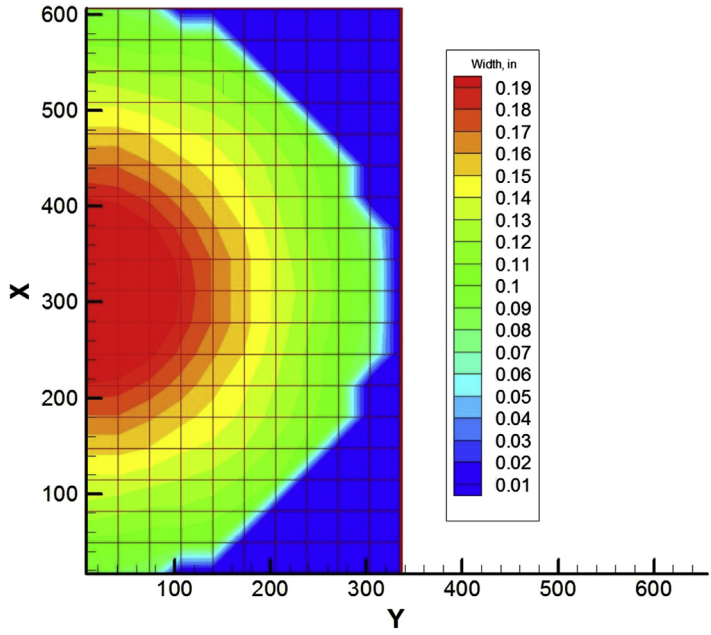

FIGURE 8.9 Fracture width after 30 min of injection.

fractures with no leak-off from Geertsma and de Klerk (1969) and obtained good agreement. Fig. 8.11 is the comparison of our results with the analytical solution. Our results track the analytical solution well, with our fracture radius increasing in discrete jumps, a characteristic of our finite difference formulation.

8.17.2 PKN-Like Fracture Propagation

The PKN-like fracture propagation problem is a simulation of fracture propagation in a zone bounded above and below by layers at much higher stresses (Ribeiro and Sharma, 2012). An analytical solution to this problem was derived by Nordgren (1972). The zone height is 150 ft (45.72 m), the minimum stress is 5000 psi (34.47 MPa), and the minimum stress in the zones above and below are 6000 psi (41.37 MPa). The system is also isothermal, and slurry consists of one incompressible Newtonian fluid component with 40 cp (0.04 Pa s) viscosity and no proppant. Young's modulus is 2.5×10^6 psi (17.24 GPa), Poisson's ratio is 0.25, and slurry is injected at 20 bbl/min (0.053 m^3/s) for 30 min (1800 s). Gridblocks are square with length of 16.40 ft (5 m). Fig. 8.12 is the comparison of fracture half-length between our results and the analytical solution. Our results track the analytical solution at smaller times with some deviation at larger times. The discrete jumps in simulated

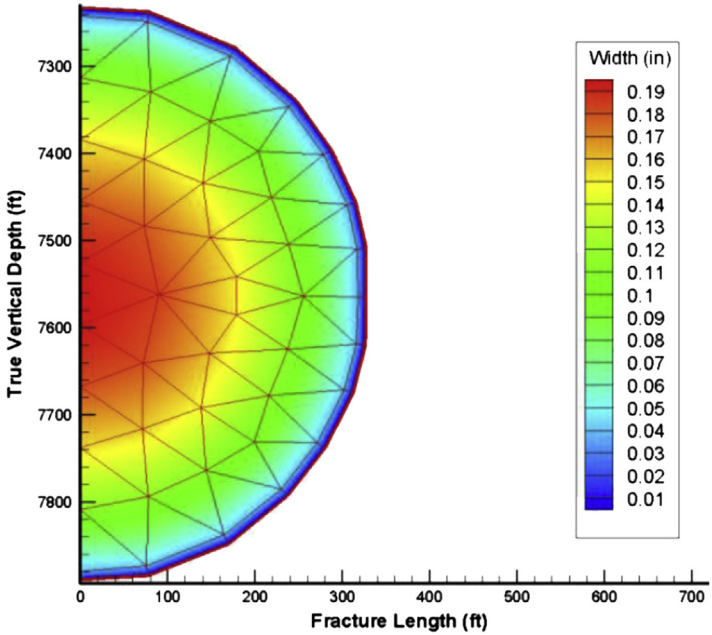

FIGURE 8.10 Fracture width after 30 min of injection. *From Ribeiro, L.H., Sharma, M.M., 2012. A new three-dimensional, compositional, model for hydraulic fracturing with energized fluids. In: Presented at SPE Annual Technical Conference and Exhibition, October 8–10, 2012, San Antonio, Texas, USA. SPE 159812.*

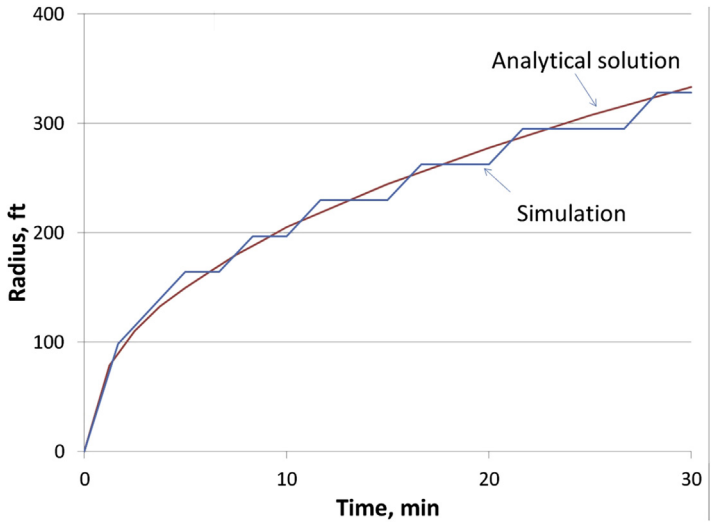

FIGURE 8.11 Comparison between simulation and analytical solution for fracture radius versus time.

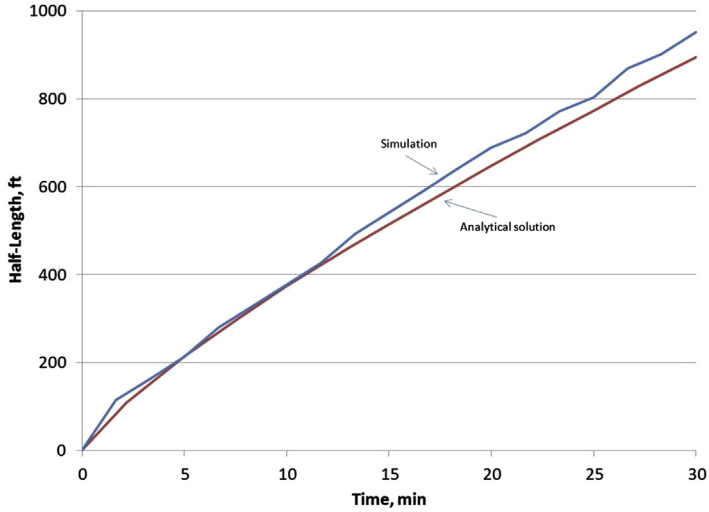

FIGURE 8.12 Comparison of fracture half-length between analytical solution and simulation.

half-length are smaller than in the previous example because the gridblocks in this example are smaller (half the length) than in the previous one. Fig. 8.13 shows the fracture width profile after 30 min of injection. This profile differs significantly from that simulated by Ribeiro and Sharma (2012), shown in Fig. 8.14. However, their simulator significantly underestimates half-length

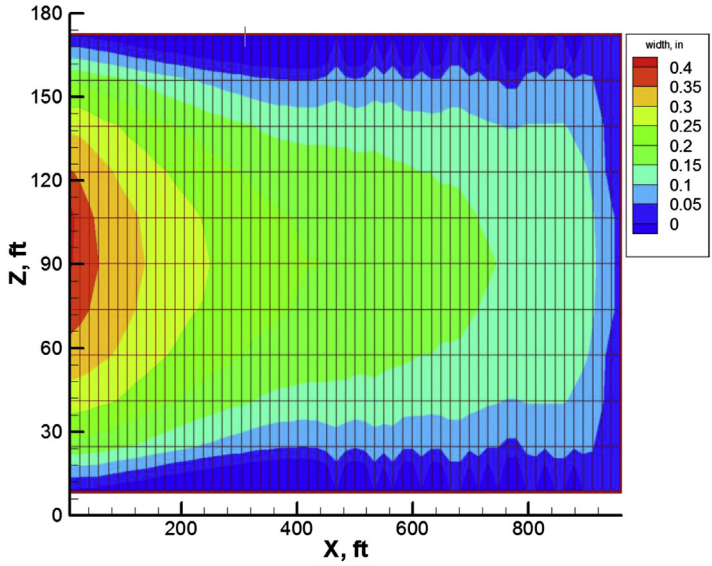

FIGURE 8.13 Fracture width after 30 min of injection.

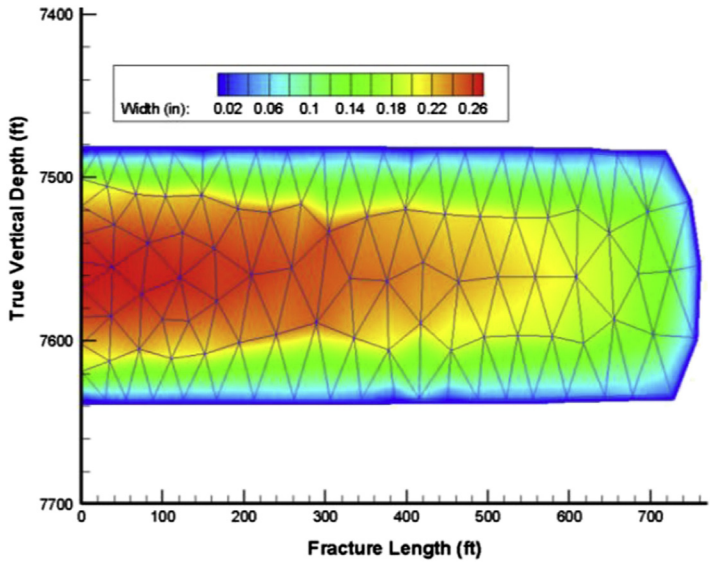

FIGURE 8.14 Fracture half-width after 30 min of injection. *From Ribeiro, L.H., Sharma, M.M., 2012. A new three-dimensional, compositional, model for hydraulic fracturing with energized fluids. In: Presented at SPE Annual Technical Conference and Exhibition, October 8–10, 2012, San Antonio, Texas, USA. SPE 159812.*

after 30 min of injection. The analytical solution then is 894 ft, our result is 951 ft, and their result is about 750 ft.

8.17.3 Field-Type Simulation

We present a simulation that is representative of that from a field. In this simulation, slurry consists of a single fluid component and a single proppant component. The fluid component is incompressible with density 1000 kg/m^3 and has power law rheology with index 0.1306 Pa s, exponent 0.4775, and maximum viscosity 0.1306 Pa s. The proppant component density is 2600 kg/m^3 and the proppant diameter is 0.0006 m.

The well consists of four segments. The first one is a vertical segment from the surface to 1778 m measured depth. The second (as well as the rest) is oriented 90 degrees (east) and this segment ends at 3360 m true vertical depth and 4058 m measured depth. The next two segments are horizontal and end at measured depths of 4559 and 4734 m, respectively. The outer diameter of the first three segment is 0.06955 m and that of the last segment is 0.16861 m. There are three completed intervals, from measured depth 4270–4280, 4350–4360, and 4430–4440 m. Heat loss from the wellbore occurs through a uniform medium with density, heat capacity, and thermal conductivity of

1200 kg/m^3, 2400 J/kgK, and 4500 W/mK, respectively. Friction along the well was neglected.

Rock-related properties that are constant are porosity (0.05), Young's modulus (41.58 GPa), Poisson's ratio (0.20), rock density (2720 kg/m^3), and Biot's coefficient (1.0). Rock-related properties that are piecewise-constant over true vertical depth are shown in Table 8.1. Rock-related properties that are piecewise-linear over true vertical depth are shown in Table 8.2.

The *1*-direction stress is oriented along the global *x*-direction and the 2-direction stress is oriented along the global *y*-direction. Because the minimum stress is along the global *x*-direction and the well trajectory at the completed intervals is also along that direction, the fractures emanating from those intervals will be parallel to each other and lie in the global *yz*-plane.

The slurry injection schedule consists of 14 segments; information about them is shown in Table 8.3. All completed intervals are open to slurry injection for the entire simulation duration.

The fracture gridblocks are square with length 10 m. Reservoir compressibility is 10^{-9} Pa^{-1} and reservoir viscosity is 0.0001 Pa s. The fracture front displacement coefficient and exponent in Eq. (8.37) are 10 m and 1, respectively. The maximum proppant fraction is 0.6 and the exponent in Eq. (8.4) (effect of proppant fraction on slurry viscosity) is −2.1.

The fractures emanating from the three completed intervals, from measured depth 4270−4280, 4350−4360, and 4430−4440 m, are referred to as "Fracture 1," "Fracture 2," and "Fracture 3," respectively. Fig. 8.15 shows the width profile for Fracture 1 at 3026 s, the end of the simulation. The coordinate system used in this figure and those upcoming is a relative one. Slurry

TABLE 8.1 Piecewise-Constant Rock-Related Properties as a Function True Vertical Depth (TVD)

TVD Range (m)	Permeability (m^2)	Tensile Strength (MPa)	Toughness (MPa)	Heat Treatment Coefficient (W/m^2)
0−1200	$1\cdot10^{-16}$	6.85	15.0	1.57
1200−3280	$8\cdot10^{-15}$	6.85	15.0	1.57
3280−3320	$8\cdot10^{-15}$	6.85	15.0	1.57
3320−3345	$8\cdot10^{-14}$	3.85	2.0	1.57
3345−3360	$8\cdot10^{-14}$	3.85	2.0	1.57
3360−3450	$8\cdot10^{-16}$	6.85	15.0	1.57
3450−4560	$8\cdot10^{-16}$	6.96	15.0	1.75

TABLE 8.2 Piecewise-Linear Rock-Related Properties as a Function True Vertical Depth (TVD)

TVD (m)	Reservoir Pressure (MPa)	Temperature (°C)	1-Stress (MPa)	2-Stress (MPa)	zz-Stress (MPa)
1200	32.0	40.0	3.5	5.5	22.00
3280	32.0	80.0	12.99	14.99	59.95
3320	32.0	85.0	13.17	15.17	60.68
3345	32.0	86.0	13.28	15.28	61.13
3360	32.0	87.0	13.35	15.35	61.41
3450	32.0	88.0	13.76	15.76	63.05
4560	32.11	91.8	19.24	21.24	84.95

TABLE 8.3 Slurry Segment Information

Segment	Volume (m^3)	Injection Rate (m^3/s)	Proppant Volume Fraction	Temperature (°C)
1	25.0	0.1333	0.0	20
2	20.0	0.1333	0.0385	20
3	25.0	0.1333	0.0	20
4	20.1	0.1333	0.0385	20
5	25.0	0.1333	0.0	20
6	20.0	0.1333	0.0385	20
7	25.0	0.1333	0.0	20
8	40.1	0.1333	0.0385	20
9	47.7	0.1333	0.0462	20
10	29.7	0.1333	0.0923	20
11	36.0	0.1333	0.1385	20
12	33.3	0.1333	0.1615	20
13	28.3	0.1333	0.1846	20
14	28.3	0.1333	0.2077	20

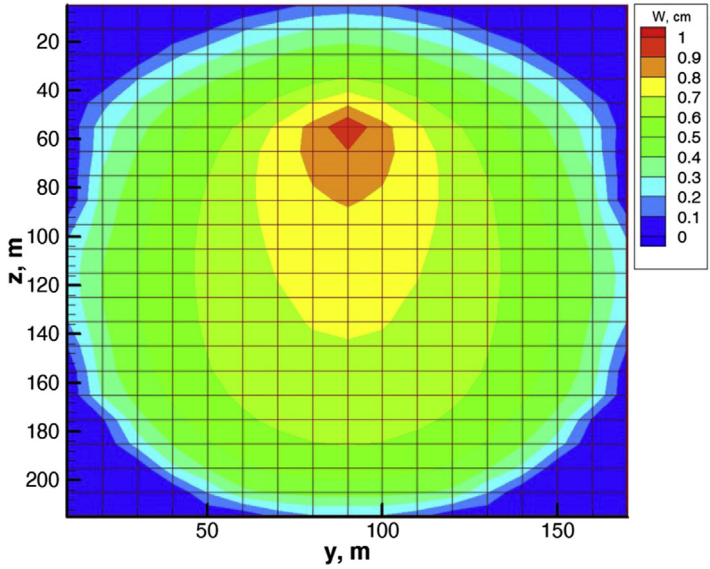

FIGURE 8.15 Width profile for Fracture 1.

enters the fracture at the gridblock that contains the completions and is centered at point (90, 60). The width is maximum there and the fracture extends preferentially downward (as opposed to upward), a consequence of the variation of the input stress field with true vertical depth. Fig. 8.16 shows the proppant volume fraction profile. Proppant is denser than fluid, so it settles to the lower portion of the fracture. Fig. 8.17 shows the temperature profile. The slurry enters the wellhead at 20 degrees and is heated by the formation as it traverses the wellbore. It enters the fracture around 52 degrees and is heated further by the formation through the fracture faces. Slurry temperature change depends on fracture width (the larger the width, the more mass, hence less temperature change per unit transfer of heat), proppant fraction (proppant has a lower heat capacity than fluid and proppant tends to move downward due to gravity), time (fracture gridblocks exchange heat with the surroundings after they become activated), and convection between neighboring gridblocks. Slurry temperature is highest around the fracture boundary, where fracture width is the smallest and lowest around the completions, where the entering slurry had a much smaller area (the well outer surface) to exchange heat.

Fig. 8.18 shows the width profile for Fracture 2. Fracture 2 has a smaller width than Fracture 1 (and Fracture 3) due to the stress shadow effect. The sum of the induced stresses from the other two fractures is greatest for Fracture 2, which lies between Fracture 1 and Fracture 3; hence, the minimum stress values are larger for this fracture than for the others, and the fracture widths are then smaller.

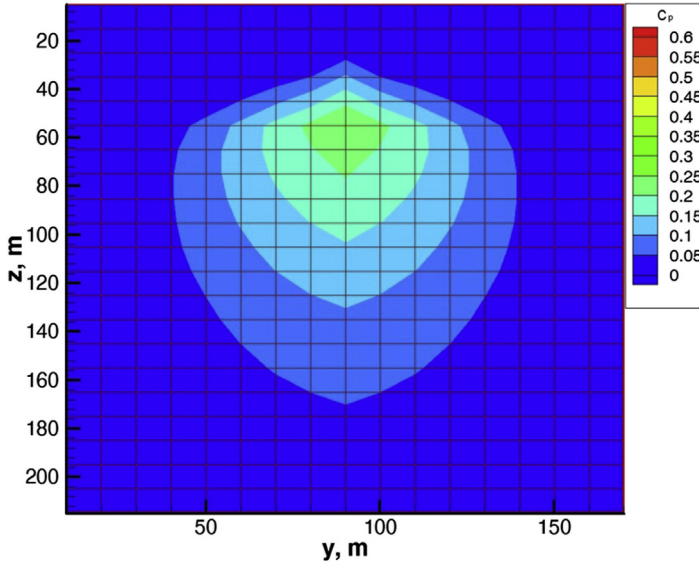

FIGURE 8.16 Proppant fraction profile for Fracture 1.

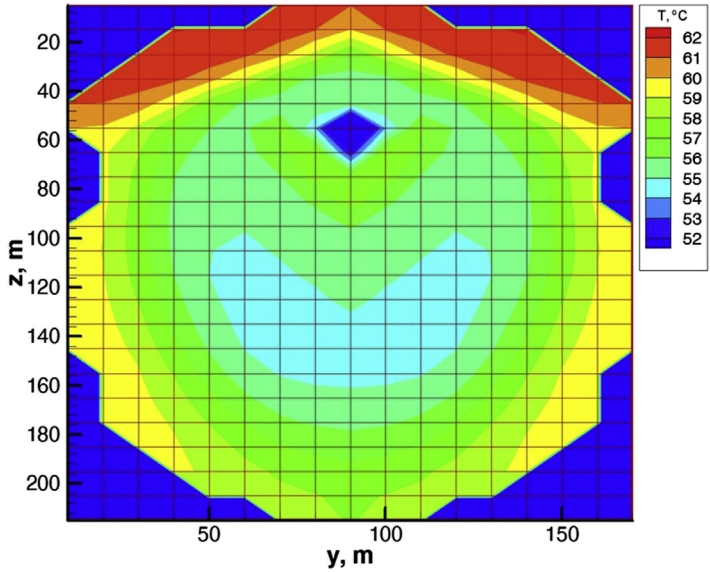

FIGURE 8.17 Temperature profile for Fracture 1.

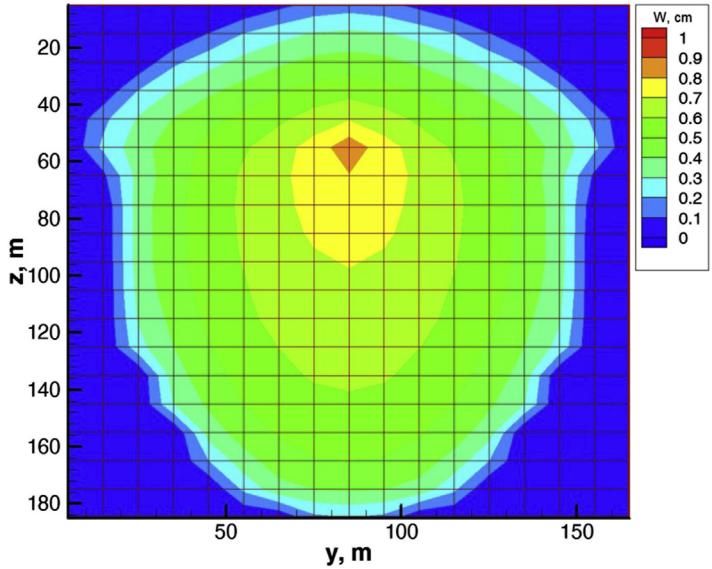

FIGURE 8.18 Width profile for Fracture 2.

Each of the three fractures induces a stress field change that decreases with distance, the stress shadow effect. The induced stress field felt for a given fracture is the sum of those induced for the other two. The induced stress field for the middle fracture has the greatest magnitude because the distance between it and the others is the smallest. The induced stress field for the two outer fractures have the same magnitude, but smaller than the middle one, and act in opposite directions.

Fig. 8.19 is a *xy*-cross section of Fracture 1 at 3400 m depth, in global coordinates with the *x*-direction, as well as the well, due east. The curve is located at the midpoint of the fracture faces. The distance between these faces, the fracture width, is too small to resolve at the distance scale of the figure. The other two fractures are located at larger *x*-values, so the stress shadow effect causes the fracture to bend to the left. Fig. 8.20 is a *xy*-cross section of Fracture 2 at 3400 m depth. The other two fracture are located on each side of this one and equal distances from it. Due to this symmetry, there is no fracture bending from the stress shadow effect, but this effect causes this fracture to be smaller than Fracture 1 because the minimum stress is larger. Fig. 8.21 is a *xy*-cross section of Fracture 3 at 3400 m depth. The other two fractures are located to the left of this one, so the stress shadow effect causes the fracture to bend to the right. The magnitude of the stress shadow effect is the same as that for Fracture 1 but acts in the opposite direction.

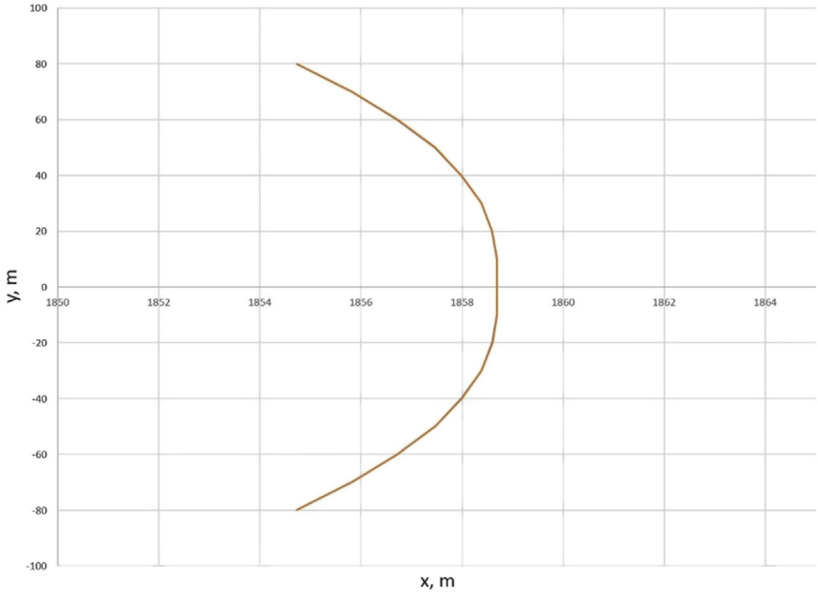

FIGURE 8.19 Fracture 1 *xy*-cross section at 3400 m depth.

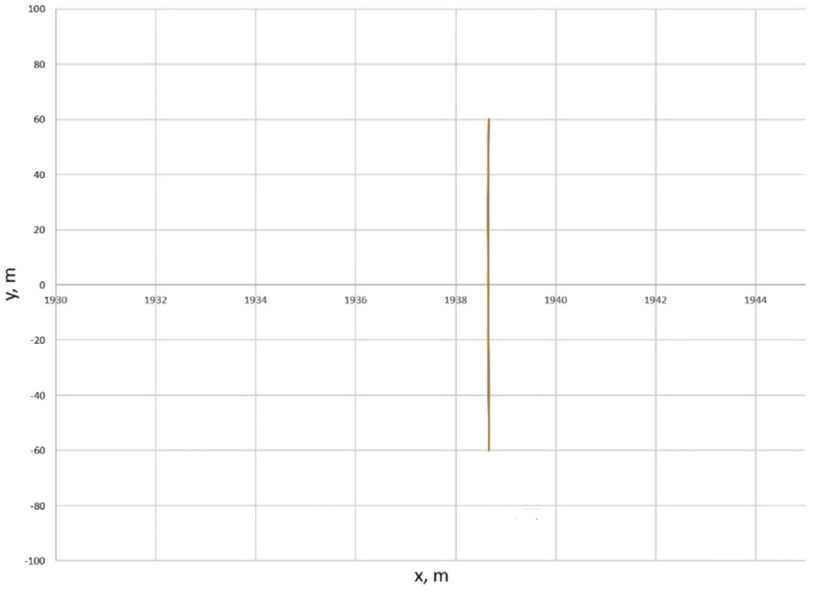

FIGURE 8.20 Fracture 2 *xy*-cross section at 3400 m depth.

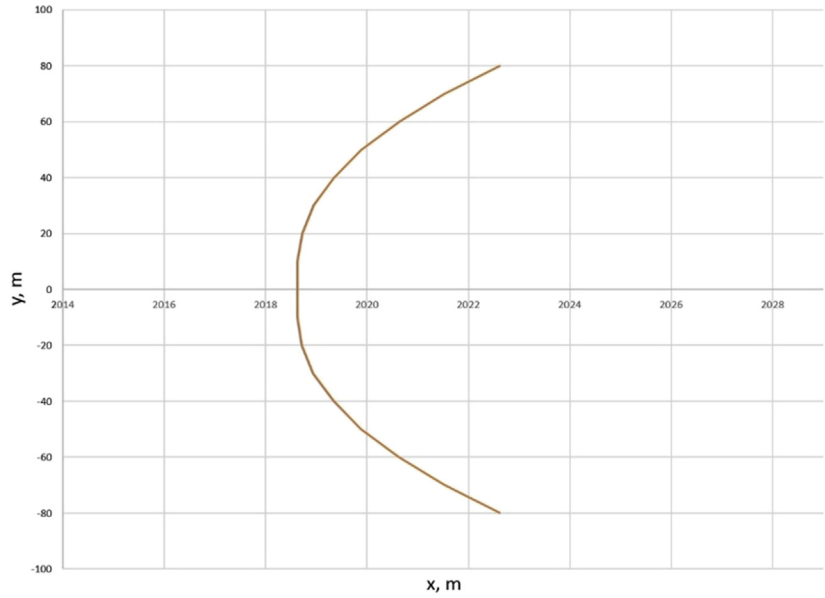

FIGURE 8.21 Fracture 3 *xy*-cross section at 3400 m depth.

8.18 SUMMARY AND CONCLUSIONS

We developed a general three-dimensional hydraulic fracturing model that accounts for fluid flow and heat transfer in the wellbore and the fracture, and the geomechanics of fracturing including fracture initiation, growth, and propagation, as well as the stress shadow effect.

We ran two simulations to provide model verification: a radial fracture propagation and a PKN-like fracture propagation. We compared results from these with analytical solutions and obtained good agreement. We then ran a simulation of field-type data that illustrated some of the simulator capabilities, including the stress shadow effect. We injected slurry into three fractures simultaneously and found the middle fracture, which felt the largest stress shadow effect, was smaller than the other two. In addition, this effect caused these other fracture to deviate from planar due to the alteration of the principal stress directions from the induced stresses.

ACKNOWLEDGMENTS

This work was supported by EMG Research Center in Colorado School of Mines and CNPC-USA.

REFERENCES

Daneshy, A.A., January 1973. On the design of vertical hydraulic fractures. Journal of Petroleum Technology 83–97. SPE 3654.

Friehauf, K.E., 2009. Simulation and Design of Energized Hydraulic Fractures (Ph.D. thesis). The University of Texas at Austin.

Geertsma, J., de Klerk, F., 1969. A rapid method of predicting width and extent of hydraulically induced fractures. Journal of Petroleum Technology 21 (12), 1571–1581.

Horner, D.R., 1951. Pressure buildup in wells. In: Proc. Third World Pet. Cong., The Hague, pp. 503–521. Sec. II.

Khristianovic, S.A., Zheltov, Y.P., 1955. Formation of vertical fractures by means of highly viscous liquid. In: Proceedings of the Fourth World Petroleum Congress, Rome, Italy, pp. 579–586.

Lord, D.L., McGowan, J.M., 1986. Real-time treating pressure analysis aided by new correlation. In: Presented at the 61st SPE ATCE Held in New Orleans, LA, October 5–8, 1986. SPE 15367.

Mastrojannis, E.N., Keer, L.M., Mura, T., 1980. Growth of planar cracks induced by hydraulic fracturing. International Journal of Numerical Methods in Engineering 15, 41–54.

Mack, M.G., Warpinski, N.R., 2000. Mechanics of hydraulic fracturing. In: Economides, N. (Ed.), Reservoir Stimulation, third ed. Wiley, Chichester (Chapter 6).

McClain, C., 1963. Fluid Flow in Pipes. The Industrial Press, New York, New York.

Narashimhan, T.N., Witherspoon, P.A., 1976. An integrated finite difference method for analysis of fluid flow in porous media. Water Resource Research 12, 57–64.

Nicodemo, L., Nicolais, L., Landel, R.F., 1974. Shear rate dependent viscosity suspensions in Newtonain and non-Newtonian liquids. Chemical Engineering Science 29, 729–735.

Nordgren, R., 1972. Propagation of a vertical hydraulic fracture. Society of Petroleum Engineers Journal 12 (4), 306–314.

Perkins, T.K., Kern, L.R., 1961. Widths of hydraulic fractures. Journal of Petroleum Technology 13 (9), 937–949. SPE 89.

Pruess, K., 1991. TOUGH2—A General Purpose Numerical Simulator for Multiphase Fluid and Heat Flow, Report LBL-29400. Lawrence Berkeley National Laboratory, Berkeley, CA.

Ribeiro, L.H., Sharma, M.M., 2012. A new three-dimensional, compositional, model for hydraulic fracturing with energized fluids. In: Presented at SPE Annual Technical Conference and Exhibition, October 8–10, 2012, San Antonio, Texas, USA. SPE 159812.

Schechter, R.S., 1992. Oil Well Stimulation. Prentice Hall, Englewood Cliffs, NJ.

Simonson, E.R., Abou-Sayed, A.S., Clifton, R.J., 1978. Containment of massive hydraulic fractures. Society of Petroleum Engineers Journal 18 (1), 27–32. SPE 6089.

Sneddon, I.N., 1946. The distribution of stress in the neighbourhood of a crack in an elastic solid. Proceedings of the Royal Society of London. Series A 187, 229–260.

Timoshenko, Goodier, 1951. Theory of Elasticity. McGraw-Hill Book Company, Inc., New York, NY.

Valko, P., Economides, M.J., 1995. Hydraulic Fracture Mechanics. John Wiley &Sons Inc.

Warpinski, N.R., Branagan, P.T., September 1989. Altered-stress fracturing. Journal of Petroleum Technology 990–997.

Winterfeld, P.H., Wu, Y.-S., 2015. Simulation of coupled thermal-hydrological-mechanical phenomena in porous and fractured media. In: Presented at the SPE Reservoir Simulation Symposium held in Houston, Texas, USA, 23–25 February 2015. SPE 173210_MS-MS.

Yew, C.H., 1997. Mechanics of Hydraulic Fracturing. Gulf Publishing Company, Houston, TX.

Chapter 9

Modeling Rock Fracturing Processes With FRACOD

Baotang Shen[1,2]
[1]*Shandong University of Science and Technology, Qingdao, China;* [2]*CSIRO Energy, Queensland Centre for Advanced Technologies, Brisbane, QLD Australia*

9.1 INTRODUCTION

Rock fracture mechanics is a promising outgrowth of rock mechanics and fracture mechanics, and it has developed rapidly in recent years, driven by the need for in-depth understanding of rock mass failure processes in both fundamental research and rock engineering designs. As rock engineering extends into more challenging fields (such as mining at depth, radioactive waste disposal, geothermal energy, and deep and large underground spaces), it requires knowledge of the rock mass's complex coupled thermal–hydraulic–chemical–mechanical processes. Rock fracture mechanics plays a crucial role in these complex coupled processes simply because rock fractures are the principal carrier (e.g., fluid flow) and common interface (e.g., heat exchange between rock and fluid).

To date, the demand for rock fracture mechanics–based design tools has outstripped the very limited number of numerical tools available. Most of those tools were developed for civil engineering and material sciences and deal with substances such as steel, ceramic, glass, ice, and concrete, which differ markedly from rocks in their fracturing behavior.

Since the early 1990s, a new approach has been taken to develop a practical numerical approach using fracture mechanics principles to predict rock mass failure processes. The development was based on several laboratory studies and new understandings about rock fracture propagation and coalescence mechanisms (Reyes and Einstein, 1991; Shen et al., 1995), in particular the acceptance of the existence of shear fracture (mode II) propagation in rock masses and its critical role in rock mass failure in a compressive stress environment. Led by this understanding, a new fracture criterion was proposed (Shen, 1993; Shen and Stephansson, 1994), which predicts both tensile and shear fracture propagations, overcoming the shortcomings of traditional

Hydraulic Fracture Modeling. https://doi.org/10.1016/B978-0-12-812998-2.00009-6

fracture criteria that predict only tensile failure. This approach has proved to be very effective in simulating the behavior of multiple fractures in rocklike materials in laboratory tests (Shen and Stephansson, 1993).

Development of this modeling approach with a view to engineering application was initially driven by proposals for radioactive waste disposal in Sweden and Finland, where the activation and propagation of fractures initiated by thermal loadings and glaciations are considered a major risk factor (Rinne, 2000; Rinne et al., 2003; Shen et al., 2004). During this period, an earlier version of the code FRACOD was developed, which was capable of simulating fracture propagation, fracture initiation, and acoustic emission (AE). This code capability was then expanded to include time-dependent rock behavior and subcritical crack growth (Rinne, 2008). In the course of this development process, many application case studies were conducted using FRACOD, including the well-known Äspö Hard Rock Laboratory's Pillar Spalling Experiments (APSE) in Sweden (Rinne et al., 2004), the DECOVALEX International Collaboration Project (Rinne and Shen, 2007), and the Mizunami Underground Research Laboratory (MIU) Investigations in Japan (Stephansson et al., 2008; Shen et al., 2011).

This fracture mechanics approach was further expanded to other application fields of rock engineering such as tunneling and geothermal energy. In an attempt to investigate the stability of a tunnel under high horizontal stresses, FRACOD successfully predicted the same "log-spiral" type of fracturing pattern around the tunnel that was observed in the laboratory (Barton, 2007). When applied to the back analysis of in situ stresses in a 4.4-km-deep geothermal well in Australia, this approach was shown to realistically simulate the borehole breakout, thereby accurately predicting the rock mass stress state (Shen, 2008).

The concerns about global warming have significantly increased the worldwide interest in alternative energy sources and storage methods. Thus, accurate prediction of the coupled behavior of rock fracturing, fluid flow, and thermal processes is now a vital scientific endeavor. FRACOD seeks to address the complex design issues that are being faced in various emerging developments in energy-related industries including geothermal energy, liquefied natural gas (LNG) underground storage, and CO_2 geosequestration.

Since 2007, the focus of FRACOD development has shifted to the coupling between rock fracturing, fluid flow, and thermal loading, thanks to the establishment of an international collaboration project with participants from Australia, Europe, and South Korea. Coupling functions of mechanical–thermal–hydraulic (M–T–H) processes have been developed in FRACOD (Shen et al., 2009, 2012). Several application case studies related to hydraulic fracturing (HF), LNG underground storage, and nuclear waste disposal (underground borehole spalling experiments) in Finland have been conducted (Xie et al., 2014; Shen et al., 2008; Siren et al., 2014).

Development and application of the fracture mechanics approach are also being extended to a three-dimensional (3D) version of FRACOD for modeling true 3D problems (Shi and Shen, 2014; Shi et al., 2014).

This chapter summarizes the key physical and theoretical foundation behind FRACOD and describes several application cases solving actual industry problems, with a focus on hydraulic fracture modeling. For those who wish to read more details about FRACOD, please refer to the book *Modelling Rock Fracturing Processes* by Shen et al. (2014).

9.2 ROCK FRACTURE PROPAGATION MECHANISMS AND FRACTURE CRITERION

Fractures in rock masses often exhibit different behaviors from those in other engineering materials such as steel and glass. Fractures in underground rock masses are mostly under compression, and they may propagate in tensile, shear, or tearing modes. Unlike in other materials, shear fracture is one of the common types of fractures observed in the rock mass, caused by high compressive stresses existing deep underground. Although the tensile strength of rock is much less than its shear strength, under compressive and confined conditions in underground rock masses, tensile stresses may not always exist and hence rock mass failure is often dominated by shear fracture initiation and propagation.

A number of laboratory tests have been conducted to investigate the fracture propagation mechanisms in compression using brittle geomaterials. Petit and Barquins (1988) used a sandstone specimen with a single preexisting fracture, which was loaded in uniaxial compression. They observed two types of fractures: wing cracks, approximately in the direction of loading, and secondary cracks in the direction of about 45 degrees from the loading direction. Shen et al. (1995) used specimens made of artificial rock with two parallel and aligned preexisting fractures and applied a uniaxial load until failure. It was found that the rock bridge between the two preexisting fractures failed due to shear fracture propagation that was initiated at the tips of the preexisting fractures. The shear fracture is clearly recognizable by its rough surfaces with the associated pulverized materials from the shearing of asperities, compared with the tensile crack (wing crack) that had clean and smooth surfaces (Fig. 9.1). Rao (1999) carried out several shear tests on rock specimens with a single preexisting fracture and found that, with a sufficiently high normal stress, the preexisting fracture propagated in its original plane and it is dominated by a shear failure mode. Backers et al. (2002) developed a method for testing the shear fracture toughness by using a punch-through test setup of a preslotted core specimen. With high confinement stress, they found that shear fractures will develop and propagate in the rock bridge between the aligned slots. All these laboratory and field observations demonstrate that

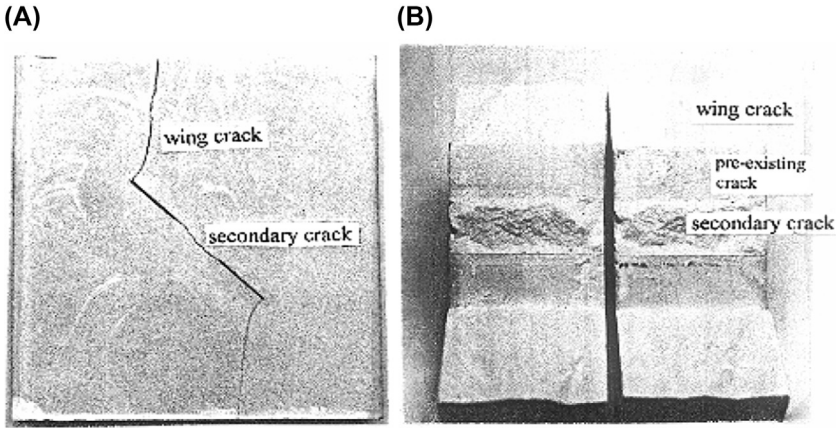

FIGURE 9.1 Fracture formation during a uniaxial loading test of a specimen with two aligned preexisting cracks. (A) Fracture pattern after failure; (B) fracture surface characteristics. *After Shen, B., Stephansson, O., Einstein, H.H., Ghahreman, B., 1995. Coalescence of fractures under shear stresses in experiments. Journal of Geophysics Research 100 (B4), 5975–5990.*

shear fracturing does occur in rocks with confinement when loaded in compression.

In modeling fracture propagation in rock masses where both tensile and shear failure are common, a fracture criterion for predicting both tensile (mode I) and shear (mode II) fracture propagation is needed. The existing fracture criteria in the macroapproach can be classified into two groups: the principal stress (strain)-based criteria and the energy-based criteria. The first group consists of the maximum principal stress criterion and the maximum principal strain criterion; the second group includes the maximum strain energy release rate criterion (G-criterion) and the minimum strain energy density criterion (S-criterion). The principal stress (strain)-based criteria are only applicable to the mode I fracture propagation that relies on the principal tensile stress (strain). To be applied for the mode II propagation, a fracture criterion has to consider not only the principal stress (strain) but also the shear stress (strain). From this point of view, the energy-based criteria seem to be applicable for both mode I and II propagation because the strain energy in the vicinity of a fracture tip is related to all the components of stress and strain.

Both the G-criterion and the S-criterion have been examined for application in the mode I and mode II propagation (Shen and Stephansson, 1993), and neither of them is directly suitable. In a study by Shen and Stephansson (1994), the original G-criterion has been improved and extended. The original G-criterion states that when the strain energy release rate in the direction of the maximum G-value reaches the critical value G_c, the fracture tip will propagate in that direction. It does not distinguish between mode I and mode II fracture critical energies (G_{Ic} and G_{IIc}). In fact, for most of the engineering materials,

the mode II fracture toughness is much higher than the mode I toughness due to the differences in the failure mechanism. In rocks, for instance, G_{IIc} is found in laboratory scale to be at least two orders of magnitude higher than G_{Ic} (Li, 1991). Applied to the mixed mode I and mode II fracture propagation, the G-criterion is difficult to use because the critical value G_c must be carefully chosen between G_{Ic} and G_{IIc}.

A modified G-criterion, namely the F-criterion, was proposed (Shen and Stephansson, 1994). Using the F-criterion the resultant strain energy release rate (G) at a fracture tip is divided into two parts, one due to mode I deformation (G_I) and the other due to mode II deformation (G_{II}). Then the sum of their normalized values is used to determine the failure load and its direction. G_I and G_{II} can be expressed as follows (Fig. 9.2): if a fracture grows a unit length in an arbitrary direction and the new fracture opens without any surface shear dislocation, the strain energy loss in the surrounding body due to the fracture growth is G_I. Similarly, if the new fracture has only a surface shear dislocation, the strain energy loss is G_{II}. The principles of the F-criterion can be stated as follows:

1. In an arbitrary direction (θ) at a fracture tip, there exists an F-value, which is calculated by

$$F(\theta) = \frac{G_I(\theta)}{G_{Ic}} + \frac{G_{II}(\theta)}{G_{IIc}} \tag{9.1}$$

2. The possible direction of propagation of the fracture tip is the direction ($\theta = \theta_0$) for which the F-value reaches its maximum.

$$F(\theta)|_{\theta=\theta_0} = \max. \tag{9.2}$$

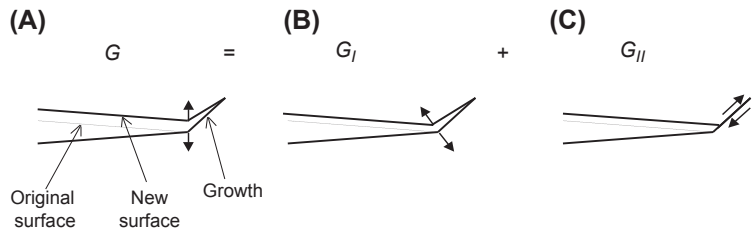

FIGURE 9.2 Definition of G_I and G_{II} for fracture growth. (A) G, the growth has both open and shear displacement; (B) G_I, the growth has only open displacement; (C) G_{II}, the growth has only shear displacement.

3. When the maximum F-value reaches 1.0, the fracture tip will propagate, i.e.,

$$F(\theta)|_{\theta=\theta_0} = 1.0 \tag{9.3}$$

The F-criterion is actually a more general form of the G-criterion and it allows us to consider mode I and mode II propagation simultaneously. In most cases, the F-value reaches its peak either in the direction of maximum tension ($G_{\mathrm{I}} =$ maximum while $G_{\mathrm{II}} = 0$) or in the direction of maximum shearing ($G_{\mathrm{II}} =$ maximum while $G_{\mathrm{I}} = 0$). This means that a fracture propagation of a finite length (the length of an element, for instance) is either pure mode I or pure mode II. However, the fracture growth may oscillate between mode I and mode II during an ongoing process of propagation, and hence form a path that exhibits the mixed mode failure in general.

9.3 THEORETICAL BACKGROUND OF FRACOD

The FRACOD code is essentially a boundary element method (BEM) program, and thus it follows the BEM principals. Specifically, it uses the displacement discontinuity method (DDM), which is an indirect boundary element technique. The fracture mechanics theories and the F-criterion are incorporated into the code to model fracturing process.

The DDM used in FRACOD is based on the analytical solution of stresses and displacements caused by a constant displacement discontinuity over a finite line segment (e.g., crack) in an infinite elastic solid body in 2D. The displacements in the solid body are continuous everywhere except over the line segment where they differ by a constant value, which is defined as the displacement discontinuity. The explicit solution of the given problem was provided by Crouch and Starfield (1983). The stresses and displacements of a specific point can be found using Eq. (9.4).

$$\begin{aligned} \sigma_s &= A_{ss}D_s + A_{sn}D_n \\ \sigma_n &= A_{ns}D_s + A_{nn}D_n \\ u_s &= B_{ss}D_s + B_{sn}D_n \\ u_n &= B_{ns}D_s + B_{nn}D_n \end{aligned} \tag{9.4}$$

where D_s and D_n are the shear and normal components of displacement discontinuity. A_{ss}, A_{sn}, etc., and B_{ss}, B_{sn}, etc., are the boundary influence coefficients for the stress and displacement, respectively. The coefficients are the functions of elastic properties of solid body and the position of the point relative to the line segment. They represent the stresses or displacements of the point caused by a constant unit displacement discontinuity.

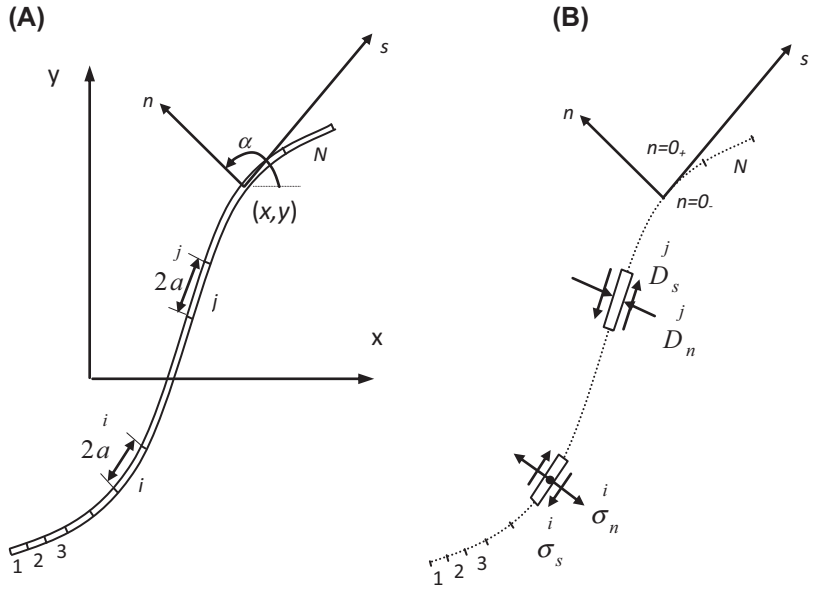

FIGURE 9.3 Representation of a curved crack by N displacement discontinuity elements.

For a crack of any shape, it is acceptable to represent it by N straight segments joined end by end as shown in Fig. 9.3, provided that the number of line segments is sufficient. For each line segment, an elemental displacement discontinuity exists (D_s^j and D_n^j). Based on the principle of superposition and applying Eq. (9.4), the stresses and displacements at any point in the infinite body can be obtained. Applying the expressions to points on the line segments along the crack, the stresses and displacements have the form

$$\begin{aligned}
\sigma_s^i &= \sum_{j=1}^{N} A_{ss}^{ij} D_s^j + \sum_{j=1}^{N} A_{sn}^{ij} D_n^j \\
\sigma_n^i &= \sum_{j=1}^{N} A_{ns}^{ij} D_s^j + \sum_{j=1}^{N} A_{nn}^{ij} D_n^j \\
u_s^i &= \sum_{j=1}^{N} B_{ss}^{ij} D_s^j + \sum_{j=1}^{N} B_{sn}^{ij} D_n^j \\
u_n^i &= \sum_{j=1}^{N} B_{ns}^{ij} D_s^j + \sum_{j=1}^{N} B_{nn}^{ij} D_n^j \quad \text{for } i = 1 \text{ to } N
\end{aligned} \tag{9.5}$$

The equations compose a system of simultaneous linear equations with 2N unknowns. They are the elemental displacement discontinuity components D_n^j and D_s^j and can be solved by applying appropriate 2N equations from Eq. (9.5)

to the specified traction and/or displacement conditions on the crack. For a problem of simulating discontinuities in the rock mass, various constraints to the stress in the equations can be added:

For an open crack where no stresses can be transmitted through it, the stress components in Eq. (9.5) are zero.

$$\begin{aligned} \sigma_s^i &= 0 \\ \sigma_n^i &= 0 \end{aligned} \tag{9.6}$$

For the crack surface of elastic contact, the stress components depend on the crack stiffness (K_s, K_n) and the displacement discontinuities and have the form

$$\begin{aligned} \sigma_s^i &= K_s D_s^i \\ \sigma_n^i &= K_n D_n^i \end{aligned} \tag{9.7}$$

A crack with its surface sliding, adopts the Coulomb's failure criterion.

$$\begin{aligned} \sigma_s^i &= c + K_n D_n^i \tan\phi \\ \sigma_n^i &= K_n D_n^i \end{aligned} \tag{9.8}$$

where ϕ is the crack friction angle and c is the cohesion strength.

Finally, with the appropriate boundary stresses and displacements, the unknowns of elemental displacement discontinuities (D_n^i and D_s^i) are obtained by solving the system of stress-governing equations in Eq. (9.5) using conventional numerical techniques for linear equations.

The key step in using the F-criterion is to determine the strain energy release rate of mode I (G_{I}) and mode II (G_{II}) at a given fracture tip. As G_{I} and G_{II} are the only special cases of G, the problem is then how to use DDM to calculate the strain energy release rate G.

The G-value, by definition, is the change of the strain energy in a linear elastic body when the crack has grown one unit of length. Therefore, to obtain the G-value the strain energy must first be estimated.

By definition, the strain energy, W, in a linearly elastic body is

$$W = \iiint_V \frac{1}{2}\sigma_{ij}\varepsilon_{ij}dV \tag{9.9}$$

where σ_{ij} and ε_{ij} are the stress and strain tensors and V is the volume of the body. The strain energy can also be calculated from the stresses and displacements along its boundary

$$W = \frac{1}{2}\int_s (\sigma_s u_s + \sigma_n u_n)ds \tag{9.10}$$

where σ_s, σ_n and u_s, u_n are the stresses and displacements, respectively, in tangential and normal directions along the boundary of the elastic body.

Applying Eq. (9.10) to a single straight crack in an infinite body with far field stresses in the shear and normal directions of the crack, $(\sigma_s)_0$ and $(\sigma_n)_0$, the strain energy, W, in the infinite elastic body is

$$W = \frac{1}{2}\int_0^a \left[\left((\sigma_s - (\sigma_s)_0)D_s + (\sigma_n - (\sigma_n)_0)D_n\right)da\right] \tag{9.11}$$

where a is the crack length, D_s is the shear displacement discontinuity, and D_n is the normal displacement discontinuity of the crack. When DDM is used to calculate the stresses and displacement discontinuities of the crack, the strain energy can also be written in terms of the element length (a_i) and the stresses and displacement discontinuities of the ith element of the crack. Then the strain energy from the whole crack is the sum of the energies of all elements:

$$W \approx \frac{1}{2}\sum_i \left(\overset{i}{a}\left(\overset{i}{\sigma_s} - \left(\overset{i}{\sigma_s}\right)_0\right)\overset{i}{D_s} + \overset{i}{a}\left(\overset{i}{\sigma_n} - \left(\overset{i}{\sigma_n}\right)_0\right)\overset{i}{D_n}\right) \tag{9.12}$$

It is noted that the far field stresses are resolved along the elemental directions for each element.

The G-value in the direction θ at a crack tip can be estimated by

$$G(\theta) = \frac{\delta W}{\delta a} \approx \frac{[W(a + \Delta a) - W(a)]}{\Delta a} \tag{9.13}$$

where $W(a)$ is the strain energy governed by the original crack, while $W(a + \Delta a)$ is the strain energy governed by new crack consisting of the original crack and a small extension at the crack tip with length of Δa in the direction θ (Fig. 9.3). In Fig. 9.4, a "fictitious" element is introduced to the tip of the original crack with the length Δa in the direction θ. Both $W(a)$ and $W(a + \Delta a)$ can be determined easily by directly using DDM and Eq. (9.12).

In the earlier calculation, if we restrict the shear displacement of the "fictitious" element numerically to zero, the result obtained using Eq. (9.13) will be $G_{\mathrm{I}}(\theta)$. Similarly, if we restrict the normal displacement of the "fictitious" element to zero, the result obtained will be $G_{\mathrm{II}}(\theta)$. After obtaining both $G_{\mathrm{I}}(\theta)$ and $G_{\mathrm{II}}(\theta)$, the F-value in Eq. (9.1) can be calculated using the given fracture toughness values G_{Ic} and G_{IIc} of a given rock type. Then the

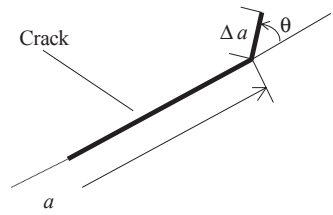

FIGURE 9.4 Fictitious crack increment Δa in direction θ with respect to the initial crack orientation.

maximum value of F and the corresponding direction can be sought. If the maximum value is greater than unity, then the crack will propagate in the maximum direction at the tip.

9.4 COUPLING BETWEEN ROCK FRACTURING AND THERMAL AND HYDRAULIC PROCESSES

Over the past several decades, coupled M−T−H processes in rock masses have been a focus of research, particularly in the field of underground nuclear waste disposal, and significant advances have been achieved (Min et al., 2005; Rutqvist et al., 2005; Tsang et al., 2005). However, the past studies have mostly treated the rock mass as a continuum or a discontinuum with predefined discontinuities. The process of explicit rock fracturing, which is the dominant mechanism in hard rock failure, has not been adequately addressed during the simulation of complex coupled processes. Understanding and predicting the effects of the interactive processes between explicit rock fracturing, temperature change, and fluid flow (coupled fracturing [F]−thermal [T]−hydraulic [H] processes) remain to be a key challenge for industries such as geothermal energy extraction, geological CO_2 sequestration, underground LNG storage, and deep geological disposal of nuclear waste.

In a fractured rock mass, rock fracturing, fluid flow, and rock temperature change are closely correlated (Fig. 9.5). Rock fractures will enhance the fluid flow by creating new flow channels and/or widening the channels, whereas the fluid pressure may stimulate fracture growth. A temperature change will result in thermal stress in the rock mass, which could lead to fracture propagation. Secondary interaction among the three processes also exists, for example, fluid flow changes temperature, which in turn affects the rock stress state and may cause fracture propagation. Coupling between these processes in numerical modeling are necessary to study the industrial issues mentioned previously.

To increase the knowledge on the aforementioned issues and to understand the coupled F−T−H processes in rocks on an engineering scale, recent

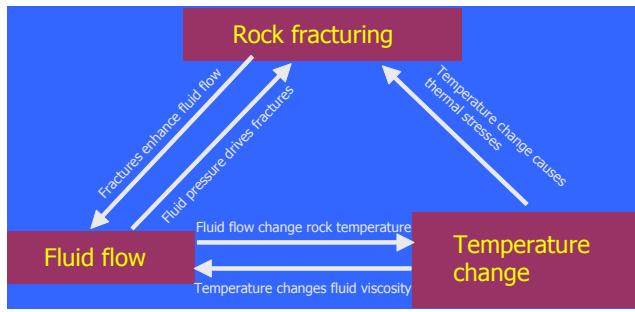

FIGURE 9.5 Interaction between rock fracturing and fluid flow and rock temperature changes.

development of FRACOD has been focused on the coupled processes between rock fracturing and thermal and hydraulic processes. This section summarizes theoretical background and numerical considerations of the coupled $F-T-H$ functions in FRACOD.

9.4.1 Rock Fracturing–Thermal Coupling

The direct coupling between rock fracturing and thermal processes is a one-way coupling with stresses dependent on the temperature field following thermoelasticity principles. As the DDM used in FRACOD is an indirect BEM, an indirect method is also used to simulate the temperature distribution and thermal stresses due to internal and boundary heat sources. With this method, fictitious heat sources with unknown strength over the boundary of domain are used, and it is therefore easier to consider the problem with internal heat sources (Shen et al., 2013b). The 2D fundamental solutions for temperature, stresses, and displacements induced by a point heat source with unit strength located at the origin of the coordinate system in thermoelasticity are given as follows.

$$T = \frac{1}{4\pi k} Ei\left(\xi^2\right) \tag{9.14}$$

$$\sigma_{xx} = \frac{E\alpha}{8\pi k(1-\nu)} \left\{ \left(1 - \frac{2x^2}{r^2}\right) \frac{1 - e^{-\xi^2}}{\xi^2} - Ei\left(\xi^2\right) \right\} \tag{9.15}$$

$$\sigma_{xy} = \frac{E\alpha}{8\pi k(1-\nu)} \left\{ \left(-\frac{2xy}{r^2}\right) \frac{1 - e^{-\xi^2}}{\xi^2} \right\} \tag{9.16}$$

$$\sigma_{yy} = \frac{E\alpha}{8\pi k(1-\nu)} \left\{ \left(1 - \frac{2y^2}{r^2}\right) \frac{1 - e^{-\xi^2}}{\xi^2} - Ei\left(\xi^2\right) \right\} \tag{9.17}$$

$$u_x = \frac{\alpha(1+\nu)}{4\pi k(1-\nu)} r \left\{ \frac{x}{r} \frac{\left(1 - e^{-\xi^2}\right)}{2\xi^2} + \frac{1}{2} Ei\left(\xi^2\right) \right\} \tag{9.18}$$

$$u_y = \frac{\alpha(1+\nu)}{4\pi k(1-\nu)} r \left\{ \frac{y}{r} \frac{\left(1 - e^{-\xi^2}\right)}{2\xi^2} + \frac{1}{2} Ei\left(\xi^2\right) \right\} \tag{9.19}$$

where T is the temperature (°C); σ_{xx}, σ_{xy}, and σ_{yy} are the stresses (Pa); u_x and u_y are the displacements (m); α is the linear thermal expansion coefficient (1/°C); k is the thermal conductivity (W/m°C); ν is the Poisson's ratio; $r = \sqrt{x^2 + y^2}$; $\xi^2 = \frac{r^2}{4c_r t}$; $c_r = \frac{k}{\rho_r c_p}$, c_r is the thermal diffusivity (m^2/s), with ρ_r being the

density (kg/m^3) and c_p being the specific heat capacity (J/kg°C), t is time (s); and $Ei(u) = \int_u^\infty \frac{e^{-z}}{z} dz$.

Eqs. (9.14)–(9.19) constitute the fundamental equations to be used in all the formulations of the numerical process for $F-T$ coupling problems.

For an internal problem as shown in Fig. 9.6, the boundary of a finite body is discretized into n elements. Before any mechanical boundary condition is considered, each element is assumed to be in an infinite, isotropic, and homogeneous medium to make use of the aforementioned fundamental solutions. Let us consider that a constant line heat source with unit heat strength is placed along element j at time $t_0 = 0$. At any given time t, the temperature, stresses, and displacements at the center point of another element (element i) is known based on the fundamental solutions given in Eqs. (9.14)–(9.19).

In the fictitious heat source method, it is assumed that a line heat source has been applied along each boundary element. The strengths of these line sources are the unknowns and need to be solved for. The total temperature change, stresses, and displacements at element i due to the fictitious line sources and mechanical boundary conditions can be calculated by superimposing the effect of all individual heat sources as shown in the following:

$$T^i = \sum_{j=1}^{n} T^{ij} H^j \tag{9.20}$$

$$\sigma_s^i = \sum_{j=1}^{n} \left(A_{ss}^{ij} D_s^j + A_{sn}^{ij} D_n^j + F_s^{ij} H^j \right) \tag{9.21}$$

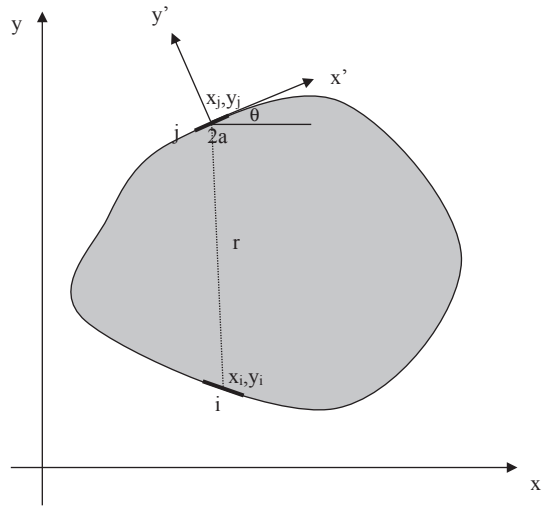

FIGURE 9.6 Elements along a solid body boundary and local coordinate system of the boundary element.

$$\sigma_n^i = \sum_{j=1}^{n} \left(A_{ns}^{ij} D_s^j + A_{nn}^{ij} D_n^j + F_n^{ij} H^j \right) \tag{9.22}$$

$$u_s^i = \sum_{j=1}^{n} \left(B_{ss}^{ij} D_s^j + B_{sn}^{ij} D_n^j + G_s^{ij} H^j \right) \tag{9.23}$$

$$u_n^i = \sum_{j=1}^{n} \left(B_{ns}^{ij} D_s^j + B_{nn}^{ij} D_n^j + G_n^{ij} H^j \right) \tag{9.24}$$

where H^j is the strength of the line heat source at element j. $T^{ij}, A_{ss}^{ij}, A_{sn}^{ij}, A_{ns}^{ij}, A_{nn}^{ij}, B_{ss}^{ij}, B_{sn}^{ij}, B_{ns}^{ij}, B_{nn}^{ij}, F_s^{ij}, F_n^{ij}, G_s^{ij}, G_n^{ij}$ are "influence coefficients," representing the temperature, stress, and displacement at the center of the element i due to a unit line source (thermal and mechanical) at element j. They are calculated based on Eqs. (9.14)–(9.19) and Eq. (9.4). For example, the coefficient A_{ns}^{ij} gives normal stress at the midpoint of the ith element $\left(\sigma_n^i\right)$ due to a constant unit shear displacement discontinuity over the jth element $\left(D_s^j = 1\right)$.

Because the strength (H^j) of the fictitious heat sources is only dependent on the thermal conditions, they can be solved separately by only using thermal boundary conditions. If the temperature along the problem boundary is known, using Eq. (9.20), there will be n equations with n unknowns. The fictitious heat source strength along each element can then be obtained by solving the system of n linear equations. Their values can then be used in Eqs. (9.21)–(9.24) to solve for the displacement discontinuities D_s^j and D_n^j.

Alternatively, heat flux rather than the temperature may be prescribed on part or whole of the boundary. In this case, the flux condition is used to replace Eq. (9.20) for temperature. The heat flux in the normal direction of element i due to a unit line source at element j is given by Eq. (9.25):

$$Q_{ij} = -k\frac{\partial T}{\partial n} = \frac{(x_i - x_j)\cos\theta_i + \left(y_i - y_j\right)\sin\theta_i}{8\pi k t^2} Ei\left(\xi^2\right) \tag{9.25}$$

The basic principle of the indirect boundary element approach for thermoelastic analysis is the assumption that a fictitious line heat source exists at each element. The strengths of the line sources are unknown and should be determined based on the boundary conditions. For example, if the temperature at all boundary elements is zero, the combined effect of all the line heat sources on the boundary elements should result in a zero temperature. Once the strength of each fictitious heat source is determined, the temperature, thermal flux, and thermal-induced stresses and displacements at any given location in the rock mass can be calculated. By applying mechanical boundary conditions, the displacement discontinuities on the elements can also be

determined, and the total stresses and displacements at any position can then be calculated.

9.4.2 Fracturing–Hydraulic Flow Coupling

In fractured hard rock such as granite, fluid flow occurs predominantly through explicit fractures rather than through intact rock due to the low permeability of the intact rock. Fluid pressure in rock fractures may cause rock fracture movement, increase fracture aperture, or even cause fracture propagation. On the other hand, fracture movement and propagation will change the fracture hydraulic conductivity and create new flow paths. The two-way interaction between fracture mechanical response and fluid flow is critically important in studying the coupled fracturing–hydraulic flow (F–H) processes.

Two fundamental approaches have been used in modeling the hydromechanical coupling in fractured rock medium. The first is the implicit approach, where fluid flow equations are solved together with mechanical equations for rock matrix and fractures. Most of the finite element codes designed for modeling the porous flow using Darcy's law are based on this approach.

The second is the explicit approach, where both fluid flow and mechanical response are simulated using a time-marching iteration process. The well-known commercial code UDEC by Itasca (2004) is based on this approach. The explicit approach is mathematically simpler and easier to adopt the complicated (and evolving) model boundary conditions than the implicit approach. However, it often requires significantly longer computational time as small time steps are required to achieve convergence for the flow solution.

The explicit approach is used in FRACOD. The mechanical calculation (including rock deformation and fracture propagation) is done using the DDM with an iteration scheme for modeling fracture propagation processes. The fracture fluid flow calculation is conducted through the time-marching iteration based on the cubic law (Louise, 1969). The study is focused on fluid flow, predominantly in rock fractures. However, leakages from fracture channels to the rock matrix are also considered.

During the mechanical numerical simulation using the DDM, a fracture is discretized into a number of DD elements. In the flow calculation, each DD element is considered as a hydraulic domain and adjacent domains are connected hydraulically (see Fig. 9.7). Fluid may flow from one domain to another depending on the pressure difference between the two domains.

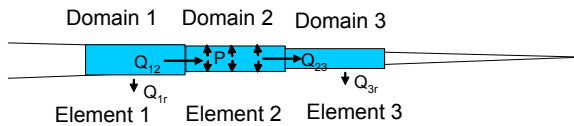

FIGURE 9.7 Domain division for fluid flow simulation.

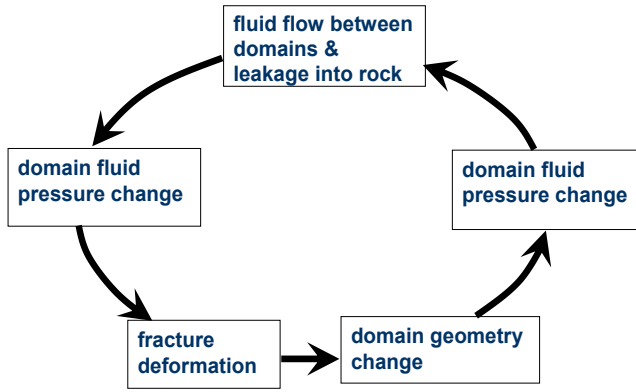

FIGURE 9.8 Iteration process for a coupled fracturing−hydraulic process.

The solution of a coupled $F-H$ problem can be achieved numerically using the iteration scheme shown in Fig. 9.8, and the iteration steps are described as follows.

Step 1. Fluid flow occurs between fracture domains and fluid leaks into the rock matrix. The fluid flow between fracture domains is calculated using the cubic law. The flow rate (Q) between two domains is calculated using Eq. (9.26):

$$Q = \frac{e^3}{12\mu}\frac{\Delta P}{l} \tag{9.26}$$

where e is fracture hydraulic aperture of the element domain, l is element length, ΔP is fluid pressure difference between the two element domains, and μ is fluid viscosity.

The leakage from a fracture domain into the rock matrix is calculated using Eq. (9.27):

$$Q_{\text{leak}} = \frac{k_w}{\mu}\frac{P - P_0}{d} \tag{9.27}$$

where k_w is rock permeability, d is effective leakage distance, P is domain fluid pressure, and P_0 is initial pore pressure. The effective leakage distance d is based on the assumption that at a distance d from the fracture surface, the fluid pressure equals the initial pore pressure. Obviously, the effective leakage distance is closely related to the flow time and the fracture system configuration. In the case of a long fracture with a constant fluid pressure within, the effective leakage distance may be estimated using one-dimensional porous flow equations, and it varies with flow time. For the case with irregular fracture systems, accurate estimate of the effective leakage distance will be much more difficult. In this case, one may consider this option as a rough guide only.

Step 2. Fluid flow causes changes in domain fluid pressure. The new domain pressure due to fluid flow during a small time duration Δt is calculated using Eq. (9.28):

$$P(t+\Delta t) = P_0 + E_w Q\frac{\Delta t}{V} - E_w Q_{\text{leak}}\frac{\Delta t}{V} \tag{9.28}$$

where E_w is the fluid bulk modulus and V is the domain volume.

Step 3. Change in fluid pressure causes fracture deformation. The fracture deformation is calculated using the DDM where the new fluid pressures in fracture domains are the input boundary stresses. After considering the fluid pressure in the fracture domains (elements), the system of equations for calculating the element displacement discontinuities is given in Eq. (9.29):

$$\begin{cases} \overset{i}{(\sigma_s)_0} = \sum_{j=1}^{N} \overset{ij}{A_{ss}}\,\overset{i}{D_s} + \sum_{j=1}^{N} \overset{ij}{A_{sn}}\,\overset{i}{D_s} - K_s\overset{i}{D_s} \\ \overset{i}{(\sigma_n)_0} + P(t+\Delta t) - P_0 = \sum_{j=1}^{N} \overset{ij}{A_{ns}}\,\overset{i}{D_s} + \sum_{j=1}^{N} \overset{ij}{A_{nn}}\,\overset{i}{D_n} - K_n\overset{i}{D_n} \end{cases} \tag{9.29}$$

During this step, the additional fracture deformation caused by any fracture propagation has also been considered and incorporated into the solutions.

Step 4. Fracture deformation changes the domain volume and hence changes the fluid pressure in domains. The new domain pressure is calculated using Eq. (9.30)

$$P'(t+\Delta t) = P(t+\Delta t) - E_w\frac{\Delta e \cdot l}{V} \tag{9.30}$$

Here Δe is the change of the fracture aperture at the element. The new domain fluid pressures are then used to calculate the flow rate between domains in Step 1. Steps 1 to 4 are iterated until the desired fluid time is reached and a stable solution is achieved.

During the fluid flow calculation, a proper time step is needed for the iteration process to converge to the final solution. The time step should meet the following condition:

$$\Delta t < \frac{12\mu \cdot l^2}{E_w \cdot e^2} \tag{9.31}$$

The convergent time step is sensitive to fluid bulk modulus and fracture aperture. High fracture aperture and fluid bulk modulus will require a small time step. For water at room temperature, if the fracture aperture is 50 μm and the element length is 0.1 m, the maximum time step for fluid calculation will be 2.4×10^{-5} s.

The time step determined using Eq. (9.31) is for dynamic fluid calculation. For transient flow or steady state flow problems, the time duration is often days

to months. This time step could be too small to reach a final solution in a feasible time. One way to improve the calculation speed is to use an artificially reduced fluid bulk modulus. Experience indicates that a fluid with a low bulk modulus is also much more stable in the coupled calculation with mechanical deformation.

9.4.3 Hydraulic Flow–Thermal Coupling

Fluid flow in rock fractures may alter the temperature of the rock, if the injected fluid has a different temperature from that of the rock. Equally, fluid may be heated or cooled when flowing through the rock fractures, drawing or releasing heat from/to the rock mass. This is the basic principle of the geothermal energy operation where cold fluid is injected into a hot rock reservoir and hot fluid is extracted from the reservoir.

Coupling of F–H flow in FRACOD considers the fracture flow only. The porous flow through rock matrix has not been taken into account. Heat transfer in rock is assumed to be a pure thermal conduction process, whereas heat transfer in fluid in the fractures is considered as a pure thermal convection process. Because rock fractures often have a very small aperture, the fluid layer in a fracture is very "thin" and hence the temperature over this layer thickness is assumed to be uniform and the same as the temperature of the rock walls.

Let us consider a simple case as shown in Fig. 9.9 where fluid flows from fracture Domain i to Domain j. The rock temperatures at element i and j are T_i and T_j, respectively. The fluid entering Domain j from Domain i has a temperature of T_i. When the fluid has traveled from one end of Domain j to the other, the fluid has been heated by the rock walls. By the time the fluid reaches the other end, the fluid temperature becomes T_j.

During this process, the fluid through the fracture Domain j has drawn thermal energy from surrounding rock. It will act as a negative heat source for the rock and in the next step will cause the rock temperature to reduce. For a duration of Δt, the fluid flow rate entering Domain j from Domain i is Q_{ij}, see Fig. 9.9. The net flow volume entering Domain j is calculated by Eq. (9.32):

$$\Delta V_j = Q_{ij}\Delta t \tag{9.32}$$

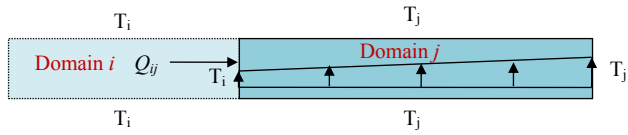

FIGURE 9.9 Fluid flow inside Domain j.

The temperature of this amount of fluid changes from T_i to T_j in Domain j, and this will cause the change of the thermal energy of fluid in Domain j. The change of total thermal energy in the fluid can be calculated by Eq. (9.33):

$$\begin{aligned}\Delta W_j &= c_w \rho_w (T_j - T_i) \Delta V_j \\ &= c_w \rho_w (T_j - T_i) Q_{ij} \Delta t\end{aligned} \tag{9.33}$$

where c_w is specific heat of the fluid and ρ_w is fluid density.

This is the thermal energy transferred from the rock mass to the fluid in Domain j. Note that Eq. (9.33) does not include the contribution from rock matrix flow (leakage) because there is no temperature difference between the fracture surface and the fluid from rock matrix.

The heat strength of this temporary heat source over the duration Δt will be calculated by Eq. (9.34).

$$H^j = \frac{\Delta W_j}{\Delta t} = c_w \rho_w (T_j - T_i) Q_{ij} \tag{9.34}$$

Note that when calculating at a time step $n\Delta t$, accumulated heat strength from all the previous steps should be used. This is consistent with the time-marching scheme used in the code for thermal elasticity analysis.

The process of thermal exchange between fluid and rock mass is an interactive process. Fluid within a fracture will be heated by the higher temperature rock. On the other hand, fluid flow will draw the thermal energy from the rock mass and hence cool down the rock mass. With the temperature in the rock mass gradually cooled down, less thermal energy can be withdrawn by the fluid, and the temperature of the fluid will be reduced accordingly. An iteration process is required to capture this interactive time-dependent process to achieve the final solution.

Due to the nature of the BEM, it is impossible to use very small time steps to march to the final solution. A practical way to achieve a final solution with a reasonable accuracy is to divide the problem time into a few rather large time steps. Due to the limited number of thermal steps permitted by the time-marching approach in the BEM, one will need to optimize the arrangement of the time steps. In general, the thermal strength curve should be more accurately modeled at the time closer to the problem time. The curve before this time duration may be simplified as they have less effect on the final solution. As such, the most efficient way to achieve an accurate result is to use smaller time steps closer to the problem time and larger time steps before it.

9.5 VALIDATION AND DEMONSTRATION EXAMPLES

Over many years, FRACOD has been used to model the rock failure field testing and was proven to be useful in predicting brittle failure (Rinne et al., 2003), borehole breakouts (Shen et al., 2002; Klee et al., 2011; Barton, 2007), stability of large shaft and galleries (Stephansson et al., 2003), pillar spalling

(Rinne et al., 2003; Siren et al., 2014), rock mass permeability change due to fracturing (Shen et al., 2011), fundamental creep behavior of rock samples (Rinne, 2008), and HF (Xie et al., 2014). This section lists a few of these application examples.

9.5.1 Modeling Biaxial Compressive Test

FRACOD has been used to simulate biaxial compressive tests. The study used numerical "specimens" with sizes similar to the real specimens in laboratory. The "specimens" were loaded in biaxial compression until failure.

The tests were performed using a "specimen" with a length of 120 mm and width of 60 mm. The top and bottom boundaries were restricted in shear movement to simulate the nonlubricated contact conditions (i.e., strong friction) in laboratory tests. A vertical stress was applied on the top and bottom boundaries. The applied stress was increased by 5 MPa in every incremental step until the "specimen" collapsed. A confinement stress of 10 MPa was used on the side boundaries. The intact rock was assumed to have a Young's modulus $E = 60$ GPa, Poisson's ratio $\nu = 0.25$, cohesion $c = 30$ MPa, internal friction angle $\phi = 30$ degrees, and tensile strength $\sigma_t = 13.4$ MPa. A Mohr–Coulomb strength criterion was used. Random fracture initiation function in FRACOD was used, and the initiation level was set to start at 50% rock strength. The predicted process of fracture initiation and propagation during loading is plotted in Fig. 9.10. The locations and relative magnitude of AE events during the test are also given in Fig. 9.10. For the particular parameters used in this test, fracture initiation starts at a stress level of 80 MPa. Extensive failure occurred at an axial stress of 130 MPa.

Fig. 9.11 shows the predicted stress–strain curve during the numerical loading test. At the stress level of 80 MPa when fracture initiation occurred,

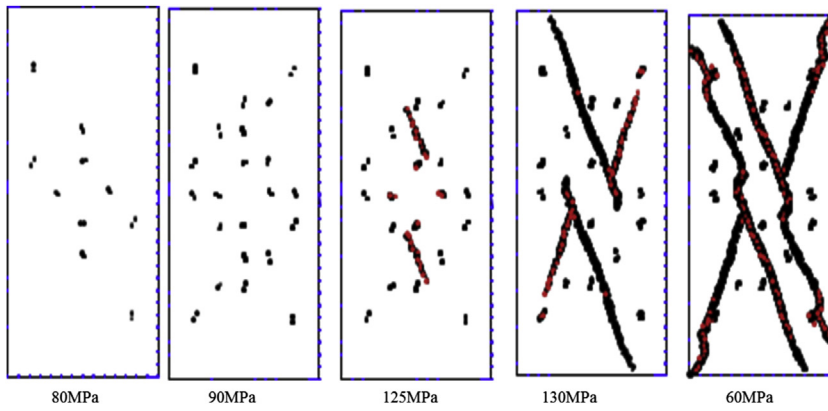

FIGURE 9.10 Predicted process of fracture initiation, propagation, and final failure of a rock specimen subjected to biaxial compressive stress. Axial stress is reported, final figure is after softening with continuing axial strain, postpeak strength.

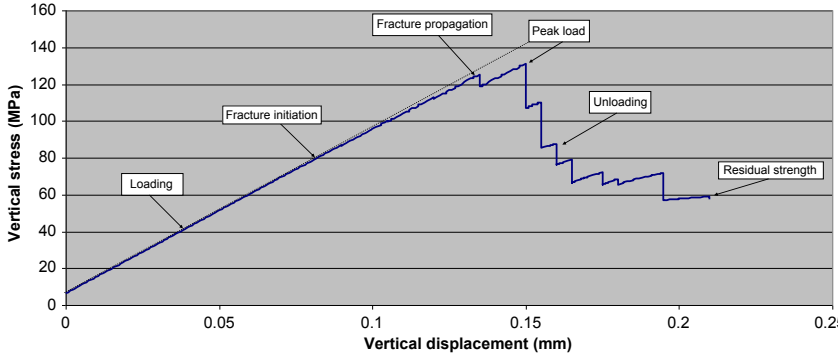

FIGURE 9.11 Stress–strain curve obtained in numerical biaxial compression tests.

the stress–strain curve deviated away from the initial linear relation and became nonlinear. This phenomenon is consistent with the typical laboratory observations. At about 125 MPa, fractures started to propagate and coalesce and formed large shear failure planes at the peak axial load of 130 MPa. The fractures continued to propagate with reduced loading capacity in the postpeak stage. Eventually, the specimen totally failed with a residual strength of about 60 MPa.

9.5.2 Modeling Borehole Breakouts

FRACOD was used to study borehole breakouts in deep granite during hot-dry-rock geothermal energy extraction in Australia for the purpose of back analyzing the in situ stresses (Shen, 2004). The breakout width of an injection well at a depth of 4500 m was obtained by acoustic scan and the breakout depth was measured by calipers. A typical breakout scan image is shown in Fig. 9.12A where the breakout azimuth angle is about 62 degrees. The measured breakout depth is about 23% of the borehole radius.

FRACOD was used to reproduce the typical breakouts as observed in the injection well. The values of the key mechanical properties used in this study are listed as follows:

Young's modulus = 65 GPa
Poisson's Ratio = 0.25
Cohesion = 31 MPa
Friction angle = 35 degrees
Uniaxial compression strength = 120 MPa
Mode I fracture toughness = 1.35 MPa $m^{1/2}$
Mode II fracture toughness = 3.07 MPa $m^{1/2}$

A large number of combinations of the maximum and minimum horizontal principle stresses were used in the FRACOD model as part of a sensitivity

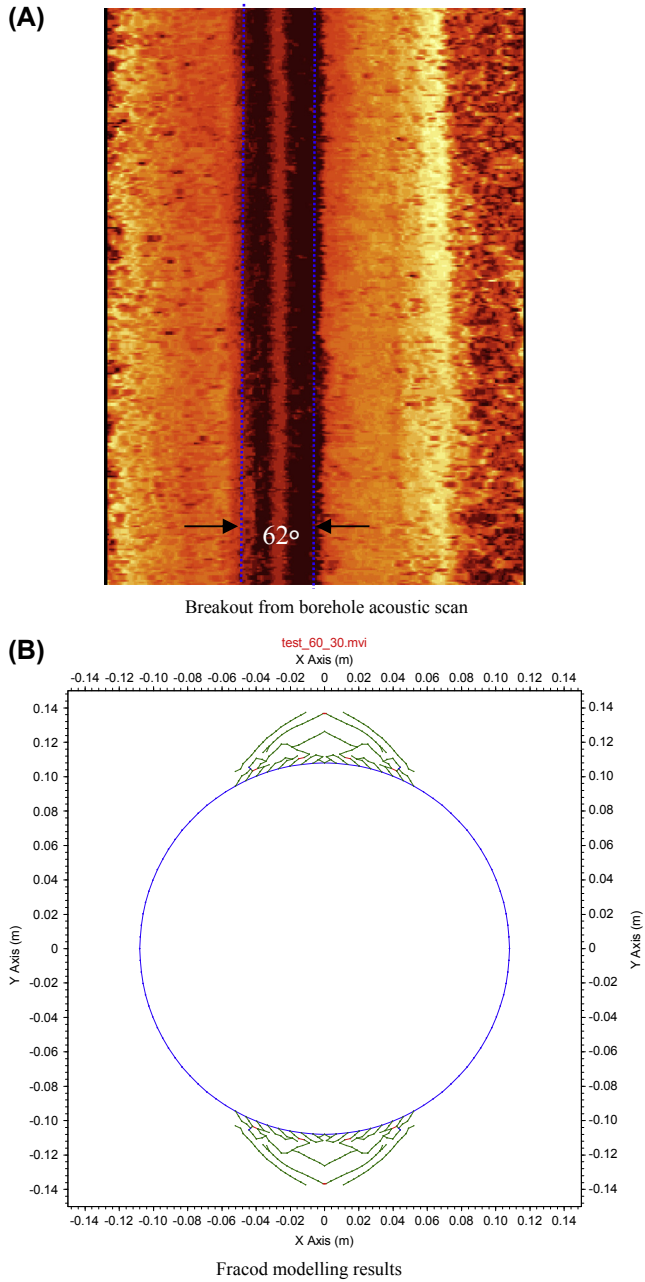

FIGURE 9.12 Comparison between the observed borehole breakout and the FRACOD prediction. (A) Breakout from borehole acoustic scan and (B) FRACOD modeling results.

study. For a combination of $\sigma_{H\max} = 60$ MPa, $\sigma_{h\min} = 30$ MPa, the predicted breakout angle and depth are 58 degrees and 26% of the borehole radius, see Fig. 9.12B. These stress magnitudes agree with expectation in deep granite where the well is located based on other existing data and knowledge. In this example, the thermal effect occurred during drilling is not considered. The final breakouts were formed after the drilling was completed, and the temperature in the borehole was equal to the in situ rock temperature.

9.5.3 Cooling Fractures in Borehole Wall

A borehole drilled into hot geothermal reservoir is investigated with FRACOD to study the possibility of fracture initiation and propagation due to thermal stress in the borehole wall from cooling. The borehole has a radius $r = 0.1$ m in the hot rock with an in situ rock temperature $T_0 = 200°C$. The borehole wall is cooled by drilling fluid and maintained at temperature $T_w = 80°C$. The mechanical and thermal properties used in this simulation are listed in Table 9.1.

Six different cooling times were considered: 10, 10^2, 10^3, 10^4, 10^5, and 10^6 s. During the last step of the modeling, fracture initiation and propagation were considered. Fig. 9.13 shows the predicted pattern of thermal cracks in the immediate vicinity of the borehole wall due to the cooling effect. Note that the initial major fracture initiations occurred at the borehole wall. These fractures

TABLE 9.1 Mechanical and Thermal Properties Used in Cooling Fracture Analysis in Borehole Wall

Property	Value
Thermal conductivity (k)	10.07 W/m°C
Specific heat (C_p)	790.0 J/(kg°C)
Linear thermal expansion coefficient (α)	2.4×10^{-5}/°C
Young's modulus (E)	37.5 GPa
Poisson's ratio (ν)	0.25
Tensile strength (σ_t)	12.5 MPa
Cohesion (c)	33 MPa
Internal friction angle (ϕ)	33 degrees
Fracture mode I toughness (K_{Ic})	1.5 MPa $m^{0.5}$
Fracture mode II toughness (K_{IIc})	3.0 MPa $m^{0.5}$
In situ stresses ($\sigma_{xx} = \sigma_{yy}$)	10 MPa

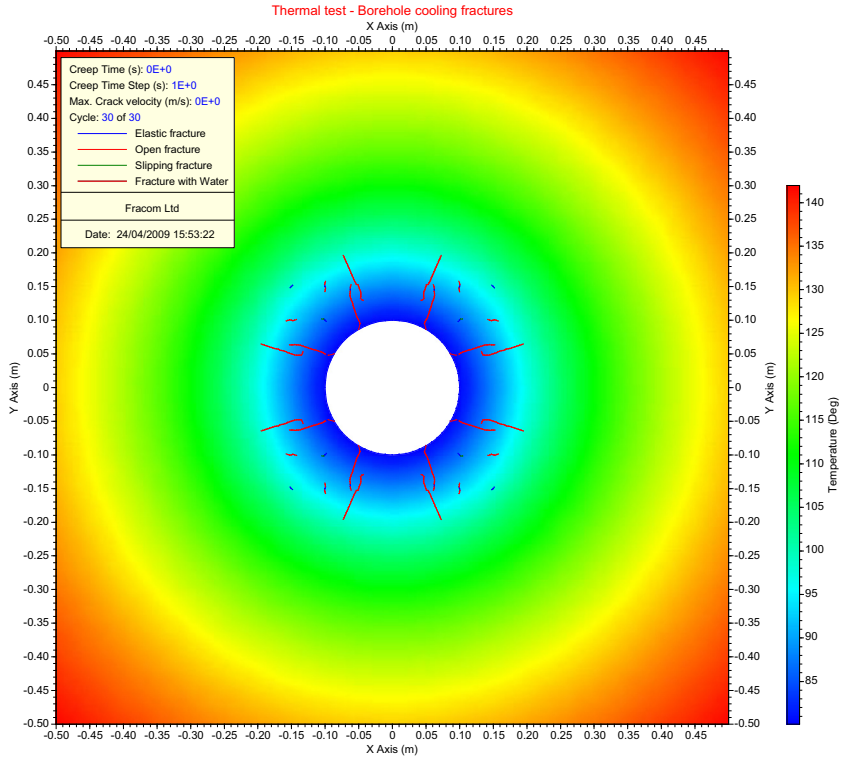

FIGURE 9.13 Cooling of a borehole. Predicted process of thermal cracks growth after 10^6 s of cooling.

then propagated in radial direction and coalesced with other newly initiated short fractures, eventually forming several long radial fractures.

9.5.4 Rock Mass Cooling Due to Fluid Flow

As part of the validation test of the hydrothermal coupling in FRACOD, a simple case of geothermal production was considered where a single open fracture exists in a homogeneous and isotropic impermeable rock mass. The initial temperature of the rock is T_{rock}. Fluid with a lower temperature (T_{inj}) is injected into the fracture, and it flows through the fracture at a constant flow rate (Q). During the flow process, the fluid will be heated up by the hot rock, whereas the rock in the vicinity of the fracture will be cooled down by the fluid.

For this problem, heat conduction occurs in the rock mass, and heat convection is dominant in the fracture by the carrying fluid. By neglecting the heat conduction in the fluid and the conduction in the rock mass along fracture

direction, Bodvarsson (1969) provided an analytical solution for the temperature along an infinite long fracture, as given below:

$$T(x) = T_{\text{rock}} - (T_{\text{inj}} - T_{\text{rock}}) \cdot erfc\left[\left(\frac{k}{c_w Q \rho_w}\right)\frac{x}{\sqrt{ct}}\right] \tag{9.35}$$

Here $T(x)$ is the temperature along the fracture at a distance x from injection point (°C), T_{rock} the initial rock temperature (°C), T_{inj} is the temperature of injection fluid (°C), k is the thermal conductivity of rock (W/m•°C), c_w is the specific heat of fluid (J/kg•°C), Q is the flow rate in fracture (m^3/s), ρ_w is the density of fluid (kg/m^3), and c is the thermal diffusivity of rock (m^2/s).

For comparison between the analytical solution and the FRACOD model, it is considered that the single fracture has a length of 200 m and a constant aperture of 100 μm. Cold water is injected from one end of the fracture at a pressure of 50 MPa. Hot water is then extracted from the other end of the fracture at a constant pressure of 0 MPa.

Other rock and fluid properties used are listed as follows:

$T_{\text{rock}} = 200°\text{C}$;
$T_{\text{inj}} = 80°\text{C}$;
$k = 2.631$ W/m•°C;
$c_w = 4187$ J/kg•°C;
$Q = 4.24 \times 10^{-3}$ m^3/s;
$\rho_w = 1000$ kg/m^3;
$c = 1.48 \times 10^{-6}$ m^2/s.

The flow time of 0.5, 1, 2, 5, 10, 20, and 50 years are modeled. The modeled temperature variation along the fracture is given in Fig. 9.14 for each modeled time, and it is compared with the analytical solution by Bodvarsson (1969).

The numerical results agree in general with the analytical solutions. However, because the FRACOD model considers a 200-m-long fracture, whereas the analytical model assumes that the fracture is infinite, some differences between the numerical and analytical results are observed particularly when the flow time is longer, e.g., 20 or 50 years.

Fig. 9.15 shows the modeled temperature distribution in the vicinity of the fracture at different time. The cooling zone is gradually increasing with time. After 10 years, the cooling zone reached the extraction well at the right end of the fracture, and the fluid temperature at the extraction well starts to drop. After 50 years, the temperature of the extracted fluid is predicted to be around 145°C.

Cooling of the rock mass due to fluid flow may cause localized tensile stress, which could drive the preexisting fractures to propagate. This case is investigated by adding a preexisting fracture close to the main fracture (see Fig. 9.16). After 10 years production, the thermal stress that develops in the

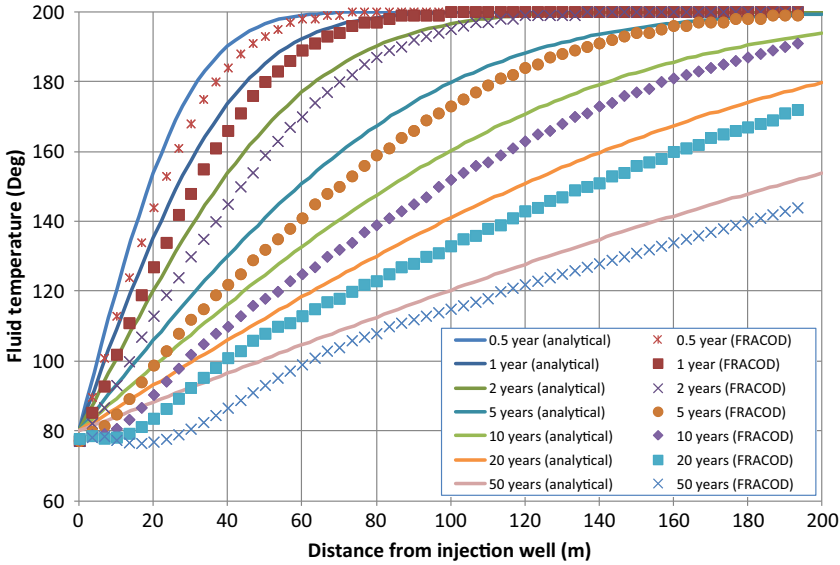

FIGURE 9.14 Temperature distribution along a single fracture due to cool water injection in a geothermal reservoir. Comparison of FRACOD results with analytical solutions.

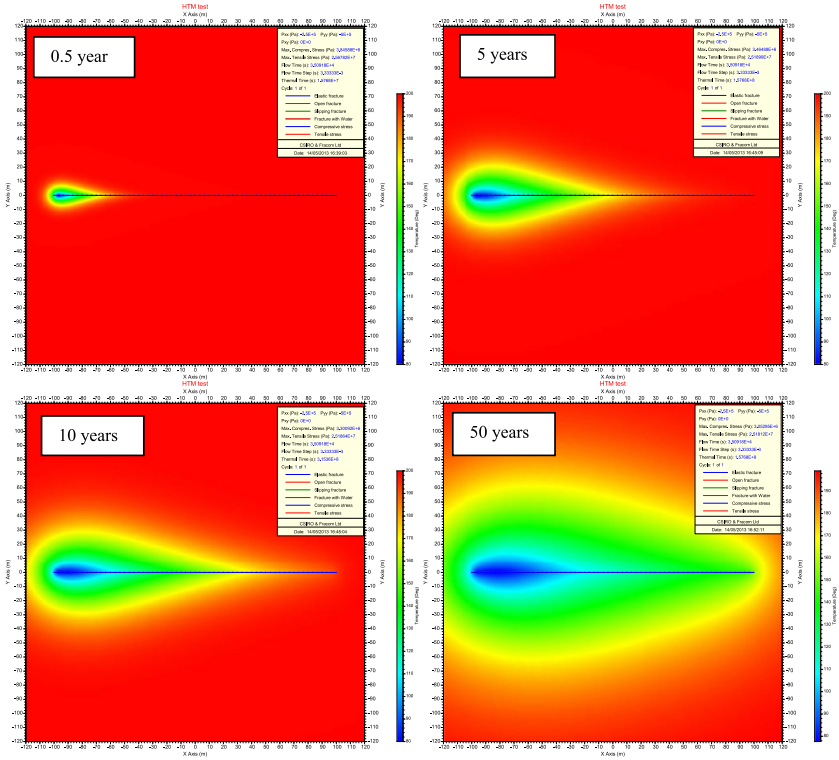

FIGURE 9.15 Modeled temperature distribution in the vicinity of the fracture.

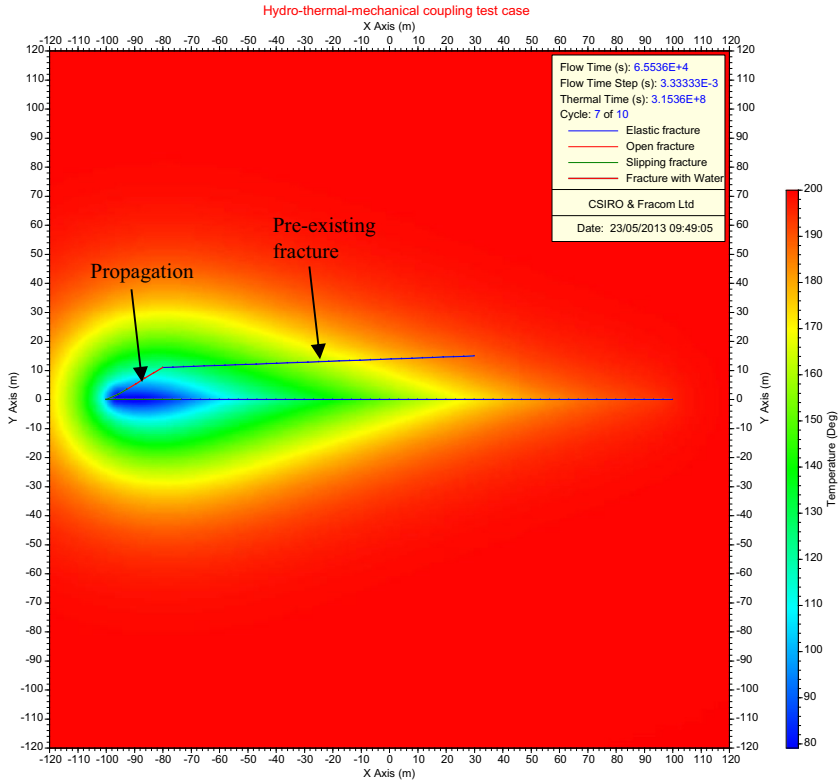

FIGURE 9.16 Propagation of preexisting fracture due to cooling stress near the injection hole.

vicinity of the injection hole due to cooling is sufficient enough to cause the preexisting fracture to propagate and coalesce with the main fracture. At the production hole side of the fracture, however, the thermal stress is much less and is not sufficient to propagate the preexisting fracture.

9.6 MODELING HYDRAULIC FRACTURING USING FRACOD

HF has been extensively used as a key technique for improving the well productivity of oil and gas reservoirs in a variety of host rocks (Valko and Economides, 1995; Warpinski and Teufel, 1987). HF means initiating and propagating artificial fractures in the reservoir by fluid injection, which aims to increase the permeability of the reservoir. One important emerging application is the unconventional gas reservoir engineering such as shale gas stimulation. Shale gas is the natural gas trapped within shale formations whose natural permeability is extremely low, and thus stimulation techniques using HF are essential to make gas recovery possible and economically viable. Because of

ubiquitous natural fractures in the reservoir, understanding the interactions between hydraulically induced fractures and natural ones are important for the success of stimulation.

HF is a complicated coupling process that involves (1) mechanical deformation induced by the fluid pressure on the fracture surfaces, (2) fluid flow within the fracture, and (3) fracture propagation (Adachi et al., 2007). The geometry of the induced fracture is dominated by the host rock mechanical properties, in situ stress, the applied fracturing fluid properties, and local geological features such as natural fractures and bedding planes (Dahi-Taleghani, 2009). Observations suggest that these natural discontinuities can significantly impact the overall patterns of hydraulic fractures and multiple fractures or segments can propagate simultaneously (e.g., Warpinski and Teufel, 1987; Fast et al., 1994; Gale et al., 2007; Jeffrey et al., 2009). Understanding complex hydraulic fracture behavior in the presence of natural fractures is critical to the optimum stimulation design.

This section describes an attempt by Xie et al. (2016) using FRACOD to investigate various aspects of HF. The Khristianovich–Geertsma–de Klerk (KGD) model of the propagation of a single fracture driven by hydraulic injection is presented to verify the code. Then a demonstration example that involves the interaction between hydraulic and preexisting fractures is presented.

9.6.1 Verification Example—Hydraulic Fracturing in Intact Rock

The classic HF theory predicts that a plane fracture is generated perpendicular to the direction of the minimum principal stress (compressive stress as positive) in the intact homogeneous rock, where the impacts of various kinds of discontinuities are ignored. For HF, simulations that are performed on vertical wells aligned with the maximum or intermediate principal stress are commonly simplified as 2D plane strain problems with geometry of a cross section through the vertical well.

The injection pressure required to initiate a vertical fracture from the wall of a vertical well or the breakdown pressure is predicted using Eq. (9.36) in the case of nonpenetrating fluid (Haimson and Fairhurst, 1967).

$$P_b = 3S_{h\min} - S_{H\max} + \sigma_t \tag{9.36}$$

where $S_{h\min}$ and $S_{H\max}$ are field minimum and maximum horizontal stresses and σ_t is the tensile strength of the intact rock.

During the application of HF, several pumping cycles are typically conducted. In this cyclic process, another parameter of interest is the fracture reopening pressure where the effect of tensile strength is removed. This pressure is expressed as

$$P_r = 3S_{h\min} - S_{H\max} \tag{9.37}$$

A numerical model was established which represents a horizontal cross section through a vertical well, to simulate HF process of intact rock in FRACOD. As shown in Fig. 9.17A, the whole model is subjected to an anisotropic stress condition ($S_{h\min}$ of 15 MPa and $S_{H\max}$ of 20 MPa), and fluid

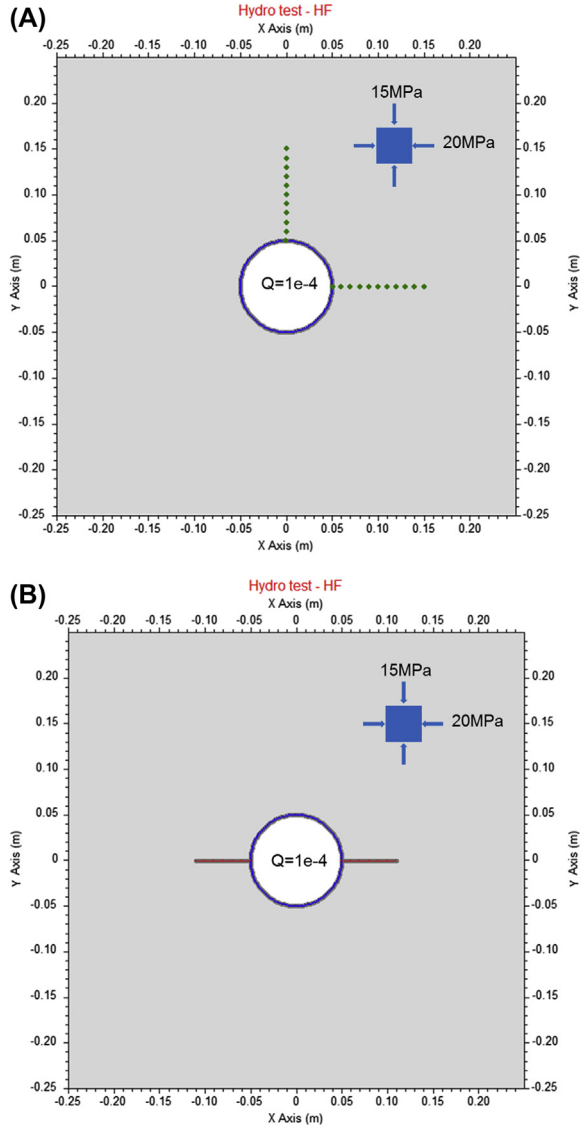

FIGURE 9.17 FRACOD model of hydraulic fracturing (HF) in intact rock. (A) Model initial configuration, *green* (gray in print version) *points* representing two sets of monitoring location and (B) hydraulic fracture developing normal to far field minimum principle stress.

TABLE 9.2 Key Input Parameters of Simulated Rock and Injection Fluid

E (GPa)	v	σ_t (MPa)	K_{Ic} (MPa·m$^{0.5}$)	K_{IIc} (MPa·m$^{0.5}$)	μ (Pa·s)	K_w (GPa)
37.5	0.25	10	1.5	3.0	0.001	0.02

is injected with a constant flow rate of 0.1 L/s into a well with the diameter of 0.1 m. The key input parameters of this simulation are listed in Table 9.2, including the properties of modeled rock and applied injection fluid. After 0.27 s of injection, the FRACOD simulation successfully produces horizontal hydraulic fractures (Fig. 9.17B), which is consistent with the statement of HF theory with respect to the orientation of a newly created fracture.where E is the elastic modulus, v is the Poisson's ratio, σ_t is the tensile strength, K_{Ic} is the mode I fracture toughness, K_{IIC} is the mode II fracture toughness, μ is the fluid dynamic viscosity, and K_w is the fluid bulk modulus.

To confirm the accuracy of the simulation, the stress distribution close to the borehole computed by the simulator is compared with that from analytical solutions just before breakdown. The stress state on the borehole wall is directly related to the prediction of fracture initiation. The injection pressure is detected to be 34.96 MPa for the modeling cycle before the fracture element is initiated on the borehole wall. Thus a pressure of 34.96 MPa is applied on the borehole wall before breakdown.

The problem of calculating the stresses in the vicinity of a circular hole excavated in the infinite elastic solid, which is subjected to given far field stresses is provided by the Kirsch solution (Jaeger et al., 2007). Superposing the additional stresses caused by injection pressure, the analytical solutions are obtained.

The stress analysis results on horizontal ($y = 0$) and vertical ($x = 0$) lines are extracted, shown as green point sets in Fig. 9.17A, and then the FRACOD computation is compared with analytical solutions (Fig. 9.18). The results demonstrate that there is a very good agreement between the numerical and analytical predictions, which indicates good accuracy of FRACOD stress analysis software.

When looking at the fracturing process more closely with respect to the injection pressure history as shown in Fig. 9.19, it is found that FRACOD modeling successfully captures some general features of the pressure response during HF tests. The simulated breakdown pressure P_b (34.96 MPa) for fracture initiation and the fracture reopening pressure P_r (25.38 MPa) for propagation in FRACOD are in close agreement with that estimated using Eqs. (9.36) and (9.37), respectively. Modeling also demonstrates that the fracture reopening pressure decreases due to the reduction in stress concentration as the

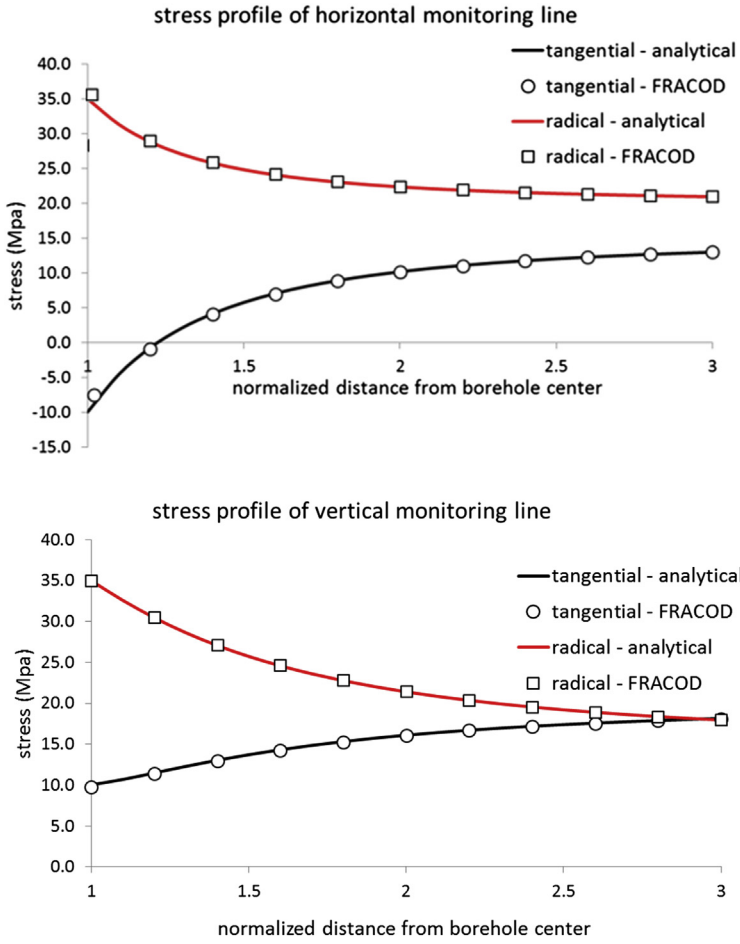

FIGURE 9.18 Comparison of stresses computed by FRACOD and the analytical results just before breakdown, 34.96 MPa injection pressure applied on borehole wall. Horizontal axis represents normalized distance from the borehole center with respect to the borehole radius.

fracture propagates away from the injection well. In FRACOD, the fracturing process is modeled explicitly and the fracture extends by a preset element length for each propagation. In the injection pressure history plot, several pressure drop−increase cycles are observed where each sharp drop corresponds to adding one fracture element at the crack tip. In addition, a constant injection pressure is observed after shut-in at 0.27 s, which is expected because the model is dealing with HF in hard rock without considering the effect of fluid leakage into the rock matrix.

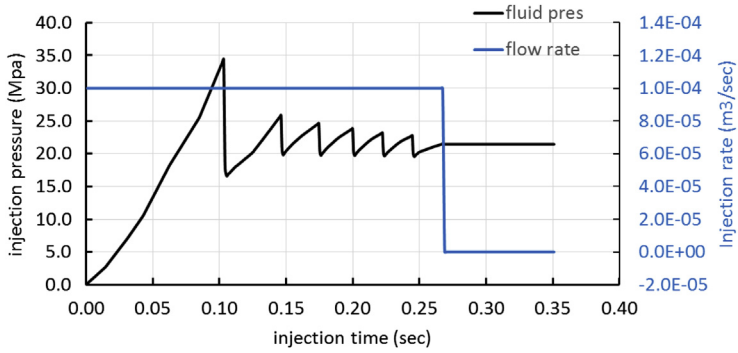

FIGURE 9.19 Monitored injection pressure response for a constant rate injection in FRACOD.

9.6.2 Verification Against the Khristianovic–Geertsma–de Klerk Model

As the HF problem is complex, it is necessary to simplify the geometry of fractures to make it mathematically tractable. Two conceptualizations of hydraulic fracture geometry, Perkins–Kern–Nordgren (PKN) and KGD geometries, have been widely accepted and used for the design of HF. The so-called KGD model was initially elaborated by Khristianovich and Zheltov (1955) and further developed by Geertsma and de Klerk (1969). It addresses the fracture geometry for a single fracture driven by a Newtonian fluid injection at a constant flow rate. The KGD model is chosen in this verification test because it considers a 2D fracture geometry, same as the FRACOD model. The PKN model assumes a 3D elliptical fracture geometry that is obviously different from the FRACOD model. As depicted in Fig. 9.20, the KGD model treats the

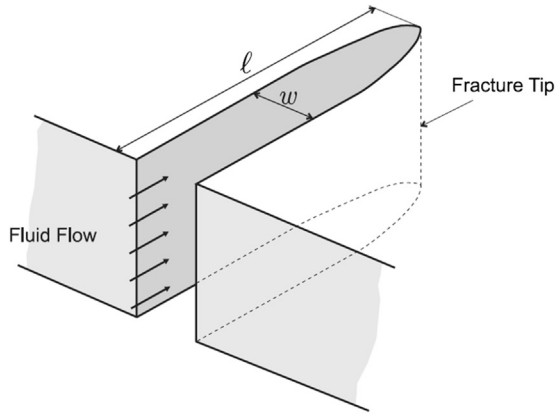

FIGURE 9.20 A schematic to show the Khristianovich–Geertsma–de Klerk geometry. *After Adachi, J., Siebrits, E., Peirce, A., and Desroches, J., 2007. Computer simulation of hydraulic fractures. International Journal of Rock Mechanics and Mining Sciences 44 (5), 739–757.*

fractures with the same width or opening at any vertical coordinate, which results in a rectangular shape of vertical cross section. It is assumed that the fracture has an elliptical profile for horizontal cross section and the width is maximum at the center, deceasing to zero at the fracture tip. The KGD model is the suitable simplification for fractures that are short horizontally but long vertically where the plane strain condition is applicable to horizontal sections.

In addition, assumptions of constant net pressure and equal flow rate distribution along the fracture, although not necessarily realistic, are enforced to derive the explicit formulas for fracture length $l(t)$ (Eq. 9.38), fracture width at the wellbore $w_0(t)$ (Eq. 9.39), and net pressure at injection location P_0 (Eq. 9.40), see Valko and Economides, 1995.

$$l(t) = 0.539\left(\frac{Q^3E'}{\mu}\right)^{\frac{1}{6}} t^{\frac{2}{3}} \tag{9.38}$$

$$w_0(t) = 2.36\left(\frac{Q^3\mu}{E'}\right)^{\frac{1}{6}} t^{\frac{1}{3}} \tag{9.39}$$

$$P_0 = 1.09\left(E'^2\mu\right)^{\frac{1}{3}} t^{-\frac{1}{3}} \tag{9.40}$$

where Q is the applied constant injection rate, E' is plane strain modulus of elasticity, μ is fluid dynamic viscosity, and t is time. In this section, we numerically simulate the KGD model to compare with the earlier equations.

The model configuration is shown in Fig. 9.21. A small-size injection borehole is placed in the center of a line fracture and a constant injection rate of 10 L/s is applied to drive the fracture growth horizontally. To guarantee a horizontal fracture path, an anisotropic far field stress state of small magnitude is also applied. Net pressure on the fracture plane is treated as the difference of monitored inner pressure and the far field minimum principal stress (Valko and Economides, 1995). Table 9.3 has the details of the input parameters for KGD problem simulation. It should be noted that the limited geometry size shown in Fig. 9.21 (10 m × 10 m) is only for the display plot, in theory, the model geometry can extend infinitely because the model represents an inner boundary problem using the BEM.

The monitored evolutions of hydraulic fracture length, fracture width at the wellbore, and injection pressure with injection time are recorded in Fig. 9.22, where the counterparts computed using Eqs. (9.38)−(9.40) are also included. In general, the FRACOD modeling results show good agreement with the analytical solutions, with a good match for the injection pressure results, in particular. The numerical simulation estimates a smaller width than KGD model equation while the modeled fracture length is generally longer than the analytical solution.

In KGD model, the injected fluid volume corresponds to fracture volume because the leak off and fluid compressibility are neglected. In the FRACOD

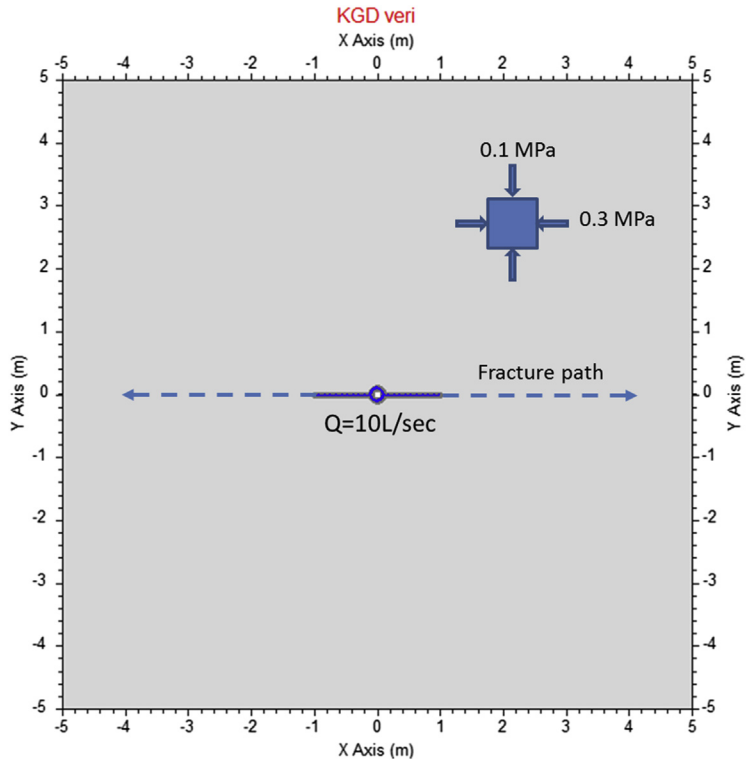

FIGURE 9.21 Numerical model for simulating Khristianovich–Geertsma–de Klerk (KGD) problem in FRACOD.

TABLE 9.3 Key Input Parameters of Simulated Rock and Injection Fluid for Khristianovich–Geertsma–de Klerk Problem

E (GPa)	v	K_{Ic} (MPa·m$^{0.5}$)	K_{IIc} (MPa·m$^{0.5}$)	μ (Pa·s)	K_w (GPa)	e_0 (mm)
20	0.25	1	2.0	0.001	0.02	0.1

where E is the elastic modulus, v is the Poisson's ratio, K_{Ic} is the mode I fracture toughness, K_{IIc} is the mode II fracture toughness, μ is the fluid dynamic viscosity, K_w is the fluid bulk modulus, and e_0 is the initial hydraulic aperture.

simulation, the fracture volume is mainly governed by injected fluid volume. Due to the smaller predicted fracture width, the fracture length needs to be greater to maintain the volume balance. FRACOD considers fluid compressibility, which is closer to the reality, by inputting the parameter of fluid bulk modulus. By considering the fluid compressibility, the fracture volume should

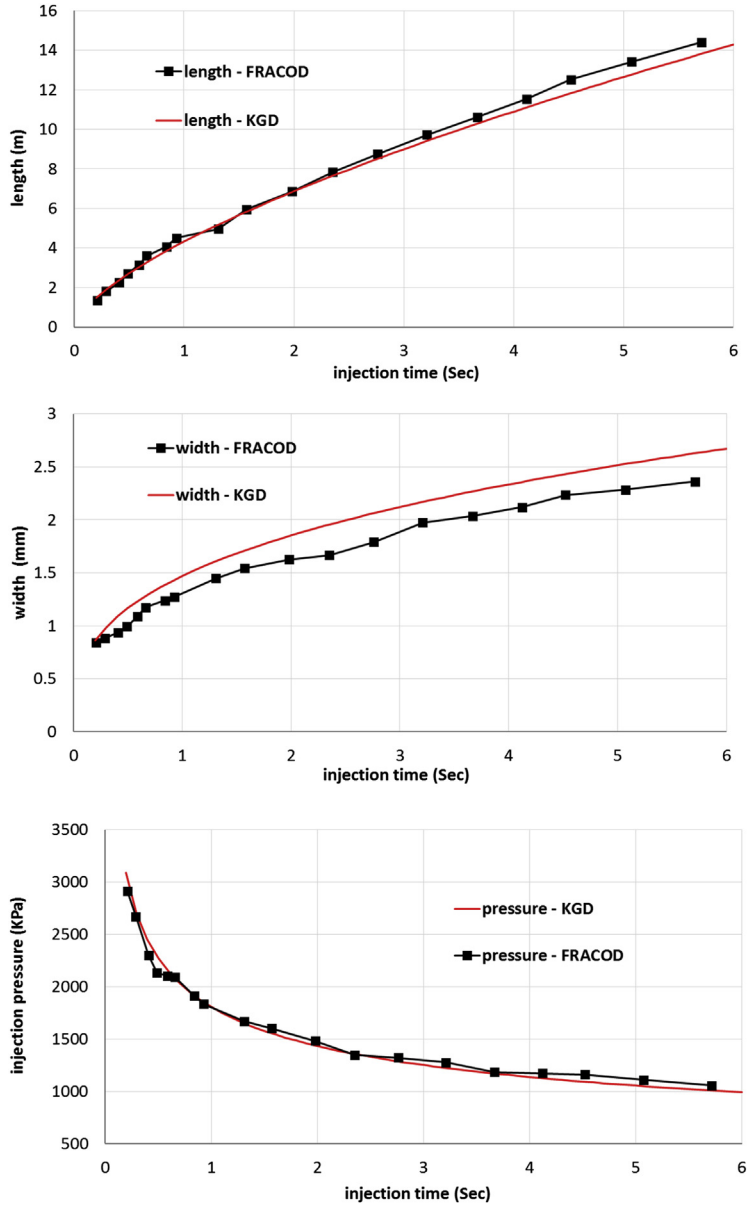

FIGURE 9.22 Comparison of evolutions of fracture length, width, and injection pressure as a function of injection time. *KGD*, Khristianovich–Geertsma–de Klerk.

always be smaller than the injected fluid volume. This probably explains that the discrepancy of fracture width is more significant than the difference of fracture length between the FRACOD and KGD models.

To demonstrate the reason that FRACOD modeling generates smaller width than the KGD model solution, the distributions of fluid pressure, fracture width (aperture), and flow rate along the fracture are studied. Fig. 9.23 shows

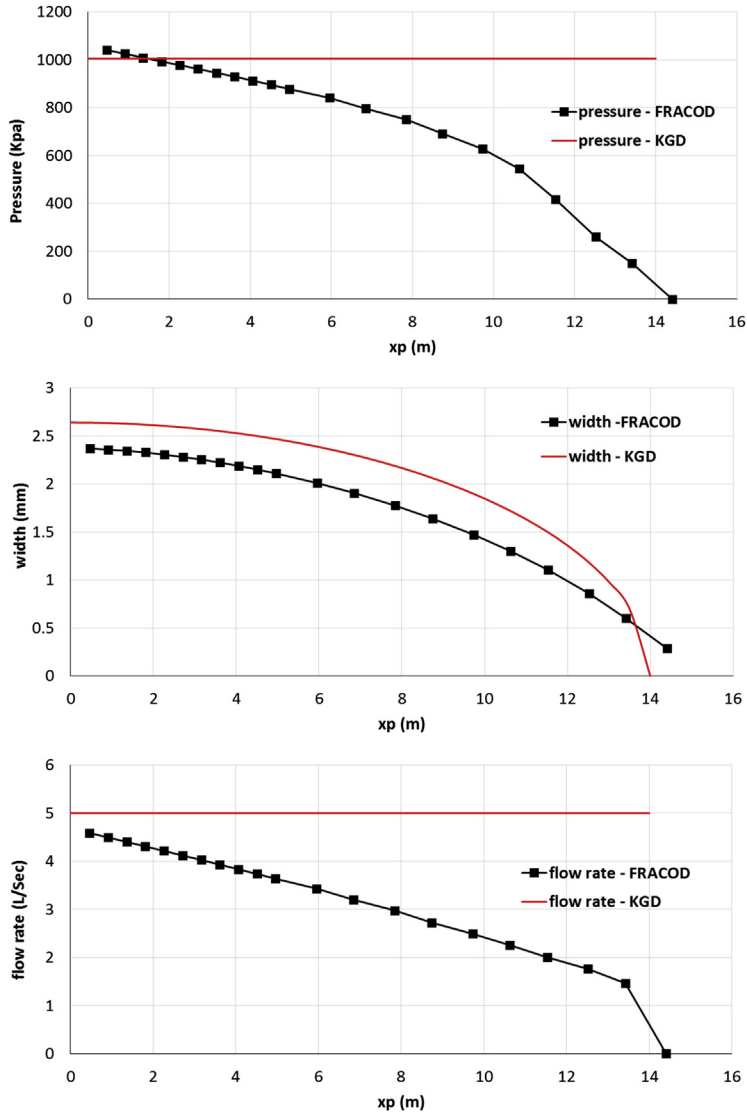

FIGURE 9.23 Comparison of pressure, fracture width, flow rate distributions along the fracture after 5.7 s injection. Horizontal axis represents the distance from the injection location.

the numerical results when the length of fracture is 14.4 m (after 5.7 s injection) and those from analytical solutions after 5.7 s injection (14.0 m fracture length). The numerical analysis shows pressure drop along the fracture while the KGD model adopts constant pressure distribution assumption. The pressure drop along the fracture is considered to be closer to the reality because of the flow resistivity. The constant pressure distribution condition overestimates the pressure magnitude on the fracture plane, resulting in a larger fracture opening or width. Indeed, the comparison of fracture width distribution shows the KGD model predicts bigger fracture width along the fracture. It is interesting that the shape of fracture width profile provided by FRACOD simulation is similar to a half ellipse, which is generally consistent with that of KGD model. These interpretations can be further confirmed by the comparison of linear elasticity solutions of crack width distribution between constant pressure case and linear pressure drop condition (Valko and Economides, 1995). For a crack with linear pressure drop, the crack width is smaller than that with constant pressure condition while the width profile is very similar. In addition, the KGD model assumes the flow rate is equal to the injection rate everywhere in the fracture, which is not entirely accurate as it ignores the storage effect in practice. The FRACOD simulation shows a reduced flow rate along the fracture, which can include the storage effect.

The general agreement of the simulation results with the KGD model solutions demonstrates that the FRACOD can handle the hydromechanical coupling process during the development of a hydraulically driven fracture. Moreover, the numerical analysis can capture more realistic pressure and flow rate distribution than the analytical model and hence tends to produce better prediction of fracture propagation. This feature has also been reported in Dahi-Taleghani (2009) and Fu et al. (2011).

9.6.3 Modeling Fracture Diversion

It is well known that the existence of natural fractures can change the HF behavior significantly. In this section, the previous KGD problem simulation is extended by including two preexisting fractures in the model (Fig. 9.24A shows the right half section of the model with symmetry) to demonstrate the potential capability of FRACOD to model the intersections of induced and natural fractures. All the model parameters are the same as the previous KGD problem simulation (Table 9.3). The center of natural fracture is 4 m away from the injection well, and it is inclined 30 degrees clockwise from the horizontal axis. Also the natural fracture is assumed to have a very small initial aperture, and it is basically not conductive unless opened by hydromechanical effects due to fluid injection.

Fig. 9.24B shows the fracture flow pattern after applying the injection for 2 s, where a red line represents the induced-fracture flow path by continuous injection. Obviously, the hydraulic fracture grows horizontally until it

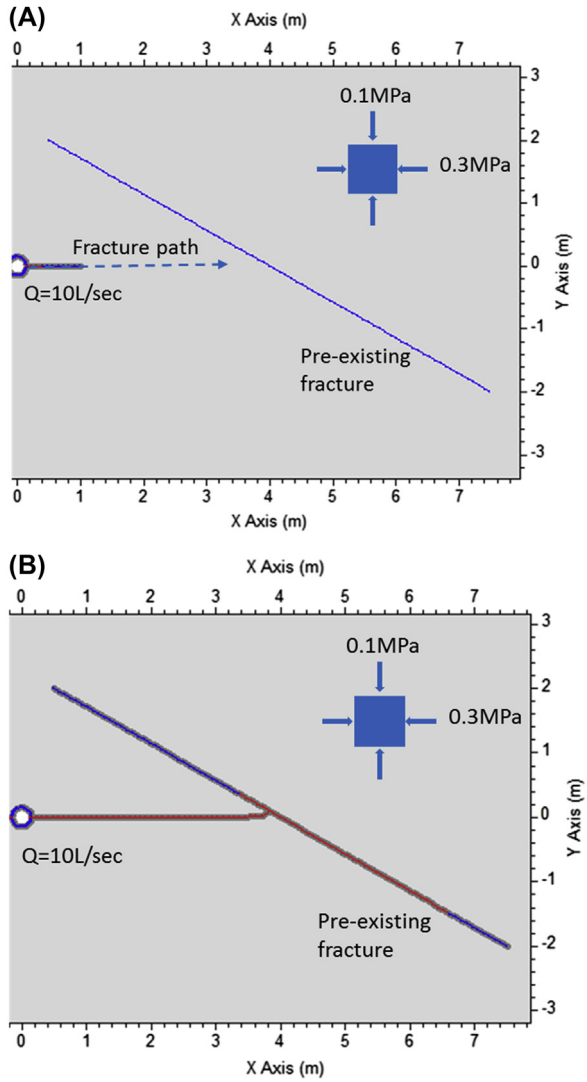

FIGURE 9.24 Numerical model for simulating hydraulic fracture diversion. Because of the symmetry, the left section of the model is not shown in the plot. (A) Model initial setting with a preexisting fracture (inclined 30 degrees from the horizontal axis), (B) fracture pattern after 2 s of injection, the right wing of hydraulic fracture diverting to southeast.

intersects the preexisting fracture, and then the fracture flow diverts into the southeast branch of the preexisting fracture. With the propagation of horizontal hydraulic fracture, the fracture width or aperture increases. When the hydraulic fracture intersects the preexisting fracture, the rock above hydraulic fracture plane detaches from that below the fracture plane. This causes the

block above the horizontal fracture plane to move upward while the one below moves downward. The upward movement of the upper block tends to compress the northwest branch of the inclined preexisting fracture while the downward movement of lower block helps to pull the southeast branch open. This effect can be very significant because of the cubic relationship between fracture conductivity and its width. More fluid flows into the southeast branch when the horizontal hydraulic fracture intersects the preexisting fracture and then pressure accumulates there, which makes it more conductive. This fracture diversion is the result of the coupling of fluid injection and block deformation.

The existence of a natural fracture not only alters the hydraulic fracture path but also influences the injection pressure and fracture length (Fig. 9.25). In Fig. 9.25, the simulation results are compared with those without the nature fracture (KGD modeling result presented in the previous section). The horizontal hydraulic fracture intersects the preexisting fracture after 0.8 s injection.

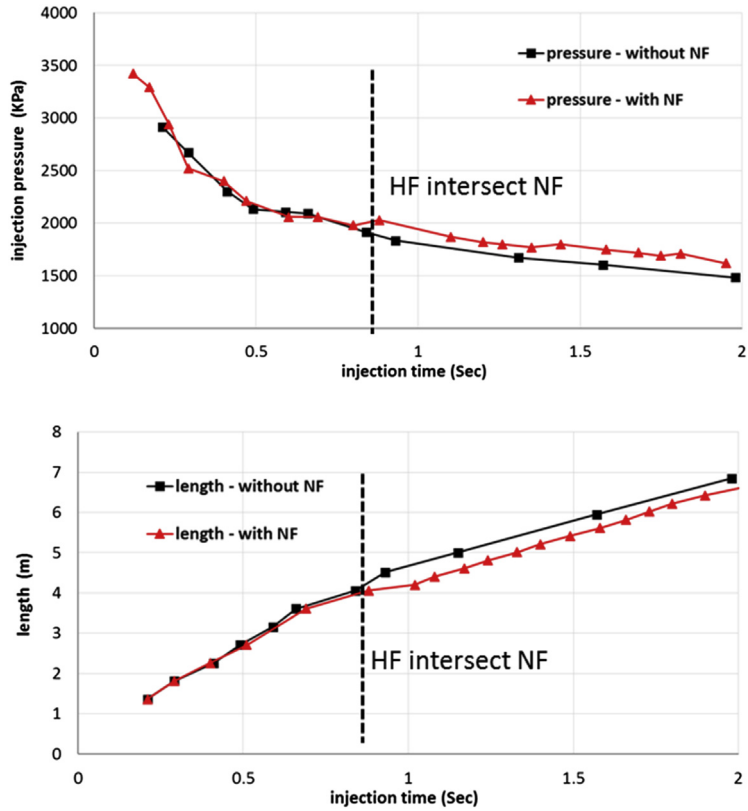

FIGURE 9.25 Comparison of injection pressure and fracture length development for the simulation with preexisting natural fracture (NF) against those without NF. Horizontal hydraulic fracture (HF) intersects a natural fracture after 0.8 s injection (*vertical dashed line*).

It requires higher injection pressure to propagate the fracture after it diverts away from the most prevailing direction. This increase of injection pressure produces a larger fracture width. The fracture length is accordingly shortened to maintain the fracture volume, which is basically equal to the injected fluid volume because no leakage in the rock matrix is considered. Therefore, it may be concluded that the hydraulic fracture decelerates when it intersects with natural ones. Similar simulations and results were also reported in Dahi-Taleghani and Olson (2011), where a simulator based on extended finite-element method was used to model the hydraulic fracture propagation accounting for the interaction between induced and natural fractures.

9.7 MODELING CO_2 GEOSEQUESTRATION EXPERIEMENT USING FRACOD

Geological storage of carbon dioxide (CO_2) has been proposed as a potential method of reducing greenhouse gas emissions. The Naylor Field in the Otway Basin, Victoria, Australia, has been chosen as a demonstration site (The Otway Project) for the geological storage of CO_2 by the Cooperative Research Centre for Greenhouse Gas Technologies (CO2CRC) (Cook, 2014). The Naylor Field is a small depleted natural gas field, with the original gas cap area estimated at 40 ha, which originally held a methane-rich gas accumulation. This resource was exhausted before the injection of CO_2. The field is a fault-bound gas trap (Fig. 9.26) (Vidal-Gilbert et al., 2010). The Naylor Field is bound to the west

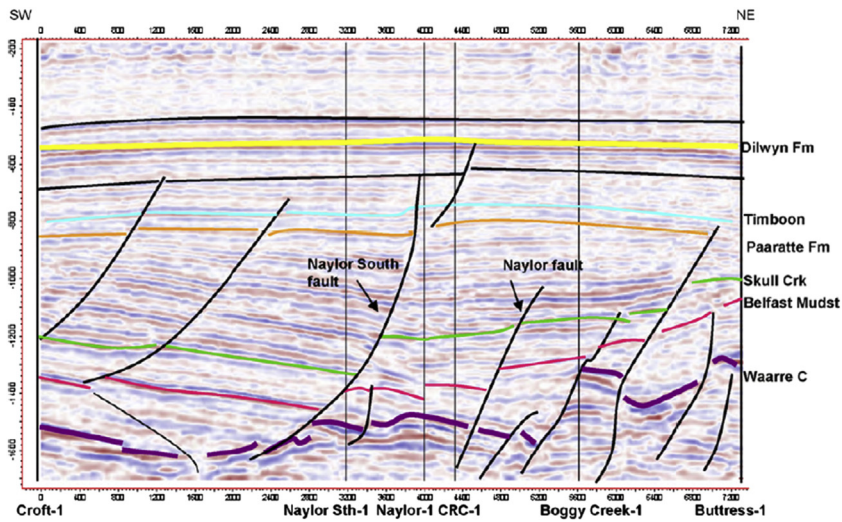

FIGURE 9.26 Major faults identified by the 3D seismic reflection survey and drilling of four wells. *After Vidal-Gilbert, S., Tenthorey, E., Dewhurst, D., Ennis-King, J., Ruth, P.V., Hillis, R., 2010. Geomechanical analysis of the Naylor field, Otway Basin, Australia: implications for CO_2 injection and storage. International Journal of Greenhouse Gas Control 4, 827–839.*

by a north–south trending normal fault (Naylor Fault in Fig. 9.26). The Naylor Fault has an effective juxtaposition seal because the fault throw is insufficient to completely offset the seal (Belfast mudstone). The Naylor Fault forms part of the structural closure that contains the injected CO_2 plume and is required to act as a long-term seal. The Naylor structure is also cut to the east by a normal fault (Naylor East Fault), and it is bound to the South by the Naylor South Fault (Fig. 9.26). Neither the Naylor East Fault nor the Naylor South Fault is in the expected migration pathway of the injected CO_2 plume. The faults bounding the Naylor field supported the initial natural gas column, and the injected volume of CO_2 at subsurface conditions was smaller than the volume of produced methane under the same conditions. Therefore, the faults bounding the Naylor Field should have sufficient sealing capacity to hold the CO_2 volume injected.

The target horizon for CO_2 injection is the Late Cretaceous Waarre Formation (Fig. 9.27). The Waarre Formation is overlain by the Flaxmans Formation and the Belfast mudstone. This site was selected as the location for a CO_2 injection pilot project due to the good porosity and permeability of its reservoir rock (the average permeability was more than 1 Darcy). Furthermore, the reservoir is overlain by the laterally extensive and thick Belfast mudstone,

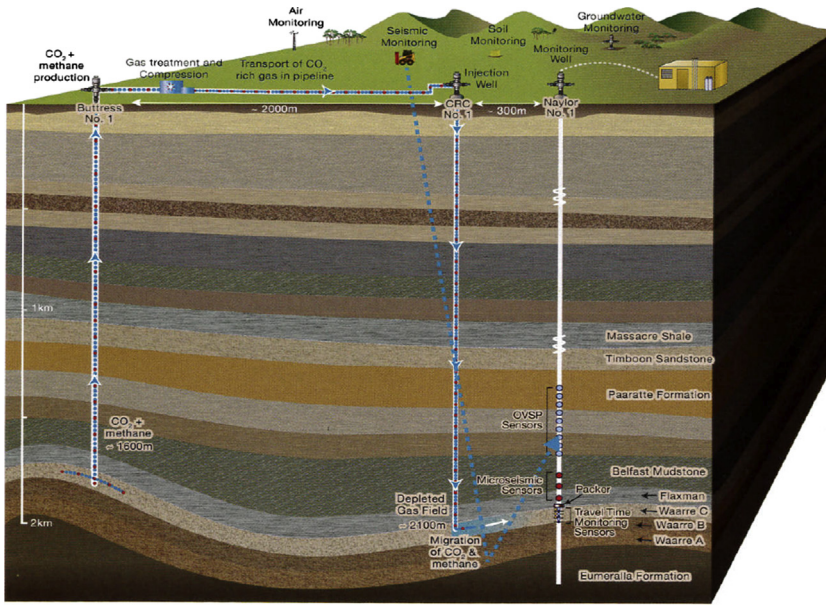

FIGURE 9.27 Geological setting in the CO2CRC Otway Project area. *After Cook, P.J., 2014. Geologically Storing Carbon – Learning from the Otway Project Experience. CSIRO Publishing, Melbourne. ISBN:978-1-48-430230-7.*

which, based on laboratory analyses, should be able to support a CO_2 column height in the range of 607−851 m with an average of 754 m (Daniel, 2007).

There are three wells in the Naylor Field: Naylor-1 being the updip monitoring well, Naylor South-1 and CRC-1 used as the CO_2 injection wells. CO_2-rich gas has been produced from a nearby field and injected into the CRC-1 borehole within the Naylor structure to demonstrate the viability of geological sequestration of CO_2 in Australia. The reservoir was monitored before, during, and after injection via downhole pressure and temperature gauges in the injection well, fluid sampling from the reservoir at the Naylor-1 observation well (via a three level U-tube assembly), and various geophysical methods including 3D seismic and microseismic equipment.

The orientation of maximum horizontal stress was determined to be N142 ± 5°E and is approximately parallel to the strike direction of Naylor fault and Naylor South fault. The magnitudes of the maximum and minimum horizontal stresses have been estimated by various means (Vidal-Gilbert et al., 2010):

$$\sigma_{H\max} = 18.5 \times Z(\text{MPa}),\ \sigma_{h\min} = 14.5 \times Z(\text{MPa}),\ \sigma_v = 21.45 \times Z(\text{MPa})$$

where $\sigma_{H\max}$ is the maximum horizontal stress, $\sigma_{h\min}$ is the minimum horizontal stress, σ_v is the vertical stress, and Z is depth in km.

A case study applying FRACOD to the Otway Project has been conducted by Shen and Shi (2016). Using the FRACOD code, a 2D numerical model for the injection area is created. The model plane is taken as a vertical cross section in the direction of the minimum horizontal principal stress (N48°E) as shown in Fig. 9.28. The Naylor fault and Naylor South fault are assumed to be planar for simplicity, and they are approximately perpendicular to the model cross section and hence can be well represented in the FRACOD model. With this model, $\sigma_{h\max}$ is in the direction perpendicular to the model plane and thus only $\sigma_{h\min}$ and σ_v have effect in the computation. The two faults are dipping 70 and 80 degrees to the SW. The injection well, CRC-1, is located along the y-axis of the coordinate system, as shown in Fig. 9.29 for a simplified model.

The reservoir Waarre C formation is a permeable layer with thickness of about 35 m. It is relatively thin at the model scale, so this layer is simplified as a fracture with a preset hydraulic aperture that results in the same hydraulic conductivity as a permeable layer. Due to this simplification, the modeling flow time will be significantly different from the actual flow time. Hence, this study will only investigate the quasistatic processes of the fracture fluid flow and mechanical response of the caprock and the faults. No attempt is made to study the fully dynamic fluid processes. The strength of the existing faults is critically important for investigation of the possibility of fault reactivation during CO_2 injection. Friction angle of 31 degrees and cohesion of 0.001 MPa used by Aruffo et al. (2014) for the faults at Otway project site are used here for both the Naylor fault and the Naylor South fault.

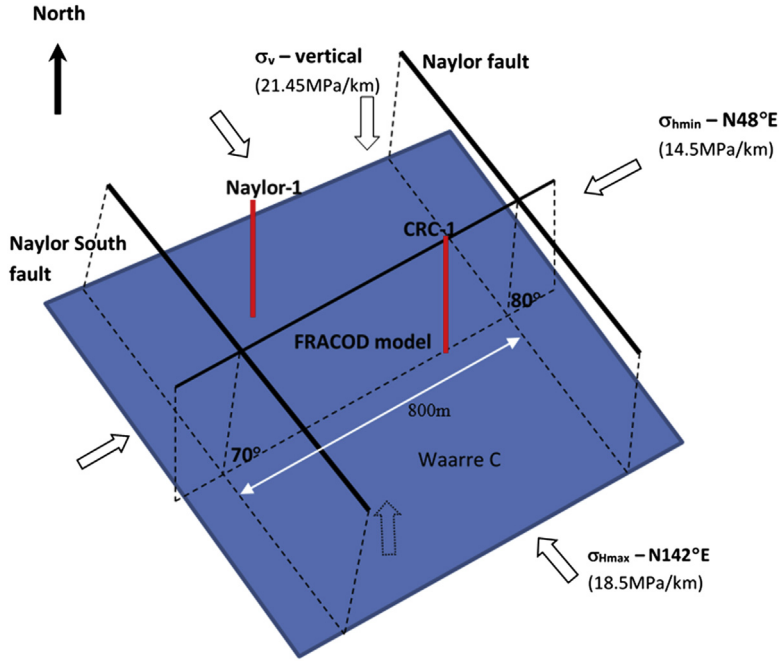

FIGURE 9.28 Geometric relationship of faults planes, wellbores, FRACOD model, and in situ stresses.

The caprock within a distance of 500 m above the reservoir consists of several different rock formations including Belfast Mudstone, Flaxman formation, Skull Creek Formation, and Paaratte Formation. For consideration of stability of the sequestration structure, only the immediate overlaying rock formation (i.e., the Belfast Mudstone and Flaxman formation) is likely to be affected significantly by CO_2 injection. Therefore, uniform rock mass mechanical properties representing those of Belfast Mudstone and Flaxman formation are assumed for the whole model. The rock mass is assumed to be transversely isotropic with parameter values used by Aruffo et al. (2014) or estimated with the experimental data of shale by Islam and Skalle (2013). Key input parameters used in this simulation are listed in Table 9.4, and it should be noted that the CO_2 under the conditions in the reservoir is at liquefied or near-liquefied state.

At the time of injection starting for the demonstration project, the reservoir pressure was 16 MPa. This pressure together with its hydraulic gradients is taken as the initial pore pressure in the fractures and faults in the model. For sensitivity studies, however, a case with zero initial pore pressure has also been investigated. During the actual injection the reservoir pressure increased from the initial pressure of 16 MPa to about 19.2 MPa at the end of the injection. A

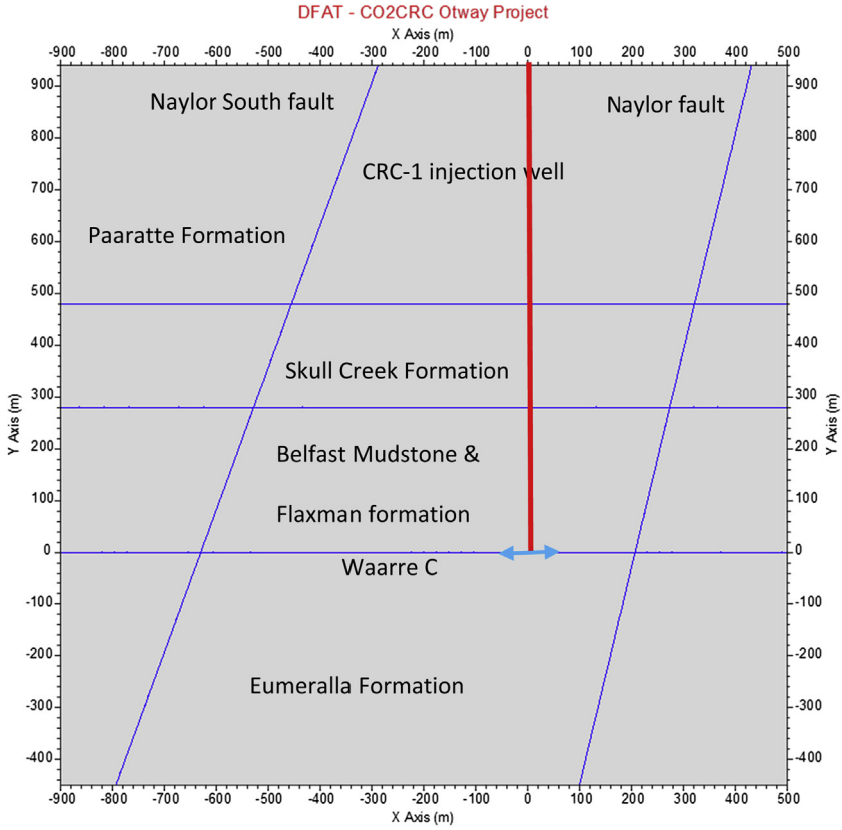

FIGURE 9.29 FRACOD model with simplified geology.

fluid pressure boundary condition is used for the fracture (Waarre C) element at the injection well to simulate the injection process. The difference between the injection pressure and the reservoir pressure will drive the fluid flowing into neighboring elements in the Waarre C formation and later into the Naylor and Naylor South faults. We consider two stability issues for the CO_2 geo-sequestration project: fault reactivation and caprock fracturing.

9.7.1 Fault Reactivation

The stability of the faults is related to the fluid pressure in the faults. Increasing the fluid pressure reduces the effective normal stress and can lead to shear failure of a fault. Fault shearing is often associated with dilation of the material in the fault and hence the increase of hydraulic aperture of the fault. If the fluid pressure is higher than the in situ normal compressive stress, faults will open, and this will dramatically increase their hydraulic conductivity. In

TABLE 9.4 Input Parameters for Modeling Otway CO_2 Geosequestration Project

Parameter	Value Used
Rock Mechanical Parameters	
Young's modulus, E_x (GPa) (in horizontal plane)	6.58
Young's modulus, E_y (GPa) (in vertical direction)	16.07
Poisson's ratio, ν_{xz} (in horizontal plane)	0.21
Poisson's ratio, ν_{yx} (in vertical plane)	0.30
Shear modulus, G_{xy} (GPa)	4.5
Uniaxial compressive strength, (MPa) (horizontal and vertical)	14.83
Tensile strength, σ_t (MPa) (horizontal and vertical)	4.44
Internal friction angle (degrees) (horizontal and vertical)	28.1
Fracture toughness mode I, K_{Ic} (MPa/m$^{1/2}$) (horizontal and vertical)	0.75
Fracture toughness mode II, K_{IIc} (MPa/m$^{1/2}$) (horizontal and vertical)	1.5
Density, ρ (kg/m^3)	2186
Acceleration of gravity, g (m/s^2)	9.81
Reservoir depth (m)	2010
Fracture Parameters	
Normal stiffness, K_n (GPa/m) (Waarre C)	0.345
Shear stiffness, K_s (GPa/m) (Waarre C)	0.345
Fracture aperture, a (m) (Waarre C)	7.29×10^{-3}
Dilatation angle, ψ (deg) (Waarre C)	0
Fracture cohesion, c (MPa) (Waarre C)	5
Friction angle, ϕ (deg) (Waarre C)	37.2
Normal stiffness, K_n (GPa/m) (Naylor and Naylor South fault)	15
Shear stiffness, K_s (GPa/m) (Naylor and Naylor South fault)	40
Fracture aperture a (m) (Naylor and Naylor South fault)	0.1×10^{-3}
Dilatation angle, ψ (deg) (Naylor and Naylor South fault)	1
Fracture cohesion, c (MPa) (Naylor and Naylor South fault)	0.001
Friction angle, ϕ (deg) (Naylor and Naylor South fault)	31

TABLE 9.4 Input Parameters for Modeling Otway CO_2 Geosequestration Project—cont'd

Parameter	Value Used
Hydraulic Fracture Parameters	
Fluid density, ρ_w (kg/m^3)	773
Dynamic viscosity of the fluid, μ (Pa•s)	0.09922×10^{-3}
Initial pore pressure, P_0 (MPa)	16
Fluid bulk modulus, E_w (MPa)[a]	20
Equivalent hydraulic aperture for Waarre C formation (m)	7.29×10^{-3}
Caprock hydraulic conductivity (m/s)	1.0×10^{-19}

[a]*Low fluid bulk modulus is used for faster fluid modeling convergence and better model stability.*

both cases, the faults could become the path of CO_2 flow into the upper rock formation and cause leakage of the injected CO_2 toward the surface.

Actual injection pressure at the site was 19.2 MPa with initial pore pressure of 16.0 MPa. To investigate possibility of reactivation of the faults, a number of fluid injection pressures from 19.2 to 30 MPa have been considered in FRACOD simulation. In addition, initial pore pressure and fault aperture have been varied to study their sensitivities on the fault reactivation. The values of these parameters and the corresponding modeling results are shown in Table 9.5. Overall, with an injection pressure of 19.2 MPa, neither the Naylor South nor the Naylor fault is predicted to have any shear or opening failure regardless of the magnitude of fault aperture and/or existence of pore pressure. This is consistent with other study results obtained by Aruffo et al. (2014) and Vidal-Gilbert et al. (2010) and the actual injection experiment data. Therefore, under the assumptions used in the modeling, the injection pressure of CO_2 at Otway site is considered to be appropriate and unlikely to cause fault reactivation.

If there is no pore pressure and the faults are relatively impermeable (aperture = 0.1 mm), then when the injection pressure is increased to 25 MPa, very limited shear failure is predicted to occur in the Naylor South fault above Waarre C but not in Naylor fault and Naylor South fault below Waarre C. If the faults have a high permeability (aperture = 1 mm), both Naylor South and Naylor faults are predicted to experience some shear failure. The shear failure has a large extension above Waarre C in the Naylor South fault. At this level of injection pressure and no pore pressure, the faults remain closed. When the injection pressure reaches 30 MPa, both the faults are predicted to experience shear failures within a limited distance (30 m) from Waarre C for a relatively

TABLE 9.5 Summary of Modeling Results on Fault Reactivation

Injection Pressure (MPa)	Pore Pressure = 0		Pore Pressure = 16 MPa	
	Fault Aperture = 0.1 mm	**Fault Aperture = 1 mm**	**Fault Aperture = 0.1 mm**	**Fault Aperture = 1 mm**
19.2	*Fault shearing* Nil *Fault opening* Nil	*Fault shearing* Nil *Fault opening* Nil	*Fault shearing* Nil *Fault opening* Nil	*Fault shearing* Nil *Fault opening* Nil
25	*Fault shearing* Naylor South: AC Nil BC 0–30 m Naylor: Nil *Fault opening* Nil	*Fault shearing* Naylor South: AC 340 m BC 80 m Naylor: AC 50 m BC 40 m *Fault opening*: Nil	*Fault shearing* Naylor South: AC 50 m BC 30 m Naylor: AC 30 m BC 30 m *Fault opening*: Nil	*Fault shearing* Naylor South: AC 800 m BC 500 m Naylor: AC 350 m BC 150 m *Fault opening* AC 200 m BC 150 m
30	*Fault shearing* Naylor South and Naylor: AC 30 m BC 30 m *Fault opening* Naylor South: AC 15 m BC Nil Naylor: Nil *High fluid pressure in faults* AC 30 m BC 60 m	*Fault shearing* Naylor South and Naylor: AC 230 m BC 210 m *Fault opening*: Nil	*Fault shearing* Naylor South: AC 800 m BC 500 m Naylor: AC 130 m BC 70 m *Fault opening* Random in shearing region of both faults	*Fault shearing* Naylor South and Naylor: AC 800 m BC 500 m *Fault opening*: Random in shearing region of both faults

AC, within the distance above Waarre C; *BC,* within distance below Waarre C.

low fault permeability assumption and over an extensive region for a high fault permeability.

The presence of initial pore pressure in the Waarre C reservoir and the two subvertical faults accelerates the injected fluid pressure propagation in the reservoir and further into the faults. In this study, the pore pressures in the reservoir and faults are assumed to be the same. Modeling results tabulated in Table 9.5 indicate that with pore pressure of 16 MPa, the extent of fault shearing and opening is greater than those cases of zero pore pressure for injection pressure of 25 and 30 MPa.

The model was run for 100 cycles for each combination of injection pressure, pore pressure, and fault permeability. It was found that 100 cycles were sufficient for the fluid pressure (in the Waarre C reservoir) to propagate well beyond the Naylor fault and Naylor South fault. Note that each cycle includes one mechanical step (fracture movement and/or propagation) and 50,000 fluid flow calculation steps. In these simulations, we did not attempt to replicate the real flow time as discussed previously. Hence the faults are under full injection pressure, at least at their intersections with the Waarre C formation. Depending on the aperture (permeability) of the fault, the fluid pressure may be able to penetrate into the fault causing large-scale fault shearing. One typical case of the fluid pressure distribution and fault shearing is shown in Fig. 9.30 where the initial pore pressure is assumed to be zero and the injection pressure is 30 MPa. At the early stage of the injection, modeling predicts that the injected CO_2 quickly spreads in the Waarre C formation (fracture). After about 35 cycles, fluid starts to penetrate into the Naylor fault and Naylor South fault. The Naylor South fault is the first one to start having limited shearing at the intersection due to its more favorable dip angle (70 degrees). Then the Naylor fault also experiences limited shearing. Shearing, however, is predicted to be limited only to a distance of several tens of meters above and below the Waarre C formation. This is because the faults have a low permeability (hydraulic aperture = 0.1 mm), and the injected fluid can only penetrate a short distance. This fault is almost vertical (dip = 80 degrees); therefore when the fluid pressure in the fault is close to the minimum horizontal stress ($\sigma_{h\min} = 30.45$ MPa at the depth of Waarre C formation), it may open in tension. Close to the end of the simulation, the part of the Naylor fault at the intersection with Waarre C is predicted to fail in tension, see Fig. 9.30.

A case where the injected CO_2 penetrates into the faults and causes major fault shearing is shown in Fig. 9.31. In this simulation the hydraulic aperture of both faults is set to be 1 mm. As the hydraulic conductivity is proportional to the cube of the fracture hydraulic apertures based on the cubic law, the actual hydraulic conductivity has increased to 1000 times from the value for that used for Fig. 9.30. Due to the significantly higher fault hydraulic conductivity, it is predicted that the injected CO_2 penetrates into the faults at an early stage and eventually results in a significant length of the faults being reactivated by shearing.

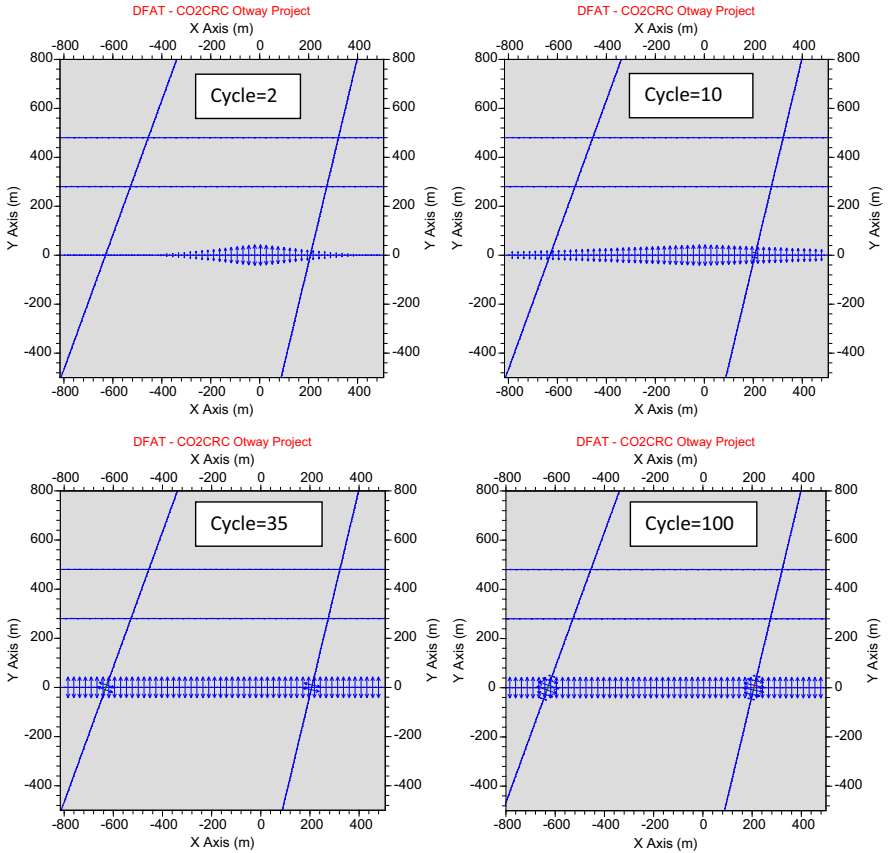

FIGURE 9.30 Modeled fluid pressure distribution and the resultant fault shearing and opening. Initial pore pressure = 0 MPa, injection pressure = 30 MPa, and fault hydraulic aperture = 0.1 mm. Green (gray in print version) indicates fracture shearing and red (dark gray in print version) for fracture opening.

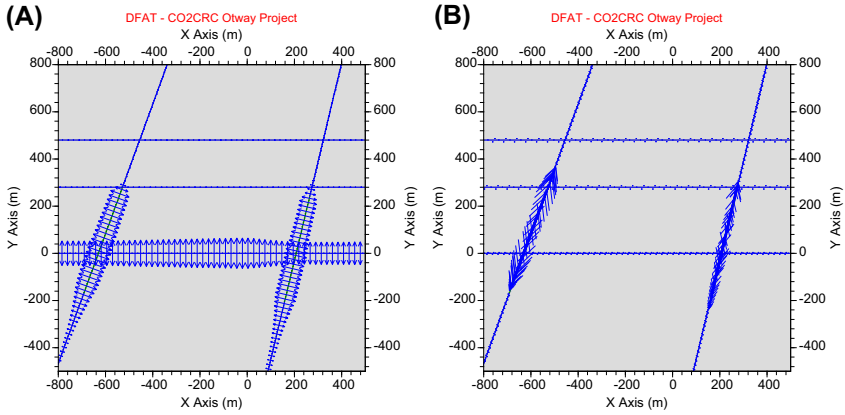

FIGURE 9.31 Modeled fluid pressure distribution and the resultant fault shearing at 35 cycles. Initial pore pressure = 0 MPa, injection pressure = 30 MPa, and fault hydraulic aperture = 1 mm.

9.7.2 Caprock Stability

Injection of pressurized CO_2 into the Waarre C reservoir will increase local fluid pressure and hence will change the effective stress in the reservoir. This will cause a change in the stress field of the surrounding rock mass, including the caprock. It is noticed that an injection pressure of 19.2 MPa into a reservoir with pore pressure of 16 MPa does not necessarily mean that it will apply an additional 3.2 MPa vertical stress to the caprock. This is because the total vertical stress in the caprock is from overall deformation caused by the overburden gravity force, in situ stresses, and the injection pressure. A change of the fluid pressure in the reservoir will cause uneven deformation of the Waarre C layer and may lead to an increase of vertical stress in some areas and a decrease in other areas.

Depending on the magnitude of injection pressure, the actual increase in vertical stress in the caprock immediately above the Waarre C reservoir is predicted to be less than 0.17, 0.35, and 0.54 MPa for injection pressures of 19.2, 25, and 30 MPa, respectively. This maximum vertical stress change occurs only in the early stage of the injection and near the injection well, as seen in Fig. 9.32, which shows the predicted change of vertical stress in the caprock immediately above the Waarre C reservoir for injection pressure of 30 MPa. During the initial stages of injection, the high fluid pressure is only distributed in the vicinity of the injection well and has not yet spread into a wide area of the reservoir. At later stages of injection when the fluid pressure is spread more evenly into the reservoir, the induced vertical stress change gradually diminishes.

Comparing with the magnitude of the in situ vertical stress at the Waarre C depth (43.1 MPa) and the uniaxial compressive strength of the caprock (14.8 MPa), a change of vertical stress of less than 0.5 MPa due to CO_2 injection is insignificant. It is therefore not expected that the injection pressure up to 30 MPa would cause intact rock failure and compromise the integrity of the caprock.

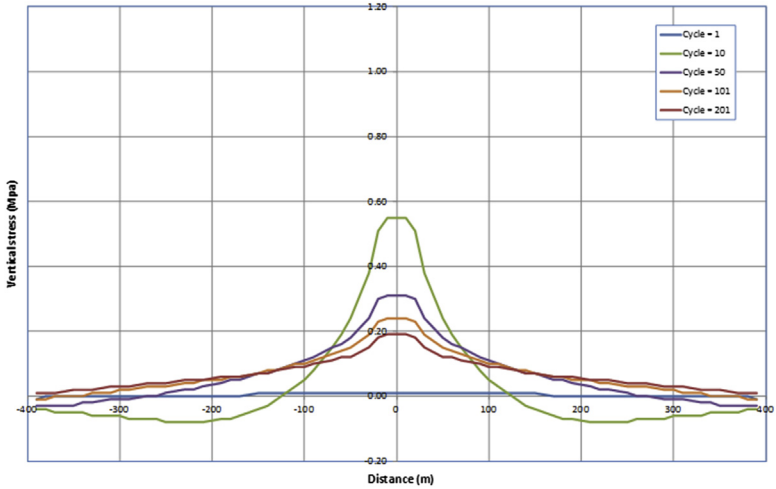

FIGURE 9.32 Predicted change of vertical stress in the caprock immediately above the Waarre C reservoir. Initial pore pressure = 16 MPa; injection pressure = 30 MPa. Note the distribution of the stress change with flow process after different modeling cycles.

These findings are for intact rocks. However, the caprock may contain discontinuities such as joints and weak bedding planes and the strength of the caprock could be dominated by the strength of these discontinuities rather than that of intact rock. To investigate the possibility of caprock failure due to discontinuities, a case with a preexisting joint near the injection well has been modeled, see Fig. 9.33. Three joint dip angles (45, 60 and 90 degrees) are simulated. The joint has a length of 144 m, and its strength parameters are assumed to be the same as those for the Naylor and Naylor South faults. The possibility of shearing and propagation of this joint has been studied with different injection pressures.

Results are shown in Table 9.6. With an injection pressure of 19.2 MPa, no shear or opening failure is predicted for the joint regardless of its dip angle. If the injection pressure is 25 MPa or higher, when the joint dip angle is 45 or 60 degrees, the joint is predicted to experience shear failure but no opening in tension or propagation. When the joint is vertical, no shear failure is expected because of the lack of shear stress in the joint plane for the values of injection pressure. At injection pressure of 25 MPa, the vertical joint is predicted to remain closed. When the injection pressure is increased to 30 MPa, which is close to the minimum principal horizontal stress at the Waarre C reservoir, the joint is predicted to open up but not propagate.

We have also investigated the possibility of caprock failure in another situation where the rock contains a set of very weak bedding planes. In sedimentary rocks such as that at the Otway Project site, bedding planes are fairly common. In most cases, the bedding planes are horizontal or sub-horizontal. At the Otway project site, subhorizontal bedding planes in the

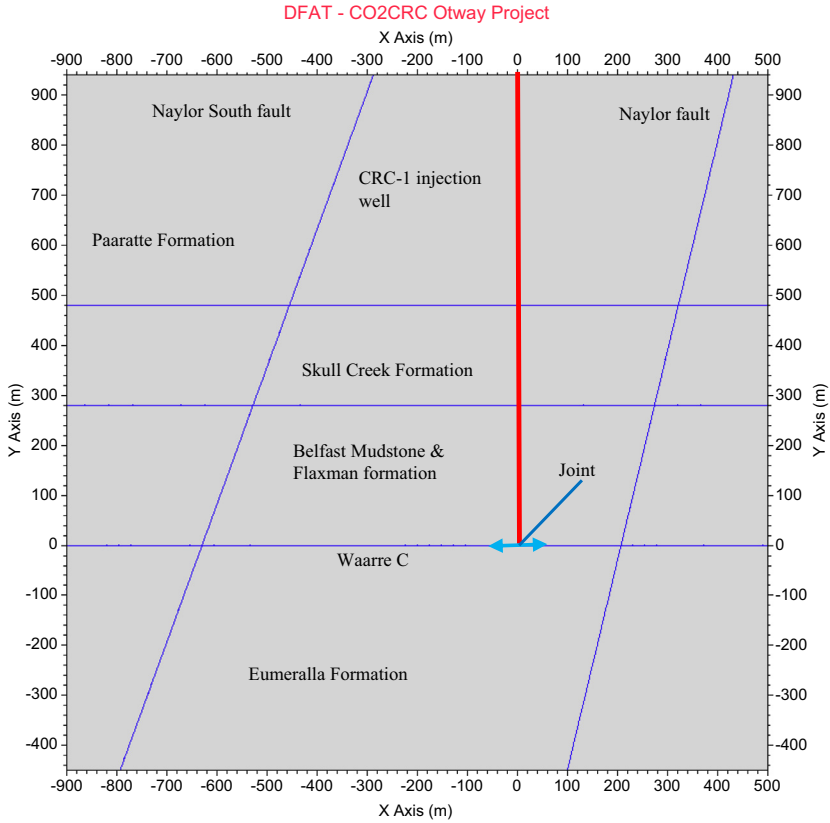

FIGURE 9.33 Numerical model with an inclined joint in caprock. The joint dip angle varies from 45 to 90 degrees.

TABLE 9.6 Summary of Modeling Results on Joint Stability

Injection Pressure (MPa)	Joint Dip Angle = 45 degrees	Joint Dip Angle = 60 degrees	Joint Dip Angle = 90 degrees
19.2	*Joint shearing*: Nil *Joint opening*: Nil *Joint propagation*: Nil	*Joint shearing*: Nil *Joint opening*: Nil *Joint propagation*: Nil	*Joint shearing*: Nil *Joint opening*: Nil *Joint propagation*: Nil
25	*Joint shearing*: **Yes** *Joint opening*: Nil *Joint propagation*: Nil	*Joint shearing*: **Yes** *Joint opening*: Nil *Joint propagation*: Nil	*Joint shearing*: Nil *Joint opening*: Nil *Joint propagation*: Nil
30	*Joint shearing*: **Yes** *Joint opening*: Nil *Joint propagation*: Nil	*Joint shearing*: **Yes** *Joint opening*: Nil *Joint propagation*: Nil	*Joint shearing*: Nil *Joint opening*: **Yes** *Joint propagation*: Nil

caprock are unlikely to fail because they align with the principal stress directions and very limited shear stress exists along the bedding planes. The CO_2 injection in Waarre C reservoir will not significantly change the stress magnitude as discussed previously. For this reason, we do not expect any failure on the bedding plane for an injection pressure up to 30 MPa.

However, in some special cases where the bedding planes are extremely weak and are inclined (say, 45 degrees), there is a possibility of fracturing along the bedding planes. To investigate this possibility, a number of cases with different bedding plane strength and bedding angle have been investigated. It was found that with a bedding plane angle of 45 degrees, fracture initiation could occur in the caprock if the bedding plane has a friction angle of 11 degrees or less and no cohesion. New fractures are formed in the vicinity of the injection well in the caprock. These fractures are all formed along the bedding plane direction (see Fig. 9.34).

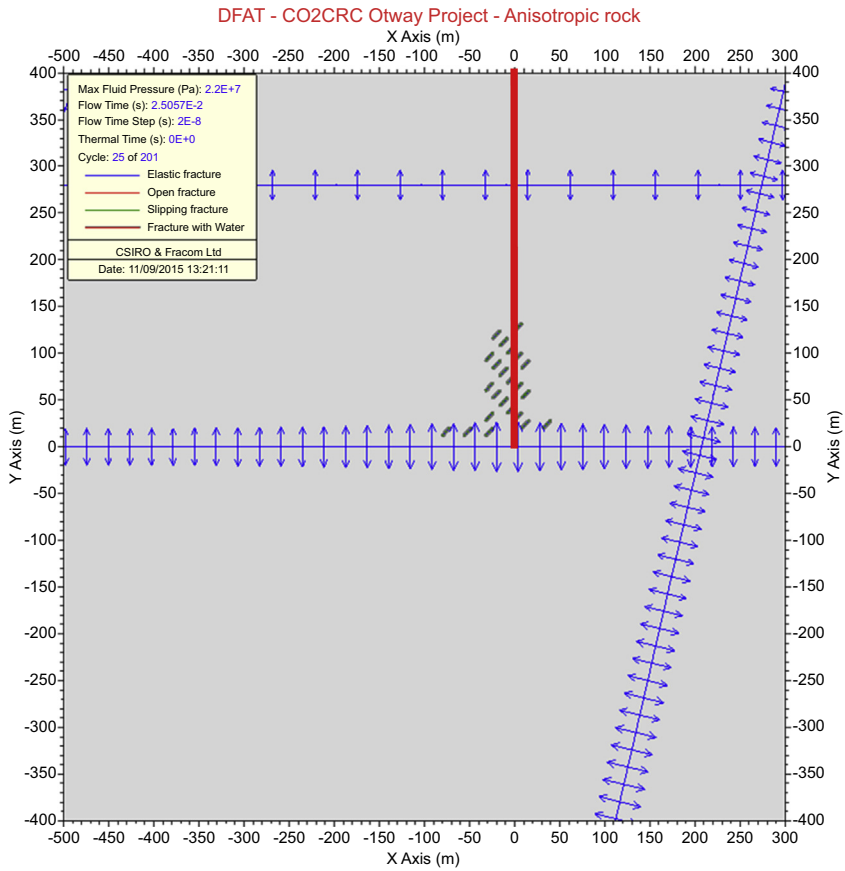

FIGURE 9.34 Predicted fracture initiation along weak bedding planes. Bedding plane friction angle is 11 degrees, cohesion = 0, and bedding angle = 45 degrees. Injection pressure = 25 MPa, initial pore pressure = 16 MPa.

Fig. 9.34 is a special case where the bedding planes are in a critical balanced state before injection. The small stress increase (0.37 MPa with injection pressure of 25 MPa) in the immediate caprock disturbs this subtle balance and causes caprock fracturing. This case is considered to be extremely rare and should not be taken as a likely scenario at Otway Project site.

9.8 CONCLUSIONS

Rock fractures propagate in both tension and shear modes. Effectively handling mode II fracture is critically important for predicting the rock mass failure processes. The fracture propagation code, FRACOD, is designed to simulate the rock mass failure by means of modeling the explicit fracturing process using fracture mechanics principles. It uses an energy-based fracture criterion, the *F*-criterion, to predict the complex mixed mode fracture propagation in jointed rock masses.

New functions of F−T−H coupling have been recently developed and implemented in FRACOD. The $F-T$ one-way coupling was achieved using an indirect method: the fictitious heat source method. The $F-H$ coupling was achieved using an explicit approach and it uses an iterative scheme for both fluid flow and fracture propagation. The new function is capable of simulating fluid flow in complex fracture networks and fracture movement and propagation driven by fluid pressure. A simple mechanism of fluid leakage into intact rocks has also been implemented.

Coupling of $T-H$ flow in FRACOD considers the fracture flow only where heat transfer in rock is assumed to be a pure thermal conduction process whereas heat transfer in fluid in the fractures is considered as a pure thermal convection process. The implicit method used in thermal analysis is combined with the explicit method in the fracture flow analysis by using an iterative method with limited time steps. This scheme is found to be effective in predicting $T-H-$coupled process with acceptable accuracy.

The capability of FRACOD and its $F-T-H-$coupled functions have been demonstrated through several application examples in this chapter, including biaxial loading tests, borehole breakout, borehole cooling fractures, and fluid flow and heat extraction in a fractured geothermal reservoir system.

Two detailed case studies have been given in this chapter. The first is the modeling of HF processes in a rock mass with and without natural preexisting fractures. The second is the modeling of a CO_2 geosequestration field experiment in Australia. These case studies have shown that FRACOD is capable of effectively predicting fracture propagation and fault activation under fluid injection pressure.

Recent development of FRACOD has been focusing on the extension to 3D, which will enable us to model the true 3D fracture propagation and the actual 3D geometry of underground excavations.

ACKNOWLEDGMENTS

The author would like to thank Prof. Ove Stephansson and Prof. Mikael Rinne for the long-time support and contributions to the development and applications of FRACOD. I would also like to thank our collaboration partners in the International Collaboration Project on Coupled Fracture Mechanics Modeling, including, but not limited to, Prof. Yunliang Tan, Dr. Johannes Suikkanen, Dr. Eui Seob Park, Dr. Yongbok Jung, Dr. Kwang Yeom Kim, Dr. Li Zhuang, Prof. Xiaochun Li, Dr. Bin Bai, Prof. Chun'an Tang, Prof. Ki-Bok Min, Dr. Linmao Xie, Dr. Jonny Rutqvist, Prof. Simon Loew, Dr. Martin Ziegler, Dr. Mohammadreza Jalali, Prof Günter Zimmermann, Dr. Arno Zang, and Prof. Weiguo Liang. My appreciation is extended to my colleagues Dr. Hua Guo and Dr. Jingyu Shi for their involvement and support. This work is partially supported by Shandong Province's Taishan Scholar Talent Team Support Plan for Advantaged & Unique Discipline Areas.

REFERENCES

Adachi, J., Siebrits, E., Peirce, A., Desroches, J., 2007. Computer simulation of hydraulic fractures. International Journal of Rock Mechanics and Mining Sciences 44 (5), 739–757.

Aruffo, C.M., Rodriguez-Herrera, A., Tenthorey, E., Krzikalla, F., Minton, J., Henk, A., 2014. Geomechanical modelling to assess fault integrity at the CO2CRC Otway Project, Australia. Australian Journal of Earth Science: An International Geoscience Journal of the Geological Society of Australia 61, 987–1001. https://doi.org/10.1080/08120099.2014.958876.

Backers, T., Stephansson, O., Rybacki, E., 2002. Rock fracture toughness testing in mode II-punch-through shear test. International Journal of Rock Mechanics and Mining Sciences 39 (6), 755–769.

Barton, N., 2007. Rock Quality, Seismic Velocity, Attenuation and Anisotropy. Taylor & Francis Group, London, ISBN 0-415-39441-4.

Bodvarsson, G., 1969. On the temperature of water flowing through fractures. Journal of Geophysical Research 74 (8), 1987–1991.

Cook, P.J., 2014. Geologically Storing Carbon – Learning from the Otway Project Experience. CSIRO Publishing, Melbourne, 9781484302307.

Crouch, S.L., Starfield, A.M., 1983. Boundary Element Methods in Solid Mechanics. George Allen & Unwin.

Dahi-Taleghani, A., 2009. Analysis of Hydraulic Fracture Propagation in Fractured Reservoirs: An Improved Model for the Interaction between Induced and Natural Fractures (Ph.D. dissertation). University of Texas, Austin.

Dahi-Taleghani, A., Olson, J.E., 2011. Numerical modeling of multistranded-hydraulic-fracture propagation: accounting for the interaction between induced and natural fractures. SPE Journal 16 (03), 575–581.

Daniel, R.F., 2007. Carbon Dioxide Seal Capacity Study. CRC-1, CO2CRC Otway Project, Otway Basin, Victoria. CO2CRC Report No: RPT07–0629.

Fast, R.E., Murer, A.S., Timmer, R.S., 1994. Description and analysis of cored hydraulic fractures, Lost Hills field, Kern County, California. SPE Production & Facilities 9 (02), 107–114.

Fu, P., Johnson, S.M., Carrigan, C.R., 2013. An explicitly coupled hydro-geomechanical model for simulating hydraulic fracturing in arbitrary discrete fracture networks. International Journal for Numerical and Analytical Methods in Geomechanics 37 (14), 2278–2300.

Gale, J.F., Reed, R.M., Holder, J., 2007. Natural fractures in the Barnett Shale and their importance for hydraulic fracture treatments. AAPG Bulletin 91 (4), 603–622.

Geertsma, J., De Klerk, F., 1969. A rapid method of predicting width and extent of hydraulically induced fractures. Journal of Petroleum Technology 21 (12), 1−571.

Haimson, B., Fairhurst, C., 1967. Initiation and extension of hydraulic fractures in rocks. Society of Petroleum Engineers Journal 7 (03), 310−318.

Islam, M.A., Skalle, P., 2013. An experimental investigation of shale mechanical properties through drained and undrained test mechanisms. Rock Mechanics and Rock Engineering. https://doi.org/10.1007/s00603-013-0377-8.

Itasca, 2004. UDEC Version 4.0 − Theoretical and Background (Fluid Flow in Joints). Itasca Consulting Group, Inc., Minneapolis, MN 55401, USA.

Jaeger, J.C., Cook, N.G., Zimmerman, R., 2007. Fundamentals of Rock Mechanics − fourth Edition. John Wiley & Sons.

Jeffrey, R.G., Bunger, A., Lecampion, B., Zhang, X., Chen, Z., van As, A., Thiercelin, M.J., 2009. Measuring hydraulic fracture growth in naturally fractured rock. In: SPE Annual Technical Conference and Exhibition. Society of Petroleum Engineers.

Khristianovich, S.A., Zheltov, Y.P., 1955. Formation of vertical fractures by means of a highly viscous fluid. In: Proc. 4th World Petroleum Congress, vol. 2, pp. 579−586.

Klee, G., Bunger, A., Meyer, G., Rummel, F., Shen, B., 2011. In situ stresses in borehole blanche-1/south Australia derived from breakouts, core discing and hydraulic fracturing to 2 km depth. Rock Mechanics and Rock Engineering 44, 531−540.

Li, V.C., 1991. Mechanics of shear rupture applied to earthquake zones. In: Atkinson, K.B. (Ed.), Fracture Mechanics of Rock. Academic Press, London, pp. 351−428.

Louise, C., 1969. A Study of Groundwater Flow in Jointed Rock and its Influence on the Stability of Rock Masses. Imperial College, Rock Mech. Research Report No.10, 1969.

Min, K.-B., Rutqvist, J., Tsang, C.-F., Jing, L., 2005. Thermally induced mechanical and permeability changes around a nuclear waste repository—a far-field study based on equivalent properties determined by a discrete approach. International Journal of Rock Mechanics and Mining Sciences 42, 765−780.

Petit, J.-P., Barquins, M., 1988. Can natural faults propagate under mode II conditions? Tectonics 7 (6), 1243−1256.

Rao, Q., 1999. Pure Shear Fracture of Brittle Rock − a Theoretical and Laboratory Study (Ph.D. thesis). Lulea University of Technology.

Reyes, O., Einstein, H.H., 1991. Failure mechanism of fractured rock — a fracture coalescence model. In: Proc. 7th Int. Con. on Rock Mechanics, vol. 1, pp. 333−340.

Rinne, M., 2000. Propagation of rock fractures in the vicinity of a canister hole for spent nuclear fuel (Licentiate thesis). Royal Institute of Technology, Engineering Geology, Stockholm, Sweden, ISBN 91-7170-617-8.

Rinne, M., 2008. Fracture Mechanics and Subcritical Crack Growth Approach to Model Time-dependent Failure in Brittle Rock (Doctoral dissertation). Helsinki University of Technology, Rock Engineering, ISBN 978-951-22-9434-3. http://lib.tkk.fi/Diss/2008/isbn9789512294350/.

Rinne, M., Shen, B., 2007. Numerical simulation of core tests using FRACOD in understanding and characterizing of the excavation disturbed zone (EDZ). DECOVALEX Task B Phase 2 report. In: Hudson and Jing 2007. SKI Report 2007:08. Swedish Nuclear Power Inspectorate.

Rinne, M., Shen, B., Lee, H.-S., Jing, L., 2003. Thermo-mechanical Simulations of Pillar Spalling in SKB APSE Test by FRACOD. In: GeoProc International Symposium, Stockholm, Sweden, August 2003.

Rinne, M., Shen, B., Lee, H.-S., 2004. Modelling of Fracture Development of APSE by FRACOD. Äspö Pillar Stability Experiment. R-04−04. Swedish Nuclear Fuel and Waste Management Co (SKB), Stockholm, Sweden.

Rutqvist, J., Chijimatsu, M., Jing, L., De Jonge, J., Kohlmeier, M., Millard, A., Nguyen, T.S., Rejeb, A., Souley, M., Sugita, Y., Tsang, C.-F., 2005. Numerical study of the THM effects on the near-field safety of a hypothetical nuclear waste repository − BMT1 of the DECOVALEX III project. Part 3: effects of THM coupling in fractured rock. International Journal of Rock Mechanics and Mining Sciences 42, 745−755.

Shen, B., 1993. Mechanics of Fractures and Intervening Bridges in Hard Rocks (Doctorate thesis). Royal Institute of Technology, ISBN 91-7170-140-0.

Shen, B., 2004. Using Borehole Breakout Data to Estimate In Situ Stresses in Deep Granite at Habanero #1 Hot Dry Rock well. CSIRO Exploration and Mining Report 1166C.

Shen, B., 2008. Borehole Breakout and In Situ Stresses, vol. 1. SHIRMS, pp. 407−418.

Shen, B., Shi, J., 2016. Analysis of fracturing-hydraulic coupling in transversely isotropic Rocks and A Case study on CO_2 sequestration. International Journal of Rock Mechanics and Mining Sciences 206−220.

Shen, B., Stephansson, O., 1993. Numerical analysis of mixed mode I and mode II fracture propagation. Special issue for the 34th U.S. Symposium of rock mechanics. International Journal of Rock Mechanics and Mining Sciences 30, 861−867.

Shen, B., Stephansson, O., 1994. Modification of the G-criterion of crack propagation in compression. International Journal of Engineering Fracture Mechanics 47 (2), 177−189.

Shen, B., Stephansson, O., Einstein, H.H., Ghahreman, B., 1995. Coalescence of fractures under shear stresses in experiments. Journal of Geophysics Research 100 (B4), 5975−5990.

Shen, B., Stephansson, O., Rinne, M., 2002. Simulation of borehole breakouts using FRACOD2D. In: Oil & Gas Science and Technology − Revue de l'IFP, special issue for International Workshop of Geomechanics in Reservoir Simulation − December 5−7, 2001 − IFP. Rueil-Malmaison, France, vol. 57. No. 5, pp. 579−590.

Shen, B., Stephansson, O., Rinne, M., Lee, H.-S., Jing, L., Roshoff, K., 2004. A fracture propagation code and its applications to nuclear waste disposal. International Journal of Rock Mechanics & Mining Sciences 41 (3), 448−449. Paper 2B 02 — SINOROCK 2004 Symposium.

Shen, B., Kim, H.-M., Park, E.-S., et al., 2008. Coupled Thermal-Fracture Behaviour of Rock: Laboratory Tests and Numerical Code Development. CSIRO Exploration and Mining Report P2008/2677.

Shen, B., Kim, H.M., Lee, J.M., Lee, H.S., Junker, R., Rinne, M., Backers, T., Stephansson, O., 2009. Coupled thermal/fracturing process of rocks. In: 43rd US Rock Mechanics Symposium, Asheville, ARMA 09-65, pp. 1−8.

Shen, B., Stephansson, O., Rinne, M., Amemiya, K., Yamashi, R., Toguri, S., Asano, H., 2011. FRACOD modelling of rock fracturing and permeability change in excavation-damaged zone. International Journal Geomechanics 11, 302−331.

Shen, B., Kim, H.M., Park, E.S., Kim, T.K., Wuttke, M., Rinne, M., Backers, T., Meier, T., Stephansson, O., 2012. Multi-region boundary element analysis for coupled thermal-fracturing processes in geomaterials. Rock Mechanics and Rock Engineering 46, 135−151.

Shen, B., Guo, H., Ko, T.Y., Lee, S.C., Kim, J., Kim, H.M., Park, E.S., Wuttke, M., Backers, T., Rinne, M., Stephansson, O., 2013. Coupling rock fracture propagation with thermal and fluid flow processes. International Journal of Geomechanics. 13, 794−808.

Shen, B., Stephansson, O., Rinne, M., 2014. Modelling Rock Fracturing Processes: A Fracture Mechanics Approach Using FRACOD. Springer, ISBN 978-94-007-6903-8, p. 173.

Shi, J., Shen, B., 2014. Approximation schemes of stresses on elements for the three dimensional displacement discontinuity method. Engineering Analysis With Boundary Elements 48, 63−72.

Shi, J., Shen, B., Stephensson, O., Rinne, M., 2014. A three-dimensional crack growth simulator with displacement discontinuity method. Engineering Analysis With Boundary Elements 48, 73–86.

Siren, T., Uotinen, L., Rinne, M., 2014. Fracture mechanics modelling of in situ shotcrete spalling experiment. Rock Mechanics and Rock Engineering Special Issue in Honour of Ove Stephansson 48 (4), 1423–1438.

Stephansson, O., Shen, B., Rinne, M., et al., 2003. Geomechanical evaluation and analysis of research shafts and galleries in MIU Projects, Japan. In: Environmental Rock Engineering. Proceedings the 1st Kyoto International Symposium on Underground Environment – Role of Geo-technology to the Underground Environment. March 17018, 2003/Kyoto Japan, pp. 39–45.

Stephansson, O., Shen, B., Rinne, M., Amemiya, K., Yamashi, R., Toguri, S., 2008. FRACOD modelling of rock fracturing and permeability change in excavation damage zone. In: 12th International Conference of International Association for Computer Methods and Advances in Geomechanics, Goa, India.

Tsang, C.-F., Jing, L., Stephansson, O., Kautsky, F., 2005. The DECOVALEX III Project: a summary of activities and lessons learned. International Journal of Rock Mechanics and Mining Sciences 42 (5–6), 593–612.

Valko, P., Economides, M.J., 1995. Hydraulic Fracture Mechanics. Wiley, New York.

Vidal-Gilbert, S., Tenthorey, E., Dewhurst, D., Ennis-King, J., Ruth, P.V., Hillis, R., 2010. Geomechanical analysis of the Naylor field, Otway Basin, Australia: implications for CO2 injection and storage. International Journal of Greenhouse Gas Control 2010 (4), 827–839.

Warpinski, N.R., Teufel, L.W., 1987. Influence of geologic discontinuities on hydraulic fracture propagation (includes associated papers 17011 and 17074). Journal of Petroleum Technology 39 (02), 209–220.

Xie, L.M., Min, K.-B., Shen, B., 2014. Displacement discontinuity method modelling of hydraulic fracturing with pre-existing fractures. In: Proceeding of 48th US Rock Mechanics/Geomechanics Symposium, ARMA 14–7464.

Xie, L., Min, K.B., Shen, B., 2016. Simulation of hydraulic fracturing and its interactions with a pre-existing fracture using displacement discontinuity method. Journal of Natural Gas Science and Engineering 36 (B), 1284–1294.

Chapter 10

An Integrated Study for Hydraulic Fracture and Natural Fracture Interactions and Refracturing in Shale Reservoirs

Azra N. Tutuncu, Binh Bui, Theerapat Suppachoknirun[a]
Colorado School of Mines, Golden, CO, United States

10.1 INTRODUCTION

The combined implementation of horizontal drilling and multistage fracturing has played a significant role in economically viable production from shale gas and tight oil reservoirs. The presence of natural fractures with varying density and distributions, in addition to their impact on the hydraulic fracturing process, creates significant complexities in reservoir characterization and production forecasting in these tight reservoirs. To account for these complexities and the associated large in situ stress alterations as a result of drilling, hydraulic fracturing, and production processes, a consistent model incorporating these alterations and complexities is needed for reliable production forecasting and field development strategy. The traditional approaches used in evaluating fracturing techniques have been typically based on a fracture network that is preestablished at a fixed location with constant reservoir properties. The validity of stimulated reservoir volume (SRV) and production performance can be significantly undermined without a representative model for naturally fractured shale formations.

The concept of SRV was first introduced by Fisher et al. (2004) to relate production performance using microseismic data collected during Barnett shale hydraulic fracturing operations. The estimation of SRV from microseismic mapping can be correlated to well performance, drainage volume, and

a. Now with PTT Exploration and Production, Bangkok, Thailand.

Hydraulic Fracture Modeling. https://doi.org/10.1016/B978-0-12-812998-2.00010-2

ultimate recovery. However, Cipolla and Wallace (2014) highlighted the potential of misapplication of this concept and suggested that the SRV is not the real stimulated volume that contributes to the production enhancement of the hydraulic fracturing operations. The main reason for this mismatch is that microseismic mapping area is a small portion of the hydraulic fracture propagation zone. Hence, SRV obtained from microseismic measurements and validated should be considered as microseismic volume (MV) rather than the SRV (Cipolla and Wallace, 2014). The MV can be used as a guide to hydraulic fracturing model and provide preliminary estimation of the fracture distribution and conductivity.

The hydraulic fracture propagation path is highly affected by the interactions between the natural fractures and the approaching propagating fracture, fracturing fluid and proppant selection, and their interactions with the formation and the native formation fluids. Local anisotropic rock properties and reservoir mineralogy and natural fractures are the key parameters determining fluid transport and proppant placement, associated in situ stress alterations during fracturing process, and production in unconventional tight oil and shale gas reservoirs. Most of the hydraulic fracturing models do not incorporate any of these key parameters into account. Excluding these important factors in this naturally fractured tight organic-rich formations results in planar symmetric bi-wing fractures similar to those in high permeability conventional reservoirs. The predicted propagation path and fracture network created in these reservoirs then become unreliable as they will not reflect any of the complexities of the tight reservoirs, and reservoir engineers may transfer this information into their simulations using the effective medium concept resulting in misleading production forecasting, recovery factors, and development plans.

In this chapter, an integrated workflow is recommended to simulate the production after hydraulic fracturing treatments in an organic-rich reservoir. The emphasis is on the integration of multiple data and a more accurate modeling of the coupled physics, fluid transport, and geomechanics in different scales. The fracture propagation and interaction during hydraulic fracturing operations are modeled using the real field data to more accurately represent the fracture network after the treatment. This process requires the solution of coupled transport and geomechanics equations, including conservation of mass, momentum, and energy. The fracture network created by this modeling procedure is then validated with microseismic data used as the input for reservoir simulator to forecast the production. A history matching procedure using production data is then used to validate the fracturing model. A customized model accounting for several factors in the fracturing of tight oil reservoirs is reported. Specifically, the simulation results obtained using the model for a case study conducted are presented based on the field data obtained from a well pad in the oil window of the Eagle Ford reservoir formation. After the field case is created for fracturing, reservoir simulation has been conducted to perform a history match using the first 4 years' production

data. Owing to the significant drop in the production rates during the first 2 years, a refracturing operation has been simulated to determine how much more oil and gas can be produced from this well pad if the wells are refractured.

An accurate understanding of the complex fracture network structure is critical for providing the prefracture reservoir characteristics to present the discrete fracture network (DFN) model for a well pad in the Eagle Ford oil window for hydraulic fracturing simulation. The production forecast for oil and gas and the role of fracture geometry are discussed for both fracturing and refracturing using the combined DFN model, and the obtained combined fracture network is validated first using the field and laboratory data and then using it as an input for production performance. The refractured production simulation is also performed after 2 years of production for recovery improvement.

10.2 BACKGROUND

One of the earliest horizontal multistage fracturing operations was conducted as part of the US Department of Energy research study in the Marcellus shale using eight stages with cemented sliding sleeve to determine the recovery efficiency of the natural fracture systems and the impact of the hydraulic fracture on the production (Yost et al., 1988). Since the pilot study, there has been an evolution of fracturing methodologies to improve the efficiency of the multistage fracturing process. The density and distribution of natural fractures before the implementation of the hydraulic fracturing operation is critical because natural fractures will act as weakness planes influencing the hydraulic fracturing growth path. In production forecasting, the conventional dual-porosity continuum approach may not be the best methodology capturing the complex nature of natural fracture network because unconventional reservoirs are highly heterogeneous with complex fracture fabric consisting of several fracture families with different spatial distribution and conductivity. Moreover, highly idealized dual-porosity model does not explicitly allow modeling the geometry of the discrete fractures, dissolved pore space, and bedding controlling flow pathway geometries. DFN model comprises the fracture network complexity providing a detailed representation of the fracture network. DFN model can be developed using a combination of deterministic, directly imaged seismic, imaging logs; full wave dipole sonic logs; local and regional geological data; and seismic surveys.

In naturally fractured medium, when the hydraulic fracture is propagating, the angle at which the hydraulic fracture approaches the natural fracture is one of the key parameters determining the hydraulic fracturing path. Gu and Weng (2010) reported an analytical method to determine whether the hydraulic fracture will cross over or be arrested with the presence of an existing natural fracture at their intersection incorporating the principal stress ratio, approaching

angle, coefficient of friction, and cohesion. According to this model, when a hydraulic fracture is approaching to an existing natural fracture, it will propagate across the existing natural fracture (i.e., a new fracture is created on the opposite side of the interface) provided that the maximum principal stress is not less than the rock tensile strength. In other words, the stress acting on the fracture surface is able to transmit its tip stress across the interface to create the fracture on the other side of the natural fracture. Depending on the variations of the approaching angle and local principal stress magnitude changes taking place due to the fracturing, the strength variation due to the heterogeneity, and the saturation variations along the fracture (cohesion, friction angle), the hydraulic fracture will propagate in one of the four scenarios depending on the stress state and formation properties at the intersection as shown in Fig. 10.1.

- Fracture will be crossing the natural fracture.
- Fracture will be arrested at the natural fracture contact plane.
- Fracture will be dilating the natural fracture.
- Fracture can propagate and rotate to a different direction (branching). It is for this reason that naturally fractured reservoirs are difficult to investigate.

Eagle Ford shale was formed in the Upper Cretaceous series with gas, condensate, and oil windows overlain by Austin Chalk and underlain by Buda Limestone covering a region of 400-mile-long and 50-mile-wide strip in SW−NE trend in Texas. The thickness of the formation varies between 50 ft. in the NE and 330 ft. in the SW (Martin et al., 2016). Kerogen maturation−induced natural fractures and thinly laminated layering introduce a high degree of geomechanical and wave propagation anisotropy bringing further complications to hydraulic fracturing for enhancement of nano-Darcy permeability in

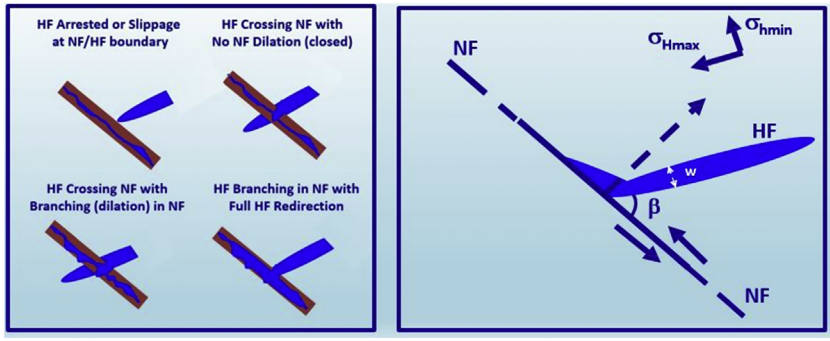

FIGURE 10.1 The interaction of hydraulic fracture with natural fractures determines the direction of the hydraulic fracture propagation. *Modified after Weng, X., Kresse, O., Cohen, E., Wu, R., Wu, H., 2011. Modeling of hydraulic-fracture-network propagation in a naturally fractured formation. SPE-140253. SPE Production & Operations 26 (4), 368−380.*

Eagle Ford formation. Horizontal microfractures are initiated in the abnormally stressed lower Eagle Ford, propagating parallel to the interfaces of the bedding planes during the hydrocarbon migration as discussed in detail by Padin et al. (2014).

Brazilian tensile failure measurements performed on preserved core samples from several naturally fractured shale reservoirs at the Unconventional Natural Gas and Oil Institute (UNGI) research group are used to investigate the effects of natural fractures on the direction and growth of hydraulic fracture. The samples with natural sealed fractures present approximately half of the tensile strength of the intact core samples (Mokhtari and Tutuncu, 2016; Mokhtari et al., 2014). On contrary to the fracture mechanics models using the elastic medium approach, the observed fractures grow away from the central plane instead of along the loading direction, or a mixture of tensile and shear fractures reorientated when natural fractures were intersected by the propagating fracture as a result of the natural fractures in the core samples tested. A few photos of the tensile fractures introduced indicate good agreement paths to the Gu and Weng (2010) model, presenting the angle dependence to the natural fracture in the tensile fracture tests as shown in Fig. 10.2. Although the existing natural fracture orientation has a strong influence in this reorientation, the size of the natural fractures appeared to have a negligible effect.

First the natural fracture DFN was established, then it was used for obtaining the hydraulic fracture path more accurately. The combined natural fracture—hydraulic fracture DFN was used for performance forecasting. As the wells in the well pad were fractured using zipper fracture geometry, the hydraulic fracturing geometry using the zipper fracturing pattern was used for the production forecasting.

Zipper fracturing pattern is the most preferred hydraulic fracturing geometry implemented in shale gas and tight oil formations. It is a fracturing pattern to stimulate two parallel horizontal wells simultaneously from toe to heel of the laterals (Waters et al., 2009). In this technique, created fractures in each cluster propagate toward each other to induce stresses near the tips and force fracture propagation to a direction perpendicular to the main fracture (Rafiee et al., 2012).

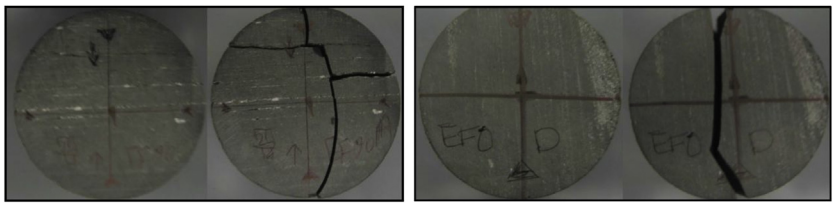

FIGURE 10.2 Tensile failure of an Eagle Ford shale sample with horizontal (left) and vertical (right) laminations (Mokhtari and Tutuncu, 2016).

In the following sections, first the investigated methodology will be briefly discussed, and then the performance predictions from the model will be presented for original zipper fracturing geometry. After 2 years of production, simulation output was history matched with the field data. The wells are then refractured and brought back to production for two more years.

10.3 COUPLED GEOMECHANICAL AND FLUID FLOW MODEL

The application of multistage hydraulic fracturing in horizontal wells has empowered production enhancements that enabled economically viable production from shale reservoirs initiating a new era in the oil industry. Yet, the methodology for optimum recovery efficiency through these operations is still under investigation. Coupling geomechanics in engineered stimulation design has been quickly recognized after quite a number of failed trials in several US shale basins, going back to Barnett shale fracturing operations in the late 1980s and early 1990s. The complex primary fracture network that preexists in shale reservoirs as a result of source rock maturation process over the geologic times is typically further complicated with the introduction of the secondary induced fractures during the hydraulic fracturing operations impacting the initiation and propagation. Simultaneously, fluid flow in the integrated fracture network will also be equally complicated as it is directly coupled with geomechanical behavior of the fractured reservoir, associated deformation, and failure in response to the fracturing operation. Therefore, a realistic prediction of production performance should take into consideration the combined primary natural fracture network and secondary introduced hydraulic fracture network.

A fractured formation is a discontinuous media with large blocks that may act as a continuum within the formation and may be disconnected from the adjoining blocks. The numerical modeling study must represent the two types of mechanical behavior: first the behavior of the formation matrix of the blocks and second the behavior of the fractures. The continuum models typically are not suitable for addressing the explicit mechanical behavior of these discontinuous fractures as they need to distinguish the behavior of interfaces between the discrete blocks making up the formation. Hence, DFN modeling is often regarded as the most representative way of incorporating the fractured formation behavior into reservoir flow simulators to properly characterize the fluid flow in tight naturally fractured formations.

In this study, first a DFN model has been created to represent the naturally fractured Eagle Ford shale formation in the well pad area investigated. Then, the DFN was used as an input for a coupled geomechanics and fluid flow model, a UNGI in-house developed model with commercial component for the optimization of production through the evaluation of several hydraulic fracture patterns with a focus on the stress and strain variations within the reservoir affecting porosity and permeability that ultimately influence the fluid flow

and production. Several fracture patterns, including alternate, zipper, Texas two-step, and modified zipper fracturing, have been used in creating a combined DFN incorporating the complex natural and hydraulic fracturing interactions for production optimization. The results are discussed in detail in Suppachoknirun and Tutuncu (2016) and Suppachoknirun et al. (2016).

Different workflows have been proposed to model the hydraulic fracturing and refracturing treatments (Cipolla et al., 2011; Malpani et al., 2015; Pankaj et al., 2016). Cipolla et al. (2011) presented a seismic-to-simulation workflow for unconventional reservoir modeling. Malpani et al. (2015) presented a six-step workflow for refracturing simulation. Pankaj et al. (2016) extended the workflow proposed by Cipolla et al. (2011) to obtain a workflow for refracturing simulation accounting for the effect of production and pressure depletion on stress and rock mechanical properties. Morales et al. recommended an extension of the workflow proposed by Marongiu-Porcu et al. (2016) for studying the refracturing in the Eagle Ford shale oil. One similarity in the recent proposed workflow is the integration of additional data to better characterize the fracture network and accurately represent the formation. Therefore, the workflow can be varied depending on the formation, available measurements, and simulation tools, as well as computing power. A workflow incorporating multiple sources of the data often results in better modeling outcome. Because most workflows are trial and error procedures, they are typically misinterpreted as the key for success of the refracturing project. In fact, the accurate characterization of the reservoir and good physics-based models representing the physical phenomena under the reservoir conditions are the most important factors. Hence, it is emphasized in this chapter that comprehensive formation characterization and representative fracture model resulted from coupled modeling are essential for the success of the workflow.

This chapter concentrates on the real case fracture geometry, zipper fracturing pattern, implemented in the three wells in the Eagle Ford well pad. The simulation model development is built using the workflow illustrated in Fig. 10.3. Three groups of input data are used to create a complex fracture network model, which is subsequently validated against the microseismic fracture mapping. The unstructured production grid generated based on the successfully validated complex fracture network geometry is input into a reservoir simulator to perform the production forecast. The forecast results are validated with production data using a history matching procedure. Based on this workflow, the validation of both the complex fracture and the fluid flow simulation model is conducted through the repeated adjustments of the reservoir parameters to obtain the final version that best represents the field characteristics. Fracture and fluid flow models are created, calibrated, and validated through the complete workflow before the complex fracture model for the new hydraulic fracture pattern is developed. The refracturing simulation is conducted after a 2-year period of production. The reservoir model after the production period is then used as the input for refracturing simulation

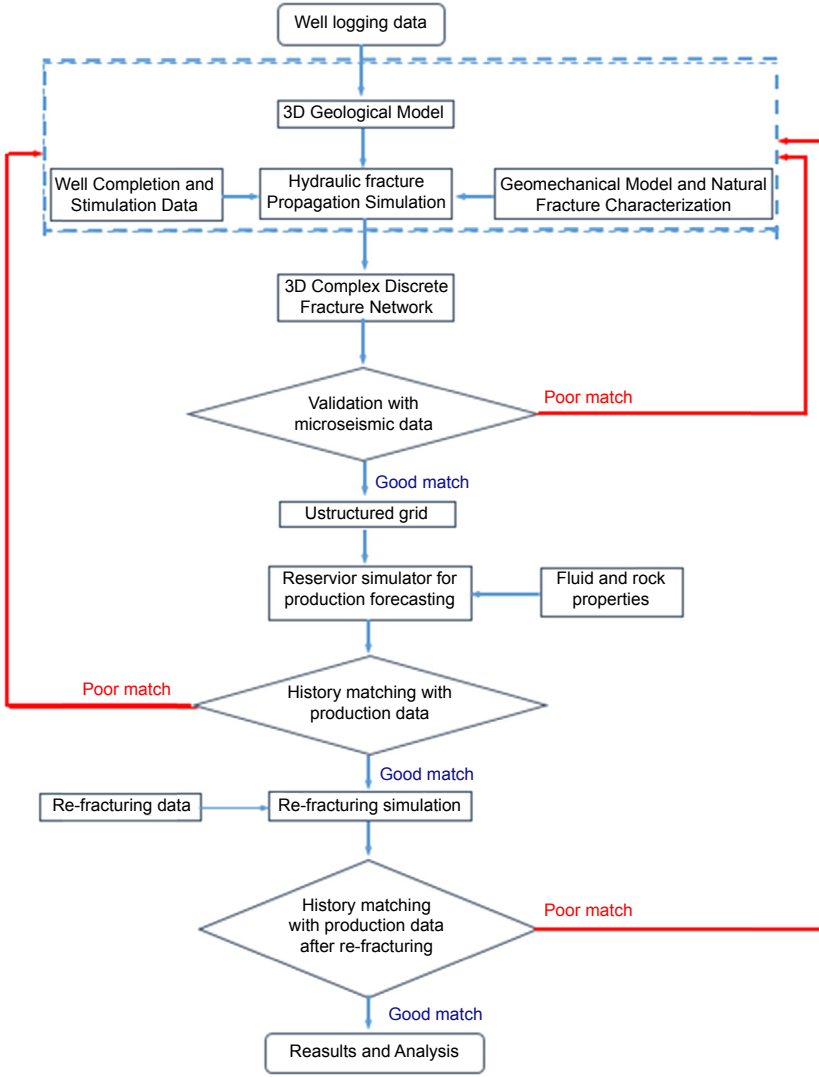

FIGURE 10.3 Workflow of integrated coupled fracture (discrete fracture network [DFN]) and reservoir simulation for refracturing.

along with the refracturing data. A new fracture network is then generated and validated with microseismic data when such data are available followed by a new production forecast after refracturing is performed, and a new history matching procedure is used to validate the refracturing simulation.

Accurate representation of the complex fracture network resulting from hydraulic fracturing operations in the naturally fractured formation was

accomplished by developing a DFN taking into account the hydraulic fracture propagation mechanics, the fluid and proppant transport inside the fracture, stress shadow effect, and the natural and hydraulic fracture interactions. These have been considered based on the reservoir properties, formation parameters, and characterization of the preexisting fractures specific to the Eagle Ford well pad investigated as the case study.

A numerical model has been developed based on conservation of mass, conservation of momentum, and volumetric balance incorporating the model introduced. Conservation of mass has been applied by considering the mass balance of the fluid flow in the fractures and the fluid leaking out of the fractures into the formation. In conservation of momentum, flow rate and pressure gradient relationship is based on the fluid flow in laminar regime. The volumetric balance was satisfied by equating the total fluid volume being pumped into the system to the fluid volume within the system. Layered medium without the variation of Young's modulus in each layer has been assumed. The stress intensity factors at the tips were calculated as a function of the pressure inside the fracture, the fracture geometry, and the layer stresses.

10.4 CASE STUDY: THE EAGLE FORD SHALE WELL PAD MODELING

The Eagle Ford case study elaborating the modeling process has been conducted based on the data from a well pad with multiple horizontal wells located in the Eagle Ford oil window in McMullen County, Texas. The data have been provided as part of the UNGI Coupled and Integrated Multiscale Measurements and Modeling (CIMMM) Consortium use by the consortium sponsors. The data consist of well logs, hydraulic fracture reports, microseismic data, and production data. The well pad was completed in a zipper well fashion consisting of four wells, wells B1, B2, B3, and B4, that lie within the lower Eagle Ford shale at a true vertical depth (TVD) of approximately 10,800 ft (Fig. 10.4). Well B4 was used as the microseismic monitoring well for wells B1 (14 stages), B2 (13 stages), and B3 (14 stages) during plug and perforation limited entry hybrid fracture treatment (Fig. 10.4). Two separate modeling studies have been conducted at this time to determine the role of induced fractures and the impact of the predefined use of the hydraulic fracture geometry on the production performance. In the first study, input data, including mechanical earth model, natural fracture characterization, and well completion and stimulation strategy, have been used in creating a complex DFN model. The DFN model is subsequently validated against the field microseismic fracture mapping. The unstructured production grid blocks specifically introduced to the particular DFN geometry have been used to perform the production forecast. The model has been finalized and confirmed on achieving the matched production forecasting results with the production history data.

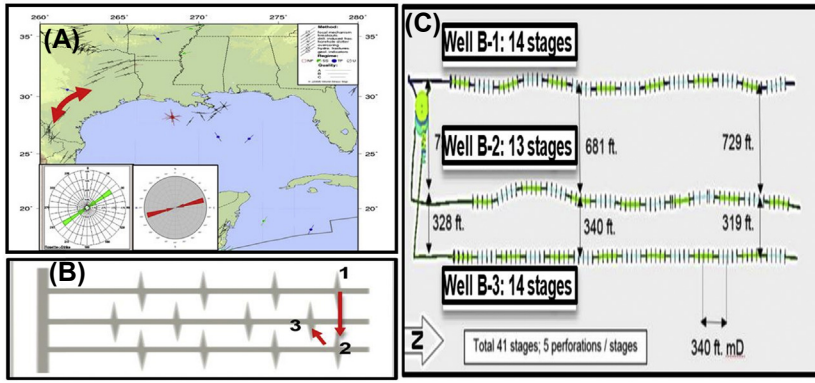

FIGURE 10.4 (A) The σ_{hmax} orientation obtained from well logs collected in the pad and using the World Stress Map. (B) The modified zipper pattern fracturing was implemented in the hydraulic fracturing of the three wells studied. (C) The distance between the wells and the stages in the three wells.

The complex DFN model and the integrated DFN and fluid flow model, along with the input data set, have been validated against microseismic fracture mapping and commingled production data obtained from the studied well pad. The delay borate cross-link (DBC) fluid system, using hydroxypropyl guar (HPG) gelling agent, was used as the fracturing fluid. With the high-viscosity fluid with temperatures up to 300°F and the cross-linked gel filter cake cleaning with the water production, DBC provided good fracture conductivity. Premium white sand proppant with 40/70, 30/50, and 20/40 sizes were used. After pumping the pad, slurry was pumped into the well in multiple stages with gradually increasing proppant concentration by 0.06 gr/cm^3 (0.5 ppg) increments to the maximum of 0.42 gr/cm^3 (3.5 ppg).

10.4.1 Complex Discrete Fracture Network Model With Predetermined Fracture Geometry

A logarithmically spaced, locally refined, dual permeability (LS-LR-DK) coupled reservoir model was created to simulate hydraulic fracturing in Eagle Ford wells in the well pad area studied using GEM compositional fluid interface of CMG reservoir simulator. The logarithmic spacing allowed fine gridding in near vicinity of the hydraulic fractures. The LS-LR-DK "tartan" gridding in CMG simulator was used as shown in Fig. 10.5 with predetermined linear geometries. Flow from fracture to fracture, matrix to matrix, and matrix to fracture was modeled by a mass transport model assigning a matrix and fracture porosity in each grid block. An assumption was made for hydraulic fracture to be not arrested by natural fractures when intersected. However, the complex interactions at the intersection were taken into account. The model

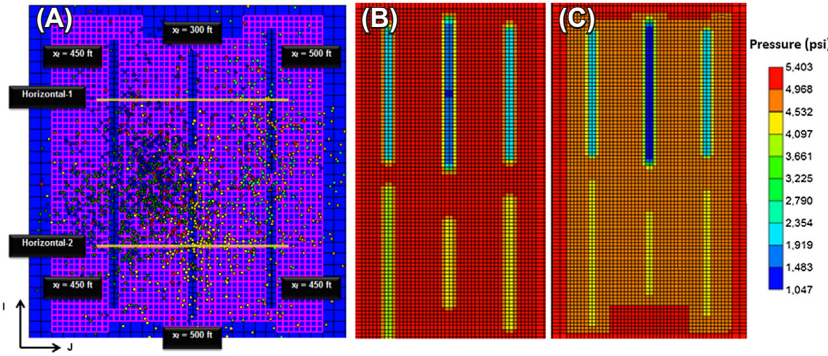

FIGURE 10.5 (A) CMG grid system where the Eagle Ford well pad was calibrated with the microseismic data for stimulated reservoir volume (SRV) (Curnow and Tutuncu, 2016). (B) The pressure distribution calculated from the reservoir simulator built is shown for 10 years and (C) 20 years. Associated validation of the oil production rates and cumulative oil production is shown in Figs. 10.6–10.8.

for the investigation area in Eagle Ford was customized because natural fractures parallel to bedding are often calcite-filled and impermeable to flow until they are reactivated through the hydraulic fracturing process (Mokhtari et al., 2014; Padin et al., 2014; Mokhtari and Tutuncu, 2016). Taking advantage of these features for simulation times, unrefined grid blocks were used outside the SRV to represent the natural fractures that were not activated and remained closed.

Minimum horizontal stress was calculated iteratively with the change of fluid pressure using a vertically transverse anisotropy with data obtained through coupled experimental measurements and well logging and other field data from the wells in the Eagle Ford well pad.

$$\sigma_h = \frac{E_h \nu_v}{E_v(1-\nu_h)}\left[\sigma_v - \alpha(1-\xi)p_p\right] + \alpha p_p + \frac{E_h}{1-v_h^2}\varepsilon_{H\max} + \frac{E_h \nu_h}{1-\nu_h^2}\varepsilon_{h\min} \tag{10.1}$$

where h and v denote the horizontal and vertical directions of Young's modulus (E) and Poisson's ratio (ν), respectively, p_p is defined as the pore pressure gradient (psi/ft), and ξ is the poroelastic constant (Waters et al., 2011). The data were obtained from the experimental tests conducted for horizontal and vertical samples at UNGI.

The geomechanics and fluid flow calculations are coupled through the pressure and porosity functions using the two-way iterative coupling method in a simulator. The fluid flow calculation updated the input pressures to start with over a time interval, and the calculated pressures are used in the geomechanics model updating the formation–deformation in response to the new pressures, and the new deformation was used back in the fluid flow

calculations for the next time interval. The porosity is calculated in the fluid flow model as a function of the new pressure with pore volume, or mass, conserved between time steps. Thus, the geomechanical deformation response was captured in the fluid flow calculations through changing parameters within the porosity function. The deformation response was accounted for in each block because each grid block has its own set of porosity function parameters, which depends on pressure, temperature, and total mean stress. The Barton−Bandis model was used to specify the relationship between fracture opening and the permeability of the fracture system. When the pressure increases in the formation, the normal stresses on the fracture increase exceeding the failure strength of the formation causing the fracture to propagate. As the fracture propagates, the fluid is allowed to flow through the fracture system, in addition to the underlying matrix system coupling geomechanics calculations h to the matrix blocks.

Zipper fracture pattern is typically used to create far-field complexity in the region near the tips of the fractures as they propagate toward each other from opposing lateral wells. We have used the coupled simulator calibrating the results using microseismic data collected in the well pad during the hydraulic fracturing (Fig. 10.5) and validated the production forecast with history matched oil and gas production from the Eagle Ford well pad data. The oil production model against field data is shown in Fig. 10.6. The predicted gas production also presents a good agreement to the field data. The 20-year oil, gas, and water production forecast using zipper fracture pattern is presented in Fig. 10.7.

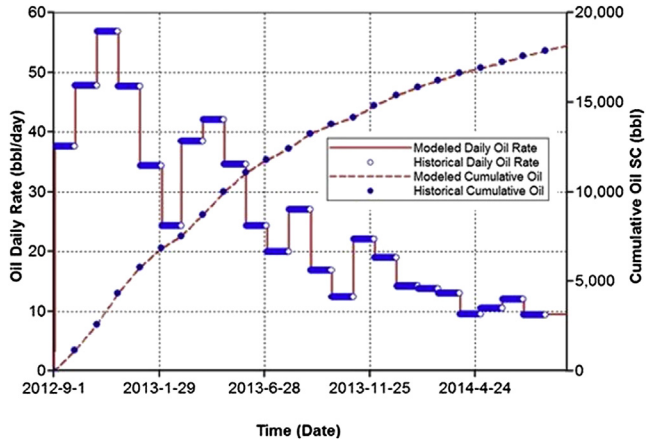

FIGURE 10.6 Two-year history match conducted between the daily and cumulative oil rates for the modeled production forecast and field production in one of the investigated wells in Eagle Ford well pad (Curnow and Tutuncu, 2016).

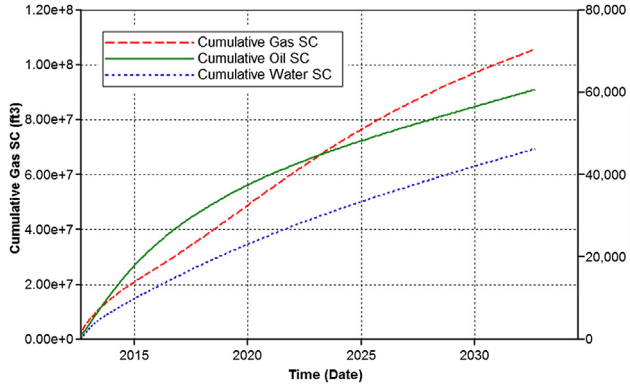

FIGURE 10.7 Cumulative gas, oil, and water production rates for 20 years using the zipper fracturing pattern (Curnow and Tutuncu, 2016).

Hydraulic fracturing introduces alteration in stress anisotropy owing to the stress shadow effect that is ascribed to the introduction and propping of the fracture in the formation. The additional minimum stress that is introduced reduces the stress anisotropy in the formation. However, this stress alteration can also result in the reorientation of the fracture resulting in a more complex geometry as discussed in detail by Curnow and Tutuncu (2016), Suppachoknirun et al. (2016), and Suppachoknirun and Tutuncu (2016). Although coupling of the geomechanics and fluid flow is accomplished using this approach, the assignment of predetermined planar fracture path in the flow simulation implies that fracture propagation path and associated friction effects have not been taken into account introducing deficient representation of nonplanar fractures with planar fractures.

The early production of three patterns is very similar as shown in Fig. 10.8. The production prediction has the same initial peaks in both oil and gas production for the first few months after completion. However, the exponential decline for the zipper pattern significantly affects the long-term production. The complex fracture network is far from the wells resulting in the early decline. The Texas two-step and modified zipper fracture patterns incorporate more fractures nearby the wells contributing more toward the early oil and gas production with higher gas production.

10.4.2 Complex Discrete Fracture Network Model With Coupled Fracture Growth Simulations

The DFN developed for natural fractures in the well pad area has been introduced into a coupled fracturing model to simulate initiation and propagation of the hydraulic fractures with representative natural fracture distribution to capture the nonplanar form and to capture the complexities and

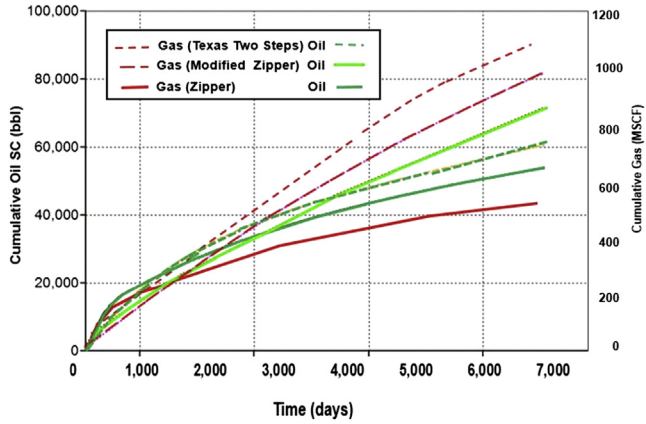

FIGURE 10.8 Cumulative gas and oil production rates for 20 years using the zipper, Texas Two-step, and modified zipper fracturing patterns (Curnow and Tutuncu, 2016).

nonplanar nature of the final fracture network. An integrated DFN model was then created incorporating all natural and hydraulically induced fractures in the well pad at the end of the fracturing simulation as shown in Fig. 10.9. The light blue fractures in the DFN are fractures that were not reactivated during hydraulic fracture propagation.

The grid blocks obtained from the integrated DFN model were introduced to the zipper fracture geometry to conduct the production forecast. The geomechanics-coupled fracture and fluid flow model were then verified through history match achieving good agreement between production forecasting results and the field data. Detailed information on the model development and validation process has been described in Suppachoknirun and Tutuncu (2016).

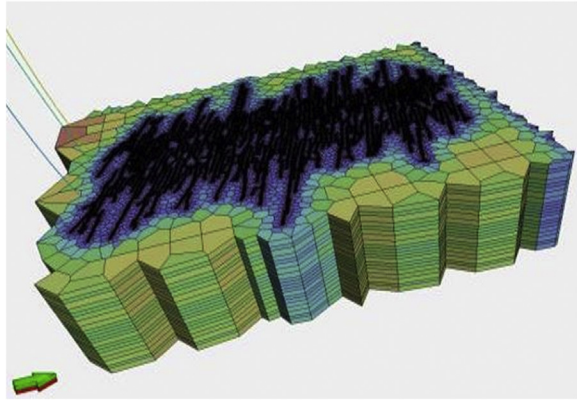

FIGURE 10.9 The production unstructured grid system created using the discrete fracture network developed to use in the coupled reservoir simulator for production performance.

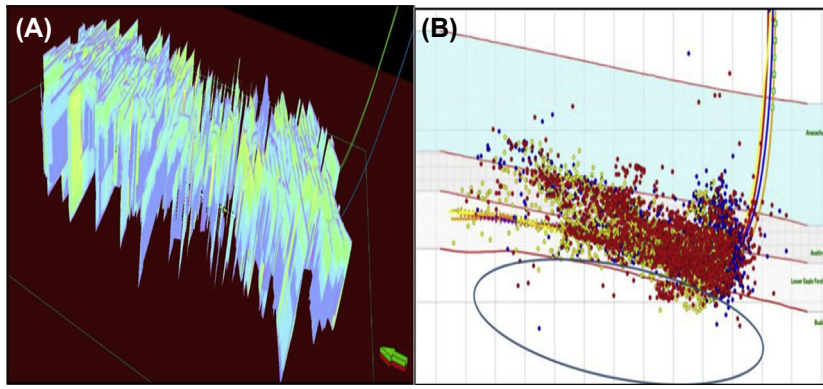

FIGURE 10.10 The integrated discrete fracture network (DFN) developed in this study including the natural fractures and hydraulic fractures in the three wells. (A) The microseismic data from the wells have been used to calibrate the DFN and the fracture containment (B) (Suppachoknirun and Tutuncu, 2016).

The vertical extent of the hydraulic fractures has been contained within the Eagle Ford and Austin Chalk with the average height of 275 ft as observed and calibrated using the microseismic mapping in the well pad (Fig. 10.10).

The simulation grid of the integrated fracture and fluid flow models shown in Fig. 10.9 consisted of 4,439,320 grid cells. Variable grid blocks with varying shapes and sizes were used near perforations and open fracture areas, whereas larger cells were used away from the wells. Inside the fractures, shape and properties of the fracture grid cells were specified by considering regional treatment results, including the variation in fracture dimensions, the length of proppant-filled areas, and the types of proppants used in the fractures. All the variables used for the parametric analysis have been shown to influence the fracture conductivities.

Production optimization has been conducted using production from one well compared with that of the commingled production at the same timeframe. The fluid pressure for all three wells at the start of the production and after 1 year and 2 years of production in the well pad is shown in Fig. 10.11. The corresponding results of the commingled and individual well production in the same timeframe are presented in Figs. 10.12–10.14. Because the wells were reported to unequally contribute to the commingled amount of the production at the pad at a given time, the proportionality specific to a particular time step was used to obtain the production forecast.

10.4.3 Refracturing

One of the adverse aspects of unconventional shale gas and tight oil horizontal well fracturing is their rapid production decline with low recovery rates. The low permeability of the reservoir plays a significant role in this decline as the

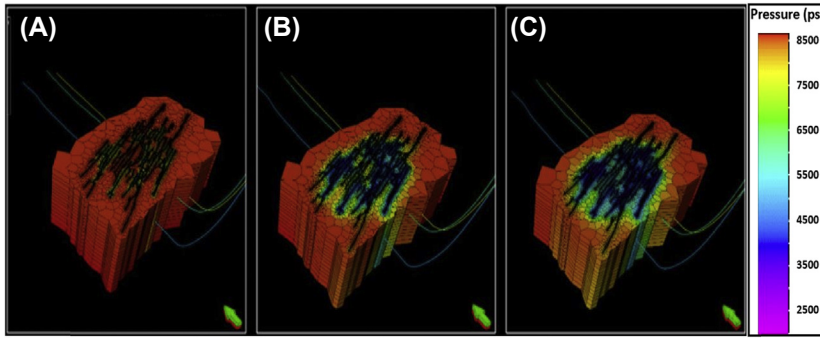

FIGURE 10.11 The variation in the reservoir pressure at three different timeframe in the well pad studied: (A) at the start of the production (0 day), (B) 1 year (360 days), (C) 2 years (720 days). Corresponding oil, gas, and water production is presented in Figs. 10.11–10.13 (Suppachoknirun et al., 2016).

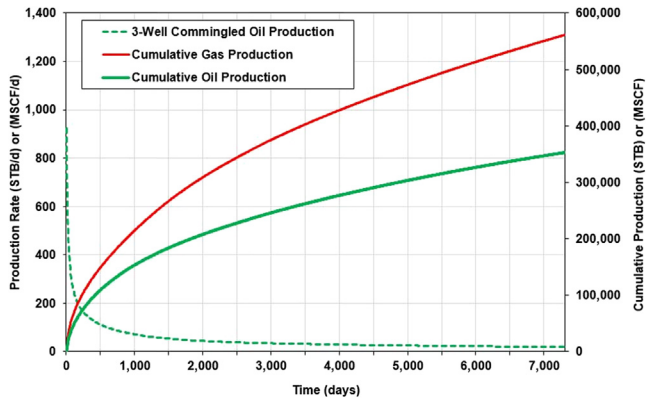

FIGURE 10.12 Cumulative commingled oil production and production rates from the three wells in the Eagle Ford well pad for 20 years using the zipper fracturing pattern implemented in the operation.

drainage area does not extend far enough into the reservoir. Therefore, the shape and size of the hydraulic fractures and the natural fractures and their interactions with the hydraulic fractures impact the production decline. A typical strategy to eliminate the decline in the field is to drill and complete large number of wells. Given the size of the resource in unconventional formations and the cost of drilling and completing new wells versus refracturing the existing wells, the refracturing candidate needs to be carefully selected to assure that the refracturing will pay off all the additional expenses, along with the large amount of oil left behind from the original fracturing in the wells to be produced, for the refracturing treatment to be a success instead of drilling a new well in the same area.

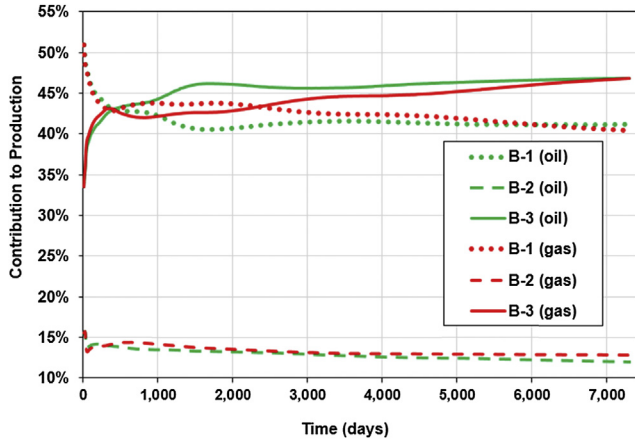

FIGURE 10.13 Calculated contributions from each well to oil and gas production from the Eagle Ford well pad for 20 years using the coupled model introduced in this study. The associated pressure variations for the first 2 years are shown in Fig. 10.11.

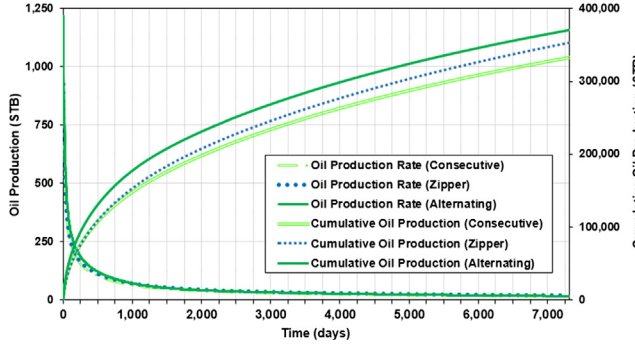

FIGURE 10.14 Cumulative oil production and production rates from three wells fractured using consecutive, zipper, and alternating patterns in the Eagle Ford well pad.

Refracturing is not a new implementation concept in the oil industry. Similar to the conventional hydraulic fracturing used for damage removal in later part of the well life after 10–20 years to enhance the production, refracturing is being implemented in much earlier life of the wells in unconventional reservoirs due to the rapid production drop in tight formations. Lindsay et al. (2016) conducted a statistical study on more than 100 refractured horizontal wells in the United States and evaluated the success of refracturing in six formations including Bakken, Barnett, Eagle Ford (in oil window), Fayetteville, Haynesville, and Woodford. They showed that the Haynesville and Eagle Ford have the highest rate of return after refracturing followed by Bakken, Woodford, and Fayetteville, whereas Barnett shows the

lowest rate of return after refracturing. Identifying a candidate well for refracturing is one of the most challenging tasks for a successful operation. Lindsay et al. (2016) suggested that a well's rapid production decline does not indicate for its candidacy for refracturing. The most important factors to consider for the selection of refracturing candidate are wellbore configuration, wellbore integrity, completion designs, formation damage, fractures, formation pressure, stress and temperature, hydrocarbon in place, geohazard risk, production decline, production data, and economic factors.

Vincent (2011, 2015) conducted a review of Bakken and Eagle Ford wells that were refractured to determine the optimum parameters for the candidate selection for refracturing. Most of the investigated refractured wells indicated positive incremental net present value (NPV) based on the EUR increase, which was 53% for the Eagle Ford and 69% for the Bakken plays. Among the existing refractured wells that were analyzed, there was no discernible correlation between the times a well is produced before the refracturing treatment as shown in Fig. 10.15 in Eagle Ford wells. A good decline curve analysis was obtained with the same b-factor postrefracturing, and secant decline rates were typically lower after refracturing.

Based on our past experience, part of the poor responses in refracturing was allocated to the poor-strength low-quality sand selection as the proppant in the fracturing treatments by the operator. Although the rapid reduction in production rates is only partially associated with the fracture conductivity reduction from the crushing of the proppants, as the continuation of the Eagle Ford study, we have used the DFN and production profiles to select 2 years as a good period for the well to be refractured and have followed the same

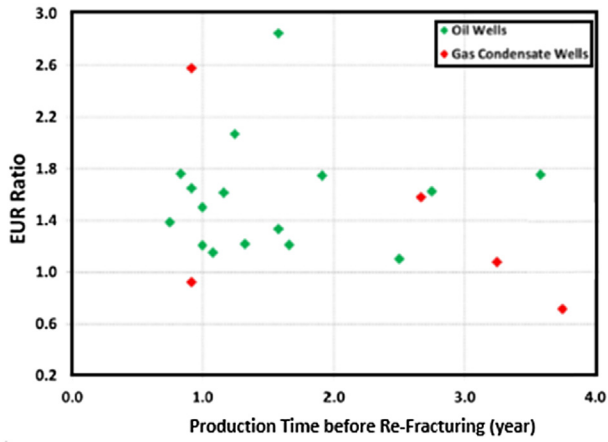

FIGURE 10.15 EUR Ratio as a function of time of production before refracturing treatment applied in Eagle Ford wells. *After Vincent, M., 2015. Restimulating horizontal oil Wells – success and failure. In: AAPG/STGS Geoscience Workshop Presentation.*

process we have followed in the original fracturing treatment for the refracturing treatment. The added SRV obtained after the refracturing treatment was provided as an input into the reservoir simulator to determine the incremental changes in the production between the original fractured wells and the refractured wells in the well pad. A third step was added by changing the proppant from sand to ceramic with similar size proppants and keeping the fracturing fluid the same as before as discussed earlier in this section. The pressure distribution after 720 days of production before refracturing treatment was input to represent the new combined fracture network for reservoir simulation for the refractured wells. The fracture distribution and pressure at the 720th day production is shown in Fig. 10.16. A comparison of the fracture conductivity after hydraulic fracturing and after refracturing is presented in Figs. 10.17–10.19. It is evident from the comparison of the fractures in both cases that refracturing creates longer hydraulic fractures with higher fracture conductivity even when the pumping and treatment schedules are kept the same. Refracturing with ceramic proppant results in higher fracture conductivity than that with sand proppant because the embedment of ceramic proppants is typically less than that of sand proppants. The corresponding comparison of the oil production rates and cumulative productions are presented in Figs. 10.20 and 10.21. It can be observed that refracturing results in significant increase in the production rate and cumulative recovery. The strong role of proppant on the recovery after refracturing is also evident in Figs. 10.20 and 10.21. When ceramic proppants are used, the cumulative production 2 years after refracturing with sand proppants is approximately 10% higher than that in the earlier period with sand proppant.

10.5 DISCUSSIONS AND CONCLUDING REMARKS

It is evident from the results presented in this study that the created fracture network geometry is significantly different than the ideal design with transverse planar fractures introduced in the network at a predetermined location. These differences affect the accuracy of the input used for the reservoir simulations to predict the production and impact the prediction reliability when such production forecasts are used in a parametric studies or the evaluation of well placement techniques.

In the case study discussed in this chapter, the primary orientation of the fracture network is greatly influenced by the orientation of principal horizontal stress and the primary set of natural fractures introduced in the DFN model. The secondary set of natural fractures that are with N 20° W orientation along with the stress shadow effect are among the key reasons for the secondary fractures in the DFN, particularly in the area between the wells where the effects of stress shadow from the neighboring stages and other perforations in the same stage are intense during the fracture propagation.

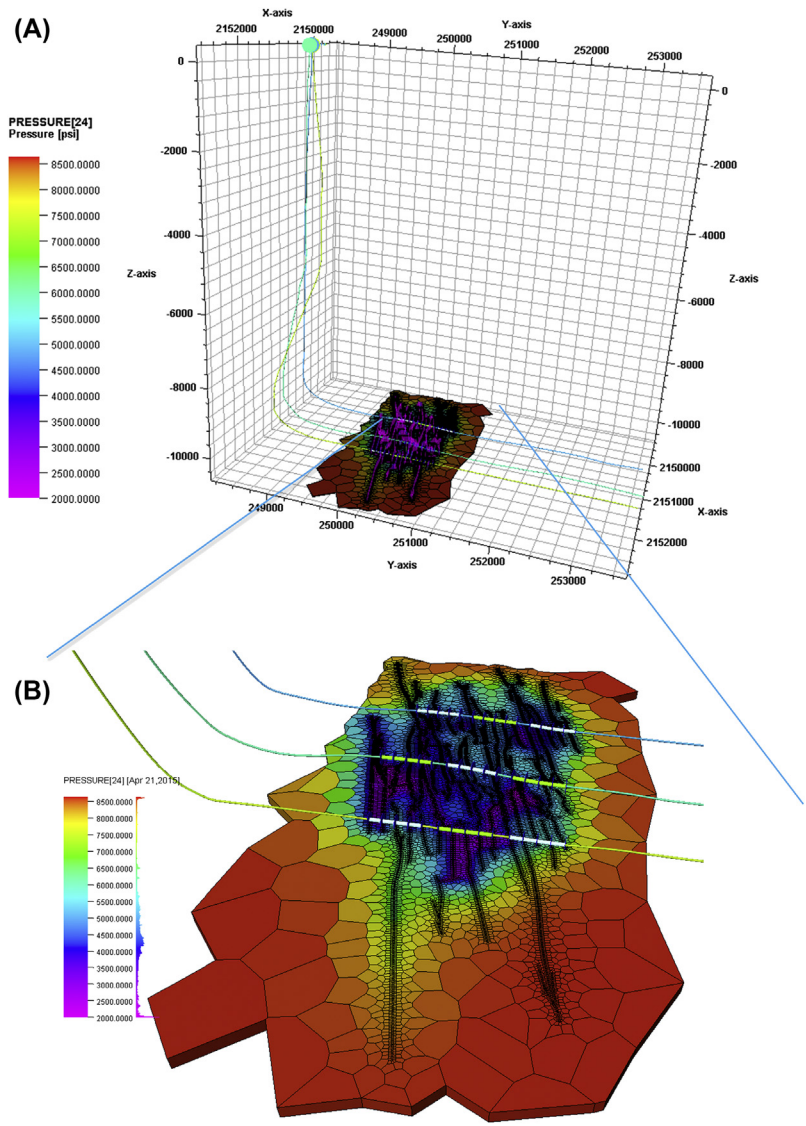

FIGURE 10.16 (A) Pressure distribution after 720 days of production before refracturing treatment in the Eagle Ford well pad. (B) A closer look at the production area in the well pad.

Based on the investigation, it is evident that the DFN geometry is substantially sensitive to the parameters concerning the natural fracture network that include orientation, diversity in the orientation, and its density. Other properties including the friction coefficient, cohesion, toughness, and their coupled combination also affect the characteristics of the final coupled DFN

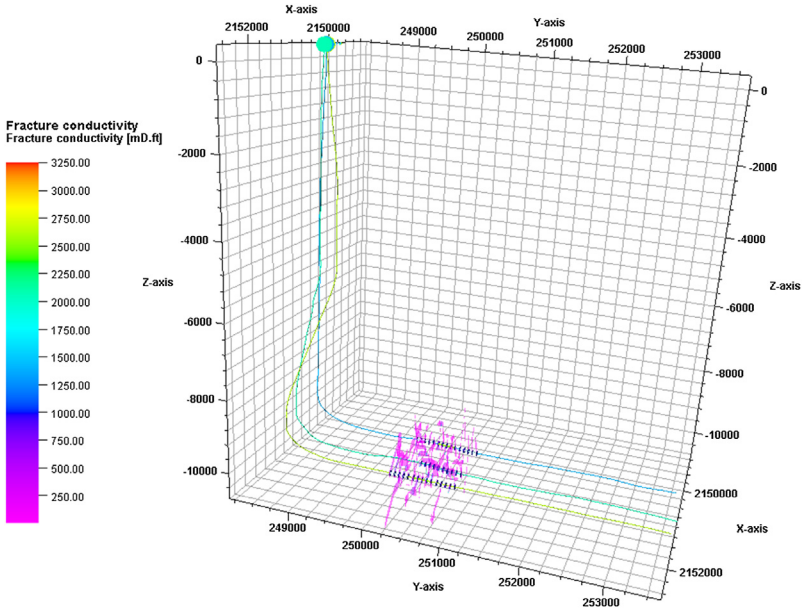

FIGURE 10.17 Fracture conductivity after the original hydraulic fracturing treatment.

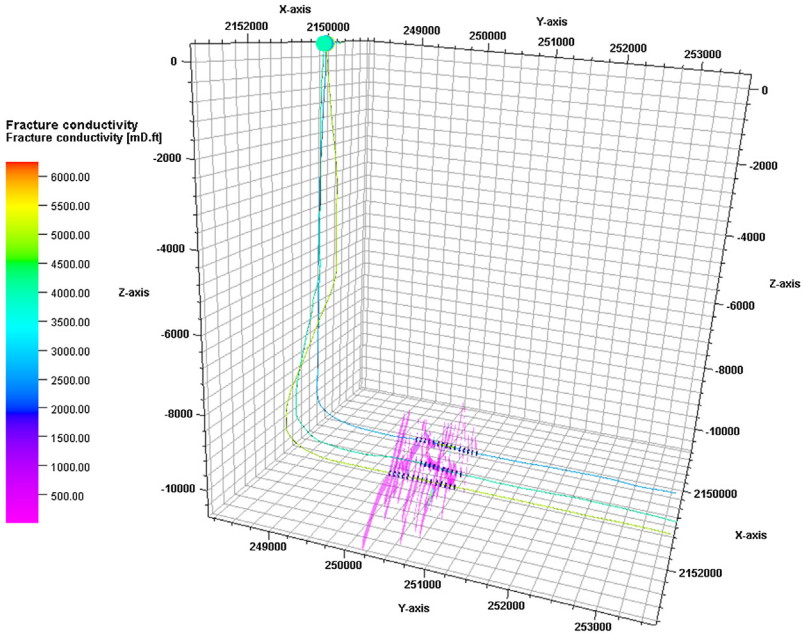

FIGURE 10.18 Fracture conductivity after the original refracturing treatment using sand proppant.

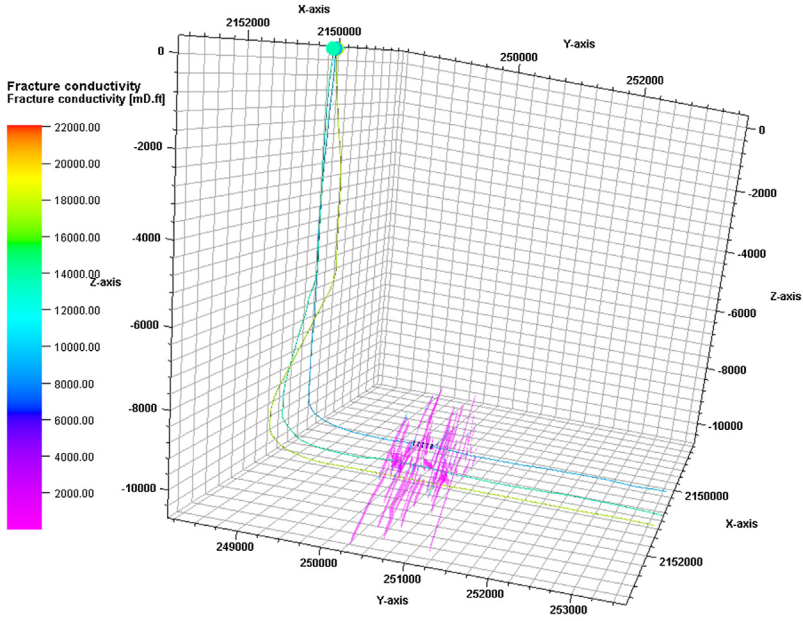

FIGURE 10.19 Fracture conductivity after the original refracturing treatment using ceramic proppant.

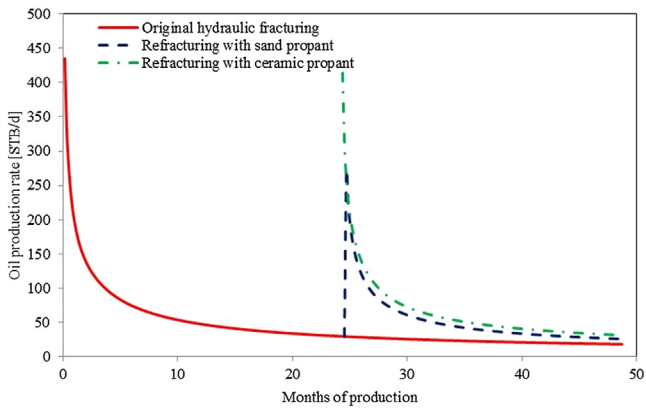

FIGURE 10.20 Comparison of the oil production rates from three wells originally fractured and 2 years after refracturing using zipper fracturing pattern in the Eagle Ford well pad.

geometry. When planning the hydraulic fracturing strategies and operational plans for a particular reservoir, especially in a newly developed field in tight formations, well stimulation strategy should be carefully studied. The design should be coupled with geomechanical characteristics of the formations

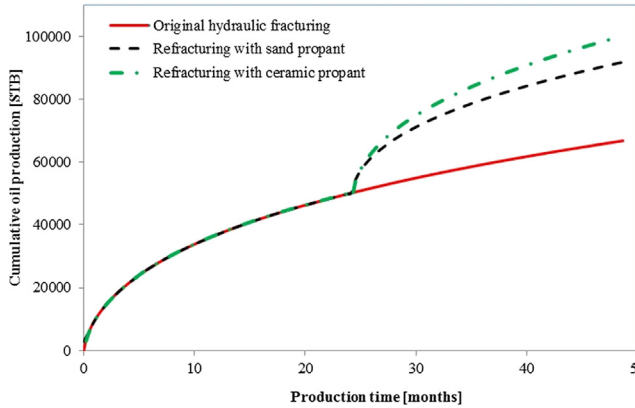

FIGURE 10.21 Comparison of the cumulative oil production from three wells originally fractured and 2 years after refracturing using zipper fracturing pattern in the Eagle Ford well pad.

through inclusion of the natural fractures in a realistic manner to better characterize the created hydraulic fractures and the integrated DFN.

It is critical to emphasize that the complex fracture network geometry presented in Fig. 10.8 has been acquired by using zipper fracturing process where the operation must follow the specific sequence of the patterns followed in the field case study investigated here. If the aforementioned simulations presented in both Model 1 and Model 2 had been performed in each well individually, the final DFN would not incorporate the stress shadow from the first stage introduced in the B1 well, resulting in a exclusion of the interactions of the existing fractures with hydraulic fracture and associated integration of the multiple wells and stages.

The natural fractures illustrated in Fig. 10.8 have been characterized in an attempt to represent the characteristics of the natural fractures in the formation that can significantly impact the propagation of hydraulically induced fractures and the complex fracture network geometry.

The interwell interference during hydraulic fracturing is an important issue affecting the success of a refracturing treatment. With the lack of computing power and a good physical model, the investigation of well-to-well interference may provide some knowledge for fracturing operations. However, in this modeling study, the well-to-well interference is incorporated in the model by solving the coupled equations for the entire reservoir. In other words, all factors are accounted in the model. Therefore, the discussion on the interwell interference is limited in the study. We emphasize on the importance of reservoir characterization including well logging and laboratory measurements and the coupled model that is the best representation of the real physical processes in the reservoir.

The results of our comparative study indicate that the modified zipper pattern generate a highly conductive secondary complex fracture network allowing the optimum recovery from the study well pad. In comparison to the zipper and Texas two-step patterns, the stress anisotropy is decreased when modified zipper pattern is used aiding in the fracture generation process. When coupled with the higher drilling density, the modified zipper provides a distinguished preferential fracture geometry for the development of the Eagle Ford shale. In the presence of similar density and distribution of the natural fractures, modified zipper will also potentially provide optimum production in basins analogous to the Eagle Ford similar to the oil window interval of Vaca Muerta formation. The Model 1 with which the predefined fractures are used in most of the reservoir simulators, introduces an underestimation of the oil production in the same well pad where the Model 2 introduced in this chapter provides more accurate performance prediction and can also be used for refracturing in pursuit of optimizing the refracturing design to reflect the desired DFN for optimum cumulative production.

The selection of proper proppant type for hydraulic fracturing is important. The simulation results presented in this chapter for refracturing with sand and ceramic proppant indicate a strong impact of the proppant quality on the oil and gas recovery. Hence, for improving the recovery in shale reservoirs, especially in the Eagle Ford shale reservoir, higher quality proppant use is recommended.

ACKNOWLEDGMENTS

The authors would like to thank the Unconventional Natural Gas and Oil Institute (UNGI) Coupled Integrated Multiscale Measurements and Modeling (CIMMM) Consortium sponsors and collaborators for the field data and computational tools used in the research study presented in this chapter.

REFERENCES

Curnow, J.S., Tutuncu, A.N., 2016. A coupled geomechanics and fluid flow modeling study for hydraulic fracture design and production optimization in an Eagle Ford shale oil reservoir. In: Paper SPE 179165-MS Presented at the SPE Hydraulic Fracture Technology Conference, Woodland, Texas, USA.

Cipolla, C.L., Fitzpatrick, T., Williams, M.J., 2011. Seismic-to-simulation for unconventional reservoir development. In: Paper SPE-146876-MS Presented at the SPE Reservoir Characterization and Simulation Conference and Exhibition, Abu Dhabi, UAE.

Cipolla, C., Wallace, J., 2014. Stimulated reservoir volume: a misapplied concept?. In: Paper SPE-168596-MS Presented at the SPE Hydraulic Fracturing Technology Conference, February 4–6, 2014, Woodlands, Texas, USA.

Fisher, M.K., Heinze, J.R., Harris, C.D., Davidson, B.M., Wright, C.A., Dunn, K.P., 2004. Optimizing horizontal completion techniques in the Barnett shale using microseismic fracture mapping. In: Paper SPE-90051-MS Presented at the SPE Annual Technical Conference and Exhibition, September 26–29, 2004, Houston, Texas.

Gu, H., Weng, X., 2010. Criterion for fractures crossing frictional interfaces at Nonorthogonal angles. In: Paper ARMA-10–198 Presented at the 44th US Rock Mechanics Symposium and 5th US–Canada, Salt Lake City, Utah, USA.

Lindsay, G.J., White, D.J., Miller, G.A., Baihly, J.D., Sinosic, B., 2016. Understanding the applicability and economic viability of refracturing horizontal wells in unconventional plays. In: Paper SPE-179113-MS Presented at the Hydraulic Fracturing Technology Conference, the Woodlands, Texas, USA.

Malpani, R., Sinha, S., Charry, L., Sinosic, B., Clark, B., Gakhar, K., 2015. Improving hydrocarbon recovery of horizontal shale wells through Re-fracturing. In: Paper SPE-175920-MS Presented at the SPE/CSUR Unconventional Resources Conference, Calgary, Alberta, Canada.

Marongiu-Porcu, M., Lee, D., Shan, D., Morales, A., 2016. Advanced modeling of interwell fracturing interference: an Eagle Ford shale oil study. Paper SPE-174902-PA. SPE Journal 21 (05), 1567–1582.

Martin, R., Baihly, J., Mulpani, R., Lindsay, G.J., Atwood, W.K., 2011. Understanding production from Eagle Ford-Austin chalk system. In: Paper SPE-145117-MS Presented at the SPE Annual Technical Conference and Exhibition, Denver, Colorado, USA.

Mokhtari, M., Tutuncu, A.N., 2016. Impact of laminations and natural fractures on rock failure in Brazilian experiments: a case study on Green River and Niobrara formations. Journal of Natural Gas Science and Engineering 36, 79–86.

Mokhtari, M., Bui, B.T., Tutuncu, A.N., 2014. Tensile failure of shales: impacts of layering and natural fractures. In: Paper SPE-169520-MS Presented at the SPE Western North American and Rocky Mountain Joint Meeting, Denver, Colorado, USA.

Padin, A., Tutuncu, A.N., Sonnenberg, S., 2014. On the mechanisms of shale microfracture propagation. In: Paper SPE-168624-MS Presented at the SPE Hydraulic Fracturing Technology Conference, the Woodlands, Texas, USA.

Pankaj, P., Gakhar, K., Lindsay, G., 2016. When to Refrac? Combination of reservoir geomechanics with fracture modeling and reservoir simulation holds the answer. In: Paper SPE-182-161-MS Presented at the SPE Asia Pacific Oil & Gas Conference and Exhibition, Perth, Australia.

Rafiee, M., Soliman, M.Y., Pirayesh, E., 2012. Hydraulic fracturing design and optimization: a modification to zipper frac. In: Paper SPE-159786-MS Presented at the SPE Annual Technical Conference and Exhibition, San Antonio, Texas, USA.

Suppachoknirun, T., Tutuncu, A.N., 2016. Evaluation of multistage hydraulic fracture patterns in naturally fractured tight oil formations utilizing a coupled geomechanics-fluid flow model – case study for an Eagle Ford shale Well Pad. In: Paper ARMA 14–782, Presented at the 50th US Rock Mechanics/Geomechanics Symposium, Houston, Texas, USA.

Suppachoknirun, T., Tutuncu, A.N., Kazemi, H., 2016. Evaluation of multistage hydraulic fracturing techniques for production optimization in naturally fractured reservoirs using coupled geomechanics fracture and flow model. In: Paper IPTC-18916, Presented at the International Petroleum Technology Conference, Bangkok, Thailand.

Vincent, M., 2011. Restimulation of Unconventional Reservoirs, Paper SPE-136757-PA. Journal of Canadian Petroleum Technology 50, 36–96.

Vincent, M., 2015. Restimulating Horizontal Oil Wells – Success and Failure. In: AAPG/STGS Geoscience Workshop Presentation.

Water, A.G., Dean, B.K., Downie, R.C., Kerrihard, K.J., Austbo, L., McPherson, B., 2009. Simultaneous Hydraulic Fracturing of Adjacent Horizontal Wells in the Woodford Shale. In: Paper SPE-119635-MS Presented at the SPE Hydraulic Fracturing Technology Conference, the Woodlands, Texas, USA.

Yost, A.B., Overby, W.K., Wilkins, D.A., Locke, C.D., 1988. Hydraulic fracturing of a horizontal well in a naturally fractured reservoir: gas study for multiple fracture design. SPE-17759. In: Proc. SPE Gas Technology Symposium. https://doi.org/10.2118/17759-MS.

Chapter 11

Development of a Coupled Reservoir–Geomechanical Simulator for the Prediction of Caprock Fracturing and Fault Reactivation During CO_2 Sequestration in Deep Saline Aquifers

Philip H. Winterfeld, Yu-Shu Wu
Colorado School of Mines, Golden, CO, United States

11.1 INTRODUCTION

A promising option for reducing atmospheric anthropogenic carbon dioxide is to inject it underground into a deep saline aquifer. Although this carbon dioxide would be a supercritical fluid when injected, it is still less dense than the native brine and would tend to rise upward. Thus, an aquifer suitable for underground carbon dioxide sequestration needs to be overlain by sealing caprock for the duration of the carbon sequestering process. A homogeneous caprock layer with a sufficiently small permeability would inhibit sequestered carbon dioxide from leaking through. However, geological systems often are heterogeneous and discontinuous and may contain fractures and faults. Carbon dioxide injection pressurizes the reservoir, and this pressurization can reactivate existing faults and fractures and provide flow paths that allow leakage of carbon dioxide from the saline aquifer. In addition, if the pressurization is sufficiently high, the caprock can fracture.

A simulation model that can predict caprock failure and fault reactivation would be a useful tool in enhancing our ability to predict reservoir conditions and integrity, and enhance the performance of life cycle storage operations for

Hydraulic Fracture Modeling. https://doi.org/10.1016/B978-0-12-812998-2.00011-4

carbon dioxide geologic storage. Such a model would couple fluid flow with geomechanics, as well as having criteria for caprock failure and fault reactivation.

To simulate coupled fluid flow with geomechanics, the two sets of equations, fluid and heat flow, and geomechanics, are both solved on a discretized medium. The different ways these two sets of equations can be coupled have been described by Settari and Walters (1999) and Tran et al. (2005). Three of these methods are iterative, explicit, and full coupling. In iterative coupling (for example, Chin et al., 2000), the fluid and heat flow, and geomechanical equations are solved iteratively and sequentially until solutions for both sets converge. In explicit coupling (for example, Minkoff et al., 1999), one set of equations is solved for first and the other set is solved for next using the updated variables of the previously solved for set. In full coupling (for example, Gutierrez and Lewis, 1996), both sets of equations are solved simultaneously.

Examples of coupled fluid flow−geomechanical simulators that have been reported in the literature are TOUGH2-FLAC3D (Rutqvist et al., 2002), a linkage of TOUGH2, a well-established code for geohydrological analysis with multiphase, multicomponent fluid flow and heat transport, and FLAC3D, a widely used commercial code that is designed for rock and soil mechanics with thermomechanical and hydromechanical interactions; TOUGH−RDCA (Pan et al., 2014), a linkage of TOUGH2 and RDCA, developed for simulating the nonlinear and discontinuous geomechanical behavior of rock; CODE-BRIGHT (Olivella et al., 1994), a finite element code that simulates nonisothermal multiphase flow of brine and gas in deformable media; Code_Aster (Sayedi et al., 2009), a thermal−mechanical finite element code that was coupled to TOUGH2 to simulate thermohydromechanical processes under multiphase flow; finite element heat and mass transfer (Bower and Zyvoloski, 1997), a coupled thermal−hydrologic−mechanical dual porosity finite element code that allows permeability of up to two perpendicular fracture planes vary with normal stress; and OpenGeoSys (Wang and Kolditz, 2007; Goerke et al., 2011), an object-oriented open source thermal−hydrological−mechanical (THM) finite element code.

In this chapter, we present a coupled fluid flow−geomechanical simulation model that can predict caprock failure and fault reactivation. A fully coupled fluid flow−geomechanical simulator was presented by Winterfeld and Wu (2014) and Hu et al. (2013). In their approach, the geomechanical equations relating stresses and displacements were combined to yield an equation for mean stress, a primary variable, and volumetric strain, a rock property. This formulation was then extended by Winterfeld and Wu (2016) to calculate the stress tensor components efficiently and is the geomechanical formulation

for our simulator. We begin by detailing this geomechanical formulation, along with the associated fluid and heat flow formulation, and then present the formulation used to predict caprock fracturing and fault reactivation. Example problems then provide verification of our coupled fluid flow–geomechanical formulation. Two are comparisons of simulation results to analytical solutions: displacement by a uniform load on a semiinfinite elastic medium and the two-dimensional Mandel–Cryer effect. The next two are comparisons of our simulator to published results: a single-phase depletion problem and a simulation of CO_2 injection into a depleting gas field. Next, we provide simulation examples of our caprock failure and fault reactivation formulation including a simulation of caprock leakage from carbon dioxide injection taken from the literature, a demonstration of the simulator's ability to predict of shear failure, and a simulation of an experiment of pressure-induced fracturing of a concrete block.

11.2 GEOMECHANICAL FORMULATION

11.2.1 Mean Stress Equation

Our simulator's geomechanical formulation is based on the linear theory of elasticity applied to multiporosity nonisothermal (thermomultiporoelastic) media. The first two fundamental relations in this theory are the relation between the strain tensor and the displacement vector $\boldsymbol{u}$:

$$\boldsymbol{\varepsilon} = \frac{1}{2}(\nabla \boldsymbol{u} + \nabla \boldsymbol{u}^t) \tag{11.1}$$

and the static equilibrium equation:

$$\nabla \cdot \boldsymbol{\tau} + \boldsymbol{F}_b = 0 \tag{11.2}$$

where $\boldsymbol{F}_b$ is the body force.

The last fundamental relation in this theory is the relation between the stress and strain tensors. For an isothermal elastic material, this relation is Hooke's law:

$$\boldsymbol{\tau} = 2G\boldsymbol{\varepsilon} + \lambda(tr\boldsymbol{\varepsilon})\boldsymbol{I} \tag{11.3}$$

where G is shear modulus and λ is the Lamé parameter. Biot and Willis (1957) extended Hooke's law to isothermal poroelastic materials—porous elastic materials such as fluid-filled porous rocks—by adding a pore pressure term to Eq. (11.3). Norris (1992) extended Hooke's law to thermoelastic materials—elastic materials subject to changes in both temperature and stress—by adding a temperature term to Eq. (11.3). McTigue (1986) extended Hooke's law to a thermoporoelastic material—a porous elastic material subject to changes

in both temperature and stress—by adding both the temperature term from McTigue (1986) and the pore pressure term from Biot and Willis (1957) to Eq. (11.3):

$$\boldsymbol{\tau} - \alpha P\boldsymbol{I} - 3\beta K(T - T_{\text{ref}})\boldsymbol{I} = 2G\boldsymbol{\varepsilon} + \lambda(tr\boldsymbol{\varepsilon})\boldsymbol{I} \tag{11.4}$$

where α is the Biot coefficient, T_{ref} is reference temperature for a thermally unstrained state, K is bulk modulus, and β is linear thermal expansion coefficient.

Bai et al. (1993) extended Hooke's law to isothermal multiporosity materials, a common example of which is a double-porosity material consisting of a network of fractures and a rock matrix, by summing the Biot and Willis (1957) pore pressure terms over the multiporosity continua. Finally, Winterfeld and Wu (2014) extended Hooke's law to a thermomultiporoelastic material by including the Norris (1992) temperature term in the Bai et al. (1993) summation:

$$\boldsymbol{\tau} - \left[\sum_j (\alpha_j P_j + 3\beta K \omega_j (T_j - T_{\text{ref}}))\right]\boldsymbol{I} = 2G\boldsymbol{\varepsilon} + \lambda(tr\boldsymbol{\varepsilon})\boldsymbol{I} \tag{11.5}$$

where the subscript j refers to porous continuum and ω_j is the porous continuum volume fraction. Wilson and Aifantis (1982) derived expressions for the porous continuum Biot coefficients in a double-porosity material:

$$\alpha_1 = 1 - \frac{K}{K_*} \tag{11.6}$$

$$\alpha_2 = \frac{K}{K_*}\left(1 - \frac{K_*}{K_s}\right) \tag{11.7}$$

where K_s is the solid modulus, K_* is the modulus of the porous material without the fractures, the subscript 1 refers to the fractures, and the subscript 2 refers to the matrix. These coefficients sum to the Biot coefficient of a single-porosity material:

$$\alpha = \alpha_1 + \alpha_2 = 1 - \frac{K}{K_*} + \frac{K}{K_*}\left(1 - \frac{K_*}{K_s}\right) = 1 - \frac{K}{K_s} \tag{11.8}$$

We substitute Eq. (11.1) into Eq. (11.5) and then into Eq. (11.2) to obtain the thermomultiporoelastic version of the Navier equation:

$$\nabla\left[\sum_j (\alpha_j P_j + 3\beta K \omega_j T_j)\right] + (\lambda + G)\nabla(\nabla \cdot \boldsymbol{u}) + G\nabla^2\boldsymbol{u} + \boldsymbol{F}_b = 0 \tag{11.9}$$

We then take the divergence of Eq. (11.9) to obtain:

$$\nabla^2\left[\sum_j(\alpha_j P_j + 3\beta K\omega_j T_j)\right] + (\lambda + 2G)\nabla^2(\nabla\cdot\boldsymbol{u}) + \nabla\cdot\boldsymbol{F}_b = 0 \tag{11.10}$$

Eq. (11.10) contains the divergence of the displacement vector. This term, shown below, is the sum of the normal strain components and is equal to the volumetric strain:

$$\nabla\cdot\boldsymbol{u} = \frac{\partial u_x}{\partial x} + \frac{\partial u_y}{\partial y} + \frac{\partial u_z}{\partial z} = \varepsilon_{xx} + \varepsilon_{yy} + \varepsilon_{zz} = \varepsilon_v \tag{11.11}$$

We sum the normal stress terms in Eq. (11.5) and obtain a relation between mean stress, volumetric strain, pore pressures, and temperatures:

$$K\varepsilon_v = \tau_m - \sum_j(\alpha_j P_j + 3\beta K\omega_j(T_j - T_{\text{ref}})) \tag{11.12}$$

where the mean stress is given by:

$$\tau_m = \frac{\tau_{xx} + \tau_{yy} + \tau_{zz}}{3} \tag{11.13}$$

and the bulk modulus is equal to the following:

$$K = \frac{(3\lambda + 2G)}{3} \tag{11.14}$$

Finally, we substitute Eq. (11.12) into Eq. (11.11) and then into Eq. (11.10), use the relationship between Poisson's ratio, υ, shear modulus, and Lamé parameter:

$$\frac{\lambda}{G} = \frac{2\upsilon}{(1-2\upsilon)} \tag{11.15}$$

and obtain an equation relating mean stress, pore pressures, temperatures, and body force—the Mean Stress Equation:

$$\nabla\cdot\left[\frac{3(1-\upsilon)}{1+\upsilon}\nabla\tau_m + \boldsymbol{F}_b - \frac{2(1-2\upsilon)}{1+\upsilon}\nabla\left[\sum_j(\alpha_j P_j + 3\beta K\omega_j T_j)\right]\right] = 0 \tag{11.16}$$

The Mean Stress Equation is derived from the static equilibrium equation, which is a momentum conservation equation. It is the primary geomechanical equation for our simulator, and Eq. (11.12) is an associated property relation. Mean stress is the primary variable associated with the former equation, and volumetric strain is the property associated with the latter.

11.2.2 Stress Tensor Components

Here we derive additional geomechanical equations for the individual stress tensor components. Eq. (11.9), the thermomultiporoelastic version of the Navier equation, is a vector equation, so each component of that equation is zero. These components in Cartesian coordinates are:

$$\frac{\partial}{\partial x}[h(\mathbf{P},\mathbf{T})] + (\lambda + G)\frac{\partial}{\partial x}(\nabla\cdot\mathbf{u}) + G\nabla^2 u_x + F_{b,x} = 0 \tag{11.17}$$

$$\frac{\partial}{\partial y}[h(\mathbf{P},\mathbf{T})] + (\lambda + G)\frac{\partial}{\partial y}(\nabla\cdot\mathbf{u}) + G\nabla^2 u_y + F_{b,y} = 0 \tag{11.18}$$

$$\frac{\partial}{\partial z}[h(\mathbf{P},\mathbf{T})] + (\lambda + G)\frac{\partial}{\partial z}(\nabla\cdot\mathbf{u}) + G\nabla^2 u_z + F_{b,z} = 0 \tag{11.19}$$

where

$$h(\mathbf{P},\mathbf{T}) = \sum_j (\alpha_j P_j + 3\beta K \omega_j (T_j - T_{\text{ref}})) \tag{11.20}$$

Differentiating Eq. (11.17) by x and eliminating strains and displacements in favor of stresses using Eqs. (11.1), (11.5), and (11.12) yields an equation relating the xx-normal stress component, mean stress, pore pressures, and temperatures:

$$\begin{aligned}\frac{\partial^2 h(\mathbf{P},\mathbf{T})}{\partial x^2} + \frac{3}{2(1+\upsilon)}\frac{\partial^2}{\partial x^2}[\tau_m - h(\mathbf{P},\mathbf{T})] \\ + \frac{1}{2}\nabla^2\left[\tau_{xx} - \frac{3\upsilon}{1+\upsilon}\tau_m + \left(\frac{2\upsilon-1}{1+\upsilon}\right)h(\mathbf{P},\mathbf{T})\right] + \frac{\partial F_{b,x}}{\partial x} = 0\end{aligned} \tag{11.21}$$

Differentiating Eq. (11.18) by y and performing the same elimination as above yields an equation relating the yy-normal stress component, mean stress, pore pressures, and temperatures:

$$\begin{aligned}\frac{\partial^2 h(\mathbf{P},\mathbf{T})}{\partial y^2} + \frac{3}{2(1+\upsilon)}\frac{\partial^2}{\partial y^2}[\tau_m - h(\mathbf{P},\mathbf{T})] \\ + \frac{1}{2}\nabla^2\left[\tau_{yy} - \frac{3\upsilon}{1+\upsilon}\tau_m + \left(\frac{2\upsilon-1}{1+\upsilon}\right)h(\mathbf{P},\mathbf{T})\right] + \frac{\partial F_{b,y}}{\partial y} = 0\end{aligned} \tag{11.22}$$

Differentiating Eq. (11.19) by z and performing the same elimination as above yields an equation relating the zz-normal stress component, mean stress, pore pressures, and temperatures:

$$\begin{aligned}\frac{\partial^2 h(\mathbf{P},\mathbf{T})}{\partial z^2} + \frac{3}{2(1+\upsilon)}\frac{\partial^2}{\partial z^2}[\tau_m - h(\mathbf{P},\mathbf{T})] \\ + \frac{1}{2}\nabla^2\left[\tau_{zz} - \frac{3\upsilon}{1+\upsilon}\tau_m + \left(\frac{2\upsilon-1}{1+\upsilon}\right)h(\mathbf{P},\mathbf{T})\right] + \frac{\partial F_{b,z}}{\partial z} = 0\end{aligned} \tag{11.23}$$

Differentiating Eq. (11.18) by x, differentiating Eq. (11.17) by y, averaging the two, and performing the same elimination as above yields an equation relating the xy-shear stress component, mean stress, pore pressures, and temperatures:

$$\frac{\partial^2 h(\mathbf{P},\mathbf{T})}{\partial x \partial y} + \frac{3}{2(1+\upsilon)}\frac{\partial^2}{\partial x \partial y}[\tau_m - h(\mathbf{P},\mathbf{T})] + \frac{1}{2}\nabla^2 \tau_{xy} + \frac{1}{2}\left(\frac{\partial}{\partial x}F_{b,y} + \frac{\partial}{\partial y}F_{b,x}\right) = 0 \tag{11.24}$$

Differentiating Eq. (11.18) by z, differentiating Eq. (11.19) by y, averaging the two, and performing the same elimination as above yields an equation relating the yz-shear stress component, mean stress, pore pressures, and temperatures:

$$\frac{\partial^2 h(\mathbf{P},\mathbf{T})}{\partial y \partial z} + \frac{3}{2(1+\upsilon)}\frac{\partial^2}{\partial y \partial z}[\tau_m - h(\mathbf{P},\mathbf{T})] + \frac{1}{2}\nabla^2 \tau_{yz} + \frac{1}{2}\left(\frac{\partial}{\partial y}F_{b,z} + \frac{\partial}{\partial z}F_{b,y}\right) = 0 \tag{11.25}$$

Differentiating Eq. (11.19) by x, differentiating Eq. (11.17) by z, averaging the two, and performing the same elimination as above yields an equation relating the xz-shear stress component, mean stress, pore pressures, and temperatures:

$$\frac{\partial^2 h(\mathbf{P},\mathbf{T})}{\partial x \partial z} + \frac{3}{2(1+\upsilon)}\frac{\partial^2}{\partial x \partial z}[\tau_m - h(\mathbf{P},\mathbf{T})] + \frac{1}{2}\nabla^2 \tau_{xz} + \frac{1}{2}\left(\frac{\partial}{\partial x}F_{b,z} + \frac{\partial}{\partial z}F_{b,x}\right) = 0 \tag{11.26}$$

The normal stress tensor components are obtained from Eqs. (11.21)–(11.23), and the shear stress tensor components are obtained from Eqs. (11.24)–(11.26). Each of these equations consists of the Laplacian of the stress tensor component plus various derivatives of the terms (mean stress, body force, and the pore pressure-temperature term Eq. 11.20) that appear in the Mean Stress Equation. This feature, as will be shown later, enables efficient calculation of stress tensor components after the mean stress and associated primary variables are solved for.

11.3 FLUID AND HEAT FLOW FORMULATION

Our simulator's fluid and heat flow formulation is based on the TOUGH2 formulation (Pruess et al., 1999) of mass and energy conservation equations that govern fluid and heat flow in general multiphase, multicomponent, multiporosity systems. The conservation equations for mass and energy can be written in differential form as:

$$\frac{\partial M^k}{\partial t} = \nabla \cdot \boldsymbol{F}^k + q^k \tag{11.27}$$

where M^k is conserved quantity k per unit volume, q^k is source or sink per unit volume, and $\boldsymbol{F}^k$ is flux.

Mass per unit volume is a sum over phases:

$$M^k = \phi \sum_l S_l \rho_l X_l^k \tag{11.28}$$

where ϕ is porosity, the subscript l denotes a phase, S is phase saturation, ρ is mass density, and X is the mass fraction of the component k. Energy per unit volume accounts for the internal energy in rock and fluid and is the following:

$$M^{N+1} = (1-\phi) C_r \rho_r T + \phi \sum_l S_l \rho_l U_l \tag{11.29}$$

where ρ_r is rock density, C_r is rock specific heat, T is temperature, U is phase specific internal energy, and N is the number of mass components with energy as conserved species $N+1$.

Fluid advection is described with a multiphase extension of Darcy's law; in addition, there is diffusive mass transport in all phases. Advective mass flux is a sum over phases:

$$\boldsymbol{F}_{\text{adv}}^k = \sum_l \boldsymbol{F}_l X_l^k \tag{11.30}$$

and phase flux, $\boldsymbol{F}_l$, is given by Darcy's law:s

$$\boldsymbol{F}_l = -k \frac{k_{rl} \rho_l}{\mu_l} \left(\nabla P + \nabla P_{c,l} - \rho_l \boldsymbol{g} \right) \tag{11.31}$$

where k is absolute permeability, k_r is phase relative permeability, μ is phase viscosity, P is pore pressure, P_c is phase capillary pressure, and $\boldsymbol{g}$ is gravitational acceleration. The pressure in phase l:

$$P_l = P + P_{c,l} \tag{11.32}$$

is relative to a reference phase, which is the gaseous phase. Diffusive mass flux is given by:

$$\boldsymbol{F}_{\text{dis}}^k = \sum_l \rho_l \boldsymbol{D}_l^k X_l^k \tag{11.33}$$

where $\boldsymbol{D}_l^k$ is the dispersion tensor. Heat flux occurs by conduction and convection, the latter including sensible as well as latent heat effects, and includes conductive and convective components:

$$\boldsymbol{F}^{N+1} = -\lambda \nabla T + \sum_l h_l \boldsymbol{F} \tag{11.34}$$

where λ is thermal conductivity and h_l is phase l specific enthalpy.

The description of thermodynamic conditions is based on the assumption of local equilibrium of all phases. Fluid and formation parameters can be arbitrary nonlinear functions of the primary thermodynamic variables.

11.4 DISCRETIZATION AND SOLUTION OF GOVERNING EQUATIONS

11.4.1 Discretization of Simulator Conservation Equations

Our simulator's mass, energy, and momentum conservation equations are discretized in space using the integral finite difference method (Narashimhan and Witherspoon, 1976). In this method, the simulation domain is subdivided into Cartesian grid blocks, and the conservation equations (Eq. 11.27 for fluid components and energy, Eq. 11.16 for momentum) are integrated over grid block volume, V_n, with flux terms expressed as an integral over grid block surface, Γ_n, using the divergence theorem:

$$\frac{d}{dt}\int_{V_n} M^k dV = \int_{\Gamma_n} \boldsymbol{F}^k \cdot \boldsymbol{n} d\Gamma + \int_{V_n} q^k dV \tag{11.35}$$

Volume integrals are replaced with volume averages:

$$\int_{V_n} M^k dV = M_n^k V_n \tag{11.36}$$

and surface integrals with discrete sums over surface averaged segments:

$$\int_{\Gamma_n} \boldsymbol{F}^k \cdot \boldsymbol{n} d\Gamma = \sum_m A_{nm} F_{nm}^k \tag{11.37}$$

where the subscript n denotes an averaged quantity over volume V_n, A_{nm} is the area of a surface segment common to volumes V_n and V_m, and the double subscript nm denotes an averaged quantity over area A_{nm}. The definitions of the geometric parameters used in this discretization are shown in Fig. 11.1.

Strictly speaking, the integrals in Eqs. (11.35)–(11.37) apply to control volumes with fixed geometry. Due to the addition of the geomechanical equations to our formulation, control volume geometry is no longer fixed, so we introduce strain dependence into the volumes, areas, and distances that arise when the integrals in Eqs. (11.35)–(11.37) are evaluated and perform

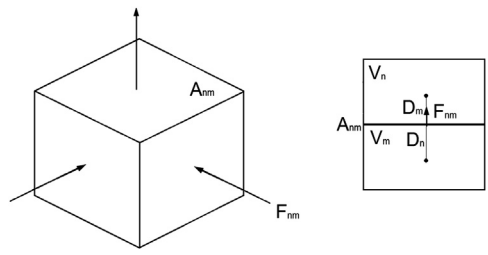

FIGURE 11.1 Parameter definitions for the integral finite difference method. The figure on the right shows two neighboring grid blocks and the interface between them.

the integrations over the fixed Cartesian grid. These dependencies are based on strains for volume, area, and length (V, A, and L, respectively):

$$V_n = V_{n,0}\left(1 - \varepsilon_{v,n}\right) \tag{11.38}$$

$$A_{nm} = A_{nm,0}\left(1 - \varepsilon_{A,nm}\right) \tag{11.39}$$

$$D_l = D_{l,0}\left(1 - \varepsilon_{ll}\right) \tag{11.40}$$

where the subscript 0 refers to zero strain, subscript n refers to a grid block, subscript nm refers to the interface between grid blocks n and m, and subscript l refers to the linear dimensions of grid block n. Volumetric strain is given by Eq. (11.11); the area strain for a given Cartesian direction is the sum of the normal strains in the other two directions. Substituting these definitions into Eqs. (11.36) and (11.37) yields:

$$\int_{V_n} M^k dV = M_n^k\left(1 - \varepsilon_{v,n}\right)V_{n,0} \tag{11.41}$$

and

$$\int_{\Gamma_n} \boldsymbol{F}^k \cdot \boldsymbol{n} d\Gamma = \sum_m A_{nm,0}\left(1 - \varepsilon_{A,nm}\right)F_{nm}^k \tag{11.42}$$

Substituting Eqs. (11.41) and (11.42) into Eq. (11.35) and using the standard difference approximation for the time derivative yields the finite difference approximation of Eq. (11.35):

$$\begin{aligned} &\frac{\left\{M_n^k\left(1 - \varepsilon_{v,n}\right)\right\}\Big|_{j+1} - \left\{M_n^k\left(1 - \varepsilon_{v,n}\right)\right\}\Big|_j}{\Delta t} \\ &= \left\{\frac{1}{V_{n,0}}\sum_m A_{nm,0}\left(1 - \varepsilon_{A,nm}\right)F_{nm}^k + q_n^k\left(1 - \varepsilon_{v,n}\right)\right\}\Bigg|_{j,j+1} \end{aligned} \tag{11.43}$$

where j refers to time step number. Some terms on the right-hand side of Eq. (11.43) are evaluated at the current time step $(j + 1)$ and others at the previous one (j).

The finite difference approximations for the normal stress components are obtained next. The equations for these components have the general form:

$$\frac{\partial^2 \Phi}{\partial s^2} + \nabla^2 \Theta_{ss} + \frac{\partial F_{b,s}}{\partial s} = 0; \quad s = x, y, z \tag{11.44}$$

where

$$\Phi = h(\mathbf{P},\mathbf{T}) + \frac{3}{2(1+\upsilon)}\left[\tau_m - h(\mathbf{P},\mathbf{T})\right] \tag{11.45}$$

and

$$\Theta_{sw} = \frac{1}{2}\left[\tau_{sw} - \frac{3\upsilon}{1+\upsilon}\tau_m + \left(\frac{2\upsilon-1}{1+\upsilon}\right)h(\mathbf{P},\mathbf{T})\right] \tag{11.46}$$

Eq. (11.44) is integrated over the grid block volume with flux terms expressed as an integral over the grid block surface using the divergence theorem:

$$\int_{\Gamma_n} \nabla\Theta_{ss}\cdot\mathbf{n}d\Gamma + \int_{V_n}\left(\frac{\partial^2\Phi}{\partial s^2} + \frac{\partial F_{b,s}}{\partial s}\right)dV = 0 \tag{11.47}$$

Evaluating the integrals in Eq. (11.47) using Eqs. (11.38)–(11.40) yields:

$$\begin{aligned}\frac{1}{V_{n,0}}\sum\nolimits_m A_{nm,0}\left(1-\varepsilon_{A,nm}\right)\nabla\Theta_{ss,nm} \\ + \left(\frac{\partial^2\Phi}{\partial s^2} + \frac{\partial F_{b,s}}{\partial s}\right)\Bigg|_n \left(1-\varepsilon_{v,n}\right) = 0\end{aligned} \tag{11.48}$$

Let grid block n in the Cartesian grid be denoted by index I in direction s. It has, in general, two neighbors in direction s, denoted by indices $I+1$ and $I-1$, as shown in Fig. 11.2. The first and second partial derivatives in Eq. (11.48) are then evaluated using standard differences:

$$\left.\frac{\partial F_{b,s}}{\partial s}\right|_n = \frac{1}{2}\left(\frac{F_{b,s}\big|_{I+1} - F_{b,s}\big|_I}{s_{I+1}-s_I} + \frac{F_{b,s}\big|_I - F_{b,s}\big|_{I-1}}{s_I - s_{I-1}}\right) \tag{11.49}$$

and

$$\left.\frac{\partial^2\Phi}{\partial s^2}\right|_n = \frac{2\left(\dfrac{\Phi|_{I+1}-\Phi|_I}{s_{I+1}-s_I} - \dfrac{\Phi|_I - \Phi|_{I-1}}{s_I - s_{I-1}}\right)}{s_{I+1}-s_{I-1}} \tag{11.50}$$

where s_I refers to the center of grid block with index I.

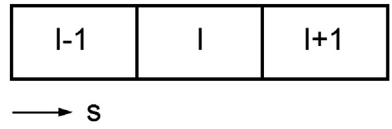

FIGURE 11.2 Grid block indices for numerical first partial derivative.

The finite difference approximations for the shear stress components are obtained similarly to that for normal stress components. The shear stress component equations have the general form:

$$\frac{\partial^2\Phi}{\partial s\partial w}+\nabla^2\Theta_{sw}+\frac{1}{2}\left(\frac{\partial F_{b,w}}{\partial s}+\frac{\partial F_{b,s}}{\partial w}\right)=0;\quad s,w=x,y,z;\quad w\neq s \tag{11.51}$$

Eq. (11.51) is integrated over the grid block volume with flux terms expressed as an integral over the grid block surface using the divergence theorem:

$$\int_{\Gamma_n}\nabla\Theta_{sw}\cdot\boldsymbol{n}d\Gamma+\int_{V_n}\left[\frac{\partial^2\Phi}{\partial s\partial w}+\frac{1}{2}\left(\frac{\partial F_{b,w}}{\partial s}+\frac{\partial F_{b,s}}{\partial w}\right)\right]dV=0 \tag{11.52}$$

Evaluating the integrals in Eq. (11.52) using Eqs. (11.38)–(11.40) yields:

$$\begin{aligned}&\frac{1}{V_{n,0}}\sum_m A_{nm,0}\left(1-\varepsilon_{A,nm}\right)\nabla\Theta_{sw,nm}\\&\quad+\left(\frac{\partial^2\Phi}{\partial s\partial w}+\frac{1}{2}\left(\frac{\partial F_{b,w}}{\partial s}+\frac{\partial F_{b,s}}{\partial w}\right)\right)\Big|_n\left(1-\varepsilon_{v,n}\right)=0\end{aligned} \tag{11.53}$$

Let grid block n be denoted by index I in direction s, and index J in direction w. It has, in general, eight neighbors in directions s and w including diagonal neighbors. They are denoted by the index pairs $(I-1,\ J-1)$, $(I,J-1)$, $(I+1,\ J-1)$, $(I-1,\ J+1)$, $(I,\ J+1)$, $(I+1,\ J+1)$, $(I-1,\ J)$, and $(I+1,\ J)$ as shown in Fig. 11.3. The two first partial derivatives in Eq. (11.53) are evaluated as before:

$$\left.\frac{\partial F_{b,w}}{\partial s}\right|_n=\frac{1}{2}\left(\frac{F_{b,w}\big|_{I+1,J}-F_{b,w}\big|_{I,J}}{s_{I+1,J}-s_{I,J}}+\frac{F_{b,w}\big|_{I,J}-F_{b,w}\big|_{I-1,J}}{s_{I,J}-s_{I-1,J}}\right) \tag{11.54}$$

and

$$\left.\frac{\partial F_{b,s}}{\partial w}\right|_n=\frac{1}{2}\left(\frac{F_{b,s}\big|_{I,J+1}-F_{b,s}\big|_{I,J}}{w_{I,J+1}-w_{I,J}}+\frac{F_{b,s}\big|_{I,J}-F_{b,s}\big|_{I,J-1}}{w_{I,J}-w_{I,J-1}}\right) \tag{11.55}$$

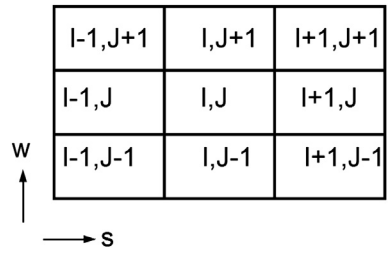

FIGURE 11.3 Grid block indices for numerical cross derivatives.

The cross derivative in Eq. (11.53) is also evaluated using standard differences:

$$\left.\frac{\partial^2\Phi}{\partial s\partial w}\right|_n = \frac{1}{4}\left(\begin{array}{l} \dfrac{\Phi|_{I,J+1}-\Phi|_{I-1,J+1}}{s_{I,J+1}-s_{I-1,J+1}} - \dfrac{\Phi|_{I,J}-\Phi|_{I-1,J}}{s_{I,J}-s_{I-1,J}} \Big/ \dfrac{w_{I,J+1}+w_{I-1,J+1}}{2} - \dfrac{w_{I,J}+w_{I-1,J}}{2} + \dfrac{\Phi|_{I+1,J+1}-\Phi|_{I,J+1}}{s_{I+1,J+1}-s_{I,J+1}} - \dfrac{\Phi|_{I+1,J}-\Phi|_{I,J}}{s_{I+1,J}-s_{I,J}} \Big/ \dfrac{w_{I+1,J+1}+w_{I,J+1}}{2} - \dfrac{w_{I+1,J}+w_{I,J}}{2} + \\ \dfrac{\Phi|_{I,J}-\Phi|_{I-1,J}}{s_{I,J}-s_{I-1,J}} - \dfrac{\Phi|_{I,J-1}-\Phi|_{I-1,J-1}}{s_{I,J-1}-s_{I-1,J-1}} \Big/ \dfrac{w_{I,J}+w_{I-1,J}}{2} - \dfrac{w_{I,J-1}+w_{I-1,J-1}}{2} + \dfrac{\Phi|_{I+1,J}-\Phi|_{I,J}}{s_{I+1,J}-s_{I,J}} - \dfrac{\Phi|_{I+1,J-1}-\Phi|_{I,J-1}}{s_{I+1,J-1}-s_{I,J-1}} \Big/ \dfrac{w_{I+1,J}+w_{I,J}}{2} - \dfrac{w_{I+1,J-1}+w_{I,J-1}}{2} \end{array}\right) \tag{11.56}$$

11.4.2 Solution of Simulator Conservation Equations

Our simulator's governing equations consist of Eq. (11.43) (fluid and heat flow, mean stress), Eq. (11.48) (normal stress components), and Eq. (11.53) (shear stress components). The primary variables associated with each of those equations are summarized in Table 11.1. Because mean stress is a primary variable (associated with the Mean Stress Equation) only two out of the three normal stress components are solved for.

This set of equations is nonlinear and is expressed in residual form as:

$$\boldsymbol{R}\left(\boldsymbol{x}^{j+1}\right) = 0 \tag{11.57}$$

where $\boldsymbol{x}^{j+1}$ is the primary variable vector at time level $j+1$. Eq. (11.57) is solved by the Newton–Raphson method. The Newton–Raphson method is an iterative procedure used to solve systems of nonlinear equations. Denoting the

TABLE 11.1 Equations and Associated Primary Variables for *N* Mass Components

Equation	Associated Primary Variables
Mass conservation (Eq. 11.43)	Pressure, $N-1$ mass fractions
Energy conservation (Eq. 11.43)	Temperature
Mean stress (Eq. 11.43)	Mean stress
Normal stresses (Eq. 11.48)	*xx, yy, zz* normal stresses
Shear stresses (Eq. 11.48)	*xy, yz, xz* shear stresses

iteration number by the subscript p, the following system of equations result from applying the Newton–Raphson method to Eq. (11.57):

$$\boldsymbol{J}\left(\boldsymbol{x}_p^{l+1}\right)\left(\boldsymbol{x}_p^{l+1}-\boldsymbol{x}_p^{l}\right)=-\boldsymbol{R}\left(\boldsymbol{x}_p^{l+1}\right) \tag{11.58}$$

where the Jacobian matrix, $\boldsymbol{J}(\boldsymbol{x})$, is defined as:

$$[\boldsymbol{J}(\boldsymbol{x})]_{ij}=\frac{\partial R_i(\boldsymbol{x})}{\partial x_j} \tag{11.59}$$

Elements of the Jacobian matrix are evaluated by numerical differentiation:

$$\frac{\partial R_i(\boldsymbol{x})}{\partial x_j}\approx\frac{R_i(\boldsymbol{x}(\forall\, i\neq j),\ \ x_j+\delta_j)-R_i(\boldsymbol{x})}{\delta_j} \tag{11.60}$$

where δ_j is the increment for primary variable x_j. The iteration is converged when all residuals R_i are less than a prescribed tolerance:

$$R_i\left(\boldsymbol{x}_{p+1}^{l+1}\right)\leq\boldsymbol{\delta}_{\text{tol}} \tag{11.61}$$

where $\boldsymbol{\delta}_{\text{tol}}$ is a vector of tolerances.

The Newton–Raphson method is applied to the system of equations represented by Eq. (11.57) in a sequential manner. First, conservation of mass, energy, and the Mean Stress Equation are solved. All primary variables appearing in the right-hand side of Eq. (11.43) are evaluated implicitly except for normal and shear stress components, which are evaluated explicitly. Solution of these equations yields pressure, mass fractions, temperature, and mean stress. The Jacobian submatrix size for this step in the solution is two plus the number of mass components. Normal and shear stress equations, Eqs. (11.48) and (11.53), are solved next. Pressure, mass fractions, temperature, and mean stress are evaluated implicitly, as well as the normal and shear stress components in these equations that originated from the Laplacian terms in Eqs. (11.21)–(11.26). Other instances of those stress components are evaluated explicitly. Consequently, each normal or shear stress component is independent of the others, so each is solved separately. The Jacobian submatrix size for each is one. Furthermore, the residual functions for these components are linear, so the Newton–Raphson method converges in one iteration. Fig. 11.4 shows a flow chart of this solution sequence.

Our simulator is massively parallel, with domain partitioning using the METIS and ParMETIS packages (Karypis and Kumar, 1998, 1999). Each processor computes Jacobian matrix elements for its own grid blocks, and exchange of information between processors uses Message Passing Interface and allows calculation of Jacobian matrix elements associated with interblock

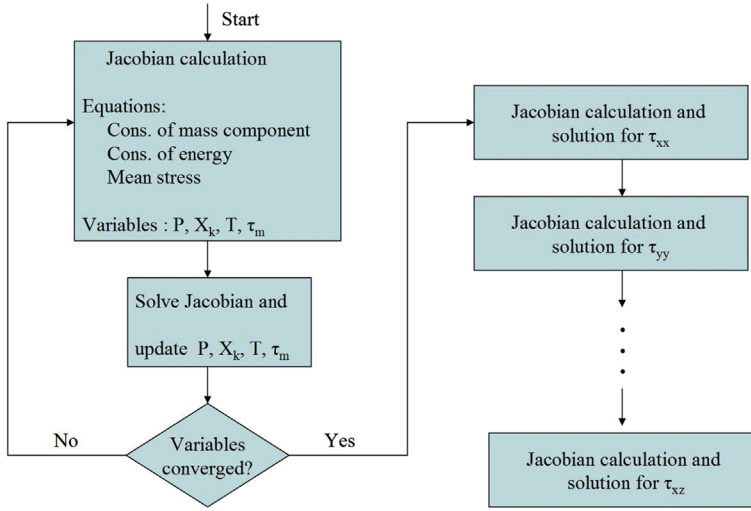

FIGURE 11.4 Flow chart for the solution of simulator governing equations.

connections across domain partition boundaries. The Jacobian matrix is solved in parallel using an iterative linear solver from the Aztec package (Tuminaro et al., 1999).

11.4.3 Geomechanical Boundary Conditions and Stress Field Initialization

The Mean Stress Equation (Eq. 11.16) is the divergence of a momentum flux, and applying the integral finite difference method to the Mean Stress Equation yields an integral of that momentum flux over the grid block surface that is approximated as a discrete sum over surface averaged segments. Grid block surface segments are common to another grid block or border the surroundings. The Eq. (11.43) summation term as is applies to surface segments that are common to another grid block. For grid block surface segments that border the surroundings, we modify that term by applying the geomechanical boundary conditions.

We conceptualize the surroundings as consisting of grid blocks that are reflections of the ones that contain surface segments bordering the surroundings, and momentum is exchanged between a grid block and its reflection. There are four terms that comprise this momentum exchange: the body force, the mean stress, pressure, and temperature difference terms. The reflection and the grid block are at the same elevation, so the body force term is zero. Surface segments bordering the surroundings generally have no fluid flowing through them (fluid loss to the surroundings is generally represented as a constant

pressure sink), so there would be no pore pressure communication between a grid block and the surroundings. Consequently, we neglect the pressure difference term as well. Finally, we assume the temperature and stress tensor of the surroundings are the grid block's initial values.

The stress field is initialized at the beginning of a simulation. We assume no shear stress and normal stresses have z-direction dependence only. In addition, pore pressure is in hydrostatic equilibrium. The equilibrium equation (Eq. 11.2) for the normal z-direction stress then becomes:

$$\frac{\partial \tau_{zz}}{\partial z} + F_{b,z} = 0 \tag{11.62}$$

We integrate Eq. (11.62) from a reference elevation, at which normal stresses and pressure are specified, to a given elevation to get the normal z-direction stress there:

$$\tau_{zz} = \tau_{zz,0} - \int_{z_0}^{z} \rho F_{b,z} dz \tag{11.63}$$

We obtain equations for the x- and y-direction normal stresses from Eqs. (11.21) and (11.22) with the assumptions outlined above:

$$\frac{d^2}{dz^2}\left[\tau_{xx} - \frac{3\upsilon}{1+\upsilon}\tau_m + \left(\frac{2\upsilon - 1}{1+\upsilon}\right)h(\mathbf{P}, \mathbf{T})\right] = 0 \tag{11.64}$$

$$\frac{d^2}{dz^2}\left[\tau_{yy} - \frac{3\upsilon}{1+\upsilon}\tau_m + \left(\frac{2\upsilon - 1}{1+\upsilon}\right)h(\mathbf{P}, \mathbf{T})\right] = 0 \tag{11.65}$$

Eqs. (11.64) and (11.65) are integrated twice to yield:

$$\tau_{xx} - \frac{3\upsilon}{1+\upsilon}\tau_m + \left(\frac{2\upsilon - 1}{1+\upsilon}\right)h(\mathbf{P}, \mathbf{T}) = D_1(z - z_0) + D_2 \tag{11.66}$$

$$\tau_{yy} - \frac{3\upsilon}{1+\upsilon}\tau_m + \left(\frac{2\upsilon - 1}{1+\upsilon}\right)h(\mathbf{P}, \mathbf{T}) = E_1(z - z_0) + E_2 \tag{11.67}$$

where D_i and E_i are constants of integration. Constants with the subscript 2 are evaluated at the reference conditions and the normal x- and y-direction stresses are obtained from solving Eqs. (11.66) and (11.67) simultaneously:

$$\tau_{xx} = \frac{D_2 + \upsilon E_2}{1-\upsilon} + \frac{D_1 + \upsilon E_1}{1-\upsilon}(z - z_0) + \frac{\upsilon}{1-\upsilon}\tau_{zz} - \frac{2\upsilon - 1}{1-\upsilon}h(\mathbf{P}, \mathbf{T}) \tag{11.68}$$

$$\tau_{yy} = \frac{E_2 + \upsilon D_2}{1-\upsilon} + \frac{E_1 + \upsilon D_1}{1-\upsilon}(z - z_0) + \frac{\upsilon}{1-\upsilon}\tau_{zz} - \frac{2\upsilon - 1}{1-\upsilon}h(\mathbf{P}, \mathbf{T}) \tag{11.69}$$

Constants with the subscript 1 are evaluated from the condition that the ratio of vertical to horizontal stress change is given at the reference point:

$$\lim_{z \to z_0} \frac{\tau_{xx} - \tau_{xx,0}}{\tau_{zz} - \tau_{zz,0}} = R_{xz} \tag{11.70}$$

$$\lim_{z \to z_0} \frac{\tau_{yy} - \tau_{yy,0}}{\tau_{zz} - \tau_{zz,0}} = R_{yz} \tag{11.71}$$

where R_{xz} and R_{yz} are the x- and y-directions ratios, respectively.

11.5 PERMEABILITY AND POROSITY DEPENDENCIES

Poroelastic media can deform when either the stress field or the pore pressure changes. For instance, when the stress increases, the medium is compressed and both the bulk volume and the pore volume decrease; when the pore pressure increases, the medium expands and both the bulk volume and the pore volume increase. In addition, the change in pore volume is accompanied by a change in cross-sectional area available for flow. Thus, rock properties that characterize pore volume, such as porosity, and the cross-sectional area available for flow, such as permeability, would depend on both the stress field and the pore pressure. We consider the dependence of permeability and porosity on stress and pressure for both isotropic porous media and fractured media. Fractured media may be isotropic if the fracture orientation is randomly distributed or anisotropic if the fracture orientation is in a preferred direction.

11.5.1 Isotropic Porous Media

The concept of effective stress was initially introduced by Terzaghi (1936) and was generalized by Biot and Willis (1957) as the difference between mean stress and pore pressure terms:

$$\tau'_m = \tau_m - \alpha P \tag{11.72}$$

Correlations have been developed for permeability as a function of either effective stress or porosity, and porosity as a function of effective stress and other variables. There are numerous examples of the above correlations, with each developed for a given rock type under a specific set of conditions. Fig. 11.5, from Rutqvist and Stephansson (2003), shows permeability versus effective stress data for shale, granite, and tight gas sand.

Data such as those shown in Fig. 11.5 can be fitted in various ways, such as by an exponential function of the form (Louis et al., 1977):

$$k = k_0 e^{-c\left(\tau'_m - \tau'_{m,0}\right)} \tag{11.73}$$

where the subscript 0 refers to a reference value and c is a parameter.

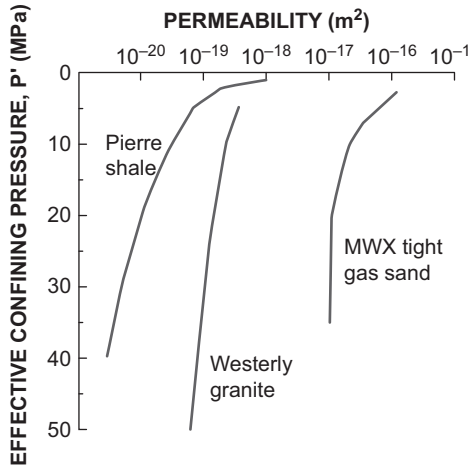

FIGURE 11.5 Permeability versus effective confining pressure for Pierre shale (Neuzil, 1986), Westerly granite (Brace et al., 1968), and MWX tight gas sand (Kilmer et al., 1987), from Rutqvist and Stephansson (2003).

Permeability can also be correlated to porosity. One early example of this is the Carman−Kozeny equation (Scheidegger, 1974), in which permeability varies with porosity according to:

$$k \sim \frac{\phi^3}{(1-\phi)^2} \tag{11.74}$$

Davies and Davies (2001) presented an exponential function for permeability in terms of porosity from laboratory experiments on sedimentary rock:

$$k = k_0 e^{c\left(\frac{\phi}{\phi_0}-1\right)} \tag{11.75}$$

Verma and Pruess (1988) presented a power law expression relating permeability to porosity:

$$\frac{k-k_\infty}{k_0-k_\infty} = \left(\frac{\phi-\phi_\infty}{\phi_0-\phi_\infty}\right)^n \tag{11.76}$$

where k_∞ and ϕ_∞ are asymptotic values of permeability and porosity, respectively.

Davies and Davies (2001) also presented the following function for porosity as a function of effective stress from their laboratory experiments on sedimentary rock:

$$\phi = \phi_1 + (\phi_0 - \phi_1)e^{-c\tau'} \tag{11.77}$$

where the reference porosity, ϕ_0, is at zero effective stress porosity, and ϕ_1 is porosity at high effective stress.

An expression for porosity versus effective stress and other variables was obtained starting with the definition of porosity (Winterfeld and Wu, 2014). Porosity is the ratio of fluid volume to bulk volume, and because fluid volume plus solid volume equals bulk volume, porosity can be written as:

$$\phi = 1 - \frac{V_s}{V} \tag{11.78}$$

where V is bulk volume and V_s is solid volume. Gutierrez and Lewis (2001) presented expressions for solid volume change with pressure and effective stress. These expressions can be integrated to yield the following:

$$V_s = V_{s,0}\left(1 + \frac{1-\phi_0}{K_s}(P - P_0) - \frac{1}{K_s}\left(\tau'_m - \tau'_{m,0}\right)\right) \tag{11.79}$$

Combining Eqs. (11.78), (11.79), and (11.38), the relation between bulk volume and volumetric strain, yields porosity as a function of pore pressure and effective stress:

$$\phi = 1 - (1-\phi_0)\frac{\left(1 + \frac{1-\phi_0}{K_s}(P - P_0) - \frac{1}{K_s}\left(\tau'_m - \tau'_{m,0}\right)\right)}{(1-\varepsilon_v)} \tag{11.80}$$

Permeability and porosity are also used to scale capillary pressure according to the relation by Leverett (1941):

$$P_c = P_{c0}\sqrt{\left(\frac{\phi}{k}\right)\left(\frac{k}{\phi}\right)_0} \tag{11.81}$$

11.5.2 Fractured Media

A fractured medium can be conceptualized as consisting of flow channels that are thin slits through which fluid flows. Fluid flow through these slits is often laminar, and the volumetric flow rate is proportional to the slit width, or fracture aperture, cubed. Experimental investigation (Witherspoon et al., 1980, for example) has confirmed the validity of this cubic dependence.

Rutqvist et al. (2002) presented correction factors for fractured rock permeability, porosity, and capillary pressure that account for changes in the stress field and pressure. These corrections depend on reference and current fracture apertures in the x-, y- and z-directions. For porosity, the correction is a simple ratio of fracture apertures:

$$\phi = \phi_0 \frac{b_x + b_y + b_z}{b_{x,0} + b_{y,0} + b_{z,0}} \tag{11.82}$$

where b_i is the fracture aperture in direction i. The corrections for permeability are a ratio of fracture apertures cubed due to the cubic dependence of

volumetric flow rate to fracture aperture and the permeability in one direction only depends on fracture apertures in the other two directions:

$$k_x = k_{x,0}\frac{b_y^3 + b_z^3}{b_{y,0}^3 + b_{z,0}^3} \tag{11.83}$$

$$k_y = k_{y,0}\frac{b_x^3 + b_z^3}{b_{x,0}^3 + b_{z,0}^3} \tag{11.84}$$

$$k_z = k_{z,0}\frac{b_x^3 + b_y^3}{b_{x,0}^3 + b_{y,0}^3} \tag{11.85}$$

The correction for capillary pressure is similar to that for isotropic porous media (Eq. 11.81):

$$P_c = P_{c0}\sqrt{\left(\frac{k_{x,0}}{k_x}\frac{k_{y,0}}{k_y}\frac{k_{z,0}}{k_z}\right)^{\frac{1}{3}}\left(\frac{\phi}{\phi_0}\right)} \tag{11.86}$$

Fracture apertures were correlated to normal effective stress using an exponential function:

$$b_x = b_{x,0} + \Delta b_x\left(e^{c\tau'_{xx}} - e^{c\tau'_{xx,0}}\right) \tag{11.87}$$

$$b_y = b_{y,0} + \Delta b_y\left(e^{c\tau'_{yy}} - e^{c\tau'_{yy,0}}\right) \tag{11.88}$$

$$b_z = b_{z,0} + \Delta b_z\left(e^{c\tau'_{zz}} - e^{c\tau'_{zz,0}}\right) \tag{11.89}$$

where normal effective stress is given by:

$$\tau'_{kk} = \tau_{kk} - \alpha P; \quad k = x, y, z \tag{11.90}$$

and Δb_i is the direction i aperture increase.

11.6 CAPROCK FRACTURING AND FAULT REACTIVATION

In this section, we describe our modeling of caprock fracturing and fault reactivation. Although sequestered carbon dioxide is supercritical when injected into the storage aquifer, it is still less dense than the native brine, and therefore an aquifer suitable for carbon dioxide sequestration would need to be overlain by sufficient low-permeability, sealing caprock throughout the time frame of the process. However, geological systems such as caprock contain heterogeneities and discontinuities such as fractures and faults, and the reservoir pressurization associated with carbon dioxide sequestration can

potentially activate these fractures and faults, providing paths for carbon dioxide migration outside the storage zone. In addition, sufficiently large reservoir pressurization can hydraulically fracture the caprock and create the aforementioned pathways. The modes of caprock integrity loss that we model here are tensile failure of caprock from excess pressurization, fault reactivation, and shear failure of a fault or caprock.

11.6.1 Caprock Tensile Failure

Caprock can undergo tensile failure, forming hydraulic fractures, when pressurization from CO_2 injection becomes too large. A common assumption (for example, Chin et al. (2012) and Rutqvist et al. (2008)) is that tensile failure could occur when the fluid pressure exceeds the least compressive principal stress. Such an assumption, a conservative one, is based on the notion that the grain–grain interfaces in the caprock have negligible tensile strength and those interfaces will break as soon as the effective stress in one direction becomes zero. In our formulation, we include a more general caprock tensile failure criterion that allows for nonzero tensile strength:

$$P \geq \sigma_3 + \sigma_{tn} \tag{11.91}$$

where σ_{tn} is tensile strength and σ_3 is the least compressive principal stress. We apply Eq. (11.91) to each grid block. When Eq. (11.91) is satisfied, we then conceptualize the initialization of a single uniform fracture, perpendicular to the minimum principle stress direction, in the grid block. We estimate the width of this fracture using an expression (Settari and Warren, 1994; Goodarzi et al., 2012) based on the two-dimensional Perkins and Kern (1961) fracture model:

$$w_{fr} = \frac{4(1-\upsilon^2)h_{fr}}{E}(P-\sigma_3) \tag{11.92}$$

where E is Young's modulus, ν is Poisson's ratio, h_{fr} is the fracture half height, and w_{fr} is the fracture width. The initialization of this fracture modifies the grid block permeability and porosity. The overall porosity of this grid block is obtained from the volume of the fracture, the grid block matrix pore volume, and the grid block matrix bulk volume:

$$\phi = \frac{w_{fr}A_{fr} + V_m\phi_m}{w_{fr}A_{fr} + V_m} \approx \phi_m + \frac{w_{fr}A_{fr}}{V_m} \tag{11.93}$$

where A_{fr} is the fracture face area and m refers to the grid block matrix. We model permeability by conceptualizing flow as occurring through both the fracture and the grid block matrix. For flow orthogonal to the principle

minimum stress direction, we average the fracture and grid block matrix permeabilities in parallel with cross-sectional area weighting:

$$k_k = \frac{k_{fr} w_{fr} \Delta x_{lj} + k_m \Delta x_l \Delta x_j}{\Delta x_{lj} + \Delta x_l \Delta x_j} \tag{11.94}$$

where k, l, and j each refer to a Cartesian direction, Δx is grid block length, and Δx_{lj} is the height of the fracture when projected into the lj-face. Permeability is unchanged for flow along the principle minimum stress direction, because fracture permeability is assumed to be much greater than the grid block matrix permeability and flow through the matrix and fracture is in series. Fracture permeability is obtained from the well-known expression for laminar flow through a slit:

$$k_{fr} = \frac{w_{fr}^2}{12} \tag{11.95}$$

Continued injection of fluid would cause the fracture width to increase and the fracture to extend. We allow fractures to extend into neighboring grid blocks that do not already contain a fracture. We track a fracture front position for this extension. When the front exceeds the appropriate dimension of the neighboring grid block, a fracture is initiated in that grid block. The criterion for the movement of a fracture front is given by Mastrojannis et al. (1980), who correlated the velocity of the extending fracture front as:

$$v = C\left(\frac{K_I - K_{IC}}{K_{IC}}\right)^n \tag{11.96}$$

where C and n are parameters that depend on the medium, K_{IC} is rock toughness, and K_I is stress intensity factor at the fracture tip. Yew and Weng (2015) gives an expression for this stress intensity factor:

$$K_I = \frac{E}{8(1-\upsilon^2)}\left(\frac{2\pi}{r}\right)^{\frac{1}{2}} w_{fr}(r) \tag{11.97}$$

where r is distance from the fracture front. We evaluate stress intensity factor using the fracture width calculated from Eq. (11.92), and the grid block half dimension along the direction of fracture front propagation plus the fracture front propagation distance for the distance r from the fracture front.

11.6.2 Fault and Fracture Reactivation

Faults are complex systems consisting of a relatively thin inner core zone that has a low permeability and is surrounded by a fractured damage zone (Wibberley et al., 2009). Injection into a reservoir containing faults would alter the stress and pressure fields and can change the flow properties of a fault, such as reactivating it by increasing its ability to transmit fluid. We conceptualize

the faulted or fractured caprock region as consisting of a network of fractures that may be randomly oriented or have a preferred direction. The permeability and porosity of this region can change with changes in the stress and pressure, and we generalize these dependences as:

$$\phi = \phi(\boldsymbol{\tau}, P) \tag{11.98}$$

and

$$k_j = k_j(\boldsymbol{\tau}, P) \tag{11.99}$$

where the subscript j refers to a Cartesian direction ($j = 1$, 2, or 3). One instance of such dependence, outlined previously, is from Rutqvist et al. (2002), which conceptualized the fractured medium as an array of cubic blocks with the fractures being the interfaces between them. These fractures are equally spaced and oriented normal to each Cartesian direction. A fracture aperture is associated with each interface, and correlations for fracture porosity and permeability were based on those apertures and appear in Eqs. (11.82)–(11.85).

11.6.3 Caprock Shear Failure

Faults or weak zones in caprock can undergo shear failure when the shear stress acting on a caprock plane exceeds its shear strength. The most common shear failure criterion is the Coulomb (1773) one. Shear failure is likened to a sliding mass on a plane. The force acting on the mass is friction, which resists sliding, and is given by its weight multiplied by a friction factor, and a force exerted on the mass in the direction of the plane that causes it to slide. For the Coulomb criteria, the sliding force is the shear stress on the caprock plane, the frictional force is the normal stress on the caprock plane, and an additional term is added that represents the cohesive strength of the material. In addition, when applied to poroelastic media, the normal stress is replaced by the effective normal stress (Terzaghi, 1936):

$$\tau = C_0 + \mu\sigma' \tag{11.100}$$

where C_0 is the cohesion and μ is the coefficient of internal friction. If the orientation of the caprock plane is specified, such as when considering a fault with a given orientation, the stress acting on that plane can be obtained by taking the dot product of the effective stress tensor with that plane's normal vector. That stress has components normal to that plane (the normal effective stress in Eq. (11.100)) and along that plane (the shear stress in Eq. (11.100)). For cases in which there is no specified plane, for example, caprock containing randomly oriented fractures, shear failure would occur when the shear and effective normal stresses acting on an arbitrary plane in the caprock satisfy Eq. (11.101). These effective normal and shear stresses

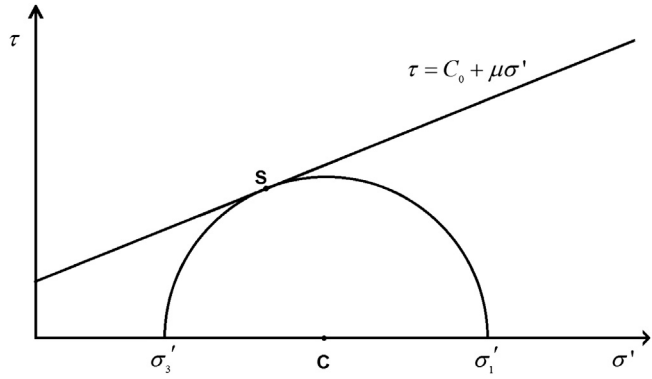

FIGURE 11.6 Mohr–Coulomb failure diagram in shear stress–normal effective stress space, with the Mohr circle centered at point "C" and failure line tangent to Mohr circle at point "S" when shear failure would occur. The Mohr circle range is from the minimum normal effective stress (subscript 3) to the maximum (subscript 1).

are obtained from the well-known Mohr circle (Jaeger et al., 2007), which in equation form is:

$$\sigma' = \frac{(\sigma_1' + \sigma_3')}{2} + \frac{(\sigma_1 - \sigma_3)}{2}\cos 2\,\theta \tag{11.101}$$

and

$$\tau = -\frac{(\sigma_1 - \sigma_3)}{2}\sin 2\,\theta \tag{11.102}$$

where the subscript 1 refers to the maximum principal stress, the subscript 3 refers to the minimum principal stress, and θ is the angle measured from the first principal stress direction. Shear failure can be represented graphically as the intersection of the Mohr circle (Eqs. 11.101 and 11.102) with the Coulomb criterion (Eq. 11.100), shown in Fig. 11.6.

Shear failure may be accompanied by irreversible mechanical changes, including activating old fractures, forming new ones, as well as wave propagation, ground motion, and even earthquakes (Häring et al., 2008). The prediction of shear failure is simulated in our model; however, because our geomechanical formulation is based on an elastic medium, the simulation of these irreversible mechanical changes is beyond the scope of it.

11.7 EXAMPLE SIMULATIONS

We provide example problems for code verification and demonstration of simulator capabilities here. The first two problems are comparisons of simulation to analytical solutions to verify our geomechanical formulation. These are the displacement caused by a uniform load on a semiinfinite elastic medium and the two-dimensional Mandel–Cryer effect. The next two, intended to further verify our geomechanical formulation, show comparisons

of our simulator to published results. These are a single-phase depletion problem and a simulation of CO_2 injection into a depleting gas reservoir. Following these are problems for the verification of our caprock fracturing and fault reactivation formulation. We run a simulation, from the literature, of caprock leakage resulting from carbon dioxide injection, match published results, and demonstrate the simulator's capability of predicting shear failure. We then run a variant of that problem where we simulate normal effective stress dependence of fracture permeability and porosity. Finally, we simulate an experiment of pressure-induced fracturing of a concrete block that includes tensile failure.

11.7.1 Displacement From a Uniform Load on a Semiinfinite Elastic Medium

Given a semiinfinite elastic medium, the displacement caused by a uniform load acting on its surface over a circular area of radius a is given by Timoshenko and Goodier (1951) as:

$$w(r) = \frac{4(1-\nu^2)pr}{\pi E}\left[\int_0^{\frac{\pi}{2}} \sqrt{1-\frac{r^2}{a^2}\sin^2\theta}\, d\theta\right], \quad r < a$$

$$w(r) = \frac{4(1-\nu^2)pr}{\pi E}\left[\int_0^{\frac{\pi}{2}} \sqrt{1-\frac{a^2}{r^2}\sin^2\theta}\, d\theta - \left(1-\frac{a^2}{r^2}\right)\int_0^{\frac{\pi}{2}} \frac{d\theta}{\sqrt{1-\frac{a^2}{r^2}\sin^2\theta}}\right], \quad r > a \tag{11.103}$$

where p is the load, $w(r)$ is displacement at a radius r from the center of the circle, and the integrals in the brackets are elliptic integrals of the first and second kind. The normal z-direction stress along the z-axis at the center of the circle is given as well:

$$\tau_{zz} = p\left[-1+\frac{z^3}{(a^2+z^2)^{\frac{3}{2}}}\right] \tag{11.104}$$

We used this analytical solution to verify the calculation of normal stress tensor components. We approximated the semiinfinite medium as a large rectangular parallelepiped 194 m in the x- and y-directions and 1320 m in the z-direction. We subdivided this medium into a $200 \times 200 \times 800$ Cartesian grid. Grid block x- and y-direction length in the vicinity of the center was 0.1 m and increased further away from it. Grid block z-direction length was 0.2 m in the vicinity of the surface and increased further away from it. The loaded circle was located at the center of the top xy-face and had a 1.0 m radius. Because our grid was Cartesian, we approximated this circle as 314 loaded squares of radius 0.1 m, as shown in Fig. 11.7. The rest of the medium's surface had no load exerted on it.

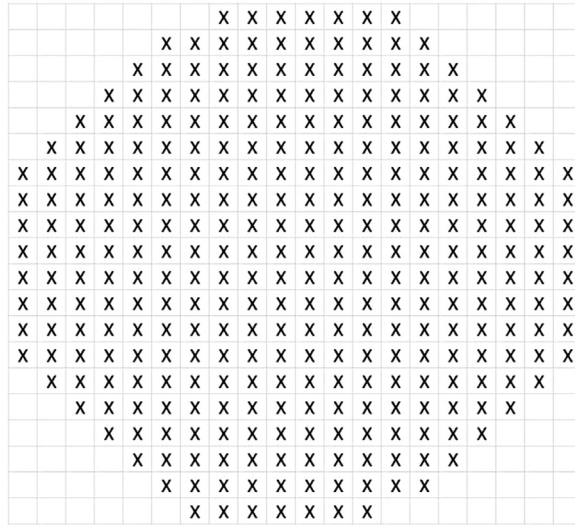

FIGURE 11.7 Approximation of loaded 1.0-m-radius circle by 314 square grid blocks of length 0.1 m.

Our geomechanical formulation requires boundary conditions for mean stress and those stress tensor components that are calculated. We specified a mean stress of 0.48 MPa and a normal z-direction stress (the load) of 0.6 MPa over the loaded circle. The equal x- and y-direction normal stresses were then 0.42 MPa. There is no fluid or heat flow in this problem, so only mean stress and stress tensor components are solved. We solve the mean stress first, and calculate stress tensor components next using the mean stress solution. Because grid block geometry depends on stress tensor components that are evaluated at the previous time step, we must repeat these calculations over a number of time steps until the stress tensor components do not change between successive time steps. This converged solution is the fully coupled or fully implicit solution to these stress equations.

The displacement caused by the load is the change of the medium's overall length in the direction of the applied load, given by:

$$w = \sum D_{0,z}\varepsilon_{zz} \tag{11.105}$$

where $D_{0,z}$ is grid block unstrained length in the z-direction and the sum is over a z-direction column of grid blocks. The z-direction normal strain is calculated from Hooke's law:

$$\varepsilon_{zz} = \frac{1}{E}(\tau_{zz} - \upsilon(\tau_{xx} + \tau_{yy})) \tag{11.106}$$

The analytical and simulated displacements are shown in Fig. 11.8 and those for the z-direction normal stresses are shown in Fig. 11.9. In both cases, they are hardly distinguishable.

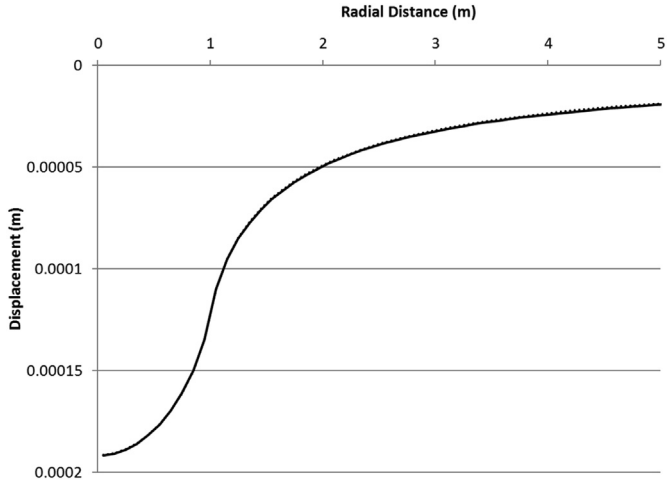

FIGURE 11.8 Analytical (*solid line*) and simulated (*dotted line*) displacements for a semiinfinite medium subjected to circular load.

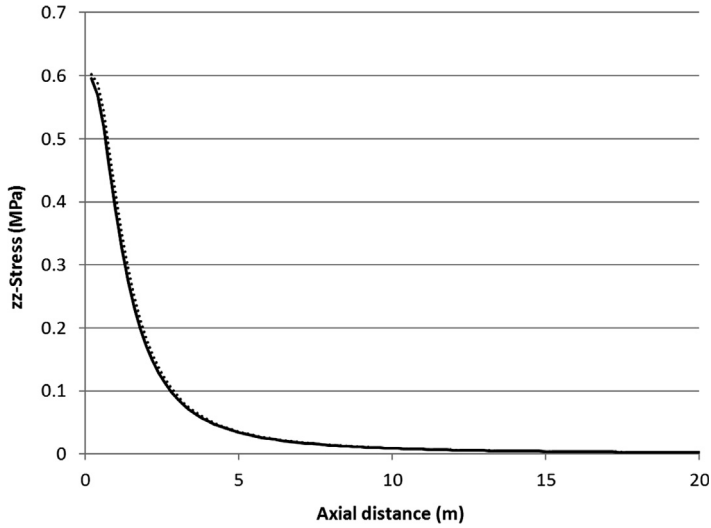

FIGURE 11.9 Analytical (*solid line*) and simulated (*dotted line*) *z*-direction normal stresses for a semiinfinite medium subjected to circular load.

11.7.2 Two-Dimensional Mandel–Cryer Effect

Consider a fluid-filled poroelastic material with a constant compressive force applied to the top and bottom. There is an instantaneous compression and uniform pore pressure increase due to the force. Afterward, the material is allowed to drain laterally. Drainage is accompanied by a decrease in pore

pressure near the edges and the material becomes less stiff, resulting in a load transfer to the center and a pore pressure increase that reaches a maximum and then declines. This pore pressure behavior is the Mandel–Cryer effect (Mandel, 1953) and Abousleiman et al. (1996) derived an analytical solution to it. We use this analytical solution to verify our coupled fluid flow and geomechanics calculations.

Our simulation domain is 1000 m square and is subdivided into a uniform Cartesian 200 × 200 grid. Rock properties are the following: porosity is 0.094, permeability is 10^{-13} m^2, Young's modulus is 5.0 GPa, Poisson's ratio is 0.25, and the Biot coefficient is 1.0.

We simulate the compression and then the drainage. The initial unstrained state is pore pressure and normal stress components at 2.0 MPa. The compressive portion of the simulation, with an imposed mean stress of 5.0 MPa at the top and bottom, is run until equilibrium is reached. The pore pressure increases to 3.28 MPa in this step and the mean stress becomes a uniform 5.0 MPa throughout the simulation domain. Because the lateral boundaries are free, the x- and y-direction effective stresses are zero, so the normal stresses in those directions are 3.28 MPa, and the normal z-direction stress is therefore 8.44 MPa.

In the drainage portion of the simulation, the initial pore pressure (2.0 MPa) is imposed at the lateral boundaries. Because the effective stresses are zero, the x- and y-direction normal stresses have that value. The normal z-direction stresses at the top and bottom remain at 8.44 MPa. The drainage simulation is run for 100,000 s with 100-s time steps. Fig. 11.10 shows the match of centerline pore pressure with the analytical solution. The

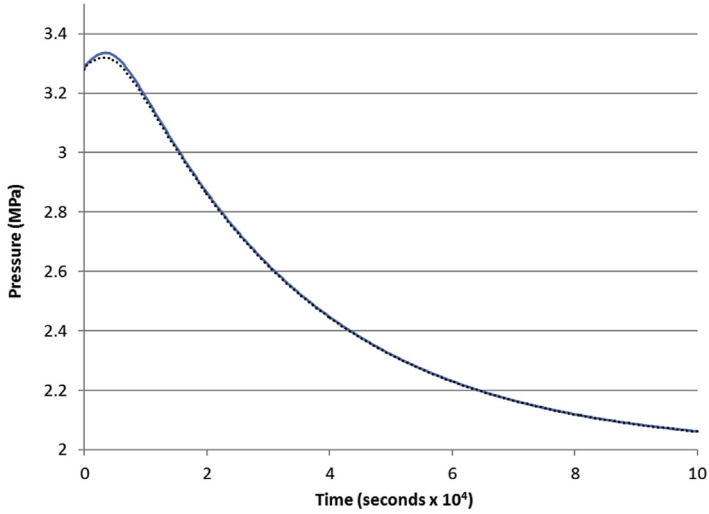

FIGURE 11.10 Match of simulated centerline pore pressure (*dotted line*) with analytical solution (*solid line*) for Mandel–Cryer effect.

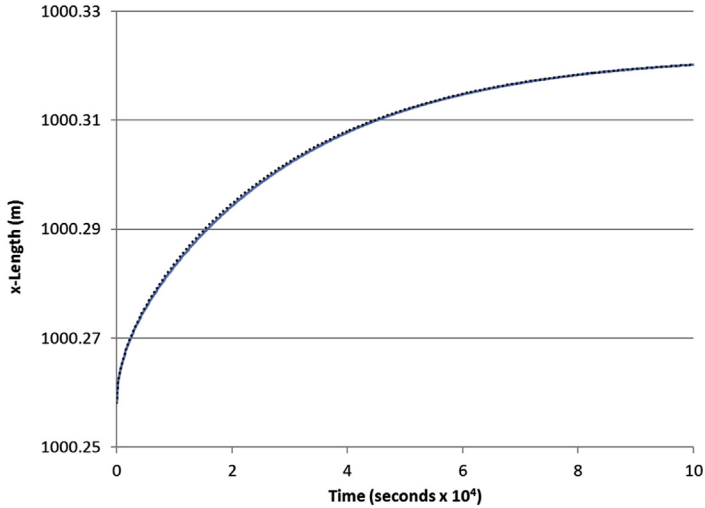

FIGURE 11.11 Match of simulated *x*-direction displacement (*dotted line*) with analytical solution (*solid line*) for Mandel–Cryer effect.

displacements in the *x*- and *z*-directions are calculated as was done in the previous example problem. The applied stress causes the system to contract in the *z*-direction and expand in the *x*-direction. The expansion, shown in Fig. 11.11, is matched almost perfectly and the match of the contraction, shown in Fig. 11.12, shows only a small deviation from the analytical solution at early times.

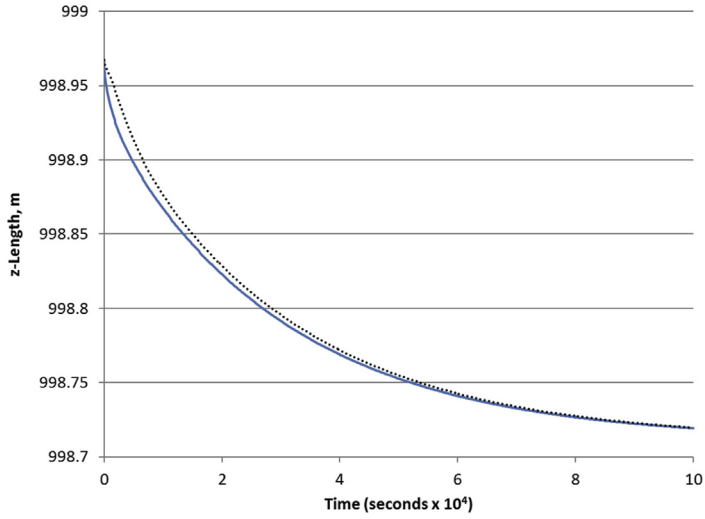

FIGURE 11.12 Match of simulated *z*-direction displacement (*dotted line*) with analytical solution (*solid line*) for Mandel–Cryer effect.

11.7.3 Depletion of a Single-Phase Reservoir

We ran the depletion of a single-phase reservoir, adapted from Dean et al. (2006), as a comparison of our simulator to published results. A single-phase (water) reservoir, 671 m^2 in area and 61 m thick, with a single vertical well at the center and completed along the entire thickness, was produced at a constant rate of 27.59 kg/s for 500 days. Reservoir porosity was initially 0.20, horizontal permeability was $5 \cdot 10^{-14}$ m^2, vertical permeability was $5 \cdot 10^{-15}$ m^2, Young's modulus was $6.87 \cdot 10^7$ Pa, Poisson's ratio was 0.30, and the rock density was 2700 kg/m^3. The z-direction stress at the reservoir top was 41.4 MPa, and the constant horizontal stresses were 27.6 MPa. Pore pressure at the reservoir top was 20.7 MPa. Pore pressure increased with increasing depth due to the hydrostatic gradient, and z-direction stress increased with increasing depth due to the overburden.

Our Cartesian grid was $11 \times 11 \times 10$ with constant grid block dimensions, and our time step size was 50 days. We used the same relations for porosity and grid block volume as was used by Dean et al. (2006); grid block volume was constant and porosity varied with volumetric strain as:

$$\phi = \phi_i + \varepsilon_{v,i} - \varepsilon_v \tag{11.107}$$

where the subscript "i" refers to initial conditions.

Fig. 11.13 shows a comparison of average reservoir pressure, and Fig. 11.14 shows a comparison of subsidence around the well, between our simulation and that of Dean et al. (2006). The average reservoir pressure match necessitated the usage of the above grid block volume and porosity relations

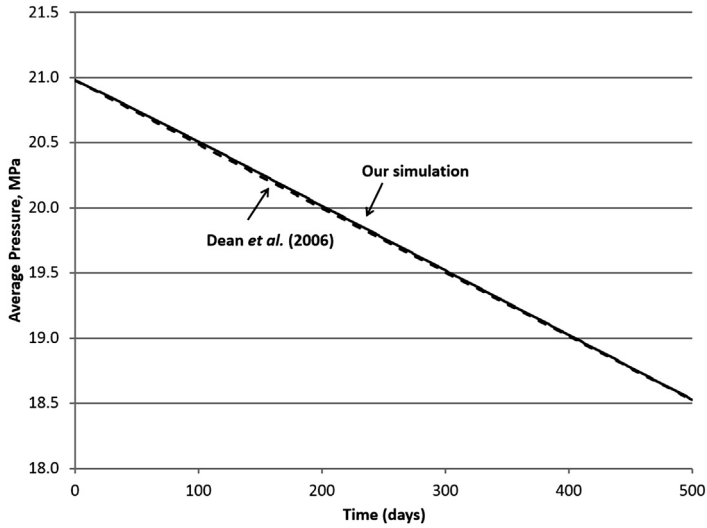

FIGURE 11.13 Average pore pressure from our simulation compared to that of Dean et al. (2006).

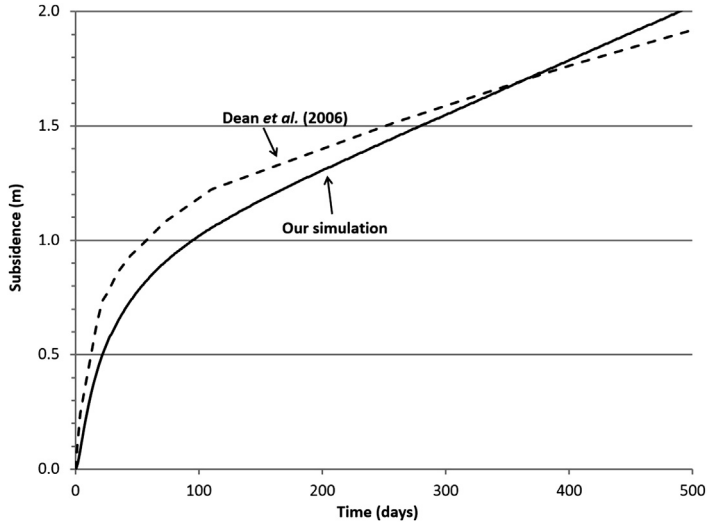

FIGURE 11.14 Subsidence from our simulation compared to that of Dean et al. (2006).

and would not have been as good if grid block volume varied with volumetric strain and porosity varied with effective stress using a different correlation. Our subsidence is very similar to the published results and differs by about 5% at 500 days.

11.7.4 In Salah Gas Project

The In Salah Gas Project, located in central Algeria, is a CO_2 storage project. Natural gas produced nearby is high in CO_2 and this CO_2 is injected back into the water leg of a depleting gas field for geological storage. Surface uplift from CO_2 injection has been measured by satellite-based interferometry, and Rutqvist et al. (2010) did a reservoir-geomechanical analysis of In Salah CO_2 injection and surface uplift using the TOUGH2-FLAC numerical simulator (Rutqvist et al., 2002) to determine if the uplift can be explained by pressure changes and deformation in the injection zone only. We reran their analysis on our simulator to match their simulated results.

The domain was $10 \times 10 \times 4$ km with one 1.5 km horizontal injection well at 1810 m depth and in the domain center. The domain consisted of four geological layers, Shallow Overburden, Caprock, Injection Zone, and Base, whose properties are shown in Table 11.2. The reservoir initially contained water at hydrostatic equilibrium. The initial temperature and pressure at the injection well were 90°C and 18.5 MPa, respectively. The initial stress tensor was calculated as outlined previously with the normal stress ratios R_{xz} and R_{yz} being 1.2 and 0.8, respectively. The lateral reservoir boundaries were maintained at constant pressure, the reservoir boundaries were maintained at

TABLE 11.2 Geological Layer Properties for In Salah CO_2 Injection

Property	Shallow Overburden (0–900 m)	Caprock (900–1800 m)	Injection Zone (1800–1820 m)	Base (>1800 m)
Young's modulus (GPa)	1.5	20.0	6.0	20.0
Poisson's ratio	0.2	0.15	0.2	0.15
Biot's coefficient	1.0	1.0	1.0	1.0
Porosity	0.1	0.01	0.17	0.01
Permeability (m^2)	$1.0 \cdot 10^{-17}$	$1.0 \cdot 10^{-19}$	$0.875 \cdot 10^{-14}$	$1.0 \cdot 10^{-21}$
Residual CO_2 saturation	0.05	0.05	0.05	0.05
Residual liquid saturation	0.3	0.3	0.3	0.3
Van Genuchten (1980) (m)	0.457	0.457	0.457	0.457
Van Genuchten, P_0 (kPa)	19.9	621.0	19.9	621.0

constant stress, and CO_2 was injected at 9.734 kg/s for 3 years. Surface uplift results from changes in grid block height and is calculated using Eqs. (11.105) and (11.106).

Our simulation was over a $5 \times 5 \times 4$ km quarter symmetry element of the domain using a $50 \times 50 \times 60$ grid. In all three directions, the grid was finer in the vicinity of the well and became coarser away from it. Fig. 11.15 compares pressure change versus depth. We modified the Rutqvist et al. (2010) Injection Zone permeability somewhat to match the pressure change there after 3 years. Their simulation used a much coarser grid than ours (about 10,000 grid blocks for the entire domain) and is reflected by their piecewise-linear pressure profile. Fig. 11.16 compares vertical displacement versus depth at the injection well center after 3 years. Both simulators give similar displacement profiles.

11.7.5 CO_2 Leakage Through Fault Zones

Rinaldi et al. (2014) studied fault responses during underground carbon dioxide injection and focused on the short-term integrity of the sealing caprock and the potential for leakage. They considered stress/strain-dependent permeability and studied leakage through a fault zone as its permeability

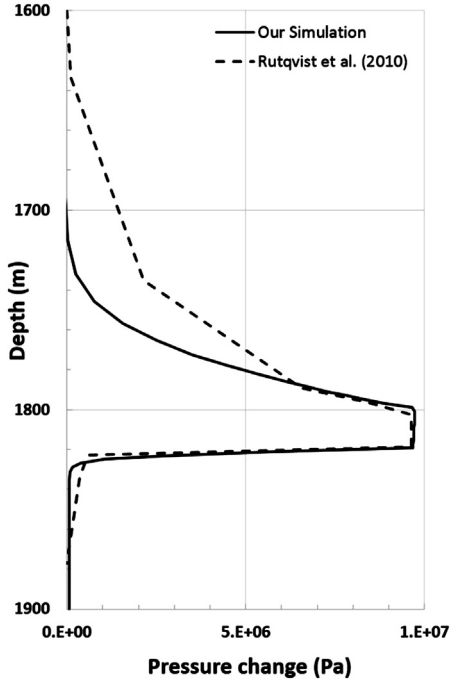

FIGURE 11.15 Pressure change at injection well center after 3 years of injection.

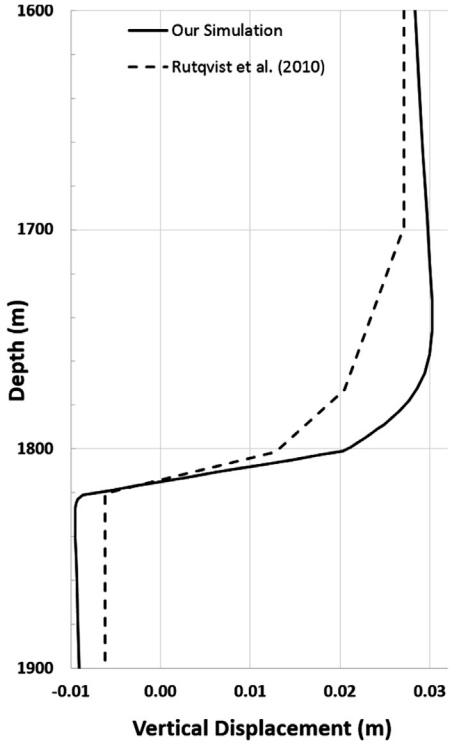

FIGURE 11.16 Vertical displacement at injection well center after 3 years of injection.

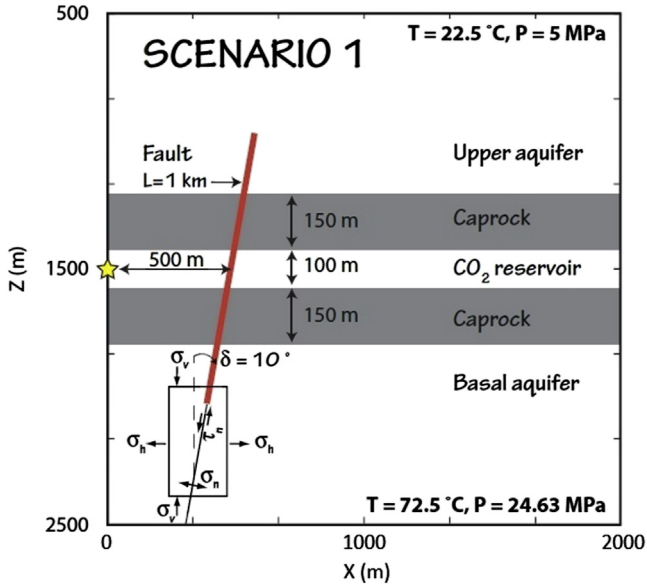

FIGURE 11.17 Schematic of "Scenario 1," showing rock layers and fault. Injection site starred point at 1500 m depth. *adapted from Rinaldi et al. (2014)*

changes during reactivation. We ran some of their simulations using our model. Their "Scenario 1" (Mazzoldi et al., 2012) was a two-dimensional system with a minor 1-km fault that intersected a 100-m-thick injection aquifer bounded above and below by a 150-m-thick low-permeability caprock, shown in Fig. 11.17, and rock properties shown in Table 11.3. Permeability and porosity depend on effective stress and is given by Eqs. (11.75) and (11.77), respectively.

We simulated this system using a 190 × 145 grid. Grid block x-direction length was 20 m, except for the *x*-direction interval the fault was located in where it was 2 m. Grid block *y*-direction length was 20 m, except for the CO_2 reservoir and caprock layers where it was 10 m. The fault was represented by a series of connected grid blocks that approximately lie on the fault line shown in Fig. 11.17. We ran two cases, the first with fault permeability 10^{-14} m^2 and CO_2 injection rate of 0.10 kg/s m, and the second with fault permeability 10^{-16} m^2 and CO_2 injection rate of 0.02 kg/s m, for 5 years. Figs. 11.18 and 11.19 compare our fault permeability change at 1 and 5 years with those from the reference. There is good qualitative agreement between the two.

We also ran this simulation with a Mohr−Coulomb failure envelope to demonstrate that capability of the simulator to predict where shear failure of the fault could occur (). The cohesion was zero and the coefficient of internal friction was 0.6. Fig. 11.20 shows the predicted failure regions at varying

TABLE 11.3 Rock Properties Used Aquifer-Caprock System

Property/Layer	Upper	Caprock	CO_2 Reservoir	Basal	Fault
Young's modulus (GPa)	10.0	10.0	10.0	10.0	5.0
Poisson's ratio	0.25	0.25	0.25	0.25	0.25
Porosity	0.10	0.01	0.10	0.01	0.10
Permeability (m^2)	10^{-14}	10^{-19}	10^{-13}	10^{-16}	10^{-14}–10^{-16}
Residual CO_2 saturation	0.05	0.05	0.05	0.05	0.05
Residual liquid saturation	0.3	0.3	0.3	0.3	0.3
Van Genuchten (1980) P_0 (kPa)	19.9	621	19.9	621	19.9
Van Genuchten (1980) (m)	0.457	0.457	0.457	0.457	0.457

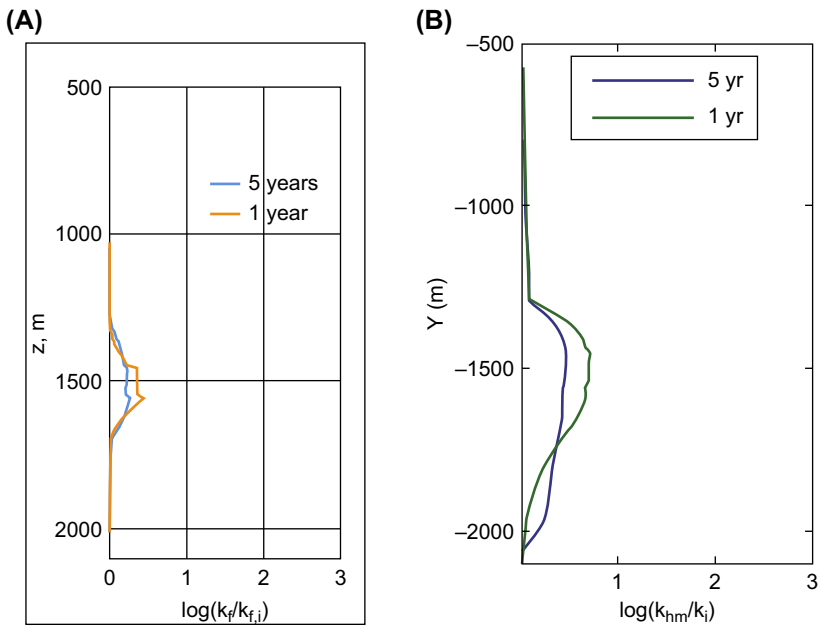

FIGURE 11.18 Fault permeability increase for our simulation (A) and reference (B) for fault permeability of 10^{-14} m^2 and CO_2 injection rate of 0.10 kg/s m.

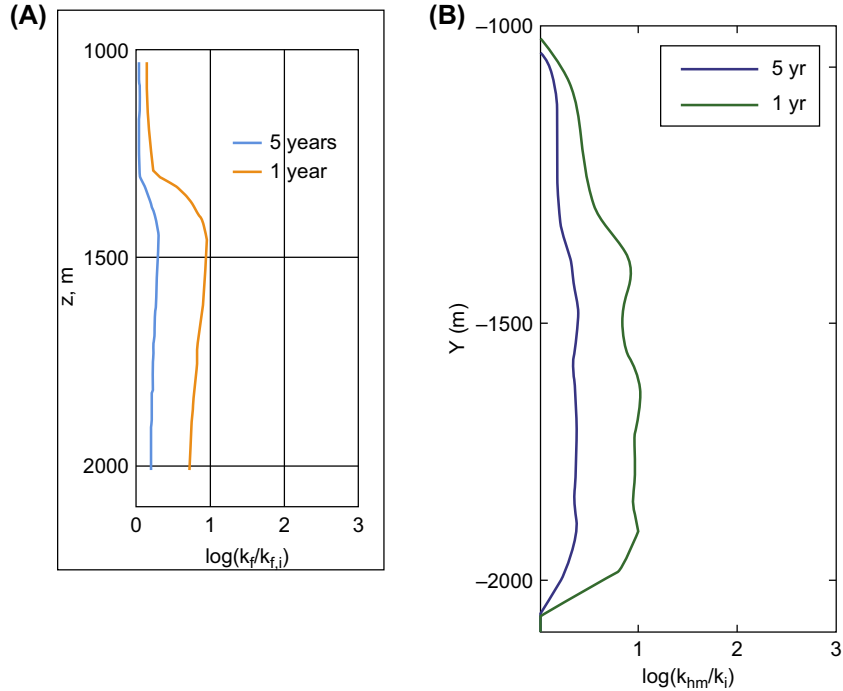

FIGURE 11.19 Fault permeability increase for our simulation (A) and reference (B) for fault permeability of 10^{-16} m^2 and CO_2 injection rate of 0.02 kg/s m.

times. These regions only lie along the fault; those outside the fault are not subject to shear failure.

We ran a variant of this problem to demonstrate the calculation of permeability and porosity as a function of normal effective stress for a fractured medium (Eqs. 11.87−11.89). The previous fault was changed to a vertical one located at x-direction 500 m and whose z-direction range is from 1000 to 2000 m and represented by a column of grid blocks. The fault permeability in the z-direction depends on normal effective stress and because the fault is vertical, it depends on the normal x-direction stress component. Fault permeability in the x-direction does not change. We reran the case with fault permeability 10^{-14} m^2 and CO_2 injection rate of 0.10 kg/s m for 5 years. Fig. 11.21 shows the gas saturation at 1 and 5 years, and Fig. 11.22 shows the permeability increase at those times.

11.7.6 Fracture of a Concrete Block

To develop a fundamental understanding of CO_2 injection pressure-induced fracturing, we are doing laboratory studies using concrete representations of

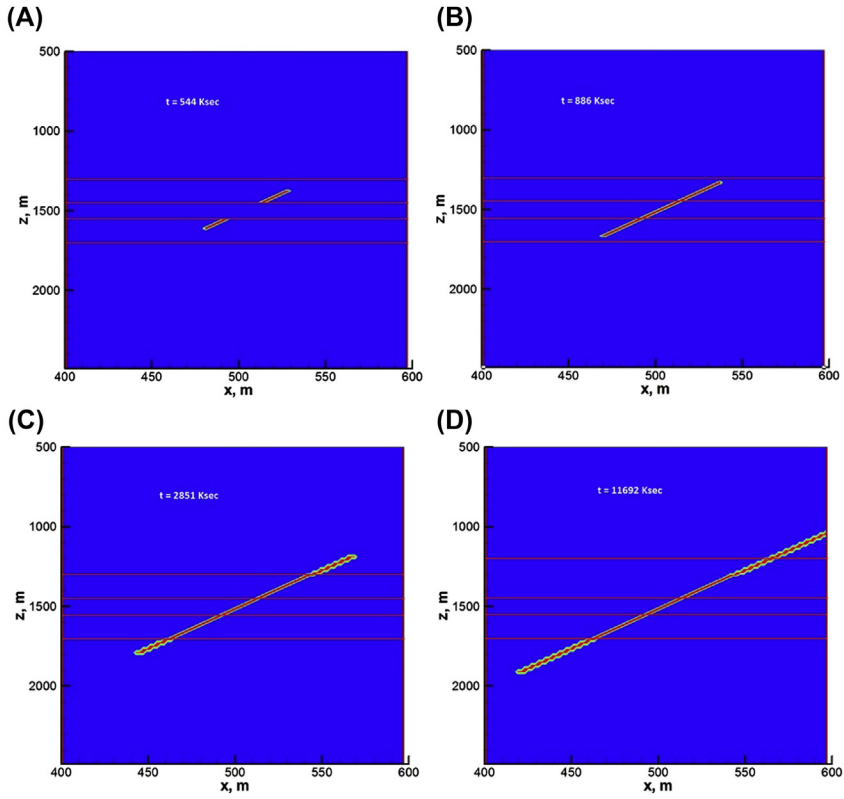

FIGURE 11.20 Mohr–Coulomb failure regions in fault shown at varying times: (A) 544 ks, (B) 886 ks, (C) 2851 ks, (D) 11692 ks.

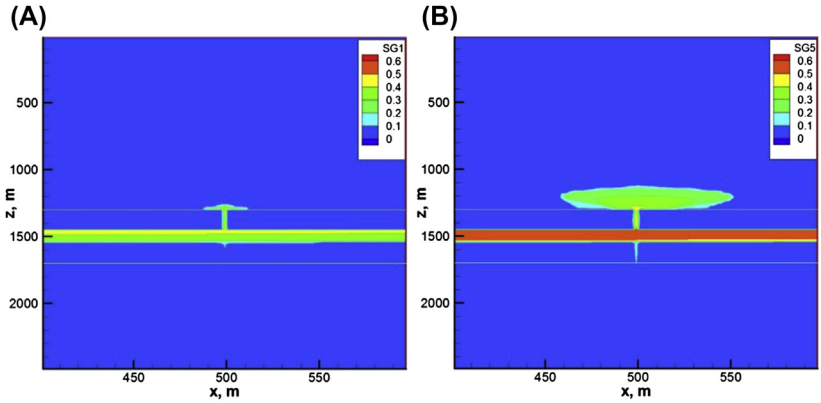

FIGURE 11.21 Gas saturation at (A) 1 and (B) 5 years. The *white lines* denote the boundaries between rock regions and the 1 km fracture, located at $x = 500$ m, is centered at $z = 1500$ m.

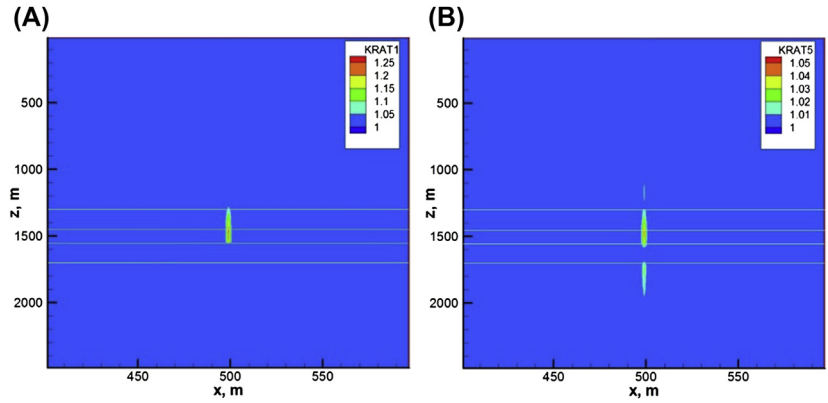

FIGURE 11.22 Permeability ratio at (A) 1 and (B) 5 years. The *white lines* denote the boundaries between rock regions and the 1 km fracture, located at $x = 500$ m, is centered at $z = 1500$ m.

caprock to determine the correlations between confining stress, fluid pressure, and fracturing initialization during CO_2 injection. The equipment used for conducting these experiments includes a triaxial loading system, an injection pump, and data acquisition devices. Initially, we use injected brine to identify the critical stress needed to initiate fractures in these caprock representations, which are 8 in. cubes that are cored in the center to create a 6 in. bore hole. We simulate one of these experiments, called "Sample 39" (Wu and Winterfeld, 2016). The cube initially contains a gaseous phase and its properties are shown in Table 11.4. The bore hole is simulated as a porous medium with much higher permeability than the surrounding concrete.

TABLE 11.4 Properties for Brine Injection Experiment

	Concrete	Bore Hole
Young's modulus (GPa)	6.0	6.0
Poisson's ratio	0.2	0.2
Porosity	0.10	0.90
Permeability (m^2)	$1.0 \cdot 10^{-15}$	$1.0 \cdot 10^{-14}$
Biot's coefficient	1.0	0.0
Tensile strength (MPa)	2.0	–
Toughness (MPa)	0.1	–
Fracture extension A (m/s)	10.0	–
Fracture extension n	1.0	–

The confining stresses are 1000 psi in x-direction, 1500 psi in y-direction, and 2000 psi in z-direction. The lateral boundaries are at constant pressure and brine is injected at 40 mL/min uniformly along the lower half of the bore hole. The $11 \times 11 \times 11$ grid is uniform in size. Because the minimum confining stress is in the x-direction, the concrete block will fracture in the yz-plane that contains the bore hole. We allow fracturing to occur only in that plane, which has the x-direction index of 6 in the grid. Fig. 11.23 shows the simulated fracture at a time of 531 s. The fracture is initiated along the bore hole and extends outward. After the experiment is completed, the concrete block is dyed and broken apart by nitrogen to reveal the fracture induced by fluid injection. Fig. 11.24 shows the result of this. The fracture is shown by the darker zone that extends a distance from the bore hole. The simulated fracture is somewhat similar to the experiment in that the overall fracture extents are similar. The simulation is a highly idealized representation of this process and is not expected to match the experiment in detail. For example, the fracture obtained by the experiment is not symmetrical about the bore hole, whereas the simulation must be due to the nature of the data input (constant rock properties, and symmetry about the bore hole).

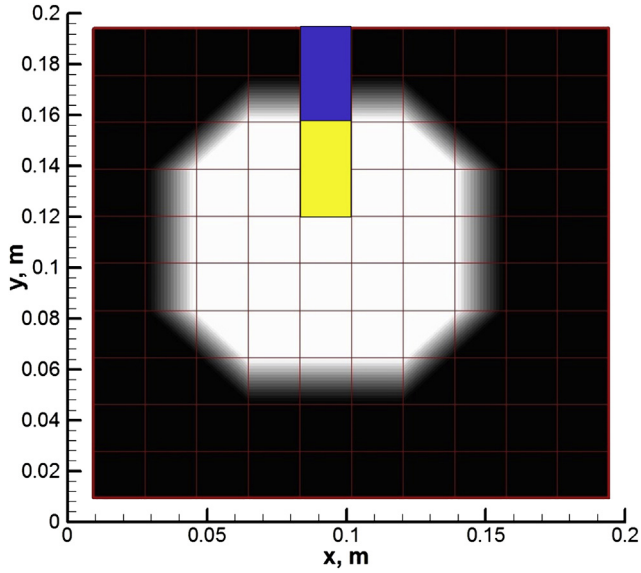

FIGURE 11.23 Simulated fracture of a concrete block. White indicates fracture, bore hole is in yellow (light gray in print version) and blue (dark gray in print version), with yellow (light gray in print version) the perforated region and blue (dark gray in print version) unperforated.

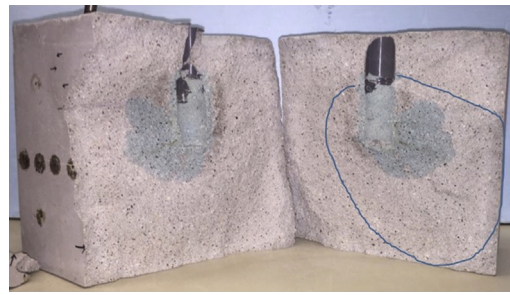

FIGURE 11.24 Internal fracture morphology of concrete sample after dyeing and gas breakdown.

11.8 SUMMARY AND CONCLUSIONS

We developed a THM reservoir simulator that is applicable to assessing the sealing capability of caprock. The geomechanical portion consists of an equation for mean stress, derived from linear elastic theory for a thermoporoelastic system, and equations for stress tensor components that depend on mean stress and other variables. The fluid and heat flow portion of our simulator is for general multiphase, multicomponent, multiporosity systems. We added the capability of simulating caprock failure scenarios, namely, tensile failure, fracture and fault reactivation, and shear failure, to the formulation.

We verified our geomechanical formulation by running two problems that had analytical solutions, the displacement caused by a uniform load on a semiinfinite elastic medium and the two-dimensional Mandel−Cryer effect, and obtained good agreement with those solutions. Then, we ran two additional problems that showed comparisons of our simulator to published results, a single-phase depletion problem and a simulation of CO_2 injection into a depleting gas reservoir, and also obtained agreement with those results. Finally, we ran problems that illustrated some of the simulator capabilities, including the normal effective stress dependence of fracture permeability and porosity and the simulation of an experiment of pressure-induced fracturing of a concrete block that includes tensile failure.

ACKNOWLEDGMENTS

This work was supported by the Foundation CMG, the EMG of the Colorado School of Mines, and the National Energy Technology Laboratory of the U. S. Department of Energy.

REFERENCES

Abousleiman, Y., Cheng, A.H.-D., Cui, L., Detournay, E., Roegiers, J.-C., 1996. Mandel's problem revisited. Géotechnique 46 (2), 187–195.

Bai, M., Elsworth, D., Roegiers, J.-C., 1993. Modeling of naturally fractured reservoirs using deformation dependent flow mechanism. International Journal of Rock Mechanics and Mining Science & Geomechanics Abstracts 30 (7), 1185–1191.

Biot, M.A., Willis, D.G., 1957. The elastic coefficients of the theory of consolidation. Journal of Applied Mechanics 24, 594–601.

Bower, K.M., Zyvoloski, G., 1997. A numerical model for thermohydro-mechanical coupling in fractured rock. International Journal of Rock Mechanics and Mining Sciences 34, 1201–1211.

Brace, W.F., Walsh, J.B., Frangos, W.T., 1968. Permeability of granite under high pressure. Journal of Geophysical Research 73, 2225–2236.

Chin, L.Y., Raghavan, R., Thomas, L.K., 2000. Fully coupled geomechanics and fluid-flow analysis of wells with stress-dependent permeability. SPE Journal 5 (1), 32–45.

Chin, L.Y., Tomberlin, T.A., Ramos, G.G., Chalaturnyk, R.J., 2012. Evaluation of caprock stability by coupled modeling of geomechanics and reservoir simulation under steam injection for producing oil sands reservoirs. In: ARMA-2012-139. 46th U.S. Rock Mechanics/Geomechanics Symposium, June 24–27, 2012, Chicago, Illinois.

Coulomb, C.A., 1773. Application des règles de maxima et minima à quelquesproblems de statiquerelatifs à l'Architecture (Application of the rules of maxima and minima tosome problems of statics related to architecture). Royal Academy of Sciences With the Memoirs of Mathematics and Physics 7, 343–382.

Davies, J.P., Davies, D.K., 2001. Stress-dependent permeability: characterization and modelling. SPE Journal 6 (2), 224–235.

Dean, R.H., Gai, X., Stone, C.M., Minkoff, S.E., March 2006. A comparison of techniques for coupling porous flow and geomechanics. SPE Journal 132–140.

Goerke, U.J., Park, C.H., Wang, W., Singh, A.K., Kolditz, O., 2011. Numerical simulation of multiphase hydromechanical processes induced by CO_2 injection into deep saline aquifers. Oil & Gas Science and Technology—Revue de l'IFP 66, 105–118.

Goodarzi, S., Settari, A., Keith, D., 2012. Geomechanical modeling for CO_2 storage in Nisku-aquifer in Wabamun lake area in Canada. International Journal of Greenhouse Gas Control 10, 113–122.

Gutierrez, M., Lewis, R.W., 1996. The role of geomechanics in reservoir simulation. In: Presented at SPE/ISRM Eurock'96, Trondheim, Norway, July 8–10, 1996, SPE/ISRM 47392.

Gutierrez, M., Lewis, R.W., June 2001. Petroleum reservoir simulation coupling fluid flow and geomechanics. SPE Reservoir Evaluation & Engineering 164–172.

Häring, M.O., Schanz, U., Ladner, F., Dyer, B.C., 2008. Characterisation of the basel 1 enhanced geothermal system. Geothermics 37, 469–495.

Hu, L., Winterfeld, P.H., Fakcharoenphol, P., Wu, Y.-S., 2013. A novel fully-coupled flow and geomechanics model in enhanced geothermal reservoirs. Journal of Petroleum Science and Engineering 107, 1–11.

Jaeger, J.C., Cook, N.G.W., Zimmerman, R.W., 2007. Fundamentals of Rock Mechanics. Blackwell Publishing, Malden, MA.

Karypis, G., Kumar, V., 1998. A parallel algorithm for multilevel graph partitioning and sparse matrix ordering. Journal of Parallel and Distributed Computing 48, 71–85.

Karypis, G., Kumar, V., 1999. A fast and high quality multilevel scheme for partitioning irregular graphs. SIAM Journal on Scientific Computing 20 (1), 359–392.

Kilmer, N.H., Morrow, N.R., Pitman, J.K., 1987. Pressure sensitivity of low permeability sandstones. Journal of Petroleum Science and Engineering 1, 65–81.

Leverett, M.C., 1941. Capillary behavior in porous media. Transactions of the AIME 142, 341–358.

Louis, C., Dessenne, J.-L., Feuga, B., 1977. Interaction between water flow phenomena and the mechanical behavior of soil or rock masses. In: Gudehus, G. (Ed.), Finite Elements in Geomechanics. Wiley, New York, pp. 479–511.

Mandel, J., 1953. Consolidation des sols (etude mathematique). Geotechnique 3287–3299.

Mastrojannis, E.N., Keer, L.M., Mura, T., 1980. Growth of planar cracks induced by hydraulic fracturing. International Journal for Numerical Methods in Engineering 15, 41–54.

Mazzoldi, A., Rinaldi, A.P., Borgia, A., Rutqvist, J., 2012. Induced seismicity within geological carbon sequestration projects: maximum earthquake magnitude and leakage potential from undetected faults. International Journal of Greenhouse Gas Control 10, 434–442.

McTigue, D.F., 1986. Thermoelastic response of fluid-saturated porous rock. Journal of Geophysical Research 91 (9), 9533–9542.

Minkoff, S.E., Stone, C.M., Arguello, J.G., Bryant, S., Eaton, J., Peszynska, M., Wheeler, M., 1999. Staggered in time coupling of reservoir flow simulation and geomechanical deformation: step 1 – one-way coupling. In: Presented at 1999 SPE Reservoir Simulation Symposium, Houston, TX, Feburary 14–17, 1999, SPE 51920.

Narashimhan, T.N., Witherspoon, P.A., 1976. An integrated finite difference method for analysis of fluid flow in porous media. Water Resources Research 12, 57–64.

Neuzil, C., 1986. Groundwater flow in low-permeability environments. Water Resources Research 22 (8), 1163–1195.

Norris, A., 1992. On the correspondence between poroelasticity and thermoelasticity. Journal of Applied Physics 71, 1138–1141.

Olivella, S., Carrera, J., Gens, A., Alonso, E.E., 1994. Nonisothermal multiphase flow of brine and gas through saline media. Transport in Porous Media 15, 271–293.

Pan, P.-Z., Rutqvist, J., Feng, X.-T., Yan, F., 2014. An Approach for modeling rock discontinuous mechanical behavior under multiphase fluid flow conditions. Rock Mechanics and Rock Engineering 47, 589–603.

Perkins, T.K., Kern, L.R., 1961. Widths of hydraulic fractures. Journal of Petroleum Technology 13 (9), 937–949.

Pruess, K., Oldenburg, C., Moridis, G., 1999. TOUGH2 User's Guide, Version 2.0. Report LBNL-43134. Lawrence Berkeley National Laboratory, Berkeley, California.

Rinaldi, A.P., Rutqvist, J., Cappa, F., 2014. Geomechanical effects on CO_2 leakage through fault zones during large-scale underground injection. International Journal of Greenhouse Gas Control 20, 117–131.

Rutqvist, J., Birkholzer, J.T., Tsang, C.-F., 2008. Coupled reservoir-geomechanicalanalysis of the potential for tensile and shear failure associated with CO_2 injection in multilayered reservoir-caprock systems. International Journal of Rock Mechanics and Mining Sciences 45 (2), 132–143.

Rutqvist, J., Stephansson, O., 2003. The role of hydromechanical coupling in fractured rock engineering. Hydrogeology Journal 11, 7–40.

Rutqvist, J., Wu, Y.S., Tsang, C.F., Bodvarsson, G., 2002. A modeling approach for analysis of coupled multiphase fluid flow, heat transfer, and deformation in fractured porous rock. International Journal of Rock Mechanics and Mining Sciences 39, 429–442.

Rutqvist, J., Vasco, D.W., Myer, L., 2010. Coupled reservoir-geomechanical analysis of CO_2 injection and ground deformations at in Salah Algeria. International Journal of Greenhouse Gas Control 4, 225–230.

Sayedi, D., Ducellier, A., Foerster, E., Guy, N., Hild, F., Rohmer, J., 2009. Coupled hydromechanical modeling to study the integrity and safety of geological storage of CO_2. Energy Procedia 1, 2451–2458.

Settari, A., Walters, D.A., 1999. Advances in coupled geomechanical and reservoir modeling with applications to reservoir compaction. In: Presented at the 1999 SPE Reservoir Simulation Symposium, Houston, TX, February 14–17, 1999, SPE 51927.

Settari, A., Warren, G.M., 1994. Simulation and Field Analysis of Waterflood Induced Fracturing. SIMTECH Consulting Services Ltd, Calgary, AB, Canada.

Scheidegger, A.E., 1974. The Physics of Flow through Porous Media. University of Toronto Press, Toronto.

Terzaghi, K., 1936. The shearing resistance of saturated soils and the angle between the planes of shear. In: Proceedings of International Conference on Soil Mechanics and Foundation Engineering. Harvard University Press, Cambridge, MA, pp. 54–56.

Timoshenko, S., Goodier, J.N., 1951. Theory of Elasticity. McGraw-Hill Book Company, Inc, New York, NY.

Tran, D., Nghiem, L., Buchanan, L., 2005. Improved iterative coupling of geomechanics with reservoir simulation. In: Presented at the 2005 SPE Reservoir Simulation Symposium, Houston, TX, January 31–February 5, SPE 93244.

Tuminaro, R.S., Heroux, M., Hutchinson, S.A., Shadid, J.N., 1999. Official Aztec User's Guide Version 2.1. Massively Parallel Computing Research Laboratory, Sandia National Laboratories, Albuquerque, NM.

Van Genuchten, M.Th., 1980. A closed-form equation for predicting the hydraulic conductivity of unsaturated soils. Soil Science Society of America Journal 44, 892–898.

Verma, A., Pruess, K., 1988. Thermohydrological conditions and silica redistribution near high-level nuclear wastes emplaced in saturated geological formations. Journal of Geophysical Research 93, 1159–1173.

Wang, W., Kolditz, O., 2007. Object-oriented finite element analysis of thermo-hydro-mechanical (THM) problems inporous media. International Journal for Numerical Methods in Engineering 69, 162–201.

Wibberley, C.A.J., Yielding, G., Di Toro, G., 2009. Recent advances in the understanding of fault zone internal structure: a review. Geological Society (London) Special Publication 299, 5–33.

Wilson, R.K., Aifantis, E.C., 1982. On the theory of consolidation with double porosity. International Journal of Engineering Science 20 (9), 1009–1035.

Winterfeld, P.H., Wu, Y.-S., 2014. Simulation of CO_2 sequestration in brine aquifers with geomechanical coupling. In: Bundschuh, J., Al-Khoury, R. (Eds.), Computational Models for CO_2 Sequestration and Compressed Air Energy Storage. CRC Press, , New York, NY, pp. 275–303 (Chapter 8).

Winterfeld, P.H., Wu, Y.-S., 2016. Simulation of coupled thermal/hydrological/mechanical phenomena in porous media. SPE Journal 21 (3), 1041–1049.

Witherspoon, P.A., Wang, J.Y., Iwai, K., Gale, J.E., 1980. Validity of cubic law for fluid flow in a deformable rock fracture. Water Resources Research 16 (6), 1016−1024.

Wu, Y.-S., Winterfeld, P.H., 2016. Quantitative Characterization of Impacts of Coupled Geomechanics and Flow on Safe and Permanent Geological Storage of CO_2 in Fractured Aquifers, Quarterly Report 2 of Year 2. Quarterly report for DOE Award Number: DE-FE0023305.

Yew, C.H., Weng, X., 2015. Mechanics of Hydraulic Fracturing, second ed. Gulf Professional Publishing, Waltham, MA.

Chapter 12

Modeling of Cryogenic Fracturing Processes

Bowen Yao, Lei Wang
Colorado School of Mines, Golden, CO, United States

12.1 INTRODUCTION

Unconventional reservoirs with low to extremely low permeability nowadays supply more than half of the oil and gas production in the United States, for which massive hydraulic fracturing is the pivotal technology. As an innovative waterless fracturing technology, cryogenic fracturing uses cryogenic fluids as fracturing fluids to create thermal shock to induce fractures in reservoir matrix. Common cryogenic fluids include liquid nitrogen and liquid carbon dioxide. When experiencing the extremely low temperature of cryogenic fluids, reservoir rocks will break due to strong thermal stress resulting from significant temperature gradient, rather than high hydraulic pressure in conventional hydraulic fracturing operations. Thus the thermomechanical properties of rocks and failure criteria play very important roles in the cryogenic fracturing process. Modeling the cryogenic fracturing process needs to simultaneously combine all these fluid and rock properties. This chapter introduces the fundamental physics of cryogenic fracturing and a numerical approach for simulating the cryogenic fracturing process of synthetic and reservoir rock samples using liquid nitrogen. Modeling results are matched with experimental results in terms of temperature and pressure distribution and fracture profiles.

12.1.1 Comparison With Hydraulic Fracturing

Traditional hydraulic fracturing uses a highly pressurized fracturing fluid to create fracture networks in reservoir rocks. With proppant carried in the fracturing fluid, the hydraulic fracture networks can be propped and therefore held open after pumping. These conductive fractures greatly increase the contact area between the reservoir and the wellbore, allowing more reservoir fluids to converge into the wellbore and get produced. Hydraulic fracturing and

Hydraulic Fracture Modeling. https://doi.org/10.1016/B978-0-12-812998-2.00012-6

its associating technologies have revolutionized the oil and gas landscape in the United States and worldwide.

As hydraulic fracturing is being widely implemented, several drawbacks rise as major concerns regarding water usage, formation damage, and environmental impacts. Most hydraulic fracturing technologies rely on water-based fracturing fluids because water is an easily accessible fluid with lowest cost in most cases. However, as water enters low permeability formations, it might cause clay swelling and thus damage the reservoir permeability. In addition, introducing water into tiny pores would lower the effective oil or gas permeability due to relative permeability effect. These formation damages caused by water-based fracturing fluids impair the oil and gas production rate and recovery efficiency. Moreover, large quantities of water usage will place stresses on local water supply, by diverting water away from other sectors. Lastly, partial fracturing fluid returns to the surface as flowback containing various kinds of contaminants, which is difficult to handle and will add extra disposal or treatment costs.

Compared with conventional hydraulic fracturing technologies, cryogenic fracturing using liquid nitrogen has the potential of overcoming all drawbacks mentioned earlier. As nitrogen does not cause clay swelling in either liquid or gas state, formation damage is avoided. Because the cryogenic fluid will eventually evaporate into gas as temperature rises, flowback process is not necessary for cryogenic fracturing. Besides, nitrogen gas can be miscible with oil and gas under certain conditions, which eliminates the relative permeability effect. Even if it cannot dissolve into formation fluid, it will have less retention and flow resistance than water-based fracturing fluids. In addition, the large gas−liquid expansion ratio of liquid nitrogen will provide pressure support for flowback and production. Cryogenic fracturing can also minimize water consumption, which will certainly have less effects on the local environment, especially for arid areas. For liquid nitrogen, it can be obtained from separation and compression of nitrogen gas from air on-site, saving the cost of transportation or pipeline development. It is believed that the cost for cryogenic fluids can be adjusted to an acceptable level once the cryogenic fracturing technology is massively implemented.

One apparent disadvantage of cryogenic fracturing technology is the lack of capability for carrying proppant due to low viscosity of cryogenic fluids (Rudenko and Shubnikov, 1934; Fenghour et al., 1998). Later experiments and field tests showed that liquid carbon dioxide can be gelled to effectively transport sand proppant (King, 1983). In fact, a cryogen could be capable of transporting adequate amount of proppant by increasing flow velocity (Gupta and Bobier, 1998). The turbulence accompanied by high velocity and fierce phase change of cryogenic fluid permits proppant to be efficiently carried from wellbore into the major fracture networks.

12.1.2 History of Cryogenic Fracturing

Cryogenic fracturing is not a newly emerged concept in the petroleum industry; the idea has been long existing since the 1980s. Several laboratory experiments and field tests have been carried out to demonstrate the possibility and feasibility of cryogenic fracturing in stimulating low permeability reservoirs.

In the late 1990s, laboratory submersion tests of coal samples into liquid nitrogen proved that using liquid nitrogen as fracturing fluid might be applicable in enhancing gas production from tight coal-bed methane wells (McDaniel et al., 1998). The thermal shock effect caused the coal samples to shrink significantly; during the submersion tests microfractures opened and propagated orthogonally to the surface exposed to liquid nitrogen. By repeating the submersion process and warming up to the ambient temperature for three times, the coal samples disintegrated into grain size particles. These tests demonstrated that using liquid nitrogen as a stimulation fluid can effectively create fractures to increase the production from coal-bed methane reservoirs. Such an effect of rubblization may also provide particles to self-propagate fractures during the cryogenic fracturing process. As a counterpart to the laboratory tests, five wells were stimulated using liquid nitrogen. Three of the five wells showed increased production rates when compared with the offset wells that underwent conventional hydraulic fracturing. One well gave equivalent production and another experienced decreased production. Among the three wells with increased production, two of them showed long-term incremental production.

Almost at the same time, cryogenic fracturing treatment was conducted in a Devonian shale well using liquid nitrogen (Grundmann et al., 1998). This field test used stainless steel tubing and special valves to transfer liquid nitrogen to the bottom hole. An 8% higher initial production rate than that of nearby offset wells fractured with nitrogen gas was observed. Due to a logistic reason, this well was subsequently shut in with no further production reports. Although it is difficult to attribute the enhanced production rate to cryogenic fracturing for various reasons, such as anisotropic stress conditions and reservoir heterogeneity over short distances, this field test showed no drawback with cryogenic fracturing as opposed to conventional hydraulic fracturing.

In a later research of cryogenic fracturing using liquid nitrogen, series of experiments were conducted extensively on synthetic concrete samples, sandstone samples, and Niobrara shale samples. The submersion tests showed visible cracks created at the surface of the concrete samples (Cha et al., 2014). The CT scan demonstrated that cryogenic fractures penetrated to the center of the 8-inch cubic block after 30 min of submersion in liquid nitrogen. Further injection tests circulated and pressurized liquid nitrogen into boreholes drilled into the center of rock samples under various confining stress conditions

(Alqahtani, 2015; Alqatahni et al., 2016; Wu et al., 2016; Wang et al., 2016; Cha et al., 2016a,b). By comparing with intact samples, liquid nitrogen–treated samples consistently exhibit noticeable lowered breakdown pressure under the same confining stress condition, indicating that cryogenic treatment weakened the rock strength by generating fractures inside the rock blocks. The overall permeability of liquid nitrogen–treated samples was improved significantly. In addition, the injection tests of liquid nitrogen at relatively high pressure (~400 psi) demonstrated remarkable permeability enhancement on synthetic concrete samples and Niobrara shale samples (Alqahtani, 2015; Yao, 2015).

12.2 PHYSICAL PROCESS OF CRYOGENIC FRACTURING

The mechanism of cryogenic fracturing is thermal expansion/contraction caused by sharp temperature gradient. Thermal expansion and fracturing mechanism on continuous single component materials, such as metal, have been well established in material science. However, given the complex composition and internal structure of reservoir rocks, cryogenic fracturing processes deviate from these well-established theories. This section describes the cryogenic fracturing process on rock samples and how it differs from typical continuous materials.

12.2.1 Fracture Initiation and Propagation

An object shrinks when it experiences low temperature. As temperature varies through different sections of the material, it will produce nonuniform shrinkage or deformation. This creates an internal thermal stress within the body of the object. As the temperature variance becomes larger, the thermal stress will also increase. Thermal stress is proportional to the local temperature variance or temperature gradient, which can be calculated in a 1-D case as:

$$\sigma_{\text{thermal}} = E\beta(T - T_o)$$

where $\sigma_{thermal}$ denotes thermal stress; E is Young's modulus; β is linear thermal expansion coefficient; T is the current temperature; T_o is the reference/original temperature.

The fracture initiation process in rocks induced by cryogenic treatment can be simplified as the process mentioned earlier. A rock sample is originally at ambient temperature, which can be either room temperature in laboratory or reservoir temperature in field. When compared with cryogen temperature, the sample can be regarded as a hot object. As cryogenic fluid is applied to the surface of the rock, temperature of the superficial layer will drop tremendously to the boiling point of the cryogen in a very short period. This cooled layer will therefore contract dramatically with the rapid temperature drop. Because the thermal conductivity of rocks is usually very low, large temperature gradient

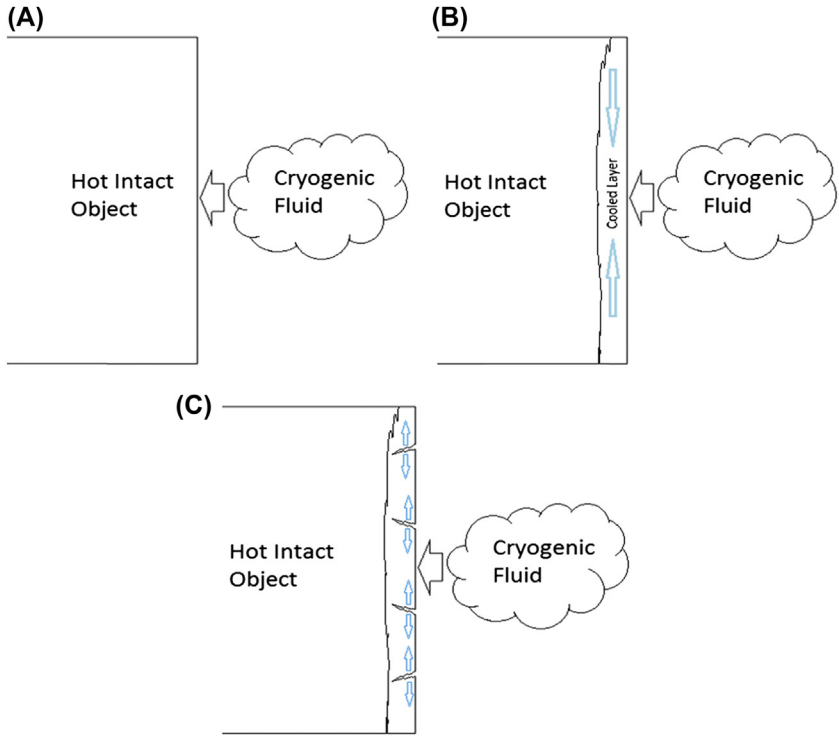

FIGURE 12.1 Schematic of fracture initiation process in cryogenic fracturing: (A) cryogenic fluid contacts the surface of a hot intact object; (B) the superficial layer is cooled down and contracts with the temperature drop creating tensile stress concentration; (C) the tensile thermal stress exceeds the tensile strength of the object, initiating fractures.

will be imposed across this thin layer of the cooled surface, concentrating enormous tensile thermal stress in the contact region. Once the tensile thermal stress exceeds the tensile strength of the rock, cracks will be initiated on the surface contacting cryogenic fluids. Fig. 12.1 shows a schematic for such a fracture initiation process.

The fracture propagation process of cryogenic fracturing is similar to the propagation process in hydraulic fracturing. As the cracks are initiated, cryogenic fluid further cools down the new surfaces of initiated fractures. The surfaces then contract with drastic temperature drop, which not only creates tensile stress, but also concentrates the stress at the tip of fractures. Fracture then propagates forward from its original tip. Fig. 12.2 demonstrates the fracture propagation process in cryogenic fracturing. Seeing that cryogenic fractures are created orthogonally to the cryogen contacted surface, they should be more complex than injection pressure−induced fractures in geometry due to Rayleigh−Bénard convection (Alqahtani, 2015).

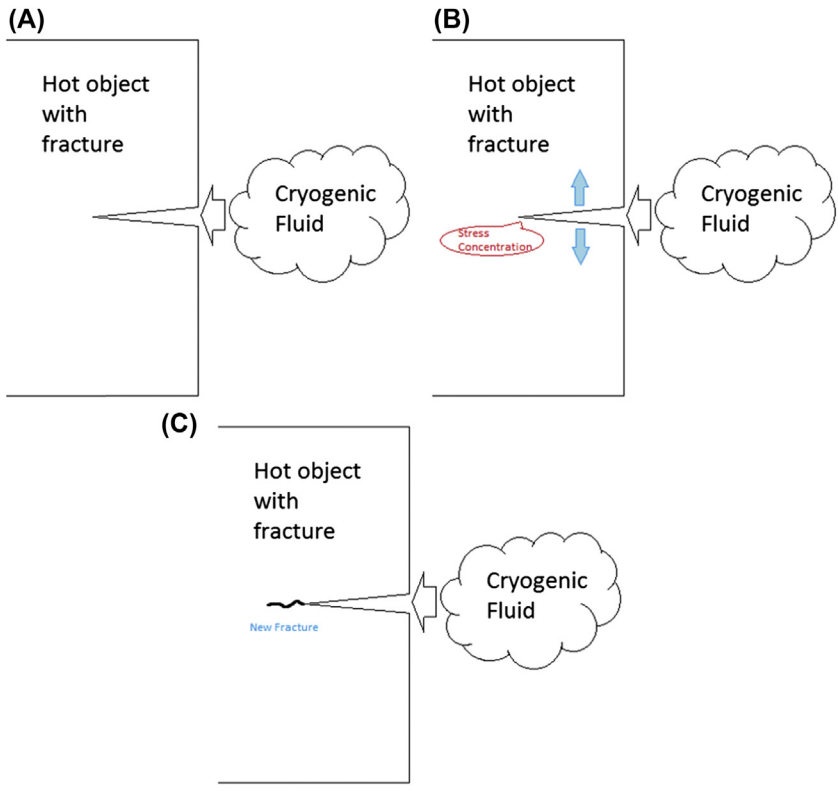

FIGURE 12.2 Schematic of fracture propagation process in cryogenic fracturing: (A) cryogenic fluid enters initiated cracks and further cools down new surfaces of the fractures; (B) new surfaces of the fractures contract, causing tensile stress concentrated at the tips; (C) fracture tip gets extended, and fracture propagates along the tip.

12.2.2 Rock Failure Characteristics

Although the fracture initiation and propagation processes of cryogenic fracturing are similar to the same processes of hydraulic fracturing, the mechanisms behind are actually different. It is generally believed that hydraulic fractures are created by both tensile failure and shear failure of formation rocks, with shear failure (also known as shear slip) dominating the fracture propagation process. Thus typical hydraulic fracturing process without preexisting fractures can be classified as Mode II in Fig. 12.3. The shear stress acts parallel to the plane of the crack and perpendicular to the crack front. Hydraulic fracturing creates macroscale interconnected planar fractures. On the other hand, during cryogenic fracturing treatment, fractures are created by the tensile thermal stress due to the contraction of rock material at cryogenic temperature. Therefore, the cryogenic fracturing process without

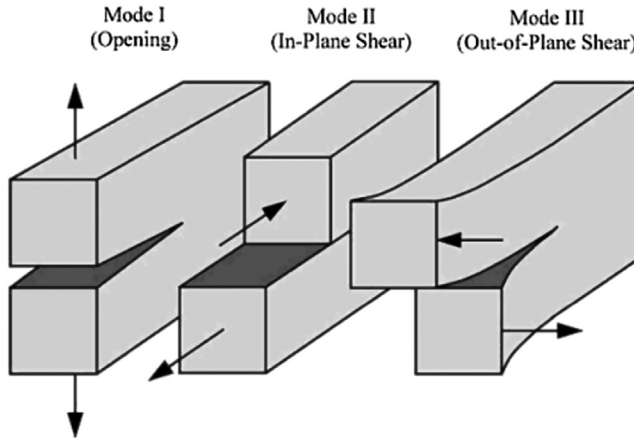

FIGURE 12.3 Three modes of loading to enable crack propagation (Anderson, 2005).

any confining stresses is more of a classical Mode I fracture propagation in Fig. 12.3, meaning that tensile stresses normal to the plane of cracks propagate the fracture.

In hydraulic fracturing, fractures are generated by fluid pressurization. After a fracture is initiated, high-pressure fracturing fluid will flow into the fracture and propagate in it. The fracture propagation pressure is generally lower than the fracture initiation pressure, which usually appears as a peak at the beginning of the fracture pressure curve. Hydraulic fractures are mostly initiated as simple and relatively large size, which depends on the volume of injected fluids. Fig. 12.4 shows a typical hydraulic fracture profile colored with blue dye in an 8-inch concrete cube, which is the same as those used for cryogenic fracturing in this chapter. The fracture propagated in one major plane that is perpendicular to the minimum horizontal stress. The hydraulic fracture extends to the boundary of the concrete sample without generating discernible branches.

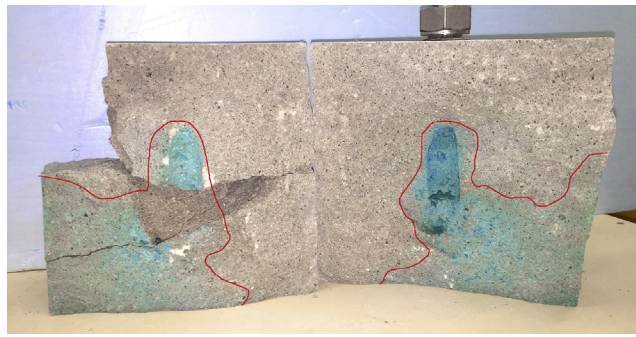

FIGURE 12.4 Typical hydraulic fracture profile on an 8-inch concrete sample under triaxial stresses.

For cryogenic fracturing, the heat transfer process under an extreme temperature gradient does not behave like pressurized fluid flow. Heat conduction does not focus solely in one direction or gets confined in an initiated direction. Instead, the temperature is much more uniformly reduced on surfaces in contact with liquid nitrogen, resulting in relatively even thermal stress around the wellbore. If the thermal stress far exceeds the horizontal stress and the tensile strength of the rock, local microfractures will be induced. This has been observed in cryogenic fracturing of concrete samples with liquid nitrogen, in which microfractures were generated in all directions around the wellbore. Nonetheless, the penetration depth of temperature change is much less than fluid pressure due to the low thermal conductivity of rocks at low injection pressure; therefore the length and width of cryogenic fractures are limited as compared with hydraulic fractures. Last but not least, because fracture initiation and propagation is dominated by the in situ stress states, penetration depths of cryogenic fractures along the maximum horizontal stress direction are longer than those in the minimum horizontal stress direction. Fig. 12.5 reveals a typical bulb-shaped cryogenic fracture plane colored by red dye, which is opened perpendicular to the minimum horizontal stress. By cutting the sample horizontally along the blue dashed line, the top view of the horizontal cross section provides us an ellipse with a semimajor axis of 1.25 inch and a semiminor axis of 1.0 inch, as shown in the inset in the figure. That is, different from hydraulic fracturing, cryogenic fracturing generates swarms of microfractures around the wellbore.

With the aid of high injection pressure, the efficacy of cryogenic fracturing can be greatly improved. High injection pressure can not only force the convection process to be more effective in the contacting area but also synergize the thermal stress with hydraulic stress in initiating and propagating fractures. As liquid nitrogen contacts rock surface of much higher temperature, it rapidly vaporizes at the rock and liquid nitrogen interface, generating a gas cushion that significantly reduces the heat transfer rate due to the low heat conductivity of gas. This phenomenon is known as Leidenfrost effect. High

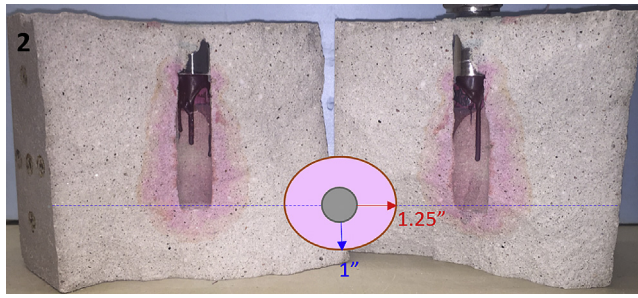

FIGURE 12.5 Cryogenic fractures around the wellbore in a concrete sample under triaxial stresses.

injection pressure can keep the fluids turbulent while in contact with rock surface, thus eliminating the Leidenfrost effect and maintaining a high cooling rate. On the other hand, high pressure gradient can further promote the propagation of created fractures or even create new fractures by hydraulic pressure. In addition, although it is not very likely for liquid nitrogen to enter the pores, increased flow rate of cold gas under high pressure can still enhance the temperature drop in rock matrix.

12.3 NUMERICAL MODELING

Cryogenic fracturing using liquid nitrogen is a physical process coupling thermodynamics, hydraulics, and rock mechanics, which can also be described as a thermo–hydraulic–mechanical (THM) process. Modeling the cryogenic fracturing process evokes assumptions to simplify the physics. In addition, the governing equations of different processes should be properly addressed. The numerical modeling of cryogenic fracturing described in this section is based on modification of TOUGH2-EGS (enhanced geothermal system), which is designed for fluid flow and heat transfer in an enhanced geothermal system.

12.3.1 Assumptions

Due to the complex physics involved in the THM process, assumptions have to been made to enable this process to be actually solvable. The following assumptions are made in the numerical scheme for the cryogenic fracturing process:

- For heat transfer, only heat conduction and convection are considered; heat radiation is neglected. Because in porous media the contacting area between fluid and rock is very large per unit volume of fluid, it indicates that heat conduction and convection play much more important roles than radiation.
- Rock material is assumed to deform elastically and obey generalized Hooke's law before it is fractured.
- In each matrix grid block, the temperature of the rock matrix is always the same as that of the fluid in the pores.
- During the fracturing process, the stress change in the rock matrix includes thermal expansion or contraction due to the change in temperature, fluid pressure in pores, and external stress condition.
- Rock properties, such as permeability, porosity, rock strength, etc., are assumed to be independent with temperature change.

12.3.2 Heat Transfer and Fluid Flow

The heat transfer and fluid flow model here is adapted from the TOUGH2-EGS simulator (Fakcharoenphol et al., 2013; Xiong et al., 2013; Zhang et al.,

2015, 2016). Both of these two processes are generalized as one diffusive governing equation (Pruess et al., 1999). Fluid flow is described by a multiphase extension of Darcy's law. Heat flow is governed by conduction and convection, with consideration of both sensible and latent heat effects. The governing equation has the following form:

$$\frac{d}{dt}\int_{V_n} Q^{\kappa} dV_n = \int_{\Gamma_n} F^{\kappa} \cdot \overrightarrow{n} d\Gamma_n + \int_{V_n} q^{\kappa} dV_n$$

where $\kappa = 1, \ldots, NK$ (total number of components); $n = 1,\ldots,$ NEL (total number of grids); V_n is an arbitrary subdomain of the system; Γ_n is the closed surface by which the subdomain is bounded; Q is the quantity that represents mass or energy per volume; F is mass or heat flux; q is the sink and/or source; $\overrightarrow{n}$ is a normal vector on surface element Γ_n pointing inward into V_n.

12.3.3 Thermal Stress

By assuming that the boundaries of each grid block deform elastically with small strain and obey the generalized Hooke's law, thermal stress can be obtained via a stress−strain relation coupled with pore pressure as the following (Zoback, 2007):

$$\sigma_{kk} - B_i \times p_p - \frac{E}{1-2v}[\beta(T - T_0)] = \frac{E}{1+v}\varepsilon_{kk} + \frac{E}{(1+v)(1-2v)}(\varepsilon_{xx} + \varepsilon_{yy} + \varepsilon_{zz})$$

where σ is the normal stress; ε is the strain; subscript kk is direction, which can be xx, yy, and zz; B_i is the Biot number of the rock; β is the linear thermal expansion coefficient of the rock; E is Young's modulus; v is Poisson's ratio; p_p is the pore pressure; T is the current temperature; T_0 is the reference or original temperature.

12.3.4 Failure Criteria

Mogi−Coulomb failure criterion (Al-Ajmi and Zimmerman, 2006), which is an octahedral failure envelope as shown in Fig. 12.6, is used here to estimate the stress condition leading to rock failure or fracture initiation for cryogenic fracturing process under confining stresses. The failure criterion has the following form:

$$\tau_{oct} = k + m\sigma_{\text{oct}}$$

where τ_{oct} is the octahedral shear stress; σ_{oct} is the octahedral normal stress; k is the Mogi−Coulomb intercept; m is the Mogi−Coulomb slope.

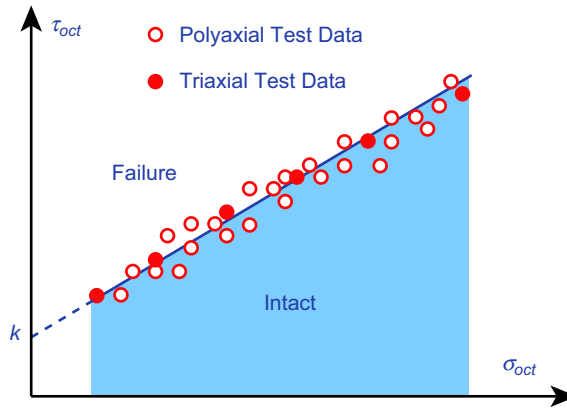

FIGURE 12.6 Failure envelope of Mogi–Coulomb criterion (Aadnoy and Looyeh, 2011).

The octahedral normal stress and shear stress can be obtained from the following equations:

$$\tau_{\text{oct}} = \frac{1}{3}\sqrt{(\sigma_v - \sigma_{H\max})^2 + (\sigma_v - \sigma_{h\min})^2 + (\sigma_{H\max} - \sigma_{h\min})^2}$$

$$\sigma_{\text{oct}} = \frac{1}{3}(\sigma_v + \sigma_{H\max} + \sigma_{h\min})$$

where σ_v is the vertical stress; $\sigma_{h\min}$ is the minimum horizontal stress; $\sigma_{H\max}$ is the maximum horizontal stress.

Mogi–Coulomb intercept and slope are obtained by regression of experimental data. If octahedral normal stress and shear stress calculated from pore pressure, thermal stress, and confining stress (in situ stress) fall below the straight line determined by Mogi–Coulomb criterion, rock material will only deform elastically and will not break down. When the stress condition changes, i.e., due to cryogenic treatment, and the calculated octahedral normal stress and shear stress fall above the failure envelope, fractures will be initiated. Mogi–Coulomb failure criterion is simple and easy to adapt in simulation and has similar accuracy to other failure criteria.

12.3.5 Numerical Scheme

The numerical simulation scheme here modifies the basic framework of TOUGH2-EGS. Modifications on fractured grids judgment according to the Mogi–Coulomb failure criterion are sequentially added into the scheme, as shown in Fig. 12.7. After reading the prepared input file, the program initializes fluid, heat, and stress variables. Then it builds a Jacobian matrix for residual equations of fluid, heat, and stress. Afterward, an iteration process was used to solve the equation system with the original thermal, hydraulic, and

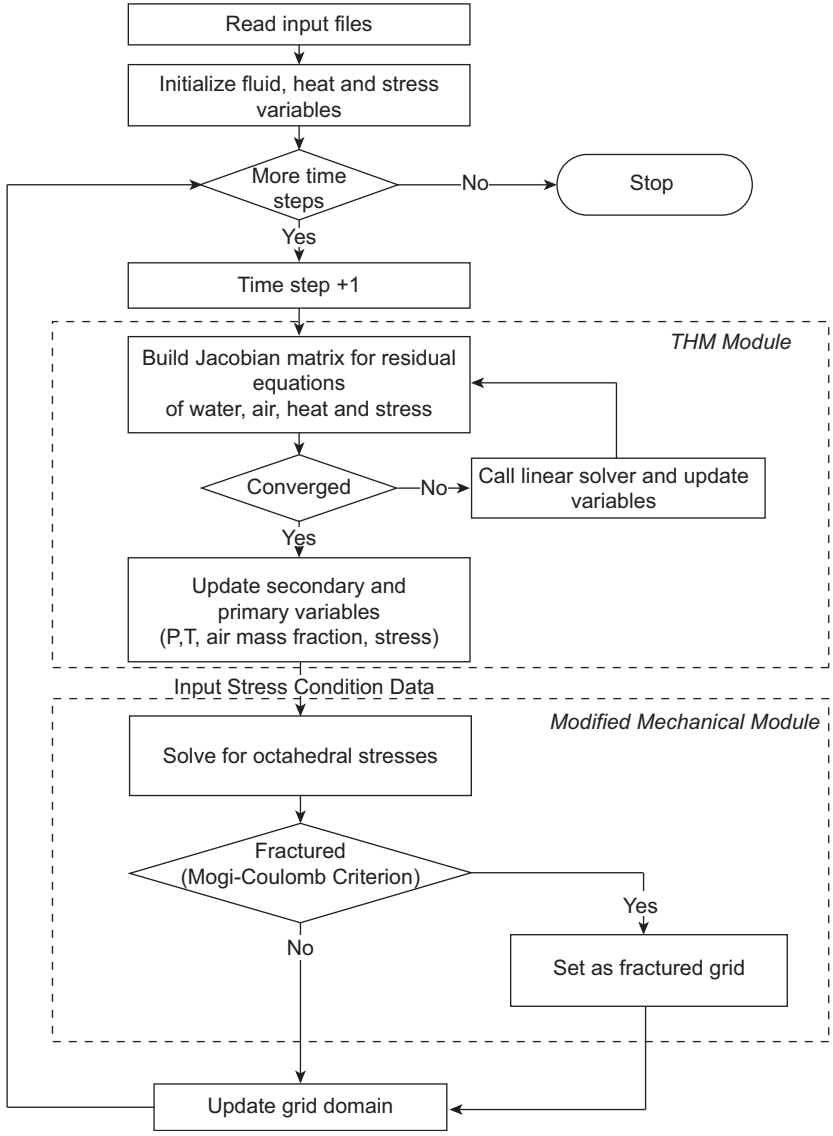

FIGURE 12.7 Simulation scheme and procedures.

mechanical modules. Once converged, the primary and secondary variables such as pressure, temperature, mass fraction, and stress are updated with new values at current time step. Then the modified mechanical module solves for the octahedral stresses for each grid with the stress condition data. Next, these data are substituted into the Mogi−Coulomb criterion. If the octahedral stresses of a grid indicate it is fractured, this grid will be set as the fractured

grid with a higher permeability. After the judgment, the grid domain will be updated, and the program continues to the next time step until the maximum time step is reached.

12.3.6 Results

The simulation results presented in this section are used to compare experimental results of cryogenic fracturing processes using liquid nitrogen on Niobrara shale samples (Yao, 2015). The 10-m-deep outcrop shale blocks were cut into 8-inch cubes, and 1-inch boreholes were drilled into the cube center for liquid nitrogen stimulation experiment. Confining stresses applied were 1000 psi in x direction, 3000 psi in y direction, and 4000 psi in z direction (vertical). The sample went through two high pressure treatments including three short cycles of high-pressure liquid nitrogen injection. Each cycle of high-pressure injection lasted for about 15 s at 450 psi with 10 min relaxation period in between. The time interval between each treatment was sufficiently long for the borehole temperature to return to the ambient temperature. The input parameters are listed in Table 12.1. Simulations were run for these two treatments.

TABLE 12.1 Input Parameters for Simulation

Properties	Value
Ambient pressure	11.8 psi (81.4 kPa)
Ambient temperature	66°F (19°C)
Rock density	2.38 g/cc
Permeability	1×10^{-3} mD
Porosity	8%
Rock compressibility	2×10^{-3} psi^{-1} (2.9×10^{-7} Pa)
Thermal diffusivity	8×10^{-7} m^2/s
Thermal expansion coefficient	2.7×10^{-5}°C^{-1}
Specific heat	990 J/(kg K)
Young's modulus	7.15×10^6 psi (4.93×10^4 MPa)
Poisson's ratio	0.268
Mogi–Coulomb constant, k	230 psi (1.59 MPa)
Mogi–Coulomb slope, m	0.58

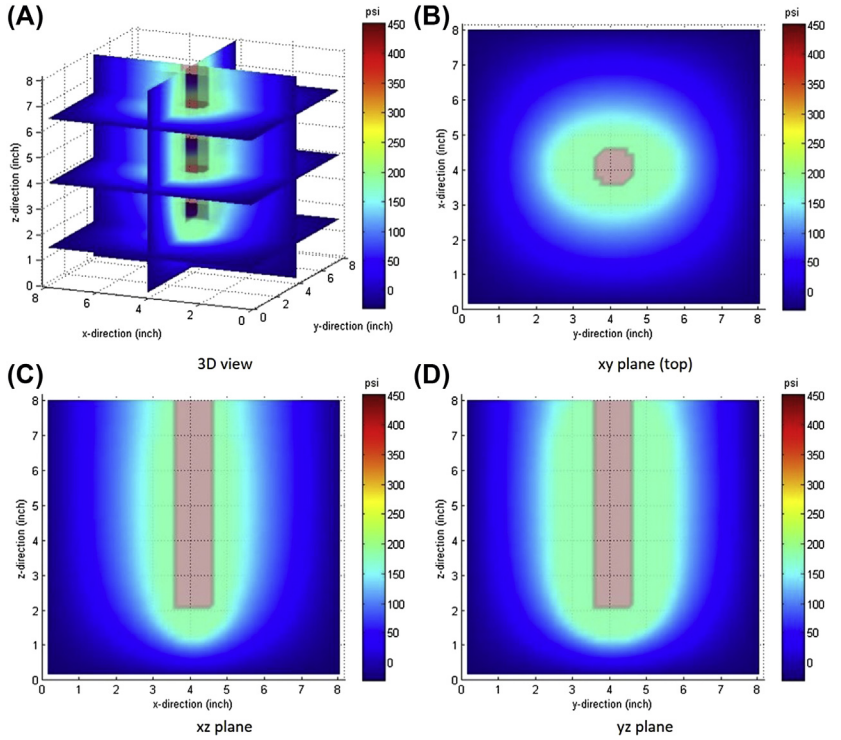

FIGURE 12.8 Simulated pressure profile in the shale sample after two treatments (Yao, 2015).

The simulation results of pressure, temperature, and fractured grid distribution inside the shale sample are shown in Figs. 12.8−12.10, respectively. All distributions of the three parameters show a bulblike shape, which is elongated into elliptical cross sections along the maximum horizontal stress. This elliptical cross section in the horizontal plane is dominantly induced by the heterogeneous triaxial stresses, along with the thermal stress and hydraulic pressurization. The distribution of fractured grids in the midplane perpendicular to the minimum horizontal stress shows a bulblike profile around the wellbore, which perfectly agrees with the observation of colored cryogenic fractures in the concrete sample as described in the previous section; however, the rock material is different. Due to the limited outreach of the dramatic temperature gradient in the near wellbore region, fracture extension is thus limited. Fig. 12.11 presents the cryogenic fracture cross section that is opened perpendicular to the minimum horizontal stress in the shale rock sample, as circled by the yellow dashed line. It is clear that the cryogenic fracture also demonstrates a bulblike shape, highly consistent with the simulation results. Although the fracture penetration into the fracture plane is not checked, it is

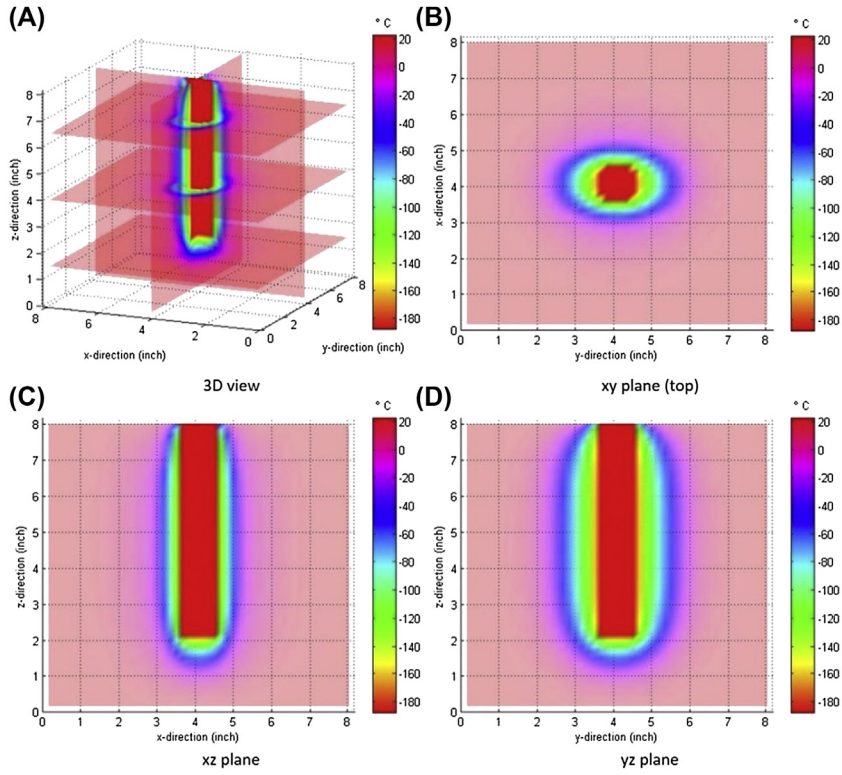

FIGURE 12.9 Simulated temperature profile in the shale sample after two treatments (Yao, 2015).

believed that it should resemble that observed for the concrete sample as illustrated in the previous section.

12.4 CONCLUSIONS

Cryogenic fracturing is still a new technology for stimulating unconventional reservoirs in view of very rare field applications. The cryogenic fracturing process involves thermal, hydraulic, and mechanical effects at the same time. This chapter illustrates the mechanisms and critical parameters pertinent to these processes and provides instructive insights for optimizing the cryogenic fracturing technique. By coupling all these processes, numerical modeling of cryogenic fracturing process successfully reproduces the experimental results of temperature and pressure profiles as well as fracture morphology inside the shale samples. In fact, permeability, porosity, rock strength, and other properties in rock samples are not uniform and are also functions of temperature and pressure. Nevertheless, due to lack of detailed experimental

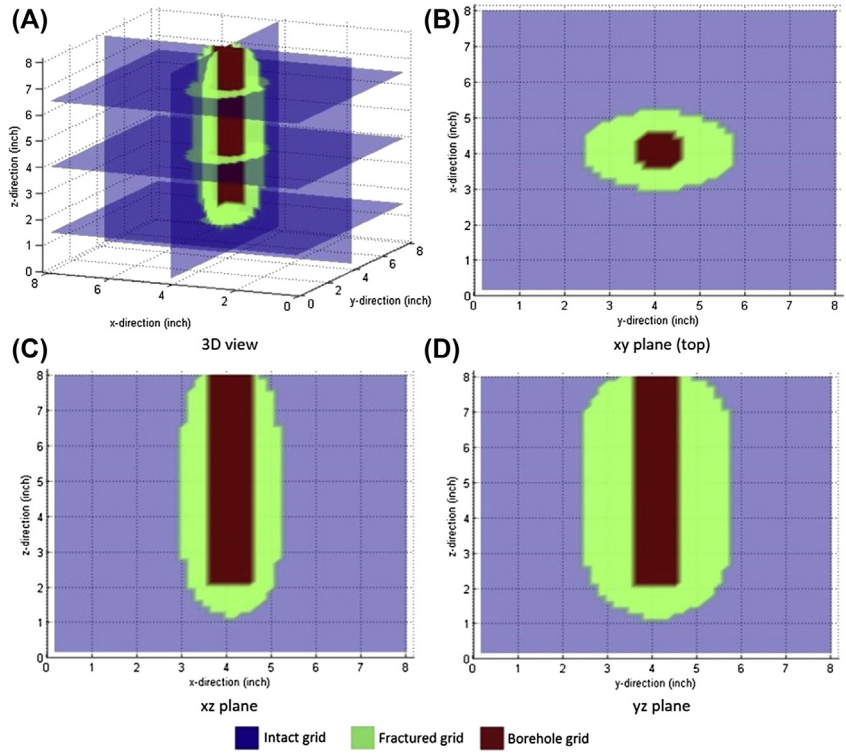

FIGURE 12.10 Simulated distribution of fractured grids in the shale sample after two treatments (Yao, 2015).

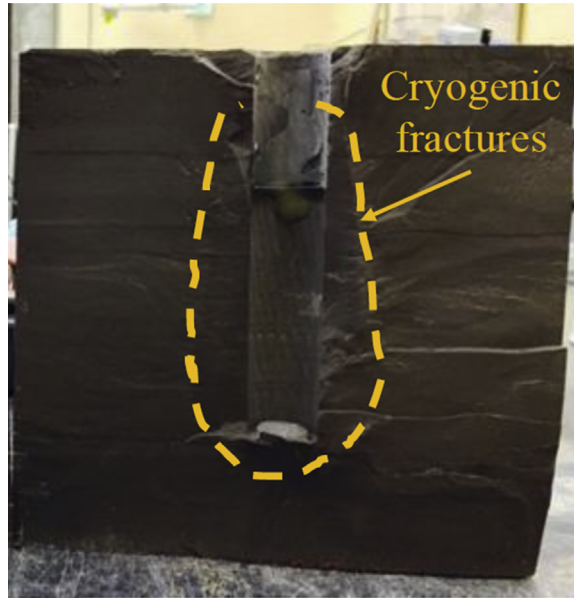

FIGURE 12.11 Cryogenic fracture cross section in the Niobrara shale sample after breakdown with high-pressure nitrogen gas (Yao, 2015).

measurements, they are not considered in the modeling of cryogenic fracturing as described in this chapter.

ACKNOWLEDGMENTS

Financial supports from the National Energy Technology Laboratory of US Department of Energy (Quantitative characterization of impacts of coupled geomechanics and flow on safe and permanent geological storage of CO_2 in fractured aquifers, Project number: DE-FE0023305) and Foundation CMG are greatly appreciated.

REFERENCES

Alqatahni, N.B., Cha, M., Yao, B., et al., 2016. Experimental investigation of cryogenic fracturing of rock specimens under true triaxial confining stresses. In: SPE Europec Featured at 78th EAGE Conference and Exhibition. Society of Petroleum Engineers. https://doi.org/10.2118/180071-MS.

Cha, M., Alqahtani, N., Yao, B., et al., 2016a. Studying cryogenic fracturing process using transparent specimens. In: Energy Geotechnics: Proceedings of the 1st International Conference on Energy Geotechnics, ICEGT 2016, Kiel, Germany, August 29−31, 2016. CRC Press.

Cha, M., Alqahtani, N., Yao, B., et al., 2016b. Development of laboratory system for cryogenic fracturing study. In: Energy Geotechnics: Proceedings of the 1st International Conference on Energy Geotechnics, ICEGT 2016, Kiel, Germany, August 29−31, 2016. CRC Press.

Aadnoy, B., Looyeh, R., 2011. Petroleum Rock Mechanics: Drilling Operations and Well Design, first ed. Gulf Professional Publishing, Houston.

Al-Ajmi, A.M., Zimmerman, R.W., 2006. Stability analysis of vertical boreholes using the Mogi-Coulomb failure criterion. International Journal of Rock Mechanics and Mining Sciences 43 (8), 1200−1211. https://doi.org/10.1016/j.ijrmms.2006.04.001.

Alqahtani, N.B., August 2015. Experimental Study and Finite Element Modeling of Cryogenic Fracturing in Unconventional Reservoirs (Ph.D. thesis). Colorado School of Mines, Golden, Colorado.

Anderson, T.L., 2005. Fracture Mechanics: Fundamentals and Applications. CRC Press.

Cha, M., Yin, X., Kneafsey, T., et al., 2014. Cryogenic fracturing for reservoir stimulation laboratory studies. Journal of Petroleum Science and Engineering 124 (1), 436−450. https://doi.org/10.1016/j.petrol.2014.09.003.

Fakcharoenphol, P., Xiong, Y., Hu, L., et al., May 2013. TOUGH2−EGS: A Coupled Geomechanical and Reactive Geochemical Simulator for Fluid and Heat Flow in Enhanced Geothermal Systems. Manual. Colorado School of Mines, Golden, CO.

Fenghour, A., Wakeham, W.A., Vesovic, V., 1998. The viscosity of carbon dioxide. Journal of Physical and Chemical Reference Data 27 (1), 31−44. https://doi.org/10.1063/1.556013.

Grundmann, S.R., Rodvelt, G.D., Dials, G.A., et al., 1998. Cryogenic nitrogen as a hydraulic fracturing fluid in the Devonian shale. In: Presented at SPE Eastern Regional Meeting, Pittsburgh, Pennsylvania, November 9−11, 1998. SPE-51067-MS. https://doi.org/10.2118/51067-MS.

Gupta, D.V.S., Bobier, D.M., 1998. The history and success of liquid CO_2 and CO_2/N_2 fracturing system. In: Presented at SPE Gas Technology Symposium, Calgary, Alberta, Canada, March 15−18, 1998. SPE-40016-MS. https://doi.org/10.2118/40016-MS.

King, S.R., 1983. Liquid CO_2 for the stimulation of low-permeability reservoirs. In: Presented at SPE/DOE Low Permeability Gas Reservoirs Symposium, Denver, Colorado, March 14–16, 1983. SPE-11616-MS. https://doi.org/10.2118/11616-MS.

McDaniel, B.W., Grundmann, S.R., Kendrick, W.D., et al., 1998. Field applications of cryogenic nitrogen as a hydraulic-fracturing fluid. Journal of Petroleum Technology 50 (3), 38–39. SPE--38623-MS. https://doi.org/10.2118/38623-MS.

Pruess, K., Oldenburg, C., Moridis, G., November 1999. TOUGH2 User's Guide Version 2. Lawrence Berkeley National Laboratory, Berkeley, CA.

Rudenko, N.S., Shubnikov, L.V., 1934. The viscosity of liquid nitrogen, carbon monoxide, argon and oxygen as a function of temperature. Physikalische Zeitschrift der Sowjetunion 6, 470–477.

Wang, L., Yao, B., Cha, M., et al., 2016. Waterless fracturing technologies for unconventional reservoirs – opportunities for liquid nitrogen. Journal of Natural Gas Science and Engineering 35, 160–174. https://doi.org/10.1016/j.jngse.2016.08.052.

Wu, Y.S., Yin, X., Kneafsey, T.J., et al., February 2016. Development of Non-contaminating Cryogenic Fracturing Technology for Shale and Tight Gas Reservoirs. Final report. US DOE, Washington, DC.

Xiong, Y., Fakcharoenphol, P., Winterfeld, P., et al., 2013. Coupled geomechanical and reactive geochemical model for fluid and heat flow: application for enhanced geothermal reservoir. In: Presented at SPE Reservoir Characterization and Simulation Conference and Exhibition, Abu Dhabi, UAE September 16–18, 2013. SPE-165982-MS. https://doi.org/10.2118/165982-MS.

Yao, B., December 2015. Experimental Study and Numerical Modeling of Cryogenic Fracturing Process on Laboratory-scale Rock and Concrete Samples (MS thesis). Colorado School of Mines, Golden, Colorado.

Zhang, R., Winterfeld, P.H., Yin, X., et al., 2015. 2015. Sequentially coupled THMC model for CO2 geological sequestration into a 2D heterogeneous saline aquifer. Journal of Natural Gas Science and Engineering 27, 579–615. https://doi.org/10.1016/j.jngse.2015.09.013.

Zhang, R., Yin, X., Winterfeld, P.H., et al., 2016. A fully coupled thermal-hydrological-mechanical-chemical model for CO_2 geological sequestration. Journal of Natural Gas Science and Engineering 28, 280–304. https://doi.org/10.1016/j.jngse.2015.11.037.

Zoback, M.D., 2007. Reservoir Geomechanics: Earth Stress and Rock Mechanics Applied to Exploration, Production and Wellbore Stability, first ed. Cambridge University Press, Cambridge.

Chapter 13

Model Validation in Field Applications

Jennifer L. Miskimins
Colorado School of Mines, Golden, CO, United States

13.1 INTRODUCTION

This chapter focuses on the use of field-scale data and diagnostics to validate numerical simulations and verify their physical accuracy. Modeling is a process, and the saying "garbage in, garbage out" aptly applies to hydraulic fracture modeling. The effort put into hydraulic fracturing simulation can range anywhere from "back of the envelope" calculations to a fully integrated model that ties with a numerical reservoir simulator and other full-scale field models.

There are a variety of ways to approach hydraulic fracture model validation; however, all of these approaches include certain similar steps. These steps include acquiring and entering data regarding the wellbore schematic, reservoir, and fracture treatment itself. With these values, preliminary modeling can be performed. However, the real validation occurs when posttreatment results such as pressure responses, geometric data, and posttreatment production values are available and incorporated. It's the intensity or level of these steps that set different models and modeling efforts (and their ultimate results) apart from each other.

13.2 PRETREATMENT MODEL INPUTS

Before pumping a hydraulic fracturing treatment, tests can be performed that will aid in quantifying both reservoir and wellbore characteristics. Such tests help to determine characteristics that are specific to a certain well and can help not only in pretreatment design but also in preventing undesired situations such as screen out and early termination of a treatment. These tests can be broken out into two broad categories, including tests that help to determine wellbore conditions and tests that aid in characterizing the reservoir conditions. In addition to values from such tests, other inputs for the wellbore and fracturing fluid and proppants systems must also be incorporated.

Hydraulic Fracture Modeling. https://doi.org/10.1016/B978-0-12-812998-2.00013-8

13.2.1 Wellbore Friction

Wellbore friction has a large impact on treatment placement and equipment design. Too much friction can lead to increased costs by requiring supplementary fluid additives and additional on-site horsepower. Wellbore friction occurs in the form of pipe friction, perforation friction, and near-wellbore tortuosity behavior.

Pipe friction is a function of rate squared when in turbulent flow. Most software packages have sufficient pipe friction models; however, the inputs into the model that are used in such friction evaluations need to be accurate for any given job. This is especially true in the case of the viscosity and fluid parameters of the treatment fluid that need to be accurately represented in the model, not only for friction calculations but also for general performance of the model. Such fluid considerations are discussed later in Section 13.2.2.

Eq. (13.1) shows the pressure drop across a set of perforations using field units. As shown in Eq. (13.1), perforation friction is a function of rate squared:

$$\Delta P_{\text{perf}} = 0.2369 \frac{\rho_{\text{fluid}} q^2}{n^2 d_{\text{perf}}^4 C_d^2} \tag{13.1}$$

where ρ_{fluid} = density of the injection fluid, ppg; C_d = discharge coefficient; d_{perf} = diameter of perforations, inches; n = number of perforations open and accepting fluid; q = injection rate, bpm; ΔP_{perf} = total friction drop across the perforations, psi.

Near-wellbore tortuosity can be the result of a variety of effects including multiple fractures, flow along cement wellbore and cement formation interfaces, cement and charge debris, perforation orientation, and perforation friction, most of which can result in a narrowing of the fracture width. Fig. 13.1 shows a schematic of this behavior. It is difficult under field conditions to determine which of these specific phenomena is actually occurring downhole; however, the overall tortuosity friction loss implications have been shown to be a function of the square root of the injection rate.

When coupling the perforation friction and near-wellbore tortuosity, the total bottomhole friction loss results in Eq. (13.2). The total friction loss in a wellbore during a hydraulic fracturing treatment is thus a function of the pipe, perforation, and tortuosity friction components as shown in Eq. (13.3).

$$\Delta P_{\text{BHFriction}} = \Delta P_{\text{perf}} + \Delta P_{\text{tortuosity}} = k_{\text{perf}} q^2 + k_{\text{tortuosity}} q^{\frac{1}{2}} \tag{13.2}$$

where k_{perf} is $0.2369 \frac{\rho_{\text{fluid}}}{n^2 d_{\text{perf}}^4 C^2}$, psi/bpm^2; $k_{\text{tortuosity}}$ is tortuosity factor, psi/bpm$^{1}/_{2}$; $\Delta P_{\text{BHFriction}}$ is total bottomhole friction drop, psi; $\Delta P_{\text{tortuosity}}$ is total friction drop due to tortuosity, psi.

$$\Delta P_{\text{total friction}} = \Delta P_{\text{pipe}} + \Delta P_{\text{perf}} + \Delta P_{\text{tortuosity}} \tag{13.3}$$

FIGURE 13.1 Schematic showing fractures (gray) exiting the perforations of a wellbore and twisting around the wellbore to eventually propagate in the direction of maximum horizontal stress (perpendicular to minimum horizontal stress). This twisting behavior and the associated pressure drop is one example of near-wellbore tortuosity behavior.

The magnitude of the total bottomhole friction losses exhibited by Eq. (13.3) can be determined by a pretreatment step rate test. Fig. 13.2 shows the raw bottomhole data from a step rate test. By subtracting the pipe friction component, which should be reasonably well known, and then solving for k_{perf} and $k_{\text{tortuosity}}$ for the treatment conditions, the total pressure losses at any rate due to the perforations and the tortuosity of that given wellbore can be determined. Fig. 13.3 shows a graph of the pressure loss versus rate for the step rate test shown in Fig. 13.2.

Once the pressure loss due to the perforation component is determined, the number of perforations actually open and taking fluid (n) can be determined by using the k_{perf} term and solving for n. Although the number of open perforations can be determined, the location of them cannot be determined, which has significant implications for limited entry designs in vertical well and in horizontal well multiperforation cluster systems.

Inclusion of correct pipe, perforation, and tortuosity friction values in a model can enhance the calibration and accuracy of a hydraulic fracturing model as the pressure that is lost to these components is not available to aid in the propagation of the fracture itself. In the case of multistage, multicluster

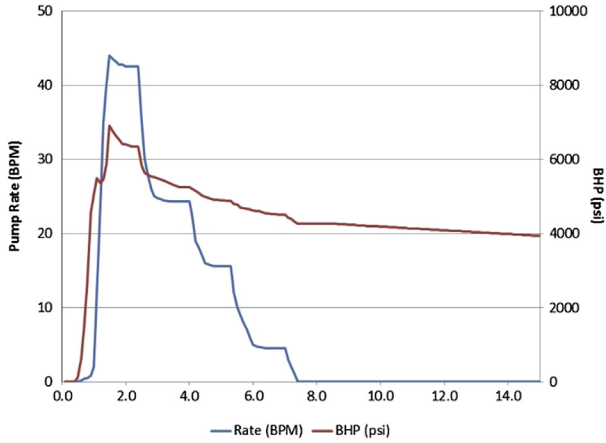

FIGURE 13.2 Bottomhole data for a step rate test. Pressure is shown in red (dark gray in print version) and rate in blue (light gray in print version). Step down tests, such as this one, are preferred to step up tests, as all of the perforations that will break down have already done so and the system is relatively stable.

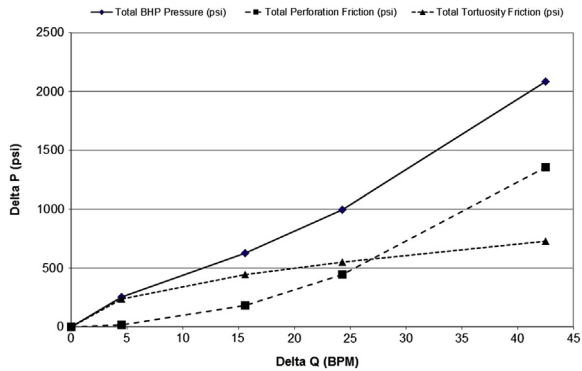

FIGURE 13.3 Individual component pressure losses for the step rate data shown in Fig. 13.2.

horizontal wells, the implications are substantial as the distribution of fluid between perforation clusters can be impacted, and therefore the fracture growth associated with each is also unevenly distributed.

Once a fracturing treatment begins, these frictional components will change via erosional effects. The perforation friction will modify via two mechanisms (Crump and Conway, 1988). First, the perforation entrance will be rounded and smoothed out, thus increasing the discharge coefficient. Second, the perforation entrance itself will be eroded and increased in size, expanding the perforation diameter. These effects will increase when larger sand concentrations or higher pressure differentials are in place.

Tortuosity will also erode during a treatment, and if not addressed, can lead to premature screen out (Cleary et al., 1993; Romero et al., 1995). Proppant slugs and gel slugs have both been shown to modify and minimize this risk (Chipperfield et al., 2000). However, if the tortuosity is extreme, it may be difficult to even get these slugs downhole in the first place.

From a modeling standpoint, the model needs to capture and acknowledge these frictional components and changing behaviors. The impacts on the overall pressure scheme can have a significant impact on the overall treatment pressure behavior. In addition, from a perforation standpoint, if less than 100% of perforations are open and taking fluid (which is likely), sensitivities can be run to determine the impact of such treatment on behavior and results to determine if corrective actions are needed.

13.2.2 Treatment and Wellbore Characterization

Determination of various pumping parameters that are anticipated to play a role in the treatment is also important from a pretreatment modeling standpoint. Such values include the anticipated leak-off characteristics and behaviors, fluid systems and their associated viscosities, anticipated proppant type and concentrations, and wellbore configurations. All of these must be correctly input into a model for that model to mimic actual field results.

Wellbore configurations are often considered as a very simple input and they generally are. Diameters and lengths of tubing or casing are known and can be accounted for in a model. The geometric components will allow for accounting of any associated pipe friction. However, other wellbore components, such as sliding sleeve seats (frequently used in multistage horizontal well treatments) or other internal diameter restrictions, must also be considered. These frictional drops are important to consider as they can impact the pressure that is being delivered to the fracture and the associated growth. They are also important to consider because modeling of such can help to determine the potential for accidently shearing sleeves and impacting treatment diversion. Correct directional surveys must also be incorporated into the model for frictional purposes, wellbore placement in the structure, and posttreatment flow behaviors.

Before pumping of an actual treatment, a model will need to incorporate an anticipated treatment schedule. This schedule can then be replaced by the actual treatment data once the treatment is completed. An example treatment schedule is shown in Table 13.1, where Stages 1−5 represent the pad and slurry stages; Stage 6, the flush stage; and Stage 7, a shut-down and 15-min shut-in pressure observation stage.

Correct characterization of the fluid system that is used in any given treatment is also a key component to correctly modeling a treatment. Most fracturing fluids are non-Newtonian fluid systems with complex viscosity behaviors. Although frequently modeled as power law fluid systems due

TABLE 13.1 Example of Hydraulic Fracturing Treatment Schedule

Stage#	Stage Time (min:s)	Fluid Type	Clean Stage Volume (gals)	Cumulative Clean Volume (gals)	Proppant Type	Slurry Concentration (ppa)	Cumulative Proppant (lbs)	Slurry Rate (bpm)
1	11:54	20# Guar	20,000	20,000	NA	0	0	40
2	12:27	20# Guar	20,000	40,000	20/40 Sand	1	20,000	40
3	12:59	20# Guar	20,000	60,000	20/40 Sand	2	60,000	40
4	13:32	20# Guar	20,000	80,000	20/40 Sand	3	120,000	40
5	14:04	20# Guar	20,000	100,000	20/40 Sand	4	200,000	40
6	11:54	2% KCl	20,000	120,000	NA	0	200,000	40
7	15:00	2% KCl	0	120,000	NA	0	200,000	0

to the simplicity of such models, most treatment fluids exhibit far more complex behaviors than can be captured by a simple power law system. Fig. 13.4 shows the viscosity profile of a commercial 30# loading guar gel system. Note the changing viscosity as a function of time. This behavior for this fluid system is not a straight line behavior as implied by a power law model, and the viscosity of the fluid at any given point in the treatment must be tracked.

The anticipated leak-off behavior of the reservoir must also be accounted for in any modeling. Matrix leak-off, associated with the Carter spurt loss equation and the Williams (1970) total leak-off coefficient, C_t, must be incorporated in the model to determine the amount of fluid that will leak into the matrix and build filter cake. Pressure-dependent leak-off (PDL) is also a critical input that can greatly affect fracture behavior. The activation pressure at which PDL initiates and the volume that will leak-off are both important to assessing field applications. These values and others can be determined by pretreatment pump-in tests as discussed in Sections 13.2.3 and 13.2.4.

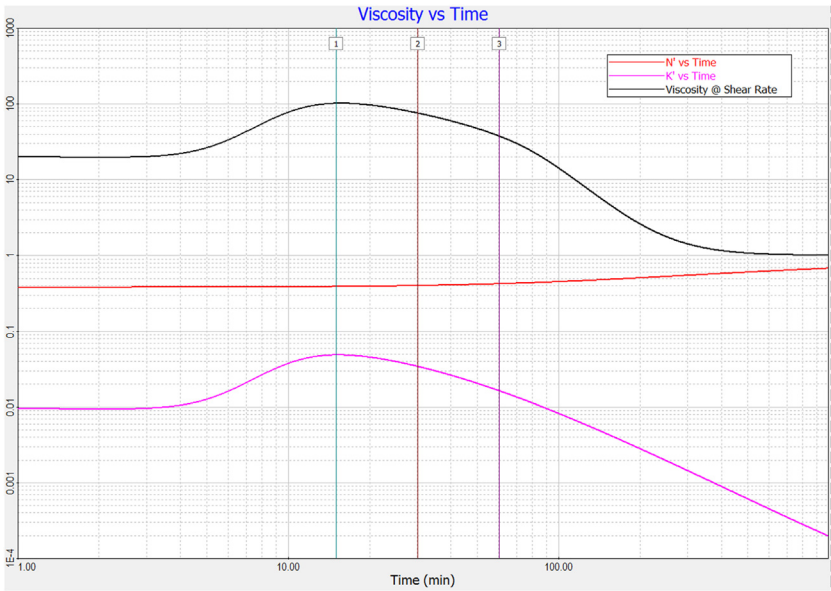

FIGURE 13.4 Viscosity (black line) versus time for a 30# linear guar system. The N′ (*red line* [dark gray in print version]) and K′ (*pink line* [light gray in print version]) values are also presented. This graph shows the variability that a treatment fluid can have during a pumping treatment. Models should have accurate curves for these values to correctly account for their behavior in the wellbore and reservoir.

13.2.3 Reservoir Characterization

In any modeling effort for petroleum applications, the characterization of the reservoir is critical, and hydraulic fracture modeling is no different in its importance. Multiple components of the reservoir need to be correctly incorporated into any modeling effort as they can have large impacts on the model results both from the treatment and posttreatment production aspects. A few of the more critical components and their impacts are discussed here.

Permeability and porosity can both impact leak-off and filter cake performance. Heterogeneities in the reservoir, and along fracture faces, can enhance or impede leak-off behaviors. Obviously, permeability will also have an impact on posttreatment analysis and production matching. Permeability values can be determined from a variety of techniques; however, in low-permeability reservoirs, diagnostic fracture injection tests (DFITs) are currently a preferred method for hydraulic fracturing applications as such tests also provide information about a variety of other model inputs (Craig and Blasingame, 2006; Barree et al., 2009; Ehlig-Economides and Liu, 2017). DFITs have found significant applicability in unconventional, low-permeability reservoirs, where they can provide such reservoir parameters in a much more convenient timescale than traditional pressure transient techniques. The permeability values provided are frequently preferred in posttreatment production, as they provide an overall effective permeability value from the G-closure times.

The subject formation's stress profile, including overburden (σ_v), maximum horizontal stress (σ_H), and minimum horizontal stress (σ_h), will have a significant impact on overall geometric fracture growth. Although generally considered as static values, these values need to be treated as dynamic for hydraulic fracturing purposes, especially if multistage treatments are being considered and "stress shadowing" is occurring. Take Eq. (13.4), for instance. This equation shows one version of closure pressure (P_c) that can also be considered to represent the minimum horizontal stress, σ_h. When a treatment is pumped, the strain and pore pressure components of the stress equation can be impacted and transformed during the treatment (Fisher et al., 2004; Wu and Olson, 2016). This behavior can cause stress shadowing and have impacts on subsequent treatments. The model should be initially calibrated to these stress values and then recalibrated after the treatment is pumped to account for changes in these values. The need for and detail of the inputs for these particular values will vary greatly by the software package being used and such needs are to be understood by the user.

$$P_c = \frac{\nu}{(1-\nu)}\left[P_{\text{ob}} - \alpha P_p\right] + \alpha P p + \varepsilon_x E + \sigma_t \tag{13.4}$$

where α, Biot's poroelastic constant; ε_x, regional horizontal strain, microstrains; σ_t, regional horizontal tectonic stress, psi; μ, Poisson's ratio;

E, Young's modulus, million psi; P_c, closure pressure, psi; P_{ob}, overburden pressure, psi; P_p, pore pressure, psi.

A final reservoir component should be incorporated in the net extension pressure or process zone stress (PZS). PZS is the value of additional pressure it takes to extend the fracture above and beyond that of closure pressure. It is generally defined as the difference between fracture pressure and closure pressure and incorporates various tip processes such as the effects of fluid lag, rock tensile strength, dilatancy, and other nonlinear stress profiles around the tip of the fracture. These effects can be incorporated individually in a model; however, it is exceedingly rare to be able to acquire values for each of them at field scales. Therefore, they are usually included as a lump term in most software packages.

13.2.4 Pretreatment Calibration Techniques

In addition to the step rate test for wellbore friction described earlier, pretreatment injection falloff tests, such as minifracs, are commonly used in pretreatment calibration of hydraulic fracturing models. Traditional minifracs are focused on fluid and leak-off characteristics, whereas DFIT tests measure these values but also assess various reservoir parameters, including pore pressure, permeability, and reservoir transmissibility as noted in the previous section. When correctly pumped and analyzed (Barree et al., 2014), DFITs can be used to calibrate numerous pretreatment model values such as fracture pressure; closure pressure; leak-off mechanisms including PDL, PZS, pore pressure, and effective permeability. Traditional minifrac falloff tests also need to be correctly pumped, and when so, can provide valuable leak-off and fluid behavior results. Obviously, such tests will not always be available for a given well; however, even regional or nearby tests can help with model calibration.

13.3 POSTTREATMENT MODEL VALIDATION

Once a fracturing treatment is pumped, most inputs need to be reassessed and the actual pumping data, incorporated. The modeling practice itself is an iterative process, with the final result taking time and effort to arrive at before a fully integrated and calibrated model is achieved.

13.3.1 Data Quality and Verification

One of the best practices for model inputs from the field is verification and validation of the treatment data curves. Most service companies will provide digital files in some type of comma-separated or delimited file. Unfortunately, there is no industry standard for these file formats, but most commercial modeling packages are capable of reading them. There is also no industry

standard for what the various data columns are named, and the user must determine what columns of data are critical to the modeling efforts. At a minimum, time, wellhead pressure, pumping rate, and proppant concentration must be incorporated, but other curves such as foam concentration, measured bottomhole pressure, and cumulative volumes may also be present and helpful to the modeling efforts. Fig. 13.5 shows an example of pump curves read from a digital treatment file.

In addition to determining what curves are required for the model runs, the quality of the data needs to be double-checked. Densitometers can have errors, and the calculated total proppant volumes can be off from actual pumped volumes (Van Domelen et al., 1989). In addition, if acid is pumped as a spearhead to the treatment, the densitometer can pick this volume up as a proppant volume due to the density differences from the fracturing fluid and what the densitometer is calibrated to. Therefore, the total pumped volumes being calculated by the model should be cross-checked with the service company—calculated volumes and associated reports. Any other unexplained abnormalities in the data should also be investigated and understood before proceeding with the rest of the modeling process.

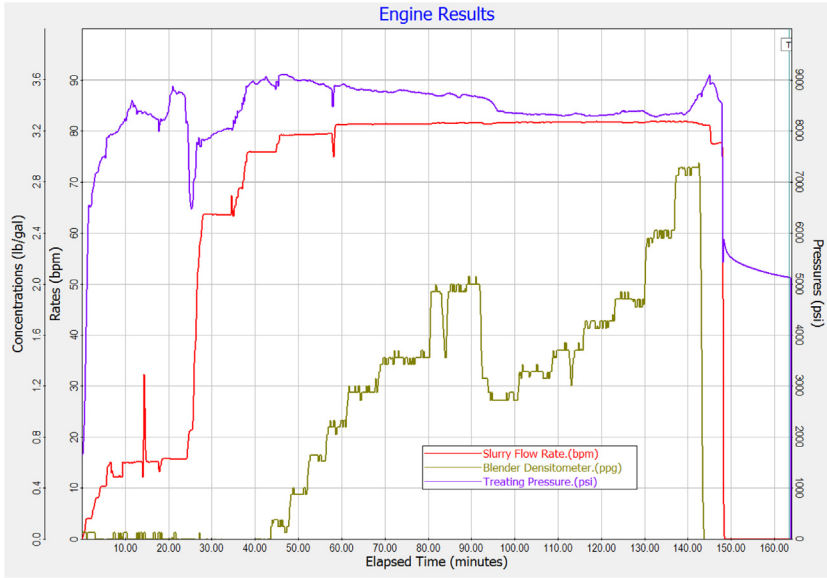

FIGURE 13.5 Raw data from the treatment pumping van. Quality control of the data is critical to the modeling process, and all curves should be verified for correctness. *From the GOHFER hydraulic fracturing modeling software.*

13.3.2 Landing Intervals

In the case of a horizontal well, the location of the well relative to the formation is a critical component for posttreatment modeling. Subtle differences in a landing depth of only a few feet can greatly impact both actual treatment and modeling results. Fig. 13.6 shows a wellbore that is landed in-zone for most of the length of the horizontal well. However, due to the distinct differences in reservoir properties, a subtle difference of only 5 feet in the vertical profile can have a significant impact on the location of the well relative to bounding stresses. The fracturing model can only be judged by the accuracy of the input data, and geosteering results have their own challenges; however, a best effort to place the well correctly in geologic space will yield the best and most accurate final modeling results.

13.3.3 Treatment Inputs

As noted earlier in this chapter and shown in Fig. 13.4, fracturing fluids are generally non-Newtonian in their behavior. The fluid viscosity can be impacted by a great number of elements including shear rate and history, the base mix water that is used, minor additive concentrations or variations, the shelf life of those chemicals, temperature, and other factors. Many commercial software packages have viscosity curves such as what is shown in Fig. 13.4, but these tend to be idealized curves for a given product. Under actual field and mix water conditions, the fluid may act significantly different. Consideration

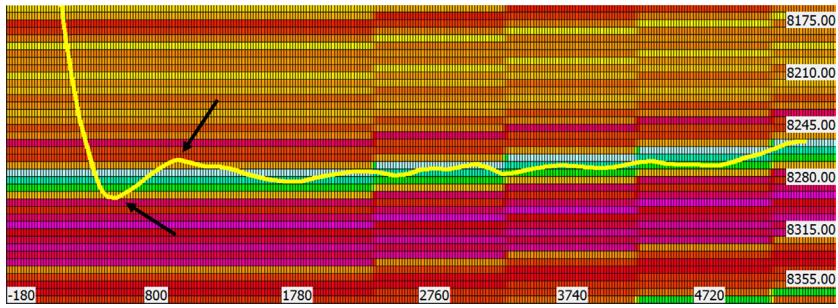

FIGURE 13.6 Grid of Poisson's ratio values (lower values in "cooler" colors) with a horizontal wellbore (yellow [light gray in print version]). Depth in feet is shown to the right; length in feet is shown along the bottom of the grid; and each grid block is 5 feet by 5 feet. The wellbore stays in the zone of interest for most of its length; however, it is out of zone toward the heel of the well (as indicated by the *arrows*). Treatments located in this section will behave differently than treatments pumped in other parts of the well. *From the GOHFER hydraulic fracturing modeling software.*

may need to be given to including a curve specific to the actual treatment. This is no easy task, as the viscosity curve needs to cover a wide variety of shear rates and time frames, much more than a common tabletop viscometer can account for. Inclusion of such information will need to involve the service company and some significant testing to account for the full range of necessary inputs. The impacts such values can have on proppant transport can be significant.

For multistage treatments that may have an impact on subsequent stages, the relaxation time between treatments needs to be considered and included in the model. Such time lapses can have large impacts on stress shadowing behaviors. For instance, if a horizontal multistage treatment is being pumped and a 3-h perforation gun run occurs between Stage 1 and Stage 2, those 3 hours need to be considered in the modeling of those stages. A model run on Stage 2 that occurs for only minutes in "model time" after Stage 1 does not correctly capture the strain relaxation and other physical behaviors that will occur before Stage 2 is pumped.

In addition to verification of the fluids and treatment timing, the proppants used in the treatment should be properly characterized. Proppant transport has a tremendous impact on the final conductivity of the model and therefore also on production and reserve recovery. The modeling software should properly handle this behavior—be it based on viscosity or velocity transport influences. Inputs such as correct specific gravities, particle sizes, sieve distributions, etc. should be reviewed and verified that they match the actual materials used in the field. All 20/40 sand proppants are not the same, and proppant libraries, just like fluid libraries, may be too general in their descriptions. Correct material properties, or at least one that are close to the reality of the treatment, should be sought out and included.

13.3.4 Pressure Calibration

Likely the most critical component of modeling actual treatments is the calibration of the pressure curves. When all reservoir and treatment parameters are correctly described, and a pressure match developed, the treatment behaviors that are occurring in the model should be a solid indication of what is actually occurring in the reservoir. This will allow the pressure that is being calculated by the model to match the actual field-measured pressures.

Bottomhole pressure data are a luxury that occurs fairly infrequently in day-to-day practice. If available, it should obviously be used in the matching and model validation process. However, even if it is available, the impacts of perforation and near-wellbore tortuosity need to be considered, along with any pipe friction between the fracture exit point and the location of the pressure gauges or dead string depth. Surface pressure, which is by far more common, additionally needs to account for hydrostatic head and pipe friction.

Assuming that the closure pressure and other reservoir components, such as permeability, have been correctly entered into the model, the most likely modification that will be needed for a pressure match is adjustment of the frictional values. The chosen software may have an excellent pipe frictional correlation included; however, as with the viscosity behavior noted earlier, this correlation and associated frictional behavior may be based on ideal fluid properties. Actual fluid properties in the field, along with other critical parameters such as pipe roughness, can alter the default frictional values in the model. This is especially true in the slurry components.

Along with pipe friction, the impacts of changing perforation and near-wellbore tortuosity need to be incorporated in the pressure match. Step rate tests can be used to determine the pretreatment frictional behavior as a starting point; however, as previously noted in Section 13.2.1, erosion will change the discharge coefficient and perforation diameter, as shown in Fig. 13.7. This is a dynamic behavior, and the model needs to account for such in the calculated pressure.

When all of these inputs are correctly captured, the calculated pressure can and should match the actual measured pressure. Fig. 13.8 is an example of a treatment match that has been pressure calibrated. Once a calibrated match is obtained, it can help to separate out things such as near-wellbore behaviors from what is actually occurring in the fracture including diagnosing issues such as causes of screen out.

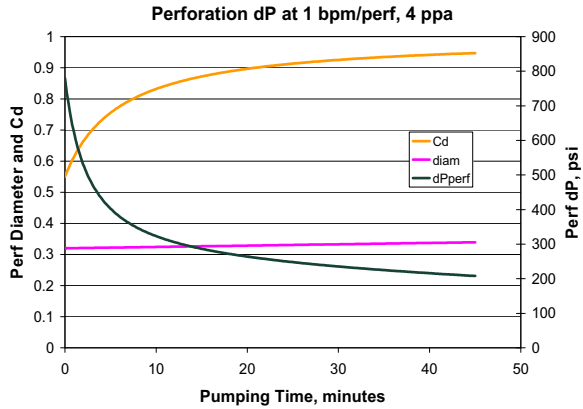

FIGURE 13.7 Graph showing the change in perforation friction (right axis, *blue line* [dark gray in print version]) due to erosion of the perforation diameter (left axis, *pink line* [light gray in print version]) and the discharge coefficient (left axis, *orange line* [gray in print version]). These results are for a rate of 1 bpm/perforation at 4 ppa proppant loading. *Based on the Crump, J.B., Conway, M.W., 1988. Effects of perforation-entry friction on bottomhole treating analysis. Journal of Petroleum Technology 40 (08), 1041–1048 model.*

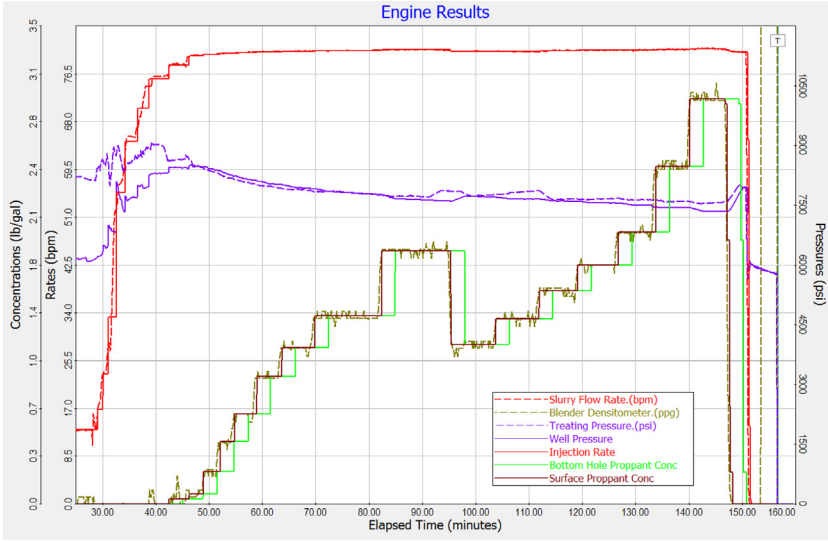

FIGURE 13.8 Treatment pressure match from one stage of a multistage horizontal well treatment. The *solid purple line* (gray in print version) (noted as "well pressure") is the output of the model; whereas, the *dashed purple line* (gray in print version) (noted as "treating pressure") is the field pressure data. *From the GOHFER hydraulic fracturing modeling software.*

13.3.5 Geometric Calibration

Although pressure calibration is the primary focus of most model validation, a variety of direct diagnostic tools that are now available also allows for geometric calibration of models when such data are acquired. When incorporating such data, consideration needs to be given to the uncertainty that goes with each measurement system. Similarly, uncertainty in the model itself almost also undergoes scrutiny. If a model does not entirely calibrate to a geometric measurement, it may simply be a result of such technique uncertainty, and forcing a match, just to have a match, may undermine the intent of the whole modeling process.

When considering the height of the fracture, data from near-wellbore tools such as temperature logs, radioactive tracer profiles, and neutron-traced proppants can be incorporated into the model and used for comparison purposes (Williams and McCarthy, 1987; Duenckel et al., 2011). Created fracture height is a consideration with all these types of tools, but in the case of radioactive tracers and neutron-traced proppants, propped fracture height can also be a potential matching parameter. The proppant transport indicated by the modeling software can be compared to results of the treatment stages that were tagged with tracers. Such comparisons can shed light on proppant settling and location of conductivity values in the vertical direction of the fracture.

"Far-field" data, such as tiltmeter and microseismic data, are also a valuable source of model calibration further away from the wellbore. As with the near-wellbore techniques, the results of the far-field techniques need to be considered in context when attempting to calibrate a model to them. For instance, microseismic events represent shear slippage events but do not necessarily mean that there is fracturing fluid or proppant at the location of the event. In addition, there can be discrepancies in the velocity model or geologic interpretation of the system that can induce additional error in the location of the event (Cipolla et al., 2011; Johnston and Shrallow, 2011). This uncertainty and other concerns such as observation of well bias need to be taken into account in the modeling results as they can result in several tens, if not hundreds, of feet of error range in the results. With this in mind, the modeler should use far-field measurement results to guide their model matches; however, forcing the model to fit all events in a microseismic acquisition could provide a false sense of calibration. Far-field results should be used as guides, not absolutes, and discussions between the microseismic interpreters and the fracturing treatment modelers will be invaluable in determining the accuracy of all integration aspects.

In addition to some of the more traditional geometric growth techniques, other methods are becoming available on the market that will be of great value in field model validation. Although not necessarily new to the industry, fiber-optic measurements are starting to be used extensively in the analysis of hydraulic fracturing treatments. These systems, specifically distributed temperature sensing (DTS) and distributed acoustic sensing (DAS), have provided significant insight into the propagation and posttreatment production of hydraulic fracturing treatment, very specifically in multistage treatments in both vertical and horizontal wellbores (Ugueto et al., 2014). DTS and DAS data can help to determine the amount of fluid and proppant volumes that are exiting any given perforation cluster set, data which can then be incorporated into the fracture modeling (Wheaton et al., 2014, 2016). In addition, DTS data can help to understand warm-back behaviors that help to interpret fluid system behaviors in field situations, information that can also be incorporated into and calibrated with fracture models.

Additional geometric measurement techniques are becoming available such as electrically and magnetically detectable proppants (Palisch et al., 2016, 2017). Although relatively new and still under development, such measurement options the opportunity to even further improve our calibration of models with field data.

In general, no matter what geometric measurements are used and calibrated to, the need for full data integration and triangulation is critical. Modelers should not just take the data that are provided to them and match their models to such. Understanding the uncertainties and issues that can go along with such

data is critical when validating field models. Ranges of modeling results should be pursued in the presence of such uncertainties, and the impacts on the outcomes of the models, including production, should be considered in the calibration process.

13.4 PRODUCTION VALIDATION

The final validation point for a hydraulic fracturing model comes in the form of production matching. Does the model correctly account for and represent the posttreatment production? Ideally, this validation point is not just focused on the flowback period but rather several months, if not a year or two, of production results.

The production modeling and validation process can be approached in a variety of ways. Most commercial hydraulic fracturing simulation software has some type of production analysis or simulation option that will provide a prediction of the anticipated production for the modeled fracturing treatment. Frequently, these models are analytical in nature. If available, they can be used to history match the actual well production. The benefits of this route are that the model has the fracturing profile already present and directly tied into the production simulation module. One of the main drawbacks, however, is because it is analytical, some of the details captured by the fracturing treatment may be lost in the transition.

The use of numerical simulation is another route for posttreatment validation and generally requires the hydraulic fracturing model results to be uploaded into another software package. One of the biggest concerns with this route is the loss of the details that the fracturing model may have captured due to the upscaling that is usually required for entry into a numerical simulator. This is unfortunate but a reality, and the modeler needs to consider this loss of detail in their overall comparisons when history matching the production results.

Other diagnostic tools can help with the history matching effort. Flowback behavior captured by techniques such as fiber optics and flowback tracers (Salman et al., 2014) can help with determining the behavior of the fluids flowing into the well. Especially in multistage horizontal well systems, these techniques can help to determine the number of stages contributing to flow, and in the fiber optics case, they can help determine even the number of perforation clusters contributing to flow (Wheaton et al., 2014).

Another posttreatment analysis option that has become popular in recent years is the use of rate transient analysis, also frequently referred to as production analysis. This technique can be coupled together with fracture modeling results to add to the analysis of what is occurring once the well starts to produce. Although such analysis provides nonunique answers, the fracture

modeling itself can help to anchor some of the production parameters such as the number of potentially contributing fractures.

No matter which postproduction technique is used, conductivity damage factors need to be considered (Barree et al., 2003; Palisch et al., 2007). This can be one of the biggest discrepancies between numerical reservoir simulation and hydraulic fracture modeling; however, it is also one of the areas where the hydraulic fracture modeling can greatly contribute to the inputs into a production simulation. Effects such as embedment, filter cake buildup, gel damage, non-Darcy flow, multiphase flow, cycle stress, and long-term degradation in the fracture need to be taken into account when incorporating the hydraulic fractures into a production simulation model as they can degrade conductivity significantly in the reservoir (+95%) as compared to surface testing. Honoring these damage mechanisms will help to calibrate the entire production system, both reservoir and fracture components, and can aid in determining where improvements to the stimulation can be made.

13.5 SUMMARY

When pulled together, the sections of this chapter provide the outline for a hydraulic model validation workflow. Fig. 13.9 shows the workflow for the processes discussed in this chapter. Although the full process described by this figure can take months (or years) due to the production requirements, it is critical if the full impacts of the fracturing design and treatment are to be determined and improved. "Look backs" and posttreatment analysis at multiple intervals during the development of a field can be performed by using this approach.

The process starts with determining treatment goals and acquiring as much pretreatment data as economically and technically possible. These pretreatment data include not only treatment parameters, but also reservoir and wellbore data. Obviously, not every modeling project can afford to acquire all of the preliminary data that can be attained; however, the modelers (and their company) must determine the value of the information that such data can provide. This type of data will aid in developing the initial fracture model. From here, an initial design can be developed.

Then once the treatment is pumped, it can be calibrated against multiple levels of outcomes. The first, and basically always available, outcome will be the pressure, which should be the starting point for model validation. Then if available, geometric measurements can and should be incorporated to the limit of the available data quality. The final, and probably most insightful, validation comes when the model is calibrated to actual production. Such calibration can be performed with a simple decline curve analysis or through a full-blown numerical simulation. In any case, such as the treatment pressure,

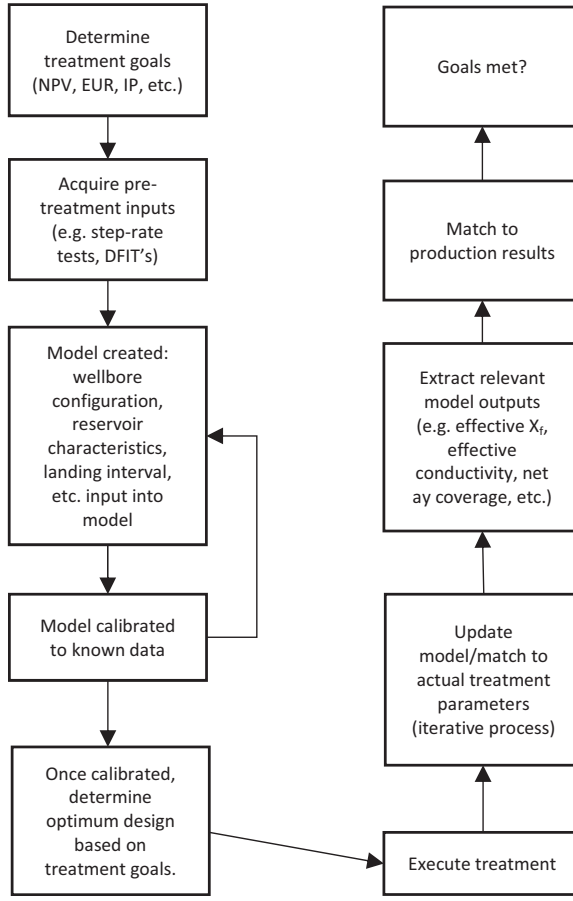

FIGURE 13.9 Model validation workflow for the processes/steps discussed in this chapter.

production data are always available and any model should ultimately be calibrated to the final well and reservoir results.

No matter the fracturing software used, the data available, or the extent of the effort put into model development, it needs to be stressed that hydraulic fracture modeling is an iterative process! It is extremely rare to arrive at a fully valid model with one run through this workflow. In addition, it is sometimes rare to see the loop fully closed with the addition of the production data incorporation. All valid data, no matter the source, need to be incorporated into the workflow, and the answer should triangulate into a set of valid conclusions. Such a process can take considerable time but will result in extremely accurate and valuable models that will improve treatment design and implementation in any given field area.

NOMENCLATURE

α Biot's poroelastic constant
ε_x Regional horizontal strain, microstrains
ρ_{fluid} Density of the injection fluid, ppg
σ_h Minimum horizontal stress, psi
σ_H Maximum horizontal stress, psi
σ_t Regional horizontal tectonic stress, psi
σ_v Overburden stress, psi
μ Poisson's ratio
C_d Discharge coefficient
C_t Total leak-off coefficient, 1/psi
d_{perf} Diameter of perforations, inches
E Young's modulus, million psi
k_{perf} $0.2369\frac{\rho_{\text{fluid}}}{n^2 d_{\text{perf}}^4 C^2}$, psi/bpm^2
$k_{\text{tortuosity}}$ Tortuosity factor, psi/bpm$^{1}/_{2}$
n Number of open perforations
$\Delta P_{\text{BHFriction}}$ Total bottomhole friction drop, psi
ΔP_{perf} Total friction drop across the perforations, psi
$\Delta P_{\text{tortuosity}}$ Total friction drop due to tortuosity, psi
P_{c} Closure pressure, psi
P_{ob} Overburden pressure, psi
P_p Pore pressure, psi
PZS Process zone stress, psi
q Injection rate, bpm
X_f Fracture half-length, ft

REFERENCES

Barree, R.D., Barree, V.L., Craig, D.P., 2009. Holistic fracture diagnostics: consistent interpretation of prefrac injection tests using multiple analysis methods. SPE Production & Operations Journal 24 (03), 396–406.

Barree, R.D., Miskimins, J.L., Gilbert, J., 2014. Diagnostic fracture injection tests: common mistakes, misfires, and misdiagnoses. SPE Production & Operations Journal 29 (04), 1–15.

Barree, R.D., Co, S.A., Barree, V.L., Conway, M.W., 2003. Realistic Assessment of Proppant Pack Conductivity for Material Selection. SPE Paper No. 84306.

Chipperfield, S.T., Roberts, G.A., Miller II, W.K., Vandersypen, R.S., 2000. Gel Slugs: A Near-Wellbore Pressure-loss Remediation Technique for Propped Fracturing. SPE Paper No. 59777.

Cipolla, C., Maxwell, S., Mack, M., Downie, R., 2011. A Practical Guide to Interpreting Microseismic Events. SPE Paper No. 144067.

Cleary, M.P., Johnson, D.E., Kogsboil, H.H., Owens, K.A., Perry, K.F., de Pater, C.J., Stachel, A., Schmidt, H., Tambini, M., 1993. Field Implementation of Proppant Slugs to Avoid Premature Screen-Out of Hydraulic Fractures with Adequate Proppant Concentration. SPE Paper No. 25892.

Craig, D.P., Blasingame, T.A., 2006. Application of a New Fracture-Injection/Falloff Model Accounting for Propagating, Dilated, and Closing Hydraulic Fractures. SPE Paper No. 100578.

Crump, J.B., Conway, M.W., 1988. Effects of perforation-entry friction on bottomhole treating analysis. Journal of Petroleum Technology 40 (08), 1041–1048.

Duenckel, R.J., Smith Jr., H.D., Warren, W.A., Grae, A.D., 2011. Field Application of a New Proppant Detection Technology. SPE Paper No. 146744.

Ehlig-Economides, C.A., Liu, G., 2017. Comparison Among Fracture Calibration Test Analysis Models. SPE Paper No. 184866.

Fisher, M.K., Heinze, J.R., Harris, C.D., Davidson, B.M., Wright, C.A., Dunn, K.P., 2004. Optimizing Horizontal Completion Techniques in the Barnett Shale Using Microseismic Fracture Mapping. SPE Paper No. 90051.

Johnston, R., Shrallow, J., 2011. Ambiguity in Microseismic Monitoring. SEG Annual Meeting, San Antonio, TX, pp. 1514−1518.

Palisch, T., Duenckel, R., Bazan, L., Heidt, H.J., Turk, G., 2007. Determining Realistic Fracture Conductivity and Understanding its Impact on Well Performance − Theory and Field Examples. SPE Paper No. 106301.

Palisch, T., Al-Tailji, W., Bartel, L., Cannan, C., Czapski, M., Lynch, K., 2016. Recent Advancements in Far-field Proppant Detection. SPE Paper No. 179161.

Palisch, T., Al-Tailji, W., Bartel, L., Cannan, C., Zhang, J., Czapski, M., Lynch, L., 2017. Far-Field Proppant Detection Using Electromagnetic Methods − Latest Field Results. SPE Paper No. 184880.

Romero, J., Mack, M.G., Elbel, J.L., 1995. Theoretical Model and Numerical Investigation of Near-Wellbore Effects in Hydraulic Fracturing. SPE Paper No. 30506.

Salman, A., Kurtoglu, B., Kazemi, H., 2014. Analysis of Chemical Tracer Flowback in Unconventional Reservoirs. SPE Paper No. 171656.

Ugueto, G.A., Ehiwario, M., Grae, A., Molenaar, M., McCoy, K., Huckabee, P.A., Barree, R., 2014. Application of Integrated Advanced Diagnostics and Modeling to Improve Hydraulic Fracture Stimulation Analysis and Optimization. SPE Paper No. 168603.

Van Domelen, M.L., Jantz, E.L., Murphy, K.S., 1989. Onsite Design, Analysis, and Automation Maximizes Efficiency of Fracturing Operations. SPE Paper No. 18863.

Wheaton, B., Haustveit, K., Deeg, W., Miskimins, J., Barree, R., 2016. A Case Study of Completion Effectiveness in the Eagle Ford Shale Using DAS/DTS Observations and Hydraulic Fracture Modeling. SPE Paper No. 179149.

Wheaton, B., Miskimins, J., Wood, D., Lowe, T., Barree, R., 2014. Integration of Distributed Temperature and Distributed Acoustic Survey Results with Hydraulic Fracture Modeling: A Case Study in the Woodford Shale. URTeC Paper No. 1922140.

Williams, B.B., 1970. Fluid loss from hydraulically induced fractures. Journal of Petroleum Technology 22 (07), 882−888.

Williams, R.L., McCarthy, J.T., 1987. Using multiple radioactive tracers to Optimize stimulation designs. SPE Paper No. 16383.

Wu, K., Olson, J.E., 2016. Mechanisms of simultaneous hydraulic-fracture propagation from multiple perforation clusters in horizontal wells. SPE Journal 21 (03), 1000−1008.

Chapter 14

Hydraulic Fracturing: Experimental Modeling

Hazim Abass, Christopher Lamei
Colorado School of Mines, Denver, CO, United States

This chapter presents the experimental modeling of hydraulic fracture characteristics in conventional and unconventional rock samples. There are distinct features associated with hydraulic fracture initiation and propagation in rock formations that are classified as homogenous and heterogeneous, brittle and ductile, consolidated and unconsolidated, permeable and tight, and intact and naturally fractured. Understanding the features of induced fractures in these formations is vital to design effective fracture stimulation treatments. The main logical difference between fracture stimulation of conventional versus unconventional reservoirs is that in conventional reservoirs a fracture is introduced for the hydrocarbon to sense and flow toward it; whereas in unconventional reservoirs, a fracture is introduced to reach where the hydrocarbon is located. Therefore, hydraulic fracturing in relatively permeable reservoirs is mostly used for modifying the fluid flow pattern in the reservoirs; while in tight formations it is aimed at shearing existing microfractures to get closer to the trapped hydrocarbon and bringing more reservoir volume in contact with created fracture network.

14.1 THEORETICAL BACKGROUND

In this section, fundamentals of fracture propagation will be discussed and followed with laboratory observation related to fracture initiation and propagation. A hydraulic fracture will initiate at the wellbore as a result of tensile failure developed at certain locations around the wellbore. When a wellbore is introduced into a formation, a new stress state around the wellbore is developed, causing a portion of the wellbore to have preferential failure mode at different locations around the wellbore.

In 1898, Kirsch described the stress state around a vertical wellbore parallel to the principal vertical stress, S_v, in an isotropic, elastic medium. This theory states that when a cylindrical opening such as a wellbore is created, it

Hydraulic Fracture Modeling. https://doi.org/10.1016/B978-0-12-812998-2.00014-X

causes the stress trajectories to bend around the wellbore wall causing a cylindrical stress field around the wellbore that is different from the original Cartesian stress field. Stress distortion can be illustrated as bunching up of stress trajectories in the direction of $S_{h\min}$ and creating strong compression, and spreading out of stress trajectories at the direction of $S_{H\max}$ causing a reduction in compressive stress. The following mathematical equations are provided to calculate the new near-wellbore stresses based on the elastic theory considering an infinite plate with a hole in the center (Zoback, 2010):

$$\sigma'_{rr}(r,\theta) = \frac{1}{2}\left(\sigma'_{H\max} + \sigma'_{h\min}\right)\left(1 - \frac{r_w^2}{r^2}\right) + \frac{1}{2}\left(\sigma'_{H\max} - \sigma'_{h\min}\right) \times \left(1 - \frac{4r_w^2}{r^2} + \frac{3r_w^2}{r^4}\right)\cos 2\,\theta + \frac{(P_w - P_r)r_w^2}{r^2}$$

$$\sigma'_{\theta\theta}(r,\theta) = \frac{1}{2}\left(\sigma'_{H\max} + \sigma'_{h\min}\right)\left(1 + \frac{r_w^2}{r^2}\right) - \frac{1}{2}\left(\sigma'_{H\max} - \sigma'_{h\min}\right) \times \left(1 + \frac{3r_w^2}{r^4}\right)\cos 2\,\theta - \frac{(P_w - P_r)r_w^2}{r^2}$$

$$\tau_{r\theta}(r,\theta) = \frac{1}{2}\left(\sigma'_{H\max} - \sigma'_{h\min}\right)\left(1 + \frac{2r_w^2}{r^2} - \frac{3r_w^2}{r^4}\right)\sin 2\,\theta$$

$$\sigma_{zz} = \sigma'_v - 2\nu\left(\sigma'_{H\max} - \sigma'_{h\min}\right)\left(\frac{r^2}{r_w^2}\right)\cos 2\,\theta$$

As seen from the above equations, the magnitude of the new stress field around the wellbore is related to the fluid pressure in the wellbore. During a hydraulic fracturing treatment, wellbore pressure is constantly increasing until tensile failure reaches. Fig. 14.1 shows stress concentration around a wellbore for a case, where $S_{H\max}$ and $S_{h\min}$ are 2.3 and 1.2 times the vertical stress, respectively. Negative values show the state of stress around part of the wellbore in tensile mode (Grandi et al., 2002).

Tensile failure occurs when tangential stress (hoop stress) around the wellbore (blue lines in Fig. 14.1) equals or exceeds the tensile strength of the rock, which is usually in the order of one-tenth of compressive strength.

$$\sigma_{zz} = \sigma'_v - 2\nu\left(\sigma'_{H\max} - \sigma'_{h\min}\right)\left(\frac{r^2}{r_w^2}\right)\cos 2\,\theta$$

Breakdown pressure may be calculated where a maximum tensile stress occurs, which is perpendicular to the direction of minimum horizontal stress.

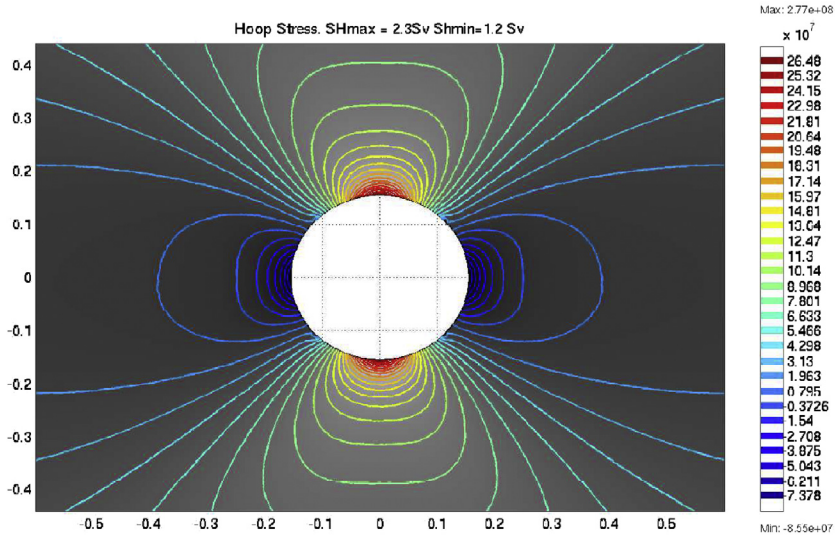

FIGURE 14.1 Stress state around a vertical wellbore, also known as Hoop stress (Grandi et al., 2002).

Breakdown pressure then can be calculated as given below from Kirsch equation, having $r = r_w$, and $\theta = 0$

$$\sigma(r_w, 0) = 3\sigma'_{h\min} - \sigma'_{H\max} - P_w + P_r$$

The breakdown pressure can be written as

$$P_{bd} = 3\sigma'_{H,\min} - \sigma'_{H,\mathrm{Max}} + T + P_r$$

Or, in terms of total stresses,

$$P_{bd} = 3\sigma_{H,\min} - \sigma_{H,\mathrm{Max}} + T - P_r$$

And the fracture propagation pressure can be described as

$$P_f = \sigma_{H,\min} + \Delta P_{net} + \Delta P_{fr} + \Delta P_{tip}$$

The term, ΔP_{fr}, is a lump sum of pressure losses due to friction at the perforation, near wellbore, and along fracture. If we assume fracture stops propagating after shut-in, then friction pressure becomes zero and the instantaneous shut-in pressure, ISIP, is

$$\mathrm{ISIP} = \sigma_{H,\min} + \Delta P_{net}$$

and

$$P_f = \mathrm{ISIP} + \Delta P_{fr} + \Delta P_{tip}$$

ΔP_{net} is required to keep the fracture open at a given width. ΔP_{tip} is the pressure at the tip required to propagate the fracture (Economides et al., 1998). Once a fracture is initiated, it will propagate in a manner that is perpendicular to least principal stress. Even if a fracture is initiated from an oriented perforation at an angle to least principal stress, it will reorient itself to find the path to propagate perpendicular to least principal stress.

14.2 BREAKDOWN AND PROPAGATION PRESSURES

The following laboratory tests show the fundamentals of fracture propagation. In the first test shown in Fig. 14.2, a cased horizontal well has been drilled parallel to the principal maximum horizontal stress. Pressure profile is shown in Fig. 14.3 and breakdown pressure is recorded as 3322 psi. Using the breakdown pressure equation, P_{bd} can be calculated as below.

$$P_{bd} = 3\sigma_{H,\min} - \sigma_{H,\text{Max}} + T - P_r$$

where

$$\sigma_{H,\min} = 1800 \text{ psi}$$

$$\sigma_{H,\text{Max}} = 3000 \text{ psi}$$

$$T = 780 \text{ psi}$$

$$P_r = 0 \text{ psi}$$

$$P_{bd} = 3(1800) - 3000 + 780 - 0 = 3180 \text{ psi}$$

The pressure value of 3180 psi is comparable to the 3324 psi breakdown pressure observed in the pressure–time record of this test, confirming the

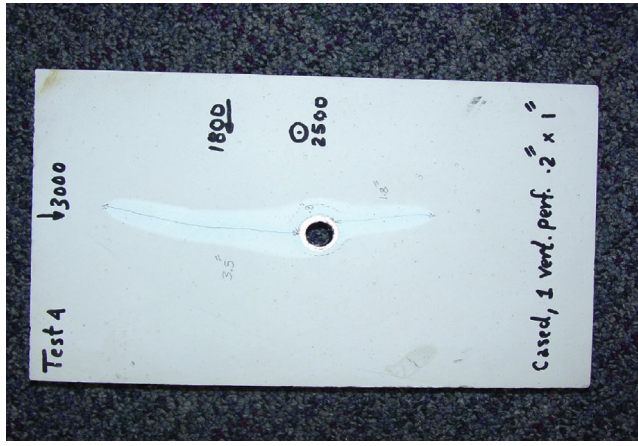

FIGURE 14.2 Fracture propagation from a cased horizontal wellbore.

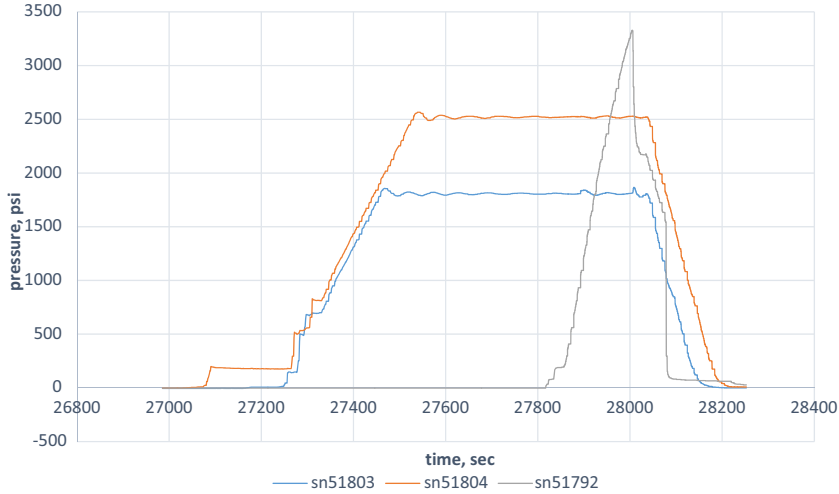

FIGURE 14.3 Fracturing pressure profile during lab-scale fracturing test of a cased horizontal wellbore in Fig. 14.2.

application of the breakdown pressure derived from Kirsch's equations. The difference in pressure reflects friction pressure from fracture tip to where the pressure is measured. The resulting fracture geometry is a longitudinal fracture along the horizontal wellbore in the direction of maximum horizontal stress of 2500 psi or perpendicular to the direction of minimum horizontal stress of 1800 psi.

In the next test, shown in Fig. 14.4, another important fundamental rule associated with hydraulic fracturing is presented. Hydraulic fractures will always find the weakest point along the wellbore. In this test, a horizontal wellbore with open hole section was cast in a hydrostone rock sample. A plug was set at the end of the open hole section. Fig. 14.4 shows the fracture propagation pattern. The fracture is initiated at a location where a plug is used to bind the open hole section. The contact between the plug and open hole provides a weak point for the fracture to initiate from. As discussed by Soliman et al. (2012), this is analogous to a packer/open hole contact, which requires careful packer placement to prevent fracture initiation at certain locations along the horizontal well. If certain location is selected to initiate a fracture, a hydrojetting technique may be used to help a fracture initiate at that location. The hydrojetting process reduces tensile strength at that point causing it to be the preferential fracture initiation point.

The fracture propagated perpendicular to the minimum horizontal stress of 1800 psi. Because the shape of the fracture resembles "T," it is called T-shape fracture. The blue part around the open hole section is due to fluid leak-off (Figs. 14.4 and 14.5).

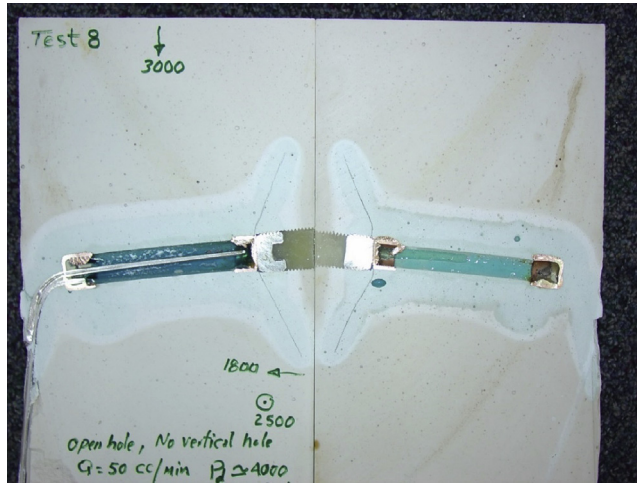

FIGURE 14.4 Fracture propagation in an open hole with a plug at the end, test 8.

FIGURE 14.5 T-shaped fracture created under the influence of a packer (Soliman et al., 2012).

In the pressure profile, the breakdown pressure is 3933 psi (Fig. 14.6). Using the equations provided earlier in this section, the breakdown pressure can be estimated as

$$P_{bd} = 3\sigma_{H,\min} - \sigma_{H,\text{Max}} + T - P_r$$

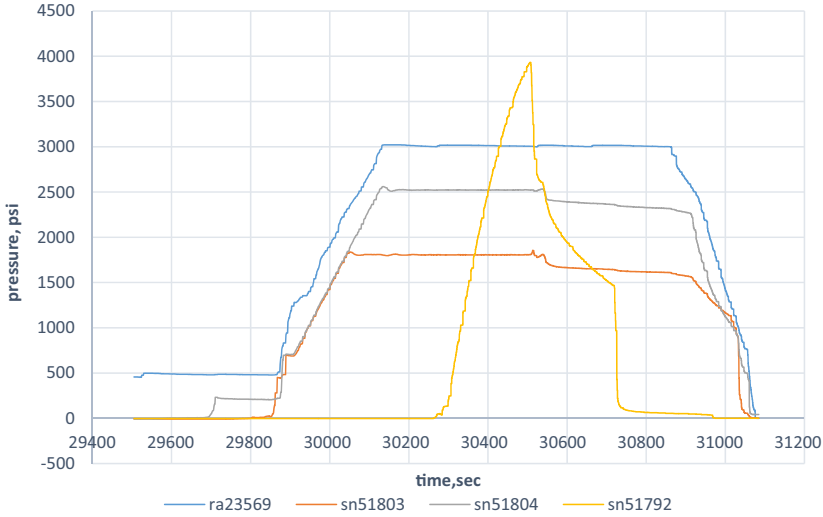

FIGURE 14.6 Pressure profile for test 8.

where

$$\sigma_{H,\min} = 2500 \text{ psi}$$

$$\sigma_{H,\text{Max}} = 3000 \text{ psi}$$

$$T = 870 \text{ psi}$$

$$P_r = 0 \text{ psi}$$

$$P_{bd} = 3(2500) - 3000 + 870 - 0 = 5370 \text{ psi}$$

It is obvious that the fracture has found an easier breakdown point right at the plug shoe, rather than breaking within the open hole section which needs a higher pressure to breakdown. This is due to the weak point at the interface of packer and formation (Li et al., 2011).

Fracturing a deviated wellbore could be challenging and sometimes can result in high treating pressure and sometimes premature screen outs as shown in the following experiments, which are done on hydrostone samples of $6 \times 6 \times 10$ in (Brumley and Abass, 1996), and the properties of the rock sample are listed in Table 14.1.

Once testing is completed, all samples were cut perpendicular to the fracture plane and parallel to the wellbore to study the induced fractures. Also, parallel slices away from the wellbore were cut to observe the propagation pattern of the created fractures. In this series of experiments, α is the angle

TABLE 14.1 Properties of the Rock Samples for Fracturing From Deviated Wellbore

Porosity	26.5%	Permeability	3.9 md
Grain density	2.32 gm/cc	Bulk density	1.71 gm/cc
E	2.7×10^6	ν	0.21
Unconfined compressive strength	8032 psi	Tensile strength	807.6 psi
Injection fluid viscosity	1300 cp	Rate	10 cm^3/min
S_v	3000 psi	S_h	1400 psi
S_H	2500 psi	Testing temperature	78°F

between the wellbore and vertical line and β is the angle between maximum horizontal stress and wellbore direction.

In fracture propagation modeling, there are two extreme fracture orientations that limit all other possible orientation: transverse fracture, in which fractures are perpendicular to wellbore orientation, and longitudinal fractures, in which fracture are aligned with the wellbore. These two orientations limit the other possible fracture orientations caused by deviated wellbore, which we refer them as the complex fracture orientations.

Complex fractures result from initiation of multiple fractures in deviated and open hole wellbores. The number of created fractures depends on the week point in the wellbore and can lead to reduced fracture width for individual fractures. Table 14.2 summarizes the experimental modeling of hydraulic fracturing propagation in deviated wellbores.

TABLE 14.2 Fracture Breakdown Pressure

	Beta, Deviation From SH				
Alpha	**0.00**	**22.50**	**45.00**	**67.50**	**90.00**
0.00	2585.00				
22.50	2803.00	2622.82	2660.53	2899.38	2974.81
45.00	2903.00	3020.90	3184.00	3385.45	3297.46
67.50	3154.99	3138.23	3347.74	3536.30	3641.06
90.00	3205.27	3134.00	3569.80	3567.82	3812.86

14.2.1 Fracture Initiation Pressure

Fracture initiation pressure or breakdown pressure increases as the angle between maximum horizontal stress and wellbore increases.

As it is shown in Table 14.2 and Fig. 14.7, fracture initiation pressure is a function of wellbore inclination and wellbore azimuth. Highest fracture breakdown pressure is observed when well is highly deviated from the vertical axis and is perpendicular to maximum horizontal stress.

14.2.2 Relief in Pressure

Relief-in-pressure concept is related to fracturing of all wells. It has been described by Abass et al. (1996) as the difference between breakdown pressure and the pressure at which post−breakdown pressure curve starts deviating from the straight line. Thus, this pressure can be considered as connectivity of the fracture, which shows the ability of the fracture to take the fluid. The near effectiveness of the fracture can be attributed to the value of relief pressure. The higher the value of relief in pressure, the less communication between a fracture and wellbore, which is an indication of a transverse fracture geometry (Fig. 14.8). Fig. 14.9 shows experimental testing for oblique perforation studies.

Planar and nonplanar fractures can affect the interpretation of conventional microfracture testing. Fig. 14.10 shows a typical response of pressure falloff data in a conventional microfracture for a planar fracture. A closure of

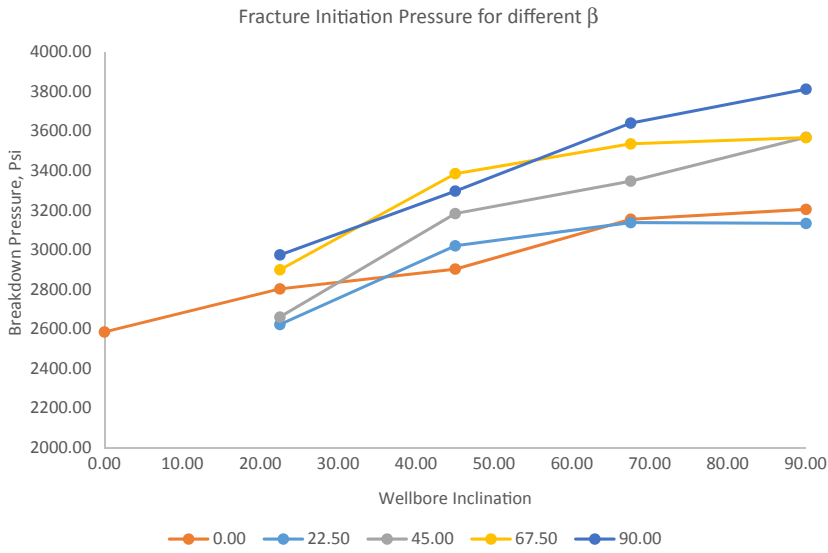

FIGURE 14.7 Fracture breakdown pressure in deviated wellbore.

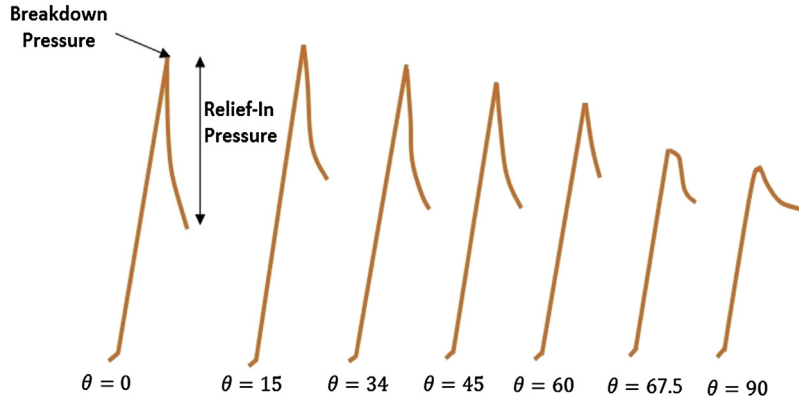

FIGURE 14.8 The concept of relief-in-pressure (Abass et al., 1996).

1300 psi was seen in the experiment which was relatively close to the 1400 psi minimum stress, which was imposed to the block. The same experiment was performed on the block with wellbore cast in it, which made an angle of 15 degrees with respect to maximum horizontal stress. This deviation caused the microfracture to go under reorientation after initiation from the wellbore. Fig. 14.11 shows the pressure falloff data for the reoriented microfracture.

There are two closures that can be observed in this test. One closure is at the wellbore and one fracture away from the wellbore. Closure seen at 1800 psi does not represent the minimum horizontal stress, but closure at 1400 psi can be considered a true measurement of minimum horizontal stress.

14.3 FRACTURE GEOMETRIES

Creating a complex fracture network is desirable in the tight formation such as shale. However, in conventional resources, creating multiple fractures often is undesirable and can lead to creating narrow fractures more prone to screen out, increasing in fluid leak-off, and operational problems due to reoriented fractures. Multiple fractures in conventional reservoirs are mainly created due to the short length of the perforation interval and perforation orientation. In the next section, different fracture geometries of planar and nonplanar fractures will be discussed. Nonplanar fractures are usually responsible for premature screen out and excessive pressure during fracturing. Nonplanar fractures will often cause multiple fractures, which have a narrow width and high leak off volume prone to a premature screen out. In the case they result in reoriented fractures, friction pressure can increase significantly (Abass et al., 1996). Nonplanar fractures also showed limited communication with the wellbore due

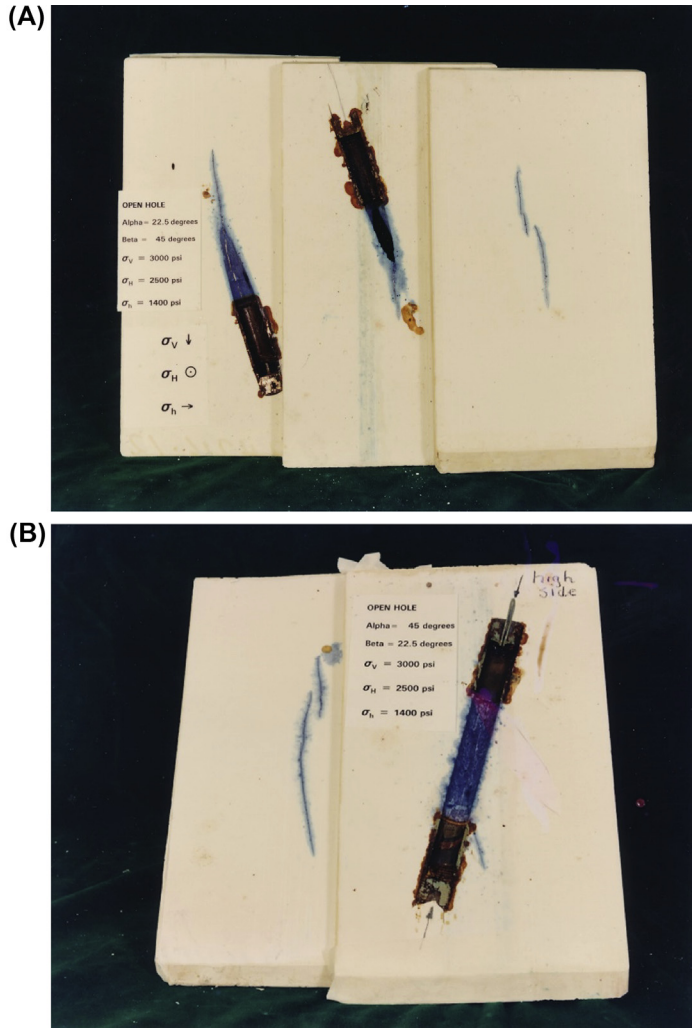

FIGURE 14.9 Oblique perforation test (A–D).

to reduced number of communicating perforations, reduced width, and tortuosity created near the wellbore (Veeken et al., 1989).

14.3.1 Planar Geometries

Planar fractures result when the wellbore is aligned with one of the principal stresses. Usually, the created fracture is single and has a clear and wide connection to the wellbore through the perforation or even in an open hole completion. Fig. 14.12 shows a typical planar bi-wing single planar fracture.

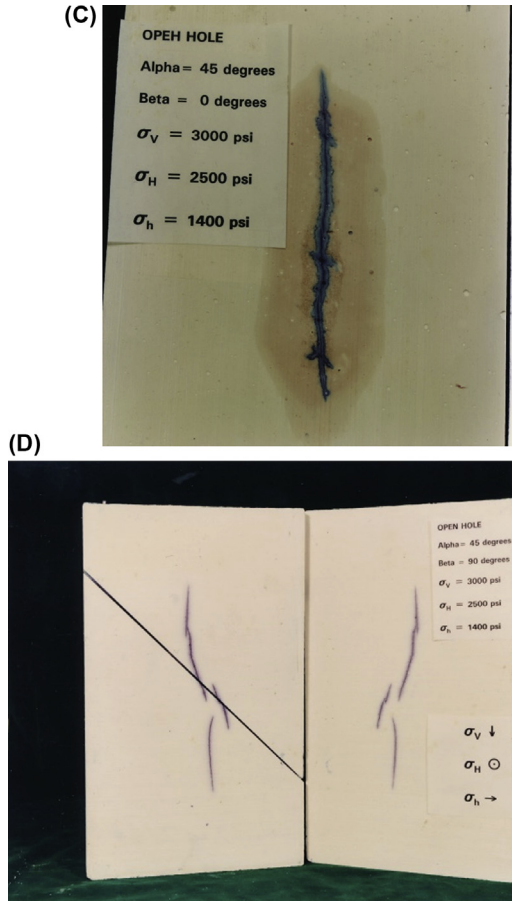

FIGURE 14.9 cont'd

14.3.2 Nonplanar Fracture Geometries

Nonplanar fractures in conventional hydraulic fracturing treatment are categorized as multiple fractures, reoriented fractures creating steps, and T-shaped fractures. When multiple fractures are created (they are usually created due to perforation orientation, which will be discussed later in the chapter), they result in reduced width. Fig. 14.13 shows multiple fractures initiated from an oblique cased hole and an open hole. Although it might not be visible in the picture, this test resulted in multiple fractures initiated from each perforation. These propagating fractures ultimately formed one fracture as they propagated away from the wellbore (Abass et al., 1996).

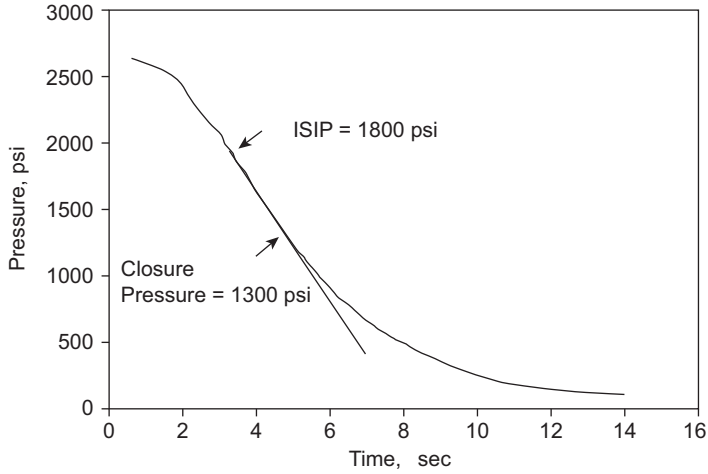

FIGURE 14.10 Microfracture pressure falloff for a conventional planar fracture, showing closure close to applied minimum horizontal stress (Abass et al., 1996).

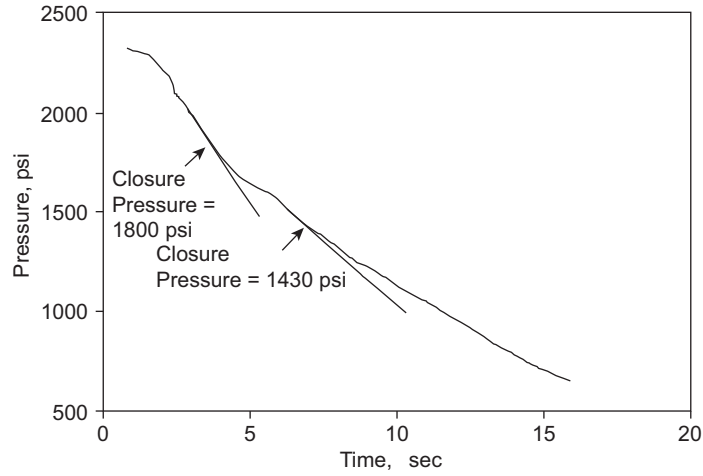

FIGURE 14.11 Microfracture pressure falloff for a reoriented fracture showing two different closures, one for the reoriented fracture and the next one for the initial fracture initiated from the wellbore (Abass et al., 1996).

The segmentation nature of fracture was also observed in larger-scale treatment. Shah et al. (2010), in a back mining effort, discovered that six different perforations created five separate fractures (Fig. 14.14). However, in conventional reservoirs, segmented fractures are often treated as a single planar fracture.

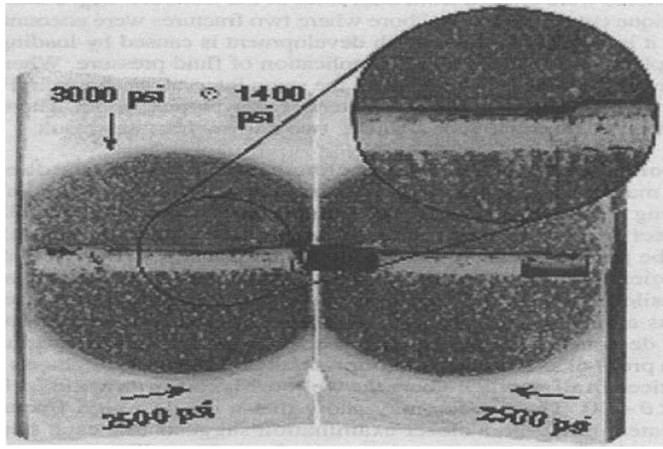

FIGURE 14.12 A typical planar fracture created during lab experimental modeling (Abass et al., 1996).

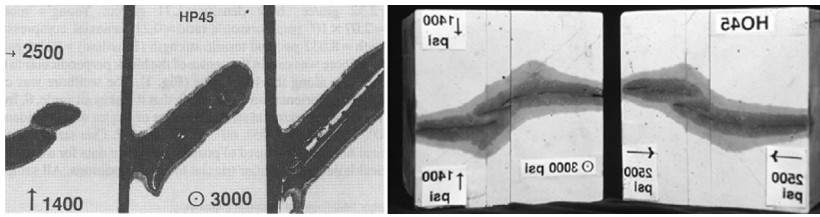

FIGURE 14.13 Multiple fractures from a cased wellbore (left) and open hole (right) (Abass et al., 1996; Soliman et al., 2004).

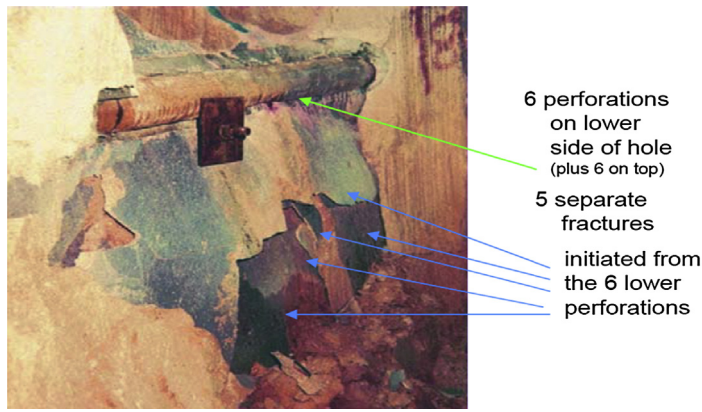

FIGURE 14.14 Back mining observation of multiple fractures propagating from a wellbore (Shah et al., 2010).

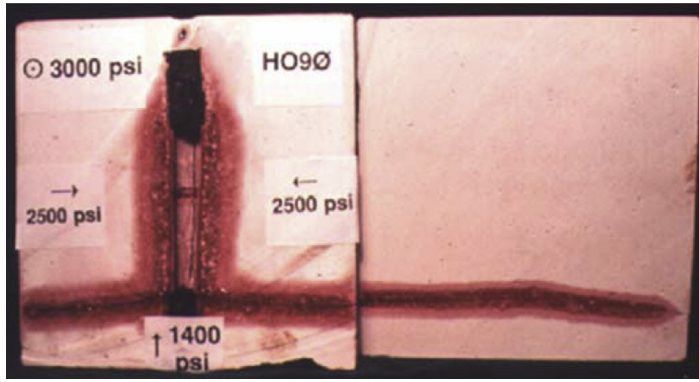

FIGURE 14.15 T-shaped fracture, a longitudinal fracture, is initiated at the open hole section and a transverse fracture initiated at the plug (Abass et al., 1994).

T-shaped fracture is one of the unfavorable fracture shapes that can happen frequently. If an open hole section is plugged at the end, a T-shaped fracture could form. In this scenario, a longitudinal fracture will be initiated at the open hole section and a transverse fracture will form at the end, where the plug is placed. Fig. 14.15 shows a typical T-shaped fracture observed in lab block fracturing.

Another complexity, which has been observed in lab block testing, is generating multiple fractures. This process happens when a fracture initiates at an angle to the least principal stress. Then, multiple fractures at the wellbore or near a wellbore may result as the fracture reorients itself to orient itself perpendicular to the minimum principal stress. The reorientation process in fracturing lab-scale rock samples with deviated wells was described by Daneshy (1972) as shown in Fig. 14.16.

Fig. 14.17 shows experimental studies by Hubbert and Willis on the left and by Abass on the right, which shows the segmentation nature of the fractures (Wu, 2006).

Fig. 14.18 shows multiple fractures resulting from cryogenic fracturing treatment where liquid N_2 was used as a fracturing fluid. Created fractures orient themselves to be perpendicular to the direction of least stress (Alqatahni et al., 2016).

In the conventional fracturing, the focus is on creating a single planar fracture that penetrates deep in the reservoir. Therefore, fracture design was to prevent fracture complexity such as T-shaped, multiple, and reoriented fractures. Additionally, a pressure loss due to flow convergence in a transverse fracture can be significant. A cavity fracturing method was introduced by Abass et al. (1995) where several hydrojetted slots were created along the wellbore in a carbonate formation. Fig. 14.19 shows the concept of this application.

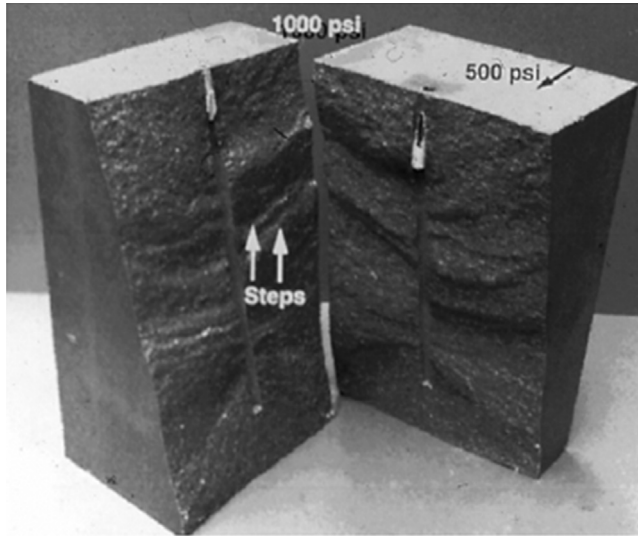

FIGURE 14.16 A fracture tries to reorient itself to be perpendicular to the minimum principal stress (Daneshy, 1972).

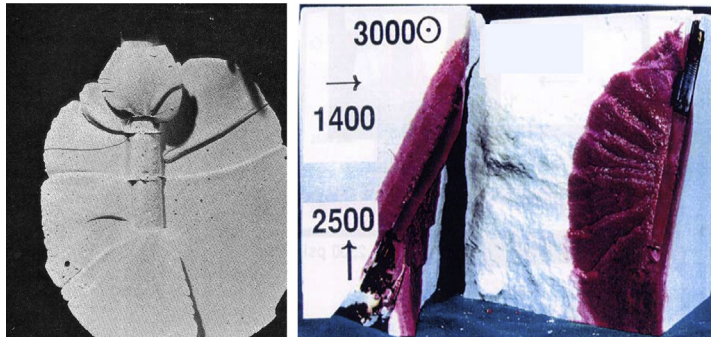

FIGURE 14.17 Segmented fractures are shown in laboratory tests (Hubbert and Willis – Abbas) (Wu, 2006).

Acid is injected and left for some time to create a cavity around the wellbore to provide a source for fracture initiation. The cavity is then packed with proppant to provide conductive zone at the transverse fracture/well area. A fracture should initiate from this cavity. This created cavity can ease the near-wellbore stress concentration and avoid creating T-shaped and multiple fractures. Furthermore, this cavity was able to create a single fracture from its surface perpendicular to the minimum horizontal stress. It also created a nonrestricted zone between the fracture and wellbore (Fig. 14.20).

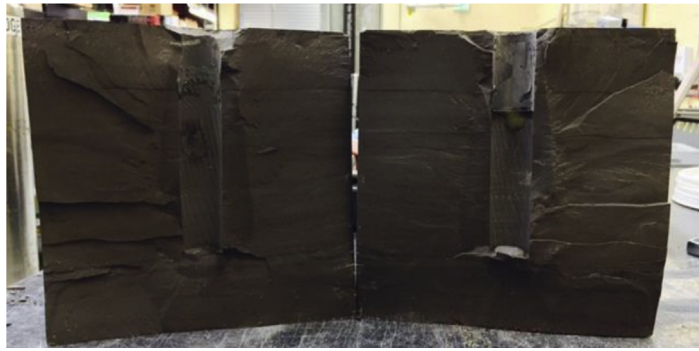

FIGURE 14.18 Cryogenic fracturing techniques (Alqatahni et al., 2016).

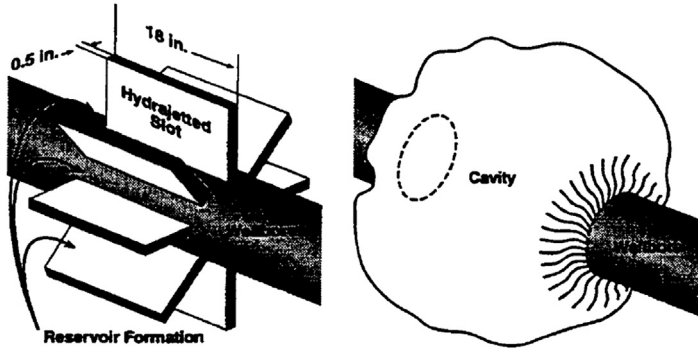

FIGURE 14.19 Cavity fracture concept: (left) hydrojetted slots and (right) cavity created using acid.

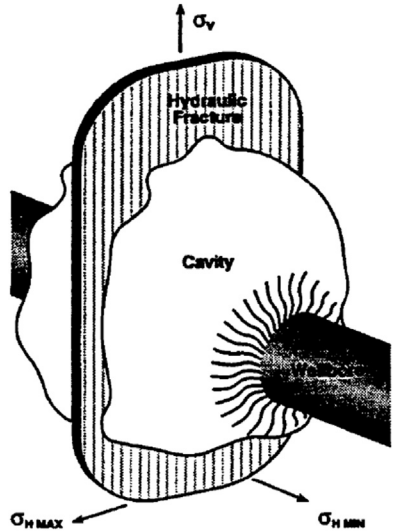

FIGURE 14.20 Single fracture created using cavity fracturing technique.

Restricted zones exist due to the limited connectivity of transverse fractures to the wellbore. Fluid from the reservoir flow linearly to the fracture, and once it reaches the fracture, fluid flow turns into the radial flow. This radial flow causes additional pressure drop, which is also known as convergence skin. Creating of such cavity can ease this limitation and reduce this convergence skin inside the transverse fractures (Abass et al., 1995). Based on the simulation results for the cavity technique in a horizontal wellbore, production was increased by 3.5-fold in comparison with the vertical wellbore. This increase was achieved by using cavity technique and eliminating the convergence skin problems and creation of multiple fractures. There are other complexities associated with fracture propagation mainly due to perforation orientation. These complexities are described in perforation orientation section.

Once fracture is created, it can change the stress state in the reservoir rock surrounding the fracture, and subsequent fracturing stages can be affected by the new stress field (El Rabaa W, 1989). Also, different mechanisms can affect the shape and propagation of hydraulic fractures including heterogeneity of the rocks and preexisting fracture seen commonly in unconventional reservoirs (Li et al., 2015). If the rock does not show the elastic behavior and creeps rather than showing a brittle behavior, a different form of fracture will be created.

Other parameters affecting the overall fracture propagation can be the existence of natural fractures. The extent of natural fractures and their filling materials can affect the overall hydraulic fracture propagation. Hydraulic fractures can be arrested or deviated or they can cross preexisting natural fractures. They can contribute to the overall permeability of the fracture network and at the same time increase the leak-off volume and reduce the extent of natural fractures (Li et al., 2015).

14.4 FRACTURE CONFINEMENT

Fracture confinement could be due to stress contrast or the existence of weakness planes and beddings, in particular when they are overpressured. In reservoirs with relatively high degree of homogeneity, stress contrast cause fractures height confinement and dictate the fracture propagation pattern. Following are some laboratory tests that show how stress contrast can result in different fracture geometry and height growth.

Fig. 14.21 shows a penny shape and an elliptical shape fracture propagated almost identically in upper and lower boundaries. There is no stress contrast between the lower and upper boundaries (both identical 1200 psi). Therefore, there is no stress dictating the preferred height growth pattern. If the rock fabric is relatively identical and there is no structural barrier such as a bedding plane or planes of weakness, fracture identically propagates in both directions.

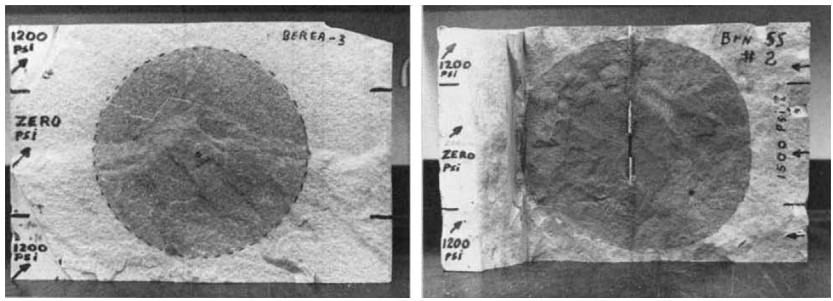

FIGURE 14.21 Penny shape (left) and elliptical shape (right) fractures (El Rabaa, 1987).

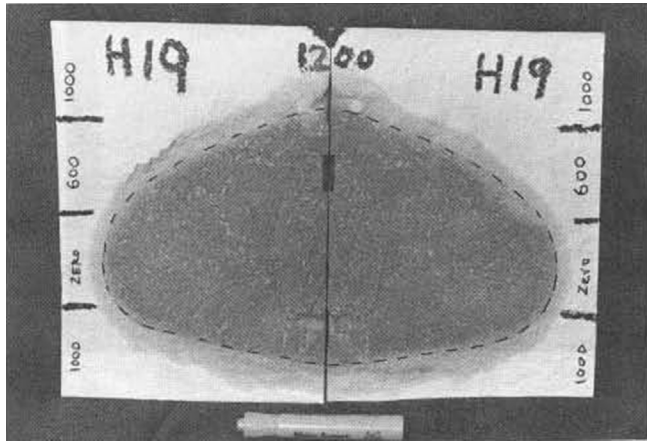

FIGURE 14.22 Fracture height confinement, fracture propagated upward as there is less resistance force opposing its growth (El Rabaa, 1987).

Fig. 14.22 shows an example where there is a stress contrast between upper and lower boundaries. Dark slot shows the injection point into a layer with 600 psi stress. The lower layer has zero stress, thus the fracture completely propagated toward this layer and not the upper layer (El Rabaa, 1987).

Fracture height confinement is critical when there is nonhydrocarbon zone adjacent to the reservoir layer. If fracture grows into an unfavorable layer, not only the production expected from fracturing treatment will not be achieved, but also it can cause huge water production.

14.5 PERFORATION DESIGN FOR FRACTURING

Single wide fracture in conventional reservoirs is the superior stimulation technique that can create a conductive path for flow from the matrix to the

wellbore. Nonplanar fracture geometries such as T-shape fractures and reoriented fractures can adversely affect the created hydraulic fracture. In this part, orientated perforation is presented as a way to create a planar fracture. It has been suggested that oriented perforation can effectively prevent sand production (Abass et al., 1994).

In this section, three sets of experiments are described to investigate the effect of oriented perforation in stimulation and completion of the wellbore. In the first experiment, a vertical with 180-degree perforation was created. Perforation was aligned with maximum horizontal stress direction, and then angle was increased to all the way to be perpendicular to the maximum horizontal stress direction. In the second set of experiment, a horizontal well was drilled in a different direction with respect to maximum horizontal stress but perforation constantly remained in the direction of maximum horizontal stress. In the third set of experiments, perforation was clustered in the high and low sides of the horizontal wellbore (Abass et al., 1994).

14.5.1 Vertical Wellbore

A hydrostone sample of 6×6×10 in. was created and a wellbore was drilled and cased with a casing of 0.61 in. in ID and 0.746 in. in OD. The casing was perforated in a 2-in. interval of the wellbore with 10 shots and 180-degree phasing. Perforations were 0.5 in. deep and 0.135 in. in diameter. Series of different angles with maximum horizontal stress were used in perforation tests, which are listed in Table 14.3.

Samples were placed in a triaxial unit with 3000 psi vertical, 2500 psi horizontal stress and 1400 psi minimum horizontal stress. During fracturing, minimum horizontal stress was monitored and it showed an increase during

TABLE 14.3 Properties of Hydrostone Sample With Different Wellbore Angles to Maximum Stress

Porosity	0.277
K	9 md
E	2.52×10^6 psi
ν	0.228
θ	0, 15, 30, 45, 60, 75 and 90
Injection rate	30 cc/min

pumping which suggests the creation of width, and it is reflected in net pressure. The net pressure is related to fracture width as

$$W_f = \frac{2D}{E}(P_f - \sigma_{h\min})$$

By differentiating both sides with respect to time, width function can be defined as

$$\frac{W_f}{dt} = \frac{2D}{E}\frac{d}{dt}(P_f - \sigma_{h\min})$$

Observation for these tests showed that width function for the hydrostones tests has a positive increasing rate as the fracture propagates. For perforation orientation larger than 45 degrees, width function showed a dramatic decrease and even gets negative for 90 degrees. If the direction of the perforation with maximum horizontal stress is no larger than 30 degrees, fracture width is increasing with time. As shown in Figs. 14.23–14.26 a single planar fracture was achieved for orientation angles of 0, 15, and 30 degrees.

The perforation diameter and depth can be used to investigate a tolerance angle beyond which fracture loses its full communication with the wellbore. This angle can be defined as

$$\alpha = \tan^{-1}\frac{d}{L}$$

From this relation, it is obvious that larger hole will result in more tolerance in the wellbore and fracture communication.

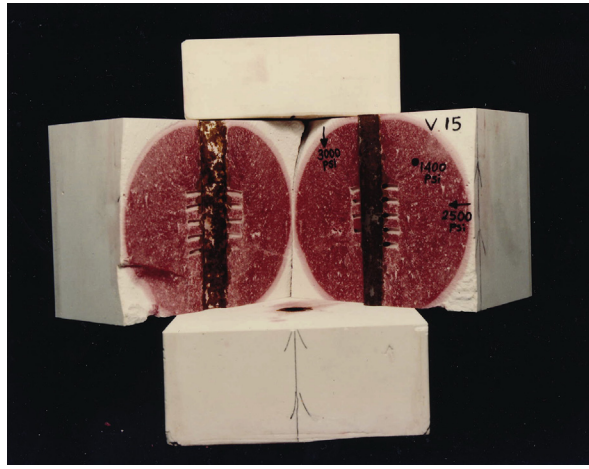

FIGURE 14.23 Fracture propagation in hydrostone with a wellbore at an angle of 15 degrees with respect to maximum horizontal stress.

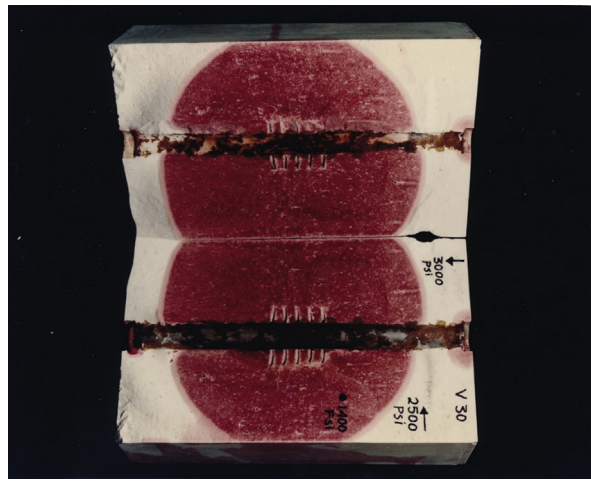

FIGURE 14.24 Fracture propagation in hydrostone with a wellbore at an angle of 30 degrees with respect to maximum horizontal stress.

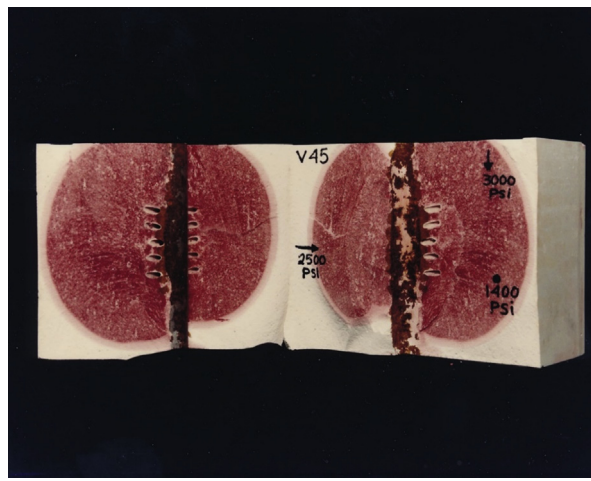

FIGURE 14.25 Fracture propagation in hydrostone with a wellbore at an angle of 45 degrees with respect to maximum horizontal stress.

14.5.2 Horizontal Wells

14.5.2.1 Oblique Perforations

Hydrostone samples used in horizontal well experiments had same properties as described above in vertical wellbore section. A wellbore at different angles of 0, 15, 30, 45, 60, 75, and 90 degrees to maximum horizontal stress was cast in these samples with 0.8125 in. ID and 0.9375 in. OD. A line of five

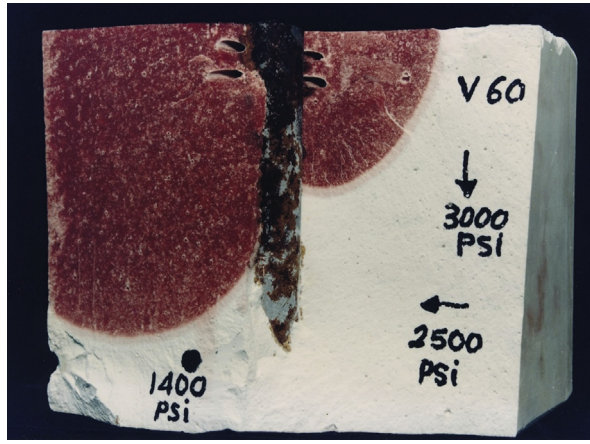

FIGURE 14.26 Fracture propagation in hydrostone with a wellbore at an angle of 60 degrees with respect to maximum horizontal stress.

perforations was created at the high low side of the horizontal wellbore in the direction of maximum horizontal stress regardless of the wellbore orientation. These oblique perforations caused different perforation depth in these samples. In all these tests, a single planar vertical fracture was initiated. The difference in these tests was breakdown pressure. Breakdown pressure for the tests up to 30 degrees averaged 3200 psi, whereas for larger angles it averaged around 4000 psi. This difference comes from friction pressure as the perforated interval becomes smaller for higher angles.

In the following test shown in Fig. 14.27, an oblique wellbore was cast in a hydrostone sample. The wellbore was created at an angle of 45 degrees with

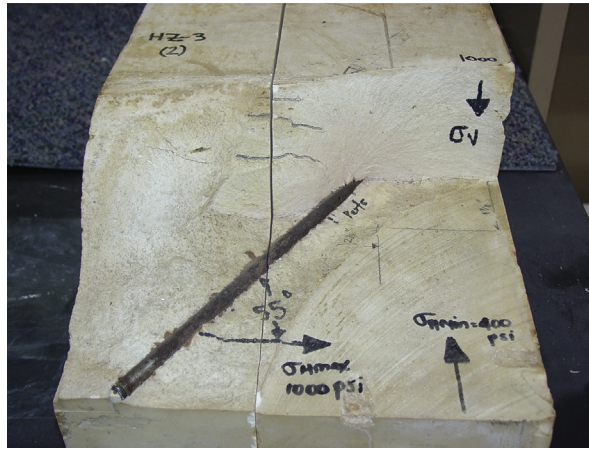

FIGURE 14.27 An oblique wellbore at an angle of 45 degrees to maximum horizontal stress.

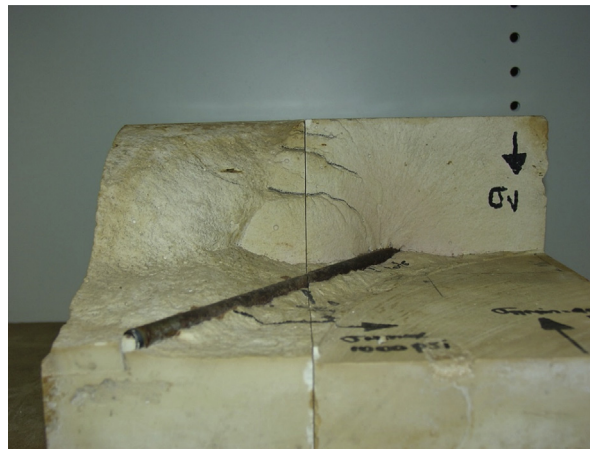

FIGURE 14.28 Multiple fractures are shown in the 45-degree wellbore.

the maximum horizontal stress. Maximum horizontal stress and vertical stress was held constant at 1000 psi and minimum horizontal stress of 400 psi in the triaxial system.

After starting the fracturing fluid injection, multiple fractures were initiated at the perforation (Figs. 14.28 and 14.29). These multiple fractures are connected to the wellbore and initiated at the perforation. This multiple fracture initiation is considered as complexity in fracturing treatment. Multiple fractures are unfavorable in conventional reservoirs as they often compete against each other resulting in multiple narrow fractures instead of creating one single wide fracture.

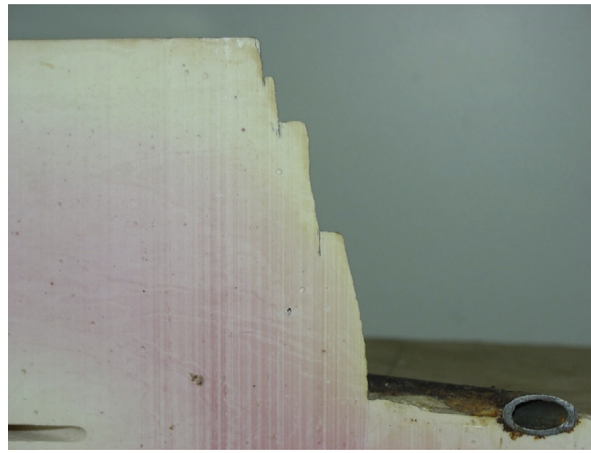

FIGURE 14.29 Cross-sectional view of the oblique wellbore, showing multiple fractures.

The same phenomena can be observed in unconventional reservoir hydraulic fracturing treatment. Instead of creating multiple fractures, there might be several natural fractures, which can intersect with the induced fracture and create a network of fractures. However, in this case, multiple fracture or fracture network can be considered as favorable fracturing treatment as the scope of hydraulic fracturing treatments in unconventional resources demands more fractures to access more volume of the reservoir (Soliman et al., 2012).

Fig. 14.29 shows clearly how these fractures initiated and die out as the other fractures were propagating. In conventional reservoirs, hydraulic fracturing treatments, which resulted in multiple fractures and multiple segmentations, could happen for two primarily reasons: heterogeneity of the materials and stress heterogeneity (Wu, 2006).

14.5.2.2 Clustered Perforations

In this set of tests, clustered perforation was made on the high and low sides of the horizontal wellbore in the same direction regardless of wellbore direction. The wellbore direction changed from the direction of maximum horizontal stress with increments of 22.5 degrees. For 0 and 90 degrees, a single fracture was created, and for other angles between, multiple fractures were observed with no link-up. This observation suggests that even with multiple perforations if they are not created closely enough, multiple fractures will be created.

14.5.3 Practical Applications of Oriented Perforations in Stimulation Techniques

Perforations can be designed based on the purpose of the completion and stimulation techniques. They can be designed to make the connection to the reservoirs, in which reservoir characteristics are important, or to fulfill the objective of the gravel pack. They also can be designed for stimulation purposes such that nonplanar fracture geometries, including multiple fractures, T-shape fractures, and other undesirable fracture orientation, are avoided.

Oriented perforation for stimulation techniques was investigated to identify different fracture orientations.

1. Longitudinal orientation—For vertical wells, it was observed that perforation in the direction of maximum horizontal stress should be used. For horizontal wells, it is recommended to align perforation with 180-degree phasing and in the high and low sides of the wellbore. Wellbore should be drilled in the direction of maximum horizontal stress.
2. Peripheral (transverse) orientation—To produce transverse fractures, wellbore must be drilled in the direction of minimum horizontal stress and perforations are recommended to cover the whole 360 degrees of the wellbore. It is also recommended to have a short interval of perforation to avoid multiple fractures.

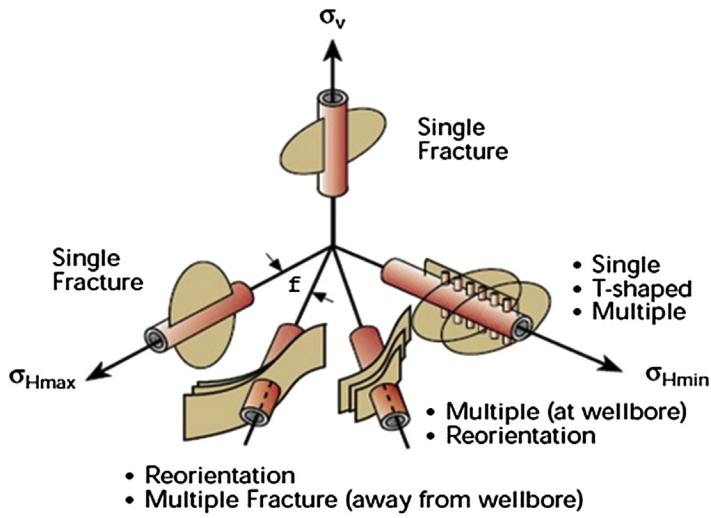

FIGURE 14.30 Perforation orientation in stimulation techniques for different wellbore directions, Abass et al. (1996).

3. Angular orientation—This applies to wells that are drilled at an angle to the either of principal stresses. In this case, there will be no advantage of perforating the whole horizontal section of the wellbore. Instead, perforation should be made in the direction of anticipated fractures. These applications are shown in Fig. 14.30.

14.5.4 Gravity-Orientated Clustered Perforations

This technique was introduced by Abass et al. (1994) in which regardless of wellbore orientation, a single planar fracture could be initiated. In this technique, a small vertical hole from any position along the deviated wellbore will be created using clustered perforations or one or two large perforations, or hydrojetting technique (Fig. 14.31).

This vertical hole will be aligned with principal vertical stress and will encourage creating a singular planner vertical fracture, which is essential to fracturing treatment. There is no need to collect in situ stress data, and there is no requirement to drill in certain orientation for fracturing because the fracture will be guided by the vertical hole. A simple orientation technique based on gravity can be used to orient the perforations for the hydrojetting tool. A single planar vertical fracture will be initiated from the small vertical wellbore. A large size vertical hole can be created to allow for high injection rate needed for hydraulic fracturing treatment.

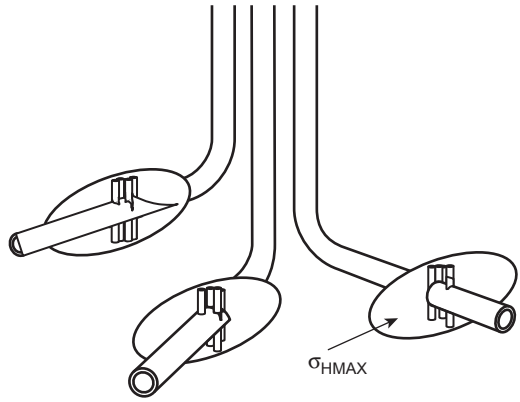

FIGURE 14.31 Gravity-orientated clustered perforation.

The application of gravity-oriented clustered perforations has been investigated extensively in laboratory experiments and showed very promising results. Following tests showed the applications of this method of perforation and creating a small vertical hole in stimulation design. In Fig. 14.32, three principal stresses are shown as 3000 psi vertical stress acting from top to bottom, the 2500 psi maximum horizontal stress acting parallel to the plane of sample cross section and 1800 psi minimum horizontal stress which is pointing into the cross section of the sample. Wellbore was cast in hydrostone sample in an angle of 45 degrees to maximum horizontal stress. A vertical

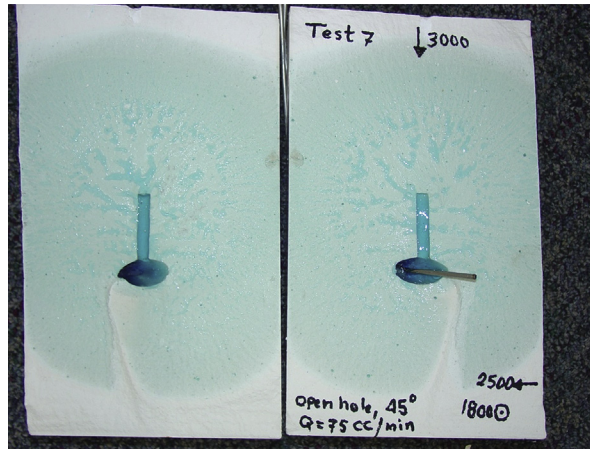

FIGURE 14.32 Application of gravity-assisted perforation technique in oblique wellbore with 45 degrees.

1.5-in. hole was created as shown in Fig. 14.32. Once pumping started, the fracture was initiated from this small vertical hole, perpendicular to the direction of least principal stress regardless of the wellbore orientation.

Fracture wings continued from the upper part of the wellbore to bottom part. The bottom part is showing the leak-off and extension of the upper fracture, and it is not a separate fracture. Fracture pressure profile and the propagation geometry of this test are shown in Figs. 14.33 and 14.34.

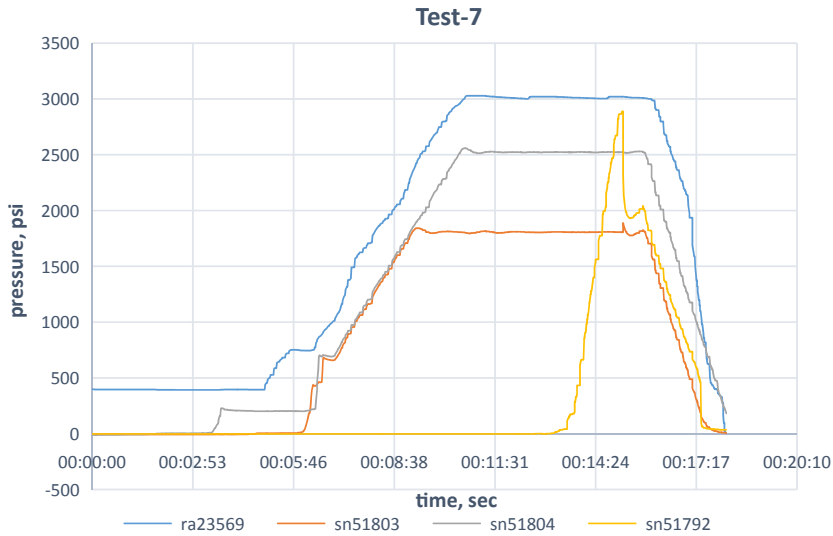

FIGURE 14.33 Pressure profile for 45-degree wellbore with gravity-assisted perforation.

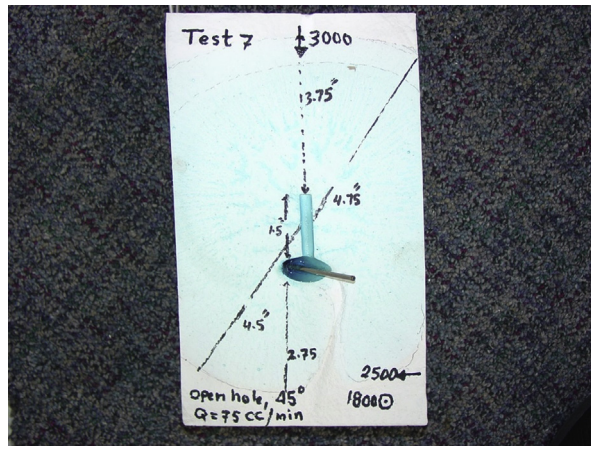

FIGURE 14.34 Application of gravity-assisted perforation technique in oblique wellbore with 45 degrees.

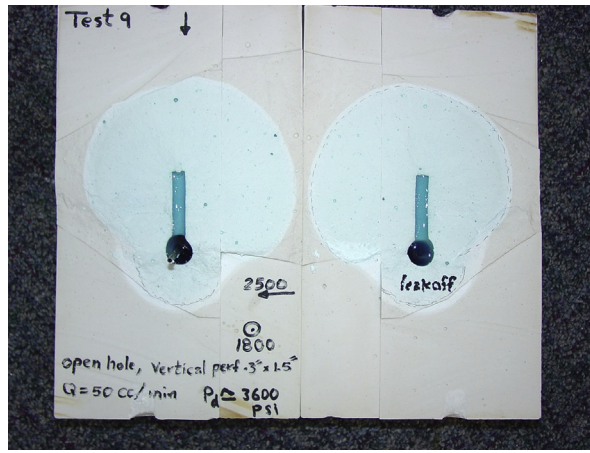

FIGURE 14.35 Application of gravity-assisted perforation in an open hole completion and limiting the fracture growth.

This test is showing the application of this technology as applied in conventional reservoirs, in which creating a single planar fracture is critical for a successful hydraulic fracturing treatment. This technique was further investigated in additional experimental modeling. Next two tests are showing how this technique can be applied in controlling the growth of a fracture and limit its propagation from propagating into neighboring zones that may not be hydrocarbon-bearing formations. Fig. 14.35 shows a successful application of gravity-oriented perforation in restricting the fracture propagation pattern. A hole with 0.3-in. diameter and 1.5-in. length was created in the vertical direction. Fracture started propagating from this hole in the upper side of the wellbore with the minimal leak-off in the lower side, and fracture confinement from one side was successfully achieved. This technique can be used to avoid creating a fracture in unfavorable zones. Pressure profile for this test is shown in Fig. 14.36.

The following test is showing same principle of restricting fracture propagation with a top view of the wellbore cross section. In this test, a shorter vertical hole was created, and as a result, a smaller fracture was also created at the upper side of the wellbore (Fig. 14.37).

This test indicates that to delay a fracture from invading the lower side of a wellbore, a fracture is started from the vertical hole, then it started propagating on the other side of the open hole (Fig. 14.38).

14.5.5 Simulation of Oriented Perforation

Extended finite element method (XFEM) was used to simulate experimental modeling for perforation orientation. Fig. 14.39 shows experimental modeling

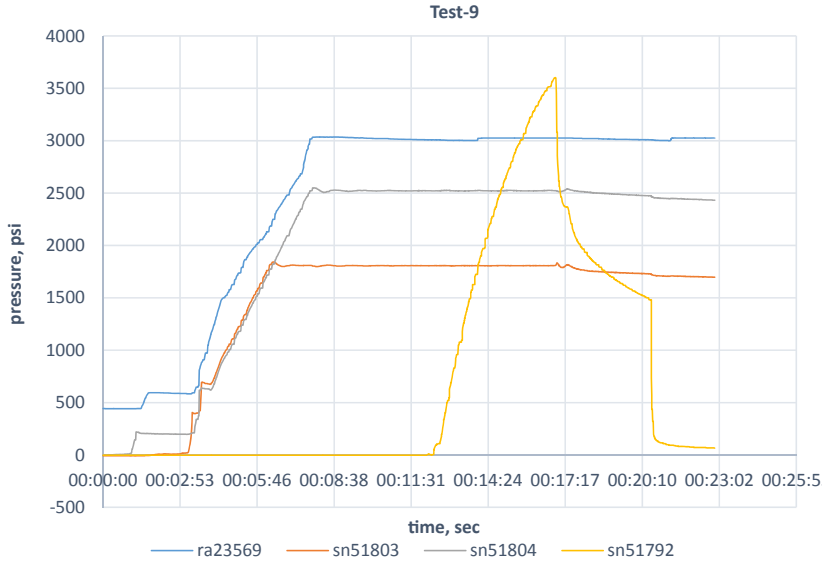

FIGURE 14.36 Pressure profile for limiting application of gravity-assisted perforation.

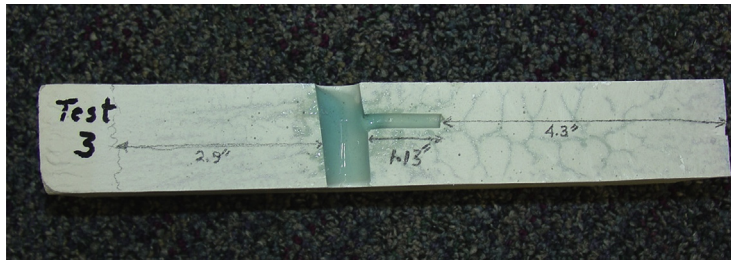

FIGURE 14.37 Smaller hole caused creation of the fracture in both sides.

by Abass et al. (1994) along with its XFEM modeling done by Sepehri et al. (2015).

Experimental modeling validates the simulation modeling. In oriented perforation, the fracture will initiate at an angle to the least principal stress, but once it passes through near-wellbore region, it reorients itself to propagate in the path of least resistance (Sepehri et al., 2015).

14.6 UNCONVENTIONAL RESOURCES FRACTURING

14.6.1 Shale Fracturing

There are fundamental differences between fracturing unconventional and conventional reservoirs. Although mechanical rock modeling, discussed

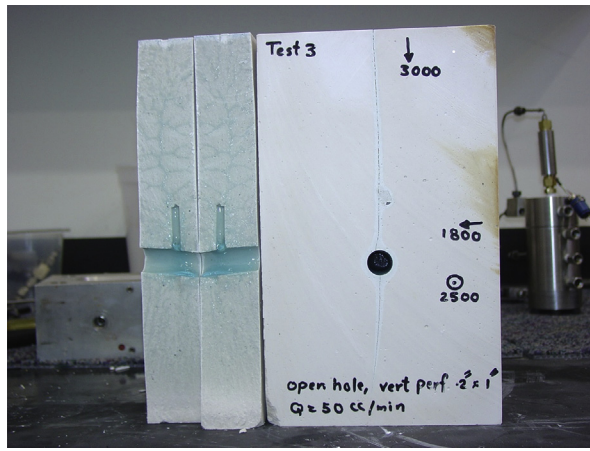

FIGURE 14.38 Top view of the created fracture.

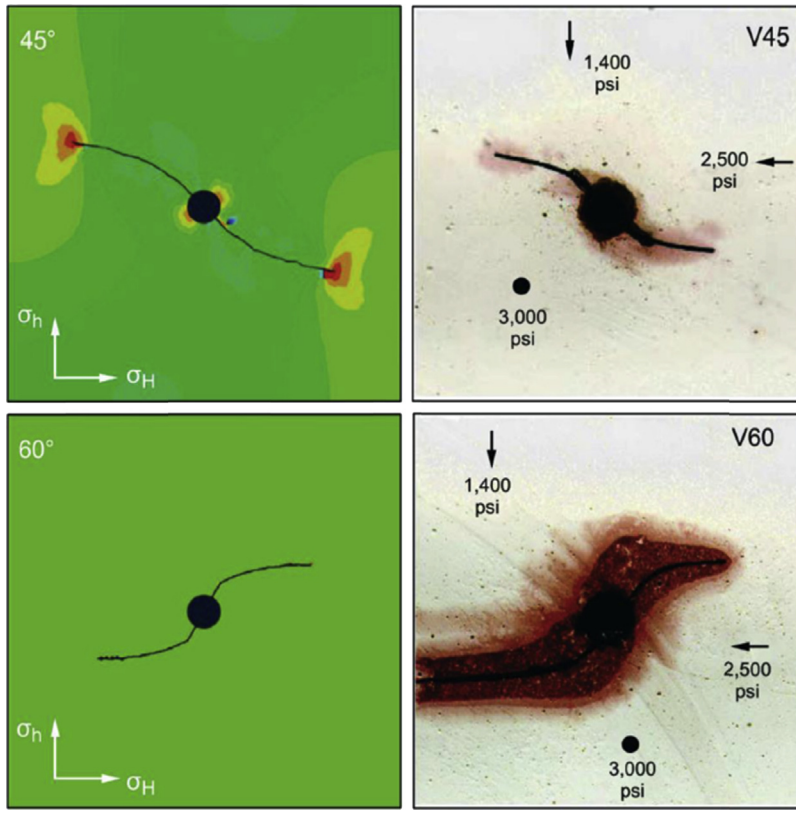

FIGURE 14.39 Simulation of oriented perforations.

earlier, still applies to shale formations, the design of hydraulic fracturing treatments in shale formation is fundamentally different than fracturing conventional rock formations.

Economical production from unconventional reservoirs including shale gas and shale oil formations requires horizontal wells with massive multistage proppant hydraulic fracturing stimulation. Fracturing involves generating sufficient stimulated reservoir volume (SRV), which is achieved by placing a large number of hydraulic fractures along multilaterals drilled from a single pad to achieve the commercial production rate. Because of the extremely low permeability, induced fractures should activate existing natural fractures to reach entrapped and adsorbed oil and gas within shale matrix. Therefore, production rate and recovery depend on the size of the created SRV. One major factor in increasing the size of SRV is the existing natural fractures and their connectivity to the main induced fractures. Numerous studies have been conducted on the importance of natural fractures in unconventional reservoirs, and most have indicated that existence and connectivity of natural fractures can significantly impact well production (Veselinovic et al., 2016; Walton and McLennan, 2013; Medeiros et al., 2007). During hydraulic fracturing treatments, due to extremely low leak-off, pressure gradually dissipates around the main fractures. The high-pressure zone around the main fracture will cause natural fractures to slip and create a network of complex fractures around the main fracture. Thus, stimulating these natural fractures and creating more of this complex network will be of great importance in designing hydraulic fracturing treatments in shale formations.

Another complication with hydraulic fracturing techniques is water flowback, and fracture clean up process after injecting a tremendous amount of fracturing fluid, which is primarily water that imbibes into the nanopores and microfractures. Due to very high capillary pressure, the imbibition process causes water blockage to be generated reducing the relative permeability of the hydrocarbon (oil or gas) causing substantial reduction of flow rate from matrix domain to the fractures domain of shale porous media. Water flowback process usually results in 20%−40% of water recovery such that more than half of the water injected stays in the reservoir.

Creating complex fractures instead of planar bi-wing fractures in unconventional reservoirs is of great importance because accessing the reservoirs by creating a larger SRV substantially impacts the production and well economics. However, hydraulic fracturing goal in conventional reservoirs as discussed in first part of this chapter is creating a bi-wing planar fracture. Furthermore, flow in unconventional reservoirs is not following Darcy's fluid flow, and instead, fluid flow should be considered in microscale pores. In this part of experimental modeling of hydraulic fracturing, physics of important processes in unconventional reservoirs including water cleanup and recovery will be discussed. Then, experimental works in creating complex fracture network and fluid flow in unconventional reservoirs at pore scale level will be discussed.

14.6.1.1 Fracturing Fluid Flowback and Cleanup Process

The first experimental modeling in unconventional reservoirs presented here is focusing on the nanoscale interaction between fracturing fluids and shale formations. Spontaneous imbibition is the resultant phenomena of interaction between rock and fracturing fluid and is considered as the main reason for water blockage and low fracturing fluid recovery and flowback. Capillary forces and osmosis pressure are created once fluid and rock are in contact and they are contributing factors to spontaneous imbibition (Zhou et al., 2014).

It is studied by several authors that fracturing fluid recovery after hydraulic fracturing treatment can be 10%−50% of total pumped fluid and more than 50% of the fluid will remain in the reservoir. Part of this remaining fluid will be in natural fractures, and induced fracture network and another part will be imbibed into the matrix (Zhou, 2016). Shale samples in following section are from Horn River Formation, Woodford, and Niobrara Formation (Figs. 14.40−14.42).

Fracturing fluid used in these tests are 2% KCL, 0.07% friction reducer, and 2% KCL substitute fluids. Samples were immersed in the fracturing fluids, and their weight was constantly monitored with time. The change in the weight can be converted to represent the imbibed water saturation. Results of the experiment are shown in the following figures. The samples with higher clay content are imbibing more fluids due to clay ability to expand and hold water-based fluids. Different fluid had different degrees of imbibition into the shale samples. However, all of them showed the similar behavior as the clay content of the shale samples were increased (Figs. 14.43−14.45).

Furthermore, contact angle, which is a measure of wettability of the rock, was measured, and it was shown the more water wet the formation, the faster the imbibition rate (Figs. 14.46 and 14.47).

FIGURE 14.40 Horn River Shale samples for imbibition studies (Zhou, 2016).

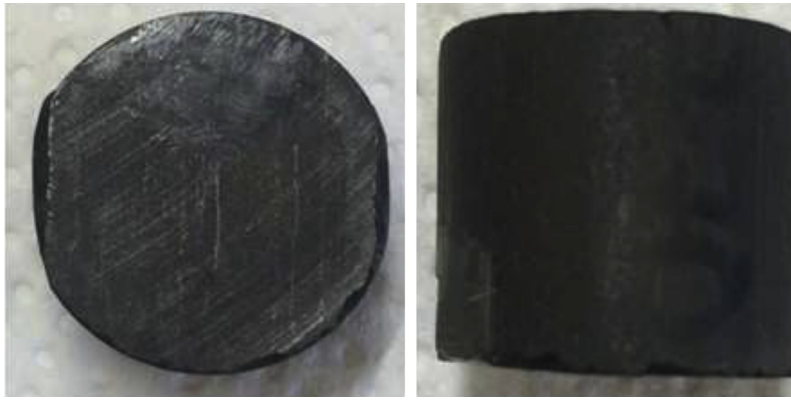

FIGURE 14.41 Woodford Shale samples for imbibition studies (Zhou, 2016).

FIGURE 14.42 Niobrara Shale samples for imbibition studies (Zhou, 2016).

And finally, the experiments showed that the type of the fluid also is affecting the imbibition process.

Imbibition process in shale formation is considered to be the main factor affecting fluid loss and low fluid recovery. Capillary imbibition and osmosis are contributing factors in whole imbibition process, and their combining effect is different in the different shale formations. For example, Fig. 14.48, from an experiment on a Horn River Shale sample, shows that capillary imbibition and osmosis alternatively controlled the imbibed water saturation.

At first, the capillary pressure was controlling the process. Once capillary pressure caused a high volume of water imbibes into the sample, then water saturation was increased, and subsequently, the capillary pressure decreased. In this stage, osmosis process became the major controlling factor and pushed

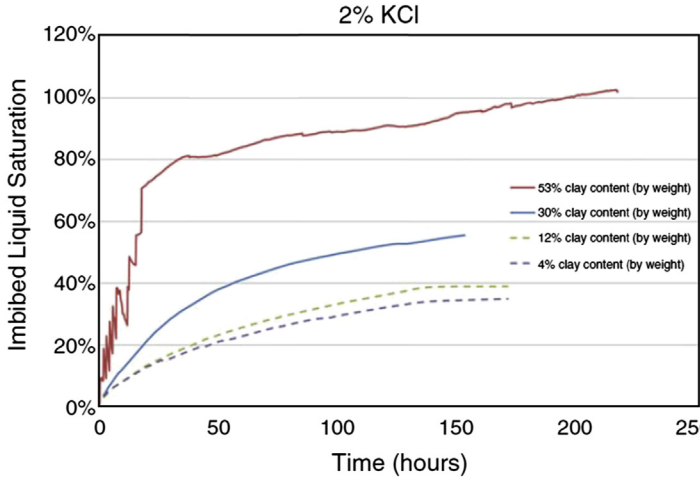

FIGURE 14.43 Imbibed liquid saturation change with time for 2% KCL fracturing fluids in different samples with different clay contents (Zhou, 2016).

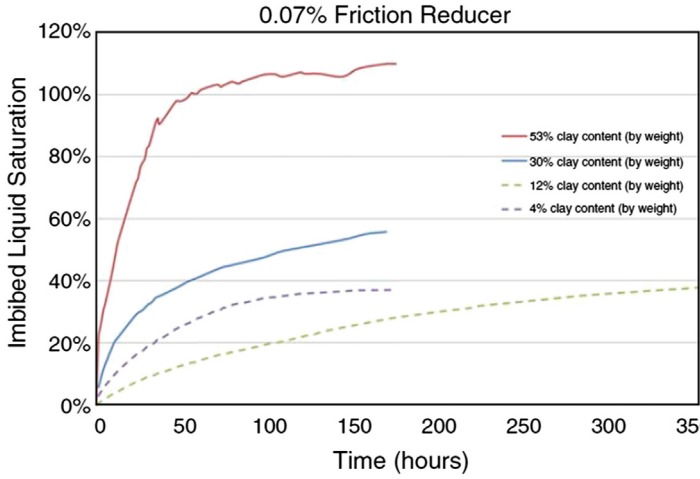

FIGURE 14.44 Imbibed liquid saturation change with time for 0.07% friction reducer fracturing fluids in different samples with different clay contents (Zhou, 2016).

back some of the imbibed water till capillary pressure was increased again and took over the process.

The combination of these two phenomena resulted in spontaneous imbibition process in shale formation once fracturing fluids come into contact with the formation. This imbibition process can cause water blockage and low fluid recovery up to 50% of the original volume pumped during hydraulic fracturing

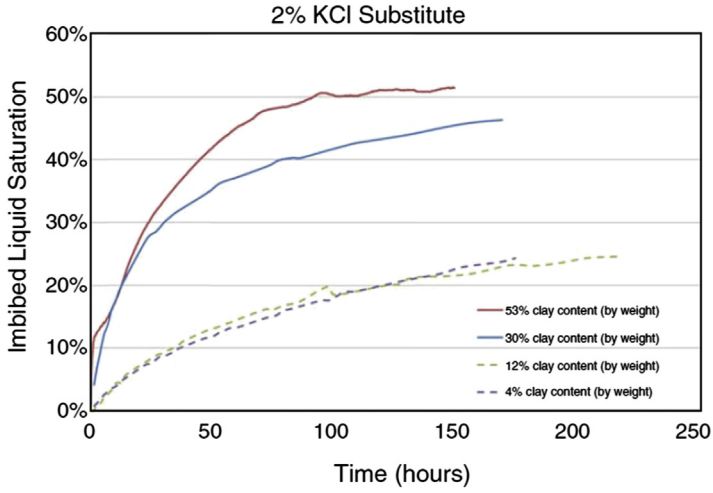

FIGURE 14.45 Imbibed liquid saturation change with time for 2% KCL substitute fracturing fluids in different samples with different clay contents (Zhou, 2016).

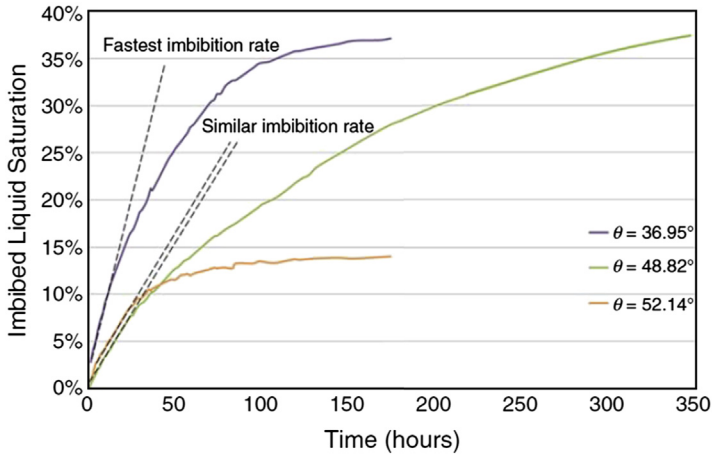

FIGURE 14.46 2% KCL fluid in contact with samples with different wettabilities (Zhou, 2016).

treatments. Imbibition process is further investigated using nuclear magnetic resonance (NMR) test in the following section.

14.6.1.2 Spontaneous and Forced Imbibition Tests

In order to determine oil recovery, capillary pressure, and fluid saturation for tight cores in spontaneous and forced imbibition tests, Amott cell, a high-speed centrifuge, and a 2-MHz NMR device were used (Karimi et al., 2015, 2016).

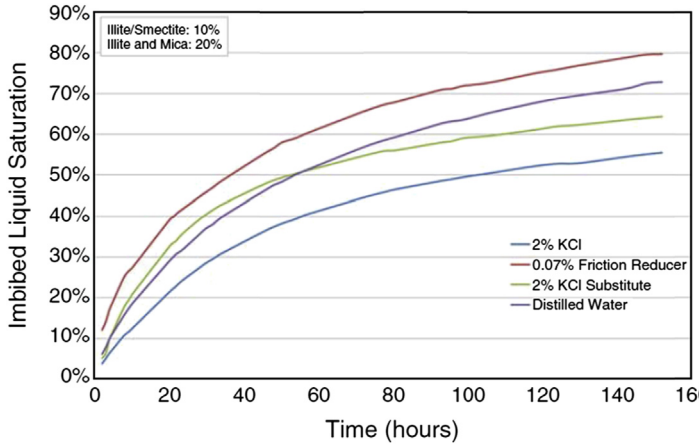

FIGURE 14.47 Samples with same clay structure in contact with different fluids (Zhou, 2016).

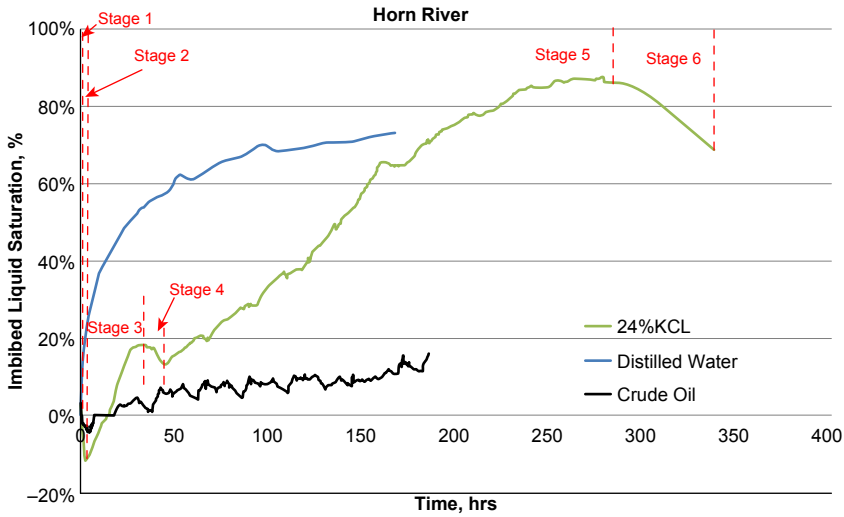

FIGURE 14.48 Altering imbibition process for Horn River samples (Zhou, 2016).

Bakken Formation is an unconventional hydrocarbon resource, which is located in the Williston Basin. Formation brine has a salinity of 300,000 to 400,000 ppm, and Bakken oil is a light oil. The formation consists of two shale members and a tight member in the middle, which is a mixture of carbonate, sandstone, and clays (mostly Illite). The Middle Bakken member has low porosity (<10% porosity) and low permeability (<0.01 mD) (Sonnenberg, 2014). Spontaneous imbibition test was conducted for three preserved core plugs from the Middle Bakken member.

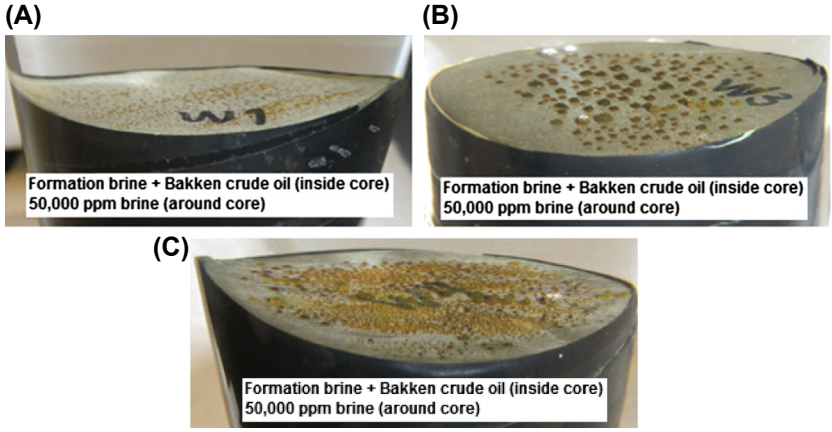

FIGURE 14.49 Images of Core 1 (A), Core 2 (B), and Core 3 (C) in Amott cell showing oil production. All cores were immersed in 50,000-ppm KCl brine for 2 weeks (Karimi et al., 2017).

The preserved cores were saturated with Bakken oil to establish initial fluid saturation, and then they were immersed in 50,000-ppm KCl brine in Amott cell for 2 weeks. Fig. 14.49 shows images of the cores producing oil in Amott cell.

Oil and brine saturation of the cores at native state, after hydrocarbon saturation, and after spontaneous imbibition test were determined from NMR studies as shown in Table 14.4. NMR tests are fairly fast compared to the centrifuge. They are nondestructive and do not change fluid and rock properties.

TABLE 14.4 Water and Oil Saturations of the Cores at Different Test Stages Determined From Nuclear Magnetic Resonance Measurements

Core Status	Parameters (%)	Core 1	Core 2	Core 3
Native state	So	17.41	22.63	15.14
	Sw	43.15	45.77	45.69
	Sair	39.44	31.60	39.17
Hydrocarbon resaturated	So	56.85	54.23	54.31
	Sw	43.15	45.77	45.69
After spontaneous imbibition with 50,000-ppm KCl in deionized water	So	46.13	49.22	47.98
	Sw	53.87	50.78	52.02

TABLE 14.5 Oil Recovery Factor (Percentage of Oil in Place) and Produced Oil (Percentage of Pore Volume) From Preserved Middle Bakken Cores in Spontaneous Imbibition Experiment Using Low Salinity Synthetic Brine

Core	Nuclear Magnetic Resonance Porosity (%)	Oil Recovery Factor (%) (Percentage of Oil in Place)	Produced Oil (%) (Percentage of Pore Volume)
1	2.13	18.86	10.72
2	8.15	9.23	5.01
3	7.40	11.66	6.33

Table 14.5 provides spontaneous imbibition—produced oil volumes from each core. Saturation of the cores was estimated using NMR CPMG (Carr and Purcell, 1954; Meiboom and Gill, 1958) sequence before and after the test to determine oil recovery from each core. Oil recovery factor (ratio of produced oil to oil in place) in spontaneous imbibition test was 18.86%, 9.23%, and 11.66% for Core 1, Core 2, and Core 3, respectively. Oil production as percentage pore volume for Core 1, Core 2, and Core 3 was 10.72%, 5.01%, and 6.33%. Core side walls were jacketed, and only top and bottom faces of the cores were exposed to brine. Immersing cores saturated with hyper salinity brine in low salinity brine resulted in high oil recovery from the cores.

The rock matrix capillary pressure was measured using a high-speed centrifuge. In forced imbibition test, 50,000 KCl brine was used similar to spontaneous imbibition test. Our results indicate that tight rocks have very high capillary pressure, and it is very difficult to displace fluids in tight rocks.

Fig. 14.50 shows measured centrifuge data in solid black line. Each point on the graph represents saturation data measured at 1 rpm. Centrifuge tests for unconventional rocks are time-consuming and expensive. By using a centrifuge, capillary pressure versus core average water saturation is determined. The capillary pressure versus core inflow-face saturation is shown in the figure with dashed lines. The reason for the discrepancy between the two graphs is that water saturation at the inflow-face of the cores is higher than core average water saturation. Because centrifugal force changes with distance from the center of rotation and the highest capillary pressure occurs at the core inflow-face. Fig. 14.50 shows that while saturation of the inflow-face changed up to about 25%, the average core saturation changed only up to about 7%. This indicates the difficulty of pore accessibility in the tight matrix.

Tables 14.6 and 14.7 show core saturations and oil recovery for each core after forced imbibition test.

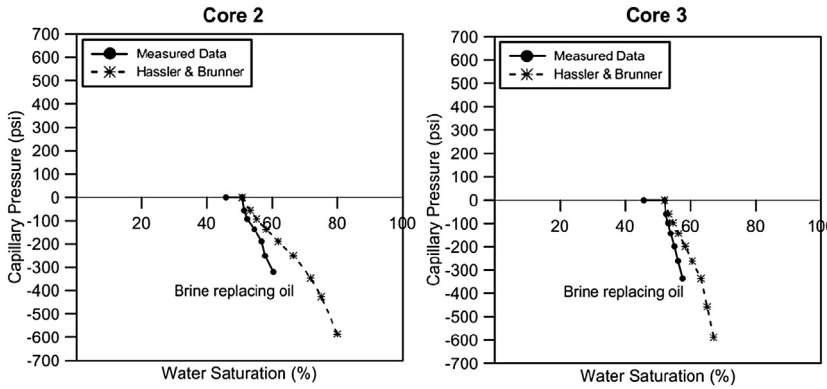

FIGURE 14.50 Imbibition capillary pressure versus measured average and corrected inflow-face core water saturation for Core 2 and Core 3. Water saturation is corrected for inflow-face saturation using Hassler and Brunner method (Hassler, 1945).

TABLE 14.6 Water and Oil Saturations of the Cores After Forced Imbibition Test Determined From Nuclear Magnetic Resonance Measurements

Core Status	Parameters	Core 1	Core 2	Core 3
After forced imbibition with 50,000-ppm KCl in deionized water	So (%)	34.90	42.59	43.32
	Sw (%)	65.10	57.41	56.68

TABLE 14.7 Oil Recovery Factor (Percentage of Oil in Place) and Produced Oil (Percentage of Pore Volume) From Preserved Middle Bakken Cores in Forced Imbibition and Secondary Air-Liquid Drainage Experiments

	Forced Imbibition	
Core	Oil Recovery Factor (%) (Percentage of Oil in Place)	Produced Oil (%) (Percentage of Pore Volume)
1	12.73	6.9
2	9.58	5.20

Table 14.8 compares saturation change estimated from NMR technique with a centrifuge for forced imbibition test, and the two methods provided similar results. It is important to note the tests were conducted at ambient laboratory conditions, and NMR technique must be used with proper

TABLE 14.8 Fluid Saturation Change Determined From Nuclear Magnetic Resonance (NMR) and Centrifuge Experiments at Various Stages of the Experiments

	Core 2		Core 3	
	Centrifuge	NMR	Centrifuge	NMR
Tests	Saturation Change (% Pore Volume)	Saturation Change (% Pore Volume)	Saturation Change (% Pore Volume)	Saturation Change (% Pore Volume)
Spontaneous imbibition	–	5.01	–	6.33
Forced imbibition	6.9	6.62	5.20	4.66

calibration when dealing with hypersalinity formation brine at reservoir pressure and temperature conditions.

The results indicate that using low-salinity brine in fracturing fluid, when formation brine is a hypersaline brine and there is not a risk of clay swelling, oil can be extracted from the rock matrix in the early stages of fracturing. The high capillary pressure of the tight matrix prevents fluid from successful displacing of oil in the matrix. However, water saturation at the fracture faces can be high.

14.6.1.3 Fracture Propagation in Shale Reservoirs

Unlike the conventional reservoirs, fracture propagation in unconventional reservoirs is more complicated. In fracture modeling software, often fractures are simulated as planar fractures even in unconventional reservoirs. However, experimental studies and microseismic mapping have proven that hydraulic fractures in shale reservoirs have a complex pattern for propagation. Shale formations are often heterogeneous materials which exhibit nonuniform distribution of properties (Soliman et al., 2010). Also, stress state could dramatically change from location to location in unconventional reservoirs. Unconventional reservoirs and in particular shale formations can contain numerous interfaces, which are called planes of weakness. These interfaces result from mineral- or organic-filled microfractures. These planes of weakness often change the direction of induced fractures or cause confinement and change the geometry, resulting in the creation of nonplanar fractures with multiple branches, which are considered as a fracture network.

Laboratory modeling of hydraulic fractures showed that interaction between rock fabric and structures, which are seen as interfaces in the formation with the induced fracture, is causing fracture confinement and complexity. In conventional reservoirs with relatively high degree of homogeneity, stress contrast is responsible for hydraulic fracture confinement and propagation. Stress contrast also exists in unconventional reservoirs, but usually due to overpressure nature of shale formations, this contrast becomes diminished, and rock fabric plays the controlling factor. In another word, when stress contrast is high, fracture propagates in the path of least resistance, whereas in the case where we have low stress contrast, fracture propagates according to the fabric of the formation (Suarez-Rivera et al., 2013).

14.6.1.4 Shale Samples

Few testing on shale samples are provided here. In the first set of test, shale cores with a dimension of 6 in. long and 2.6 in. in diameter were cast into hydrostone samples of $6 \times 6 \times 10$ in. Fracturing tests then were done on these shale plugs. Two different approaches were used in these tests, one for open hole and one for oriented perforation in the direction of anticipated fracture.

Oriented perforation test resulted in breakdown pressure of 2300 psi and extension pressure of 1850 psi. On the other hand, the open hole samples showed breakdown pressure of 5200 psi, and after breakdown, several cycles of pressure loading and releasing were observed, which is an indication of opening the natural fractures. Multiple fractures were competing to achieve more width resulting in building up the pressure. Once a new fracture propagated, a release in pressure was observed. Fig. 14.51 shows the propagated fracture initiated from the shale sample and through hydrostone sample.

In the next test, shale samples in Fig. 14.52 went under fracturing test, while there is no stress contrast imposed on these samples. Two heterogeneous shale samples were placed in thick wall cylinders with uniform stress applied around cylinder. On the left core, the sample was cut perpendicular to the bedding planes. Fracture is first initiated in the path of high density material interface, and then changes its direction to low density material interface. This change in fracture direction was only due to the fabric and structure of interfaces in the samples. The core sample on the right side of Fig. 14.52 is cut parallel to the bedding plane. As it can be seen, rock fails in the direction of weakness planes and fracture complexity develops as two weakness planes reached a single point (Suarez-Rivera et al., 2013).

Microstructural and CT scanning observations have shown that the degree of fabric anisotropy in shale reservoirs can vary significantly. Different material composition in shale directly impacts their elastic properties as well (Sone and Zoback, 2013a,b).

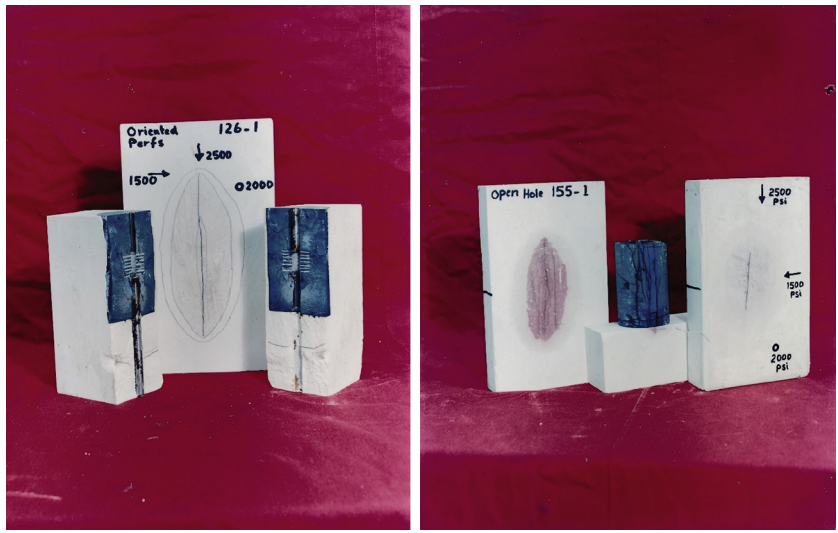

FIGURE 14.51 Oriented perforation (left) versus open hole fracturing (right) in shale sample cast in hydrostone.

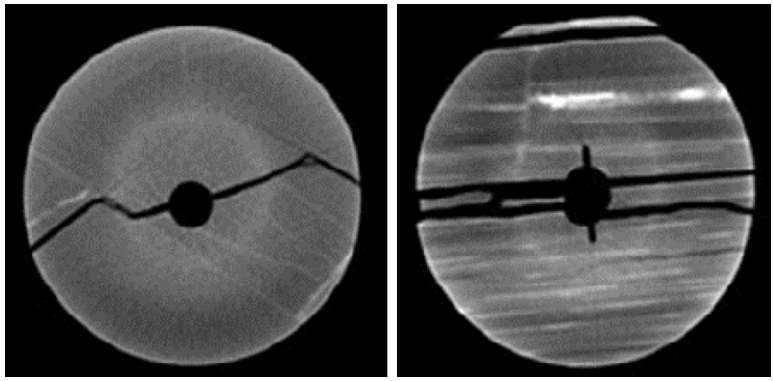

FIGURE 14.52 Fracture propagation in the direction of weakness planes when there is no stress contrast. The core is plugged perpendicular to bedding plane (left) and in the right core was plugged parallel to bedding planes (right) (Suarez-Rivera et al., 2013).

In large-scale shale block fracturing (Figs. 14.53 and 14.54), it was observed in the presence of stress contrast, the primary fracture propagates in the direction of least principal stress. However, if there is the plane of weakness present in parallel to the direction of minimum horizontal stress, then short and discontinuous fractures are formed following the planes of weakness.

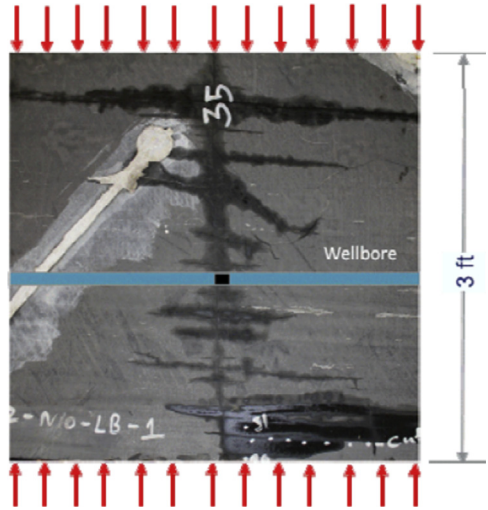

FIGURE 14.53 Shale block fracturing, *red arrows* (dark gray in print versions), showing maximum stress. Fracture propagates perpendicular to least stress; however, due to existence of planes of weakness parallel to minimum stress direction, several short and discontinuous fractures are formed (Suarez-Rivera et al., 2013).

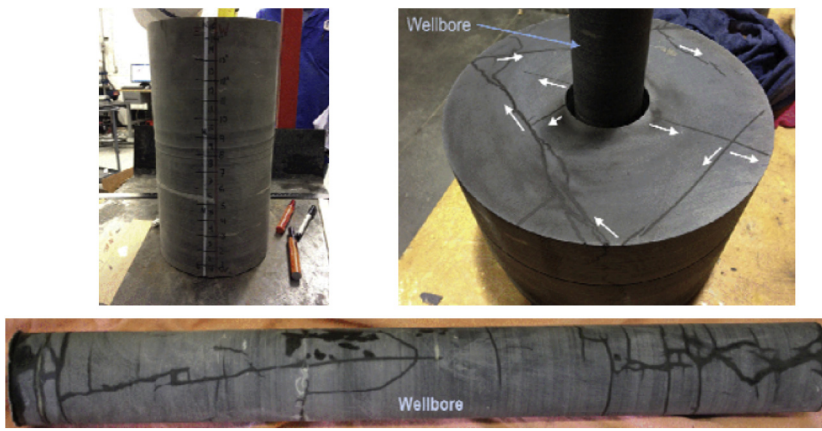

FIGURE 14.54 Large shale block fracturing showing complex propagation pattern within shale formation (Suarez-Rivera et al., 2013).

Further studies of shale formation composition and fabric structure revealed that brittleness and ductility of shale formation are not only dependent on the composition of the shale formations but also on the fabric anisotropy (Sone and Zoback, 2013a,b).

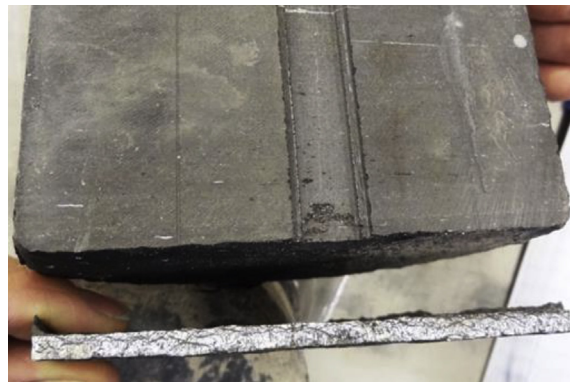

FIGURE 14.55 A detached interface which was placed between two mudstone layers. This is an example of a weak interface, which can easily slip by hydraulic fracturing treatments (Ptaszynska et al., 2016).

The composition of these weak interfaces within unconventional reservoirs has been studied. Weak interfaces are defined as low shear strength between adjusting layers and lithology and can be slipped easily if subjected to shear stress caused by hydraulic fracturing treatments. Not all interfaces in the shale formation are prone to slip. When changes in composition and physical properties at the interface are more transitional and smooth, the interface is acting as strong binding. But when the changes in density, elastic stiffness, and unconfined strength are abrupt, the interface is relatively week (Ptaszynska et al., 2016). In another word, the interface can be considered as critically stressed (Fig. 14.55).

14.6.1.5 Shale Block Fracturing and Studying Stimulated Reservoir Volume Maximizing Methods

As it was discussed earlier, the major distinction between hydraulic fracturing techniques in conventional reservoirs and unconventional reservoirs is the goal of hydraulic fracturing technique. In conventional reservoirs, a single bi-wing and a planar fracture are the optimum designs. However, in unconventional reservoirs, the goal is to create a complex fracture network by hydraulic fracturing. Due to the extremely low permeability of the unconventional reservoirs, more reservoirs must be exposed to hydraulic fractures. This technique leads to the definition of SRV in unconventional reservoirs. Creating a more complex network of fractures, as depicted in Fig. 14.57, could substantially enlarge the created SRV (Fisher et al., 2004).

The creation of SRV and fracture complex network was first discussed in Barnett shale formation, and their importance of final production was observed. Fig. 14.57 shows the microseismic mapping of hydraulic fracturing

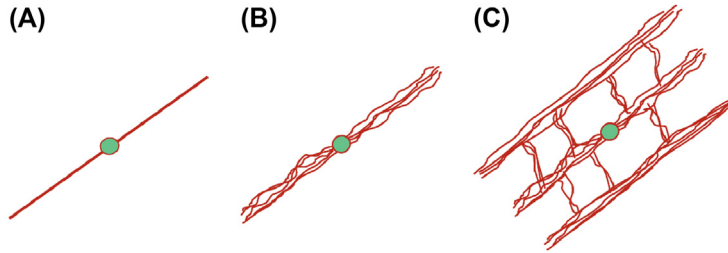

FIGURE 14.56 Fracture network and created stimulated reservoir volumes (Fisher et al., 2004). (A) Simple Fracture. (B) Complex fracturing. (C) Extremely complex.

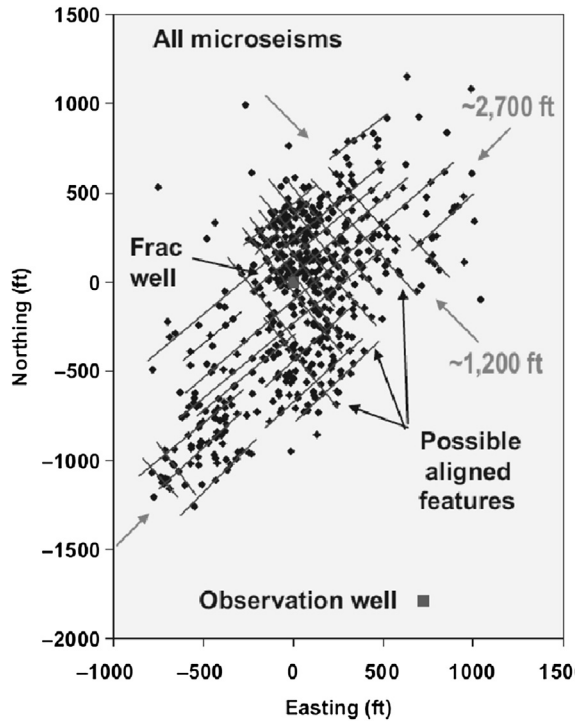

FIGURE 14.57 Microseismic mapping of a fracture network (Mayerhofer et al., 2008).

in a vertical well in a shale formation, which indicates the creation of complex fracture network (Mayerhofer et al., 2008).

In creating a complex fracture network, sliding existing natural fractures is critical. Fluid injection has an impact on the change of friction coefficient and subsequently influences the sliding of natural fractures during hydraulic fracturing (Padin et al., 2014; Mokhtari and Tutuncu, 2016).

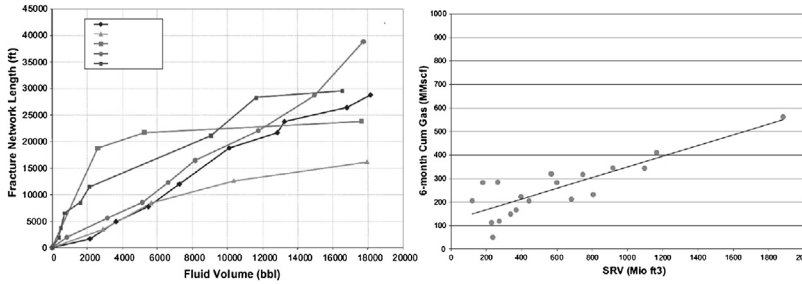

FIGURE 14.58 Fluid volume and created length of the fracture network, legend shows five different wells (left), size of the stimulated reservoir volume (SRV), and its impact on production (right) (Mayerhofer et al., 2008).

It is worth mentioning that the application of microseismic in mapping fracture network was questioned in recent years; however, microseismic still can be used to assess the success of the fracturing operation other than mapping the fracture network (Vermylen, 2011).

To create optimum SRVs, horizontal fracturing with massive hydraulic fracturing treatments, which could be up to 30–50 hydraulic fracturing stages, were employed. This method, although it was successful in creating a larger SRV, resulted in substantially increasing the treatment cost and complexity regarding water needed and high volume of water waste back from hydraulic fracturing treatments.

Fig. 14.58 shows the relationship between job size and the size of created SRV, which indicates a direct effect of increasing the size of the treatment in final fracture network created. It was also observed that bigger SRV resulted in higher 6 months' cumulative gas production.

To eliminate the costly operation to increase the SRV size, several experimental modeling studies have been done to decrease the treatment fracturing volume without decreasing the SRV size. In later sections, experimental modeling of several methods, which are proposed to reduce the water-based fracturing method, is presented.

14.6.2 Coal Fracturing

Coalbed methane is considered another form of unconventional resources along the gas and oil shale and tight formations. It provides a high-quality methane resource. Hydraulic fracturing in coalbed methane is also trying to connect the complex network of natural fractures or cleats to the wellbore (Abass et al., 1991). Figs. 14.59 and 14.60 show a typical coal sample with a network of cleats and fractures connected to the wellbore in the center.

Coal is characterized by interacted system of coal grains, micropores, and cleats. Gas is absorbed on the large surface area of the grain, and the cleat

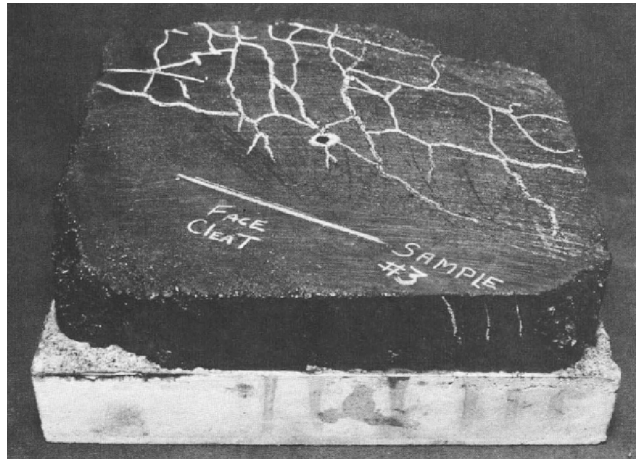

FIGURE 14.59 Typical coalbed methane with cleat network (Abass et al., 1991).

FIGURE 14.60 Cleat network in coal samples (Fang and Khaksar, 2011).

system is water saturated. To initiate the gas desorption process, it is necessary to recover water and drop the pressure below the onsite of gas desorption process.

Due to cleated nature of coal, it is a discontinuous medium. Fracture created in shallow coal may stay open mainly due to this discontinued nature and lack of confinement at shallow depth. Experimental modeling of coal fracturing was done by Abass et al. (1991) on coal blocks of $9 \times 6 \times 5$ in. In one test, where four different injection cycles were designed, it was observed in the tests that treating pressure is increasing for each cycle while fluid was leaking off from sides of the sample.

This increase in treating pressure shown in Fig. 14.61 is indicating that in every cycle, a new system of fractures and cleats are getting connected and a larger SRV is created. Similar behavior has been seen in a minifrac test in an actual field operation (Fig. 14.62). However, it was indicated by the authors that this increase in treating pressure is due to creating high-stress regions in the vicinity of saturated fracture network (Fang and Khaksar, 2011).

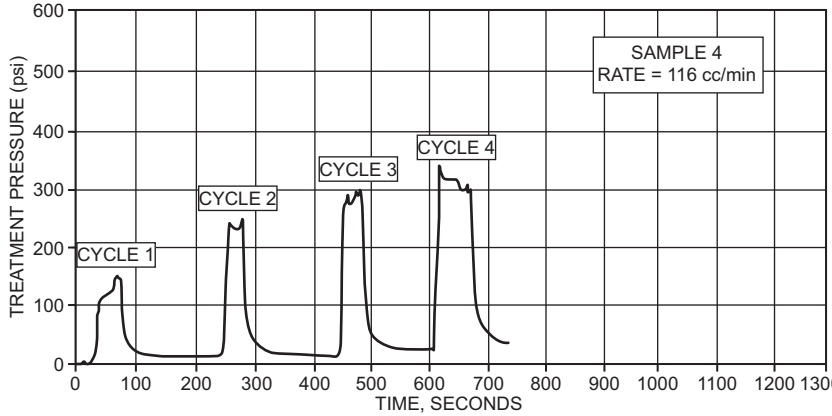

FIGURE 14.61 Injection cycles in the same core sample. Increasing the treating pressure for each consecutive cycle is due to increasing the stimulated reservoir volume and opening a new set of fracture system.

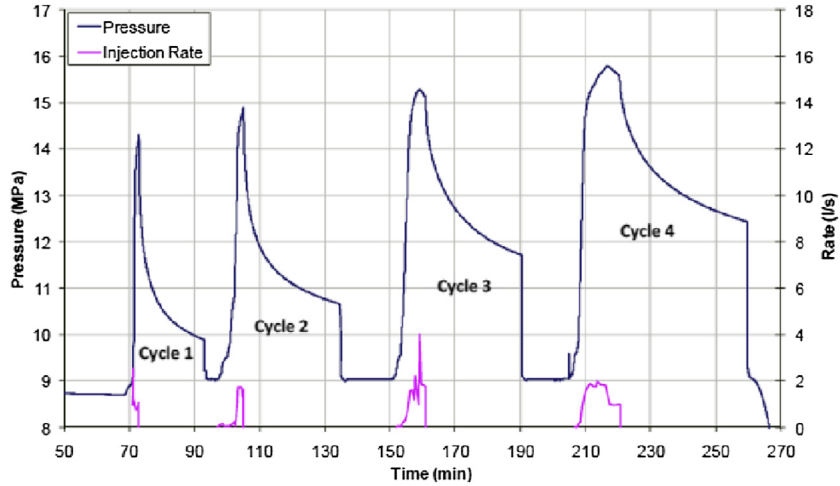

FIGURE 14.62 Injection cycles in an actual minifrac test in a coal formation. Showing the same increase in injection pressure trend (Fang and Khaksar, 2011).

14.7 WATERLESS FRACTURING

14.7.1 Chemically Induced Pressure Pulse Fracturing

In this section, experimental modeling of a chemically induced pressure pulse to increase SRV will be discussed. This method includes triggering an exothermic reaction in situ, which generates gas, heat, and localized pressure, which is sufficient enough to break down the formation and initiate multiple

fractures. Additionally, this technique helps the cleanup process of fracturing gel, as the generated heat completely breaks the fracturing fluid gel.

There are mainly three fracturing techniques regarding pressurizing the wellbore and breaking the formation. Pressurizing rate in hydraulic fracturing is less than 1 MPa per second. The second technique is pressurizing through explosive that has the pressuring rate of more than 107 MPa per second. The third technique is using a propellant that has an intermediate pressuring rate of 102−106 MPa per second. It has been observed that the higher the pressuring rate, the more fractures initiated. However, in chemically induced pressure pulse technique, this pressurizing rate and the number of created fractures can be controlled.

Experiments below show application of this technique. These tests were done on Indiana Limestone, Berea Sandstone, and shale blocks at the unconfined and confined environment. The first test was done on a white cement block, and breakdown pressure was recorded as 5400 psi. The block properties are listed in Table 14.9.

Fig. 14.63 shows this block before and after fracturing with chemically induced pressure pulses. Created fractures are longitudinal and perpendicular to the cased vertical wellbore. Also, fractures propagated to the end of the samples show that generated pressure use greater than the compressive strength of the rock samples.

Next test shows Indiana Limestone samples. The breakdown pressure for this sample was recorded as 4700 psi (Table 14.10).

Fig. 14.64 shows this block before and after fracturing techniques, which indicates multiple fractures generated in the block.

The final test was done on a shale sample from Mancos. The breakdown pressure was recorded as 6600 psi, and its mechanical properties are listed in Table 14.11.

Fig. 14.65 shows shale block before and after treatment using chemically induced pressure pulse method.

TABLE 14.9 White Cement Properties

Porosity	29%
Bulk density	1.82 gm/cc
Young's modulus	1.92×10^6
Poisson's ratio	0.26
Unconfined compressive strength	3299 psi
Cohesive strength	988 psi
Internal friction angle	28 degrees

FIGURE 14.63 White cement block before (top) and after (bottom) applying fracturing technique using chemically pulsed pressure.

CT scanning tests on core samples showed significant density reduction in the samples. Voids scattered around the treated area were obvious. MR-CT microscopy of the treated blocks showed a significant increase in core pores and a created network of otherwise isolated micro and macropores. The following figures show the CT scanning pictures of the core sample before and after the treatment (Figs. 14.66 and 14.67).

It was also observed that the generated heat was able to sufficiently break the fracturing gel. The fracturing gel viscosity after the treatment dropped to 10 cp. The chemical component can be incorporated into the fracturing gel. Fracturing gel will carry the proppant down to tips of the initial fracture, and once the chemical reaction triggered and created a large network of new fracture, the generated heat can break the gel completely (Fig. 14.68).

TABLE 14.10 Indiana Limestone Properties	
Porosity	28%
Bulk density	1.82 gm/cc
Young's modulus	1.92×10^6
Poisson's ratio	0.26
Unconfined compressive strength	3299 psi
Cohesive strength	1067 psi
Internal friction angle	23 degrees
Tensile strength	271 psi

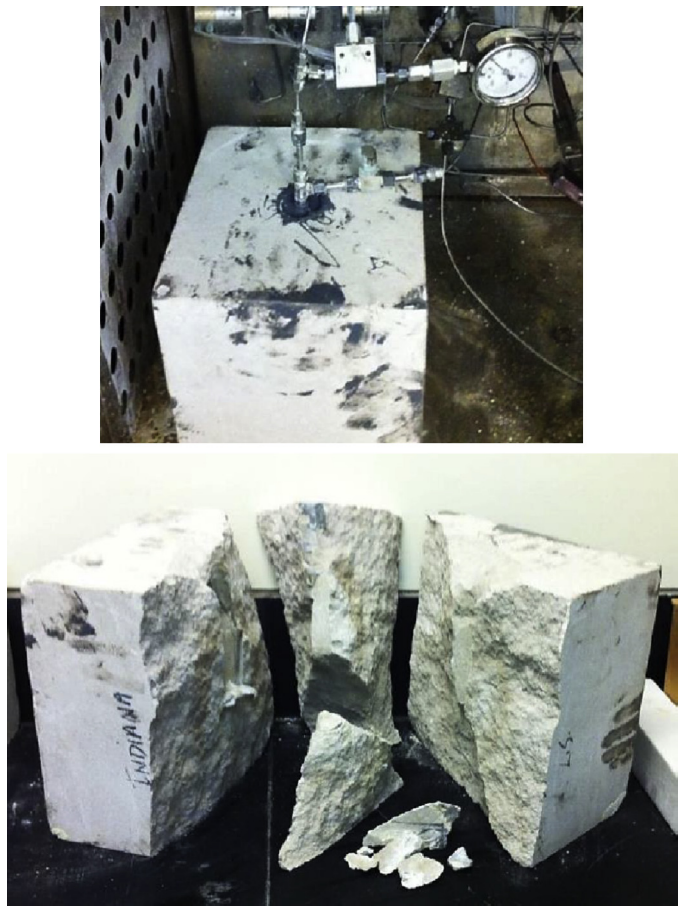

FIGURE 14.64 Indiana Limestone block before (top) and after (bottom) applying fracturing technique using chemically pulsed pressure.

TABLE 14.11 Shale Sample Properties

Porosity	3.8%
Bulk density	2.50 gm/cc
Young's modulus	2.66×10^6
Poisson's ratio	0.20
Unconfined compressive strength	4965 psi
Cohesive strength	1268 psi
Internal friction angle	36 degrees

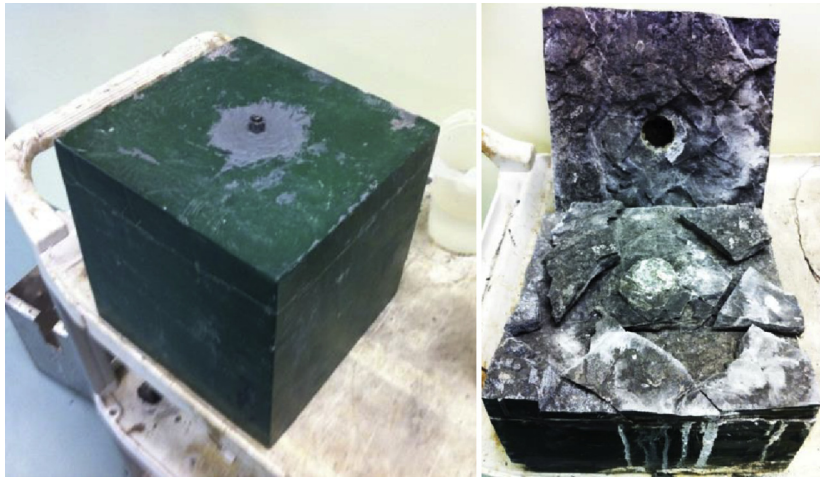

FIGURE 14.65 Shale block before and after fracturing with chemically induced pressure pulse.

This technique can be completely controlled to create a sufficiently large SRV. One important factor in this technique is how to control the activation time.

This chemical reaction needs a triggering temperature to be activated. In the field application, this triggering temperature can be achieved by pre-flushing the wellbore and cooling down the reservoirs, and then as reservoir temperature is recovering to the initial temperature then the reaction will take place. This lag in activation time can result in better controlling the pressure pulse generated (Al-Nakhli et al., 2014).

14.7.2 Cryogenic Fracturing to Increase Stimulated Reservoir Volume

In this section, experimental studies on cryogenic fracturing as well as their numerical simulations in Niobrara Shale will be presented. Cryogenic

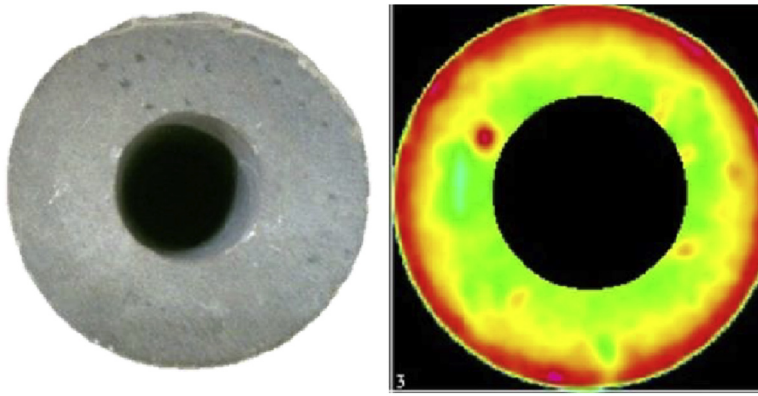

FIGURE 14.66 The CT scanning on the core plug before the treatment.

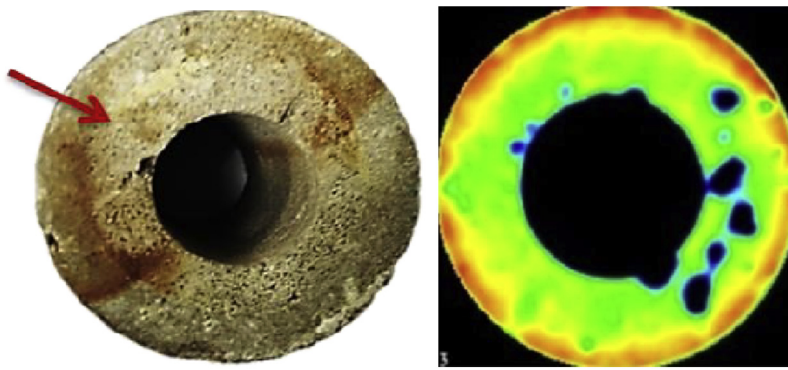

FIGURE 14.67 The CT scanning on the same core plug after the treatment.

fracturing is described as the result of a thermal shock on the hot surface of the rock by introducing a cryogen. The rapid heat transfer will cause the surface of the rock to shrink, and eventually rocks fails in tension. Orthogonal fractures will form on the plane of contact of the cryogen and the rock (Yao et al., 2016).

Cryogenic fracturing experiment was first started using liquid gel CO_2 on sandstone rocks and liquid N_2 on coal samples (King, 1983) (McDaniel et al., 1997). In this work, the governing equation of mass and heat transfer is described as (Xiong et al., 2013)

$$\frac{d}{dt}\int_{V_n} Q^K \, dV_n = \int_{\Gamma_n} F^K \cdot \vec{n} \, d\Gamma_n + \int_{V_n} q^K dV_n$$

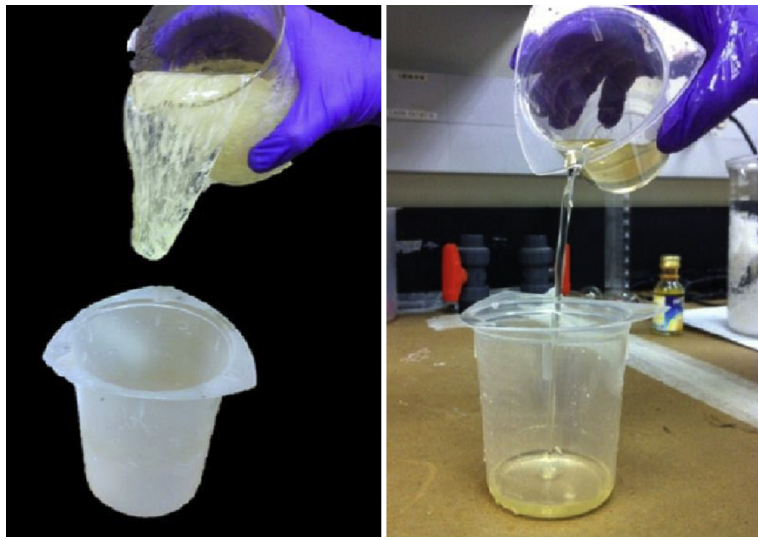

FIGURE 14.68 Breaking the fracturing gel using the generated heat from the reaction.

Thermal stress is that portion of stress, which is resultant of thermal effects or temperature change. Thermally induced stress can be integrated into the stress−strain relation as (Zoback, 2010)

$$\sigma_{kk} - B_i \times P_p - \frac{E}{(1-2v)}[\beta(T-T_0)] = \frac{E}{(1+v)}\varepsilon_{kk} + \frac{E}{(1+v)(1-2v)}(\varepsilon_{xx}+\varepsilon_{yy}+\varepsilon_{zz})$$

Then, the failure criterion of Mogi−Coulomb was integrated into the TOUGH2-EGS simulation, a coupled geomechanical simulator for fluid and heat flows in the enhanced geothermal system (Xiong et al., 2013; Yao et al., 2017; Zhang et al., 2016, 2015), to describe the failure mode when the stress exceeds the strength by this criterion (Al-Ajmi and Zimmerman, 2006). In this modeling, only conduction was considered and every single grid was considered as a homogenous grid. The natural fractures were ignored due to the complexity associated with simulating natural fractures (Yao et al., 2016). Results of actual experimental block fracturing on 8 in. by 8 in. by 8 in. shale blocks from Niobrara to the simulation are provided.

The test presented here was done on a shale sample with two rounds of high-pressure liquid nitrogen injection. The values of confining stress applied

on the block were 1000 and 3000 psi in a horizontal plane and 4000 psi in a vertical plane. The visual observation for the created fracture is in Fig. 14.69. The breakdown pressure recorded for this test was 1417 psi (Yao et al., 2016).

The simulation result of this test is shown in Fig. 14.70.

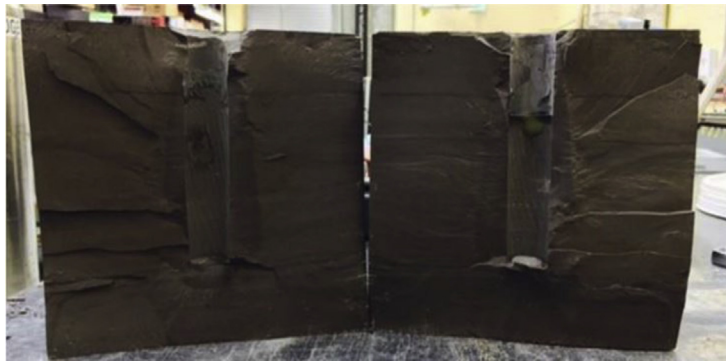

FIGURE 14.69 Visual observation for the shale sample fracturing using cryogenic method (Alqatahni et al,. 2016).

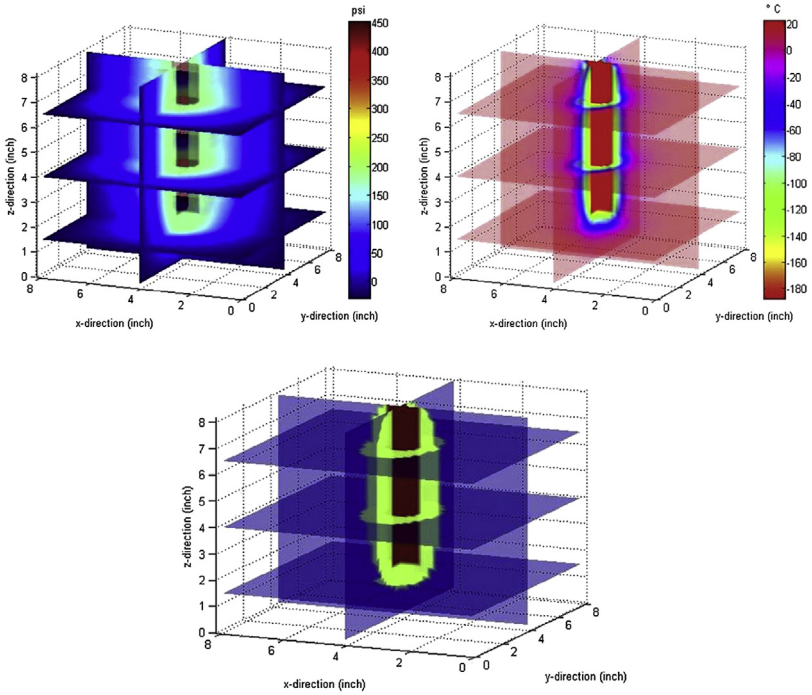

FIGURE 14.70 Simulation results for shale sample fracturing using cryogenic fracturing technique showing pressure (top left), temperature (top right), and grid (bottom) distributions (Yao et al., 2016).

REFERENCES

Abass, H.H., Hagist, P., Harry, J., Hunt, J.L., Shumway, M., Gazi, N., 1995. A case history of completing and fracture stimulating a hariozntal well. In: SPE Production Operations Symposium, SPE 29443. Oklahoma City, OK.

Abass, H.H., Hedayati, S., Meadows, D.L., 1996. Nonplanar fracture propagation from a horizontal wellbore: experimental study. SPE Production & Facilities 11 (03), 133–137.

Abass, H.H., Kim, C.M., Hedayati, S., 1991. Experimental simulation of hydraulic fracturing in shallow coal seams. Rock Mechanics as a Multidisciplinary Science 261–270.

Abass, H.H., Meadows, D.L., Brumley, J.L., Hedayati, S., Venditto, J.J., 1994a. Oriented perforations – a rock mechanics view. In: SPE Annual Technical Meeting. New Orleans, LA.

Al-Ajmi, A.M., Zimmerman, R.W., 2006. Stability analysis of vertical boreholes using the Mogi–Coulomb failure criterion. International Journal of Rock Mechanics and Mining Sciences 43 (8), 1200–1211.

Al-Nakhli, A.R., Abass, H.H., Khan, M., Hilab, V., Rizq, A., 2014. Chemically-induced pressure pulse to increase stimulated reservoir volume in unconventional reservoirs. In: SPE Unconvnetional Resources Technology, URTec 1922369. Denver, CO.

Alqatahni, N.B., Cha, M., Yao, B., Yin, X., Kneafsey, T.J., Wang, L., Miskimins, J.L., 2016. Experimental investigation of cryogenic fracturing of rock specimens under true triaxial confining stresses. In: 78th EAGE Conference and Exhibition. Vienna, Austria.

Brumley, J.J., Abass, H.H., 1996. Hydraulic fracturing of deviated wells: interpretation and initial fracture opening pressure. In: SPE 37363. Columbus, OH.

Carr, H.Y., Purcell, E.M., 1954. Effects of diffusion on free precession in nuclear magnetic resonance experiments. Physical Review 94 (3), 630.

Daneshy, A.A., 1972. A study of inclined hydraulic fractures. In: SPE-AIME 47th Annual Fall Meeting, SPE 4062. San Antonio, TX.

Economides, M.J., Watters, L.T., Dunn-Norman, S., 1998. Petroleum well construction. In: Economides, M.J., Watters, L.T., Dunn-Norman, S. (Eds.), Petroleum Well Construction. John Wiley & Sons, pp. 143–1712.

El Rabaa, W., 1987. Hydraulic fratcure propagation in the presence of stress variation. In: SPE Annual Technical Conference and Exhibition. Dallas, TX.

El Rabaa, W., 1989. Experimental study of hydraulic fracture geometry initiated. In: Annual Technical Conference and Exhibition, SPE. San Antonio, TX.

Fang, Z., Khaksar, A., 2011. Complexity of minifrac tests and implications for in-situ horizontal stresses in coalbed methane reservoirs. In: International Petroleum Technology Conference, IPTC 14630. Bangkok, Thailand.

Fisher, M.K., Heinze, J.R., Harris, C.D., Davidson, B.M., Wright, C.A., Dunn, K.P., 2004. Optimizing horizontal completion techniques in the Barnett shale using microseismic fracture modeling. In: SPE Annual Technical Conference and Exhibition, SPE 90051. Houston, TX.

Grandi, S., Rao, R.V., Toksoz, M.N., 2002. Geomechanical Modeling of In-situ Stresses Around a Borehole. Massachusetts Institute of Technology. Earth Resources Laboratory.

Hassler, G.L., 1945. Measurement of capillary pressures in small core samples. Transactions of the AIME 160 (01), 114–123.

Karimi, S., Kazemi, H., Simpson, G.A., 2017. Capillary pressure, fluid distribution, and oil recovery in preserved middle bakken cores. In: SPE Oklahoma City Oil and Gas Symposium. Oklahoma City, OK.

Karimi, S., Saidian, M., Kazemi, H., 2016. Experimental study of the effect of core aging on fluid distribution in middle bakken cores. In: SPE Low Perm Symposium, SPE 180269. Denver, CO.

Karimi, S., Saidian, M., Prasad, M., Kazemi, H., 2015. Reservoir rock characterization using centrifuge and nuclear magnetic resonance: a laboratory study of middle bakken cores. In: SPE Annual Technical Conference and Exhibition, SPE 175069. Houston, TX.

King, S.R., 1983. Liquid CO_2 for the stimulation of low-permeability reservoirs. In: SPE/DOE Low Permeability Gas Reservoirs Symposium, SPE 11616. Denver, CO.

Li, G., Allison, D., Soliman, M.Y., 2011. Geomechanical study of the multistage fracturing process for horizontal wells. In: 45th US Rock Mechanics/Geomechanics Symposium. American Rock Mechanics Association, San Francisco, CA.

Li, Q., Xin, H., Liu, J., Liu, X., 2015. A review on hydraulic fracturing of unconventional reservoir. Ke Ai − Advanced Research Evolving Science, Petroleum 1, 8−15.

Mayerhofer, M.J., Lolon, E.P., Warpinski, N.R., Cipolla, C.L., Waiser, D., Rightmire, C.M., 2008. What is stimulated reservoir volume?. In: SPE Shale Gas Production, SPE 119890. Fort Worth, TX.

McDaniel, B.W., Grundmann, S.R., Kendrick, W.D., Wilson, D.R., Jordan, S.W., 1997. Field applications of cryogenic nitrogen as a hydraulic fracturing fluid. In: SPE Annual Technical Conference and Exhibition. San Antonio, TX.

Medeiros, F., Kurtoglu, B., Ozkan, E., Kazemi, H., 2007. Pressure-transient performances of hydraulically fractured horizontal wells in locally and globally naturally fractured formations. In: International Petroleum Technology Conference.

Meiboom, S., Gill, D., 1958. Modified spin-echo method for measuring nuclear relaxation times. Review of Scientific Instruments 29 (8), 688−691.

Mokhtari, M., Tutuncu, A.N., 2016. Impact of laminations and natural fractures on rock failure in Brazilian experiments; a case study on green river adn Niobrara formations. Natural Gas and Science and Engineering 36, 79−86.

Padin, A., Tutuncu, A.N., Sonnenberg, S., 2014. On the mechanism of shale microfarcture propagation. In: SPE Hydraulic Fractuirng Technology Conference, SPE 168624. Woodland, TX.

Ptaszynska, A., Green, S., Hupka, J., Suarez-Rivera, R., 2016. Mineral and organic matter constituents in weak interfaces in shales. In: 50th US Rock Mechanics/Geomechanics Symposium. American Rock Mechanics Association, Houston, TX.

Sepehri, J., Soliman, M.Y., Morse, S.M., 2015. Application of extended finite element method to simulate hydraulic fracture propagation from oriented perforations. In: SPE Hydraulic Fracturing Technology Conference. Woodlands, TX.

Shah, S.N., Vincent, M.C., Rodriquez, R.X., Palisch, T.T., 2010. Fracture orientation and proppant selection for optimizing production in horizontal wells. In: SPE Oil and Gas India Conference and Exhibition, SPE 128612. Mumbai, India.

Soliman, M.Y., Daal, J., East, L., 2012. Impact of fracturing and fracturing techniques on productivity of unconventional formations. In: SPE/EAGE European Unconventional Resources Conference & Exhibition. Vienna, Austria.

Soliman, M.Y., East, L., Adams, D., 2004. GeoMechanic aspects of multiple fratcuring of horizontal and vertical wells. In: SPE International Thermal Operations and Heavy Oil Symposium, SPE 86992. Bakersfield, CA.

Soliman, M.Y., East, L.E., Augustine, J.R., 2010. Fracturing design aimed at enhancing fracture complexity. In: SPE EUROPEC/EAGE Annual Conference and Exhibition. Vienna, Austria.

Sone, H., Zoback, M.D., 2013a. Mechanical properties of shale-gas reservoir rocks—Part 1: static and dynamic elastic properties and anisotropy. Geophysics 78 (5), D381−D392.

Sone, H., Zoback, M.D., 2013b. Mechanical properties of shale-gas reservoir rocks—Part 2: ductile creep, brittle strength, and their relation to the elastic modulus. Geophysics 78 (5), D393–D402.

Sonnenberg, S., 2014. The upper bakken shale resource play, Williston basin. In: Unconventional Resources Technology Conference, URTeC 1918895. Denver, CO.

Suarez-Rivera, R., Burghardt, J., Stanchits, S., Edelman, E., Surdi, A., 2013. Understanding the Effect of Rock Fabric on Fracture Complexity for Improving Completion Design and Well Performance. International Petroleum Technology, IPTC 17018, Beijing, China.

Veeken, C., Davies, D., Walters, J., 1989. Limited communication between hydraulic fracturing and (deviated) wellbore. In: SPE Joint Rocky Mountain Regional/Low Permeability Reservoirs Symposium and Exhibition. Denver, CO.

Vermylen, J.P., 2011. Geomechanical Studies of the Barnett Shale. Stanford University, Texas, USA.

Veselinovic, D., Green, D., Dick, M., 2016. Determination of natural fracture porosity using NMR. In: Unconventional Resources Technology Conference, URTEC-2447768-MS.

Walton, I., McLennan, J., 2013. The role of natural fractures in shale gas production. International Society for Rock Mechanics.

Wu, R., 2006. Some Fundamental Mechanisms of Hydraulic Fracturing. Georgia Institute of Technology.

Xiong, Y., Fakcharoenphol, P., Winterfeld, P., Zhang, R., Wu, Y.S., 2013. Coupled geomechanical and reactive geochemical model for fluid and heat flow: application for enhanced geothermal reservoir. In: SPE Reservoir Characterization and Simulation Conference and Exhibition. Abu Dhabi, UAE.

Yao, B., Wang, L., Patterson, T., Kneafsey, T.J., Yin, X., Wu, Y., 2017. Experimental study and modeling of cryogenic fracturing treatment of synthetic rock samples using liquid nitrogen under tri-axial stresses. In: SPE Unconventional Resources Conference. Abu Dhabi, UAE.

Yao, B., Wang, L., Yin, X., Wu, Y.S., 2016. Numerical modeling of cryogenic fracturing process on laboratory-scale Niobrara shale samples. Journal of Natural Gas Science and Engineering.

Zhang, R., Winterfeld, P.H., Yin, X., Xiong, Y., Wu, Y.S., 2015. Sequentially coupled THMC model for CO_2 geological sequestration into a 2D heterogeneous saline aquifer. Journal of Natural Gas Science and Engineering 27, 579–615.

Zhang, R., Yin, X., Winterfeld, P.H., Wu, Y.S., 2016. A fully coupled thermal-hydrological-mechanical-chemical model for CO_2 geological sequestration. Journal of Natural Gas Science and Engineering 28, 280–304.

Zhou, Z., 2016. The Impact of Capillary Imbibition and Osmosis During Hydraulic Fracturing of Shale Formations. Colorado School of Mines.

Zhou, Z., Hoffman, B.T., Bearinger, D., Li, X., 2014. Experimental and numerical study on spontaneous imbibition of fracturing fluids in shale gas formation. In: SPE/CSUR Unconventional Resources Conference, SPE 171600. Calgary, Canada.

Zoback, M.D., 2010. Reservoir geomechanics. In: Zoback, M.D. (Ed.), Reservoir Geomechanics. Cambridge University Press, pp. 167–196.

Chapter 15

Laboratory Studies to Investigate Subsurface Fracture Mechanics

Timothy J. Kneafsey
Lawrence Berkeley National Laboratory, Berkeley, CA, United States

15.1 INTRODUCTION

Since the late 1940s, laboratory studies on the nature of fracturing applicable to hydrocarbon production or enhanced geothermal systems have been performed. Most of these studies are applicable to hydraulic fracturing with the focus on improving the understanding of the fracturing process to enhance hydrocarbon recovery. This chapter walks through the literature of laboratory fracture experiments conducted over the last six decades. A good number of studies are reviewed in this chapter, but the intention is not to include every study.

In the laboratory, tests have been performed to investigate numerous subsurface conditions to gain understanding on many of the conditions of interest in the subsurface, including homogeneous media using gelatins, hydrostone, cement, natural samples, poly(methyl methacrylate) (PMMA); anisotropic media using gelatins, hydrostones, cements, and natural samples; and media with specific weaknesses, fractures, and flaws, various stress conditions, and various borehole angles with respect to principal stresses. Sample sizes range from centimeter-scale cores under hydrostatic and triaxial stresses in some earlier tests to nearly meter-scale blocks under true triaxial stresses in more recent tests. Applied stresses range from those implemented utilizing rubber bands to in situ reservoir stresses and far beyond. Viscous fluids and slickwater have been investigated by many, and nonwater fluids such as supercritical CO_2 ($scCO_2$) and liquid nitrogen have been investigated to a limited extent. Because the experimental matrix for full understanding and testing each parameter to capture the possible fracturing conditions and fluids is very large, it is of course incomplete.

Hydraulic Fracture Modeling. https://doi.org/10.1016/B978-0-12-812998-2.00015-1

In a long-view looking back on fracture testing, Warpinski stated, "When rocks are fairly simple, the fractures behave the way we expect them to. We did a fairly good job of predicting how they would propagate. Conversely, when the geology gets very complicated, you have lots of natural fractures and the hydraulic fracturing became very unpredictable and complicated" (King, 2014).

In evaluating the literature for the laboratory studies on hydraulic fracturing, de Pater et al. (1994) stated, "We conclude from the literature survey that very few valid tests have been conducted. Moreover, many tests have been performed to study complicated situations without properly representing the conditions for simple propagation. It might be possible that such tests yielded some correct conclusions; e.g., regarding fracture containment. The possibility exists that the results of these experiments bear no worthwhile relation to field-size hydraulic fractures." In this chapter, laboratory tests will be reviewed more broadly, and although many of the covered studies do not meet de Pater et al. (1994) standards for validity, some truths of fracturing have been revealed and recorded.

In this chapter, the studies summarized are presented chronologically. With the number of independent variables that can be investigated, the studies are difficult to group. A header is provided for each study; however, these headers are often oversimplified. The final section of the chapter crosscuts through the studies, attempting to generalize some of the results. The terms "horizontal" and "vertical" are used from the perspective of vertical wellbores, generally considering the vertical lithostatic stress as the maximum principal stress.

15.2 LABORATORY STUDIES OF FRACTURING

15.2.1 Homogeneous Medium and Anisotropic Medium

In a very early laboratory fracturing demonstration, Hubbert and Willis (1957) examined hydraulic fracturing in quite an elegant way. A hardened 12% gelatin solution was used as the medium and it was contained in a 2-gallon polyethylene bottle with the top cut off. Using appropriate glass tubing, the gelatin was hardened with a well in the center. Stresses were applied by either squeezing the container to make its circular cross section elliptical, causing one horizontal stress to exceed the other, or by wrapping a stretched rubber tubing around the plastic bottle to stretch it vertically, minimizing the vertical stress. Plaster of paris was injected into the well as the fracturing fluid resulting in a solid impression of the resulting fracture.

With the horizontal stresses uneven and smaller than the vertical stress, the expected vertical bi-wing penny-shaped fracture formed and hardened, allowing its removal and quantification. Wrapping the polyethylene bottle with a rubber tube following hardening of the gelatin caused a reduction in the magnitude of the vertical stress relative to the horizontal stresses. When fracturing was performed, a horizontal fracture perpendicular to the vertical

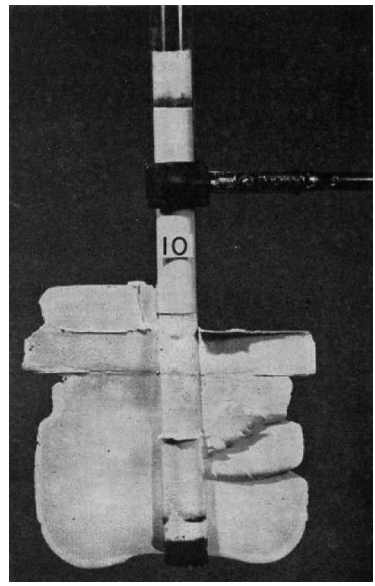

FIGURE 15.1 Solidified plaster of paris fracturing fluid from a vertical fracturing experiment. *From Hubbert, M.K., Willis, D.G., 1957. Mechanics of hydraulic fracturing. Petroleum Transactions, AIME 210, 16.*

borehole formed. To investigate anisotropy, stratified layers of alternating weak and strong gelatin were poured. As expected, this resulted in a horizontal fracture. A vertical fracture experiment considering anisotropy is shown in Fig. 15.1, identifying the importance of boundaries and geological layering.

15.2.2 Heterogeneous Flawed Media

Lamont and Jessen (1963) examined the effect of an existing fracture or joint plane on hydraulic fracture propagation. 106 model systems were investigated using as many as 6 rock types, having dimensions of $1.5 \times 3.5 \times 4$ to 8 in. The prefractures were (1) mated together, (2) filled with a layer of sand, or (3) in some cases large enough to represent vugs. In 70 tests, the hydraulic fracture extended across the existing fracture. It was noted that hydraulic fractures tended to alter direction near the discontinuity so that the plane of the hydraulic fracture intersected the plane of the existing fracture at right angles. The rates of fracturing were considerably greater than would occur in the field.

15.2.3 Homogeneous Medium

Haimson and Fairhurst (1967) presented the criteria for fracture initiation in porous-permeable materials by considering all the possible stress fields around

the wellbore. About 200 fracturing tests were performed on hydrostone (gypsum cement) cubical and cylindrical samples with a characteristic dimension of about 5 in. In these tests, the effect of hydraulic fracturing fluid viscosity (7 oil viscosities), rock strength (varied by using three hydrostone compositions), and stress orientations were investigated. In these tests, all fractures were tensile and there were no shear fractures. Vertical fractures were always oriented in a direction perpendicular to the smaller horizontal compressive load. Fractures always originated at the borehole boundary in the pressurized zone and propagated outward. "Horizontal" fractures, perpendicular to the borehole, usually occurred near the bottom end of the pressurized hole.

In a series of tests performed at constant pressurizing rate, the critical breakdown pressures ranged between theoretical breakdown pressures for impermeable and permeable rock. This was explained by the formation of a plastic region near the borehole. Larger boreholes required lower breakdown pressures, and lower pressurization rates required lower breakdown pressures.

15.2.4 Homogeneous Flawed Medium: Joint Effects

Daneshy (1974) studied the effect of the size of open and filled material flaws on hydraulic fracturing. Granite blocks $6 \times 6 \times 10$ in. were used. The blocks contained natural fractures having remaining tensile and shear strengths and the ability to flow water. Small material flaws (compared with the hydraulic fracture size) do not change the overall orientation of the hydraulic fracture. The hydraulic fracture can encircle such small defects, or if not, the influence of these flaws is local. Large material flaws, however, were observed to drastically change fracture orientation.

15.2.5 Homogeneous and Flawed Media

Zoback et al. (1977) performed tests on three types of rocks to evaluate the effect of fluid penetration into the rock prior to fracturing and the influence of preexisting cracks on hydraulic fracturing operations. The rock types included Ruhr sandstone (a fine-grained, massive, weakly bedded carboniferous sandstone from the Ruhr area of Germany), Weber sandstone (a very well-indurated Permian sandstone) used in triaxial tests, and a low-porosity South African gabbro used in tests with no external load.

Three types of tests were performed. Tests were performed on 6-cm long, 3-cm diameter, triaxially loaded specimens pre-loaded by a constant axial stress of about 40 MPa, by pressurizing a 2 to 3-mm diameter axial borehole. Larger-scale tests were performed on 12 cm cubical samples having a 1.05 cm diameter borehole through the center of the specimen perpendicular to the loading axis. These 2.5 MPa uniaxially loaded blocks were pressurized over 6.5 cm length of the borehole. This setup was used for prefractured samples as well.

The rate of borehole pressurization strongly influenced breakdown pressures, with the breakdown pressure increasing with increasing pressurization rate, as also seen by Haimson and Fairhurst (1969). When the effect of fluid penetration is negligible, the pressure at which hydraulic fractures initiate (and thus tensile strength) is independent of the rate of borehole pressurization. In tests performed on prefractured samples where the fracture was oriented such that the applied uniaxial stress would close the fracture, fractures could be formed and propagated perpendicular to the prefracture if a viscous fracturing fluid was used.

15.2.6 Homogeneous Medium: Varying Stresses

Lockner and Byerlee (1977) performed hydraulic fracturing experiments on cylindrical 3-inch diameter Weber sandstone samples at very high stress (4 kbar axial, 1 kbar radial) and showed that the resulting fracture could be followed using acoustic emissions. A further series of tests was performed using 1-inch diameter cylindrical samples at various differential stresses and injection rates. The results of these tests led to the conclusion that either shear or tensile failure could be achieved under the proper combination of injection rate and differential stress.

15.2.7 Homogeneous and Heterogeneous Media

Blanton (1982) performed hydraulic fracturing experiments on naturally fractured blocks of Devonian shale. Additionally, fracturing tests were performed on blocks of hydrostone, which could be tested in a more uniform manner. In these tests, the angle of approach of the hydraulic fracture to an existing fracture was varied systematically. Experiments in both the Devonian shale and hydrostone indicate that the hydraulic fracture morphology is strongly affected by the natural fractures. The hydraulic fractures tended to cross preexisting fractures only under high differential stresses between horizontal stress components and high angles of approach. At intermediate values of either of these, natural fractures tended to open or divert fracturing fluid or arrest hydraulic fracture propagation.

15.2.8 Anisotropic Medium: Joint Effects

Teufel and Clark (1984) performed numerous hydraulic fracturing laboratory experiments under uniaxial stress on monolithologic and dilithologic sandstone assemblies. The assemblies were composed of three layers of $20 \times 20 \times 8$ cm blocks of sandstones having the same (monolithologic) or different properties (dilithologic). Different polishing steps were taken to evaluate the effect of friction between layers on arresting vertical-traversing fractures. Weak interfacial shear strength between the layers (smooth

surfaces) required an increase in the axial stress needed for the fracture to continue. The authors concluded that a weaker interfacial layer under greater horizontal stress than the fracturing layer will tend to arrest fracture growth.

15.2.9 Homogeneous Medium: Effect of Borehole Angle

El Rabaa (1989) present results from 22 fracturing tests in $6'' \times 12'' \times 18''$ hydrostone blocks. The tests were performed to evaluate the effect of the length of a spirally perforated or open borehole region relative to the diameter and the effect of borehole angular offset from $\sigma_{h\min}$. For long perforated or open regions (length $> 4\times$ borehole diameter) multiple fractures can be created, with one fracture eventually becoming predominant. For shorter regions, one fracture is likely to occur. Perforations more closely spaced than 1 borehole diameter are likely to result in a connected fracture. An "H-shape" fracture (Fig. 15.2) can occur in open holes having a length exceeding four times the diameter oriented parallel to the minimum principal stress.

The authors presented their results schematically as shown in Figs. 15.2 and 15.3. In Fig. 15.2, for a horizontal hole drilled in the minimum principal stress direction the effect of perforated or open borehole length is shown on the horizontal axis. Short perforated lengths result in single fractures, whereas long perforated lengths result in a number of fractures, with one becoming

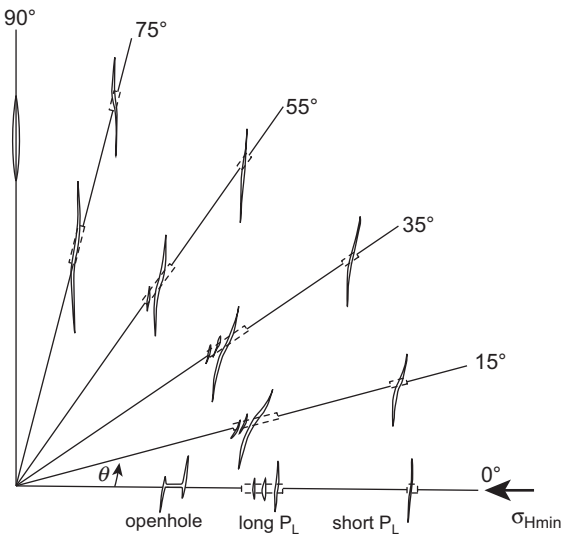

FIGURE 15.2 Top view of fractures induced at various wellbore deviation angles. P_L is the length of perforation. *From El Rabaa, W., 1989. Experimental study of hydraulic fracture geometry initiated from horizontal wells. In: 64th Annual Technical Conference and Exhibition of the Society of Petroleum Engineers. Society of Petroleum Engineers, San Antonio, TX.*

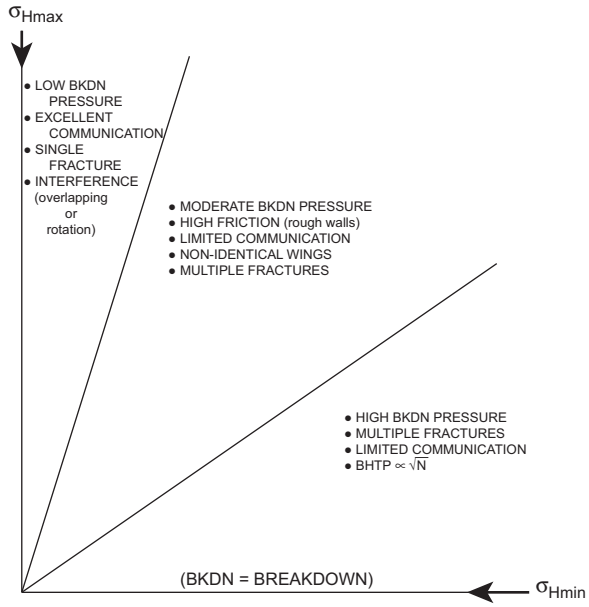

FIGURE 15.3 Principal findings of horizontal well fracturing. *From El Rabaa, W., 1989. Experimental study of hydraulic fracture geometry initiated from horizontal wells. In: 64th Annual Technical Conference and Exhibition of the Society of Petroleum Engineers. Society of Petroleum Engineers, San Antonio, TX.*

dominant. The open hole allowed a fracture that paralleled the borehole, which connected two perpendicular fractures that formed at the ends of the open hole. As the deviation angle increases, induced fractures tend to follow the borehole in the near-borehole region, and then transition to fractures propagating in the maximum horizontal stress direction. The rock in the transition zone tends to have significant roughness, which has implications for shear-slip propping. Fractures in boreholes drilled in the direction of the maximum principal stress tend to parallel the borehole as in vertical well fracturing.

15.2.10 Homogeneous Isotropic Medium

de Pater et al. (1994) derived a set of five dimensionless groups to scale planar fracture propagation ("universal scaling laws") and provided an analysis of numerous reported laboratory tests on hydraulic fracturing. Based on these scaling laws, the authors concluded that for laboratory tests at in situ stress, low fracture toughness and low permeability media should be used, with very high fracturing fluid viscosity to reduce the influence of toughness and to compensate for the low injection rate in laboratory models. Based on their evaluation of the numerous laboratory fracturing tests and based on their derivations, it was concluded that most tests neglected scaling and stability of

fracture propagation; thus the information gained from these tests is not likely to relate to hydraulic fracturing in the field. The authors point out that studying crack propagation in real rocks may be useful in terms of material science, but simplification is required to allow for repeatable measurements.

The authors performed tests in 10 cm transparent PMMA blocks and 30 cm biaxially and triaxially loaded cement blocks, and their results compare adequately to their scaling. In their tests pressure strokes were applied causing growth rings on the fracture surfaces, which allowed measurement of the radius of the fractures. Linear elastic material behavior was thought to adequately describe the fracture propagation in their tests.

15.2.11 Homogeneous Medium: Borehole Angle

Abass et al. (1996) performed hydraulic fracturing tests in $6 \times 6 \times 10$ in. hydrostone blocks with borehole angle ranging from parallel to the maximum principal strength (0 degree) to parallel to the minimum principal strength (90 degrees). Their results are similar to those of El Rabaa (1989); however, a few additional details are flushed out. For the case of the borehole perpendicular to the maximum principal stress direction, these authors also showed a "T-shaped" fracture (similar to the "H-shaped" fracture observed by El Rabaa (1989)), with an axis-parallel fracture extending about one wellbore diameter from the borehole, and a wellbore-perpendicular fracture consuming most of the energy and fracturing fluid. Fracture initiation pressure was also evaluated with respect to the borehole angle. Boreholes aligned with the maximum principal stress direction had the minimum fracture initiation pressure, with the pressure increasing as the borehole deviated from that orientation. In their measurements, there is almost a factor of 2 in the fracture initiation pressure between the borehole parallel to $\sigma_{h\max}$ and that parallel to $\sigma_{h\min}$. The authors also noted that the pressure signal during the relief in pressure events can be used to estimate the fracture angle with respect to the borehole.

15.2.12 Uniform Medium With Discontinuities

Beugelsdijk et al. (2000) examined the effect of discontinuities in rock by forming 30-cm cement cubes that were then dehydrated to form dehydration cracks. The blocks were subjected to triaxial stress of 8, 10, and 20 MPa, and a viscous fracturing fluid (100 Pa·s) was used. At low flow rates, fluid leaked off into discontinuities, hindering fracturing and lowering shear strength in the discontinuities. The authors concluded that initiating hydraulic fractures by increasing the flow rate in steps, a so-called step-rate procedure, will hamper hydraulic fracture initiation and result in unfavorable conditions or complete leak-off. At high flow rate fracturing, the fracture propagated largely as expected; thus high flow rates tend to minimize the effect of discontinuities. Discontinuities can affect fractures anywhere along the flow path; ultimately, this may affect proppant transport as well.

15.2.13 Large Discontinuous Homogeneous Block: Effect of Joint Properties

Casas et al. (2005, 2006) performed a pair of laboratory hydraulic fracturing tests on a 0.76 × 0.76 × 0.91 m (high) block of Colton Sandstone having a permeability of about 0.19 mD. In spite of the sample size, the stresses were set to realistic stresses – $\sigma_v = 35.9$ MPa, $\sigma_{h\max} = 29.0$ MPa, and $\sigma_{h\min} = 16.5$ MPa. Two large discontinuities (slots) were cut into the rock across the top and partially through the block. These were parallel to each other and at an angular offset from the principal stresses. One was filled with a stiff grout having rocklike properties, and the other was filled with low-modulus epoxy. Tubes attached to pressure transducers were sealed in at a number of locations where the fracture was anticipated to pass to attempt to identify the time the fracture passed the location. At different times, fracturing was performed in two perpendicular directions: first by setting the stresses as stated, and then by reversing the horizontal stresses without releasing the vertical stress. A high-viscosity silicone fluid (586 Pa·s, akin to peanut butter) was used for fracturing.

Fracturing results were compared with scaling analysis given by de Pater et al. (1994). Higher pressures than predicted were required to fracture the sandstone in both tests. Of particular interest is that one of these experiments provided data that may validate the concept of a rarified region at the fracture tip of a moving fracture. For the pressure transducers that intersected the fracture, pressure decreases were observed that preceded the expected pressure increases when the fracturing fluid passed the monitored location. Both tests produced planar fractures that propagated in the directions of the larger two principal stresses. The fracture crossed the stiff rocklike grout discontinuity, which had a higher modulus than the sandstone. The hydraulic fracture was arrested, however, at the epoxy discontinuity (low-modulus) inclusion. The authors note that clays and some sandstones may behave similarly to the epoxy in arresting a fracture. The fracture tip propagation velocity was on the order of those expected in the field.

15.2.14 Large Block Homogeneous and Anisotropic Media

Athavale and Miskimins (2008) fractured one cement block and a layered sandstone/cement(s)/epoxy/polyurethane block, both having dimensions of 11″ × 11″ × 15″. Applied stresses were 1500, 2500, and 3500 psi. Two vertical fracturing experiments were performed in each block, controlled by changing the direction of $\sigma_{h\max}$ as was done by Casas et al. (2006). Scaling relationships by de Pater et al. (1994) and (Bunger et al., 2005) were considered in the experiment design, and the fracturing time (∼5–8 min) and fracturing fluid viscosity (100,000 cP ∼ somewhere between ketchup and lard) were specified from these analyses. In fracturing one direction of the

cement block, a penny-shaped bi-wing fracture was created. However, in the second fracturing test in the orthogonal direction, a single wing fracture was generated. It was noted that the borehole was not notched, and that notching the borehole may have produced a bi-wing fracture.

The results of fracturing in the layered block are as complex as the block itself. From top to bottom, the block composition includes layers of varying thicknesses of Lyons sandstone, polyurethane adhesive, 15.8 pounds per gallon (ppg) cement, Lyons sandstone, an unbonded surface, 16.2 ppg cement, Lyon sandstone, epoxy, and 15.8 ppg cement. In one test a fracture formed in the expected direction above the unbonded interface between sandstone and cement. The fracturing fluid spread in this unbonded layer, and two fractures formed beneath this layer. One of these fractures continued until it met with the low-modulus epoxy layer where it was arrested. In the perpendicular fracturing test, a small single-winged fracture formed in one direction. Interestingly, the fracturing fluid wandered in the unbonded plane during both fracture tests; however, it did not leak out on the sides that experienced limited fracturing. Stresses on this block were 1700, 2700, and 4200 psi.

15.2.15 Heterogeneous Flawed Media (Desiccated Cement)

Zhou et al. (2010) investigated the effect of natural flaws in the rock on hydraulic fractures using dessication fractures. The desiccation fractures were created by placing 30 cm cubic cement blocks in an oven at 400°C for 3 h to cause dehydration, followed by air-cooling. Consistent with Blanton (1982), the authors concluded that at intermediate and low differences between the principal horizontal stresses, and at low angles of approach, preexisting fractures tend either to open and divert fracturing fluid or arrest propagation of the hydraulic fracture.

Zhou et al. (2010) also described fracture morphology for varying stress differentials. Experiments were performed using the cement blocks over a range of K_h values from 1 to 10, where $K_h = \frac{\sigma_{h\max} - \sigma_{h\min}}{\sigma_{h\min}}$. For K_h values greater than 2.5, a vertical main fracture formed with multiple subfractures. For K_h values between 1.5 and 2.5, the hydraulic fracture tends to be a partly vertical dominating fracture (one wing) with random branches. When K_h is below 1.5, the fracture geometry is radial random fractures.

15.2.16 Heterogeneous Flawed Media: Natural Fort Hays Limestone

Frash et al. (2015) performed a hydraulic fracturing experiment on a block of Fort Hays Limestone, part of the Niobrara Shale Formation. The 30 cm cubic sample contained natural bedding planes—one of which was poorly cemented—and the borehole was oriented perpendicular to these features. The

sample was placed under triaxial stress and the fracturing was monitored with pressure and volume measurements in addition to acoustic emissions. The horizontal stresses applied were 5 and 10 MPa and the vertical stress was 13 MPa. The fracturing fluid was a black epoxy having a 90-min working time. After the test, the block was sectioned and the location and characteristics of the fractures were identified by the presence of the black epoxy. The test resulted in a complex fracture network composed of a vertical tensile penny-shaped fracture, a shear activation along a preexisting discontinuity, and dilation of two bedding plane fractures. Fracture stranding and complex fracturing zones were observed in the experiment suggesting an increased volume of stimulated rock as compared to simple singular fractures. The authors suggest that a three-dimensional fracture propagation criterion may be necessary to model multiple fracture interaction and preexisting discontinuity activation.

15.2.17 Homogeneous Media: Water Blasting

Huang et al. (2014) investigated "water blasting" and hydraulic fracturing following water blasting. Water blasting consists of setting off a small explosion in a water-saturated well. The effect of the explosion is to cause numerous microfractures and small fractures to form around the borehole. Experiments were performed in 30 cm cubic concrete specimen, with $\sigma_v = 12.31$ MPa, $\sigma_{h\min} = 3.08$ MPa, and $\sigma_{h\max} = 7.69$ MPa. Acoustic emissions were used to monitor the tests in addition to pressure monitoring. Acoustic emissions were frequent and of medium intensity when loading the block, very strong on the water blasting event, and weaker following that. With hydraulic fracturing following the water blasting, the acoustic emissions were frequent and of medium intensity, and during unloading, acoustic emissions were frequent and of low intensity. Water blasting induced small fractures and microfractures in a bulb shape around the borehole. Subsequent hydraulic fracturing occurred along several planes and followed several initial smaller fractures, resulting in a complex fracture pattern. However, it is not clear how such a pattern would scale to the field. For comparison, hydraulic fracturing without water blasting occurred as expected, with planar fractures propagating in the direction of the maximum principal stress; however, radial fractures occurred at the toe of the borehole, "blowing off" the bottom of the borehole. Hydraulic fracturing pressure and subsequent peak injection pressure for the water-blasted samples greatly exceeded those values for the hydraulic fractured cases. The increase in these values was attributed to water leak-off and loss. The water-blasted hydraulic fractured samples had numerous fractures and low integrity at the end of the tests. The hydraulic fractured blocks, on the other hand had few fractures and good integrity at the end of the tests.

15.2.18 Uniform Media: Cryogenic Fracturing

Cha et al. (2014) and Alqatahni et al. (2016) investigated cryogenic fracturing in 8-inch cement cubes. In their initial evaluation, room temperature blocks were semisubmerged in liquid nitrogen (temperature = −196°C) to induce a sharp thermal gradient, thus a sharp stress gradient. Fractures were observed at the point of submersion, and X-ray CT scanning showed that the fractures extended substantially into the block. Because of the direction of the stress gradient, some shear likely occurred. Experimental setups and procedures were developed to conduct cryogenic fracturing tests from boreholes in 20 cm cubical samples with and without confining stress, including cryogen transport, measurements, and fracture characterization. Active acoustic signals and pressure decay were used to characterize the flow properties of natural and induced fractures before and after the experiments. When cryogenic tests were performed without confining stress, cracks formed in the experimental blocks and altered the rock properties. Repeated stimulation resulted in enhanced fracturing by both creating new cracks and widening the existing cracks. Cryogenic fracturing test results from unstressed weak concrete and sandstone showed that fracture generation depends on material properties. Water in the formation may play a role because it initially expands as it freezes competing with contraction from cryogenic cooling. For cryogenic stimulation, rapid cooling is desired to achieve high thermal gradient.

Alqatahni et al. (2016) extended the work by Cha et al. (2014) and showed that in samples under triaxial stress permeability increases with liquid nitrogen treatments, in addition to lowering breakdown pressure following treatment with liquid nitrogen.

15.2.19 Homogeneous Medium: Different Fracturing Fluid Viscosities

Using 170-mm anisotropic cubes all cut similarly, Chen et al. (2015) investigated hydraulic fracturing in Kurokami-jima granite, a coarse-grained biotite granite from Yamaguchi Prefecture, Japan, using $scCO_2$, water, and hydraulic oil at 10 mL/min. The tests were performed under 3, 6, and 4 MPa triaxial stress. The fractures were filled with fluorescent epoxy, and thin sections were cut from the blocks. Microscopy was used to examine the fractures. The lowest viscosity $scCO_2$ created the most tortuous fracture paths at the scale examined, in addition to the most branching pathways. The low-viscosity $scCO_2$ was able to move around grains, whereas the water and oil tended to fracture through grains. The authors point out that the lack of a planar surface in any fracture means that there will be some shear on some scale in a tensile fracture.

15.2.20 Heterogeneous Large Block Samples: Effect of Slickwater and Gel

Wang et al. (2015) discuss the results of six large-scale (762 mm × 762 mm × 914 mm [height]) laboratory fracturing tests on two types of shale and mention the results of three large-scale laboratory fracturing tests on a tight sandstone, a fractured sandstone, and a coal sample. In the shales, two fracturing fluids were tested: slickwater (viscosity = 5 mPa·s) and a cross-linked gel (viscosity = 150 mPa·s). Two different stress regimes (13, 13, 10 MPa and 24, 24, 10 MPa), and three flow rates were used. Under low horizontal plane stress difference (3 MPa), the natural fracture system was opened by slickwater more easily and no main fracture formed. With cross-linked gel under the same conditions, a simple fracture formed and opened part of the natural fractures at the same time. Slickwater at higher horizontal stress difference (14 MPa) formed a new fracture perpendicular to the minimum horizontal stress direction. Slickwater fluid leak-off into an open discontinuity hampered the extension of the hydraulic fracture. Under the same stress regime, cross-link gel formed only a single main hydraulic fracture without any discontinuity connections. Fig. 15.4 shows a matrix of observations. Low-viscosity fracturing fluid (left side of Fig. 15.4) tends to activate

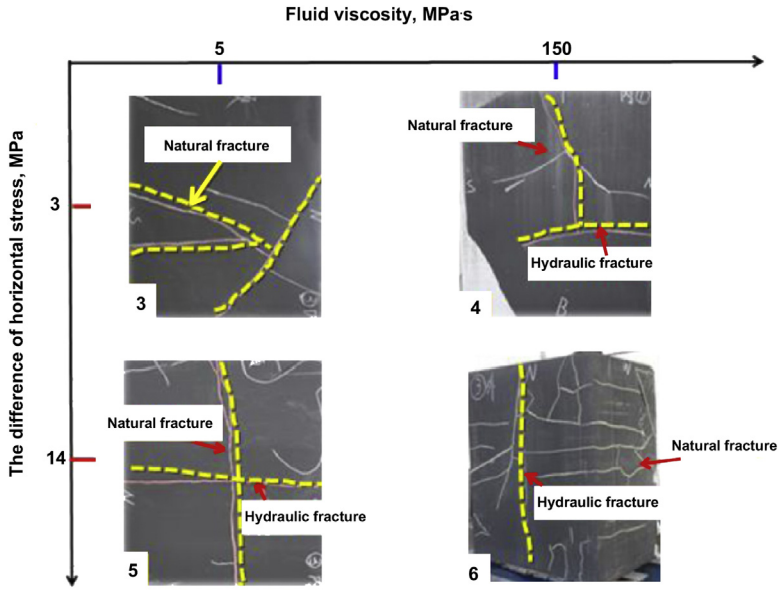

FIGURE 15.4 Matrix of results of fracturing large laboratory shale blocks. Effects of viscosity and differential horizontal stress. Low-viscosity fracturing fluid (left) tends to activate natural fractures, and under high differential stress to form hydraulic fractures. Higher-viscosity cross-linked gel (right) tended to generate hydraulic fractures (Wang et al., 2015).

natural fractures, and under high differential stress tends to form hydraulic fractures. Higher-viscosity cross-linked gel (right side of Fig. 15.4) tended to generate hydraulic fractures.

15.2.21 Direct Observation of Fracturing in Small Samples

Hyman et al. (2016) used X-ray videography to observe hydraulic fracturing in 2.5-cm-diameter samples under constant radial confining pressure and axial stress. Five samples including three acrylic samples, one shale, and one cement were fractured by applying fluid pressure to a circular notch in the sample top. A gasket was used to localize the flow. The method allows for injection of proppant; however, in the demonstration test, no proppant was taken into the fracture. This method has applicability for the study of proppant transport, hydraulic fracture toughness, and hydraulic fracture permeability as a function of confining stresses.

15.2.22 Heterogeneous Media (Shale and Sandstone): Water, Liquid CO_2, and Supercritical CO_2

Zhang et al. (2017) compared hydraulic fracturing using water, liquid CO_2 (lCO_2), and supercritical CO_2. In each test, 3×20 cm cubical shale samples were fractured. One sandstone cube was fractured with water and another with $scCO_2$. In addition, four shale samples were fractured using $scCO_2$ while varying horizontal stress ratios. The brittle shale cubes were from an outcrop of the Lower Silurian Longmaxi Formation in the Sichuan basin, China, having about 3.8% plagioclase, 11.7% calcite, 40.2% quartz, and 15.1% clay minerals. Hydraulic fracturing was accomplished through a 15-mm-diameter hole perpendicular to bedding planes drilled 110 mm in length into the center of each cube. The injection rate of all the fluids was the same (30 mL/min). Along with pressure and acoustic emissions, X-ray CT and digital radiography were used to monitor the fracturing or examine the resulting fractured system. Because of the variability of the shale, tests were repeated three times to compare the breakdown pressure for water, lCO_2, and $scCO_2$ fracturing. Interestingly, the breakdown pressure decreased significantly as the viscosity of the fracturing fluid decreased. The breakdown pressure decreased by a factor of 2 from water to lCO_2 and was reduced an additional 15% on the use of $scCO_2$. Acoustic emission monitoring showed many more events for the $scCO_2$ fracturing than the water fracturing prior to the major fracturing event, indicating the formation of a large number of smaller fractures with the less viscous $scCO_2$.

The fracture patterns from each of the fracturing liquids were different as well. With water (hydraulic fracturing), a planar fracture was formed. With lCO_2, a more complex fracturing pattern was formed. The complexity of the fracturing pattern increased even more for the $scCO_2$ with irregular and

multiple cracks that tended to connect with the natural bedding. $scCO_2$-induced fractures have larger widths and more crack volume than the hydraulic fractures. With $scCO_2$ fracturing, the acoustic emission energy ratio data showed sharp peaks in the data several times before the specimen ruptured. With respect to the ratio in horizontal stresses with a low differential stress, fractures initiated in weak locations near the borehole and propagated along paths of weakness. As the stress difference increases, the orientation of the fractures trends toward propagation in the maximum principal stress direction; however, the fracture network remains complex and includes bedding planes. This is consistent with Zhou et al. (2010) and shows some of the complexity observed by Athavale and Miskimins (2008).

15.3 DISCUSSION

Over the last six decades, many laboratory studies related to subsurface fracturing have been performed. Because the experimental matrix needed to cover all the expected conditions that could be encountered in subsurface fracturing is so large, the experiments covering that matrix are sparsely distributed. In spite of that, the tests that have been performed have yielded valuable information. One clear observation of laboratory studies is that they have evolved over the years, and the topics of study and tests have increased in complexity. Tests have evolved from the small samples from which much has been learned, to the desire for larger-scale tests (Haimson, 1981), to the realization of meter-scale tests (Wang et al., 2015). Media as simple as gelatin and hydrostone and as complex as natural shale or anisotropic assemblies of rock have been examined. Fracturing fluids and methods have evolved along with the laboratory tests. In spite of the sparsity in coverage of the experimental matrix, some take-home messages are apparent and discussed below along with references illustrating the message.

15.3.1 Stress

The directions and relative magnitudes of stress exert the strongest control on the direction and morphology of induced fractures in geologic media. Fractures will tend to open in the direction of least resistance (minimum principal stress) and propagate perpendicular to that direction (e.g., Hubbert and Willis, 1957; Haimson and Fairhurst, 1967; Zoback et al., 1977 and others). The effects of the relative magnitude of stresses has also been investigated, showing the possibility of shear or tensile fractures depending on the relative difference between stresses (Lockner and Byerlee, 1977), and the relative difference between stresses may also induce different fracture patterns (Zhou et al., 2010; Zhang et al., 2017). High stress differentials tend to result in a main fracture formed with multiple subfractures. Medium differentials tend to result in the hydraulic fracture tending to be a partly vertical dominating

fracture (one wing) with random branches, and low differentials resulted in radial random net-fractures. Larger borehole diameters result in lower critical breakdown pressures (Haimson and Fairhurst, 1969). de Pater et al. (1994) concluded that linear elastic material behavior was adequate to describe fracturing in their tests.

In large-scale tests considering the scaling laws described by de Pater et al. (1994), Athavale and Miskimins (2008) fractured a large laboratory cement block in two perpendicular directions. One test generated a penny-shaped bi-wing fracture; however, in the test in the perpendicular direction a single wing fracture was formed. This showed that even under fairly ideal conditions, the expected case is not always generated. Hyman et al. (2016) attempted to observe fracture formation directly using X-ray radiography. In their apparatus, the fracture is formed from a notch carved into the top of the sample providing a stress concentration location.

15.3.2 Anisotropy

Anisotropy has been investigated by many researchers (e.g., Teufel and Clark, 1984; Athavale and Miskimins, 2008; Hubbert and Willis, 1957). The additional complexity of varying properties was shown in very visual tests (Hubbert and Willis, 1957) using a very simple setup and a layered gelatin medium. Fig. 15.1 shows some of these complexities from this very simple system including fracturing fluid penetrating the interfaces between layers and bi-wing fractures in some layers and single wing in others. Fracturing layers of sandstone blocks with different moduli under uniaxial stress showed that frictional force between layers is important as to whether a fracture will continue between the layers (Teufel and Clark, 1984). Below a limiting combination of low normal stress and low frictional characteristics fracture arrest at the boundary between layers occurred. In the very complex system investigated by Athavale and Miskimins (2008), a number of behaviors were observed. Fracturing fluid flowed in a "wandering" pattern in the unbonded interface between sandstone and cement, resulting in a very different distribution of fracturing fluid than expected, and more fractures in the block and at different locations than from a simple pressurized borehole. Fractures perpendicular to this layer formed from various locations in the unbonded joint (more in Section 15.3.4).

15.3.3 Borehole Angle

Two studies investigating the angle between the borehole and the orientation of the principal horizontal stresses were considered (El Rabaa, 1989; Abass et al., 1996). This is very important, as it is often difficult to know the directions of the principal stresses with certainty. Boreholes that are parallel to the maximum horizontal stress direction give fractures parallel to the borehole and fracture at the lowest breakdown pressures. As the angle of the borehole

increases with respect to the maximum principal stress, fractures tend to start parallel to the borehole and turn toward the direction of the maximum principal stress. A number of fractures may initiate, with one eventually taking the majority of the fluid. In the case of the borehole being perpendicular to the maximum principal stress, a short open or perforated region will provide a fracture perpendicular to the borehole at a significantly higher pressure than for the parallel case. A longer perforated or open hole may result in a short-extent borehole-parallel fracture that will intersect borehole-perpendicular fractures. Away from the near-wellbore region, a borehole-perpendicular fracture will form and take the fracturing fluid.

15.3.4 Discontinuities

Many researchers have addressed discontinuities, as these are ubiquitous in the subsurface. In fractured sandstone with the fracture parallel to the minimum principal stress, Zoback et al. (1977) showed that fractures could be formed in the direction perpendicular to the initial fracture if the fracturing fluid were viscous enough. Daneshy (1974) showed that small discontinuities relative to the induced fracture do not significantly affect the direction of the fracture.

Blanton (1982) systematically investigated the angle of approach of a hydraulic fracture to an existing fracture. Experiments performed in both the Devonian shale and hydrostone indicate that the hydraulic fracture morphology is strongly affected by the natural fractures. The hydraulic fractures tended to cross preexisting fractures only under high differential between horizontal stress components and high angles of approach. At intermediate values of either of these, natural fractures tended to open or divert fracturing fluid or arrest hydraulic fracture propagation. Zhou et al. (2010) performed similar tests and their conclusions are in line with Blanton's (1982).

Lamont and Jessen (1963) showed that under many conditions, fractures will cross discontinuities, and they typically adjust to cross them perpendicular to the direction of the discontinuity. Teufel and Clark (1984) showed that adequate frictional forces are required to allow the fracture to cross the discontinuity. Casas et al. (2006) showed that fractures would continue through a grouted high modulus discontinuity, whereas they would be arrested at a low modulus epoxy discontinuity. The authors pointed to conditions in sandstone and clays where the clay might arrest a fracture. Athavale and Miskimins (2008) showed the impact of an unbonded interface taking up the fracturing fluid and resulting in fractures in unexpected locations in the direction of the maximum principal stresses.

Beugelsdijk et al. (2000) concluded that approaching discontinuities with an increasing step-rate procedure could enhance the impact of the discontinuity, and that high flow rate fracturing resulted in fractures in the expected directions. They expressed the concern that proppant transport will be affected by discontinuities as well.

15.3.5 Permeability and Fracturing Fluid Viscosity

The uptake of fracturing fluid by the medium is impacted by the medium permeability, injection pressure, and the fracturing fluid viscosity. The invasion of fracturing fluid into the medium reduces the breakdown pressure (Hubbert and Willis, 1957). Both Zoback et al. (1977) and Haimson and Fairhurst (1969) show data to support this from experiments performed using different viscosity fluids and different pressurization rates. Zhang et al. (2017) investigated the use of water, liquid CO_2, and $scCO_2$ as fracturing fluids, fracturing multiple cubes of brittle shale. The breakdown pressure decreased by a factor of 2 from water to liquid CO_2 and by another 15% for $scCO_2$—in order of their declining viscosities. Fracture morphology became more complex as the viscosity of the fracturing fluid decreased. Comparing fractures generated using hydraulic oil, water, and $scCO_2$ in granite at the microscale, Chen et al. (2015) found that fractures formed using hydraulic oil and water tended to go through grains, whereas fractures formed using the less viscous $scCO_2$ tended to go around grains. The fractures induced by the $scCO_2$ were the most tortuous and branched (on the microscale). At the large laboratory scale, Wang et al. (2015) compared fracturing using slickwater and gel in shale samples under a variety of conditions. The two fracturing fluids resulted in different fracturing behaviors. Slickwater under low differential horizontal stress opened the natural fracture system and did not form a main fracture. With the cross-linked gel, however, a simple fracture was formed in addition to some opening of the natural fracture system. This is conceptually in agreement with Zoback et al. (1977). Higher horizontal stress differential resulted in a simple fracture with slickwater. Slickwater fractures were more easily hampered by discontinuities.

15.3.6 Different Technologies

Although not a comprehensive study of fracturing techniques that are not purely hydraulic, two other stimulation methods were mentioned here: water blasting and cryofracturing. Both of these concepts can initiate fractures differently than hydraulic fracturing and the initial fracture location may be different as well. Because these studies were limited in extent, many questions remain, including scaling to the field.

In water blasting a small explosion is carried out in the wellbore to initiate fractures prior to hydraulic fracturing. Contrary to intuition, in the experiments by Huang et al. (2014) the subsequent hydraulic fracturing required much higher breakdown pressure and peak injection pressure than the nonwater-blasted samples. This increase in pressure was attributed to enhanced leak-off.

The use of extreme thermal gradients by applying cryogenic fluids was investigated by Cha et al. (2014). In this method, liquid nitrogen was injected into samples causing the near-wellbore rock to contract. Results indicate that

the permeability of the samples increased with the number of treatments, and that in some cases shear may occur.

15.3.7 Sample Size

Samples sizes in the tests described in this chapter range from centimeter scale to meter scale. All sample properties affect the measurements and data interpretation. Small preserved samples may represent the actual properties of the rock to be fractured well; however, they contain artifacts from unloading, machining, exposure, and reloading. Large samples are often manufactured in the laboratory or extracted from outcrops where the rock has weathered and are also unloaded and machined. From the upscaling perspective, large bock tests exhibit better similarity to field cases. Measurements on small preserved core samples while applying true triaxial stress and scaled test parameters, on the other hand, will be the most suitable to match the relevant physics realistically. Samples composed of artificial materials are useful to test models; however, the real rock formation behavior will deviate from these artificial materials behavior due to the differences in material properties. The sample material and size need to be selected to address the purpose of the data collection.

15.4 CONCLUSIONS

Laboratory studies into fracturing to support understanding of subsurface stimulation have provided important insights into the behavior of fluids and rocks during fracturing. The range of possible studies is extremely large, and the studies performed to date have covered many of the important questions.

- Stress is the overriding control of fracturing, and because it typically cannot be controlled, it must be understood and worked with. The relative differences in the principal stresses control the resulting fracture orientation and morphology. Low stress differentials result in fractures that may follow existing rock weaknesses, whereas high stress differentials may result in simple fractures opening against the minimum principal stress and propagating perpendicular to that.
- The borehole angle with respect to the stresses strongly affects the behavior of fracturing with boreholes parallel to the maximum principal stress, providing fractures parallel to that borehole and at low breakdown pressures, and boreholes perpendicular to the maximum principal stress provide very complex near-borehole fracturing at high breakdown pressure. Ultimately, these situations result in fractures perpendicular to the wellbore at a short distance away from the wellbore.
- High-viscosity fracturing fluids are less influenced by discontinuities than low-viscosity fluids, and low-viscosity fluids may provide more fracturing pathways with more fracture tortuosity.

- Discontinuities affect fracturing with less viscous fluids, more than viscous fluids. They also will affect proppant transport.
- Anisotropy can significantly alter fracturing, particularly if a layer is very weak, arresting the propagation of the fracture.
- Nontraditional methods are being investigated to improve fracturing technology. These can be more simply investigated in the laboratory than the field; however, simulation is required to help understand behavior scaled to the field.

REFERENCES

Abass, H.H., Hedayati, S., Meadows, D.L., August 1996. Nonplanar fracture propagation from a horizontal wellbore: experimental study. SPE Production and Facilities 133–137.

Alqatahni, N.B., Cha, M., Yao, B., Yin, X., Kneafsey, T.J., Wang, L., Wu, Y.-S., Miskimins, J.L., 2016. Experimental investigation of cryogenic fracturing of rock specimens under true triaxial confining stresses. In: SPE Europec Featured at 78th EAGE Conference and Exhibition. Society of Petroleum Engineers, Vienna, Austria.

Athavale, A.S., Miskimins, J.L., 2008. Laboratory hydraulic fracturing tests on small homogeneous and laminated blocks. In: 42nd US Rock Mechanics Symposium and 2nd U.S.-Canada Rock Mechanics Symposium. American Rock Mechanics Association, San Francisco.

Beugelsdijk, L.J.L., De Pater, C.J., Sato, K., 2000. Experimental hydraulic fracture propagation in a multi-fractured medium. In: 2000 SPE Asia Pacific Conference on Integrated Modelling for Asset Management. Society of Petroleum Engineers, Yokohama, Japan.

Blanton, T.L., 1982. An experimental study of interaction between hydraulically induced and preexisting fractures. In: SPE/DOE Unconventional Gas Recovery Symposium of the Society of Petroleum Engineers. Society of Petroleum Engineers, Pittsburgh, PA.

Bunger, A.P., Jeffrey, R.G., Detournay, E., 2005. Application of scaling laws to laboratory-scale hydraulic fractures. In: Alaska Rocks 2005, the 40th U.S. Symposium on Rock Mechanics (USRMS): Rock Mechanics for Energy, Mineral and Infrastructure Development in the Northern Regions. American Rock Mechanics Association, Anchorage, Alaska.

Casas, L., Miskimins, J., Black, A., Green, S., 2005. Large scale hydraulic fracturing tests on rock with discontinuities. In: Golden Rocks 2006, the 41st U.S. Symposium on Rock Mechanics (USRMS): 50 Years of Rock Mechanics – Landmarks and Future Challenges. American Rock Mechanics Association, Golden, CO.

Casas, L.A., Miskimins, J.L., Black, A.D., Green, S.J., 2006. Laboratory hydraulic fracturing test on a rock with artificial discontinuities. In: 2006 SPE Annual Technical Conference and Exhibition. Society of Petroleum Engineers, San Antonio, Texas, USA.

Cha, M., Yin, X., Kneafsey, T., Johanson, B., Alqahtani, N., Miskimins, J., Patterson, T., Wu, Y.-S., 2014. Cryogenic fracturing for reservoir stimulation – laboratory studies. Journal of Petroleum Science and Engineering 124, 436–450.

Chen, Y., Nagaya, Y., Ishida, T., 2015. Observations of fractures induced by hydraulic fracturing in anisotropic granite. Rock Mechanics and Rock Engineering 48, 1455–1461.

Daneshy, A.A., 1974. Hydraulic fracture propagation in the presence of planes of weakness. In: SPE-European Spring Meeting 1974 of the Society of Petroleum Engineers of AIME. Society of Petroleum Engineers, Amsterdam, The Netherlands.

El Rabaa, W., 1989. Experimental study of hydraulic fracture geometry initiated from horizontal wells. In: 64th Annual Technical Conference and Exhibition of the Society of Petroleum Engineers. Society of Petroleum Engineers, San Antonio, TX.

Frash, L.P., Gutierrez, M., Tutuncu, A., Hood, J., Mokhtari, M., 2015. True-triaxial hydraulic fracturing of Niobrara carbonate rock as an analogue for complex oil and gas reservoir stimulation. In: 49th US Rock Mechanics/Geomechanics Symposium. American Rock Mechanics Association, San Francisco, CA, USA.

Haimson, B.C., 1981. Large scale laboratory testing of hydraulic fracturing. Geophysical Research Letters 8, 715–718.

Haimson, B., Fairhurst, C., 1967. Initiation and extension of hydraulic fractures in rocks. SPE Journal 310–318.

Haimson, B., Fairhurst, C., 1969. Hydraulic fracturing in porous-permeable materials. Journal of Petroleum Technology 811–817.

Huang, B., Li, P., Ma, J., Chen, S., 2014. Experimental investigation on the basic law of hydraulic fracturing after water pressure control blasting. Rock Mechanics and Rock Engineering 47, 1321–1334.

Hubbert, M.K., Willis, D.G., 1957. Mechanics of hydraulic fracturing. Petroleum Transactions, AIME 210, 16.

Hyman, J.D., Jiménez-Martínez, J., Viswanathan, H.S., Carey, J.W., Porter, M.L., Rougier, E., Karra, S., Kang, Q., Frash, L., Chen, L., Lei, Z., O'malley, D., Makedonska, N., October 2016. Understanding hydraulic fracturing: a multi-scale problem. Philosophical Transactions A 374 (13).

King, L., 2014. Interview with Norm Warpinski, Director of Technology for Pinnacle: On the Early Experiments that Catalyzed the Shale Revolution (Online). . Available. thebreakthrough.org. https://thebreakthrough.org/index.php/issues/innovation-policy/interview-with-norm-warpinski-director-of-technology-for-pinnacle.

Lamont, N., Jessen, F.W., 1963. The effects of existing fractures in rocks on the extension of hydraulic fractures. Journal of Petroleum Technology 203–209.

Lockner, D., Byerlee, J.D., 1977. Hydrofracture in Weber Sandstone at high confining pressure and differential stress. Journal of Geophysical Research 82, 2018–2026.

de Pater, C.J., Cleary, M.P., Quinn, T.S., Barr, D.T., Johnson, D.E., Weijers, L., 1994. Experimental verification of dimensional analysis for hydraulic fracturing. SPE Production & Facilities 230–238.

Teufel, L.W., Clark, J.A., 1984. Hydraulic fracture propagation in layered rock: experimental studies of fracture containment. SPE Journal 19–32.

Wang, Y., Fu, H., Liang, T., Wang, X., Liu, Y., Peng, Y., Yang, L., Tian, Z., 2015. Large-scale physical simulation experiment research for hydraulic fracturing in shale. In: SPE Middle East Oil & Gas Show and Conference. Society of Petroleum Engineers, Manama, Bahrain.

Zhang, X., Lu, Y., Tang, J., Zhou, Z., Liao, Y., 2017. Experimental study on fracture initiation and propagation in shale using supercritical carbon dioxide fracturing. Fuel 190, 370–378.

Zhou, J., Jin, Y., Chen, M., 2010. Experimental investigation of hydraulic fracturing in random naturally fractured blocks. International Journal of Rock Mechanics and Mining Sciences 47, 1193–1199.

Zoback, M.D., Rummel, F., Jung, R., Raleigh, C.B., 1977. Laboratory hydraulic fracturing experiments in intact and pre-fractured rock. International Journal of Rock Mechanics and Mining Sciences & Geomechanics Abstracts 14, 49–58.

Chapter 16

Fracture Conductivity Under Triaxial Stress Conditions

Jessica Iriarte, Dina Hegazy, Daisuke Katsuki, Azra N. Tutuncu
Colorado School of Mines, Golden, CO, United States

16.1 INTRODUCTION

Conductivity is the measurement of the fracture's flow capacity, and it is obtained by multiplying the fracture permeability by the fracture width ($k_f w_f$). Decreasing fracture effectiveness due to conductivity decay is a strong contributor to the steep production decline commonly observed in shale plays. Fracture conductivity degradation results from damage mechanisms and fluid interactions that occur during hydraulic fracture operations. The conductivity of a fracture is determined experimentally by measuring the pressure drop of a fluid through a uniformly distributed proppant bed in a core with fixed length and height. By measuring conductivity in the laboratory under similar stress state to field conditions, the impact of damage mechanisms and fluid interactions can be determined to customize the fluid and proppant selection process.

There are several damage mechanisms that can be closely observed creating a controlled stress state in the laboratory. These include proppant embedment, formation spalling, proppant resistance to cyclic stress changes, fines migration, and rock−proppant−fluid interactions. These can be closely observed by creating a controlled stress state in the laboratory. As shale strength is very sensitive to the fluid introduced to the formation, the selection of the fluid will also become a factor in the mentioned damage mechanisms, particularly the proppant embedment.

A few mechanisms contributing to fracture conductivity damage in the field, including non-Darcy flow, multiphase flow, multiphase non-Darcy flow, gravity and viscous segregation, and reservoir flow capacity, are hard to measure experimentally (Baree et al., 2003).

In this chapter, details of the experimental results for two of these damage mechanisms are discussed: proppant embedment and formation spalling. When proppants embed into the fracture wall, the effective width of the

Hydraulic Fracture Modeling. https://doi.org/10.1016/B978-0-12-812998-2.00016-3

proppant pack is reduced, causing a reduction in the conductivity of the fracture. Spalling, however, occurs as the formation grain extrudes into the proppant pack and is often a consequence of the proppant embedment. Proppant fines can also be generated as the fracture is subjected to closure stress at downhole temperature. Small particles of proppant break off the proppants grains, reducing the proppant pack permeability and porosity, and these fines can migrate toward the wellbore depositing near the wellbore causing further reduction in flow and correspondingly the fracture conductivity (Terracina et al., 2010).

Several techniques have been introduced since the early days of fracturing operations to test conductivity. American Petroleum Institute (API) issued the first industry standard to measure the proppant pack conductivity. Recommended Practices for Evaluating Short Term Conductivity (API RP61) is considered short term and later replaced with a longer-term conductivity measurement API RP19D that has been adopted by the oil and gas industry as a standard and is used as a basis to compare the performance of different types of proppants provided by the various suppliers in industry (API, 1989, 2008). Most of the published research studies include fracture conductivity measurements under uniaxial stress conditions as described in the testing procedures for API RP19D opening up for modifications in selected research studies to introduce nonstandard methodologies that will represent more realistic field conditions. This also allows further investigation potential on the role of the formation interaction with various fluids introduced during the fracturing operations in addition to the varying stress conditions. The rock–fluid interactions and their impact on the mechanical and acoustic properties of organic-rich and seal shales have been extensively studied at Unconventional Natural Gas and Oil Institute (UNGI) using intact and fractured core samples performing coupled measurements in the laboratory, including compressional and shear ultrasonic wave velocities, attenuation, low-frequency Young's moduli, permeability, geomechanical properties, complex resistivity, high-field NMR and failure measurements, and field data analysis and modeling.

The results presented in this chapter is a small window looking into the UNGI coupled experiments conducted using Vaca Muerta and Niobrara shale core samples and their stress-dependent, long-term fracture conductivity comparison under triaxial stress state. The results endorse the sharp decline taking place in the fracture conductivity at the early stages of the flow through the fracture experiments that is also typically observed in the form of sharp production decline at the early stages of the production. A comparison of the conductivity measurements for the samples from these two formations indicates that the effect of conductivity damage varies not only with the mineralogy of the formation being fractured and produced

from, but also with the distribution of the minerals in the rock matrix, where the natural and hydraulic fractures are located within the formation and the rock–fluid–proppant interactions that influence the fracturing fluid and proppant selection and the effectiveness of the hydraulic fracturing operations.

16.2 FORMATIONS OVERVIEW

The Vaca Muerta formation is located in the Neuquén Basin in central west Argentina. The basin consists of strata of Late Triassic to Early Cenozoic age that were deposited in a back-arc tectonic setting. Its stratigraphic column is of 7 km and consists of carbonates, evaporites, and marine siliciclastic rocks (Manceda and Figueroa, 1995). The organic-rich Vaca Muerta is one of the main source rocks for fields in the Neuquén Basin. A typical stratigraphic column from Neuquén Basin is shown in Fig. 16.1A.

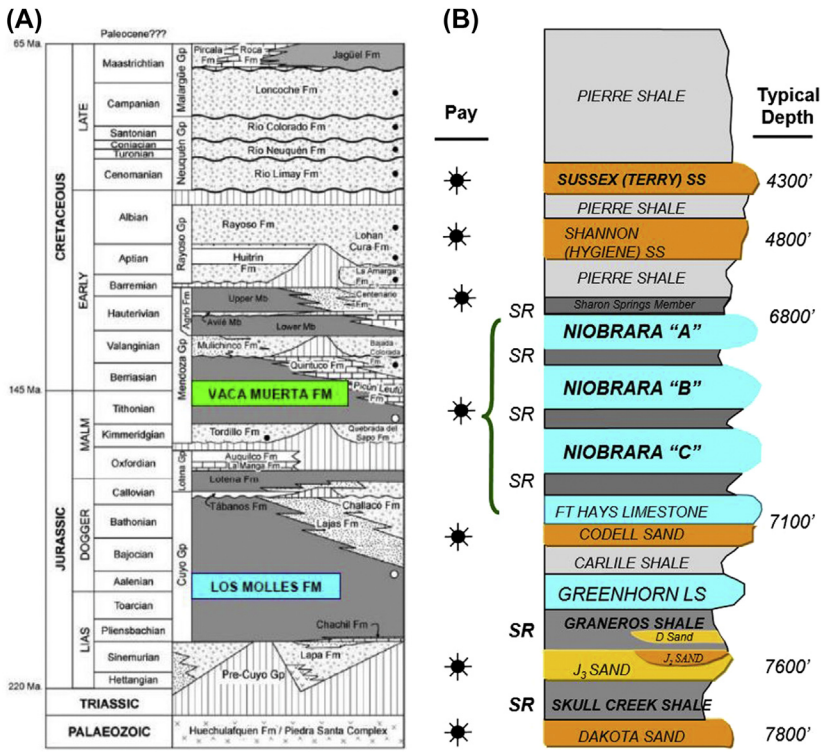

FIGURE 16.1 (A) Stratigraphic column of the Neuquén Basin, showing relative thickness of the Vaca Muerta and Los Molles formations (Howell et al., 2005) and (B) Niobrara shale, showing the combination of chalk and marl layers (Sonnenberg, 2012).

The Vaca Muerta shale is of Late Jurassic to Early Cretaceous age and could be characterized as a calcareous shale/marl with illite-type clay (Kugler, 1985; Wren, 2011). It was deposited as a propagating wedge, increasing in thickness from the south to the east toward the north and west. Looking at outcrop or core samples, it seems the shale is finely stratified, black, and dark gray and contains limestone lenses (Aguirre-Uretta et al., 2008). With permeability ranging between 50 and 200 nD, the Vaca Muerta shale can be considered an unconventional play.

The Niobrara shale is an organic-rich source rock in the Denver basin. It is an Upper Cretaceous formation in the Rockies region that consists of a combination of chalk and marl layers, as presented in Fig. 16.1B. The organic-rich marls within the Niobrara Formation act as source rocks, whereas the chalks and clay-rich limestones act as the reservoir formations (ElGhonimy, 2015; Finn and Johnson, 2005). This formation is mainly composed of calcium carbonate. Porosity in the chalks and clay-rich limestones is typically less than 10%, and permeability is typically around 0.0001−0.0007 mD, which classifies it as tight and unconventional. Because the Niobrara Formation was deposited, the ground has been uplifted, depressed, uplifted again, and tilted resulting in fractures, faults, and folding (Matthews, 2011).

Production in both basins is facilitated through the presence of abundant natural fractures that are mineralized and contain calcite. The samples used in this study are representative of the natural fracture system present in both formations. Based on the standard X-ray diffraction measurements shown in Table 16.1, the Niobrara core plug used is composed primarily of calcite and quartz, and the Vaca Muerta core plug mainly consists of quartz and mica/illite. The Vaca Muerta samples have higher clay content than the Niobrara samples. The amount of clay content strongly affects the conductivity results presented in this chapter.

16.3 SAMPLE PREPARATION FOR MEASUREMENTS

The core plugs were drilled parallel to bedding using dry air to prevent exposure to any fluid with a bit of 3.8 cm (1.5 in.) diameter. The samples were then cut using a diamond saw, ground, and polished to obtain a flat, smooth surface to achieve equal distribution of stresses throughout the core diameter during the experiment. Then, the original intact core samples were fractured using Brazilian tensile tests to obtain rough fracture faces representative of natural and hydraulic fractures in their native states in the formation, as shown in Fig. 16.2. Consequently, the fractures were filled with a proppant monolayer that was kept intact using heavy syrup, and the two halves of the core sample were brought together, as shown in Fig. 16.3. The proppant agent used in the tests is a ceramic proppant of a 20/40-mesh size. Finally, the Niobrara sample was saturated using deionized water, whereas the Vaca Muerta sample was saturated using 2% KCl water.

TABLE 16.1 Mineralogical Composition of the Niobrara and Vaca Muerta Core Sample Plugs Used in the Experiments in Weight Percentage (wt%)

Mineral Composition (wt%)									
Formation	Calcite	Dolomite	Quartz	Plagioclase Feldspar	K-Feldspar	Mica/Illite	Pyrite	Hematite	Unidentified
Niobrara	84	<3	9	0	0	<5	<1	0	<5
Vaca Muerta	20	0	33	8	<3	24	3	<3	<5

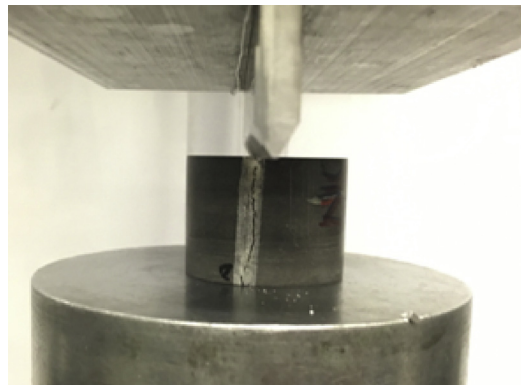

FIGURE 16.2 Brazilian tensile tests conducted to obtain naturally rough fracture surfaces or the triaxial stress state measurements (Iriarte, 2017).

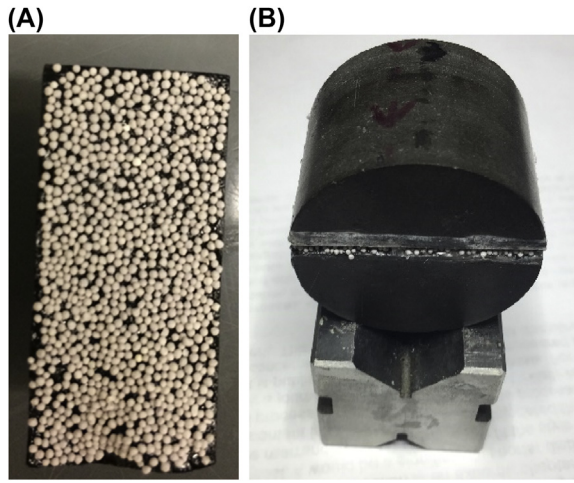

FIGURE 16.3 (A) Proppant monolayer in the fracture face of half of a core sample used (Hegazy, 2017) and (B) fracture core filled with a proppant monolayer and when wrapped with tape around the circumference (Iriarte, 2017).

16.4 TRIAXIAL TEST EXPERIMENTAL SETUP

A schematic of the coupled triaxial apparatus used in the experiments in the UNGI coupled geomechanics laboratory is shown in Fig. 16.4. The system consists of several components allowing coupled measurements to be carried out. These components include (1) a triaxial load cell, (2) a pore fluid injection system, (3) a back pressure system, (4) an axial and confining pressure system, (5) a vacuum system, and (6) a temperature control system. The triaxial cell is

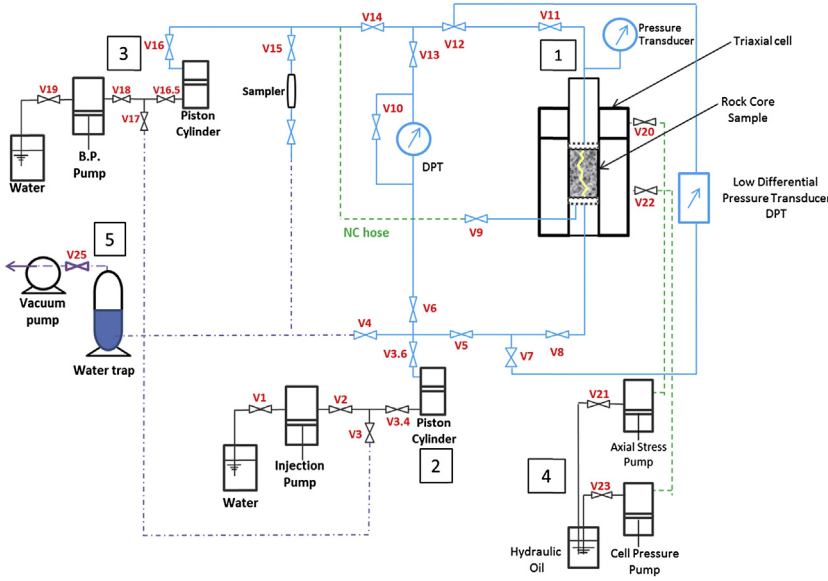

FIGURE 16.4 Schematic diagram of the UNGI coupled triaxial measurement assembly used in the experiments. *Blue lines* (light gray in print version) indicate stainless steel high-pressure lines; *green lines* (light gray dotted lines in print version) are nonconductive high pressure lines; and *purple lines* (dark gray dotted lines in print version) indicate low-pressure lines that are used for vacuuming of the entire assembly. *Modified after Padin, A., 2016. Experimental and Theoretical Study of Water and Solute Transport Mechanisms in Organic-Rich Carbonate Mudrocks (PhD thesis). Colorado School of Mines, Golden, Colorado.*

a high-pressure vessel made of thick stainless steel allowing the simultaneous application of axial stress (simulating the overburden stress) and confining pressure (representing isotropic horizontal stress conditions in the formation). The confining pressure can be increased up to 138 MPa (20,000 psi) using computer-controlled syringe pumps. The entire triaxial test assembly is placed within a polycarbonate insulation cabinet. The temperature in the system is kept constant at 40°C by circulating hot air with 0.01°C accuracy. The temperature is measured by two gauges connected to the heater and the fan controllers that are installed within the insulation cabinet.

During the triaxial measurements, the pressure in the system is increased stepwise until reaching the maximum stress for the formation in situ stress state. At each pressure step, the conductivity of the fracture is calculated assuming that all flow is taking place through the fracture and the flow going through the core matrix is negligible in the low permeability formation used. This assumption has been established using the simultaneous permeability, complex resistivity, geomechanical, ultrasonic compressional and shear wave velocities, and low-frequency Young's modulus measurements in dry and 2% KCl saturated Niobrara core samples (Katsuki and Tutuncu, 2017; Tutuncu

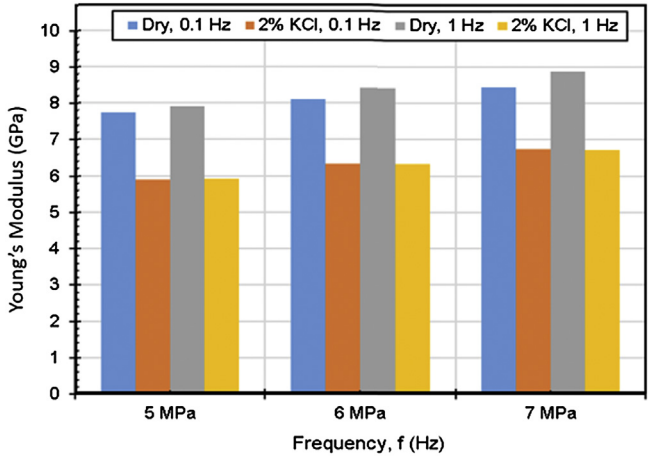

FIGURE 16.5 Effect of the pore fluid introduced on Young's modulus in Niobrara shale core samples. *After Katsuki, D., Tutuncu, A.N., 2017. Coupling complex resistivity, geomechanical and acoustic properties and permeability in sandstone and shale reservoirs, URTEC 2671521. In: Proc. Unconventional Resources Technology Conference, Austin, Texas.*

et al., 1993). Similar results have been observed for the preserved ("as is") core samples from two Eagle Ford wells in oil window and when these samples were saturated with distilled water and 2% KCl solutions (Padin, 2016; Padin et al., 2016; Tutuncu et al., 2016). The low-frequency Young's modulus measurements for intact dry and 2% KCl Niobrara shale samples presented in Fig. 16.5 indicate that Young's modulus decreases by 20%−25% compared with the dry values when samples are saturated with 2% KCl. Moreover, the dry core samples present higher frequency sensitivity than the KCl saturated samples (Katsuki and Tutuncu, 2017).

16.5 PROPPED FRACTURE CONDUCTIVITY TESTS

Darcy's law can be used directly to calculate permeability in the fracture. For this purpose, the flow area (A) is obtained by multiplying the fracture height (h_f) by the fracture width (w_f) (Eq. 16.1). In this case, the fracture height is represented by the diameter of the core sample. Because the fracture width is unknown during the experiment, the conductivity ($k_f w_f$) is calculated using Eq. (16.2), which is obtained by multiplying both sides of Eq. (16.1) by the fracture width.

$$k_f = \frac{q\mu l}{w_f h \Delta p} \tag{16.1}$$

$$k_f w_f = \frac{q\mu l}{h \Delta p} \tag{16.2}$$

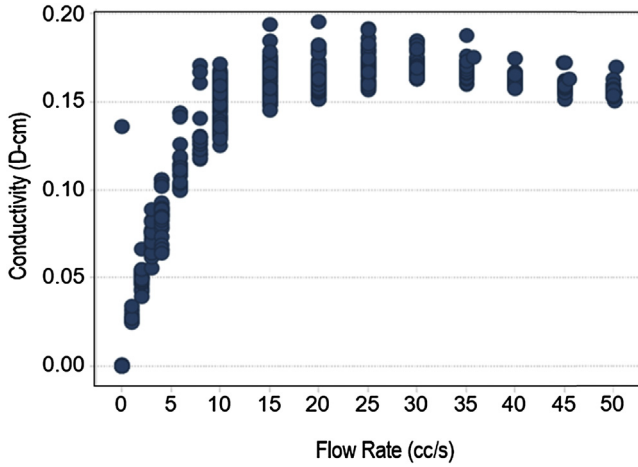

FIGURE 16.6 Apparent fracture permeability determined from Darcy's law and fluid rate in the fracture at the same stress state conditions.

Several conductivity values were obtained at each applied stress condition. The calculated apparent fracture conductivity plotted against the fluid rate is shown in Fig. 16.6. The departure from a straight line shows the presence of non-Darcy flow regime. This nonlinearity is accounted for in Forchheimer's method.

Forchheimer's equation expressed in Eq. (16.3) is used to obtain an absolute value of the conductivity for each measured stress state. The term $\mu v/k$ represents the linear Darcy pressure gradient. The second term represents nonlinear flow component in the equation and is described by the fluid density, the square of interstitial velocity, and β, which is a contrived proportionality constant with the unit of inverse distance m^{-1} (ft^{-1}).

$$\frac{dp}{dl} = \frac{\mu v}{k} + \beta \rho v^2 \tag{16.3}$$

Rewriting the Forchheimer's equation as presented in Eq. (16.4) and further simplifying this relationship by replacing v with q/A lead to Eq. (16.5). It is evident that this is a linear relationship between $1/k_{app}$ and flow rate q.

$$\frac{1}{k_{app}} = \frac{1}{k_d} + \beta \rho v \tag{16.4}$$

$$\frac{1}{k_{app}} = \frac{1}{k_d} + \frac{\beta \rho}{A} q \tag{16.5}$$

When the reciprocal apparent conductivity determined using Eq. (16.5) is plotted against the fluid rate, a linear relationship is obtained as displayed in

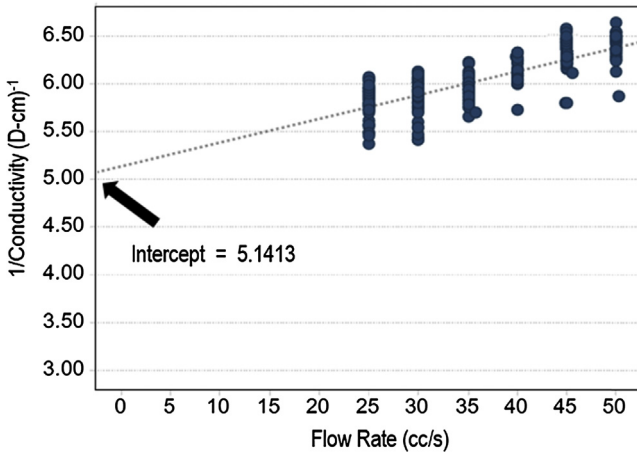

FIGURE 16.7 Determination of the absolute fracture permeability based on Forchheimer's equation.

Fig. 16.7. Then, the absolute conductivity is determined by calculating the inverse of the intercept of the y-axis.

The long-term fracture conductivity results for both Vaca Muerta and Niobrara formations are shown in Fig. 16.8. The error bars indicate the uncertainty in the values related to the flow rate variations during the test and the variation in the fracture length related to the rough surface. The sharpest decline in conductivity is observed at the lower pressure regimes 0.34−10.34 MPa (50−1500 psi), whereas more stable values have been obtained at higher pressure intervals. Although the same behavior is observed for the measurements with both formations, the Vaca Muerta samples have presented steeper conductivity decay. One explanation for this decay is the proppant embedment observed in the samples as shown in Fig. 16.9A. The high clay content present in the rock corresponds to the high embedment observed in the sample. Conversely, Niobrara samples showed little-to-no proppant embedment in the fracture wall (Fig. 16.9B), which is explained to be due to the high strength of the calcite-filled fracture where the proppants are placed.

Simultaneous measurements of compressional and shear wave velocities along with the conductivity and geomechanical properties and geochemical composition changes have also been conducted at the same stress state during the same core flow through experiments. The clay effect on the fracture conductivity is also supported through these observations, yet the details of the velocity and geochemical results of the experiments are subject of other publications in preparation.

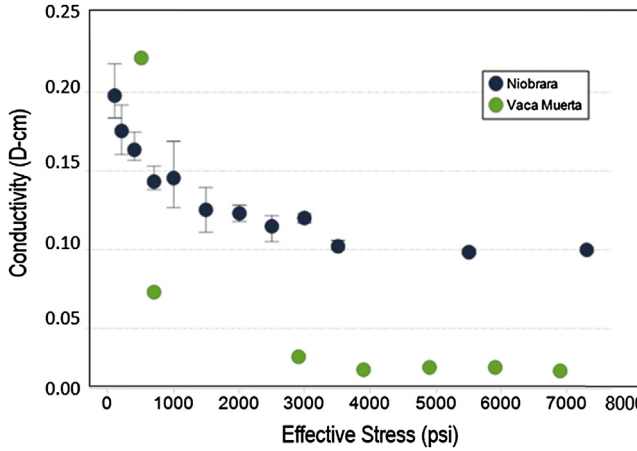

FIGURE 16.8 Effective stress dependence of the proppant-filled fracture conductivity for the Niobrara and Vaca Muerta samples used in the experiments (Iriarte, 2017).

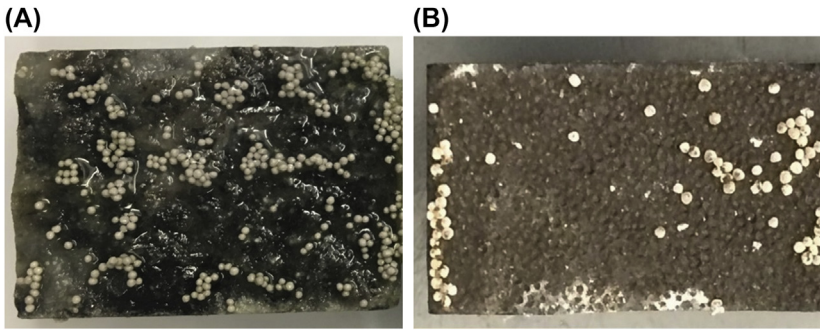

FIGURE 16.9 (A) Niobrara core sample shows little-to-no proppant embedment (Iriarte, 2017) and (B) Vaca Muerta core sample showing the high level of indentation in the rock from proppant embedment (Hegazy, 2017) in the triaxial stress conductivity experiments conducted in the research study.

16.6 CONCLUSIONS

The stress-dependent, long-term fracture conductivity shows the sharpest decline in the early stages of the experiment. A comparison with the conductivity measurements performed on the Vaca Muerta samples shows a similar behavior yet a steeper initial decay than that observed in the Niobrara samples. The difference observed between the two samples is related to the mineralogy of the formation and the high proppant embedment observed in the Vaca Muerta samples. The lack of proppant embedment in the Niobrara samples is attributed to the high strength of the calcite-filled fracture where the

proppant is placed. This illustrates how conductivity damage effects vary not only with mineralogy of the rock, but also with the mineral distribution and where the fracture is located within the formation.

ACKNOWLEDGMENTS

This research was financially supported by the Unconventional Natural Gas and Oil Institute (UNGI) at the Colorado School of Mines. Special thanks to Dr. Ali I. Mese for donating the triaxial cell to our geomechanics laboratory and CoorsTek for donating the proppants used in the tests.

REFERENCES

API RP 61, 1989. Recommended Practice for Evaluating Short-Term Proppant-Pack Conductivity. API, Washington, DC.

API RP19D, 2008. Recommended Practice for Measuring the Long-Term Conductivity of Proppants (ISO 13503−13505:2006, Identical) (Includes July 2008 Errata), first ed. API, Washington, DC.

Aguirre-Uretta, M., Price, G., Ruffel, A., 2008. Southern hemisphere early cretaceous (Valanginian-Early Barremian) carbon and oxygen isotope curves from the Neuquén Basin, Argentina. Cretaceous Research 29 (1), 87−99. https://doi.org/10.1016/j.cretres.2007.04.002.

Baree, R., Cox, S., Baree, V., Conway, M., 2003. Realistic assessment of proppant pack conductivity for material selection. Paper SPE 84306. In: Proc. SPE Annual Technical Conference and Exhibition. Colorado, Denver. https://doi.org/10.2118/84306.

ElGhonimy, R.S., 2015. Petrophysics, Geochemistry, Mineralogy, and Storage Capacity of the Niobrara Formation in the Aristocrat PC H11-07 Core, Wattenberg Field, Denver Basin, Colorado (M.S. thesis). Colorado School of Mines, Golden, Colorado.

Finn, T.M., Johnson, R.C., 2005. Niobrara total petroleum system in the Southwestern Wyoming province. In: Petroleum Systems and Geologic Assessment of Oil and Gas in the Southwestern Wyoming Province, Wyoming, Colorado, and Utah. U.S. Geological Survey Digital Data Series DDS-69-D.

Hegazy, D.A., 2017. An Experimental Study to Investigate the Effects of In Situ Stress State and Rock-Fluid Interactions on Propped Fracture Conductivity in the Vaca Muerta Formation (M.S. thesis). Colorado School of Mines, Golden, Colorado.

Howell, J., Schwar, E., Spalletti, L., 2005. The Neuquén Basin: an overview. In the Neuquén Basin, Argentina: a case study in sequence stratigraphy and basin dynamics. Geological Society, London, Special Publications 252 (1), 1−14. https://doi.org/10.1144/gsl.sp.2005.252.01.01.

Iriarte, J.G., 2017. Fluid-Shale-Proppant Interactions and the Degradation of Hydraulic Fracture Conductivity in the Niobrara Formation (M.S. thesis). Colorado School of Mines, Golden, Colorado.

Katsuki, D., Tutuncu, A.N., 2017. Coupling Complex resistivity, geomechanical and acoustic properties and permeability in sandstone and shale reservoirs, URTEC 2671521. In: Proc. Unconventional Resources Technology Conference, Austin, Texas.

Kugler, R.L., 1985. Source rock characteristics, Los Molles and Vaca Muerta shales, Neuquén Basin, west-central. AAPG Bulletin 69. https://doi.org/10.1306/ad4620ce-16f7-11d7-865000102c1865d.

Manceda, R., Figueroa, D., 1995. Inversion of the Mesozoic Neuquén Rift in the Malargue fold and thrust Belt, Mendoza, Argentina. Journal of Structural Geology, Memoir 62 (7), 369–382. https://doi.org/10.1016/j.jsg.2008.03.007.

Matthews, V., 2011. Colorado's new oil boom – the Niobrara. CGS RockTalk 13 (1).

Padin, A., 2016. Experimental and Theoretical Study of Water and Solute Transport Mechanisms in Organic-Rich Carbonate Mudrocks (Ph.D. thesis). Colorado School of Mines, Golden, Colorado.

Padin, A.D., Torcuk, M.A., Katsuki, D., Tutuncu, A.N., Kazemi, H., 2016. Experimental and theoretical study of water-solute transport in organic-rich carbonate mudrocks, SPE 181585. In: Proc. SPE Annual Technical Conference, Dubai, UAE.

Sonnenberg, S.A., 2012. The Niobrara petroleum system, a major tight resource play rocky mountain region. AAPG Search and Discovery 10355, 32.

Terracina, J., Turner, J., Collins, D., Spillars, S., 2010. Proppant selection and its effect on the results of fracturing treatments performed in shale formations. Paper SPE 135502. In: Proc. SPE Annual Technical Conference and Exhibition. https://doi.org/10.2118/135502-MS. http://www.searchanddiscovery.com/pdfz/documents/2012/80206sonnenberg/ndxsonnenberg.pdf.html.

Tutuncu, A.N., Podio, A.L., Sharma, M.M., 1993. Effect of macrofractures on acoustic properties of rocks. In: SEG Annual Meeting, Washington, DC, USA, pp. 26–30. September, SEG-1993-0765. https://doi.org/10.1190/1.1822611.

Tutuncu, A.N., Katsuki, D., Padin, A., Bui, B., McDowell, B., 2016. Coupling geomechanics and petrophysical measurements for production enhancement in organic-rich shales. SPE 2461986. In: Proc. Unconventional Resources Technology Conference, San Antonio, Texas.

Wren, E., 2011. The prospectively of unconventional oil and gas resources in the Vaca Muerta shale of the Neuquén Basin of Argentina. In: Presented at the World Shale Gas Conference and Exhibition, 7–11 November. SPE-179145-MS. https://doi.org/10.2118/179145-MS.

Index

'*Note*: Page numbers followed by "f" indicate figures, "t" indicate tables.'

D

E

F

G

H

I

J

K

L

M

N

O

P

T

U

V

W

X

Y

Z

Hydraulic Fracture Modeling

Yu-Shu Wu, Editor

Natural and hydraulic fractures are common in oil and gas reservoir formations, and with the ongoing increase in development of unconventional reservoirs, more petroleum engineers today need to know the latest technology surrounding hydraulic fracturing technology such as fracture rock modeling. There is tremendous research in the area but not all located in one place. *Hydraulic Fracture Modeling* delivers all the pertinent technology and solutions in one product to become the go-to source for petroleum, well stimulation, and reservoir engineers. Providing tools and quantitative approaches, this multi-contributed reference presents current and upcoming developments for modeling rock fracturing including their limitations as well as problem-solving applications. Covering two types of modeling technologies, various effective fracturing approaches, and model applications for fracturing, *Hydraulic Fracture Modeling* equips today's petroleum engineer with an all-inclusive product to characterize hydraulic fractures and optimize today's more complex reservoirs.

Key Features

- Understand details surrounding fracturing and fracture modeling technology including theories and quantitative methods
- Gain academic and practical perspective from multiple contributors that are at the forefront of hydraulic fracturing and rock mechanics
- Provides today's petroleum engineer with model validation tools backed by real-world case studies

About the Editor

Yu-Shu Wu is currently a Professor and the Reservoir Modeling Chair for the Department of Petroleum Engineering at the Colorado School of Mines in Golden, Colorado, USA. Yu-Shu earned a BS in petroleum engineering from Daqing Petroleum Institute, a MS in petroleum engineering from Southwest Petroleum Institute (China), and a MS and PhD both in reservoir engineering from University of California at Berkeley.

Related Titles

Belyadi, Fathi, and Belyadi, *Hydraulic Fracturing in Unconventional Shale Reservoirs: Theories, Practice, and Operations*, 978-0-12-849871-2
Yew and Weng, *Mechanics of Hydraulic Fracturing, 2nd Ed*, 978-0-12-420003-6
Tiab and Donaldson, *Petrophysics, 4th Ed*, 978-0-12-803188-9

Technology and Engineering/Petroleum

ISBN 978-0-12-812998-2

ELSEVIER

Gulf Professional Publishing
An imprint of Elsevier
elsevier.com/books-and-journals